frontiers | Research Topics

Advances in high-power lasers for interdisciplinary applications

Edited by
Shuo Liu, Tonglei Cheng, Zhenxu Bai, Bofeng Zhu,
Yi Bao and Pingxue Li

Published in
Frontiers in Physics

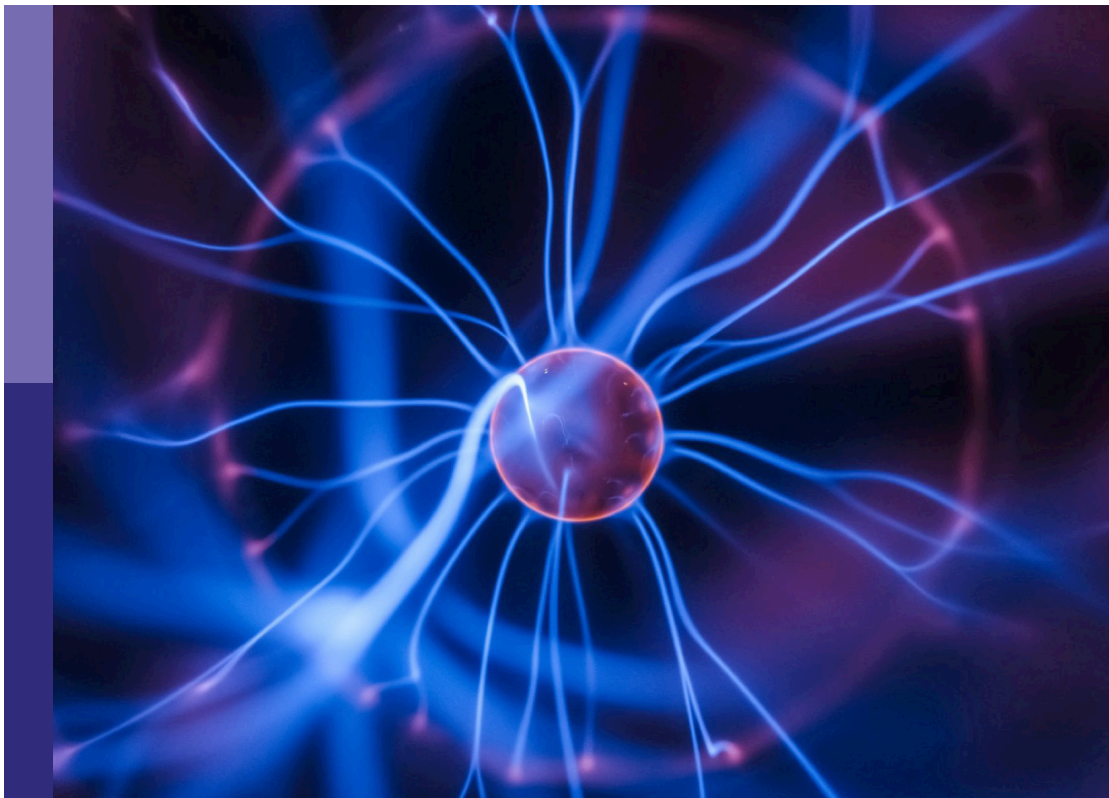

ISSN 1664-8714
ISBN 978-2-8325-4092-3
DOI 10.3389/978-2-8325-4092-3

About Frontiers

Frontiers is more than just an open access publisher of scholarly articles: it is a pioneering approach to the world of academia, radically improving the way scholarly research is managed. The grand vision of Frontiers is a world where all people have an equal opportunity to seek, share and generate knowledge. Frontiers provides immediate and permanent online open access to all its publications, but this alone is not enough to realize our grand goals.

Frontiers journal series

The Frontiers journal series is a multi-tier and interdisciplinary set of open-access, online journals, promising a paradigm shift from the current review, selection and dissemination processes in academic publishing. All Frontiers journals are driven by researchers for researchers; therefore, they constitute a service to the scholarly community. At the same time, the *Frontiers journal series* operates on a revolutionary invention, the tiered publishing system, initially addressing specific communities of scholars, and gradually climbing up to broader public understanding, thus serving the interests of the lay society, too.

Dedication to quality

Each Frontiers article is a landmark of the highest quality, thanks to genuinely collaborative interactions between authors and review editors, who include some of the world's best academicians. Research must be certified by peers before entering a stream of knowledge that may eventually reach the public - and shape society; therefore, Frontiers only applies the most rigorous and unbiased reviews. Frontiers revolutionizes research publishing by freely delivering the most outstanding research, evaluated with no bias from both the academic and social point of view. By applying the most advanced information technologies, Frontiers is catapulting scholarly publishing into a new generation.

What are Frontiers Research Topics?

Frontiers Research Topics are very popular trademarks of the *Frontiers journals series*: they are collections of at least ten articles, all centered on a particular subject. With their unique mix of varied contributions from Original Research to Review Articles, Frontiers Research Topics unify the most influential researchers, the latest key findings and historical advances in a hot research area.

Find out more on how to host your own Frontiers Research Topic or contribute to one as an author by contacting the Frontiers editorial office: frontiersin.org/about/contact

Advances in high-power lasers for interdisciplinary applications

Topic editors

Shuo Liu — Hebei University of Technology, China
Tonglei Cheng — Northeastern University, China
Zhenxu Bai — Hebei University of Technology, China
Bofeng Zhu — Nanyang Technological University, Singapore
Yi Bao — Stevens Institute of Technology, United States
Pingxue Li — Beijing University of Technology, China

Citation

Liu, S., Cheng, T., Bai, Z., Zhu, B., Bao, Y., Li, P., eds. (2023). *Advances in high-power lasers for interdisciplinary applications*. Lausanne: Frontiers Media SA.
doi: 10.3389/978-2-8325-4092-3

Table of contents

frontiers | Frontiers in Physics

TYPE Mini Review
PUBLISHED 20 December 2022
DOI 10.3389/fphy.2022.1102996

OPEN ACCESS

EDITED BY
Tonglei Cheng,
Northeastern University, China

REVIEWED BY
Lee Xiaobao,
Hunan University of Technology, China
Xuebin Sun,
Tianjin University, China
Yang Qu,
Nanjing Vocational College of Information Technology, China

*CORRESPONDENCE
Yajun Pang,
yjpang@hebut.edu.cn

SPECIALTY SECTION
This article was submitted to Optics and Photonics, a section of the journal
Frontiers in Physics

RECEIVED 19 November 2022
ACCEPTED 05 December 2022
PUBLISHED 20 December 2022

CITATION
Pang Y, Zhang K and Lang L (2022), Review of acousto-optic spectral systems and applications.
Front. Phys. 10:1102996.
doi: 10.3389/fphy.2022.1102996

Review of acousto-optic spectral systems and applications

Yajun Pang[1,2]*, Kai Zhang[1,2] and Liying Lang[1,2]

[1]Center for Advanced Laser Technology, Hebei University of Technology, Tianjin, China, [2]Hebei Key Laboratory of Advanced Laser Technology and Equipment, Tianjin, China

Acousto-optic devices represented by acousto-optic tunable filters (AOTFs), have the advantages of wide wavelength range from the ultraviolet to the long-wave infrared and fast wavelength switching speed. Nowadays, acousto-optic spectral systems have become very important scientific instruments in laboratory. There are many factors to be considered when we choose different solutions for acousto-optic spectral systems, but there is no comprehensive analysis and summary of them. This paper explains the working principle of the acousto-optic devices and summarizes the most common optical schemes for acousto-optic spectral systems. We also analyzed their characteristics of application conditions. In addition, specific applications of acousto-optic spectral systems in some common fields are presented.

KEYWORDS

spectral devices, imaging spectrometer, acousto-optic tunable filter (AOTF), optical schemes, acousto-optic effect

1 Introduction

The study of acousto-optic interactions began in the 1920s and was limited to isotropic media such as water and glass [1, 2]. When ultrasonic waves pass through the medium, the refractive index of the medium changes periodically by the modulation of the strain. The acousto-optic medium is equivalent to a dislocation grating, and diffraction occurs when light passes through it. With the emergence of lasers and high-performance acousto-optic crystals, the study of acousto-optic devices has broadened from isotropic to anisotropic media and from normal to anomalous interactions [3–5]. As the research of acousto-optic theory continues to progress, the principles of isotropic and anisotropic acousto-optic interactions need to be unified. We can consider the acousto-optic effect as a parametric interaction process, which is described by the relationship between the non-linear polarization vector and the strain [6–8].

The first AOTF was proposed by Harris and Wallace utilizing the collinear acousto-optic interaction [9]. In 1974, I. C. Chang proposed the idea of a non-collinear acousto-optic tunable filter design, which laid a solid foundation for the development of acousto-optic devices [10]. When an excitation RF signal of a certain frequency is applied to the transducer, the piezoelectric crystal transducer converts it into an ultrasonic signal of the corresponding frequency and couples it into the birefringent crystal. The refractive index of the crystal then changes periodically, which is equivalent to the formation of a bit-phase grating in the crystal, and the grating constant is the wavelength of ultrasonic waves

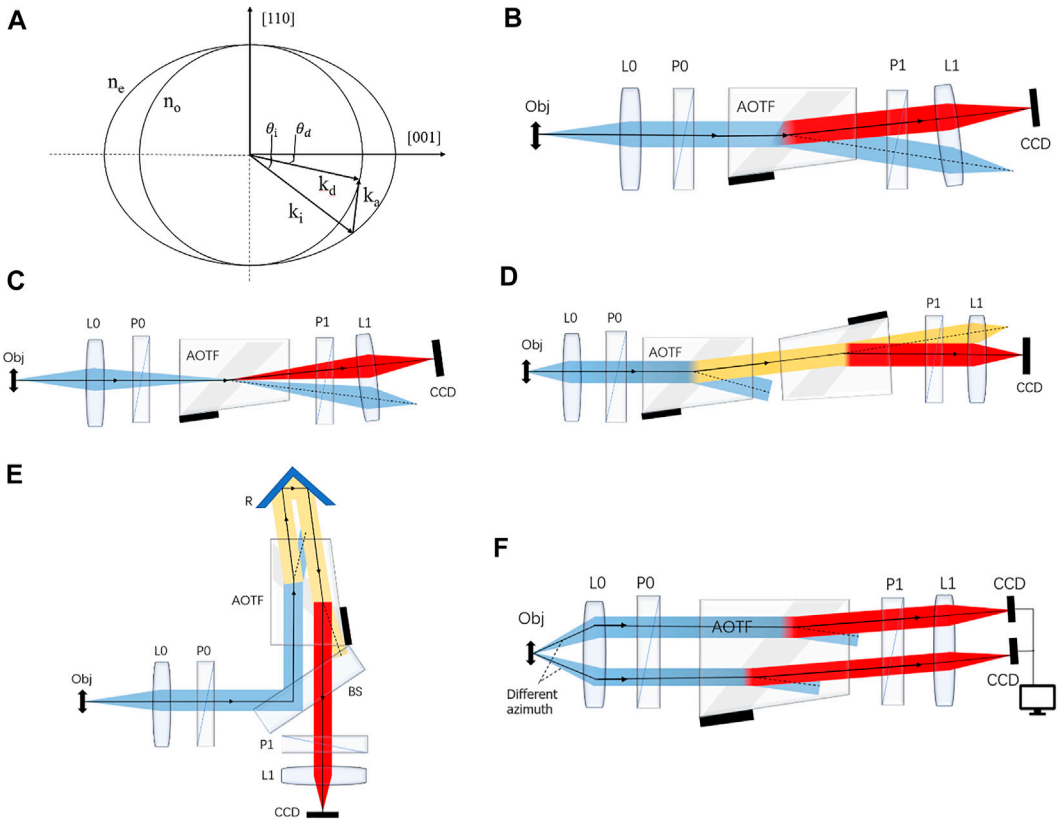

FIGURE 1
(A) Non-collinear acousto-optic interaction wave vector diagram in TeO_2, **(B)** collimating scheme, **(C)** confocal scheme, **(D)** tandem scheme, **(E)** double-pass single-crystal AOTF based spectral scheme, **(F)** double-path scheme (Obj, object; L, lens; P, polarizer; R, retroreflector; BS, beam splitter; CCD, charge-coupled device).

[11–14]. The acousto-optic interaction wave vector diagram, which takes place in AOTF, is shown in Figure 1A. The incident light wave vector $\mathbf{k_i}$, diffracted light wave vector $\mathbf{k_d}$, and the acoustic wave vector $\mathbf{k_a}$ are strictly matched to the momentum triangle closure condition:

$$\overrightarrow{k_d} = \overrightarrow{k_a} \pm \overrightarrow{k_i} \tag{1}$$

$$k_i = \frac{2\pi n_i}{\lambda}, k_d = \frac{2\pi n_d}{\lambda}, k_a = \frac{2\pi f_a}{v_a} \tag{2}$$

Where n_i is the refractive index of the crystal to the incident light, and n_d is the refractive index of the crystal to the diffracted light. The incident angle θ_i and diffraction angle θ_d are shown in Figure 1A. λ is the optical wavelength in vacuum, f_a is the acoustic frequency, and v_a is the speed of the ultrasonic wave.

In the case of collinear acousto-optic interaction, the incident light wave vector, the diffracted light wave vector and the ultrasonic wave vector are in the same direction. The momentum matching triangle at this point is simplified to a straight line. The geometric relationship between the vectors can be turned into an algebraic sum. Bringing Eq. 2 into Eq. 1, the tuning equation of the common-linear acousto-optic tunable filter can be obtained as

$$\lambda f_a = \pm v_a (n_d - n_i) \tag{3}$$

In the non-collinear case, the diffracted light and the incident light propagate in different intrinsic modes in the crystal, and the incident light wave vector and the diffracted light wave vector are not parallel. The incident light wave vector, the ultrasonic wave vector and the diffracted light wave vector are in a vector triangle relationship (i.e., momentum matching condition). Usually, in the design of AOTF, the tangents of the incident and diffracted light wavevectors are parallel to each other at the corresponding wavevector surface in order to have a large incident angle aperture. In this case, the design parameters are related as follows

$$n_i = \left[\frac{\cos^2\theta_i}{n_o^2} + \frac{\sin^2\theta_i}{n_e^2}\right]^{-1/2} \tag{4}$$

$$n_d = n_o \tag{5}$$

n_o and n_e are the refractive indices of ordinary ray and extraordinary ray which are perpendicular to the optical axis,

and they are a function of the wavelength of light. According to the tangential parallelism condition, the relationship between the diffracted light polar angle and the incident light polar angle is

$$\tan\theta_d = \left(n_o/n_e\right)^2 \tag{6}$$

The tuning relationship between optical wavelength and ultrasonic frequency can be expressed by

$$f_a = \frac{v_a}{\lambda}\left(n_i^2 + n_d^2 - 2n_i n_d \cos\left(\theta_i - \theta_d\right)\right)^{\frac{1}{2}} \tag{7}$$

Combining Eqs 1–3, we can simplify Eq. 4 to

$$f_a = \frac{v_a}{\lambda}\left(n_i - n_d\right)\left(\sin^2 2\theta_i + \sin^4\theta_i\right)^{\frac{1}{2}} \tag{8}$$

Exceptionally, when $\theta_i = 90°$, the equation reduces to the tuning relationship for the common-linear interaction. Therefore, the collinear interaction can be viewed as a special case of non-collinear interaction. The non-collinear AOTF keeps the tangents of the incident light and the diffracted light on the wave vector trajectory parallel to each other, so that when there is a small change for the incident angle, the momentum matching condition still holds.

There are many applications based on acousto-optic action, such as acousto-optic modulators, deflectors, frequency shifters, and tunable filters. The AOTFs are becoming a widely used tool for these applications. Spectral imagers based on AOTF have a wide range of applications in science and engineering [15–17]. Although there have been many reports on the generation and application of AOTF acousto-optic spectral instruments, there is no comprehensive summary of the characteristics of different schemes. In this paper, we summarize in detail the commonly used optical schemes for AOTF-based acousto-optic spectral systems and compare them with examples, and finally present specific applications in major representative fields.

2 Acousto-optic spectral system schemes

AOTFs have a variety of applications, and researchers have used a variety of different optical solutions for purposes [18, 19]. Different schemes differ in image quality, the number of coupling components, size, and alignment complexity [20–22]. To properly select the optical system for an AOTF-based spectral system, many factors must be considered [23–25]. Although various acousto-optic filtering schemes have been tested and discussed in various articles, a summary of them is not available so far. In this section, the four most common optical schemes based on the AOTF module as shown in Figure 1 are presented: collimating scheme, confocal scheme, tandem scheme, and double-path scheme. We will compare and analyze their main features with some examples. Although these schemes are derived from both collimation and confocal schemes, this division makes them easier to be summarized as well as to be understood.

2.1 Collimating scheme

For conventional acousto-optic spectral systems, the collimating scheme is the most common and structurally simple scheme, and the optical path diagram is shown in Figure 1B. The adopted scheme is to filter the light directly using a single AOTF, which is also the basis of other schemes [26, 27]. The light entering the optical system from the object under test is collimated by L0, the mutually parallel light is filtered by the AOTF, and then be focused on the CCD by the focusing lens L1. Non-uniformity of the central wavelength of the filtered light across the field of view can lead to specific image spectral distortions [28].

The conventional acousto-optic spectral system can satisfy the needs of many tasks. But, the optimization of this system is necessary, and the integration of the optimized AOTF units into other schemes can multiply the efficiency. In 2021, proposed a method for optimizing the size of piezoelectric transducers of quasi-collinear AOTF [29]. In this scheme, they used an AOTF with a large interaction length. From the experimental results, it is shown that the variation of the transducer size can minimize the RF power consumption of the AOTF. Comparing the optimized transducer dimensions with those commonly used ones in quasi-collinear AOTF, the optimized AOTF energy efficiency can be improved about twice.

2.2 Confocal scheme

Confocal optics can compensate for almost any degree of AOTF diffraction aberration. Unlike wedge compensation, this optical system does not require dispersion and can be used with any type of AOTF [30–32]. The confocal optics scheme is shown in Figure 1C. The use of telecentric confocal optics can eliminate errors caused by inaccurate focus. In addition, the system has the advantage of uniform image field with the same resolution and diffraction efficiency over the scene [33, 34]. However, the focal length of the lens in the system must be shot enough to prevent diffraction from limiting resolution.

In 2019, combined AOTF with a rigid borescope, a flexible fiberscope, and a video endoscope, and designed an acousto-optic spectral imaging endoscopic analysis system for observing cancerous tissue [35]. This scheme uses a confocal optical design that can provide high-quality spectral images. This solution can be very effective in solving different specific tasks in biomedical and industrial fields. The main aberration in the confocal scheme is from the presence of longitudinal color focus shift and lateral chromatic image drift. However, this color difference can be almost completely compensated by adjusting

the tilt of the output side of the acousto-optic unit to the input side. While, in the collimating scheme, the main aberration is the transverse chromatic aberration, which can be eliminated by choosing a different tilt angle [36, 37].

Collimating and confocal optical schemes both have their own advantages and disadvantages, the confocal scheme is not the optimization of the collimated scheme. In 2021, a super-angular aperture scheme was proposed by [38]. They used both schemes to quantify the change in radiation flux caused by the super-angular aperture scheme and the response of the AOTF element at tilted incidence. They analyzed the system response of the collimated and confocal optical schemes and verified the simulation results. The collimated optical path was found to be more suitable for the super-angular aperture scheme by comparing the two optical schemes. This is because its spectral bandwidth is better than that of the confocal optical scheme, and the central wavelength shift can be corrected by calibration.

2.3 Tandem scheme

The most common and straightforward application of the double filter structure is to connect two AOTFs in series. In 2018, Lei Shi et al. designed a series of double filtering schemes [39]. They compared the spectral widths at different frequencies by analyzing the experimental data. It was finally found that the double-filter structure reduced the spectral width by an average of 37% and improved the spectral resolution by an average of 57% compared to the single filter. By analyzing and comparing the theoretical calculations and experimental measurements of the properties of single and double filter structures, we can find that the spectral width of the double filter structure is smaller than that of the single filter structure for equal central wavelengths. This situation illustrates the superiority of the double-filter technique in improving the spectral width and in increasing the spectral resolution [40].

In 2019, Vitoid E. Pozhar et al. designed a system architecture to address the problem of creating hyperspectral optoelectronic systems for unmanned aerial vehicles [41]. The developed hyperspectrometer uses a dual compact AO monochromator as a spectral element. It consists of two identical AO cells, deployed by 180°, which provides compensation for most spatial spectral aberrations. The device's small size, low power consumption, and ability to obtain both spectral and color images with high spectral (~5 nm) and spatial (600–500 elements) resolution over a sufficiently wide wavelength range (450–850) nm make it possible to use it effectively on unmanned aerial vehicles. In fact, back in 2005, Pozhar and other researchers proposed a double-AOTF spectral imaging system for microscopic analysis in the visible and near-infrared range, and it was shown that double AOTF monochromator ensures improved image quality than single imaging AOTF [42].

Tandem AOTF is only one way to realize double filtering, in addition, there are different ways such as the single-crystal double filtering technique. The optical scheme design diagram is shown in Figure 1D. Double filtering is realized using a single crystal, but structurally it is similar to double filtering using two AOTFs. It is simpler and more economical to realize double filtering using a single crystal. Therefore, the scheme of the series connection is less used in practical applications, and nowadays, the single crystal double filtering technique is more often used.

In 2019, Xiaofa Zhang et al. designed a single-crystal double filtering hyperspectral microscopic imaging system [43]. By analyzing the experimental results of diffracted light spectrograms of single-crystal double-filtering scheme, we can find that the comparison yielded a double-filter structure with an average 32% reduction in spectral width compared to single-filtering at a fixed ultrasound frequency of 120 MHz. In the visible range, the spectral resolution can be improved by 37.08%–59.95%. In addition, in 2021, Vladislav Batshev et al. similarly devised a method to improve the spectral resolution of a single AOTF by using a single-crystal for secondary filtering [44]. The structure is similar to Figure 1E. From the results, the transmission spectral width at the 0.5 level (FWHM) is about 1.3 times smaller than that of the classical single-pass scheme.

Among the three schemes mentioned above, the series double-filtering system designed by Shi Lei et al. works best from the results. But unfortunately, the specific series filtering method does not appear in the article. The double-filtering technique can effectively improve the spectral resolution of the acousto-optic filters. In addition, the primary filtered signal after the AOTF is accompanied by an obvious side flap phenomenon, which comes from the acousto-optic interaction [45–48]. There is no way to eliminate the side flaps by using the primary filtering technique. After double-pass filtering, the side flaps are suppressed very significantly, which can improve the spectral purity of the diffracted light [49].

2.4 Double-path scheme

For double-path acousto-optic spectroscopy systems or multi-path analysis systems, they are often used in special scenarios to meet specific requirements [50, 51].

Khoptyar et al. published two articles back and forth in 2012 and 2013 on the use of double-path optical schemes to fabricate novel photon time-of-flight spectrometers for the analysis of turbid media [52, 53]. The wide spectral range of the instrument helps to characterize the structure of the sample and to obtain excellent accuracy in the measurement of absorption and scattering coefficients. Photon time-of-flight spectrometers are used for the evaluation of pharmaceutical chemical composition analysis with proven results. Therefore,

TABLE 1 Comparison of acousto-optic spectral analysis system schemes.

Type	Advantages	Disadvantages	Spectral range/nm	Angular aperture/°	Spectral band/nm	Ref
Collimating scheme	1. The structure is simple and easy to build	1. Non-uniformity of the central wavelength of the filtered light across the field of view can lead to specific image spectral distortions	700–1,150	0.04	0.3@633	[27]
	2. It is stable and can be used as a component in various systems	2. The scheme has transverse chromatic aberration				
Confocal scheme	1. The structure is simple and easy to build	1. The presence of longitudinal color focus shift and lateral chromatic image drift produce aberration	450–750	—	4.5@632	[33]
	2. Compensate for almost any degree of AOTF diffraction aberration					
Tandem scheme	1. It can reduce the spectrum width and improve the spectral resolution	1. Diffraction efficiency will be reduced	400–1,000	2.83	2.9@632.5	[37]
	2. The scheme can effectively lower the side flaps		400–1,000	3	3.44@651.62	[39]
			450–850	4	3@600	[40]
Double-path scheme	1. The structure can obtain more complete and richer spectral information	1. Specific solutions in different applications need to be designed	450–850	—	~3@625	[50]
	2. The design of the structures in different practical applications will be flexible					

10.3389/fphy.2022.1102996

double-path optical systems and triple-path spectral systems tend to demand high precision as well as wide spectrum.

In 2019, Ramy Abdlaty and Qiyin Fang both designed an AOTF-based hyperspectral imaging system [54]. Object illumination is provided from both sides to provide uniformly distributed illumination and to avoid shadowing problems. The light reflected from the object is captured by the zoom lens and beam shaping optics. Polarization beam splitter (PBS) splits the collimated beam into two orthogonally polarized beams of transmitted and reflected light. The polarization of the PBS reflected beam is rotated using a half-wave plate to match the PBS transmitted beam. The two PBS beams have the same polarization matched to the AOTF crystal, and this polarization matching allows them to come to the maximum diffraction efficiency.

In 2020, Alexander Machikhin et al. proposed a new concept of spectral stereo imaging [55]. The stereo imaging optical system is shown in Figure 1F. This stereo imaging system is based on simultaneous wide-aperture acousto-optic diffraction of two beams through a conventional AOTF. Experimental results have shown that the quality of the spectral images is quite high, which is necessary for the stereo reconstruction process. In 2021, A. A. Naumov proposed an optical stereo system [56], and this system is very similar to the structure of Figure 1E. The characteristics of such optical systems depend to a large extent on three parameters: the focal length of the incident lens, the focal length of the matrix sensor lens, and the diameter of the incident optical pupil of the acousto-optic filter. The variability of these parameters allows the optical system to be adapted to different tasks [57].

The photon time-of-flight spectrometer utilizes an AOTF module with only partial overlap of the two spectral bands, and the results of the two spectral bands are stitched together to obtain broad-spectrum information. In contrast, in the hyperspectral imaging system, the information of both line polarized beams is processed and retained to obtain the complete spectrum. The two cases of stereo imaging have the same principle, both of which collect the spectral information observed in different orientations and then reorganize them. From the previous analysis, it can be known that both double-path acousto-optic spectral analysis systems aim to obtain more complete spectral information, only the way and results are different. The double-path scheme allows for a wider spectral range than other optical schemes as well as a more complete spectral information from different angles of the same object. At the same time, the flexible placement of the device may also bring more possibilities for spectral system detection. The double pathway acousto-optic spectroscopy system has been used in practical devices for stereoscopic imaging, drug characterization, and multi-directional evaluation after continuous experimentation and is still being improved.

Each scheme have different features and resolutions, the comparison is shown in Table 1.

3 Applications

Acousto-optic devices are used more frequently in representative fields such as medical and healthcare, aerospace, and food safety. Due to the small mass, small size, absence of removable elements, and compact construction of the AOTF, acousto-optic filters are ideally suited for use with devices used to view hard-to-reach objects, such as rigid lenses and flexible fiberoptic endoscopes [58–61]. The application of acousto-endoscopic imaging spectroscopy will significantly reduce the cost of laboratory testing and increase the information density of research [62–64]. In addition, the development of space instruments based on AOTFs has enhanced the detection capabilities of various space probes. In 2019, He et al. summarized the acousto-optic spectrometers used by China in recent years for lunar exploration [65]. The study include the infrared imaging spectrometer on Chang'e 3 and Chang'e 4 lunar rovers, and the lunar mineral spectrometry analyzer on the Chang'e 5 and Chang'e 6 lunar landers. Acousto-optic devices are becoming widely used in planetary observation, laser observation, surface positioning, and remote sensing [66–69].

Acousto-optic hyperspectral imaging detection technology has also been applied to the detection of microorganisms. In 2018, Y. Seo et al. used acousto-optic spectral image processing techniques for extracting information related to morphological characteristics of 15 different foodborne bacterial species and serotypes [70]. This study achieved a cost-effective classification of foodborne bacteria. In addition, acousto-optic spectroscopy detection systems are also used to test meat, grains and even liquid foods [71–77]. For example, in 2021, I. Baek et al. proposed a short-wave infrared hyperspectral imaging system for the detection of total volatile basic nitrogen content in fresh pork. This system can be used for rapid non-destructive assessment of pork freshness and can be an effective alternative to traditional methods for assessing pork freshness [78].

In addition, acousto-optic spectroscopy systems are also widely used in agriculture, forestry, pharmaceutical analysis, and environmental monitoring [79]. Hong Liu et al. designed a drone-based hyperspectral imaging remote sensing system in 2021 [80], which can be used for activities such as water surface remote sensing, imaging, and spectral analysis. In agriculture, a commercial AOTF-based near-infrared spectrometer is already available for the non-destructive detection of agricultural products such as dried apples and olive fruit [81]. Acousto-optic spectroscopy systems are becoming more and more relevant to our lives.

With the development of various new technologies, the miniaturization and intelligence of spectrometers equipped with acousto-optic spectral analysis systems are becoming more obvious. Like the applications of acousto-optic spectral analysis instruments in various fields described

above, acousto-optic devices are now used in a large number of fields. The application of acousto-optic spectral systems is likely to be associated with the development of new materials and new energy sources in the future. Not only for the test of new materials, but also for improving the performance of acousto-optic spectral systems in combination with new materials. The acousto-optic spectral analysis systems are expected to get more long-term development.

4 Conclusion

This article focuses on review of the basic construction of four different optical schemes based on AOTF. Due to the simplicity of the acousto-optic spectral systems, these four optical schemes can be easily embedded in different application scenarios. We summarize the advantages and disadvantages of the different schemes by analyzing the characteristics of the four optical schemes. At the same time, we compare the different schemes with each other and provide theoretical references for the application in different scenarios. Acousto-optic spectral systems have great potential for development in various fields, but in order to adapt to different application scenarios, the requirements for each parameter of the acousto-optic device become higher. The relevant summary and the analysis of characteristics described are expected to provide references for further applications of acousto-optic spectral technology.

Author contributions

YP: Investigation, writing—original draft, writing—review and editing, supervision. KZ: Investigation, writing—original draft. LL: Investigation, writing—review and editing.

Funding

This work was supported by the National Natural Science Foundation of China (61905063), Natural Science Foundation of Hebei Province (F2020202055).

Conflict of interest

The authors declare that the research was conducted in the absence of any commercial or financial relationships that could be construed as a potential conflict of interest.

Publisher's note

References

1. Chang I. Acousto-optic tunable filters. *Opt Eng* (1981) 20(6):206824. doi:10.1117/12.7972821

2. Brillouin L. Diffusion de la lumière et des rayons X par un corps transparent homogène. *Ann Phys* (1922) 17(2):88–122. doi:10.1051/anphys/192209170088

3. Cheong Y., Popa B-I. Acousto-optical metasurfaces for high-resolution acoustic imaging systems. *Phys Rev B* (2021) 104(14):L140304. doi:10.1103/physrevb.104.l140304

4. Goutzoulis AP. *Design and fabrication of acousto-optic devices*. Boca Raton: CRC Press (2021).

5. V Pozhar A Machikhin, editors. Acousto-optical imaging spectroscopy. In: 2021 Wave Electronics and its Application in Information and Telecommunication Systems (WECONF). IEEE (2021).

6. S Mantsevich, V Balakshy, Y Kuznetsov, editors. Acousto-optic spectrum analyzer-the new type of optoelectronic device. In: International Conference on Photonics, Optics and Laser Technology, Porto, February 27–March 1, 2017 (Porto: SCITEPRESS) (2017).

7. Balakshy VI. Acousto-optic visualization of optical wavefronts [Invited]. *Appl Opt* (2018) 57(10):C56–C63. doi:10.1364/ao.57.000c56

8. Bader T. Acoustooptic spectrum analysis: A high performance hybrid technique. *Appl Opt* (1979) 18(10):1668–72. doi:10.1364/ao.18.001668

9. Harris S, Wallace R. Acousto-optic tunable filter. *J Opt Soc Am* (1969) 59(6):744–7. doi:10.1364/josa.59.000744

10. chang IC. Noncollinear acousto-optic filter with large angular aperture. *Appl Phys Lett* (1974) 25(7):370–2. doi:10.1063/1.1655512

11. Machihin A, Pozhar V. Spatial and spectral image distortions caused by diffraction of an ordinary polarised light beam by an ultrasonic wave. *Quan Elec (Woodbury)* (2015) 45(2):161–5. doi:10.1070/qe2015v045n02abeh015385

12. S Mantsevich, V Balakshy, editors. The peculiarities of collinear acousto-optic filtration in the presence of optoelectronic feedback. In: 2018 4th International Conference on Frontiers of Signal Processing (ICFSP), Poitiers, France, September 24-27, 2018. (Poitiers, France: IEEE) (2018).

13. Voloshinov VB, Yushkov KB, Linde BB. Improvement in performance of a Teo2 acousto-optic imaging spectrometer. *J Opt A: Pure Appl Opt* (2007) 9(4):341–7. doi:10.1088/1464-4258/9/4/006

14. Harris SE, Wallace RW. Acousto-optic tunable filter. *J Opt Soc Am* (1969) 59(6):744–7. doi:10.1364/JOSA.59.000744

15. Y Chu, L Chen, H Wang, C ZHang, W Liu, P Wang, et al. editors. Research on edge enhancement of optical image based on acousto-optic filtering. In: Twelfth International Conference on Information Optics and Photonics, Xi'an, China, July 23–27, 2021 (Xi'an, China: SPIE) (2021).

16. Machikhin A, Gorevoy A, Batshev V, Pozhar V. Modes of wide-aperture acousto-optic diffraction in a uniaxial birefringent crystal. *J Opt* (2021) 23(12):125607. doi:10.1088/2040-8986/ac3368

17. R Abdlaty, S Sahli, J Hayward, Q Fang, editors. Hyperspectral imaging: Comparison of acousto-optic and liquid crystal tunable filters. In: *Medical ImagingPhysics of medical imaging*. Houston, TX: International Society for Optics and Photonics (2018).

18. A Beliaeva, G Romanova, editors. Energy efficiency of lighting systems based on acousto-optic filtration. *J Phys Conf Ser* (2021).

19. Lingying C, Qiang Z, Yuehong Q. Design of optical system for broadband and integrated aotf imaging spectrometer. *Acta Optica Sinica* (2021) 41(7):0722002. doi:10.3788/aos202141.0722002

20. J Zhu, L Li, X Guo, W Zhu, N An, editors. A multi-field of view hyperspectral imaging system based on mid-wave infrared. In: *4th optics young scientist summit (OYSS 2020)*. Ningbo, China: International Society for Optics and Photonics (2021).

21. Beliaeva AS, Romanova GE. Batshev VI, zhukova TIComputer modelling of acousto-optical diffraction in optical systems design. In: AM Zhurkin, editor. *Optical design and testing X*. Online Only, China: International Society for Optics and Photonics (2020).

22. Chen Y, Li W, Hyyppä J, Wang N, Jiang C, Meng F, et al. A 10-nm spectral resolution hyperspectral lidar system based on an acousto-optic tunable filter. *Sensors* (2019) 19(7):1620. doi:10.3390/s19071620

23. Kulak GV, Ropot PI, Bestugin AR, Shakin OV. Acousto-optical spectrum analyzer based on bessel light beams. *Problemy Fiziki, Matematiki i Tekhniki (Problems Phys Maths Technics)* (2021)(1) 19–23.

24. L Tv KKS, Kruglov SK. Application of the flicker noise filtering algorithm by changing the modulation frequency in an acousto-optic spectrum analyzer. *IOP Conf Ser : Mater Sci Eng* (2021) 1047(1):012113. doi:10.1088/1757-899X/1047/1/012113

25. Machikhin A, Batshev V, Pozhar V, Naumov A, Gorevoy A. Acousto-optic tunable spectral filtration of stereoscopic images. *Opt Lett* (2018) 43(5):1087–90. doi:10.1364/ol.43.001087

26. V Pozhar, M Bulatov, A Machikhin, V Shakhnov, editors. Technical implementation of acousto-optical instruments: Basic types. In: Journal of Physics: Conference series. Moscow, Russian Federation: IOP Publishing (2019).

27. Voloshinov VB, Porokhovnichenko DL, Dyakonov EA. Design of far-infrared acousto-optic tunable filter based on backward collinear interaction. *Ultrasonics* (2018) 88:207–12. doi:10.1016/j.ultras.2018.04.002

28. Batshev V, Machikhin A, Gorevoy A, Martynov G, Khokhlov D, Boritko S, et al. Spectral imaging experiments with various optical schemes based on the same aotf. *Materials* (2021) 14(11):2984. doi:10.3390/ma14112984

29. Mantsevich SN, Yushkov KB. Optimization of piezotransducer dimensions for quasicollinear paratellurite aotf. *Ultrasonics* (2021) 112:106335. doi:10.1016/j.ultras.2020.106335

30. Suhre DR, Denes LJ, Gupta N. Telecentric confocal optics for aberration correction of acousto-optic tunable filters. *Appl Opt* (2004) 43(6):1255–60. doi:10.1364/ao.43.001255

31. A Beliaeva, G Romanova, A Chertov, editors. Analysis of chromatic aberrations influence on operation of the tunable aotf-based source. *J Phys Conf Ser* (2021):2091/012012. doi:10.1088/1742-6596/2091/1/012012

32. KB Yushkov, VV Gurov, VY Molchanov, editors. Engineering of aotf transfer function for phase imaging microscopy and optical trapping. In: European Conference on Biomedical Optics. Munich Germany: Optical Society of America (2021).

33. V Batshev, S Boritko, A Kozlov, M Sharikova, V Lomonov, editors. Optical system of visible and short-wave infrared aotf-based spectral imaging device. In: *2021 wave electronics and its application in information and telecommunication systems*. St. Petersburg, Russia: WECONF IEEE (2021).

34. OD Moskaletz, MA Vaganov, VI Kazakov, AS Khomutov, editors. Measurement of optical spectrum by a spectral device based on an acousto-optic tunable filter with a stepwise tuning frequency. In: *2020 systems of signals generating and processing in the field of on board communications*. Moscow, Russia (2020).

35. Khokhlov DD, Machikhin A, Batshev V, Gorevoy A, Pozhar V. *Endoscopic spectral imagers based on acousto-optic filtration of light*. SPIE (2019).

36. Batshev V, Machikhin A, Martynov G, Pozhar V, Boritko S, Sharikova M, et al. Polarizer-free aotf-based swir hyperspectral imaging for biomedical applications. *Sensors* (2020) 20(16):4439. doi:10.3390/s20164439

37. GN Martynov, AV Gorevoy, AS Machikhin, VE Pozhar, editors. On inherent spatio-spectral image distortion in aotf-based imagers. In: *Optical measurement systems for industrial inspection XII*. Online Only, Germany: International Society for Optics and Photonics (2021).

38. Xu Z, Zhao H, Jia G, Sun S, Wang X. Optical schemes of super-angular aotf-based imagers and system response analysis. *Opt Commun* (2021) 498:127204. doi:10.1016/j.optcom.2021.127204

39. Lei S, Chunguang Z, Hao W, Jiangwei Y. Hyperspectral microimaging system based on double-filtering technology of acousto-optic tunable filter and its image analysis. *Laser Optoelectronics Prog* (2019) 55(3):032303.

40. L Denes, B Kaminsky, M Gottlieb, P Metes, editors. Factors affecting aotf image quality. In: Proceedings of the First Army Research Laboratory AOTF Workshop. Adelphi, Md: Army Research Laboratory (1997). Army Research Laboratory Report ARL-SR-54.

41. Pozhar VE, Machikhin AS, Gaponov MI, Shirokov SV, Mazur MM, Sheryshev AE. Hyper-spectrometer based on an acousto-optic tuneable filters for UAVS. *Le&E* (2019) 27(3):99–104. doi:10.33383/2018-029

42. V Pustovoit, V Pozhar, M Mazur, V Shorin, I Kutuza, A Perchik, editors. *Double-aotf spectral imaging system*. Warsaw, Poland: Acousto-optics and PhotoacousticsSPIE (2005).

43. Zhang X, Zhang C, Chen Y, Wang H, Sheng Z, Huang X, et al. Study on the performance of double filtering based on an acousto-optic tunable filter. *Phys Scr* (2019) 94(11):115507. doi:10.1088/1402-4896/ab2061

44. V Batshev, A Machikhin, S Boritko, G Martynov, A Gorevoy, N Moiseeva, editors. Double-pass acousto-optic filtration for spectral imaging. In: 2021 International Conference on Information Technology and Nanotechnology, Samara, Russian Federation, September 20–24, 2021 (Samara, Russian Federation: ITNT IEEE) (2021).

45. Gupta N, Suhre DR. Effects of sidelobes on acousto-optic tunable filter imaging. *Opt Eng* (2017) 56(7):073106. doi:10.1117/1.oe.56.7.073106

46. Shi S, Lv X, Wang Z, Guo J, Huang Y. Ray tracing method for removing sidelobe laser interference in aotf-based hyperspectral imaging. *Appl Opt* (2021) 60(17):5186–94. doi:10.1364/ao.423016

47. Arellanes AO, Quintard V, Pérennou A. Spectral and temporal behavior of a quasi-collinear aotf in response to acoustic pulses: Simulations and experiments. *Appl Opt* (2022) 61(7):1687–94. doi:10.1364/ao.449028

48. SN Mantsevich, editor. Frequency locking effect in acousto-optic systems and its practical applications. In: *2019 wave electronics and its application in information and telecommunication systems (WECONF)*. St. Petersburg, Russia (2019).

49. Satorius DA, Dimmick TE, Burdge GL. Double-pass acoustooptic tunable bandpass filter with zero frequency shift and reduced polarization sensitivity. *IEEE Photon Technol Lett* (2002) 14(9):1324–6. doi:10.1109/lpt.2002.801111

50. A Machikhin, editor. Acousto-optical tunable filters: Applications in 3d imaging and multi-wavelength digital holography. In: *Digital holography and three-dimensional imaging*. Washington, D.C: Optical Society of America (2021).

51. Champagne J, Kastelik J-C, Dupont S, Gazalet J. Study of the spectral bandwidth of a double-pass acousto-optic system [Invited]. *Appl Opt* (2018) 57(10):C49–C55. doi:10.1364/ao.57.000c49

52. D Khoptyar, AA Subash, M Saleem, S Andersson-Engels editors. Wide-bandwidth diffused optical spectroscopy for pharmaceutical characterization. In: 2012 Asia Communications and Photonics Conference, Guangzhou, China, November 7-10, 2012 (Guangzhou, China: ACP IEEE) (2012).

53. D Khoptyar, A Subash, M Saleem, OHA Nielsen, S Andersson-Engels editors. Wide-bandwidth photon time of flight spectroscopy for biomedical and pharmaceutical applications. In: 2013-16th International Conference on Near Infrared Spectroscopy, La Grande-Motte, France, June 2–7, 2017 (La Grande-Motte, France) (2013).

54. R Abdlaty Q Fang, editors. *Acousto-optic tunable filter-based hyperspectral imaging system characterization*. San Francisco, CA: Design and Quality for Biomedical Technologies XIISPIE (2019).

55. Machikhin A, Batshev V, Pozhar V, Naumov A. Single-volume dual-channel acousto-optical tunable filter. *Opt Express* (2020) 28(2):1150–7. doi:10.1364/OE.383960

56. A Naumov, editor. Optical system of 3d aotf-based microscopic imager. *J Phys Conf Ser* (2021):2127/012038. doi:10.1088/1742-6596/2107/1/012038

57. Mazur M, Mazur L, Suddenok YA, Shorin V. Increase of an output optical signal of an acousto-optic monochromator upon frequency modulation of a control signal. *Opt Spectrosc* (2018) 125(4):594–8. doi:10.1134/s0030400x18100156

58. KV Zaichenko BS Gurevich, editors. Spectral selection using acousto-optic tunable filters for the skin lesions diagnostics. In: *European conference on biomedical optics*. Munich Germany: Optical Society of America (2021).

59. KV Zaichenko BS Gurevich, editors. Biochemical analyzer for medical diagnostics based on spectrophotometric principle and programmable light source. In: *European conference on biomedical optics*. Munich Germany: Optical Society of America (2021).

60. Zaichenko K, Gurevich B. *Features of electroencephalographic signals acousto-optic processing*. Online Only, France: SPIE (2020).

61. K Zaichenko B Gurevich, editors. Acousto-optic devices application for bioelectric signals wavelet processing. In: *2021 ural symposium on biomedical engineering*. Radioelectronics and Information Technology USBEREIT (2021).

62. Machikhin A, Pozhar V, Batshev V. An acousto-optic endoscopic imaging spectrometer. *Instrum Exp Tech* (2013) 56(4):477–81. doi:10.1134/s0020441213030202

63. Zaichenko K, Gurevich B. *Choice of photodetector characteristics for acousto-optic devices for bioelectric signals processing*. SPIE (2020).

64. Yushkov KB, Champagne J, Kastelik J-C, Makarov OY, Molchanov VY. Aotf-based hyperspectral imaging phase microscopy. *Biomed Opt Express* (2020) 11(12): 7053–61. doi:10.1364/boe.406155

65. He Z, Li C, Xu R, Lv G, Yuan L, Wang J. Spectrometers based on acousto-optic tunable filters for *in-situ* lunar surface measurement. *J Appl Remote Sensing* (2019) 13(2):027502.

66. Gorevoy A, Machikhin A, Martynov G, Pozhar V. Computational technique for field-of-view expansion in aotf-based imagers. *Opt Lett* (2022) 47(3):585–8. doi:10.1364/ol.438374

67. Vanhamel J, Dekemper E, Berkenbosch S, Clairquin R. Novel acousto-optical tunable filter (aotf) based spectropolarimeter for the characterization of auroral emission. *Instrumentation Sci Technol* (2021) 49(3):245–57. doi:10.1080/10739149.2020.1814809

68. Sierra JAR, Contreras GS, Rivera EKA, Isaza C, de Paz JPZ. A novel methodology to study particulate material/aerosol pollution via real-time hyperspectral acousto-optic intelligent spectrometry. In: *Health and well-being considerations in the design of indoor environments*. Hershey, Pennsylvania: Hershey, Pennsylvania: IGI Global (2021). 32

69. Korablev OI, Belyaev DA, Dobrolenskiy YS, Trokhimovskiy AY, Kalinnikov YK. Acousto-optic tunable filter spectrometers in space missions [Invited]. *Appl Opt* (2018) 57(10):C103–C19. doi:10.1364/ao.57.00c103

70. Seo Y, Park B, Yoon S-C, Lawrence KC, Gamble GR. Morphological image analysis for foodborne bacteria classification. *Trans ASABE* (2018) 61(1):5–13. doi:10.13031/trans.11800

71. Duocastella M, Surdo S, Zunino A, Diaspro A, Saggau P. Acousto-optic systems for advanced microscopy. *J Phys Photon* (2020) 3(1):012004. doi:10.1088/2515-7647/abc23c

72. AS Khomutov, VI Kazakov, OD Moskaletz, editors. Spectrometer based on acousto-optic tunable filter for contactless spectral monitoring in extreme conditions. In: *Wave electronics and its application in information and telecommunication systems (WECONF)*. St. Petersburg, Russia: (2020).

73. Bonah E, Huang X, Aheto JH, Osae R. Application of hyperspectral imaging as a nondestructive technique for foodborne pathogen detection and characterization. *Foodborne Pathog Dis* (2019) 16(10):712–22. doi:10.1089/fpd.2018.2617

74. Park B, Eady M, Oakley B, Yoon S-C, Lawrence K, Gamble G. Hyperspectral microscope imaging methods for multiplex detection of Campylobacter. *J Spectr Imaging* (2019) 8. doi:10.1255/jsi.2019.a6

75. Kang R, Park B, Ouyang Q, Ren N. Rapid identification of foodborne bacteria with hyperspectral microscopic imaging and artificial intelligence classification algorithms. *Food Control* (2021) 130:108379. doi:10.1016/j.foodcont.2021.108379

76. Erna KH, Rovina K, Mantihal S. Current detection techniques for monitoring the freshness of meat-based products: A review. *J Packag Technol Res* (2021) 5(3): 127–41. doi:10.1007/s41783-021-00120-5

77. Polschikova O, Machikhin A, Ramazanova A, Bratchenko I, Pozhar V, Danilycheva I, et al. An acousto-optic hyperspectral unit for histological study of microscopic objects. *Opt Spectrosc* (2018) 125(6):1074–80. doi:10.1134/s0030400x19020188

78. Baek I, Lee H, Cho B-k, Mo C, Chan DE, Kim MS. Shortwave infrared hyperspectral imaging system coupled with multivariable method for tvb-N measurement in pork. *Food Control* (2021) 124:107854. doi:10.1016/j.foodcont.2020.107854

79. L Chen, Y Chu, C Zhang, H Wang, S Fan, B Yan. editors. Hyperspectral imaging system based on fiber endoscope. In: Twelfth International Conference on Information Optics and Photonics, Xi'an, China, July 23-27, 2021 (SPIE) (2021).

80. Liu H, Yu T, Hu B, Hou X, Zhang Z, Liu X, et al. Uav-borne hyperspectral imaging remote sensing system based on acousto-optic tunable filter for water quality monitoring. *Remote Sensing* (2021) 13(20):4069. doi:10.3390/rs13204069

81. Ji Z, He Z, Gui Y, Li J, Tan Y, Wu B, et al. Research and application validation of a feature wavelength selection method based on acousto-optic tunable filter (aotf) and automatic machine learning (automl). *Materials* (2022) 15(8):2826. doi:10.3390/ma15082826

frontiers | Frontiers in Physics

TYPE Brief Research Report
PUBLISHED 06 January 2023
DOI 10.3389/fphy.2022.1115330

OPEN ACCESS

EDITED BY
Bofeng Zhu,
Nanyang Technological University,
Singapore

REVIEWED BY
Wenlong Tian,
Xidian University, China
Dai Tongyu,
Harbin Institute of Technology, China

*CORRESPONDENCE
Zhongwei Fan,
fanzhongwei@aoe.ac.cn
Zhenao Bai,
baizhenao@hotmail.com

SPECIALTY SECTION
This article was submitted to Optics and Photonics,
a section of the journal
Frontiers in Physics

RECEIVED 03 December 2022
ACCEPTED 20 December 2022
PUBLISHED 06 January 2023

CITATION
Fan Z, Liu X, Zhang Z, Meng W, Long M and Bai Z (2023), 10 kHz repetition rate picosecond green laser for high-accuracy satellite ranging.
Front. Phys. 10:1115330.
doi: 10.3389/fphy.2022.1115330

10 kHz repetition rate picosecond green laser for high-accuracy satellite ranging

Zhongwei Fan[1,2]*, Xiaopeng Liu[2], Zhongping Zhang[3], Wendong Meng[3], Mingliang Long[3] and Zhenao Bai[1]*

[1]Aerospace Information Research Institute, Chinese Academy of Sciences, Beijing, China, [2]College of Optoelectronics, University of Chinese Academy of Sciences, Beijing, China, [3]Shanghai Astronomical Observatory, Chinese Academy of Sciences, Shanghai, China

Picosecond pulse laser is the main light source for satellite laser ranging. In this paper, a 10 kHz repetition rate picosecond green laser with an average output power of 5.3 W is demonstrated. The laser generates a pulse width of 18.6 ps at a center wavelength of 532.20 nm with a spectral width of .066 nm. The beam quality is well preserved with M^2 of 1.1 with the beam divergence measured to be .62 mrad and pointing stability of 7 μrad over 30 min of operation. The laser system was then applied to measure the BeiDou satellite (Compass-I3) and generated a single range accuracy of 3.2 mm, which is the highest reported range accuracy for synchronous orbit satellite laser ranging.

KEYWORDS

picosecond, regenerative amplifier, second harmonic generation, green laser, satellite laser ranging

Introduction

Satellite laser ranging (SLR) which uses a laser to detect the variation of a satellite from its predicted orbit is the most accurate satellite ranging technique [1–3]. With laser as the core light source, SLR uses the time-of-flight (TOF) measurement method for ranging [4, 5]. Generally, a laser with narrower pulse width contributes to higher ranging accuracy; meanwhile, a higher repetition rate leads to a higher probability of range echoes. At present, along with the technological breakthrough of kilohertz picosecond lasers, lasers with high repetition rate are rapidly becoming the landmark light source for fourth-generation satellite laser ranging [6–11]. Mode-locking technology is the main approach to achieve picosecond pulses, but the energy of the ultrashort pulses generated by mode-locked is low (~nanojoule) [12, 13]. In order to increase the pulse energy while maintaining the narrow pulse width, laser amplifiers (viz. regenerative amplifier and traveling wave amplifiers) are usually used to amplify the pulses output from picosecond oscillators [14–17]. Regenerative amplifiers have been widely applied to amplify the picosecond pulses from the nanojoule level to the millijoule level with a peak power enhancement of 10^6 times [18, 19].

In this letter, a picosecond green laser with a high repetition rate, high beam quality, high pointing stability and high-power stability is presented. In this system, a regenerative amplifier is used to increase the single pulse energy while keeping the pulse width constant. Then, the energy is further amplified using a traveling wave amplifier. Finally, the green laser output is achieved by second harmonic generation (SHG) with a conversion efficiency of up to 81.5%. The laser generates 10 kHz repetition rate picosecond pulses with an average output power of 5.3 W and pulse width of 18.6 ps. The center wavelength of the laser is 532.20 nm with a spectral width of .066 nm. It has a beam divergence angle of .62 mrad and

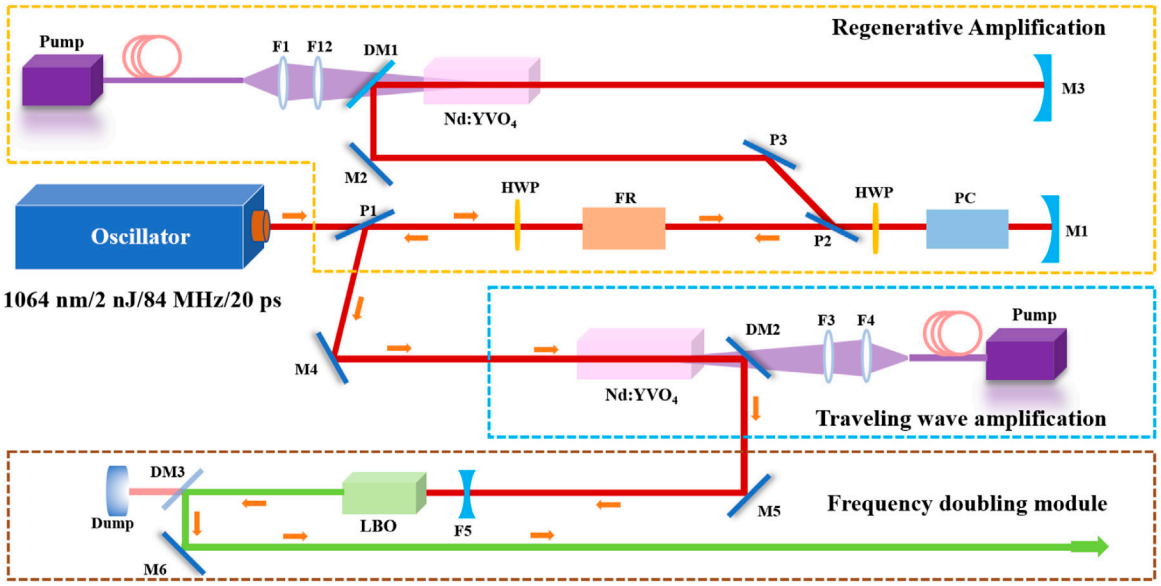

FIGURE 1
Schematic showing the layout of the laser system. PC, BBO crystal Pockels cell; HWP, half-wave plate; FR, Faraday rotator; M, mirrors; F, focus lens; P, Brewster angle polarizer.

a beam quality factor (M^2) of 1.1. The peak-to-peak energy fluctuations of the laser are 1.32% at .5 h.

Experiment and results

The experimental setup of the green picosecond laser is shown in Figure 1, which mainly consists of a picosecond seed source module, a regenerative amplifier module, a power amplifier module, and an electric control module. The seed source outputs 1,064 nm ps pulses with a pulse energy of 2 nJ and a pulse width of 20 ps at a repetition rate of 84 MHz. The seed passes through the optical isolator and then enters the regenerative amplifier. The optical isolator which is to prevent the amplified laser from returning and causing damage to the picosecond seed source consists of a polarizer, a half-wave plate, and a Faraday rotator. The regenerative amplification module consists of a polarizer, a quarter-wave plate, a gain medium, an electro-optical switch—Pockels cells (PC), a pump source, and a highly reflective mirror. The seed light pulse energy is amplified to .32 mJ in the regenerative amplification module with a repetition rate of 10 kHz. In the regenerative amplification module, the gain medium uses .3 at % doped Nd: YVO_4 crystal, which has a large excited emission cross-section and a wide pumping bandwidth. And the laser output is linearly polarized due to its natural birefringence property, which can mitigate thermogenic birefringence [20]. By using a semiconductor laser to end-pump the gain medium, a better mode matching of the pump light to the signal light is achieved and a better beam quality is obtained. The in-band pumping method is used to excite the particles directly to the upper energy level of the laser ($^4I_{9/2}\rightarrow{}^4F_{3/2}$), which can avoid the non-radiative leap process ($^4F_{5/2}\rightarrow{}^4F_{3/2}$), reduce the quantum loss, reduce the thermal effect, and improve the beam quality and stability [21, 22]. The size of Nd:YVO_4 is 3 mm × 3 mm × 20 mm. The pump light with a power of 25 W is injected into the Nd: YVO_4 crystal after being collimated and focused by a coupling lens set.

The seed light is output from the regenerative amplifier module and then enters the traveling wave amplifier module, which consists of a pump source, a gain medium, and a highly reflective mirror. Similar to the regenerative amplification module, the gain medium of the traveling wave amplification module is selected as .5 at % doped Nd: YVO_4 crystal with a size of 4 mm × 4 mm × 32 mm, using the same pumping geometry. The pump power is 90 W. After the signal light is amplified by the traveling wave module, the pulse energy is amplified to .65 mJ and the repetition rate is 10 kHz. The signal light amplified by the traveling wave amplifier module enters the frequency doubling module. It consists of a lens, a frequency doubling crystal, a dichroic mirror, and a highly reflective mirror. The frequency doubling crystal is selected as LBO crystal, which has a wide transmission range, good optical uniformity, high damage threshold, good mechanical properties, and high frequency doubling conversion efficiency [23, 24]. LBO adopts a combination of angular phase matching and temperature phase matching. The LBO is cut at $\theta = 90^\circ$ and $\varphi = 10.6^\circ$ with dimensions of 4 mm × 4 mm × 12 mm. In the experiment, the LBO achieves the best matching at around 50°C. This matching method can avoid the system disturbance caused by the high local temperature of the system, and at the same time suppress the micro-dampness of the crystal to improve the service life.

The amplified pulse is focused by the lens and then enters the LBO crystal for frequency doubling. The frequency doubled light is separated from the fundamental frequency light at the dichroic

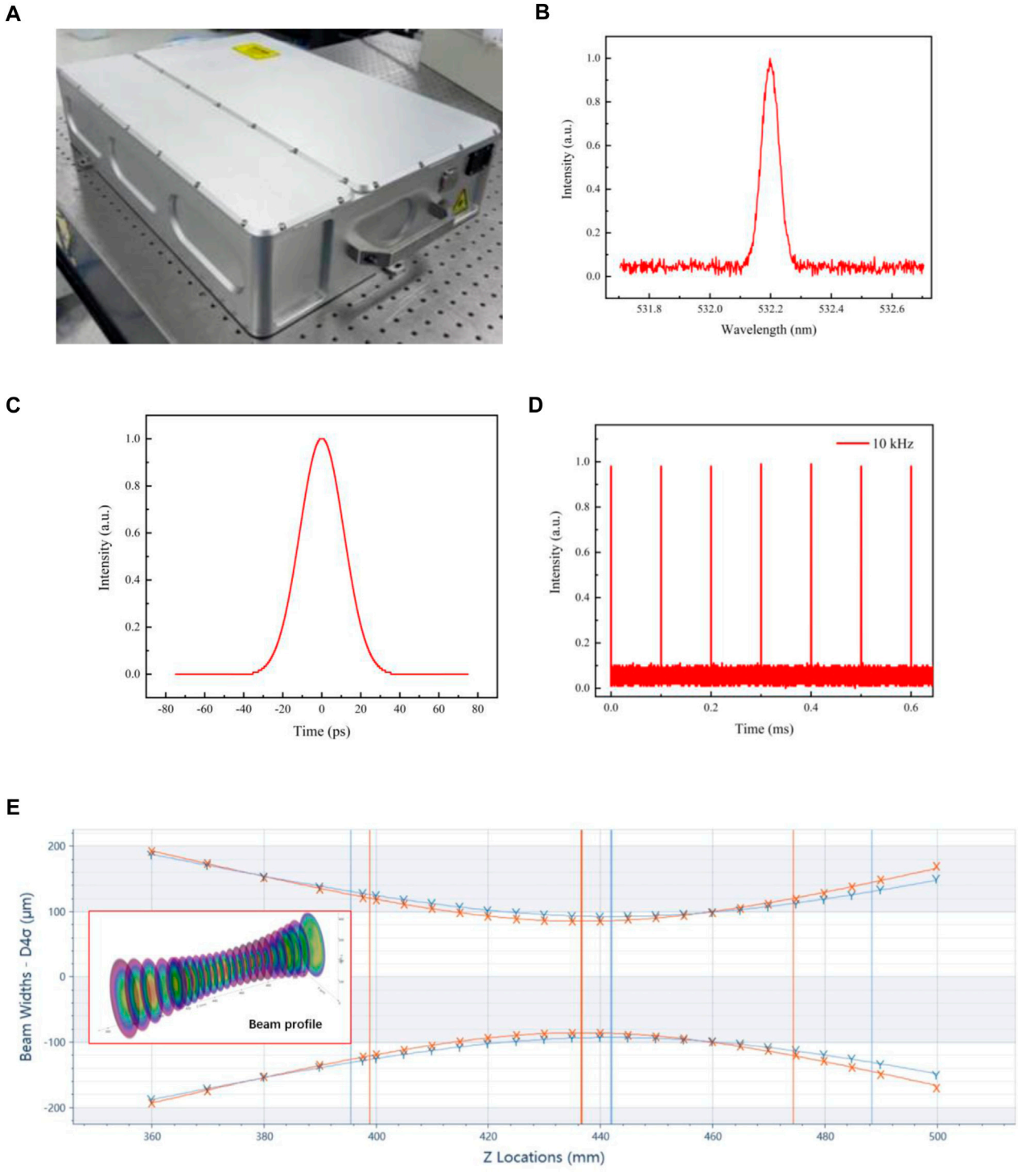

FIGURE 2
Compilation of output characteristics of the green laser. **(A)** Encapsulated lasers; **(B)** Normalized wavelength spectrum of the amplified laser output; **(C)** Characteristic of a single output pulse with an autocorrelation trace; **(D)** Normalized pulse characteristics of the output **(E)** plot of the focusing characteristics of the output beam (inset: beam profile).

mirror, and the fundamental frequency light is output at the dichroic mirror and collected by the collector, while the frequency doubled light is reflected by the dichroic mirror and then reflected and output by the high reflector. After the frequency doubling crystal, the pulse energy was converted from .65 to .53 mJ, and the frequency doubling efficiency was 81.5%. The central wavelength of green light is 532.20 nm, with a single pulse energy of .53 mJ, a repetition rate of 10 kHz, and a pulse width of 18.6 ps.

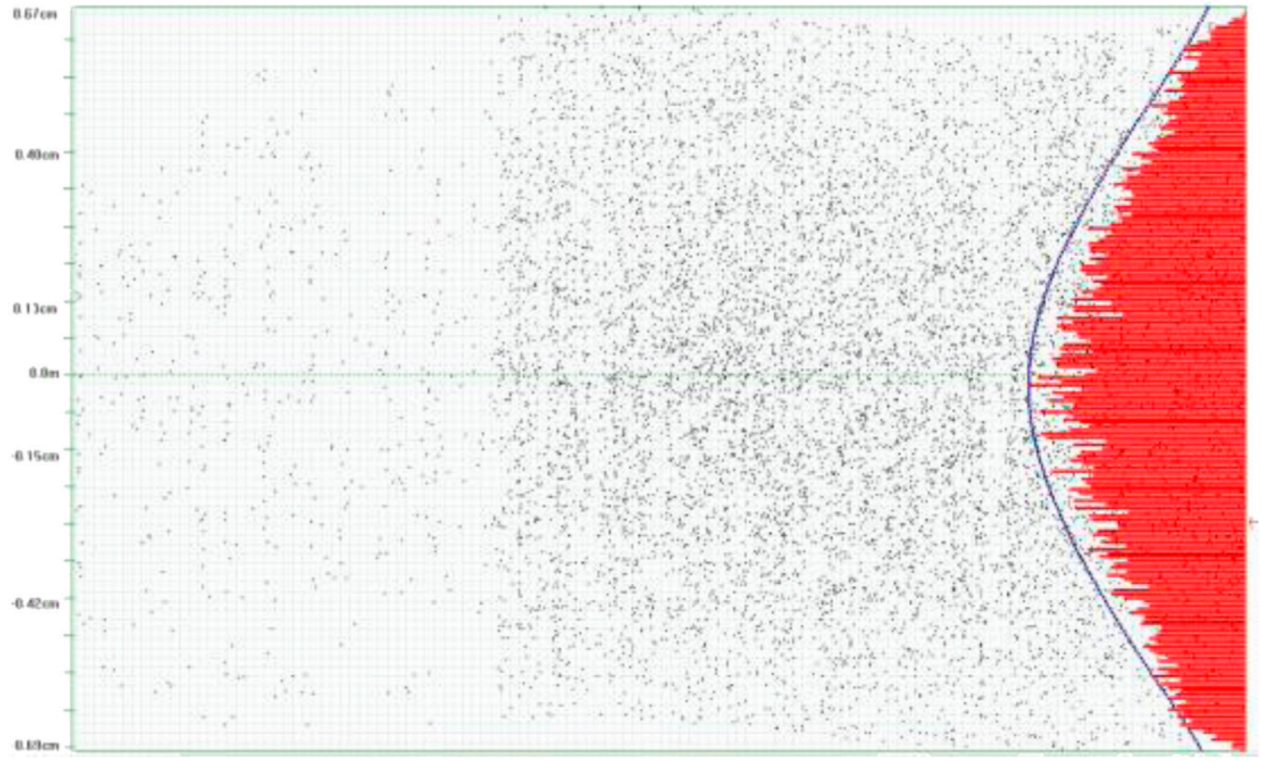

FIGURE 3
Plot of residuals from polynomial fit of measurement results.

The encapsulated laser is shown in Figure 2A. The output laser parameters are measured. The spectrum of the output laser is measured by using a spectrometer (AQ6374 OPTICAL SPECTRUM ANALYZER) as shown in Figure 2B. The central wavelength of the output laser is 532.20 nm and the linewidth is .066 nm. The pulse width of the output laser is measured by using an autocorrelator as shown in Figure 2C. The pulse width of the output laser is about 18.6 ps. The repetition rate of the output laser is measured by using an oscilloscope, as shown in Figure 2D. The beam quality of the output laser is measured by using a beam quality analyzer, as shown in Figure 2E. The beam quality factor of the output laser is M_x^2 = 1.09, M_y^2 = 1.12, and the beam divergence angle is about .62 mrad. The laser has good power stability (.11% at 2 h) and energy stability (Pulse Energy Peak—Peak Fluctuation 1.32% at .5 h). Output laser pointing stability is 7 μrad at .5 h.

According to the above experimental results, the green picosecond laser output laser has a narrow pulse width, which can improve the measurement accuracy of a single pulse; high energy stability, which can reduce the main wave timing jitter and further improve the measurement accuracy; narrower spectral width can better match the narrow band filter and improve the reception efficiency; high repetition rate of 10 kHz can obtain more effective data and reduce the fitting error. In summary, the laser can effectively improve the satellite laser ranging accuracy.

Applied to the satellite laser ranging system of Shanghai Astronomical Observatory, the Compass-I3 satellite in geosynchronous orbit (36,000 km) was measured, as shown in Figure 3, and a single ranging accuracy of 3.2 mm was obtained. To the best of our knowledge, this is the highest SLR accuracy obtained in synchronous orbit.

Conclusion

In this paper, a green picosecond laser with high beam quality, high pointing stability and high power stability is demonstrated. The final output laser has a power of 5.3 W, a central wavelength of 532.20 nm, a spectral width of .066 nm, a pulse width of 18.6 ps, and a repetition rate of 10 kHz. The laser has high beam quality and repetition rate, as well as very high power, energy, and pointing stability, and was applied to a satellite laser ranging system to measure the Compass-I3 satellite in geosynchronous orbit (36,000 km). The final single range accuracy of 3.2 mm was obtained, which is the highest range accuracy we know of for laser ranging of satellites in synchronous orbit. This research provides a high-quality laser source for high-precision space detection.

Data availability statement

The original contributions presented in the study are included in the article/supplementary material, further inquiries can be directed to the corresponding authors.

Author contributions

ZF, conceptualization, writing-original draft preparation, supervision, and funding acquisition. XL, investigation, formal

analysis, writing-review, and editing. ZZ, formal analysis, investigation, writing—review, and editing. WM, visualization and writing-original draft. ML, formal analysis, investigation, and validation. ZB, conceptualization, formal analysis, writing-review and editing, and funding acquisition. All authors have read and agreed to the published version of the manuscript.

Funding

This work was supported by the Research Group of Short Pulse Laser Technology (GJJSTD20200009), and Guangdong Key Research and Development Program (2018B090904003).

Conflict of interest

The authors declare that the research was conducted in the absence of any commercial or financial relationships that could be construed as a potential conflict of interest.

Publisher's note

References

1. Lucchesi DM, Anselmo L, Bassan M, Pardini C, Peron R, Pucacco G, et al. Testing the gravitational interaction in the field of the Earth via satellite laser ranging and the Laser Ranged Satellites Experiment (LARASE). *Classical Quan Gravity* (2015) 32(15):155012. doi:10.1088/0264-9381/32/15/155012

2. Wilkinson M, Schreiber U, Procházka I, Moore C, Degnan J, Kirchner G, et al. The next generation of satellite laser ranging systems. *J Geodesy* (2019) 93(11):2227–47. doi:10.1007/s00190-018-1196-1

3. Long M, Zhang H, Yu RZ, Wu Z, Qin S, Zhang Z. Satellite laser ranging at ultra-high PRF of hundreds of kilohertz all day. *Front Phys* (2022) 10:1036346. doi:10.3389/fphy.2022.1036346

4. Degnan J, Jan M. SLR2000: Eyesafe and autonomous single photoelectron satellite laser ranging at kilohertz rates. *Proc SPIE* (1997) 3218:63–77.

5. Lucchesi D, Anselmo L, Bassan M, Magnafico C, Pardini C, Peron R, et al. General relativity measurements in the field of earth with laser-ranged satellites: State of the art and perspectives. *Universe* (2019) 5(6):141. doi:10.3390/universe5060141

6. Deng H, Zhang H, Long M, Wu Z, Tang K, Zhang Z. 4 kHz repetition rate satellite laser ranging system and its application. *Acta Optica Sinica* (2019) 39(03):0314002. (in Chinese). doi:10.3788/aos201939.0314002

7. Sung K-P, Choi E-J, Lim H-C, Jung CG, Kim IY. Development of operation software for high repetition rate satellite laser ranging. *J Korean Soc Aeronaut Space Sci* (2016) 44(12):1103–11. doi:10.5139/jksas.2016.44.12.1103

8. Wu Z, Zhang Z, Zhang H, Li P, Meng W, Chen J. *The preliminary results of SLR with 10 kHz laser system at Shanghai station[C]//International workshop on laser ranging*. Japan: Fujiyoshida (2013).

9. Gen R, Wu Z, Tang K, Li Y, Meng W, Zhang Z Precise control of laser emission epoch in laser time transfer with high repetition rate. *Infrared Laser Eng* (2021) 50(10):135–43.

10. Long M, Zhang H, Men L, Wu Z, Deng H, Qin S, et al. Satellite laser ranging at high-repetition 10 kHz in all day. *Infrared Millim Waves* (2020) 39(6):778–85.

11. Bai Z, Chen H, Gao X, Li S, Qi Y, Bai Z. Highly compact nanosecond laser for space debris tracking. *Opt Mater* (2019) 98:109470. doi:10.1016/j.optmat.2019.109470

12. Keller U, Weingarten KJ, Kartner FX, Kopf D, Braun B, Jung I, et al. Semiconductor saturable absorber mirrors (SESAM's) for femtosecond to nanosecond pulse generation in solid-state lasers. *IEEE J Selected Top Quan Electron* (1996) 2(3):435–53. doi:10.1109/2944.571743

13. Gong M, Yu H, Wushouer X, Yan P. Passively mode-locked Nd: YVO_4 picosecond laser with oblique incidence on SESAM. *Laser Phys Lett* (2008) 5(7):514–7. doi:10.1002/lapl.200810025

14. Kim GH, Yang JH, Lee DS, Kulik AV, Sall EG, Chizhov SA, et al. Femtosecond laser based on Yb:KYW crystals with suppression of spectral narrowing in a regenerative amplifier by spectral profiling of the pulse. *J Opt Technol* (2013) 80(3):142–7. doi:10.1364/jot.80.000142

15. Kleinbauer J, Knappe R, Wallenstein R. 13-W picosecond Nd:$GdVO_4$ regenerative amplifier with 200-kHz repetition rate. *Appl Phys B* (2005) 81(2):163–6. doi:10.1007/s00340-005-1903-5

16. Hong KH, Gopinath JT, Rand D, Siddiqui AM, Huang SW, Li E, et al. High-energy, kHz-repetition-rate, ps cryogenic Yb:YAG chirped-pulse amplifier. *Opt Lett* (2010) 35(11):1752–4. doi:10.1364/ol.35.001752

17. Li K, Wang Y, Yu Y, Yue J, Song C, Cao C, et al. Amplification of high repetition-rate, picosecond laser pulses using a zig-zag slab configuration. *Opt Laser Techn* (2023) 157:108717. doi:10.1016/j.optlastec.2022.108717

18. Bai Z, Bai Z, Kang Z, Lian F, Lin W, Fan Z. Non-pulse-leakage 100-kHz level, high beam quality industrial grade Nd: YVO_4 picosecond amplifier. *Appl Sci* (2017) 7(6):615. doi:10.3390/app7060615

19. Bai Z, Bai Z, Yang C, Chen L, Chen M, Li G. High pulse energy, high repetition picosecond chirped-multi-pulse regenerative amplifier laser. *Opt Laser Techn* (2013) 46:25–8. doi:10.1016/j.optlastec.2012.04.019

20. Walter K. *Solid-state laser engineering*. New York, USA: Springer (2006). p. 54–5.

21. McDonagh L, Wallenstein R, Nebel A. 111 W, 110 MHz repetition-rate, passively mode-locked TEM_{00}Nd:YVO_4 master oscillator power amplifier pumped at 888 nm. *Opt Lett* (2007) 32:1259–61. doi:10.1364/ol.32.001259

22. Bai ZA, Fan ZW, Bai ZX, Lian FQ, Kang ZJ, Lin WR. Optical fiber pumped high repetition rate and high power Nd: YVO_4 picosecond regenerative amplifier. *Appl Sci* (2015) 5:359–66. doi:10.3390/app5030359

23. Chen CT, Wu YC, Jing A, Wu B, You G, Li R, et al. New nonlinear-optical crystal: LiB_3O_5. *J Opt Soc Am B* (1989) 6:616–21. doi:10.1364/josab.6.000616

24. Zhang Z, Bai Z, Song X, Zhang Y, Liang B, Liu T, et al. 178-W picosecond green laser with active beam-pointing stabilization. *Front Phys* (2022) 10:1084594. doi:10.3389/fphy.2022.1084594

frontiers | Frontiers in Physics

TYPE Original Research
PUBLISHED 18 January 2023
DOI 10.3389/fphy.2023.1124491

OPEN ACCESS

EDITED BY
Shuo Liu,
Hebei University of Technology, China

REVIEWED BY
Xinyang Su,
Beijing Jiaotong University, China
Lei Gao,
Chongqing University, China
Zhaohong Liu,
Hebei University of Technology, China

*CORRESPONDENCE
Yingbin Xing,
jsxyb1232008@126.com

SPECIALTY SECTION
This article was submitted to Optics and Photonics, a section of the journal Frontiers in Physics

RECEIVED 15 December 2022
ACCEPTED 09 January 2023
PUBLISHED 18 January 2023

CITATION
Zhang Z, Luo Y, Xing Y, Li H, Peng J, Dai N and Li J (2023), Experimental comparison of Yb/Al/Ce and Yb/Al/P co-doped fibers on the suppression of transverse mode instability.
Front. Phys. 11:1124491.
doi: 10.3389/fphy.2023.1124491

Experimental comparison of Yb/Al/Ce and Yb/Al/P co-doped fibers on the suppression of transverse mode instability

Zhilun Zhang, Yonghui Luo, Yingbin Xing*, Haiqing Li, Jinggang Peng, Nengli Dai and Jinyan Li

Wuhan National Laboratory for Optoelectronics (WNLO), Huazhong University of Science and Technology, Wuhan, Hubei, China

We presented an experimental comparison of the core-composition difference on the suppression of the photodarkening and transverse mode instability effects. Two core-composition fibers, entailing Yb/Al/Ce and Yb/Al/P co-doped fibers, were fabricated by MCVD process combined with solution doping technique. The parameters of two fibers were almost the same. The PD-induced loss at equilibrium was 3.94 dB/m at 702 nm in Yb/Al/Ce fiber, while it was 0.99 dB/m in Yb/Al/P fiber. To obtain a deeper understanding of the impact of PD on laser performance, a bidirectional pumping fiber amplifier was constructed. Compared with Yb/Al/Ce co-doped fiber, the TMI thresholds of Yb/Al/P co-doped fiber were enhanced in co-pumped and counter-pumped schemes. Meanwhile, the slope efficiency in bidirectional scheme was promoted by 4%. Moreover, the transmittance at 638 nm confirmed the superior PD resistance of Yb/Al/P co-doped fiber. These experimental results pave the way for the further development of high-power fiber lasers.

KEYWORDS

Yb-doped fiber, core composition, photodarkening, transverse mode instability, stimulated Raman scattering

1 Introduction

High power fiber lasers (HPFLs), attributed to their considerable advantages of excellent beam quality, high conversion efficiency, efficient heat dissipation, and compact structure [1–3], have been broadly utilized in industrial processing, military defense, medical treatment and other fields [4, 5]. With the development of the double-clad fibers, high-power laser diodes (LDs) and passive devices, the output powers of fiber lasers and amplifiers have been unprecedentedly promoted, exceeding 20 kW [6]. However, the remarkable evolutions of continuous-wave broadband fiber lasers and amplifiers are hindered by non-linear effects (NLEs), such as stimulated Raman scattering (SRS) [7–10]. In recent years, the threshold-like onset of transverse mode instability (TMI) is the main limitation for the further power scaling in the fiber laser systems [11–20].

It is well known that HPFLs are impressionable for the photodarkening (PD) effect, which might weaken the long-term stability of fiber lasers [21]. PD effect, by producing color centers, can lead to broadband absorption from the ultraviolet to the near infrared, inducing the significant decline of signal laser output power [22]. Additionally, the absorption range of color centers contains the absorption and emission band of Yb-doped fibers, which will absorb both pump light and signal light and generate a large amount of thermal load [23].

Further, PD-induced thermal load will result in a series of issues. By theoretically calculating the thermally-induced mode loss evolution, it showed that the refractive index of the Yb-doped fiber would be changed by the thermo-optic effect, which affected the waveguide structure and altered the bending loss of different modes [24]. Moreover, the phase of the beam could be distorted by PD-induced thermal load [25]. Meanwhile, PD effect would significantly increase the thermal load of the active fiber and aggravate thermally induced refractive index grating, which eventually triggered the occurrence of TMI effect [26]. It was also expected that even a slight reduction of the PD-induced loss would cause the significant increment of the TMI threshold. Furthermore, researchers theoretically demonstrated that the PD effect might bring about the quasi-static mode degradation on a time scale of minutes to hours [27]. They considered that the energy of the fundamental mode (FM) unidirectionally transferred to high order mode (HOM), which caused by a phase-shifted refractive index grating. One year later, the PD-induced mode degradation was experimentally observed [28]. After 532 nm photobleaching, the beam profile recovered to Gaussian-shape profile, which agreed with the theory of quasi-static mode degradation.

Up to now, there are many strategies to mitigate the PD effect. Firstly, efficient structural design of the active fiber was beneficial to the mitigation of the PD effect. In 2009, a novel reduced mode overlap fiber design was proposed and demonstrated, which could reduce the mode overlap and thus decrease the PD loss [29]. And after 1,500 h operation, less than 7% slope efficiency degradation was found and further 500 h operation showed no degradation. Then, photobleaching and thermal bleaching were also commonly used in bleaching the existing PD loss [22, 30, 31]. They significantly bleached the photo-darkened fiber and mitigated the PD effect of the active fiber. Additionally, the PD effect would be restrained by H_2 or O_2 loading [32–34]. Afterwards, our previous work revealed that there was no PD loss in the H_2-loaded fiber, while it was 114.4 dB/m at 702 nm in the pristine fiber [35]. Meanwhile, in the H_2-loaded fiber, the output power remained stable and no TMI was observed, while the TMI effect in the pristine fiber occurred at a lower power level. Finally, by optimizing the co-doped composition including Ce, P, Al, and Na ions, it could effectively inhibit the PD effect [36–38]. It has been demonstrated that Yb/Ce co-doped and Yb/Al/P co-doped fibers were conducive to suppress the PD effect in HPFLs [39–41]. However, there are still lack of the impacts of the PD differences of co-doped Ce and P ions on the high-power laser performances, especially in the TMI effect.

In this contribution, the experimental comparisons of the core-composition difference were carried out. The parameters of Yb/Al/Ce and Yb/Al/P co-doped fibers fabricated by MCVD process were almost the same. Then, the PD-induced excess loss, laser performance, and the transmittance at 638 nm were successively measured. The PD-induced excess loss of Yb/Al/Ce and Yb/Al/P co-doped fibers were 3.94 dB/m and 0.99 dB/m at 702 nm. The TMI thresholds of Yb/Al/Ce and Yb/Al/P fibers in co-pumped amplifier were 1,803 W and 1,934 W, while they were 2434 W and 3314 W in counter-pumped amplifier, respectively. Meanwhile, compared with Yb/Al/Ce fiber, the slope efficiency of Yb/Al/P fiber in bidirectional scheme was promoted by 4%. Moreover, the 638 nm transmittance of Yb/Al/P co-doped fiber was superior than that of Yb/Al/Ce co-doped fiber.

2 Fiber fabrication and characterization

The Yb-doped fiber preform fabrication by modified chemical vapor deposition (MCVD) combined with solution doping technique (SDT) could be composed of the following steps [42]: deposition and pre-sintering of soot layers, solution soaking, dehydration, vitrification and collapsing into preforms. Generally speaking, the uniform preform profile could be realized by controlling the dopants incorporation such as soot porosity, soot oxidation temperature, solution doping condition [43] and collapse pressure.

The refractive index profiles (RIPs) of the fabricated preform were measured by PK104 (PHOTO KINETICS), as depicted in Figure 1. The RIPs of Yb/Al/Ce co-doped and Yb/Al/P co-doped preforms, which were measured at the positions of 100 mm and 200 mm along the longitudinal direction, were almost coincidental, manifesting excellent uniformity. Compared with Yb/Al/Ce preform, there was central RIP dip in the core of Yb/Al/P preform. It was because that the sublimation of P_2O_5 would take away part of the doped Yb_2O_3 and Al_2O_3 during MCVD process [44]. Additionally, compared with Yb/Al/Ce co-doped preform, more soot layers are deposited in Yb/Al/P co-doped preform and the deposition temperature was different. Thus, it would present that the RIP of Yb/Al/P co-doped preform was more fluctuant. From the Figures 1A, B, the core NAs of Yb/Al/Ce and Yb/Al/P preforms were 0.061 and 0.06, respectively, almost the same.

Subsequently, the above-mentioned fabricated preforms would be milled into an octagonal shape, and drawn and coated to form the double-cladding Yb-doped fiber on the drawing tower. As exhibited in Figure 2, The concentration distributions of the doped elements of two fibers across the core region were characterized by electron probe microanalysis (EPMA). For the Yb/Al/Ce co-doped fiber, as described in Figure 2A, the concentrations of Yb^{3+}, Ce^{3+}, Al^{3+}, and F^{-} were measured to be ~0.75 wt%, ~0.25 wt%, ~0.3 wt%, and ~0.1 wt%, respectively. For the Yb/Al/P co-doped fiber, as shown in Figure 2B, the concentrations of Yb^{3+}, P^{5+}, Al^{3+}, and F^{-} were measured to be ~1.1 wt%, ~1.4 wt%, ~0.9 wt%, and ~0.05 wt%, respectively. The insets in Figure 2 were the microscope images of the cross sections of two fibers, respectively. The pump absorption coefficients of Yb/Al/Ce and Yb/Al/P fibers were measured to be 1.214 dB/m and 1.217 dB/m at 976 nm, respectively. For meeting the sufficient absorption, the utilized fiber lengths of two fibers were both 20 m. Notably, the Yb^{3+} ions concentration of Yb/Al/P fiber was higher than that of Yb/Al/Ce fiber. This was because that the Yb-doped fiber core with Al^{3+} and P^{5+} would alter the effective cross-sections of the fiber, which reduced the absorption of pump power [41]. Thus, it was necessary to improve a higher Yb^{3+} ion concentration to reach a certain desired pump absorption. By several exploration, Yb/Al/Ce and Yb/Al/P co-doped fibers were successfully fabricated with almost the same pump absorption, as shown in the above results. In addition, the detailed parameters of two fibers were presented in Table 1.

For purpose of a proper bending condition, bending losses at different bend radiuses were calculated using the finite element method with perfectly matched layer. In order to achieve the effective single-mode operation, the bending loss of the FM was less than 0.1 dB/m and the bending loss of the HOMs was more than 1 dB/m [45, 46]. Here, the values of core NA, core diameter, and center wavelength were set to be 0.06, 20 μm, and 1,080 nm, respectively. Thus, the normalized frequency V parameter was easily calculated to be 3.49, which indicated that there were only two transverse modes, LP_{01} and LP_{11}, supported in the fiber core. The calculated results of the bend losses and the effective mode areas

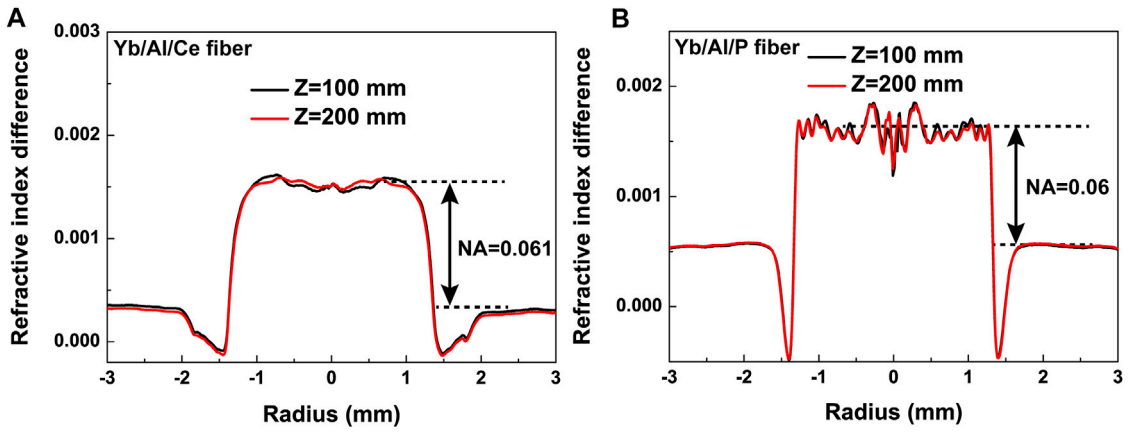

FIGURE 1
Refractive index profiles of **(A)** Yb/Al/Ce co-doped and **(B)** Yb/Al/P co-doped preforms at the positions of 100 mm and 200 mm along the longitudinal direction.

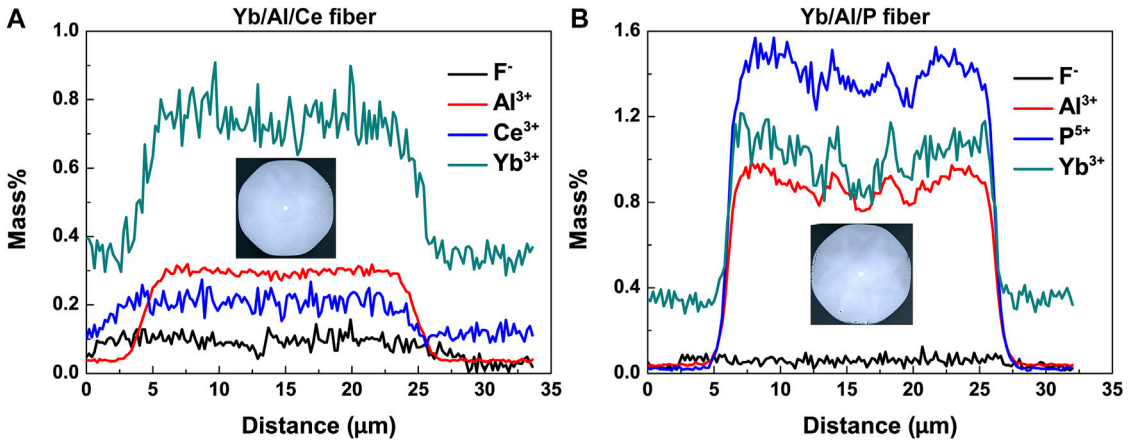

FIGURE 2
The elemental distribution of **(A)** Yb/Al/Ce co-doped and **(B)** Yb/Al/P co-doped fibers measured by electron probe microanalysis. (Insets: the microscope images of the cross sections of two fibers).

TABLE 1 Fiber parameters.

Core composition	Core diameter (μm)	Core NA	Pump absorption	Fiber length (m)
Yb/Al/Ce	21.41	0.061	1.214 dB/m	20
Yb/Al/P	21.71	0.06	1.217 dB/m	20

(EMAs) as functions of the bend radiuses were illustrated in Figures 3A, B, respectively. It was obvious that, as the increment of the bend radius, the bend losses of the transverse modes gradually decreased, while the EMAs gradually increased. From the results of Figure 3A, for the theoretical implementation of the single-mode operation, we considered that the proper bend radius region was between 4.5 cm and 8 cm and the corresponding EMA was between 256 μm^2 and 264 μm^2. Hereon, the bend radius of 5 cm was selected and corresponding LP_{01} loss, LP_{11} loss, and EMA were 0.03 dB/m, 36 dB/m, and 259 μm^2, respectively, so as to achieve the better laser performances in the laser test.

3 Experimental setup

The experimental setup for PD-induced excess loss measurement was illustrated in Figure 4. The signal light source was a halogen lamp ranging from 600 to 1,650 nm and was free spaced into a single mode fiber (SMF). Three 976 nm wavelength-locked laser diodes (LDs) could achieve 160 W pump power output, which could provide 46% population inversion. The broadband signal light from SMF and pump light from 976 nm LDs were both injected into the Yb-doped fiber through a combiner. The length of the tested fiber was kept

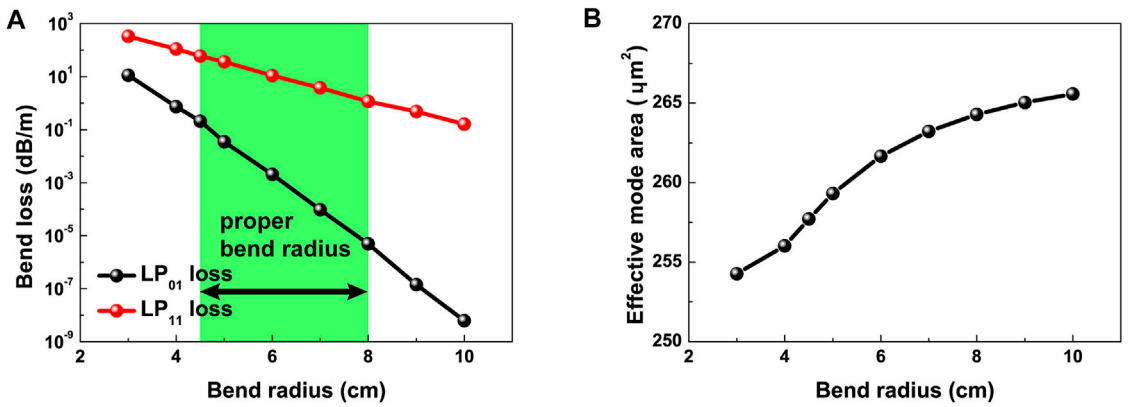

FIGURE 3
(A) The bend losses and **(B)** the effective mode areas as the functions of the different bend radiuses. Simulation parameters: core/inner cladding diameter of 20/400 μm, NA of 0.06 and center wavelength of 1,080 nm.

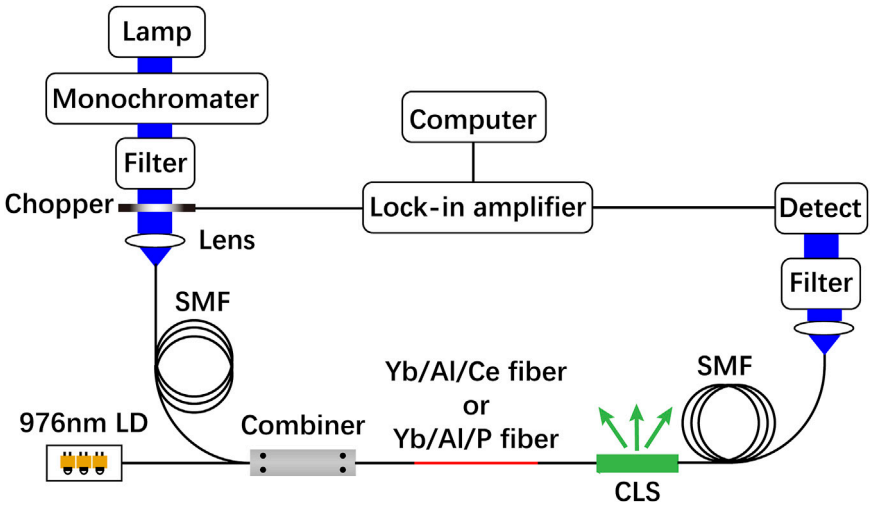

FIGURE 4
Schematic diagram of the experimental setup for PD loss measurement.

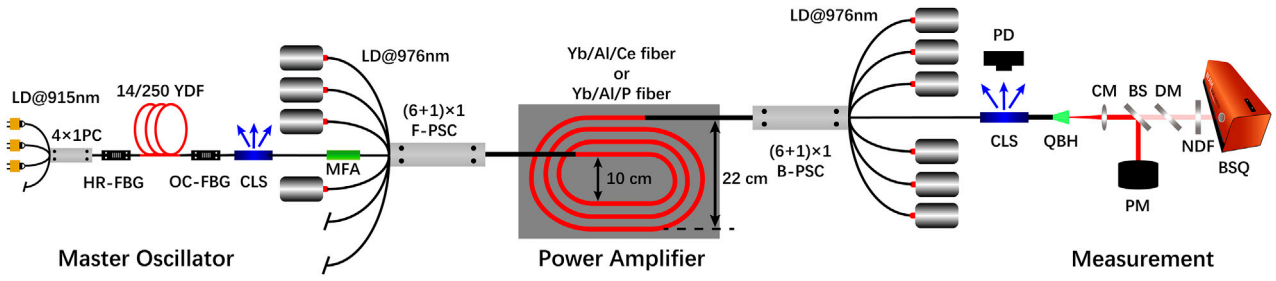

FIGURE 5
Schematic diagram of the experimental setup for laser performance measurement. LD, laser diode; PC, pump combiner; HR-FBG, high reflectivity fiber Bragg grating; OC-FBG, output coupler fiber Bragg grating; CLS, cladding light stripper; MFA, mode field adaptor; F- and B-PSC, forward- and backward-pump and signal combiner; PD, photodetector; QBH, quartz block holder; CM, collimating mirror; BS, beam splitter; DM, dichroic mirror; NDF, neutral density filter; BSQ, beam squared.

about 15 cm to maintain uniform inversion level. The cladding light would be stripped by cladding light stripper (CLS) between the Yb-doped fiber and SMF. To avoid heat accumulation, two air-cooling fans were employed to cool the LDs, Yb-doped fibers and CLS in the whole experiment. The absorption spectra of two Yb-doped fibers were recorded every 5 min.

For the measurement of laser performance, an all-fiberized bidirectional-pumped master oscillator power amplifier (MOPA) was constructed, as depicted in Figure 5. First of all, the master oscillator (MO) constituted by a pair of gratings and an active fiber was pumped by three 915-nm LDs from JDSU with each maximum pump power of 130 W. The high reflectivity fiber Bragg grating (HR-FBG) and the output coupler fiber Bragg grating (OC-FBG) fabricated by Teraxion could provide the reflectivity of 99.950% and 11.252%, the core NA of ~0.07, the center wavelength of ~1,080 nm, the core and inner cladding diameter of 14 μm and 250 μm, and the 3 dB bandwidth of 2.962 nm and 1.022 nm, respectively. The homemade 14/250 Yb-doped fiber was employed with the core NA of ~0.07 and the fiber length of 21 m. After stripped by CLS, the pure seed light in the fiber core was obtained, with the center wavelength of ~1,080 nm and the beam quality M^2 factor of ~1.2. Finally, a mode field adaptor (MFA) was used to match the signal fiber of the forward combiner, which possessed the core/cladding diameter of 14/250 μm on one end and 20/250 μm on the other.

Then, the seed light from the MO and the pump light from the forward/backward 976 nm LDs were poured into the power amplifier (PA). The forward pump and signal combiner (F-PSC) and the backward pump and signal combiner (B-PSC) were employed to permit the passage of the pump and signal lasers. Herein, the pigtails of the commercial F-PSC and B-PSC were passive fibers manufactured by Nufern and their core NAs were both about 0.06. The above-mentioned Yb/Al/Ce and Yb/Al/P fibers with the same length of 20 m were coiled in a racetrack-typed water-cooled plate with minimum and maximum bending diameter of 10 cm and 22 cm, respectively. The amplified signal laser propagated through CLS to strip the cladding light, which was received by a InGaAs photodetector to collect the time-domain signal and monitor the TMI process. Finally, the signal laser was exported through the quartz block holder (QBH).

As for the measurement of laser performance, the diverging signal laser output from QBH was collimated by a collimating mirror with the focal length of 150 mm, and then, the collimated laser was split by a high-reflectivity beam splitter (BS) with the reflectivity of >99%. A dichroic mirror (DM) was utilized to further eliminate the residual pump light, and subsequently, the purer laser was attenuated by a set of neutral density filter (NDF). The beam quality evolution was recorded by the Beam Squared (BSQ) and the optical spectra of the output laser was also measured with an optical spectrum analyzer (OSA).

4 Results and discussion

4.1 Photo-darkening excess losses of Yb/Al/Ce and Yb/Al/P fibers

Several absorption spectra of two Yb-doped fibers were obtained by PD loss measurement. Based on our previous investigation [35], the PD-induced excess losses at 633 nm, 702 nm, 810 nm, and 1,041 nm were selected to characterize the PD properties. Meanwhile, the data were also fitted by the classical stretched exponential function used in [47]. Additionally, the excess loss at 633 nm was commonly used in the characterization of PD properties. However, 633 nm was at the edge of the detection range of our measurement, and the data fluctuates greatly. Thus, for accuracy, 702 nm was chosen for comparison in this work.

The PD-induced excess losses of Yb/Al/Ce co-doped and Yb/Al/P co-doped fibers were depicted in Figures 6A, B. Overall, the excess losses of Yb/Al/Ce co-doped fiber at chosen wavelengths were more than twice as much as those of Yb/Al/P co-doped fiber. Concretely, by stretched exponential function fitting, the PD-induced equilibrium excess losses of Yb/Al/Ce co-doped fiber at 633 nm, 702 nm, 810 nm, and 1,041 nm were calculated to be 6.73 dB/m, 3.94 dB/m, 1.37 dB/m, and 0.58 dB/m, respectively. For Yb/Al/P co-doped fiber, the excess losses at 810 nm and 1,041 nm were nearly 0 and only the excess losses of 633 nm and 702 nm were fitted. And the PD-induced equilibrium excess losses of Yb/Al/P co-doped fiber at 633 nm and 702 nm were calculated to be 3.14 dB/m, 0.99 dB/m. Here, for 702 nm, the excess losses of Yb/Al/Ce and Yb/Al/P fibers were 3.94 dB/m and 0.99 dB/m, respectively, which was 3.98 times as much as that of Yb/Al/P fiber. In conclusion, the Yb/Al/P co-doped fiber presented superior PD resistance.

4.2 Laser performances of Yb/Al/Ce and Yb/Al/P fibers

For the laser performances of two fibers, we measured the laser efficiencies, the TMI thresholds and output laser spectra in co-pumped, counter-pumped, and bidirectional pumping amplifiers. For a start, the laser performances of Yb/Al/Ce and Yb/Al/P fibers were verified in co-pumped amplifier and depicted in Figure 7. The output power as a function of pump power of Yb/Al/Ce and Yb/Al/P fibers were recorded and the results were shown in Figures 7A, C, respectively. The maximum output powers of Yb/Al/Ce and Yb/Al/P fibers in co-pumped amplifier were 1,803 W and 1,934 W, with the slope efficiencies of ~78.9% and 81.7%, respectively. From the time- and frequency-domain signals as illustrated in Figures 7B, D, there were obvious fluctuations at the output power of 1803 W in Figure 7B and at the output power of 1,934 W in Figure 7D. The fluctuations in time- and frequency-domain signals indicated the onsets of TMI. Thus, we considered that the TMI thresholds of Yb/Al/Ce and Yb/Al/P fibers in co-pumped amplifier were 1,803 W and 1,934 W, respectively. Meanwhile, the further power scaling was limited by TMI effect.

Then, the laser performances of Yb/Al/Ce and Yb/Al/P fibers were verified in counter-pumped amplifier and described in Figure 8. The output powers of Yb/Al/Ce and Yb/Al/P fibers continuously increased to 2434 W and 3314 W without power rollover and the slope efficiencies were linearly fitted to ~81.5% and 84.6%, as shown in Figures 8A, C, respectively. Furthermore, the time- and frequency-domain spectra were also observed by oscilloscope and there were obvious fluctuations at the output power of 2,434 W in Figure 8B and at the output power of 3,314 W in Figure 8D, respectively. Thus, we considered that the TMI thresholds of Yb/Al/Ce and Yb/Al/P fibers in counter-pumped amplifier were 2,434 W and 3,314 W, respectively. Meanwhile, the further power scaling was limited by TMI effect.

Finally, the output laser performances of Yb/Al/Ce and Yb/Al/P fibers with bidirectional pump were measured and recorded, as exhibited in Figure 9. The output powers of two fibers as a function of pump powers were depicted in Figures 9A, D,

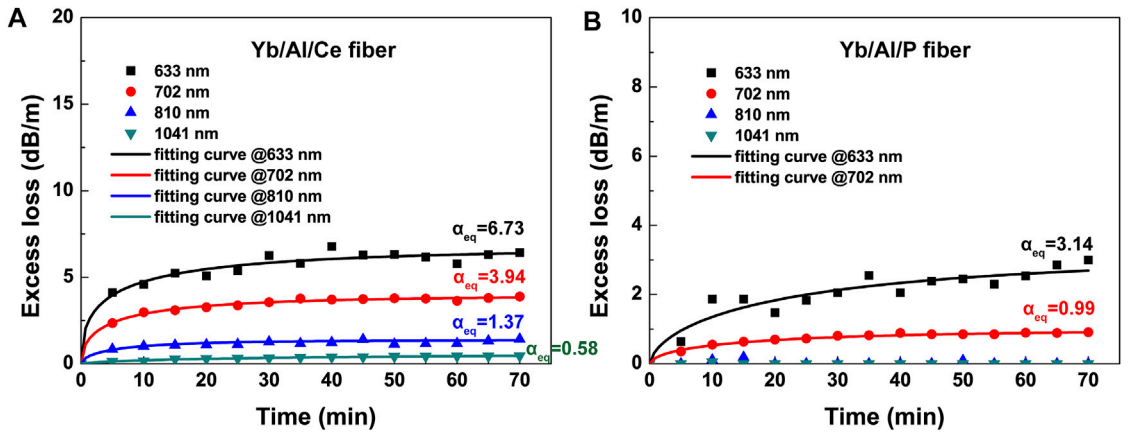

FIGURE 6
PD excess losses and fitting curves at 633 nm, 702 nm, 810 nm, and 1,041 nm of **(A)** Yb/Al/Ce co-doped fiber and **(B)** Yb/Al/P co-doped fiber.

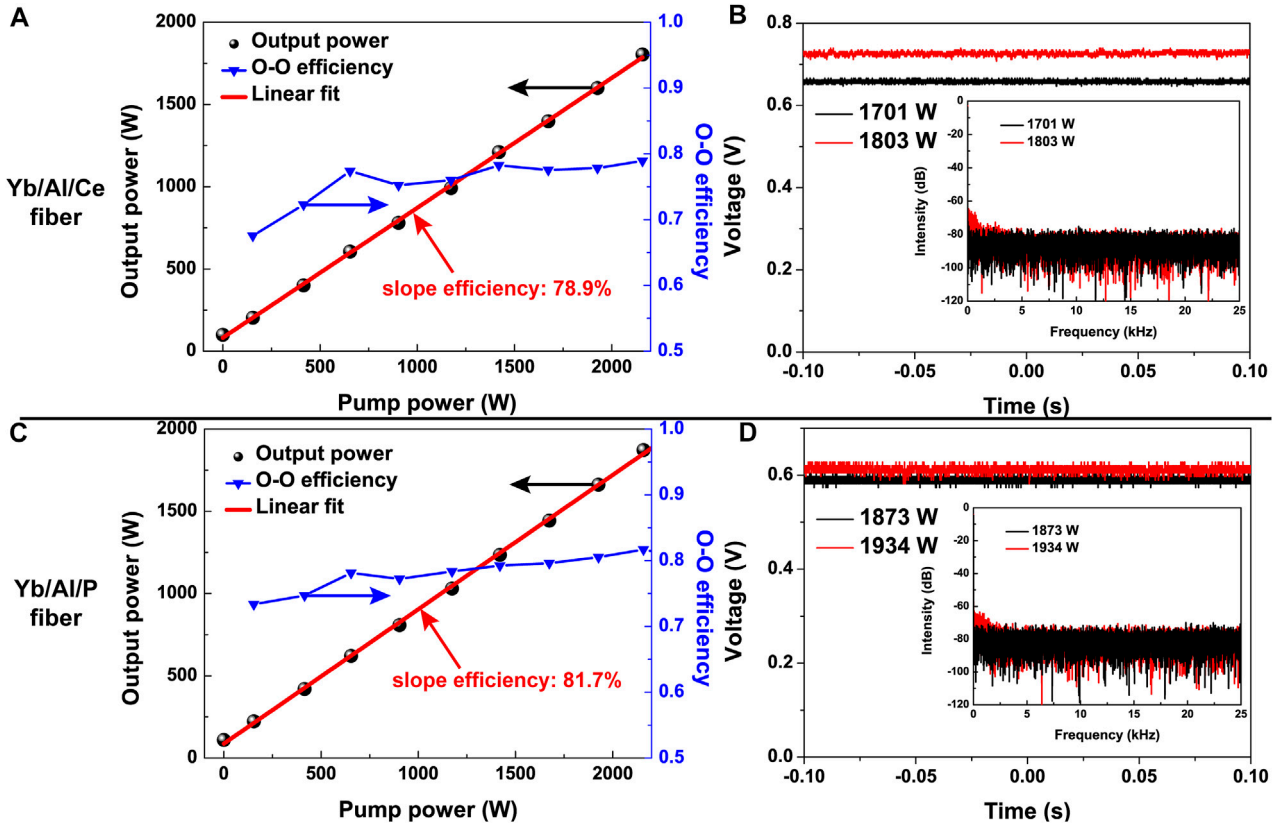

FIGURE 7
Laser performances in co-pumped amplifier. Yb/Al/Ce fiber: **(A)** output power and O-O efficiency dependence on the pump power; **(B)** time- and frequency-domain signals. Yb/Al/P fiber: **(C)** output power and O-O efficiency dependence on the pump power; **(D)** time- and frequency-domain signals.

respectively. By continuously increasing the pump powers from the bidirectional 976-nm LDs, the output powers of Yb/Al/Ce and Yb/Al/P fibers enhanced to 2846 W and 3536 W, which the slope efficiencies were linearly fitted to ~80.0% and ~84.0%, respectively. Meanwhile, the beam quality M^2 factors of Yb/Al/Ce and Yb/Al/P fibers at the maximum output powers were measured to be 1.42 and 1.45, respectively. From the Figures 9B, E, the signal lasers of Yb/Al/Ce and Yb/Al/P fibers were both centered at the wavelength of ~1,080 nm, and the full width at half maximum increased to ~3 nm of 2,846 W and ~4 nm of 3,536 W, respectively. Simultaneously, there were Raman Stokes light in the optical spectra. The Stokes intensity was ~44 dB below that of signal laser of Yb/Al/Ce fiber, while the intensity

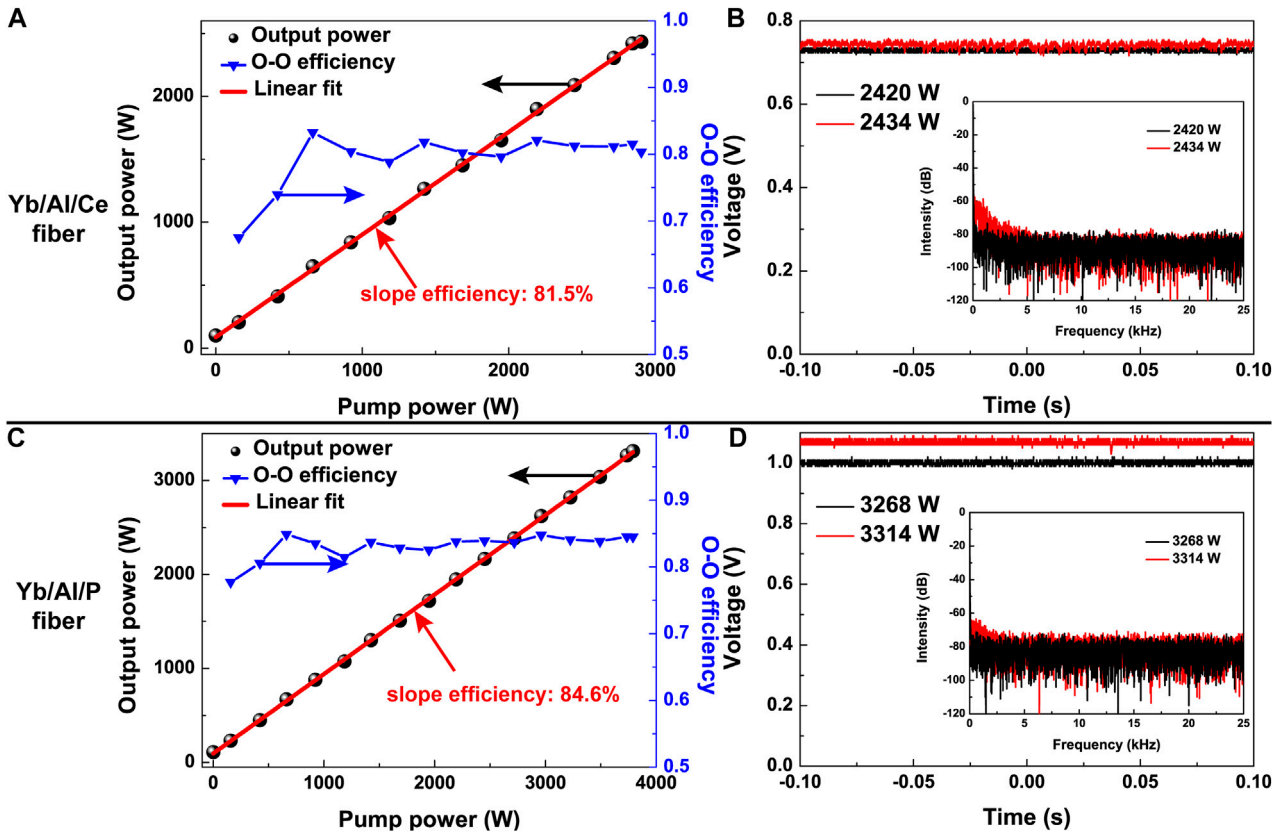

FIGURE 8
Laser performances in counter-pumped amplifier. Yb/Al/Ce fiber: **(A)** output power and O-O efficiency dependence on the pump power; **(B)** time- and frequency-domain signals. Yb/Al/P fiber: **(C)** output power and O-O efficiency dependence on the pump power; **(D)** time- and frequency-domain signals.

was ~41 dB below that of signal laser of Yb/Al/P fiber. Thus, further power scaling was not pursued to avoid the exponential increase of the Raman Stokes light. In addition, the time- and frequency-domain signals of Yb/Al/Ce fiber at the output power of 2,846 W remained stable without any fluctuation, while those of Yb/Al/P fiber at the output power of 3,536 W were also stable, as described in Figures 9C, F, respectively. The results of the time- and frequency-domain signals of two fibers indicated the absence of the TMI effect.

The output power stability of two fibers was monitored at ~2.5 kW for an hour and the power values were recorded with an interval of 0.133 s. For Yb/Al/Ce co-doped fiber, the output laser power presented a power fluctuation within a range from 2,437 W to 2,506 W, ~2.8%. For Yb/Al/P co-doped fiber, the output power was recorded from 2,488 W to 2,512 W with the power fluctuation of less 1%. It indicated that the Yb/Al/P co-doped fiber owned a better power stability.

4.3 638 nm transmittance of Yb/Al/Ce and Yb/Al/P fibers

Moreover, the 638 nm transmittances of Yb/Al/Ce and Yb/Al/P co-doped fibers were measured and compared. The experimental setup of the 638 nm transmittance was depicted in Figure 10A. 30 mW 638 nm single-mode laser was injected to two fibers by MFA. After stripped by CLS, the remanent laser was received by a milliwatt-level PM. The input end was kept unchanged and the active fiber was cut off from the output end to measure the output power at a different position. To avoid the influence of splicing loss, the output power of 638 nm laser injected in 1 cm Yb-doped fiber was measured as the initial injection power. The measured results were depicted in Figure 10B. The transmittance of Yb/Al/Ce co-doped fiber presented a rapid declining trend and the transmittance in the position of 20 m was only 30%. For Yb/Al/P co-doped fiber, the declining trend was slow and the transmittance was still up to 84% in the position of 20 m. The transmittance results demonstrated that there was more seriously distributed PD loss along the longitudinal length of Yb/Al/Ce co-doped fiber, compared with Yb/Al/P co-doped fiber.

The aforementioned experimental results were all measured by the same setups and conditions, which ensured the credibility of the contrast experiment. Thus, we considered that the PD resistance of Yb/Al/P co-doped fiber was superior to that of Yb/Al/Ce co-doped fiber, and meanwhile the TMI thresholds and laser efficiencies of Yb/Al/P co-doped fiber in co-pumped and counter-pumped amplifiers were higher than those of Yb/Al/Ce co-doped fiber. Concretely, the excess losses of Yb/Al/Ce and Yb/Al/P fibers at 702 nm were 3.94 dB/m and 0.99 dB/m, respectively. The TMI thresholds of Yb/Al/Ce and Yb/Al/P fibers in co-pumped amplifier were 1,803 W and 1,934 W, while they were 2,434 W and 3,314 W in counter-pumped amplifier, respectively. Meanwhile, by replacing Yb/Al/Ce co-doped fiber with Yb/Al/P co-doped fiber, the slope efficiency of the signal laser was also enhanced by ~4%. Moreover, the 638 nm transmittance confirmed that there was lower PD loss in the Yb/Al/P co-doped fiber.

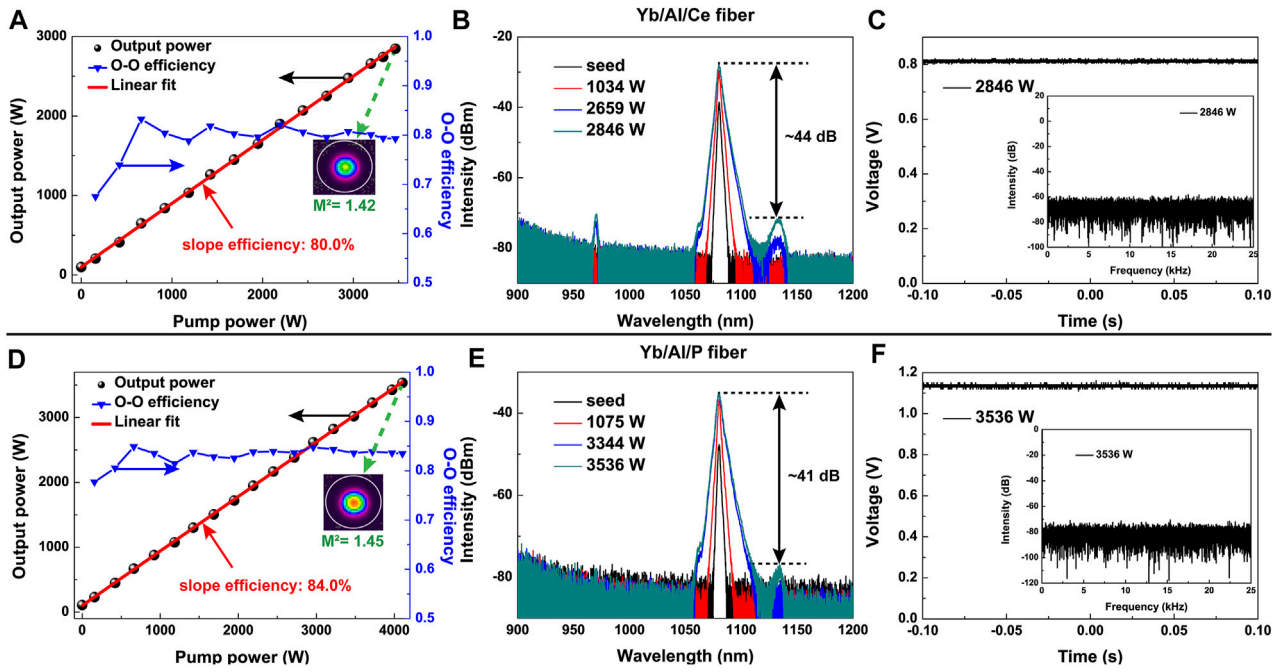

FIGURE 9
Laser performances in bidirectional pumping amplifier. Yb/Al/Ce fiber: **(A)** output power and O-O efficiency dependence on the pump power; **(B)** optical spectra at several output powers; **(C)** time- and frequency-domain signals. Yb/Al/P fiber: **(D)** output power and O-O efficiency dependence on the pump power; **(E)** optical spectra at several output powers; **(F)** time- and frequency-domain signals.

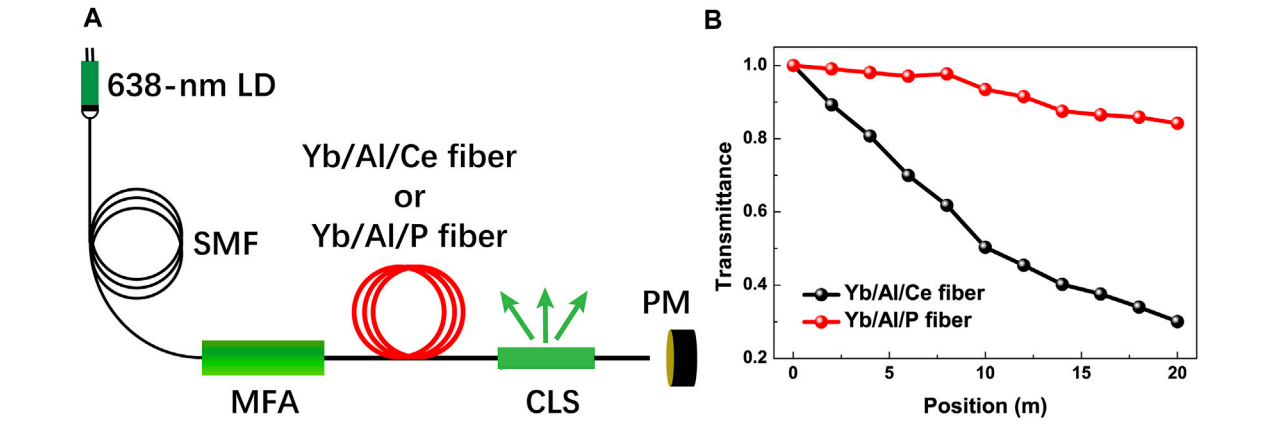

FIGURE 10
(A) Schematic diagram of the experimental setup for 638 nm transmittance measurement; **(B)** the measured results of the 638 nm transmittance of Yb/Al/Ce and Yb/Al/P co-doped fibers.

In our experiment, most of parameters of two fibers were remained the same, entailing core and inner cladding diameters, core NA, pump absorption, and fiber length. Thus, the core composition became the key point for reducing the PD loss, and further suppressing the TMI effect. Meanwhile, thanks to the superior PD resistance, the TMI thresholds of Yb/Al/P co-doped fiber were higher than those of Yb/Al/Ce co-doped fiber under co-pumped and counter-pumped schemes. For Yb/Al/Ce co-doped fiber, Ce had different valence states, Ce^{3+}/Ce^{4+}. Through their valence-state transition, both electrons and holes related to color centers could be trapped to suppress PD effect [48]. The suppression of PD effect would mitigate the TMI effect. However, Ce-doping would introduce new heat sources to Yb-doped fiber lasers [49].

For Yb/Al/P co-doped fiber, it would effectively inhibit the generation of aluminum oxygen hole centers (Al-OHCs) and Oxygen Deficiency Centers (ODCs) by forming $[AlPO_4]$ structure [39]. Meanwhile, this structure would shift the charge-transfer band to a shorter wavelength region. Thus, Yb/Al/P co-doped fiber would

present low PD sensitivity, which was beneficial for mitigating the TMI effect. Additionally, when the value of $C_{P_2O_5}/(C_{P_2O_5}+C_{Al_2O_5})$ was greater than 0.49, the PD effect would be effectively suppressed and the average heat load would also be weakened [41]. In our experiment, this value was about 0.6. Although it was not the optimal value, it still maintained a lower heat load and a higher TMI threshold, according the simulated results of Ref. [41]. Meanwhile, our experimental results manifested that, compared with Ce co-doping, P co-doping would induce a lower average heat-loaded distribution, which would contribute to mitigating the TMI effect.

5 Conclusion

In summary, we reported on an experimental comparison of the core-composition difference. Based on MCVD process combined with SDT, Yb/Al/Ce and Yb/Al/P co-doped fibers were fabricated, whose parameters were almost the same. Firstly, the PD-induced excess loss of Yb/Al/Ce and Yb/Al/P co-doped fibers were 3.94 dB/m and 0.99 dB/m at 702 nm, which indicated the superior PD resistance of Yb/Al/P fiber, Then, a bidirectional pumping fiber amplifier was constructed to verify the impact of PD on laser performance. The TMI thresholds of Yb/Al/P co-doped fiber were higher than those of Yb/Al/Ce co-doped fiber in co-pumped and counter-pumped schemes. The slope efficiency of Yb/Al/P co-doped fiber in bidirectional scheme was enhanced by 4%. In addition, the results of 638 nm transmittance manifested the lower PD loss of Yb/Al/P co-doped fiber. These experimental results could provide a good reference for realizing high-power fiber lasers.

Data availability statement

The original contributions presented in the study are included in the article/supplementary material, further inquiries can be directed to the corresponding author.

Author contributions

ZZ and YX proposed the idea. ZZ and YL performed the experiments. ZZ wrote the original manuscript. YX, HL, JP, ND, and JL revised the manuscript. All authors contributed to the article and approved the submitted version. JL and YX supervised the project.

Funding

This work is supported by National Natural Science Foundation of China under Grant nos. 61975061 and 61905080.

Acknowledgments

The authors wish to thank Xianfeng Lin and Anjun Zhang for their help during the experiment and thank Changjin Laser Ltd. for providing fibers. The authors also thank the Analytical and Testing Centre at the HUST for performing elemental characterization of fiber samples.

Conflict of interest

The authors declare that the research was conducted in the absence of any commercial or financial relationships that could be construed as a potential conflict of interest.

Publisher's note

References

1. Richardson DJ, Nilsson J, Clarkson WA. High power fiber lasers: Current status and future perspectives [invited]. *J Opt Soc Am B* (2010) 27(11):B63. doi:10.1364/josab.27.000b63

2. Jauregui C, Limpert J, Tünnermann A. High-power fibre lasers. *Nat Photon* (2013) 7(11):861–7. doi:10.1038/nphoton.2013.273

3. Codemard C, Zervas MN, Codemard CA. High power fiber lasers: A review. *IEEE J Sel Top QUANTUM Electron* (2014) 20:219–41. doi:10.1109/jstqe.2014.2321279

4. Kalisky O. The status of high-power lasers and their applications in the battlefield. *Opt Eng* (2010) 49(9):091003. doi:10.1117/1.3484954

5. Zhao K, Wang H, Yan J, Shen H. Welding fused silica glass by picosecond pulsed laser with low numerical aperture. *J Micro Nano-manufacturing* (2019) 7(4):1–8. doi:10.1115/1.4045467

6. Shiner B. The impact of fiber laser Technology on the world wide material processing market. *AF2J.* (2013) 1. doi:10.1364/CLEO_AT.2013.AF2J.1

7. Jauregui C, Eidam T, Schimpf DN, Limpert J, Tünnermann A. Derivation of Raman treshold formulas for CW double-clad fiber amplifiers. *Opt Express* (2009) 17(10):8476–90. doi:10.1364/oe.17.008476

8. Tao R, Xiao H, Zhang H, Leng J, Wang X, Zhou P, et al. Dynamic characteristics of stimulated Raman scattering in high power fiber amplifiers in the presence of mode instabilities. *Opt Express* (2018) 26(19):25098. doi:10.1364/oe.26.025098

9. Hu Q, Zhao X, Tian X, Wang M, Wang Z, Xu X. Raman suppression in high-power fiber laser oscillator by long period fiber grating. *Results Phys* (2021) 26:104460. doi:10.1016/j.rinp.2021.104460

10. Hu Q, Zhao X, Tian X, Li H, Wang M, Wang Z, et al. Raman suppression in 5 kW fiber amplifier using long period fiber grating fabricated by CO 2 laser. *Opt Laser Technol* (2022) 145:107484. doi:10.1016/j.optlastec.2021.107484

11. Eidam T, Wirth C, Jauregui C, Stutzki F, Jansen F, Otto H-J, et al. Experimental observations of the threshold-like onset of mode instabilities in high power fiber amplifiers. *Opt Express* (2011) 19(14):13218. doi:10.1364/oe.19.013218

12. Stutzki F, Otto H-J, Jansen F, Gaida C, Jauregui C, Limpert J, et al. High-speed modal decomposition of mode instabilities in high-power fiber lasers. *Opt Lett* (2011) 36(23):4572. doi:10.1364/ol.36.004572

13. Jauregui C, Eidam T, Otto H-J, Stutzki F, Jansen F, Limpert J, et al. Temperature-induced index gratings and their impact on mode instabilities in high-power fiber laser systems. *Opt Express* (2012) 20(1):440. doi:10.1364/oe.20.000440

14. Otto H-J, Stutzki F, Jansen F, Eidam T, Jauregui C, Limpert J, et al. Temporal dynamics of mode instabilities in high-power fiber lasers and amplifiers. *Opt Express* (2012) 20(14):15710. doi:10.1364/oe.20.015710

15. Otto HJ, Jauregui C, Eidam T, Stutzki F, Jansen F, Limpert J, et al. Dynamics and origin of mode instabilities in high power fiber laser amplifiers. *CLEO Sci Innov Cleo_si* (2012) 20(12):10180–92. doi:10.1364/CLEO_SI.2012.CF2N.7

16. Jauregui C, Eidam T, Otto H-J, Jansen F, Stutzki F, Limpert J, et al. On the thermal origin of mode instabilities in high power fiber lasers Fiber Lasers IX Technol. *Syst Appl* (2012) 8237:82370D.

17. Dong L. Stimulated thermal Rayleigh scattering in optical fibers. *Opt Express* (2013) 9(6):2365–70. doi:10.1364/OE.21.002642

18. Jauregui-Misas C, Stihler C, Tünnermann A, Limpert J. Origin and evolution of phase-shifts in high-power fiber laser systems: Detailed insights into TMI. *SPIE* (2019) 10897:10897043. doi:10.1117/12.2508854

19. Zervas MN. Transverse-modal-instability gain in high power fiber amplifiers: Effect of the perturbation relative phase. *APL Photon* (2019) 4(2):022802. doi:10.1063/1.5050523

20. Jauregui C, Stihler C, Limpert J. Transverse mode instability. *Adv Opt. Photon* (2020) 12(2):429–84. doi:10.1364/aop.385184

21. Ye C, Petit L, Koponen JJ, Hu I, Galvanauskas A. Short-term and long-term stability in lasers and amplifiers. *IEEE J Sel Top Quan Electron.* (2014) 20(5):1. doi:10.1109/JSTQE.2014.2310657

22. Manek-Hönninger I, Boullet J, Cardinal T, Guillen F, Podgorski M, Ermeneux S, et al. Photodarkening and photobleaching of an ytterbium-doped silica double-clad LMA fiber. *Opt Infobase Conf Pap* (2007) 15(4):1606–11. doi:10.1364/oe.15.001606

23. Montiel I Ponsoda JJ, Söderlund MJ, Koplow JP, Koponen JJ, Honkanen S. Photodarkening-induced increase of fiber temperature. *Appl Opt* (2010) 49(22): 4139–43. doi:10.1364/ao.49.004139

24. Kong L, Leng J, Zhou P, Jiang Z. Thermally induced mode loss evolution in the coiled ytterbium doped large mode area fiber. *Opt Express* (2017) 25(19):23437. doi:10.1364/oe.25.023437

25. Feng Y, Zhang BM, Nilsson J. Photodarkening-induced phase distortions and their effects in single-channel and coherently combined Yb-doped fiber chirped pulse amplification systems. *J Light Technol* (2018) 36(23):5521–7. doi:10.1109/jlt.2018.2874086

26. Otto H-J, Modsching N, Jauregui C, Limpert J, Tünnermann A. Impact of photodarkening on the mode instability threshold. *Opt Express* (2015) 23(12):15265. doi:10.1364/oe.23.015265

27. Ward B. Theory and modeling of photodarkening-induced quasi static degradation in fiber amplifiers. *Opt Express* (2016) 24(4):3488. doi:10.1364/oe.24.003488

28. Bobkov KK, Bubnov MM, Aleshkina SS, Likhachev ME. Long-term mode shape degradation in large mode area Yb-doped pulsed fiber amplifiers. *Laser Phys Lett* (2017) 14(1):015102. doi:10.1088/1612-202x/14/1/015102

29. Mattsson KE. Low photo darkening single mode RMO fiber. *Opt Express* (2009) 17(20):17855. doi:10.1364/oe.17.017855

30. Leich M, Röpke U, Jetschke S, Unger S, Reichel V, Kirchhof J. Non-isothermal bleaching of photodarkened Yb-doped fibers. *Opt Express* (2009) 17(15):12588. doi:10.1364/oe.17.012588

31. Cao R, Lin X, Chen Y, Cheng Y, Wang Y, Xing Y, et al. 532 nm pump induced photodarkening inhibition and photo-bleaching in high power Yb-doped fiber amplifiers. *Opt Express* (2019) 27(19):26523. doi:10.1364/oe.27.026523

32. Jasapara J, Andrejco M, DiGiovanni D, Windeler R. Effect of heat and H2 gas on the photo-darkening of Yb +3 fibers. In: Conf. Lasers Electro-Optics 2006 Quantum Electron. Laser Sci. Conf. CLEO/QELS; 21-26 May 2006; Long Beach, CA, USA (2006). p. 2006 2–3.

33. Yoo S, Basu C, Boyland AJ, Sones C, Nilsson J, Sahu JK, et al. Photodarkening in Yb-doped aluminosilicate fibers induced by 488 nm irradiation. *Opt Lett* (2008) 33(11):1626. doi:10.1364/ol.32.001626

34. Engholm M, Norin L. Reduction of photodarkening in Yb/Al-doped fiber lasers. *Fiber Lasers V Technol Syst Appl* (2008) 6873:68731E. doi:10.1117/12.763218

35. Cao R, Chen G, Chen Y, Zhang Z, Lin X, Dai B, et al. Effective suppression of the photodarkening effect in high-power Yb-doped fiber amplifiers by H 2 loading. *Photon Res* (2020) 8(3):288. doi:10.1364/prj.381208

36. Zhao N, Liu Y, Li M, Li J, Peng J, Yang L, et al. Mitigation of photodarkening effect in Yb-doped fiber through Na^+ ions doping. *Opt Express* (2017) 25(15):18191. doi:10.1364/oe.25.018191

37. Engholm M, Jelger P, Laurell F, Norin L. Improved photodarkening resistivity in ytterbium-doped fiber lasers by cerium codoping. *Opt Lett* (2009) 34(8):1285. doi:10.1364/ol.34.001285

38. Jetschke S, Unger S, Schwuchow A, Leich M, Kirchhof J. Efficient Yb laser fibers with low photodarkening by optimization of the core composition. *Opt Express* (2008) 16(20): 15540. doi:10.1364/oe.16.015540

39. Liu S, Peng K, Zhan H, Ni L, Wang X, Wang Y, et al. 3 kW 20/400 Yb-doped aluminophosphosilicate fiber with high stability. *IEEE Photon J* (2018) 10(5):1–8. doi:10.1109/jphot.2018.2860584

40. Li Y, Liu S, Zhan H, Peng K, Sun S, Jiang J, et al. Fiber design and fabrication of Yb/Ce codoped aluminosilicate laser fiber with high laser stability. *IEEE Photon J* (2018) 10(4): 1–8. doi:10.1109/jphot.2018.2853665

41. Jauregui C, Stutzki F, Tünnermann A, Limpert J. Thermal analysis of Yb-doped high-power fiber amplifiers with Al:P co-doped cores. *Opt Express* (2018) 26(6):7614. doi:10.1364/oe.26.007614

42. Townsend JE, Poole SB, Payne DN. Solution-doping technique for fabrication of rare-earth-doped optical fibres. *Electron Lett* (1987) 23(7):329–31. doi:10.1049/el:19870244

43. Matejec V, Kasik I, Berkova D, Hayer M, Chomat M, Berka Z, et al. Properties of optical fiber performs prepared by inner coating of substrate tubes. *Ceram Silik* (2001) 45(2):62–9.

44. Wang Y, Gao C, Tang X, Zhan H, Peng K, Ni L, et al. 30/900 Yb-doped aluminophosphosilicate fiber presenting 6.85-kW laser output pumped with commercial 976-nm laser diodes. *J Light Technol* (2018) 36(16):3396–402. doi:10.1109/jlt.2018.2823504

45. Saitoh K, Tsuchida Y, Koshiba M. Design of effectively single-mode leakage channel fibers with large mode area and low bending loss. *IEICE Electron Express* (2009) 6(7): 412–7. doi:10.1587/elex.6.412

46. Wang X, Lou S, Lu W, Sheng X, Zhao T, Hua P. Bend resistant large mode area fiber with multi-trench in the core. *IEEE J Sel Top Quan Electron.* (2016) 22(2):117–24. doi:10.1109/jstqe.2015.2461456

47. Jetschke S, Röpke U. Power-law dependence of the photodarkening rate constant on the inversion in Yb doped fibers. *Opt Lett* (2009) 34(1):109–11. doi:10.1364/ol.34.000109

48. Jetschke S, Unger S, Schwuchow A, Leich M, Jäger M. Role of Ce in Yb/Al laser fibers: Prevention of photodarkening and thermal effects. *Opt Express* (2016) 24(12):13009. doi:10.1364/oe.24.013009

49. Cao R, Wang Y, Chen G, Zhao N, Xing Y, Liu Y, et al. Investigation of photodarkening-induced thermal load in Yb-doped fiber lasers. *IEEE Photon Technol. Lett.* (2019) 31(11):809–12. doi:10.1109/lpt.2019.2906773

frontiers | Frontiers in Physics

TYPE Original Research
PUBLISHED 26 January 2023
DOI 10.3389/fphy.2023.1123818

OPEN ACCESS

EDITED BY
Shuo Liu,
Hebei University of Technology, China

REVIEWED BY
Hongbao Xin,
Jinan University, China
Xusan Yang,
Northwestern University, United States

*CORRESPONDENCE
Yifan Qin,
q1025hb007@163.com

SPECIALTY SECTION
This article was submitted to Optics and Photonics, a section of the journal Frontiers in Physics

RECEIVED 14 December 2022
ACCEPTED 13 January 2023
PUBLISHED 26 January 2023

CITATION
Zhang Y, Su W, Qin Y, Jin W, Zhang Y, Liu Z and Yuan L (2023), All-fiber probing of aluminized RDX particle micro-explosion. *Front. Phys.* 11:1123818. doi: 10.3389/fphy.2023.1123818

All-fiber probing of aluminized RDX particle micro-explosion

Yu Zhang[1], Wenjie Su[1], Yifan Qin[1]*, Wei Jin[1], Yaxun Zhang[1], Zhihai Liu[1,2] and Libo Yuan[1,3]

[1]Key Lab of In-Fiber Integrated Optics, Ministry Education of China, Harbin Engineering University, Harbin, China, [2]National Demonstration Center for Experimental Physics Education, Harbin Engineering University, Harbin, China, [3]Photonics Research Center, Guilin University of Electronics Technology, Guilin, China

Investigating the thermal decomposition characteristics and mechanisms of nano- and submicron-aluminized 1,3,5-trinitro-1,3,5-triazine (RDX) is essential to optimize the formulations and improve combustion/detonation efficiencies. However, no research has focused on the microscopic scale of a single aluminized RDX particle. We demonstrate an all-fiber probing method for the violent thermal decomposition of a single nano-aluminized micron-RDX particle, which we address as micro-explosion in this paper. We believe studying micro-explosion will be beneficial to the research of thermal decomposition. In experiments, we first characterize the micro-explosion as a three-step process, i.e., melting, first decomposition, and second decomposition. Then, we measure micro-explosion properties, i.e., shockwave-like flow velocity, initiation energy threshold, and shockwave-like flow pressure. Among the aluminized RDX particles with 0%, 5%, 10%, 15%, 20%, 25%, and 30% surface coverage ratios (SCRs), the sample with 20% surface coverage ratio shows the highest flow velocity and force, which are about 69.9 mm/s and 39.4 μN, respectively. Moreover, the threshold decreases with rising surface coverage ratios, and the mean threshold of 30% surface coverage ratio is 75 μJ. The experimental results prove that the all-fiber micro-explosion probing method is feasible, safe, and robust.

KEYWORDS

fiber optics, fiber optics sensor, aluminized RDX, nano-Al particle, thermal decomposition

1 Introduction

Energetic materials, e.g., explosives, pyrotechnics, and propellants, have a wide range of civilian and military applications. As a solid-propellant and an explosive, 1,3,5-trinitro-1,3,5-triazine (RDX) has drawn extensive attention [1, 2]. To improve combustion/detonation performance, RDX is usually mixed with metallic fuel particles (e.g., Al, Mg, B, and Zr) [3]. Al is the most popular additive for RDX due to its high enthalpy of combustion and low cost.

The combustion/detonation performance of aluminized RDX depends on the size of Al particles [4]. Coarse Al powder with a limited surface area has a high ignition threshold and low energy release rate, while nano- and submicron-Al particles with excellent dispersity have features of rapid combustion and large heat generation [5, 6]. It is known that thermal decomposition is the initial process of aluminized RDX combustion and detonation. Therefore, investigating the thermal decomposition characteristics and mechanisms of nano- and submicron-aluminized RDX is essential to optimize the formulations and improve combustion/detonation efficiencies.

Through simulations, some research has been performed to investigate the thermal pathways of nano-aluminized RDX. For example, X. -H. Ju et al. examined the thermal decomposition of RDX on nano-Al particles by reactive dynamics simulations using a parameterized reactive force field with low gradient correction (ReaxFF-lg). They confirmed

that the energy release rate of RDX was dramatically enhanced by nano-Al [7]. Then, X. -H. Ju et al. simulate the thermal decomposition of RDX systems with Al, surface-nitrided Al, and surface-oxidized Al nano-particles. They found different thermal decomposition pathways for these particles [8]. S. Zhang et al. mixed partially passivated nano-Al particles with RDX, TNT, and TNT/RDX supercells. They proved that the thermal decomposition process of TNT/RDX/nano-Al has six stages by numerical calculations [4].

Because of lacking prior knowledge, it is not easy to acquire all intermediate processes in simulations. Therefore, much work has been dedicated to nano- and submicron-aluminized RDX decomposition experiments. For instance, D. E. G. Jones et al. studied the thermal decomposition behaviors of nano-Al, submicron-Al, and aluminized RDX powders. They proved Al's reactivity decreased with rising particle diameter using differential scanning calorimetry (DSC), simultaneous thermogravimetry and differential thermal analysis (TG-DTA), and accelerating rate calorimeter (ARC) [9]. C. An et al. focused on the influence of nano-Al particles on the thermal decomposition of RDX. They found that the decomposition peak temperature of RDX was reduced by nano-Al particles [10]. H. Ren et al. integrated RDX with nano-Al particles and Viton using a two-solvent strategy. The thermal analysis indicated that nano-Al particles could accelerate the energy release of decomposition [11].

Despite the efforts on the thermal decomposition of nano- and submicron-aluminized RDX, no research has focused on the dynamic physiochemical process of a single aluminized RDX particle. Experiments of a single aluminized RDX particle could provide a better understanding of how Al particles affect the thermal decomposition of RDX.

This paper demonstrates an all-fiber probing method for the thermal decomposition of a single nano-aluminized micron-RDX particle. A microfabricated fiber probe locally coated with gold absorbs energy from laser pulses and transfers heat to the surface of an aluminized RDX particle. As a result, the particle absorbs heat rapidly and undergoes a violent thermal decomposition. We find that a single particle's violent thermal decomposition shows micro-scale phenomena (e.g., dispersion of product particles and gas flow with a shockwave-like morphology) that mimic the macro-scale phenomena of an explosion [12–14]. Thus, we define the violent thermal decomposition of a single particle as micro-explosion. Note that the definition of micro-explosion here differs from the one applied in the combustion process of slurry droplet fuels [15–18]. The micro-explosion process is simultaneously recorded by a homemade fiber Fabry-Perot (F-P) pressure sensor and a high-speed camera. The all-fiber micro-explosion probing method is cost-effective, robust, and environmentally insensitive. In addition, as the mass of the aluminized explosive is minimal, it is safe to carry out the experiments in labs without explosion protection equipment. Therefore, we believe the micro-explosion probing method could be an alternative to conventional methods (e.g., DSC, TG-DTA, ARC) for studying aluminized RDX thermal decomposition.

2 Materials and methods

2.1 Materials

2.1.1 Nano-aluminized micron-RDX particle

We use magnetron sputtering to coat nano-Al particles (purity 99.999%) on the surface of a micron-RDX particle, maximizing reactive surface area. The mean particle sizes of nano-Al and micron-RDX are about 400 nm and 10 μm, respectively. The radio frequency sputter (JS-1600, HTCY) works under vacuum conditions. Figure 1A shows the optical micrograph of an uncoated micron-RDX particle. Figure 1B shows that the surface of the micron-RDX particle is uniformly coated with nano-Al. The density of nano-Al deposited on the surface of RDX particles is controllable by adjusting the sputtering time. For subsequent experiments, aluminized micron-RDX particles with different surface coverage ratios (SCRs, i.e., 0%, 5%, 10%, 15%, 20%, 25%, and 30%) are obtained. The SCRs are calculated using micrographs like Figure 1B with ImageJ (RRID: SCR_003070).

2.1.2 The fiber probe for heat generation

We micro-fabricate a segment of single-mode fiber (SMF, FullBand G.652, YOFC) to acquire a fiber probe with a gold-coated parabolic-shaped tip using a unique three-step procedure. The SMF fiber has an effective group index of refraction of 1.476 at 1,550 nm and a mode field diameter of ~10.3 μm at 1,550 nm. The first step is selective chemical etching. The chemical etching solution comprises hydrofluoric acid (HF) and xylene C_8H_{10} [19]. The volume ratio for HF and C_8H_{10} is 1.5:1. The SMF is inserted into the etching solution for 60 min at room temperature, and a cone-shaped fiber tip is achieved. The second step is discharged current fusion molding. We generate a single arc discharge with a short fusion time using a fusion splicer (FSM-100P+, Fujikura). The arc discharge molds the cone-shaped fiber tip into a parabolic-shaped one. In the final step, we use the sputter JS-1600 to realize gold coating on the surface of the parabolic-shaped fiber tip. When pumped with a pulsed laser, the fiber probe can efficiently absorb heat from laser pulses due to multiple total reflections, generating a thermal field to initiate micro-explosion (Figure 1C). Figure 1D shows the optical micrograph of the fiber probe.

2.1.3 The fiber F-P pressure sensor

We combine an SMF (FullBand G.652, YOFC), a silica capillary, and a gelatin diaphragm to fabricate a fiber F-P pressure sensor. First, a gelatin diaphragm is fixed on an end face of a small segment of silica capillary with ultraviolet glue. The thickness of the gelatin diaphragm is 800 nm, and the glass capillary has an inner diameter of 400 μm. Then, an SMF is inserted in the silica capillary through the other end face. The position of the SMF is adjusted by a motorized micromanipulator (MP-225, Sutter Instrument). Next, we coaxially align the SMF and the silica capillary, whose end faces are separated by 89 μm. As a result, a microcavity is formed between the SMF and the gelatin diaphragm. At last, we seal the microcavity and fix the SMF with ultraviolet glue. When the SMF is pumped with a laser, the fiber F-P microcavity can detect external pressure variation through the deflection of the gelatin diaphragm (Figure 1E). Figure 1F shows the optical micrograph of the F-P pressure sensor.

2.2 Methods

As shown in Figure 2, the experimental setup comprises three parts, the micro-explosion initiation module, the pressure sensing module, and the microscope.

The micro-explosion initiation module includes a 1,550-nm pulsed laser (VFLS-1550-M-PL, Connet), the motorized micromanipulator (MP-225, Sutter Instrument), and the micro-

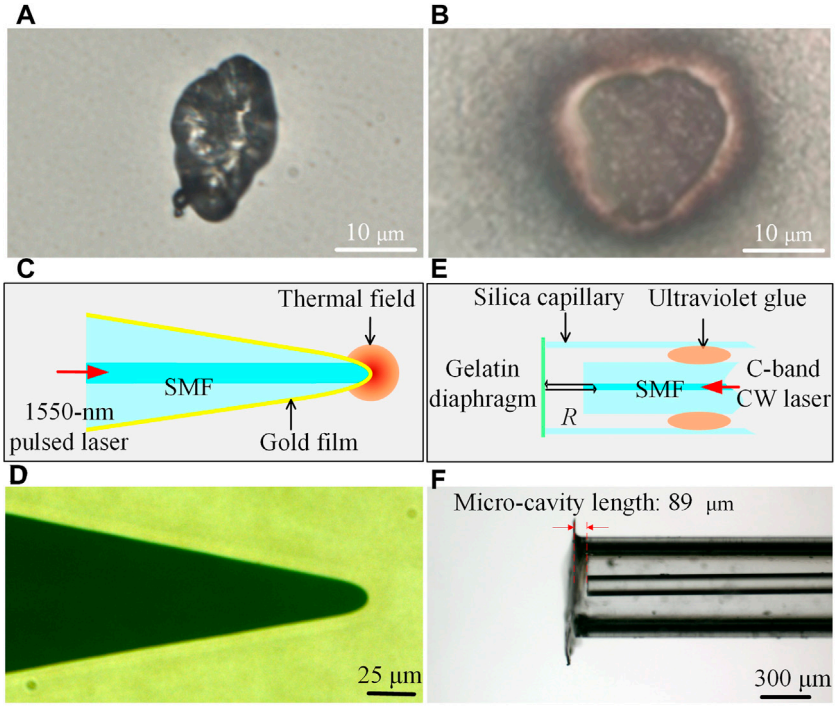

FIGURE 1
Preparation of the materials. **(A)** An uncoated micron-RDX particle. **(B)** A micron-RDX particle coated with coated nano-Al. **(C)** Schematic of the fiber probe. **(D)** Picture of the fiber probe. **(E)** Schematic of the fiber F-P sensor. **(F)** Picture of the fiber F-P sensor. The micro-cavity length is 89 μm.

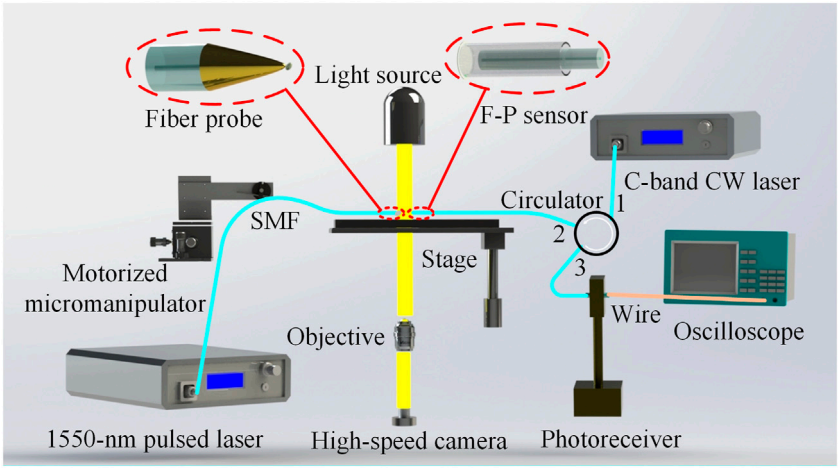

FIGURE 2
Experimental setup for probing micro-explosion. This figure is not to scale.

fabricated fiber probe. The 1,550-nm pulsed laser characterizes a 1-MHz repetition rate and a 10-ns full-width-at-half-maximum (FWHM) pulse width. The pulsed laser's single-mode pigtail (SMF-28, Corning) is spiced to the micro-fabricated fiber probe. The pulses from the laser are injected into the fiber probe, providing a thermal field to initiate the micro-explosion. The motorized micromanipulator holds part of the laser pigtail, controlling the micro-explosion initiation position on the aluminized RDX.

The pressure sensing module is composed of the fiber F-P pressure sensor, a C-band wavelength-tunable continuous wave (CW) laser (VLSP-C-M-TL, Connet), a circulator, an InGaAs photoreceiver (Model 2117-FC, New Focus), and a digital storage oscilloscope (SDS6000A, Siglent). The CW laser's single-mode pigtail (SMF-28, Corning) and the fiber sensor are spiced to Port 1 and Port 2 of the circulator, respectively. The photoreceiver and Port 3 of the circulator are connected. The laser is pumped into the microcavity of the fiber

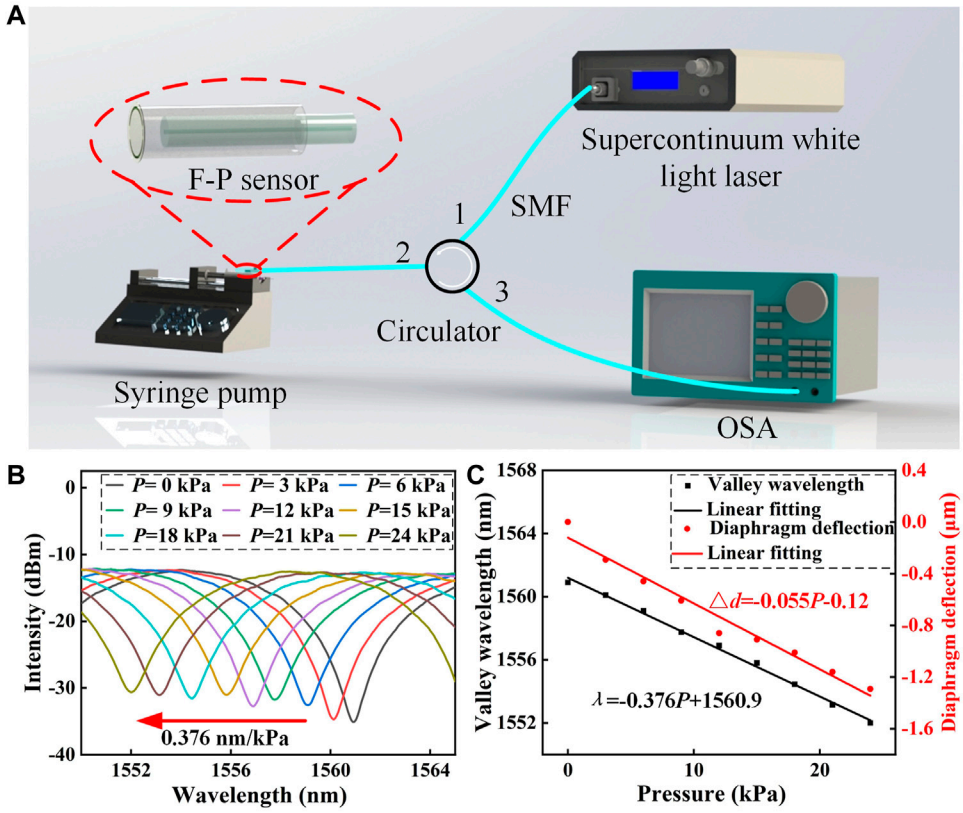

FIGURE 3
Static pressure test of the fiber F-P sensor. **(A)** Experimental setup of the static pressure test. This figure is not to scale. **(B)** Spectra collected under different pressures. **(C)** The relationship between valley wavelength λ and pressure P, and the relationship between diaphragm deflection Δd and pressure P.

F-P pressure sensor through the circulator. The photoreceiver collects the reflected light from the sensor through the circulator and sends the amplified electrical signal to the digital storage oscilloscope through a variable bandpass filter. The pressure variation originating from the micro-explosion can be acquired by interpreting the waveform.

Aluminized RDX sample is placed on a two-dimensional stage of an inverted microscope (IX73, Olympus). The fiber probe and the F-P pressure sensor, whose optical axes are aligned with each other, are located on each side of the sample. The microscope's light source illuminates the aluminized RDX sample, and a high-speed camera (Mini AX100, Photron) records the micro-explosion process through a ×40 objective. The camera's maximum frame rate is 13,600 fps for a 512 × 512 image, capable of measuring micro-explosion thresholds and velocities.

3 Results and discussion

3.1 Characterization of the fiber F-P pressure sensor

To characterize the performance of the fiber F-P pressure sensor, we conduct a static pressure test [20–22]. Figure 3A shows the static pressure test setup, including a supercontinuum white light laser (SuperK COMPACT, NKT Photonics), a circulator, a syringe pump (LSP01-1A, Longer Pump), and an optical spectrum analyzer (OSA, AQ6373, Yokogawa). We seal the pressure sensor inside the syringe pump. The supercontinuum white light laser's single-mode pigtail and the OSA are connected to Port 1 and Port 3 of the circulator, respectively. The fiber sensor is spiced to Port 2 of the circulator. We pump the laser into the microcavity of the fiber F-P pressure sensor through the circulator. The OSA collects the reflected light from the sensor through the circulator. Figure 3B shows the spectra collected under different pressures applied by the syringe pump. As the rising pressure deforms the diaphragm and reduces the F-P micro-cavity length, the fringes shift toward the shorter wavelength. Figure 3C shows the relationship between valley wavelength λ and pressure P. According to the linear fitting, the wavelength shift caused by pressure P is 0.376 nm/kPa. The length of the micro-cavity d can be demodulated by

$$d = \lambda_1\lambda_2/(2|\lambda_1 - \lambda_2|), \quad (1)$$

where λ_1 and λ_2 are adjacent valley wavelengths of the same fringe [23]. Thus, the micro-cavity length of the sensor is ~89 μm, in agreement with the value in Figure 1F. Thus, fringes and Eq. 1 can acquire the diaphragm deflection Δd originating from pressure. Figure 3C shows the relationship between diaphragm deflection Δd and pressure P. According to the linear fitting, the sensor's pressure sensitivity between 0 and 24 kPa is 0.055 μm/kPa.

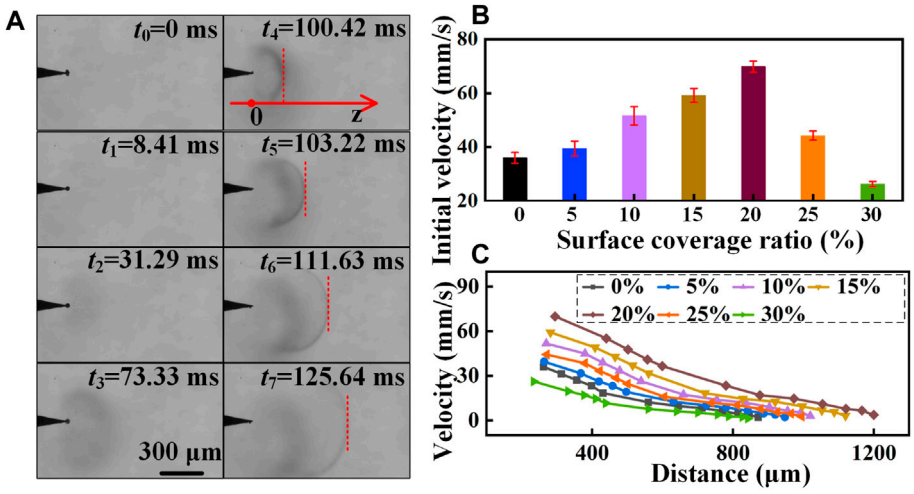

FIGURE 4
The process of micro-explosion. **(A)** Pictures of micro-explosion acquired at different moments. The dashed red lines indicate the flow fronts of shockwave-like flow. **(B)** The relationship between the initial flow velocity and surface coverage ratio. Error bars represent standard error. **(C)** The relationship between the flow velocity and the distance. The distance is calculated from the fiber probe tip to the flow front along the optical axis.

3.2 Measurement of micro-explosion properties

To prove the probing method's capability, we first characterize the process of nano-aluminized micron-RDX micro-explosion. The typical process of RDX thermal decomposition includes three steps, which are melting, first decomposition, and second decomposition [2]. Melting is an endothermic process, while first decomposition and second decomposition are exothermic processes. Figure 4A (the frame rate is 2000 frames and 1,024 × 1,024 image of the original video) confirms that micro-explosion is composed of melting, first decomposition, and second decomposition. First, the pulses from the 1,550-nm laser accumulate energy on the gold film of the fiber probe and elevate the temperature applied to the sample, causing melting. The pictures at t_0 and t_1 show the process of melting, during which the sample becomes spherical. Then, the first decomposition occurs, slowly releasing heat and spreading reaction products, as shown in pictures at t_2 and t_3. Slight mass loss can be observed during the first decomposition. At last, the second decomposition generates a gas flow with a shockwave-like morphology, which mainly propagates along the optical axis of the fiber probe. As shown in pictures at $t_4 - t_7$, some reaction products spread with the shockwave-like flow, indicating the flow front. Red dashed lines mark the locations of the flow fronts at different moments. The second decomposition is accompanied by enormous mass loss. Then, we measure micro-explosion properties, i.e., shockwave-like flow velocity, initiation energy threshold, and shockwave-like flow pressure.

3.2.1 Shockwave-like flow velocity

We measure the velocities of aluminized micron-RDX particles with different SCRs (i.e., 0%, 5%, 10%, 15%, 20%, 25%, and 30%). The shockwave-like flow velocities are acquired by frame-to-frame analysis. Figure 4B shows the relationship between the initial flow velocity and SCR. The initial velocity is acquired at the first moment (e.g., t_4) when a clear flow front forms. The measurement of each SCR is conducted 10 times. Note that the laser power stays unchanged during the 10 × 7 measurements. The mean initial velocities of 0%, 5%, 10%, 15%, 20%, 25%, and 30% SCRs are about 36.0, 39.5, 51.6, 59.1, 69.9, 44.2, and 26.2 mm/s, respectively. It can be found that the initial velocity first increases and then decreases with rising SCRs. The initial velocity reaches the maximum when the SCR is 20%. The reason for the rise of the initial velocity under 20% SCR is that the nano-Al can catalyze the micro-explosion process, enhancing the second decomposition. However, a high SCR of Al restricts the propagation of flows, reducing the initial velocity of micro-explosions.

Figure 4C shows the relationship between the flow velocity and the distance. The distance is calculated from the fiber probe tip to the flow front along the optical axis. It can be found that the velocity decreases with increasing distance. Moreover, the locations where flow fronts form are closer to the fiber probe tip with lower initial velocities.

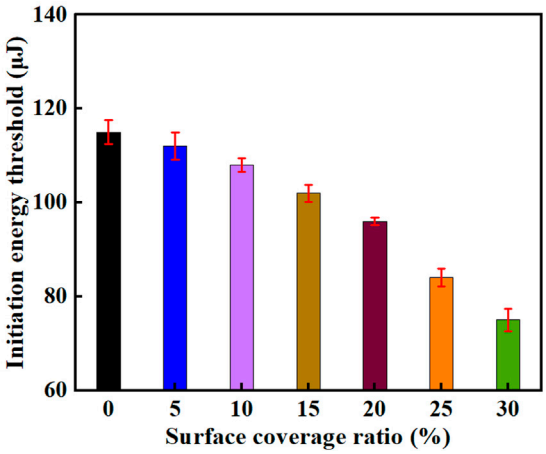

FIGURE 5
The relationship between the initiation energy threshold and surface coverage ratio. Error bars represent standard error.

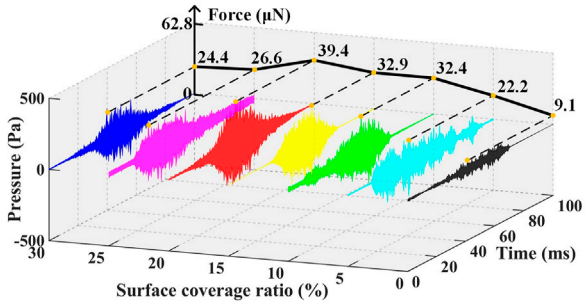

FIGURE 6
The shockwave-like flow pressures and corresponding forces of different surface coverage ratios as a function of time.

3.2.2 Initiation energy threshold

We measure the initiation energy thresholds of aluminized micron-RDX particles with different SCRs. The initiation energy threshold is the energy of laser pulses, which will lead to a micro-explosion. The energy is integrated from the moment when the laser is turned on to the beginning of the second decomposition. Figure 5 shows the relationship between the initiation energy threshold and SCR. The measurement of each SCR is conducted 10 times. Note that the laser power stays unchanged during the 10 × 7 measurements. The mean thresholds of 0%, 5%, 10%, 15%, 20%, 25%, and 30% SCRs are about 115, 112, 108, 102, 96, 84, and 75 μJ, respectively. It can be found that the threshold decreases with rising SCRs. The threshold is at the maximum when the SCR is 0%. The threshold reduction is attributed to the catalyzation of nano-Al particles.

3.2.3 Shockwave-like flow pressure

We measure the shockwave-like flow pressure using the fiber F-P pressure sensor. The distance between the sensor and the probe is about 300 μm along the optical axis. To achieve a high-frequency response to flow pressure, we replace the setup in Figure 3A with the one in Figure 2. The wavelength of the C-band CW laser is tuned to a quadrature point of the fringe of zero external pressure. The signal from the sensor is detected by the photoreceiver and displayed by the oscilloscope. The relationship between the reflected light intensity I_R and the micro-cavity length d is

$$I_R = 2R\left[1 - \cos\left(\frac{4\pi nd}{\lambda_0} + \pi\right)\right]I_0, \quad (2)$$

where R is the reflectivity of the micro-cavity, λ_0 is the wavelength of the C-band laser, n is the refractive index of the micro-cavity medium, and I_0 is the input light intensity. As mentioned above, we have acquired the relationship between diaphragm deflection Δd and pressure P. Thus, the flow pressure can be real-time demodulated using the waveform recorded by the oscilloscope and Eq. 2.

Figure 6 shows the shockwave-like flow pressures and corresponding forces of different SCRs as a function of time. Note that the laser power stays unchanged during the seven measurements. The high-frequency vibrations of the traces in Figure 6 are attributed to the impacts of the reaction products. The envelopes of the traces depict the flow propagations. The peak forces of 0%, 5%, 10%, 15%, 20%, 25%, and 30% SCRs are about 9.1, 22.2, 32.4, 32.9, 39.4, 26.6, and 24.4 μN, respectively. It can be found that the peak force first increases and then decreases with rising SCRs. The peak force reaches the maximum when the SCR is 20%. Moreover, the vibration signal duration is shorter when the peak force is larger. These experimental results correspond to those in Figures 4B, C.

4 Conclusion

In conclusion, we demonstrate an all-fiber probing method for the micro-explosion of nano-aluminized micron-RDX particles. A microfabricated gold-coating fiber probe absorbs energy from laser pulses, heating an aluminized RDX particle through thermal conduction. As a result, the particle rapidly absorbs heat and undergoes the process of micro-explosion. A homemade fiber F-P pressure sensor and a high-speed camera simultaneously record the micro-explosion process. In experiments, we first characterize the micro-explosion as a three-step process, i.e., melting, first decomposition, and second decomposition. Then, we perform measurements of micro-explosion properties, i.e., shockwave-like flow velocity, initiation energy threshold, and shockwave-like flow pressure. Among the aluminized RDX particles with 0%, 5%, 10%, 15%, 20%, 25%, and 30% SCRs, the sample with 20% SCR has the highest flow velocity and force, which are about 69.9 mm/s and 39.4 μN, respectively. These results are attributed to the tradeoff between catalyzation and restriction of nano-Al particles. Moreover, the threshold decreases with rising SCRs, and the mean threshold of 30% SCR is 75 μJ. The all-fiber micro-explosion probing method is cost-effective, robust, and environmentally insensitive. Due to the minimal mass of the aluminized RDX, it is safe to carry out the experiments without explosion protection equipment. Furthermore, the movement of the fiber probe can adjust the shockwave-like flow propagation direction, providing additional flexibility for future applications. Therefore, we believe the micro-explosion probing method will be a powerful tool for studying aluminized RDX.

Data availability statement

The original contributions presented in the study are included in the article/supplementary material, further inquiries can be directed to the corresponding author.

Author contributions

Conception, YuZ, WS, YQ, WJ, YaZ, ZL, and LY; Investigation, YuZ, WS, YQ, WJ, YaZ, ZL, and LY; Design, YuZ, WS, YQ, WJ, YaZ, ZL, and LY; Software, WS; Data acquisition, YuZ, WS, YQ, WJ, YaZ, ZL, and LY; Analysis, YuZ, WS, YQ, WJ, YaZ, ZL, and LY; Original

draft, YuZ, WS, YQ, WJ, YaZ, ZL, and LY; Review and editing, YuZ, WS, YQ, WJ, YaZ, ZL, and LY; Supervision, YuZ, YQ, YaZ, ZL, and LY; Project administration, YuZ, YQ, YaZ, ZL, and LY; Funding acquisition, YuZ, YQ, YaZ, ZL, and LY. All authors approved the submitted version.

Funding

This work was supported by the National Natural Science Foundation of China (61975039, 62175046, 62205086); China Postdoctoral Science Foundation (2022M720940); Heilongjiang Provincial Natural Science Foundation of China (YQ2020F011); the 111 Project (B13015); Fundamental Research Funds of Harbin Engineering University.

Conflict of interest

The authors declare that the research was conducted in the absence of any commercial or financial relationships that could be construed as a potential conflict of interest.

Publisher's note

All claims expressed in this article are solely those of the authors and do not necessarily represent those of their affiliated organizations, or those of the publisher, the editors and the reviewers. Any product that may be evaluated in this article, or claim that may be made by its manufacturer, is not guaranteed or endorsed by the publisher.

References

1. Khichar M, Patidar L, Thynell S. Comparative analysis of vaporization and thermal decomposition of cyclotrimethylenetrinitramine (RDX). *J Propul Power* (2019) 35: 1098–107. doi:10.2514/1.b37643

2. Pagoria PF, Lee GS, Mitchell AR, Schmidt RD. A review of energetic materials synthesis. *Thermochim Acta* (2002) 384:187–204. doi:10.1016/s0040-6031(01)00805-x

3. Hao W, Niu L, Gou R, Zhang C. Influence of Al and Al_2O_3 nanoparticles on the thermal decay of 1,3,5-trinitro-1,3,5-triazinane (RDX): Reactive molecular dynamics simulations. *J Phys Chem C* (2019) 123:14067–80. doi:10.1021/acs.jpcc.9b03575

4. Meng J, Wang C, Cheng M, Zhang S, Gou R, Chen Y, et al. The thermal decomposition behavior of the TNT-RDX-Al explosive by molecular kinetic simulation. *Int J Quan Chem.* (2021) 121:e26635. doi:10.1002/qua.26635

5. Sundaram D, Yang V, Yetter RA. Metal-based nanoenergetic materials: Synthesis, properties, and applications. *Prog Energ Combust. Sci.* (2017) 61:293–365. doi:10.1016/j.pecs.2017.02.002

6. Sergienko AV, Popenko EM, Slyusarsky KV, Larionov KB, Dzidziguri EL, Kondratyeva ES, et al. Burning characteristics of the HMX/CL-20/AP/polyvinyltetrazole binder/Al solid propellants loaded with nanometals. *Propellants Explos Pyrotech* (2019) 44:217–23. doi:10.1002/prep.201800204

7. Mei Z, An Q, Zhao F-Q, Xu S-Y, Ju X-H. Reactive molecular dynamics simulation of thermal decomposition for nano-aluminized Explosives. *Phys Chem Chem Phys* (2018) 20: 29341–50. doi:10.1039/c8cp05006f

8. Zhao Y, Zhao F-Q, Xu S-Y, Jua X-H. Molecular reaction dynamics simulation of thermal decomposition for aluminiferous RDX composites. *Comp Mater Sci* (2020) 177: 109556. doi:10.1016/j.commatsci.2020.109556

9. Kwok QSM, Fouchard RC, Turcotte AM, Lightfoot PD, Bowes R, Jones DEG. Characterization of Aluminum nanopowder compositions. *Propellants Explos Pyrotech* (2002) 27:229–40. doi:10.1002/1521-4087(200209)27:4<229::aid-prep229>3.0.co;2-b

10. Hou C, Geng X, An C, Wang J, Xu W, Li X. Preparation of Al nanoparticles and their Influence on the thermal decomposition of RDX. *Cent Eur J Energ Mater* (2013) 10: 123–33.

11. Yan T, Ren H, Liu J, Jiao Q. Facile preparation and synergetic energy releasing of nano-Al@RDX@Viton hollow microspheres. *Chem Eng J* (2020) 379:122333. doi:10.1016/j.cej.2019.122333

12. He S, Tan K, Song Q, He G, Cao W. Thermally stable and low-sensitive aluminized explosives with improved detonation performance. *Propellants Explos Pyrotech* (2021) 46: 1428–35. doi:10.1002/prep.202100047

13. Zhang K, Feng X, Zhao J, Feng B, Wang X. Effect of aluminum powder content on air blast performance of RDX-based explosive grenade charge. *Adv Mater Sci Eng* (2022) 2022:1–7. doi:10.1155/2022/1751182

14. Wang H, Liu Y, Bai F, Huang F. Study on the reaction rate model for shock initiation of aluminized hexahydro-1, 3, 5-trinitro-1, 3, 5-triazine (RDX) explosive under shock waves. *J Appl Phys* (2021) 129:215902. doi:10.1063/5.0048443

15. Kadota T, Yamasaki H. Recent advances in the combustion of water fuel emulsion. *Prog Energ Combust Sci* (2002) 28:385–404. doi:10.1016/s0360-1285(02)00005-9

16. Gan Y, Qiao L. Combustion characteristics of fuel droplets with addition of nano and micron-sized aluminum particles. *Combust Flame* (2011) 158:354–68. doi:10.1016/j.combustflame.2010.09.005

17. Morozumi Y, Saito Y. Effect of physical properties on microexplosion occurrence in water-in-oil emulsion droplets. *Energy Fuels* (2010) 24(3):1854–9. doi:10.1021/ef9014026

18. Teixeira AR, Hermann RJ, Kruger JS, Suszynski WJ, Schmidt LD, Schmidt DP, et al. Microexplosions in the upgrading of biomass-derived pyrolysis oils and the effects of simple fuel processing. *ACS Sustain Chem Eng* (2013) 1(3):341–8. doi:10.1021/sc300148b

19. Tao M, Jin Y, Gu N, Huang L. A method to control the fabrication of etched optical fiber probes with nanometric tips. *J Optics-uk* (2009) 12:015503. doi:10.1088/2040-8978/12/1/015503

20. Xu F, Ren D, Shi X, Li C, Lu W, Lu L, et al. High-sensitivity Fabry–Perot interferometric pressure sensor based on a nanothick silver diaphragm. *Opt Lett* (2012) 37(2):133–135. doi:10.1364/ol.37.000133

21. Guo F, Fink T, Han M, Koester L, Turner J, Huang J. High-sensitivity, high-frequency extrinsic Fabry–Perot interferometric fiber-tip sensor based on a thin silver diaphragm. *Opt Lett* (2012) 37(9):1505–1507. doi:10.1364/ol.37.001505

22. Ma J, Jin W, Ho HL, Dai JY. High-sensitivity fiber-tip pressure sensor with graphene diaphragm. *Opt Lett* (2012) 37(13):2493–2495. doi:10.1364/ol.37.002493

23. Jiang Y. High-resolution interrogation technique for fiber optic extrinsic Fabry-Perot interferometric sensors by the peak-to-peak method. *Appl Opt* (2008) 47(6):925–932. doi:10.1364/ao.47.000925

frontiers | Frontiers in Physics

TYPE Brief Research Report
PUBLISHED 01 February 2023
DOI 10.3389/fphy.2023.1126903

OPEN ACCESS

EDITED BY
Zhenxu Bai,
Hebei University of Technology, China

REVIEWED BY
Jianping Huang,
Northeast Forestry University, China
Lihui Wang,
Guizhou University, China

*CORRESPONDENCE
Xiaoming Sun,
sunxiaoming@hrbust.edu.cn

SPECIALTY SECTION
This article was submitted to Optics and Photonics, a section of the journal Frontiers in Physics

RECEIVED 18 December 2022
ACCEPTED 10 January 2023
PUBLISHED 01 February 2023

CITATION
Wang Y, Sun X, Duan Y and Chen Y (2023), Three-dimensional measurement method based on the singular operator and the shortest path search technique. *Front. Phys.* 11:1126903. doi: 10.3389/fphy.2023.1126903

Three-dimensional measurement method based on the singular operator and the shortest path search technique

Yongliang Wang, Xiaoming Sun*, Yan Duan and Yan Chen

Harbin University of Science and Technology, Harbin, Heilongjiang, China

Coded structured light plays a crucial role in the field of non-contact three-dimensional measurement. To improve the accuracy, we propose a novel method based on shortest path search and edge and central singular operator, which is able to detect the edge of Gray code and locate its line shift fringes more accurately. Starting from the patterns of the Gray code edge and the center of the line shift strip, we develop the corresponding singular operators and hence the cost function. The Euler distance is used as the distance condition for the adjacent key points, which are located by the fast-marching algorithm. We propose a method to compute the graph with minimum energy by finding the shortest path. The shortest path was automatically calculated and found both the edge of the Gray code and the center of the bar stripe accurately.

KEYWORDS

three-dimensional measurement, Gray code edge, line-shift stripe center, singular operator, shortest path

1 Introduction

The rapid development of machine vision has had a great influence on the development of modern industry. One of the most important tasks of intelligent image processing is to increase the accuracy of three-dimensional (3D) measurement. 3D measurement based on structured projection light is one of the most important technologies in machine vision. It is widely used in robot assembly, visual inspection, medical treatment and other fields because it is easy to use, non-contact, non-destructive and efficient. The 3D measurement method of coded structured light is widely accepted by researchers because of its large field of view, high efficiency. The common 3D measurement methods with coded structured light consist of the phase shift code and the Gray code, which is combined with line shift fringe coding. However, when the structured light is encoded by a Grayscale code or a line-shift stripe, the edge of the Grayscale code and the center of the line-shift stripe are susceptible to deformation due to the varying surface shape, texture, and other factors of the object.

Edge detection is a popular topic in the image processing community. At the pixel level, the Sobel operator and the Prewitt operator [1] can be used to eliminate the deviation of individual points from the straight template of the Roberts operator [2]; Marr.H [3] proposed the Log operator based on the Laplacian operator. The Canny operator [4] can be used to detect and extract blurry edges associated with sharp edges. At the subpixel level, researchers have proposed many basic and advanced versions of subpixel edge

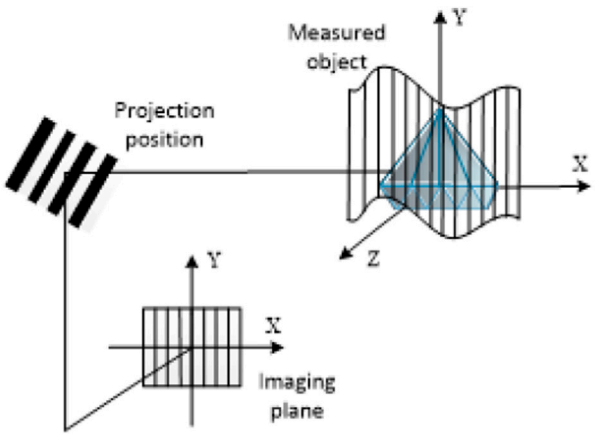

FIGURE 1
Multiline structured light measurement principle.

detection methods around interpolation and matching methods [5–7]. Jason [8] has achieved the positioning of the step edges of a given continuous space. Sui Liansheng [9] proposed the NURBS matching method to detect and locate the edge of the light strip. The Gray level moment method is an earlier moment method. In the literature [10], the suppression of pseudo edges is achieved by analyzing the influence of parameters on the positioning result during the detection process. Lyvers [11] proposed a subpixel edge detection method based on spatial moments. Zhu Hong [12] uses Zernike moment method on pixel-level edges obtained by classical operators and obtains a new recognition method. Li Jie [13] uses structural elements for image shape recognition and complete edge detection in images. There are also neural network techniques [14], Gray theory of image edge detection [15], diffuse edge detection method [16], and so on.

Despite continuous improvements, the pixel-level light streak detection method still struggles with shortcomings, such as susceptibility to noise and heavy dependence on a specific image requirement. We propose a method for detecting the edges of Gray stripes based on the techniques of singular operator and shortest path search in order to increase the positioning accuracy of the light strip edge.

2 Construction and calibration of experimental system platform

The 3D measurement system used in this work consists of three parts: Projection module, image acquisition module and image processing module.

The images encoded by the Gray scale code and the line shift strip are projected onto the surface of the object in chronological order by the projection module, and the surface image information of the measured object is acquired by the image acquisition module and transferred to the image processing module for post-processing and calculation to obtain the spatial coordinates of the sampling point of the surface of the measured object to realize 3D measurement. As is shown in Figure 1.

The principle of encoding and decoding is shown in Figure 2. In encoding, Gray code and line-shift strip do not interfere with each other. In decoding, the four-step line-shift strip is in a whole period of Gray code, which theoretically avoids the interference of position.

The experimental system is as follows: the camera and the projector are connected to the computer through serial ports; the encoded image is sequentially projected on the surface of the object to be measured, where the ball in the image is the object to be measured; the encoded image captured by the camera is decoded by the computer; the hardware configuration of the system consists of three major functional modules: the projection module is an InFocus 82 projector (resolution 1024 pixels × 768 pixels); the image capture module is a AT-200GE industrial camera (resolution 1624 × 1236); the image processing and computation module is the Dell Precision T7910. The real picture is shown in Figure 3.

3 Research on edge and centroid detection method based on shortest path search technology of singular operator

3.1 Principle of shortest path technology

As there is a phenomenon that the light stripes from the projector spread light fringes to dark stripes. Therefore, in this work, we use singular operators to improve the signal characteristics of the edge or the center, and the shortest path search technology is used to locate the sampling points of the edge or the center with high precision. The specific process is shown in figure 4:

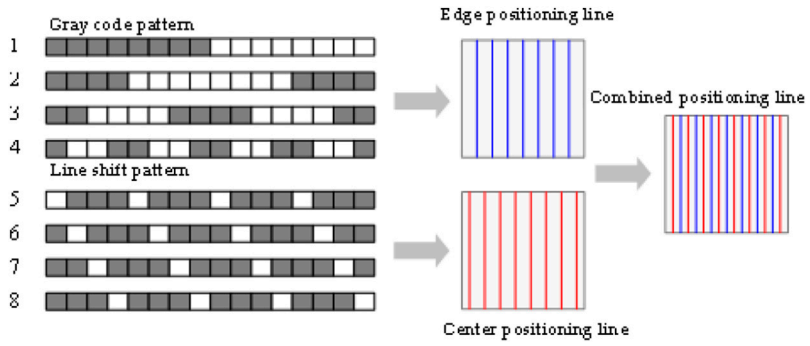

FIGURE 2
Principle of encoding and decoding by stripe edge and four-step line shift.

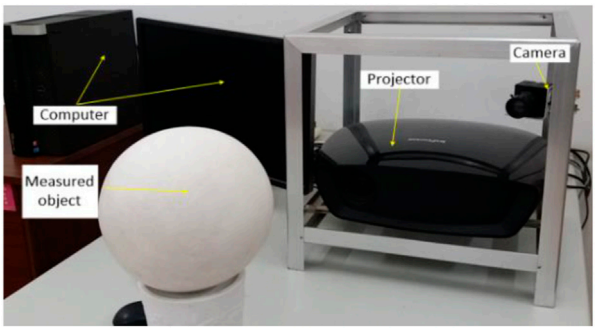

FIGURE 3
Experimental system.

Curve evolution theory is very effective in the field of image segmentation and feature extraction. Cohen [17] proposes a global minimum energy method for geometric active contours. Instead of specifying the initial path, this method only requires the key points on the path in advance and then determines the minimum energy curve between the two key points by solving the functional equation.

From the above, a brief summary of the procedure for finding the shortest path in the detection of Gray scale edges and the center of line shift fringes is given: The cost function is introduced by using the difference between the feature of the edge line or the center line and that of other positions in the image, so that the cost function at the edge or center line to be extracted is different from other values. Starting from the initial point, we solve the equation of the equation and obtain the minimum energy map. Finally, starting from the desired key points, the starting point can be obtained by searching along the direction in which the minimum energy decrease and the fastest change cannot be obtained, and the corresponding curve of the shortest path can be obtained.

3.2 Construction of shortest path cost function based on singular operators

Figure 5A is a standard gray code image. Projecting it onto the surface of the object to be measured, we get the image shown in Figure 5B.

In Figure 5A, the grayscale image at the striped edge of the scribed position Figures 6A, B, by comparing the change curve of the gray level and the gray gradient within the measurement range, it can be seen that the striped edge of the standard grayscale code has a good step property. The same treatment was performed for Figure 5B to obtain the curves in Figures 6C, D. It can be seen that the edge of the gray code stripe in the projected image corresponds to a smooth step curve.

According to the properties of the Gray level distribution of the Gray level edge in the coded image, the singularity operator of the Gray level edge is constructed as shown in Eq. 1:

$$\varphi_e(x,y,\sigma) = \frac{\left|I^e_{0,\theta,\sigma}(x,y) I^e_{1,\theta,\sigma}(x,y)\right|}{1+\left|I^e_{2,\theta,a\sigma}(x,y)\right|^2} \tag{1}$$

In the formula, a is the factor of the scale constant and the Gaussian kernel scale. $I^e_{0,\theta,\sigma}(x,y)$ is the zero-order derivative of the Gray code edge image along the direction $\theta(x,y)$ of the Gaussian kernel scale σ; $I^e_{1,\theta,\sigma}(x,y)$ is the first derivative of the Gray code edge image along the direction $\theta(x,y)$ at the Gaussian kernel scale σ; $I^e_{2,\theta,\sigma}(x,y)$ is the second derivative of the Gray code edge image along the direction $\theta(x,y)$ at the Gaussian kernel scale σ.

According to above, at the edge of the Gray code, the first derivative of the image reaches a local maximum and the second derivative goes to zero, giving a large value to singular operator; the singular operator has a solid response to the step signal and the smooth step curve and can suppress impulse signals and other noises in Gray code images, which is very suitable for stripe edge extraction.

In summary, the cost function for the shortest path of the singular Gray code edge detection operator is constructed as shown in Eq. 2:

$$P_e = \gamma I + (1-\gamma) g_e(\varphi_e(x,y,\sigma)) \tag{2}$$

In the formula, γ is a proportionality factor, a constant used to adjust the ratio of information after and before edge enhancement; $g_e(\varphi_e(x,y,\sigma))$ is a decreasing function of φ_e:

$$g_e = \max(\varphi_e(x,y,\sigma)) - \varphi_e(x,y,\sigma) \tag{3}$$

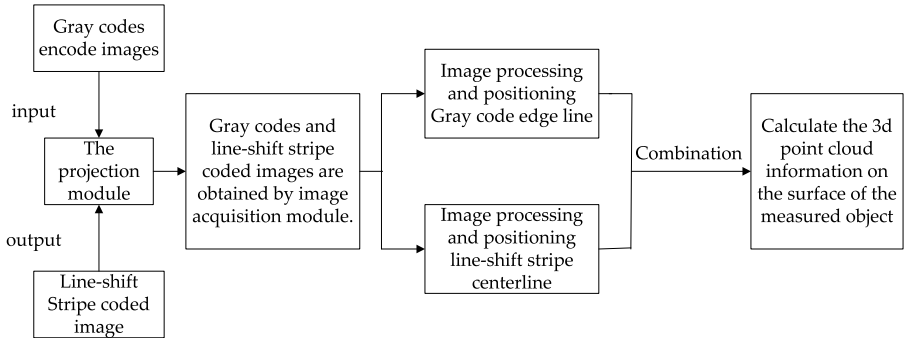

FIGURE 4
Workflow of 3D measurement system.

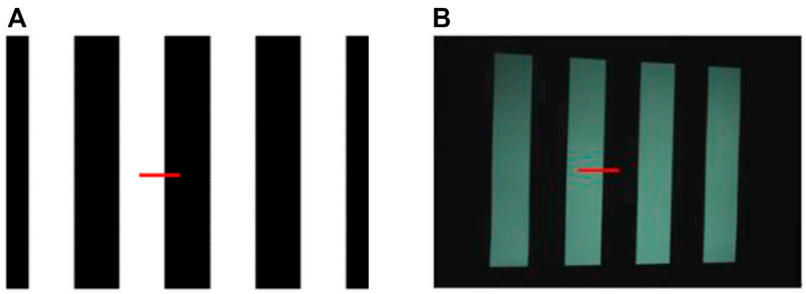

FIGURE 5
The standard image of Gray code and image projection. **(A)** Standard Gray code; and **(B)** Projection image of plane.

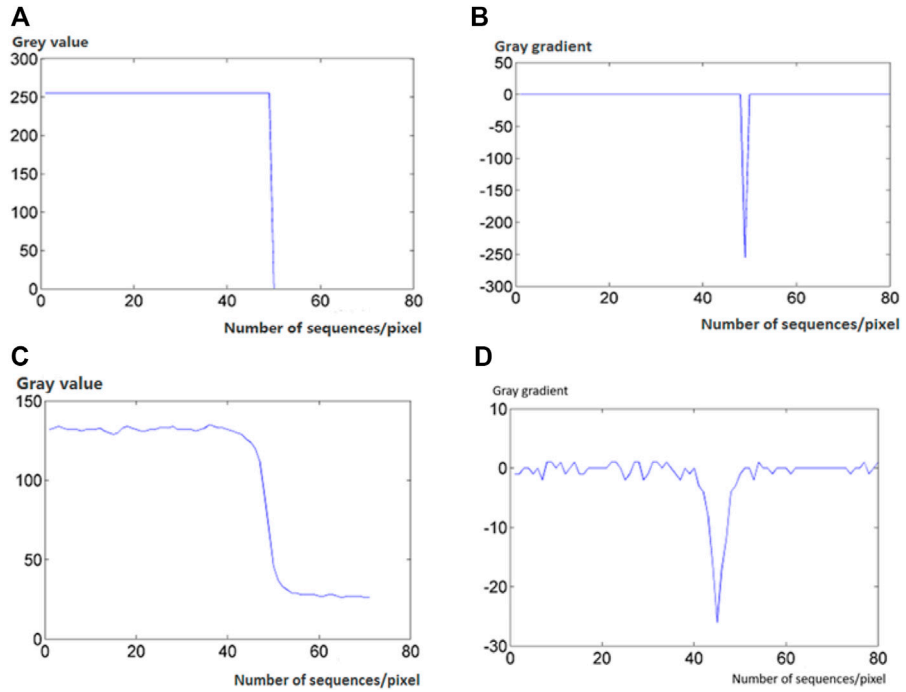

FIGURE 6
Grey value and grey gradient curve of fringe edge. **(A)** Grey value of standard Gray code; **(B)** Grey gradient of standard Gray code; **(C)** Grey value of projection plane with Gray code; and **(D)** Grey gradient of projection plane with Gray code.

3.3 Research on shortest path extraction method

3.3.1 Key point detection

Given image I, image domain $\Omega \in R$, cost function is $P \in R$, and $P > 0$ (P is taken here as I itself, i.e. $P = I$). The set S is used to represent all detected key point sets, the initial set $S = \{k_0\}$.

It is known that the initial wavefront is a circle, and the center of the circle is k_0. Combined with the fast-marching algorithm, there are the following key point detection steps:

1) To find the map with minimum energy, we set the iterative step size to t and solve the equation function U using the fast-marching algorithm. Then the technique of finding the shortest path in the reverse direction from the request point is applied and the map with the minimum energy of the initial point is obtained;
2) The energy integral E of each path is calculated using Eq. 1. The algorithm for the shortest path requires the minimum energy integral E, the corresponding boundary point is the key candidate k_p;
3) Calculate the Euler distance of the path between k_p and k_0, if the Euler distance is greater than the given threshold T, then this point is upgraded to a key point k_1. Euler's distance between two points can be calculated using Eq. 4:

$$L(k_i, k_j) = \sum_{l=1}^{n} \|x_{l+1} - x_l\| \tag{4}$$

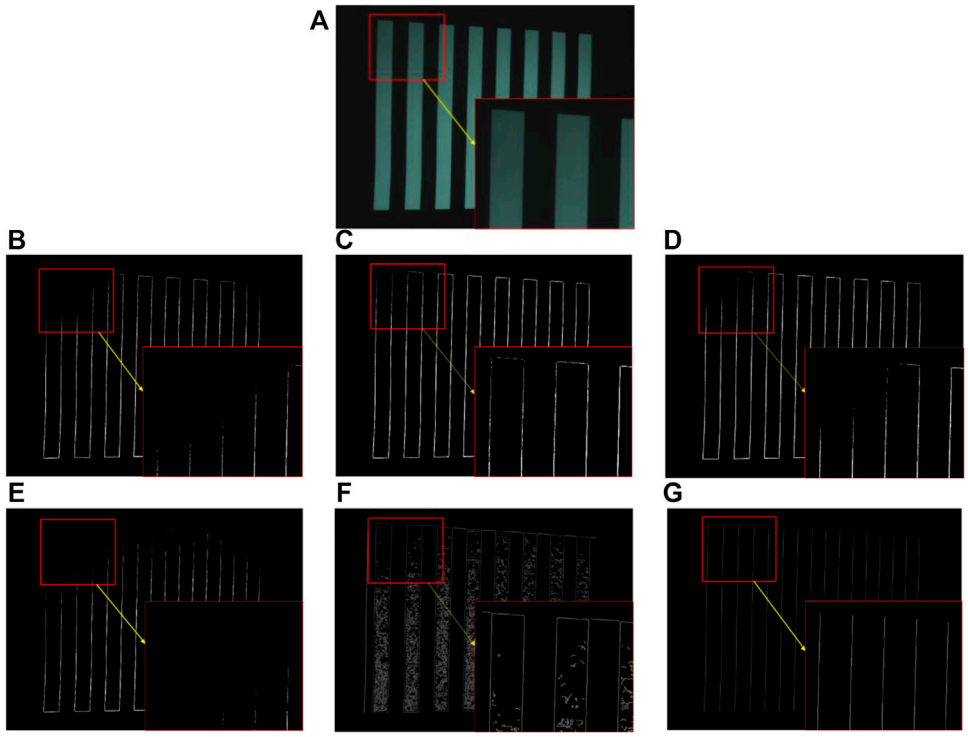

FIGURE 7
Edge detection image. **(A)** Gray projection plane; **(B)** Edge image of Sobel operator; **(C)** Edge image of Robers operator; **(D)** Edge image of Prewitt operator; **(E)** Edge image of Laplacian operator; **(F)** Edge image of Canny operator; and **(G)** The method we propose.

In the formula: n is the number of points through which the path passes.

3.3.2 Path tracking detection

After finding the key point k_1 on the path, both the key point set and the path set are updated, including: $S = \{k_0, k_1\}$, $C = \{k_0 \rightarrow k_1\}$.

The following steps are used to iteratively detect key points on the path curve:

1) The updated key point set is S, all of them are set as source points after updating. We use the fast-marching algorithm to find the minimum energy graph, calculate for each key point the shortest path integral energy E between it and the edge point of the surrounding minimum energy graph, and determine the next candidate key point in the edge point;
2) The Euler distance constraint is used to determine the candidate key points which exceed the threshold T and upgrade to the new key point k_2;
3) Update the key point set and the path set, which are: $S = \{k_0, k_1, k_2\}$, $C = \{k_0 \rightarrow k_1, k_1 \rightarrow k_2\}$;
4) The key point k_2 satisfies the stop condition and stops the path tracking monitoring;
5) If the stop condition is not met, loops a) to d), the final set of key points and the final set of paths are obtained by iteration.

3.3.3 Stop condition

The next key point in the path is identified during each loop of the path tracing, and we need to compare their Euler distance with the default threshold T. This comparison criterion makes the Euler distances between adjacent key points in the extracted shortest path approximately equal, this feature in the shortest path can be used to determine the endpoint of the path tracing.

We give two known adjacent key points p and q, k_i is the candidate key point of the adjacent key point q. If the candidate keypoint is the closest one, the Euler distance from k_i to point q should greater than the threshold T, and it satisfies $L(k_i, q) \approx T$, and $L(p, q) \approx T$, then it can be deduced that the Euler distance condition that the candidate key point k_i and the key point p should satisfy, as shown in Eq. 5:

$$L(k_i, p) \approx L(k_i, q) + L(p, q) \tag{5}$$

Since noise can easily interfere with path tracing, here is the allowable error, Eq. 5 can be changed to the standard for monitoring the stopping of path tracing, as shown in Eq. 6:

$$L(k_i, p) - L(k_i, q) - L(p, q) \leq \varepsilon \tag{6}$$

If the candidate key points do not satisfy Eq. 6, end the pursuit the path tracing.

4 Experiments and results

4.1 Contrast experiment with classical edge detection operator

We compare the edge detection method proposed in this article with various classical edge detection operators, and choose as the object of study the edge of the stripe in the projected Gray code plane.

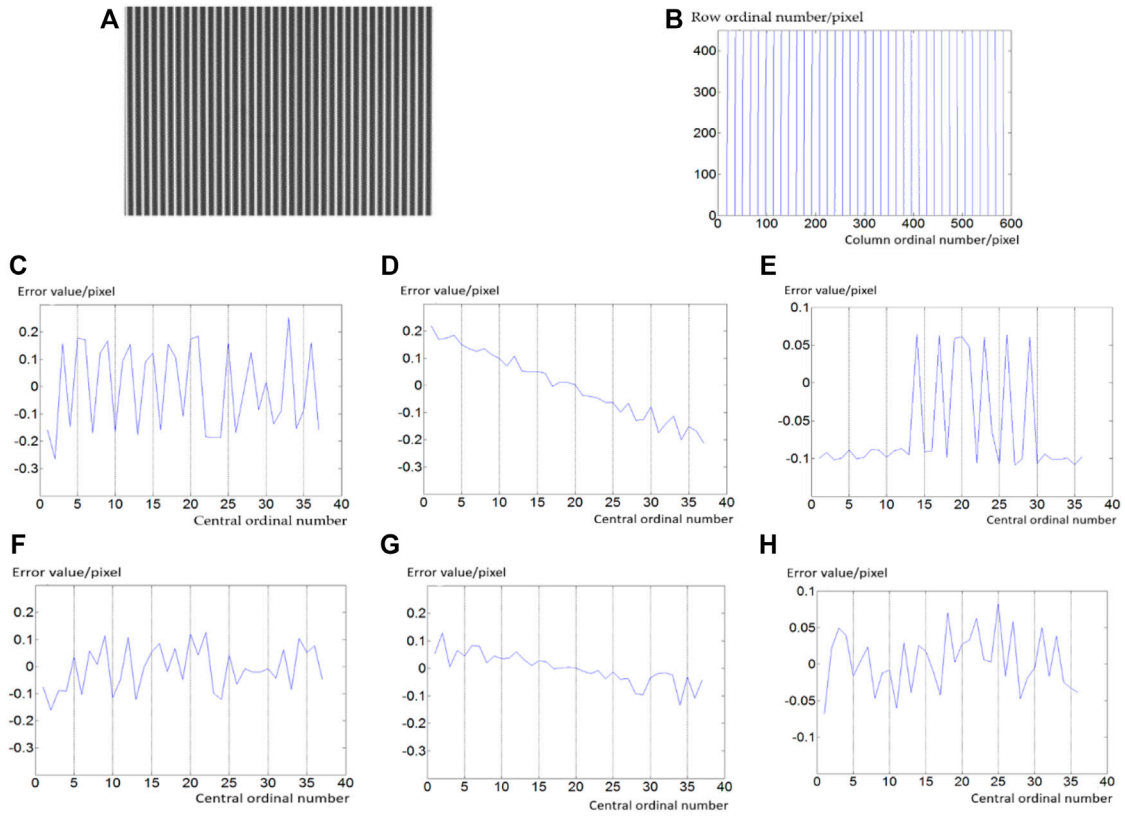

FIGURE 8
Line-shift stripe center detection. **(A)** Stripe image; **(B)** The fitting center line; **(C)** Gray Gravity method straightness; **(D)** Straightness with this article method; **(E)** Gray Gravity method parallelism; **(F)** Parallelism with this article method; **(G)** Gray Gravity method equidistance; and **(H)** Equidistance with this article method.

TABLE 1 Centre detection positioning error.

	Gray scale centre of gravity method	This article method
Straightness error/pixel	0.146	0.070
depth of Parallelism error/pixel	0.192	0.099
equidistant degree error/pixel	0.188	0.091
Comprehensive error/pixel	0.305	0.145

As shown in Figure 7, several classical operator methods for edge detection perform the detection of the stripe edge on the image shown in Figure 7A.

Figure 7G illustrates the detection results at the pixel level. The comparison shows that in the real measurement scenario, the upper left corner of the image shown in Figure 7A is darker than the other parts. The Sobel operator, the Prewitt operator, and the Laplacian operator cannot perform Gray code edge detection in this case, and the edge detected by the Roberts operator suffers from disconnection; noise in the edge images detected by the Canny operator is an obstacle. In the edge line image obtained by the method presented here, the edge line shown is the edge image drawn by matching the sub-pixel edge line with the pixels with the shortest distance. In the darker part of the image, the position of the Gray code edge can still be accurately located, and no discontinuity is observed.

4.2 Contrast experiment of central detection

Figure 8 shows that the results of the detection and localization of the strip center based on the local Gray centroid method [18] and the shortest path search technology based on the singular operator are evaluated and compared when the center line-shift strip in the 3D measurement is 4 pixels wide.

Table 1 tabulates the data of the positioning error in detecting the center of a strip with a width of 4 pixels. The method described in this article reduces the comprehensive error in detecting the center of the

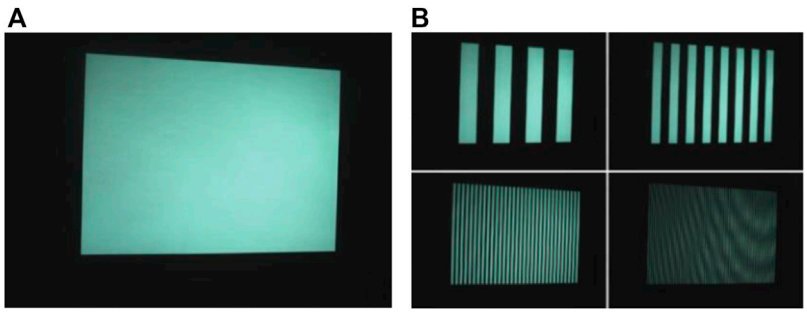

FIGURE 9
The measured plane and its encoding pattern. **(A)** Measured plane; and **(B)** Coding plan.

TABLE 2 Plane measurement errors in three-dimensional measurement.

Plane position/mm		Maximum error/mm	The mean error/mm	Mean square error (MSE)/mm
−40	the first method	1.200	0.311	0.357
	the second method	0.924	0.157	0.201
−20	the first method	1.115	0.290	0.320
	the second method	0.876	0.151	0.199
0	the first method	0.946	0.240	0.293
	the second method	0.829	0.146	0.197
+20	the first method	1.078	0.256	0.304
	the second method	0.856	0.149	0.205
+40	the first method	1.184	0.298	0.334
	the second method	0.898	0.155	0.203

stripe by the Gray barycenter method from 0.305 pixels to 0.145 pixels. Comparing the comprehensive detection and positioning errors between the two methods, the center detection position is more accurate in this article method.

4.3 Plane measurement experiments and error analysis

The shortest path search technique based on the singular operator is used to detect the edge of the Gray code and the center of the line shift fringes in the three-dimensional measurement of structured light, and realize the three-dimensional measurement of the measured object. Figure 9 is the measured plane using Cartesian coordinates, and the position of the measured plane is Z = 0. Figure 9A is the measured plane, Figure 9B is the coding diagram of the projected Gray code and line shift fringe on the measured plane.

Table 2 shows the measurement data of the plane. The first method in the table is the detection of the three-dimensional measurement plane by combining the edge detection of the intersection method and the centre detection of the gray centroid method, and the second is our proposed method. The mean plane error of the five positions measured by the second method is 0.152 mm, which is smaller than the 0.279 mm measured by the first method. The mean square plane error of the five positions measured by the second method is 0.201 mm, which is smaller than the 0.322 mm measured by the first method. The results show that our proposed method is superior in terms of accuracy.

4.4 Spherical measurement experiments

Figure 10A is the measured spherical image, Figure 10B is the encoding diagram of the Gray code and the line-shift strip of the measured spherical projection.

Figure 11A shows the reconstruction of the spherical surface by combining the edge detection of the intersection method with the center detection of the gray centroid method, Figure 11B shows the results using the edge and center detection method of the singular operator based shortest path search technology.

In Figure 11A, due to inaccurate edge or center positioning, there are many perturbations for some positions in the reconstructed object, while there are few points for adjacent positions. This leads to errors in point positioning during decoding and also to streaky protrusions or depressions in the graph. Therefore, the proposed method is more accurate in positioning and striped protrusions or depressions can be reduced or even eliminated.

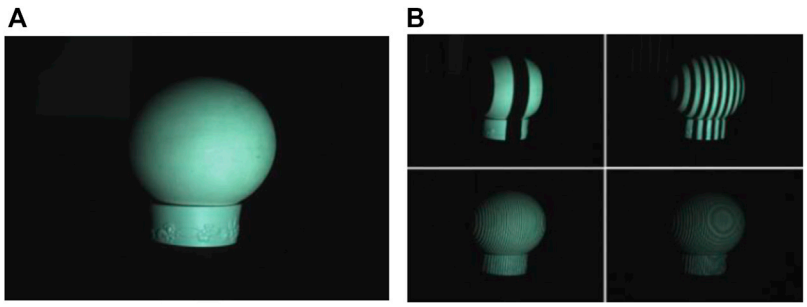

FIGURE 10
The measured sphere and its coding diagram. **(A)** Measured sphere; and **(B)** Encoding pattern.

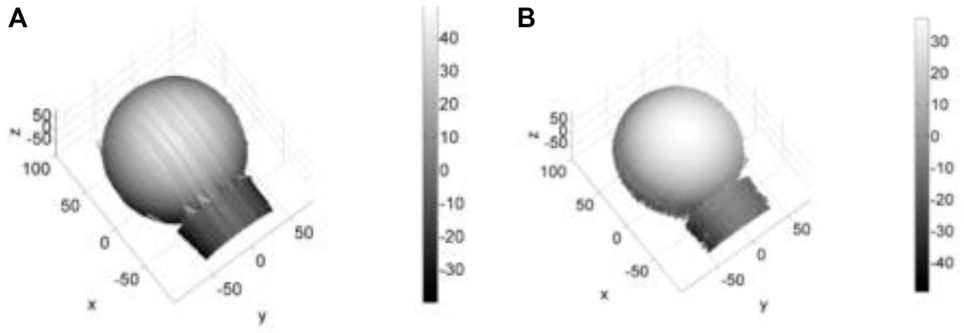

FIGURE 11
Spherical Reconstructed Image. **(A)** The method of combining Intersection method and Gray Gravity method; and **(B)** This article method.

5 Discussion

In this article, we propose the singular operators and cost functions based on a thorough review of the signal properties of the Gray code edge and the center of the line-shift strips, and then use the Euler distance as a constraint on the neighboring key points computed by the fast-marching algorithm, integrated with the computation of the minimum energy map in the shortest path search technology. The experiments show that the shortest path search method based on the singular operator for the edge and the singular operator for the center proposed in this article improves the accuracy of the positioning of the edge of the Gray scale strip and the center of the line-shift strip in 3D measurement and decoding, and thus increases the accuracy of 3D.

Data availability statement

The original contributions presented in the study are included in the article/Supplementary Material, further inquiries can be directed to the corresponding author.

Author contributions

YW: Conceptualization, Methodology, Software, Writing—Original Draft XS: Validation, Formal analysis, Investigation YD: Data Curation, Writing—Review YC: Writing—Editing.

Funding

This research was supported by the Fundamental Research Funds for the Universities in Heilongjiang Province (2018-KYYWF-1681), the University Nursing Program for Young Scholars with Creative Talents in Heilongjiang Province (UNPYSCT-2017086), and National Natural Science Foundation of China (61671190, 61571168).

Conflict of interest

The authors declare that the research was conducted in the absence of any commercial or financial relationships that could be construed as a potential conflict of interest.

Publisher's note

References

1. Rewitt JM. *Object enhancement and extraction*. New York, U.S.A: picture Processing and Psychopictoric Press (1970).

2. Roberts LG. *Machine perception of three-dimensional solid*. Boston, U.S.A: Massachusetts Institute of Technology (1965).

3. Marr D, Hildreth E. Theory of edge detection. *Proceeding R Soc Lond* (1980) 207: 187–217. doi:10.1098/rspb.1980.0020

4. Canny J. A computational approach to edge detection. *IEEE Trans Pattern Anal Machine Intel* (1986) 8:679–98. doi:10.1109/tpami.1986.4767851

5. Kong FT. Research on edge thinning algorithm in image magnification. *Comput Appl Softw* (2010) 27:261–264.

6. Chen H. *Research on image edge detection technology*. Harbin, China: Harbin Engineering University (2012).

7. Chen YH. A survey of image edge detection methods. *J Baoji Univ Arts Sci (Natural Sci Edition)* (2013) 33:16–21. doi:10.13467/j.cnki.jbuns.2013.01.001

8. Jensen K, Anastassiou D. Subpixel edge localization and the interpolation of still images. *IEEE Trans Image* (1995) 4:285–295. doi:10.1109/83.366477

9. Sui LS, Jiang ZD. Image subpixel edge extraction method based on NURBS curve fitting. *J Chin Comput Syst* (2004) 25:1502–1505.

10. Zheng XP, Bi YW. Improved algorithm about subpixel edge detection based on Zernike moments and three-grayscale pattern. In: 2009 2nd International Congress on Image and Signal Processing; 17-19 October 2009; Tianjin, China. IEEE (2009).

11. Lyvers EP, Mitchell O, Akey ML, Reeves A. Subpixel measurements using a moment-based edge operator. *IEEE Trans Pattern Anal Machine intelligence* (1989) 11:1293–309. doi:10.1109/34.41367

12. Zhu H, Zen XJ. Sub-pixel edge extraction based on Zernike moment and least squares ellipse fitting. *Comput Eng Appl* (2011) 47:148–150.

13. Li J, Peng YY. Image edge refinement based on mathematical morphology thinning algorithm. *J Comput Appl* (2012) 32:512–520. doi:10.3724/SP.J.1087.2012.00514

14. Zhang XM, Jia KF, Zhuo DF. Application of BP neural network in image edge detection. *J Comput Appl* (2011) 32:2146–2149. doi:10.16208/j.issn1000-7024.2011.06.060

15. Guo KB. *Theoretical research on image edge detection based on gray relational degree*. Kaifeng, China: Henan University (2016).

16. Lin XT, Liu T, Wang ZY. A new subpixel detection method for diffuse edge. *Chin J Sensors Actuators* (2010) 23:973–977.

17. Wu HB. *Research on three-dimensional measurement technology of gray-scale edge gray code and line-shift fringe*. Harbin: Harbin University of Science and Technology (2008).

18. Song Z, Chung R, Zhang XT. An accurate and robust strip-edge-based structured light means for shiny surface micro-measurement in 3D. *IEEE Trans Ind Electron* (2013) 60:1023–32. doi:10.1109/tie.2012.2188875

frontiers | Frontiers in Physics

TYPE Original Research
PUBLISHED 21 February 2023
DOI 10.3389/fphy.2023.1127505

OPEN ACCESS

EDITED BY
Tonglei Cheng,
Northeastern University, China

REVIEWED BY
Yue Wu,
Beijing Information Science and Technology University, China
Muguang Wang,
Beijing Jiaotong University, China
Zhongwei Tan,
Beijing Jiaotong University, China

*CORRESPONDENCE
Xiao Liang,
xiaoliang@muc.edu.cn

SPECIALTY SECTION
This article was submitted to Optics and Photonics, a section of the journal Frontiers in Physics

RECEIVED 19 December 2022
ACCEPTED 30 January 2023
PUBLISHED 21 February 2023

CITATION
Liang X and Zuo B (2023), A precision refractometer using strict dual-mode elliptical multilayer-core fibers with temperature and strain decoupled. *Front. Phys.* 11:1127505. doi: 10.3389/fphy.2023.1127505

A precision refractometer using strict dual-mode elliptical multilayer-core fibers with temperature and strain decoupled

Xiao Liang[1]* and Binzhou Zuo[2]

[1]School of Information Engineering, Minzu University of China, Beijing, China, [2]College of Science, Minzu University of China, Beijing, China

To accurately measure the surrounding refractive index (SRI), an all-fiber microstructure multi-parameters optical sensor based on Mach–Zehnder interferometer (MZI) has been designed. A homemade elliptical multilayer-core fiber (EMCF), in which only two modes could be propagated, is used in this sensor. This sensor has a sandwich structure of EMCF-SMF-EMCF (ESE). The sensitivities of RI, temperature, and strain are analyzed practically, and different from each other which would provide a basis for restraining cross-sensitivity of sensor and improving measuring precision. According to the numerical simulation, the relationship between the guided mode and relevant excitation coefficient is shown, and the sensing characteristic of the interference spectrum is well expatiated. Maximum sensitivities of ~31.83 nm per refractive index unit (RIU), ~69 pm/°C, and ~2.06 pm/με have been experimentally achieved. The monitoring system is promoted by the fact that the resonance dips have their individual sensitivities, and the standard matrix inversion method is used for simultaneous three parameters determination. Consequently, this fiber sensor could ensure the completion of accurate SRI measurements with temperature and strain decoupled.

KEYWORDS

strict dual-mode fiber, fiber sensor, mulit-parameters, axial micro-strain, in-fiber MZI

1 Introduction

The reliable and compact fiber sensors are significantly indispensable in many fields due to their unique characteristics, such as extremely high sensitivity and precision, stable electric insulation, chemical stability, resistance to electromagnetic interference, distributed measurement, and durability. Therefore, the fiber sensor has drawn a great deal of attention in various fields, such as the securities and protection monitoring [1, 2], biomedical instruments [3, 4], the construction industry [4, 5], aerospace [6, 7], etc. Apart from the above, the fiber sensor has the potential research values in measuring the surrounding refractive index (SRI). Compared with the conventional refractometer, which is mostly based on electrical and mechanical technologies [8], the fiber-optic SRI sensor has the advantages of compact size, anti-electromagnetic interference, high voltage, and corrosion resistance. However, due to the higher order modes guided in fibers, a stable clean interference spectrum would be hardly obtained. In addition, due to the temperature and axial micro-strain cross-sensitivity, the fiber-based refractometer could hardly achieve high-accuracy survey as well.

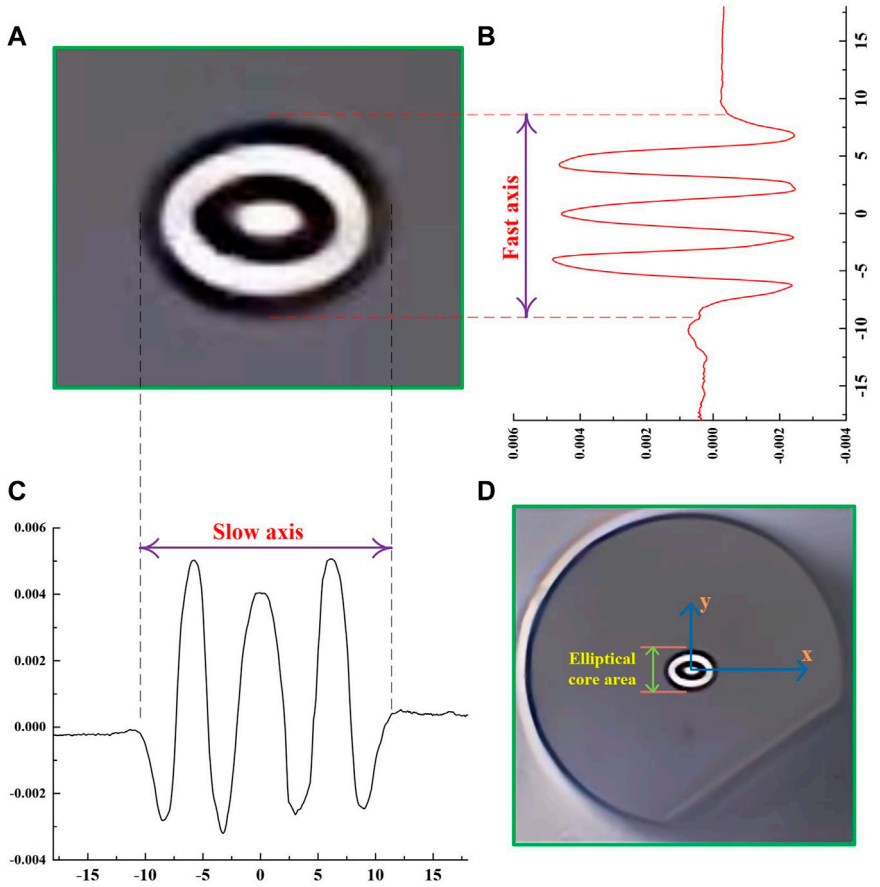

FIGURE 1
Schematic diagrams of **(A)** the cross-section micrograph of the elliptical core area; **(B)**, **(C)** the index profile along the fast/slow axis; and **(D)** the cross-section microstructure of the EMCF.

To attain a stable clean interference spectrum, the number of guided modes in the fiber must be limited, and the energy occupation of each mode should be roughly the same [9]. To restrict the number of interference modes, some solutions like using few modes fiber (FMF) have been demonstrated, such as temperature and strain sensors using an elliptical central silica core [10], gas concentration measurement based on the dual-mode Fiber Bragg Grating (FBG) structure [11], dual-parameter active fiber sensor based on a fiber ring laser [12], liquid-core optical fiber [13], and et al. A novel SRI sensor based on a specially designed polyimide coated dual-mode fiber (DMF) is presented by Lei [14]. The structure of this fiber is fabricated with an inner core, three inner claddings, and a pure silica outer cladding, which only permits the fundamental mode, LP_{01}, and the higher order core mode, LP_{02}, to propagate. However, higher order modes could be propagated in the round-core fiber, which leads to an unstable interference spectrum. In addition, the perturbance of temperature and micro-strain in the refractometer could also cause an unpredictable disturbance. Several schemes have been proposed to remove one interfering component, such as the temperature-compensated refractometer [15], and the refractometer with strain-error correction [16]. Moreover, there are some schemes proposed for the simultaneous measurement of them. A novel fiber-optic refractometer is proposed with its temperature and axial strain compensation [17]. This literature demonstrates a scheme using a tapered bend-insensitive fiber. However, numerous nanoscale gas-filled voids are embedded in its cladding, making it complex and a little repeatable. This study aims to develop a precision refractometer using homemade elliptical multilayer-core fibers (EMCF) with EMCF-SMF-EMCF (ESE) structure. Based on the in-fiber Mach–Zehnder interferometer (MZI), this refractometer is proposed and experimentally characterized.

This sensor has the advantage of a stable structure and is relatively easy to be fabricated. Furthermore, it could simultaneously measure SRI, temperature, and axial micro-strain. The transmission dips have their individual sensitivities. Thus, the temperature could be compensated, and axial micro-strain error could be corrected, which leads to an improvement in SRI measurement. In addition, by utilization of the EMCF, the higher order modes are suppressed, and it could only support the LP_{01} and LP_{11}^{even}, while the LP_{11}^{odd} would be suppressed by the elliptical fast-axis [18]. This strict dual-mode EMCF would enable this sensor to

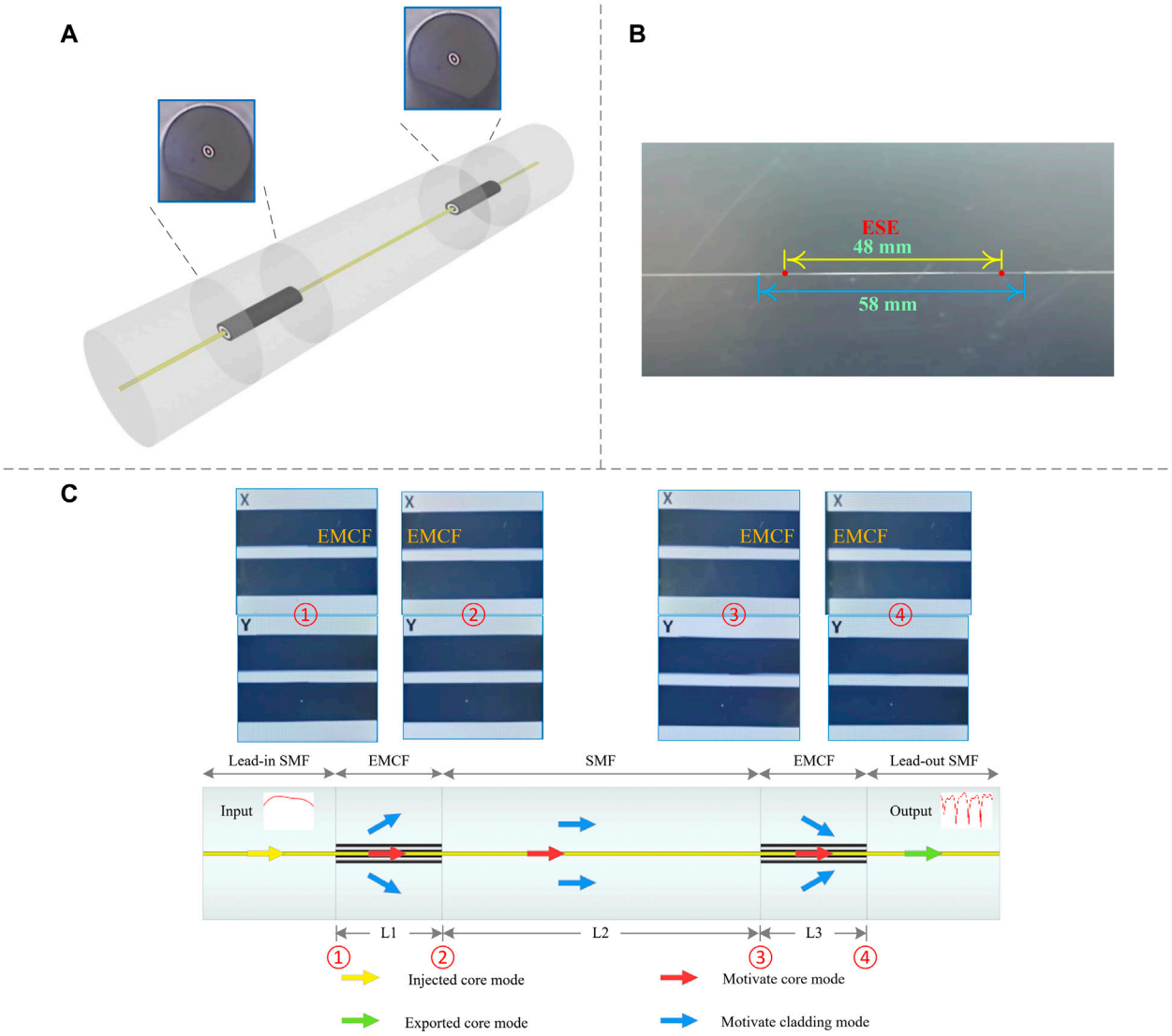

FIGURE 2
Details of the proposed sensor, **(A)** the three-dimensional structure; **(B)** the close view and geometrical sizes; **(C)** the representation and operation.

achieve a stable and clean interference spectrum [19]. Consequently, the multi-parameter monitor is easy to carry out by the wavelength shift. A detailed analysis of the mode interference is proposed. The operation mechanism and methods for characteristic compensation are demonstrated in elaborate experiments.

2 Design and principles of operation

2.1 Structure of the EMCF

This homemade strict dual-mode EMCF could be obtained with conventional modified chemical vapor deposition (MCVD) and solution-doping techniques. It is composed of an elliptical core area and conventional cladding. Figure 1A illustrates the cross-section micrograph of the elliptical core area, while the cross-section microstructure of the EMCF is shown in Figure 1D. It could be found from Figures 1A, D that the elliptical core area consists of a central elliptical core and three inner elliptical layers. The elliptical core area has a slow/fast axis with a length of 22.64/18.05 μm, and the diameter of the fiber is 125 μm. This special structure guarantees the feasibility of the strict dual-mode operation, which will be described in more detail later.

Figures 1B, C depict the distribution of the refractive index (RI), which is gained by an optical fiber analyzer (EXFO NR9200). This alternating low and high refractive index in the elliptical ring structure is acquired by doping with fluorine and germanium. The EMCF has a conventional cladding, the gray part, whose RI is 1.444. The highest RI of the slow/fast axis could achieve about 1.449/1.4485, while the lowest part could be approximately 1.4408/1.4415. The RI distribution is non-

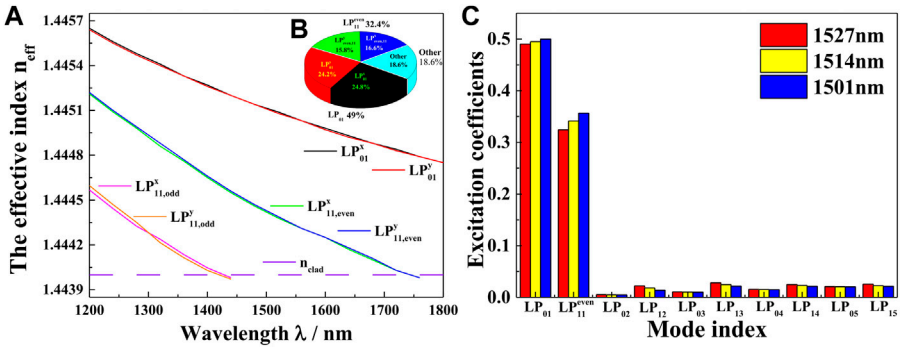

FIGURE 3
The guided-mode propagation analysis in EMCF, **(A)** the curves of λ vs. n_{eff} of the guided modes; **(B)** excitation coefficients for different modes in 1,510 nm; **(C)** excitation coefficients of various modes for various wavelength propagating in the first EMCF.

uniform and not strictly axisymmetric, which might have some influence on the mode distribution [20].

2.2 Configuration of the sensor and transmission principle

A fiber sensor, an in-fiber MZI based on ESE, has been utilized, and schematically plotted in Figure 2A and widely detailed in Figure 2C. It has a symmetrical ESE structure in that two same EMCFs are spliced to each end of a central SMF (Corning SMF-28). Then, two segments of SMF are stitched to the opposite ends of the ESE, playing the role of input and output SMF, respectively. Each segment is combined by the fiber fusion splicer (Fujikura, FSM-100M/P). As depicted in Figure 2B, the ESE is 48 mm long, which is 10 mm less than the total length of the sensor. This compact size enables this sensor to have a great potential for development and application in the field of micro-sensing. In more detail, the EMCF and central SMF lengths are 5 mm and 38 mm, respectively. This geometrical size is specially designed for an ideal coupling ratio of the propagating modes, which would be discussed in detail later.

Figure 2C shows the basic sensing principle of the sensor. A Gaussian beam is injected into the lead-in SMF, playing the role of the light source. Before reaching the central SMF, whose core and cladding act as the two arms of MZI, the fundamental modes (LP_{01}) and other cladding modes are excited by the first EMCF. As all the cladding modes have been coupled back to the core area by the second EMCF, an interference spectrum could be obtained in the lead-out SMF [21]. The SRI, temperature, and axial micro-strain could influence the optical path difference (OPD) of the LP_{01} and other modes. Hence, this device has the potential to measure the three parameters simultaneously. In addition, the fused splice losses between each EMCF and SMF, which correspond to Point 1 to Point 4, are 0.16 dB, 0.26 dB, 0.25 dB, and 0.16 dB, respectively. To have a high extinction radio MZI, the major axes of two EMCFs should be aligned, and the rotation angle of this two fibers should be specially arranged. The manufacturing approach is referenced to [22]

As mentioned above, the largest RI difference in the core area is only 0.0082, which satisfies the weakly guiding approximation [23]. By accumulating all the excited modes, which could be described as normalized and orthogonal wave functions, the total optical field distribution $\psi(x, y, z)$ is derived as

$$\psi(x, y, z) = \sum_{n}^{N} \eta_n \psi_n^E(x, y) e^{-i\beta_n z} \tag{1}$$

Where N is the number of excited modes in the EMCF. η_n, $\psi_n^E(x, y)$, β_n are excitation coefficient, guided mode distribution, and the longitudinal propagation constant in the EMCF, respectively. n represents a particular mode. Theoretically, the total field distribution is nearly the same as the incident field distribution. At the $z = 0$ position, the excitation coefficient, η_n, could have the expression in the form as [24]

$$\eta_n = \frac{\iint \psi_n^S(x, y)\psi_n^E(x, y)dxdy}{\iint \psi_n^E(x, y)\psi_n^E(x, y)dxdy} \tag{2}$$

Where $\psi_n^S(x, y)$ is the incident field distribution in the input SMF.

Figure 3A describes the curves of different effective refractive index n_{eff} vs. wavelength λ. According to the optical waveguide theory [27], the cutoff wavelengths of LP_{11}^{even} and LP_{11}^{odd} are not the same, which is different from that of the conventional circular optical fiber. This happens because the effective index is related to the geometric size of the elliptical axis. Consequently, the LP_{11}^{even} has a higher cut-off wavelength than that of LP_{11}^{odd}. With a wavelength ranging from 1,425 nm to 1,575 nm, only the LP_{01} and LP_{11}^{even} could be propagated in the elliptical waveguide system. As a result, the EMCF could be considered as a distinct dual-mode fiber, which could only support four orthogonal polarization modes.

According to the definition of the half beat length L_π [24]

$$L_\pi = \frac{\pi}{\beta_{LP_{01}} - \beta_{LP_{11}^{even}}} \tag{3}$$

Where the propagation constants of LP_{01} and LP_{11}^{even} are represented as $\beta_{LP_{01}}$ and $\beta_{LP_{11}^{even}}$, respectively. In this sensor, the EMCF is 5 mm long, which is approximate eleven times of $\frac{L_\pi}{2}$. Hence, according to the coupled mode theory [23], the coupling ratio could achieve approximately 3 dB. As shown in Figure 3B, in the first EMCF, the

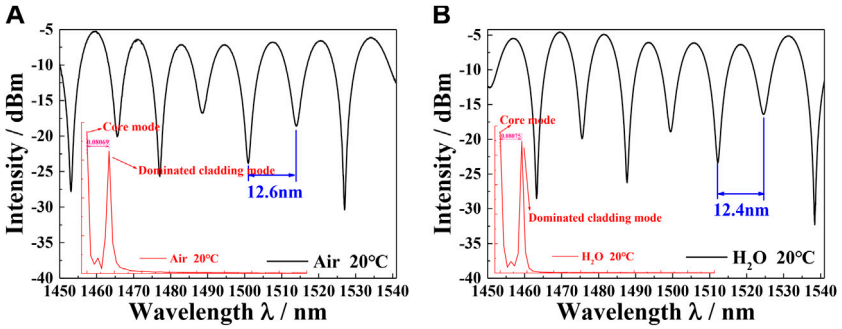

FIGURE 4
Interference-pattern analysis: the measured transmission spectrum and corresponding spatial frequency of the EMCF-based MZI in **(A)** air/ **(B)** water.

excitation coefficient of LP_{01} is 49%, and the one of LP_{11}^{even} is 32.4%. Other modes, which occupied 18.6%, are depicted in Figure 3C. Most obviously, the two mode groups, LP_{01} and LP_{11}^{even}, are dominant. In contrast, other higher order modes are so weak that they could be neglected. The reason why the higher order modes could be excited is that the coating of the EMCFs is removed completely. However, most of them would reduce exponentially because of weakly bound [9].

According to the definition of the normalized constant V_n [9]

$$V_n = \frac{2\pi}{\lambda} R\sqrt{n_{co}^2 - n_{cl}^2} \tag{4}$$

Where λ is the operation wavelength, R is the diameter geometry of the fiber, n_{co}/n_{cl} is the index of core/cladding. Since the normalized constant V_n of the EMCF varies in the different working wavelengths, the excitation coefficients among the three wavelengths are slightly different. In this case, a stable and clean interference spectrum could be gained.

Figure 4 shows the transmission spectrum and the free spectral range (FSR). As depicted, the interference spectrum is clean and stable. Since the two dominant mode groups have a close excitation coefficient, this phenomenon could be explained by the distinct dual-mode interference process. Therefore, regardless of other modes, the FSR could be described as [25].

$$FSR \approx \frac{\lambda^2}{\Delta n_{LP}^S L_S + 2\Delta n_{LP}^E L_E} \tag{5}$$

Where $\Delta n_{LP}^S/\Delta n_{LP}^E$ is the refractive index difference between modes LP_{01} and LP_{11}^{even} in the central SMF/EMCF. L_S and L_E are the lengths of the central SMF and EMCF, respectively. The FSRs in the air and water are the distance of the adjacent resonance dips, which are 12.6 nm and 12.4 nm, respectively. The spatial frequency is gained by the Fast Fourier Transform (FFT). The distance between the two peaks is 0.08069/nm in air and 0.08075/nm in water. The two peaks show that there are mainly two modes with similar power. However, there are some evanescent modes, which would cause some effect on the sensitivity and drift direction of the interference dips. To sum up, a clean and stable interference spectrum could be obtained by taking advantage of the strict dual-mode EMCF and controlling its length. The distinct FSR between each resonance dip is conducive to multi-parameter sensing because it could support a cleaner dip-drift spectrum. In addition, more accurate parameter sensitivities could be achieved. Finally, the conventional demodulation algorithm could be more simple and more precise.

2.3 Sensing principle

According to the optical waveguides theory [20], compared with LP_{01}, the LP_{11}^{even} has a lower effective refractive index, who has a low optical waveguide confinement property. Furthermore, the ESE structure has no coating, decreasing the absorption of radiation modes. As a result, LP_{11}^{even} modes could be propagated in the cladding of the central SMF. The sensing principle is based on the multimode interference (MMI) effect. The OPD between these two modes could be influenced by the environment which could change the effective refractive index and the L_S. Regardless of the much shorter part, L_E , the phase delay $\Delta\phi^{ij}$ could be expressed as [17]

$$\Delta\phi^{ij} \approx \frac{2\pi\left(n_{eff}^{01} - n_{eff}^{ij}\right)L_S}{\lambda} = \frac{2\pi\Delta n_{eff}^{ij} L_S}{\lambda} \tag{6}$$

Where n_{eff}^{01} and n_{eff}^{ij} are the effective refractive index of LP_{01} and a higher order mode, respectively. Δn_{eff}^{ij} is the effective refractive index difference between these two modes. The extinction radio of the interference spectrum could reach optimal performance, as $\Delta\phi^{ij} = 2n\pi$. Regardless of the evanescent modes, we could replace Eq. 6 by

$$\lambda_n \approx \frac{\Delta n_{eff}^{ij} L_S}{n} \tag{7}$$

Where λ_n is the wavelength of the nth resonance dip. As a result, $\lambda_n \approx \frac{\Delta n_{eff}^{ij} L_S}{n}$. In practical application, λ_n could be influenced by axial micro-strain, temperature, and SRI simultaneously.

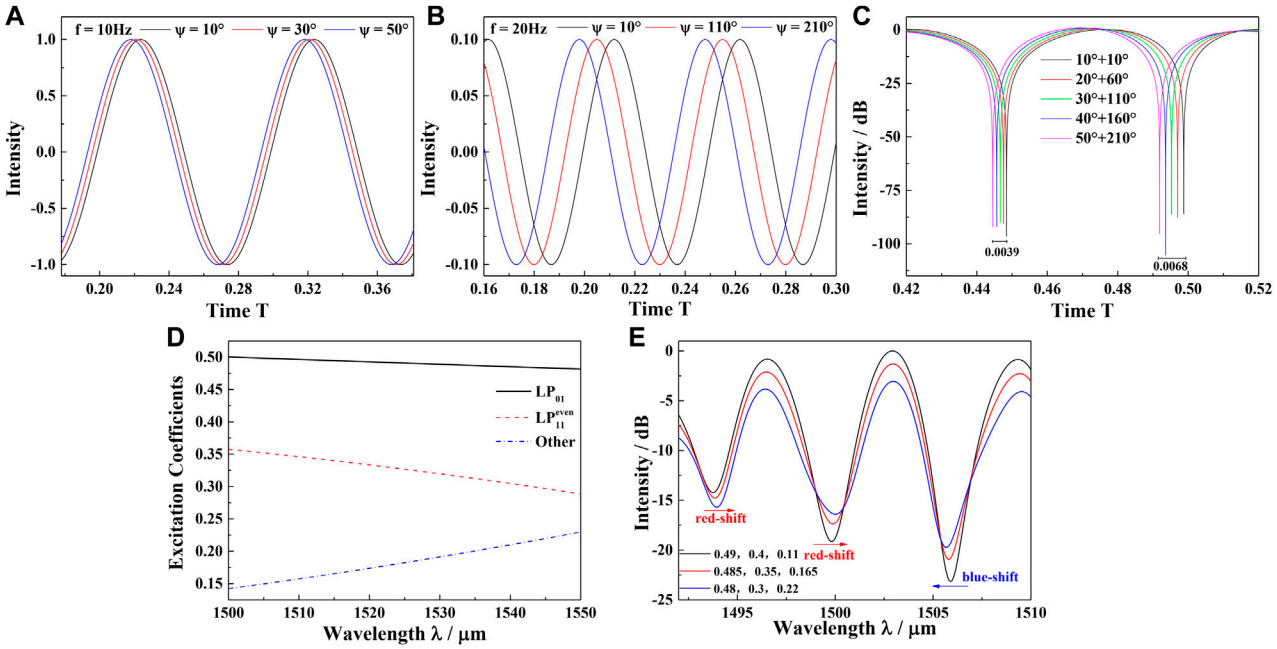

FIGURE 5
The mechanism analysis of the spectra shift, **(A)**, **(B)**, **(C)** the different sensitivities of the dips as the variation of the ψ; **(D)**, **(E)** the different shift directions as the variation of the excitation coefficients.

When axial micro-strain serves as the only source of interference, the change of λ_n caused by axial micro-strain could be described by [25]

$$\Delta\boldsymbol{\lambda}_{n,S} = -(\mathbf{1} + \mathbf{2}\boldsymbol{\mu} + \boldsymbol{p}_e)\boldsymbol{\lambda}_n\Delta\boldsymbol{\varepsilon} = \boldsymbol{C}_S^n\Delta\boldsymbol{\varepsilon} \tag{8}$$

Where $\Delta\lambda_{n,S}$ is the variation of λ_n caused by micro strain, μ is the Poisson ratio, and p_e is the effective strain-optic coefficient. For most silica fibers, μ and p_e value 0.16 and 0.22, respectively. $\Delta\varepsilon = \frac{\Delta L_{SMF}}{L_{SMF}}$, is the variation of axial micro-strain. Thus, C_S^n is a coefficient only related to material type. Therefore, the axial micro-strain could be determined by the shift of resonance wavelength.

Overlooking the affect by axial micro-strain and SRI, the change of λ_n caused by temperature, $\Delta\lambda_{n,T}$, could be obtained as [26]

$$\Delta\boldsymbol{\lambda}_{n,T} = (\boldsymbol{\delta} + \boldsymbol{\zeta})\boldsymbol{\lambda}_n\Delta\boldsymbol{T} = \boldsymbol{C}_T^n\Delta\boldsymbol{T} \tag{9}$$

Where δ and ζ are the thermal optical coefficient and dilatation coefficient respectively. For certain materials, δ and ζ are two constants. ΔT is the fluctuating temperature. C_T^n is a constant only changed by the material type. Thus, by monitoring the wavelength drift, we could obtain the exact variation of the surrounding temperature.

When only SRI is considered, n_{eff}^{01} would remain stable because of its deep location. Hence, the wavelength of the nth resonance dip influenced by SRI, $\lambda_{n,R}$, could be expressed as follows

$$\boldsymbol{\lambda}_{n,R} \approx \frac{\left(\boldsymbol{n}_{eff}^{01} - \boldsymbol{n}_{eff,R}^{ij}\right)\boldsymbol{L}_S}{\boldsymbol{n}} \tag{10}$$

Where $n_{eff,R}^{ij}$ is the effective refractive index of a higher order mode influenced by SRI. Then the variation of λ_n caused by SRI, $\Delta\lambda_{n,R}$, satisfies a similar equation [26]

$$\Delta\boldsymbol{\lambda}_{n,R} \approx \frac{-\Delta\boldsymbol{n}_{eff,R}^{ij}}{\Delta\boldsymbol{n}_{eff}^{ij}}\boldsymbol{\lambda}_n \approx \frac{-\boldsymbol{K}}{\Delta\boldsymbol{n}_{eff}^{ij}}\boldsymbol{\lambda}_n\Delta\boldsymbol{n}_R = \boldsymbol{C}_R^n\Delta\boldsymbol{n}_R \tag{11}$$

Where Δn_R is the SRI variation, K is the proportionality between Δn_R and $n_{eff,R}^{ij}$. $\frac{\lambda_n}{\Delta n_{eff}^{ij}}$ is a fixed constant as mentioned above. Generally, the relationship between Δn_R and $n_{eff,R}^{ij}$ tend to be non-linear. However, in this experiment, the range of Δn_R is strictly limited. Hence, $n_{eff,R}^{ij}$ could have a nearly linear increase with the increase of SRI. As a result, C_R^n is a fixed value as C_T^n and C_S^n. Similarly, by measuring the variation of λ_n, the SRI could be gained.

In addition, the sensitivity of each dip is different due to higher modes, which would be demonstrated with emulation and experiment results. To sum up, C_R^n, C_T^n, and C_S^n provide an opportunity to construct a character matrix for precision SRI sensing. Thus, this sensor could facilitate discrimination among the SRI, the temperature, and micro-axial strain, achieving accurate SRI measurement with temperature and axial strain compensations.

The essential condition to facilitate discrimination among these three parameters is differences in drift-sensitivity and drift-direction for environment variables. This phenomenon is caused by the higher order modes and has been analyzed in Figure 5. Based on the waveguide property, different Δn_{eff}^n would cause different interference frequencies, f. Various f could cause various phase delays, Ψ, as the variation of the environment. To better explain this phenomenon, the frequency components are taken analogous to sinusoids in the time domain. The interference pattern produced by LP_{01} and LP_{11}^{even} is depicted in Figure 5A. Qualitatively, it processes a wide range of intensity and a lower f, compared with the other interference pattern, Figure 5B, which is caused by LP_{01} modes and higher order modes. Regardless of the various intensity and other contributing factors, the MMI effect is taken analogous to sinusoids

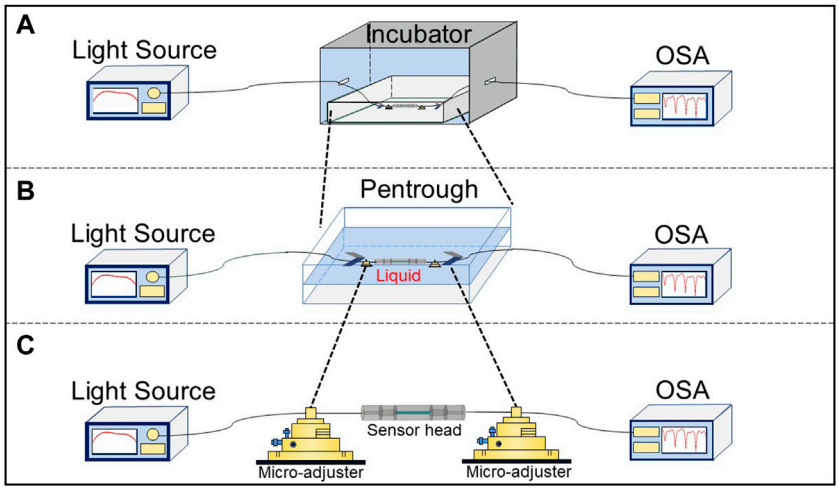

FIGURE 6
The schematic diagram of experimental setup for **(A)** temperature, **(B)** SRI, and **(C)** strain measurement.

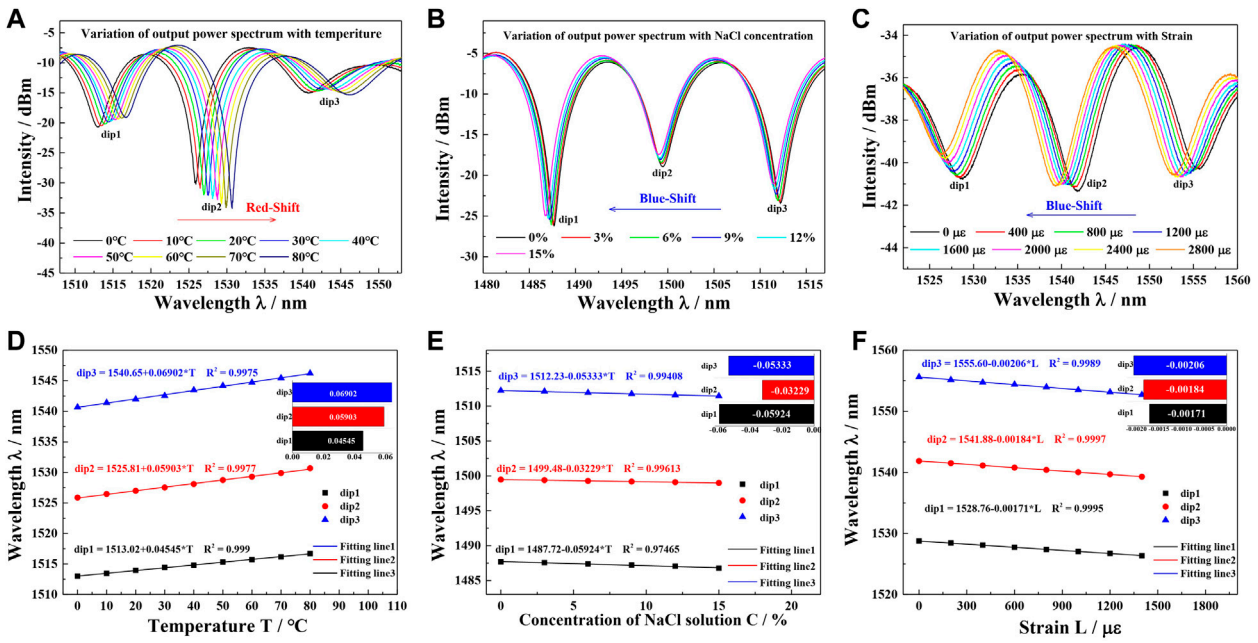

FIGURE 7
The tri-parameter monitoring results, **(A)**, **(B)**, **(C)** experimental transmission spectra under different RI/temperature/strain of surrounding areas; **(D)**, **(E)**, **(F)** the fitted line of dips wavelength shifts with different RI/temperature/strain.

mixing, and is shown in Figure 5C. The degree of drift for each resonance dip is different, demonstrating that the higher order modes could affect drift sensitivity. Figure 5D depicts the changing tendency of the excitation coefficients. With the increasing working wavelength, the effective refractive indexes of the guide modes would decrease slightly. As a result, the excitation coefficients of LP_{01} and LP_{11}^{even} would decline, and those of other modes would rise gradually. Figure 5E presents the shift directions as the variation of the excitation coefficients. One can find that the marked dips show different shift directions and different drift sensitivities. To sum up, the waveform drift is ultimately determined by the Δn_{eff}^{n} and excitation coefficients of guide modes.

3 Experimental methods and discussion

As mentioned above, a precision refractometer with temperature and strain compensated simultaneously could be accomplished with

the structure of ESE. For this purpose, this sensor has been tested under different environments with one variable controlled.

Figure 6A presents the experimental architecture for temperature measurement. The sensor is secured with two fiber clips to prevent transverse bending. The micro-adjusters are applied to obviate the disturbance of the axial micro-strain. All the devices are placed in a temperature control box (WEISS, WT1-180). A broadband source (KOHERAS, superK uersa) serves as a light source. The S + C band range is provided for the sensing system, which is used for conventional communication. As a result, this refractometer could have potential application in remote sensing system. The optical spectrum analyzer (OSA) is used for detecting the interference spectrum. The experimental transmission spectra showing a wavelength red shift corresponding to the temperature of 0°C–80°C, are presented in Figure 7A. The temperature range is divided into nine values (0, 10, 20, 30, 40, 50, 60, 70, 80°C). With the increase of the ambient temperature, the resonant wavelength increases by 4.625 nm on average. A linear relationship between the temperature and resonance wavelength is shown in Figure 7D. The line slopes represent the different drift-sensitivities, which are about ~69.02 pm/°C, ~59.03 pm/°C, and ~45.45 pm/°C, respectively. The average correlation coefficient of polynomial fitting, R^2, is above 0.998, demonstrating very accurate linearity.

Figure 6B shows the SRI experiment, in which this sensor is submerged in NaCl solutions of 0%–15% at 20.0°C with zero strain. The SRI increases in line from 1.3330 to 1.3609 with the concentration of NaCl increasing, which is measured by an Abbe refractometer. The measuring approach is referenced to [28]. In contrast with temperature sensing, the dip wavelength shows a blue shift as depicted in Figure 7B. The accurate linear relationship between SRI and the resonance dips with an average R^2 over 0.988 is shown in Figure 7E. The sensitivities of SRI for each dip are ~28.66 nm/RIU, ~17.35 nm/RIU, and ~31.83 nm/RIU, respectively.

Figure 6C illustrates the experiment of measuring axial micro-strain at room temperature. In it, the sensor could be elongated by the micro-adjuster. The axial strain experiment, Figure 7C, is carried out by elongating the ESE structure at a step of 10 μm, corresponding to 208 με. Similarly, it shows a blue shift. The linear relationship between the axial micro-strain and the resonance dips with an average R^2 over 0.999 is recorded in Figure 7F. The sensitivities for each dip are about ~2.06 pm/με, ~1.84 pm/με, and ~1.71 pm/με, respectively. The fiber-optic SRI sensor exhibits a cross-sensitivity of strain, which is consistent with previous studies [16, 22]. Therefore, an ideal refractometer should be capable of discriminating the strain induced wavelength shift.

To sum up, the linearity of this refractometer is very accurate. In both the simulation and experiment, the resonance dips have their individual sensitivities. In addition, in the experiments, the dips' drift direction is depended on the C_R^n, C_T^n, and C_S^n. As only C_T^n is positive, the interference spectrum would have a red shift as the temperature increasing, while the one would have a blue shift as the SRI or axial micro-strain increasing. However, these coefficients which would affect the experiment result are not considered in the simulation. Thus, the drift direction in the simulation is different from that of experiment. In order to give the experiment direction, the proper simplified condition would be desirable. In short, the calculated results are in good agreement with the experimental data.

The standard matrix inversion method could be used for simultaneous determination of axial micro-strain, temperature, and SRI, when taking C_R^n, C_T^n, and C_S^n as the nth dips' drift slopes. By combining Eqs. 7–9, a matrix equation could be obtained to facilitate discrimination among the three parameters as follows.

$$\begin{bmatrix} \Delta\boldsymbol{\lambda}_{n-1} \\ \Delta\boldsymbol{\lambda}_{n} \\ \Delta\boldsymbol{\lambda}_{n+1} \end{bmatrix} = \begin{bmatrix} \boldsymbol{C}_R^{n-1} & \boldsymbol{C}_T^{n-1} & \boldsymbol{C}_S^{n-1} \\ \boldsymbol{C}_R^{n} & \boldsymbol{C}_T^{n} & \boldsymbol{C}_S^{n} \\ \boldsymbol{C}_R^{n+1} & \boldsymbol{C}_T^{n+1} & \boldsymbol{C}_S^{n+1} \end{bmatrix} \begin{bmatrix} \Delta\boldsymbol{n} \\ \Delta\boldsymbol{T} \\ \Delta\boldsymbol{\varepsilon} \end{bmatrix} = \boldsymbol{M}_{\boldsymbol{R,T,S}} \begin{bmatrix} \Delta\boldsymbol{n} \\ \Delta\boldsymbol{T} \\ \Delta\boldsymbol{\varepsilon} \end{bmatrix} \tag{12}$$

Where $M_{R,T,S}$ is a coefficient matrix. As $M_{R,T,S}$ and $\Delta\lambda_n$ are available through specific experiments, the negative effects of strain and temperature cross sensitivity could be quantified. Thus, by calculating the inverse matrix of the coefficient matrix, $M_{R,T,S}^{-1}$, the error due to temperature and axial micro-strain could be compensated to negligible degree. The proposed approach shows better measurement characteristics than the previous scheme, which usually could only realize temperature or micro-strain compensation. Thus, this SRI sensor is suitable for resolving a high degree of cross-sensitivity.

4 Conclusion

In conclusion, a precision fiber refractometer with temperature and axial micro-strain compensation has been demonstrated. Based on the strict dual-mode EMCF, the in-fiber MZI could obtain a stable clean interference spectrum. This high-quality spectrum is a guarantee for multi-parameter sensing. The FFT analysis of the interference spectrum demonstrates that almost only foundation modes and LP_{11}^{even} are supported. The mechanism of MMI has been developed to interpret the various drift sensitivities and drift direction, which is a novel formulation. By measuring the three dip shifts, the coefficient matrix $M_{R,T,S}$ could be calibrated. Consequently, the three parameters could be measured simultaneously by using the method of spectrum character demodulation. Finally, this refractometer could achieve precision SRI sensing with temperature and axial micro-strain compensation. Therefore, the proposed approach shows great potential for applications in precision SRI measurement with the multi-parameter cross sensitivity [27, 28].

Data availability statement

The raw data supporting the conclusion of this article will be made available by the authors, without undue reservation.

Author contributions

XL: optical experiment, XL and BZ: guidance and revision.

Funding

The authors would like to thank the financial support by the National Natural Science Foundation of China (Grant No. 61905293), the Fundamental Research Funds for the Central University (Grant Nos. 2022QNYL32, 2022QNPY78), the Foundation of Key Laboratory of All Optical Network and Advanced Telecommunication Network, Ministry of Education, China (Beijing Jiaotong University) (Grant No. AON2022001).

Conflict of interest

The authors declare that the research was conducted in the absence of any commercial or financial relationships that could be construed as a potential conflict of interest.

Publisher's note

References

1. Peng Z, Peng Z, Jian J, Wen H, Gribok A, Wang M, et al. Distributed fiber sensor and machine learning data analytics for pipeline protection against extrinsic intrusions and intrinsic corrosions. *Opt Express* (2020) 28:27277–92. doi:10.1364/OE.397509

2. Li J, Zhang J, Sun H, Hong D, Li L, Yang Y, et al. An optical fiber relative humidity sensor based on hollow-core fiber and hydroxypropyl methylcellulose hydrogel film. *Optik* (2019) 195:163172. doi:10.1016/j.ijleo.2019.163172

3. Shang Z, Li S, Li B, Wu H, Sampaolo A, Patimisco P, et al. Quartz-enhanced photoacoustic NH3 sensor exploiting a large-prong-spacing quartz tuning fork and an optical fiber amplifier for biomedical applications. *Photoacoustics* (2022) 26(2022): 100363100363–5979. doi:10.1016/j.pacs.2022.100363,ISSN

4. Alwis LSM, Bremer K, Roth B. Fiber optic sensors embedded in textile-reinforced concrete for smart structural health monitoring: A review. *Sensors* (2021) 21:4948. doi:10.3390/s21154948

5. Chan S, William Y, Wang H-P, Xiang P. Optical fiber sensors for monitoring railway infrastructures: A review towards smart concept. *Symmetry* (2021) 13(12):2251. doi:10.3390/sym13122251

6. Rocha H, Semprimoschnig C, Nunes JP. Sensors for process and structural health monitoring of aerospace composites: A review. *Eng Struct* (2021) 237:112231. doi:10.1016/j.engstruct.2021.112231

7. Goossens S, Berghmans F, Sharif Khodaei Z, Lambinet F, Karachalios E, Saenz-Castillo D, et al. Practicalities of BVID detection on aerospace-grade CFRP materials with optical fibre sensors. *Compos Struct* (2021) 259:113243. doi:10.1016/j.compstruct.2020.113243

8. Yang H, Shin S, Kumar S, Seo D, Oh S, Lee M, et al. A CMOS image sensor based refractometer without spectrometry. *Sensors* (2022) 22(3):1209. doi:10.3390/s22031209

9. Born M, Wolf E. *Principles of optics: Electromagnetic theory of propagation, interference and diffraction of light*. Great Britain: Elsevier (2013).

10. Abbas LG, Ai Z, Mumtaz F, Muhammad A, Dai Y, Parveen R. Temperature and strain sensing with hybrid interferometer. *IEEE Sens J* (2021) 21:26785–92. doi:10.1109/JSEN.2021.3120798

11. Rani S, Haider S, Bukhari SHR, Zaidi SAA, Huda AB. Performance optimization of apodized FBG biomedical sensor for variation in temperature and presence of noise. *IEEJ Trans Electr Electron Eng* (2022) 17:847–55. doi:10.1002/tee.23573

12. Wan H, Zhang J, Chen Q, Wang Z, Zhang Z. An active fiber sensor based on modal interference in few-mode fibers for dual-parameter detection. *Opt Commun* (2021) 481:126498. doi:10.1016/j.optcom.2020.126498

13. Liu Q, Ma Z, Wu Q, Wang W. The biochemical sensor based on liquid-core photonic crystal fiber filled with gold, silver and aluminum. *Opt Laser Technol* (2020) 130:106363. doi:10.1016/j.optlastec.2020.106363

14. Lei X, Dong X, Lu C. Sensitive humidity sensor based on a special dual-mode fiber. *IEEE Sens J* (2019) 19:2587–91. doi:10.1109/JSEN.2018.2889799

15. Ouyang Y, Xu X, Zhao Y, Zhou A, Yuan L. Temperature compensated refractometer based on parallel fiber fabry–pérot interferometers. *IEEE Photon Technol Lett* (2018) 30:1262–5. doi:10.1109/LPT.2018.2844543

16. Kong L-X, Zhang Y-X, Zhang W-G, Li Z, Zhang Y-S, Yan T-Y, et al. Temperature-independent micro-refractometer based on cascaded in-fiber air cavities with strain-error correction. *IEEE Sens J* (2018) 18:8773–80. doi:10.1109/JSEN.2018.2868739

17. Harris J, Lu P, Larocque H, Xu Y, Chen L, Bao X. Highly sensitive in-fiber interferometric refractometer with temperature and axial strain compensation. *Opt Express* (2013) 21:9996. doi:10.1364/OE.21.009996

18. Geisler T, Pedersen ME, Herstrøm S. Measurement of spatial and polarization birefringence in two-mode elliptical core fibers. In: Optical Fiber Communication Conference; 17-21 March 2013; Anaheim, CA, USA. Optica Publishing Group (2013). OW1K. 3.

19. Kim YH, Song KY. Mapping of intermodal beat length distribution in an elliptical-core two-mode fiber based on Brillouin dynamic grating. *Opt Express* (2014) 22:17292. doi:10.1364/OE.22.017292

20. Kasap SO. *Optoelectronics and photonics: Principles and practices*. 2nd ed. Boston: Pearson (2013).

21. Li H, Li H, Meng F, Lou X, Zhu L. All-fiber MZI sensor based on seven-core fiber and fiber ball symmetrical structure. *Opt Lasers Eng* (2019) 112:1–6. doi:10.1016/j.optlaseng.2018.08.021

22. Liang X, Liu S, Li Y, Liu Z, Jian S. Characteristics of a high extinction ratio comb-filter based on LP01–LP11even mode elliptical multilayer-core fibers. *Opt Fiber Technol* (2015) 21:103–9. doi:10.1016/j.yofte.2014.09.005

23. Gloge D. Weakly guiding fibers. *Appl Opt* (1971) 10:2252–8. doi:10.1364/AO.10.002252

24. Li H, Ren G, Atakaramians S, Kuhlmey BT, Jian S. Linearly polarized single TM mode terahertz waveguide. *Opt Lett* (2016) 41:4004. doi:10.1364/OL.41.004004

25. Liang X, Ning T, Li J, Li Y, Liu Z. Axial micro-strain sensor based on resonance demodulation Technology via dual-mode CMECF. *Photonic Sens* (2019) 9:78–88. doi:10.1007/s13320-018-0513-x

26. Zuo B-Z, Liang X, Zhang X-R, Yin T-H. Detection of refractive index with a temperature-compensated MZI-based optical sensor using few-mode fiber. *IEEE Access* (2021) 9:158651–9. doi:10.1109/ACCESS.2021.3130371

27. Chuang SL. *Physics of photonic devices*. Hoboken, New Jersey: John Wiley & Sons (2012).

28. Wu Y, Pei L, Jin W, Jiang Y, Yang Y, Shen Y, et al. Highly sensitive curvature sensor based on asymmetrical twin core fiber and multimode fiber. *Opt Laser Technol* (2017) 92:74–9. doi:10.1016/j.optlastec.2017.01.007

frontiers | Frontiers in Physics

TYPE Original Research
PUBLISHED 22 February 2023
DOI 10.3389/fphy.2023.1134745

OPEN ACCESS

EDITED BY
Shuo Liu,
Hebei University of Technology, China

REVIEWED BY
Chunyu Guo,
Shenzhen University, China
Xiaohui Li,
Shaanxi Normal University, China

*CORRESPONDENCE
Yingbin Xing,
jsxyb1232008@126.com

SPECIALTY SECTION
This article was submitted to Optics and Photonics, a section of the journal Frontiers in Physics

RECEIVED 30 December 2022
ACCEPTED 14 February 2023
PUBLISHED 22 February 2023

CITATION
Liao S, Luo T, Xiao R, Cheng J, Shu C, Zhang Z, Zhou Y, Xing Y, Li H, Peng J, Dai N and Li J (2023), 3.2 kW, 0.22 nm narrow-linewidth MOPA configuration fiber laser with a homemade polarization-maintaining Yb-doped fiber. *Front. Phys.* 11:1134745. doi: 10.3389/fphy.2023.1134745

3.2 kW, 0.22 nm narrow-linewidth MOPA configuration fiber laser with a homemade polarization-maintaining Yb-doped fiber

Shibiao Liao, Tao Luo, Runheng Xiao, Junjie Cheng, Chang Shu, Zhilun Zhang, Yanyan Zhou, Yingbin Xing*, Haiqing Li, Jinggang Peng, Nengli Dai and Jinyan Li

Wuhan National Laboratory for Optoelectronics, Huazhong University of Science and Technology, Wuhan, China

In this work, a narrow-linewidth linearly polarized fiber amplifier with a record output power of 3.2 kW was achieved based on a homemade polarization-maintaining Yb-doped fiber corresponding to a slope efficiency of 79% and a 3 dB linewidth of 0.2227 nm. By examining various numerical aperture (NA) PMYDFs, the experimental investigation on expanding mode instability (MI) threshold in PM fiber amplifiers was put on display. And the results reveal that the MI threshold is enhanced by more than 370 W for every 0.004 decrease in core numerical aperture. Increasing the seed linewidth from 0.0454 nm to 0.0976 nm by adding 200 m polarization maintaining Ge-doped fiber the stimulated Brillouin scattering threshold increased from 805 W to above 3.2 kW. By applying the MI suppression method, a double-eight-shaped aluminum plate was adopted to coil the gain fiber, and the MI threshold increased by more than 1100 W.

KEYWORDS

polarization-maintaining Yb-doped fiber, MOPA, fiber laser, SBS, MI, NA control

1 Introduction

High-power narrow-linewidth fiber lasers or amplifiers with linearly polarized have been a major area of interest within the field of gravitational wave detection (GWD), non-linear frequency conversion (NFC), spectral beam combining (SBC), coherent beam combining (CBC) [1–6], and ultrafast lasers [7–12], etc., Over the last decade, ytterbium (Yb)-doped master oscillator power amplifiers (MOPAs) with linearly polarized ones have made great progress, and the power scaling has reached the muti-kilowatt level [13–15]. However, a number of destructive non-linear phenomena, including stimulated Raman scattering (SRS), stimulated Brillouin scattering (SBS), and thermal mode instability (MI), can jeopardize the stability of the laser system because of the high intensity in the fiber core [6, 16–18]. Among them, MI and SBS are the main limiting factors in the power scaling of a high-power narrow-linewidth linearly polarized MOPA system [18, 19].

A great deal of theoretical and experimental strategies has been carried out for mitigation of the MI or increasing its threshold power and SBS non-linearities in fiber laser systems. By taking into different strategies, some traditional methods to mitigate the MI in high-power all-fiber laser systems are to use few-mode fibers with tight coiling [18, 20], balance the heat

load of a gain fiber [21, 22], design the spiral winding shape of fiber [23, 24], and tailor the gain fiber with high laser performance [25]. To some extent, tailing the gain fibers, such as confining Yb^{3+} doping in the fiber core [26, 27], varying core size in the longitudinal dimension [28, 29], and decreasing the numerical aperture (NA) of the large mode area (LMA) [30] fiber are theoretically and experimentally demonstrated to be capable of the effective suppression of the MI effects. And there are many theoretical and experimental studies for designing the common Yb-doped fiber (YDF) to solve the MI in random polarized fiber laser systems [30, 31]. However, few studies are reported on the fiber design solutions of MI in a linearly polarized fiber laser system due to its complexity of polarization-maintaining Yb-doped fiber (PMYDF) structure manufacturing. The traditional modified chemical vapor deposition (MCVD) technology combined with the solution doping process (SDP) is considered to be an easy and effective strategy to design the core NA of fiber and manufacture the excellent PMYDF [5, 32]. The detailed experimental studies on the influence of core NA of the PMYDF have a significant impact on the further power scaling of a high-power linearly polarized fiber laser.

Taking the various strategies of seed sources into consideration, some typical approaches to realize high-power narrow-linewidth linearly polarized fiber amplifiers are to use phase-modulated single-frequency laser (PMSFL) seeds [14, 15], super-fluorescent (SF) seeds [33, 34], random fiber laser (RFL) seeds [35, 36], and fiber oscillator laser (FOL) seeds [5, 13, 32]. And the multi-stage pre-amplifier and main-amplifier schemes based on the PMSFL seeds, SF seeds, and RFL seeds make the entire system complex and expensive while the scheme based on the FOL seeds is straightforward and practical due to its one-stage amplification. However, it is well known that the SBS effect is easily stimulated in amplifiers based on a FOL seed due to its temporal instability [14, 36]. Previous theoretical studies have shown that broadening the output linewidth of the laser can effectively suppress the SBS effects [37]. Increasing the bandwidth of output coupler (OC) fiber Bragg grating (FBG) is adopted to be a common way to broaden the linewidth [38], however, which is not conducive to suppressing temporal instability. In 2019, Li et al. reported that by inserting long transmission fibers in a seed laser [39], the temporal fluctuations could be flattened, while increasing the seed linewidth. Therefore, we want to introduce the method of inserting long transmission fibers into the polarization-maintaining (PM) MOPA systems based on a FOL seed and improve the SBS threshold, which is meaningful to the wider application of high-power narrow-linewidth linearly polarized amplifiers.

In this work, a maximum output power of 3.2 kW with a 3 dB linewidth of 0.2227 nm reached by applying the combination of a homemade PMYDF and a double-eight-shaped aluminum plate, corresponding to a slope efficiency of 79%. To the best of our knowledge, this is the highest output power from a linearly polarized narrow-linewidth fiber amplifier based on a FOL seed. The beam quality factor of M^2_x and M^2_y is 1.307 and 1.285 respectively at 2024 W. During the experimental process, three different NA PMYDFs were manufactured by MCVD combined with SDP, and the experimental relationship between the core NA and MI threshold in PM systems have been investigated for the first time. The results reveal that the MI threshold can be further scaled by decreasing the core NA. The threshold power increased from 1350 W to 1752 W and 2126 W for the case where the core NA drops from 0.068 to 0.064 and 0.060. The SBS effects are well-suppressed during the power scaling by broadening the seed linewidth.

TABLE 1 Characteristic of three different NA PMYDFs.

Fiber samples	NA	Absorption@ 976 nm	Fiber length m)
PMYDF-1	0.068	1.56 dB/m	11.2
PMYDF-2	0.064	1.47 dB/m	11.9
PMYDF-3	0.060	1.35 dB/m	13.0

2 Fiber fabrication and characterization

To study the MI threshold of fibers, three different NA PMYDF were manufactured by MCVD combined with SDP. The core and inner cladding dimensions of the PMYDF were designed and found to be 20 μm and 400 μm, respectively, as the relatively large-mode area may reduce non-linear effects and an adequate NA may ensure excellent beam quality. In addition, the 20/400 μm PMYDF has been a preferable choice for the high-power narrow-linewidth fiber amplifiers, and the fiber design based on NA investigation may provide a new sight for its further scaling. The concentration of the doping components in the SiO_2 matrix directly affects the refractive index and NA during the process of solution doping. Hence, the doping components of Yb^{3+} and Al^{3+} were adopted to modulate the NA of the fiber. It should be noted that the increased Yb^{3+} will improve the absorption coefficient and NA of fiber simultaneously and excessive Yb^{3+} doping will cause crystallization. Therefore, Al^{3+} needs to be co-doped at the same time to improve the solubility of Yb^{3+} and eliminate crystallization. Meanwhile, the development of a center dip in the refractive index profile (RIP) may be avoided since Al^{3+} has minimal volatility. Since they all contribute positively to the RIP, the content of Yb^{3+} and Al^{3+} is accurately controlled so that NA can be confined to an effective range.

The technique in which PMYDF is prepared is almost identical to that described in our earlier work [32]. Specifically, the fabrication of active fiber preforms by MCVD combined with SDP can be divided into five fundamental steps: 1) barrier layer and soot layer deposition, 2) rare-earth solution doping, 3) thermal drying, 4) sintering, and 5) collapse. Different from the preparation of conventional Yb-doped fiber (YDF), the preparation of PMYDF needs to add two sets of processes: preform drilling and boron rod assembly. Subsequently, after achieving a well-prepared polarization maintaining (PM) preform, at temperatures of 1980°C, the preform assembly was pulled into a 20/400 μm fiber with a circular cladding and coated with a low-index polymer [5].

The detailed parameters of the three PMYDFs are shown in Table 1. In order to characterize the effect of NA on the MI threshold, the three kinds of PMYDF were fabricated with very close parameters for comparison. The RIP of PMYDF-3 with almost the same trend as the other two is shown in Figure 1A. The

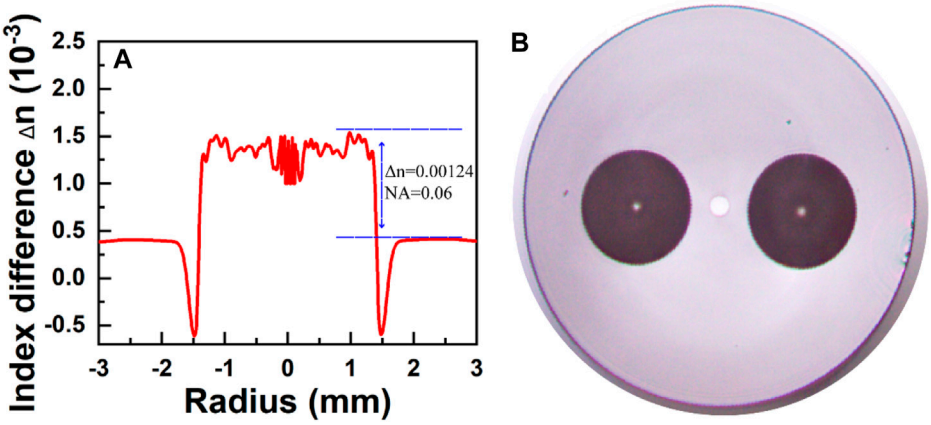

FIGURE 1
Characteristics of the PMYDF-3 (NA = 0.06) **(A)** Refractive index profile of the preform; **(B)** Image of the fiber cross-section.

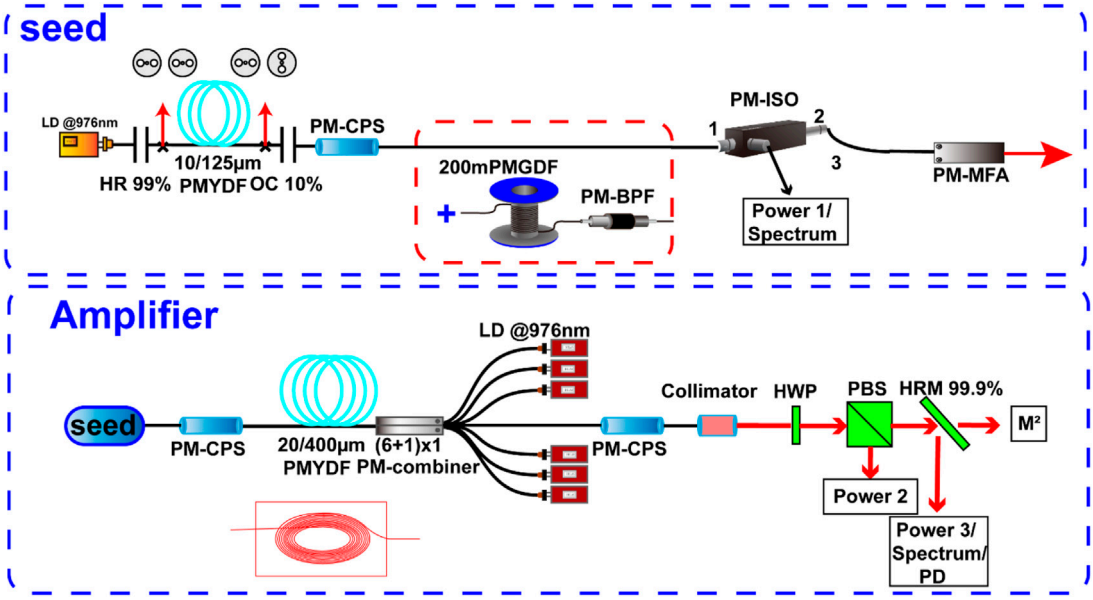

FIGURE 2
Scheme of experimental setup based on master oscillator power amplifier (MOPA). LD, laser diode; HR, high reflectivity fiber Bragg grating; OC, output coupler fiber Bragg grating; PM-CPS, polarization maintaining cladding power stripper; PMGDF, polarization maintaining Ge-doped fiber; BPF, bandpass filter; ISO, isolator; MFA, mode field adaptor; HWP, half-wave plate; PBS, polarization beam splitter; HRM, high reflection mirror; PD, photodetector.

difference between the three fibers lies in the various core ions doping concentrations, which leads to a different NA. Figure 1B presents the cross-section of the PMYDF-3 exhibiting a 20.1 μm fiber core and a 400.2 μm inner cladding. The NA of the three fibers is 0.068, 0.064, and 0.060, respectively, corresponding to the cladding absorption coefficients at 976 nm of 1.56 dB/m, 1.47 dB/m, and 1.35 dB/m. As revealed in [40], Tao et al. demonstrated that the MI threshold was independent of dopant concentration as long as the same total pump absorption was maintained. Therefore, the only variable that affects the MI threshold is the difference in NA in our experiment.

3 Experimental setup

An all-fiber high-power narrow-linewidth linearly polarized MOPA was built up as shown in Figure 2, which has been described in our previous publication [5, 32]. The system contains a PM-FOL seed and the main PM amplifier. The PM-FOL seed consisting of a linear-cavity oscillator which is composed of a pair of gratings and an active fiber of 3.2 m is pumped by a fiber-pigtailed wavelength-stabilized 976 nm laser diode (LD). For polarization selection, the fast-axis wavelength of the high reflectivity (HR) FBG fitted the slow-axis wavelength of the

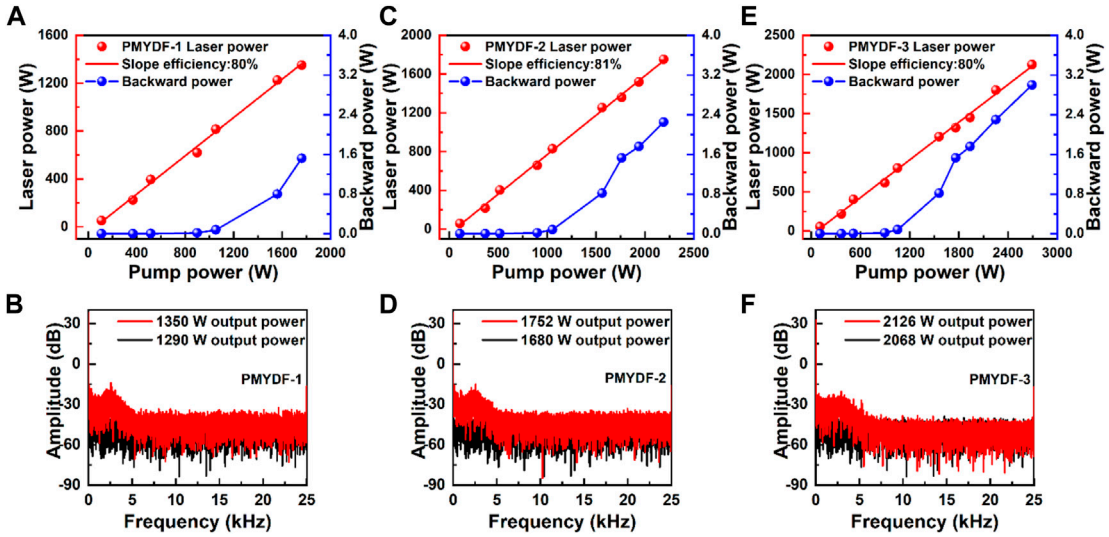

FIGURE 3
The laser and backward power of a MOPA system versus the pump power and the frequency-domain characteristics of the amplifier by applying the three different NA PMYDFs. **(A)** The laser performance of the PMYDF-1. **(B)** Frequency-domain characteristics before and after MI by applying the PMYDF-1. **(C)** The laser performance of the PMYDF-2. **(D)** Frequency-domain characteristics before and after MI by applying the PMYDF-2. **(E)** The laser performance of the PMYDF-3. **(F)** Frequency-domain characteristics before and after MI by applying the PMYDF-3.

output coupler OC FBG. The full width at half maximum bandwidth (FWHM) of the HR-FBG and the OC-FBG was 0.25 nm and 0.05 nm, respectively. The cladding absorption coefficient of the commercial PMYDF is approximately 4.95 dB/m at 976 nm. The cavity's passive fiber measures around 1 m in length. Then, a PM cladding power stripper (CPS), a PM isolator (ISO), and a PM mode field adaptor (MFA) are closely followed. When the laser beam passes through the PM ISO, the PM ISO is used not only for blocking backward light but also for monitoring the backward SBS signal which originates from a final amplifier. The PM MFA is with an input size of 10/125 μm and an output size of 20/400 μm.

The main PM amplifier is based on a counter-pumping configuration. The PM CPS after the seed is used to remove the cladding modes and pump lights in the fiber cladding which are generated by mode field mismatch from the seed and unabsorbed pump lights from the amplifier. A total pump absorption of 17.5 dB at 976 nm was adopted to trade off the laser efficiency against the SBS effects. The gain fiber length used in the amplifier is shown in Table 1. A runway-shaped aluminous plate was employed to coil the gain fiber for thermal management. The signal laser was injected from the coiled PMYDF with a diameter of ~10 cm, and the largest diameter of the coiled PMYDF was ~17 cm. The amplifier was pumped by non-wavelength-stabilized 976 nm LDs *via* a (6 + 1) × 1 PM combiner. Six 220/242 μm fibers with a NA of 0.22 make up the combiner's pump ports, while its input and output signal ports are both 25/400 μm PM fibers with NA of 0.065 for the core and 0.46 for the cladding, respectively. A CPS and a collimator with a size of 30/400 μm are spliced behind the PM combiner. The output beam passes a half-wave plate (HWP) and a polarization beam splitter (PBS) for selecting the measured polarization. The PER is determined as 10log (Power 3/Power 2) shown in Figure 2. Then, a high reflection mirror (HRM) follows. A photodetector (PD) with a pinhole of a 1.5 mm diameter was placed to receive the reflected scattering lights. Three power meters, a spectrum analyzer, an oscilloscope, and an M^2 analyzer are used to analysis of the characteristics of light. The whole MOPA system was mounted on an actively cooled heat sink with a cooling temperature of 16 °C to avoid thermal damage [32].

4 Experimental results and discussion

4.1 Laser performance and discussion of three PMYDFs

The contrast of output power characteristics: the output laser and backward power of the MOPA system versus the pump power and the frequency-domain characteristics of the amplifier by applying the three different NA PMYDFs were recorded and the results are shown in Figure 3. Since SBS has been a serious limiting factor to power scaling and is easy to be stimulated in high-power narrow-linewidth fiber amplifiers, hence, the backward power was recorded by a power meter named power 1, as depicted in Figure 2. Experimentally, it has been reported that reflectivity of 0.01%–1% indicates the amplifier working around the continuous wave (CW) SBS threshold [15]. By applying the PMYDF-1 in the amplifier, an output power of 1350 W was achieved with a slope efficiency of 80% shown in Figure 3A. The high laser efficiencies indicate that the fabricated fiber possesses a low background loss. During the power scaling experiments, a sudden increase of backward power occurred with the laser power beyond 820 W. This can be a sign of the SBS threshold. As a PM ISO was utilized to protect the seed source from damage, further power scaling was carried out for the research of fiber performance. The highest backward power was 1.52 W. It is well known that the energy transfer at a frequency of kHz level between the fundamental mode (FM) and the higher order modes

TABLE 2 Results by applying the three different NA PMYDFs.

Fiber samples	NA	MI threshold (W)	SBS threshold (W)	Highest backward power (W)
PMYDF-1	0.068	1350	820	1.52
PMYDF-2	0.064	1752	820	2.25
PMYDF-3	0.060	2126	805	3.00

(HOMs) indicates the occurrence of MI [41]. From Figure 3B, one can conclude that the frequency-domain signal remains stable at a laser power of 1290 W, and the frequency-domain signal lifting doesn't occur. The fluctuation frequency in the range of 0–5 kHz appears in the Fourier spectrum with the further increased power to 1350 W, which reveals that the MI threshold of the PMYDF-1 is 1350 W. Figure 3C displays that the output power of 1752 W was achieved with a slope efficiency of 81% by applying the PMYDF-2. The highest backward power was 2.25 W. Similarly, the SBS threshold reaches when the laser power is approximately 820 W. And in Figure 3D, it can be seen that the MI threshold of the PMYDF-2 is 1752 W. Figure 3E exhibits that an output power of 2126 W was achieved with a slope efficiency of 80% by applying the PMYDF-3. The SBS threshold reaches at the laser power of 805 W, and the highest backward power was 3 W. The MI threshold of the PMYDF-3 is 2126 W shown in Figure 3F.

The experimental results are arranged in detail shown in Table 2. There is a clear trend of elevation in the MI threshold by decreasing the NA of PMYDF, which is consistent with the finding in non-PM MOPA [30, 42]. For example, Tao et al. reported that the threshold power increases by 57%, 25%, 16%, and 11% for 20/400, 25/400, 30/400, and 30/250 fiber when the core NA decreases from 0.07 to 0.045 by numerical investigations [42]. In this work, the prominent aspect of our research is that the experimental investigations indicate MI threshold increases by more than 370 W for every 0.004 decreases in NA. This result mainly can be explained by the fact that the increased NA leads to the increasing number of modes supported by the core, which reduces the proportion of FM, so MI is more likely to occur. For the first time, accurate experimental data is given to illustrate the relationship between NA and MI threshold in 20/400 PMYDF, which is urgently needed for current power scaling in high-power narrow-linewidth linearly polarized fiber amplifiers [14, 19]. Although the gain fiber lengths employed in the amplifier have meter-scale differences, the previous experimental results show that the SBS threshold was affected little. The reasonable explanation of different backward power is that the SBS light passing through the gain fiber can be amplified, therefore, the backward power increased as the power was scaling.

4.2 The mitigation of SBS

To overcome the SBS observed in the present MOPA system, the common mitigation strategy which relied on increasing the length of 200 m polarization maintaining Ge-doped fiber (PMGDF) was applied to increase the linewidth of the laser shown in Figure 2. The PMGDF was spliced to the end of PM-CPS. As illustrated in [39], the stimulated Raman scattering (SRS) will be stimulated and accumulated due to the excessive transmission fiber. Therefore, a PM bandpass filter (BPF) was used to suppress the SRS. The 1064 nm BPF has the features of low insertion loss and 35 dB out-band suppression, with a passband of 8 nm and a maximum power handling of 30 W. Figure 4A depicts the evolution of seed linewidth before and after adding 200 m PMGDF. As is shown, the 3 dB linewidth of the original seed and broadened seed are 0.0454 nm and 0.0967 nm, respectively. In the following, we carried out the same laser experiment by applying the PMYDF-3 and investigated the improvement of the SBS threshold. As the laser power improves, as is shown in Figure 4B, the backward power keeps below the SBS threshold. And the highest backward power was 72 mW at the laser power of 2126 W. The results demonstrate the well-suppressed SBS effects and the MOPA system can afford higher laser output.

4.3 The mitigation of MI

Since the optimization of SBS effects was achieved, we considered realizing higher output power by suppressing the MI. The tight coiling method stands out due to its simplicity of implementation, which may be carried out without the construction of a more complex fiber or the selection of an exact wavelength. However, it is pointed out in [43] that the linearly polarized laser's polarization direction is parallel to the direction of stress, which might greatly lessen the bend loss of the HOMs caused by the photo-elastic effect. The MI threshold for the commercial PMYDF is lower than those of the non-PMYDF in the same coil package as a result of this effect, which lessens the impact of the coil technique on MI suppression [44, 45]. Therefore, in order to attain a higher overall bend loss and avoid the drawback of reducing the bend loss of HOMs, the MI suppression approach must be developed.

As shown in Figure 5A, the original cooling system for fiber thermal management is a runway-shaped aluminous plate with a bending diameter ranging from 10cm to 17 cm. The seed laser was injected into the coil with a bending diameter of 10 cm and exited from the coil with a bending diameter of 17 cm. To increase the HOMs loss, a double-eight-shaped aluminum plate was adopted to suppress the MI and enhance the MOPA output power shown in Figure 5B. The difference is that the seed laser was injected into the coil and exited from the coil with the same bending diameter of 10 cm, and the maximum bending diameter of the coil was only 11 cm.

Figure 6A shows the output power and backward power of the MOPA system versus the pump power, corresponding to a slope efficiency of 79%. As is shown, the SBS effects are well-suppressed during the power scaling and the backward power is 0.19 W at the laser power of 3.2 kW. To the best of our knowledge, 3.2 kW is the maximum output power of a narrow-linewidth linearly polarized fiber system based on a FOL seed. In Figure 6B, the frequency-domain spectra stay stable below the MI threshold for the laser

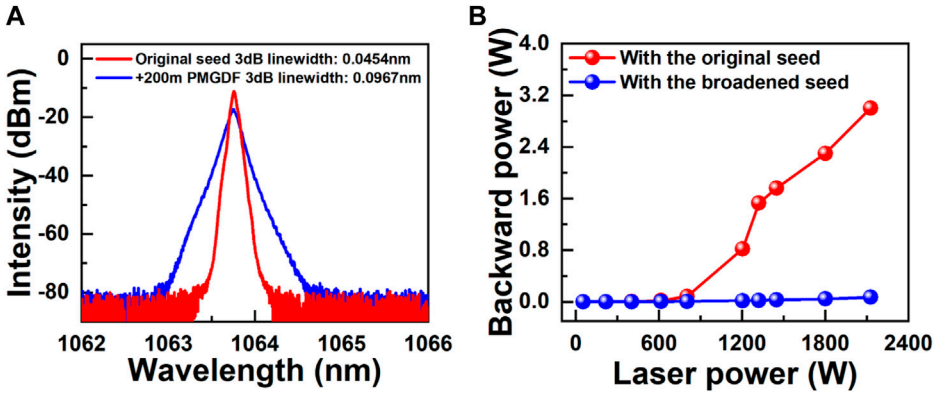

FIGURE 4
The results of the MOPA system before and after adding 200 m PMGDF. **(A)** The spectra of seed. **(B)** The backward power versus the laser power of a MOPA system by applying the PMYDF-3.

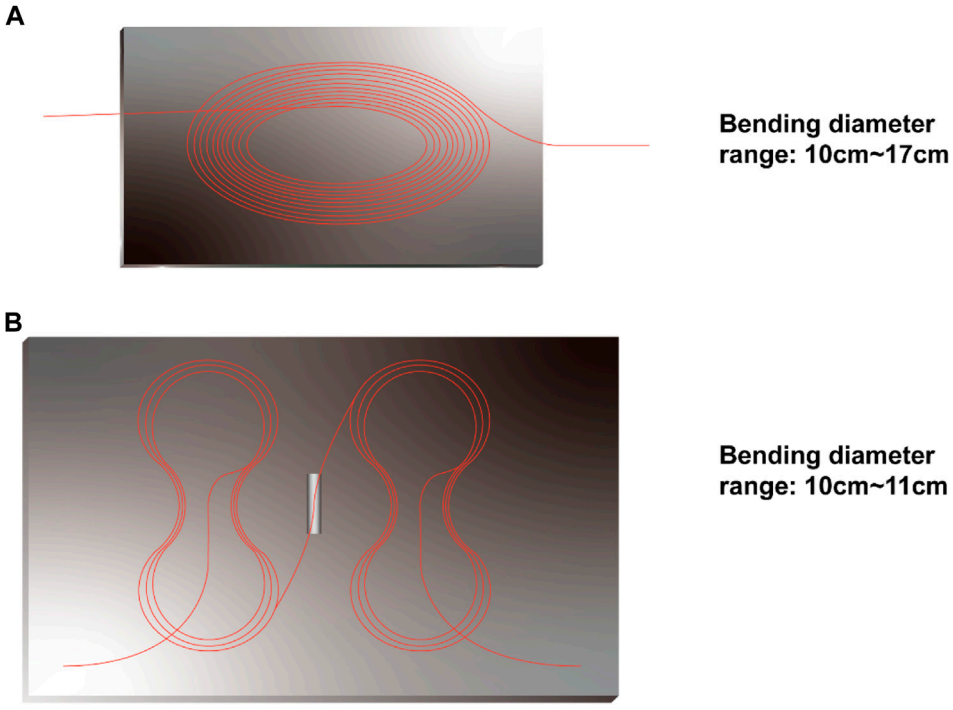

FIGURE 5
The cooling system for fiber thermal management. **(A)** A runway-shaped aluminous plate. **(B)** A double-eight-shaped aluminum plate.

power of 3.2 kW and the fluctuation frequencies appear in the range of 0–5 kHz for the laser power of 3.227 kW, which demonstrates the MI threshold is 3.227 kW. The inset of Figure 6B is a power display screenshot at the laser power of 3.227 kW.

One can conclude from the experiment that coiling the PMYDF in a double-eight-shaped aluminum plate is superior to coiling it in a runway-shaped aluminous plate, which increases the MI threshold by more than 1100 W. The reasonable explanation is that a higher total HOMs bending loss is obtained by coiling the gain fiber in a double-eight-shaped aluminum plate, which is consistent with our expectations. The coil diameter increases as the laser propagate along the fiber with a runway-shaped aluminous plate, resulting in the HOMs bending loss decreasing dramatically. However, the coil diameter remains almost unchanged with a double-eight-shaped aluminum plate, which is beneficial to realize a higher loss of HOMs.

In Figure 7A, the spectrum is shown for the 3.2 kW MI-suppressed MOPA which is achieved based on a higher loss of HOMs. The laser-to-Raman peak intensity ratio is larger than 27 dB,

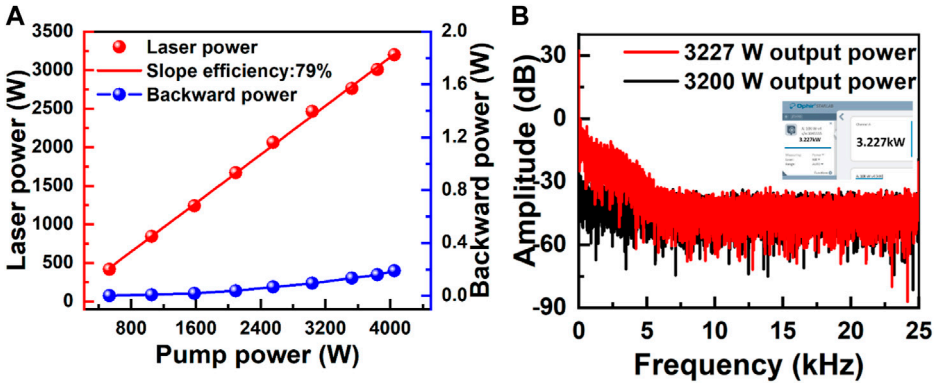

FIGURE 6
The laser performance of the PMYDF-3 when the MI is suppressed. **(A)** Laser power and backward power of a MOPA system versus the pump power. **(B)** Frequency-domain characteristics before and after MI. Inset: power display screenshot at the laser power of 3.227 kW.

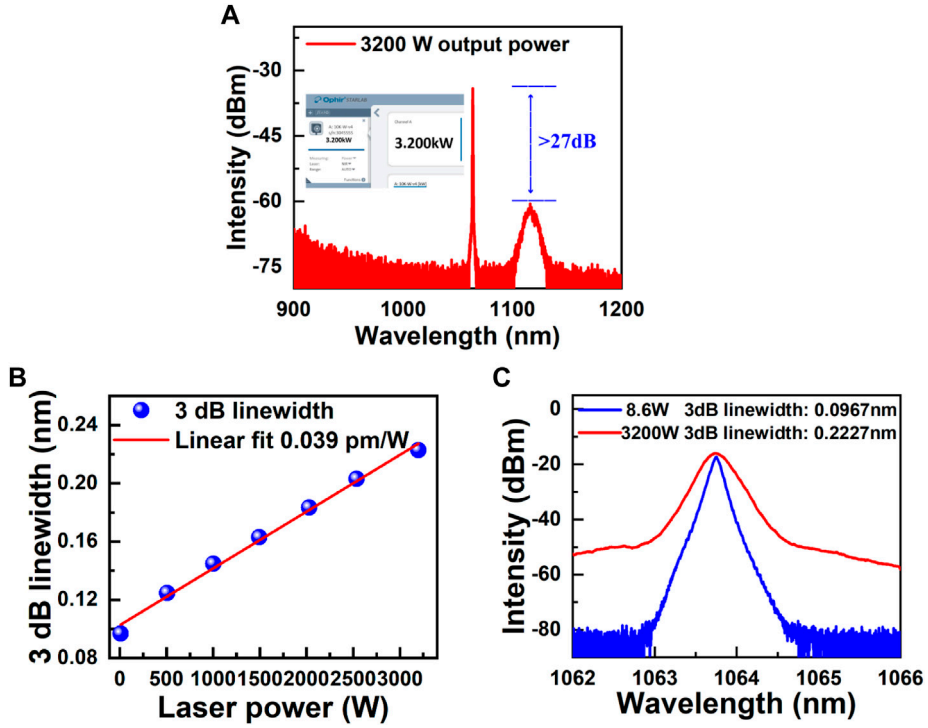

FIGURE 7
(A) Spectrum of the MOPA system at the laser power of 3.2 kW. **(B)** 3 dB linewidth versus the laser power. The 3 dB linewidths of 508 W, 1002 W, 1495 W, 2027 W, 2538 W, and 3.2 kW are 0.1247 nm, 0.1447 nm, 0.1629 nm, 0.1833 nm, 0.2030 nm, and 0.2227 nm, respectively. **(C)** Spectra of the MOPA system at the laser power of 8.6 W and 3.2 kW, and the 3 dB linewidth are 0.0967 nm, and 0.2227 nm, respectively.

and the SRS effects are severe at this power level which should be effectively suppressed if further power scaling is needed. It can be explained that the accumulated SRS was caused by the 200 m PMGDF, which is a coincidence with the results in Ref. [39]. The SRS still exists because of the inadequate inhibition effect of BPF. Meanwhile, recent research reveals that several non-linear effects can also lead to MI, such as inter-modal four-wave mixing (IM-FWM) [46], SRS [6], etc. As shown in Figure 7A, there is no characteristic peak caused by the IM-FWM effect in the spectrum, and the content of SRS is not enough to trigger MI. The linewidth of a high-power narrow-linewidth linearly polarized amplifier matters a lot for its application, such as SBC and CBC. Consequently, the 3 dB linewidth of an SBS-suppressed and MI-suppressed MOPA was measured and shown in Figures 7B, C. The 3 dB linewidth versus the laser power is depicted in Figure 7B, corresponding to a linear fitting efficiency of 0.039 pm/W. And the

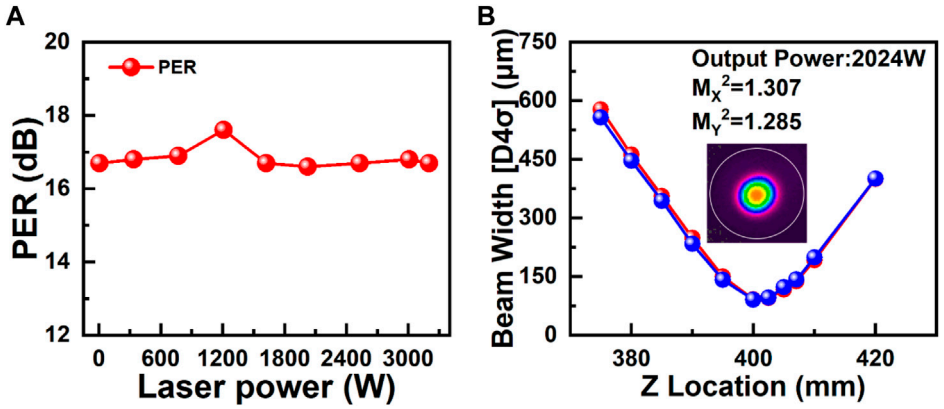

FIGURE 8
(A) PER versus laser power of a MOPA system. **(B)** Diffraction limited beam quality of the improved MOPA system at 2024 W after suppressing the SBS and mitigation of MI.

3 dB linewidth of a MOPA at 8.6 W and 3.2 kW are 0.0967 nm and 0.2227 nm, respectively.

Figure 8A reveals the evolution of the PER at different levels of laser power, and it can be seen that the PER keeps larger than 16.6 dB, which demonstrates a good polarization performance of the fiber. For the sake of the power-carrying capacity of the attenuation lens, a near-diffraction-limited output beam at the laser power of 2024 W was measured by an M^2 analyzer with the M^2_x = 1.307 and M^2_y = 1.285.

5 Conclusion

In conclusion, a maximum output power of 3.2 kW was achieved with a 3 dB linewidth of 0.2227 nm, corresponding to a slope efficiency of 79%. The PER remained larger than 16.6 dB during the power scaling. During the process of experiments, we investigated the effects of core NA on the MI of PMYDFs for the first time. It shows the MI threshold can be further scaled by decreasing the core NA, which is consistent with the results on non-PMYDF. For the case that the core NA decreases from 0.068 to 0.064 and 0.060, the threshold power increased from 1350 W to 1752 W and 2126 W. Increasing the seed linewidth from 0.0454 nm to 0.0976 nm by adding 200 m PMDGF, the SBS threshold increased from 805 W to above 3.2 kW. Compared with the method of coiling gain fiber in a runway-shaped aluminous plate, coiling it in a double-eight-shaped aluminum plate has a higher MI threshold, which enhances the output power by more than 1100 W. The results could provide a good reference for the power scaling of a narrow-linewidth linearly polarized system.

Data availability statement

The original contributions presented in the study are included in the article/supplementary material, further inquiries can be directed to the corresponding author.

Author contributions

SL: Conceptualization, Methodology, Validation, Investigation, Resources, Data Curation, Visualization. TL: Writing–Review & Editing. RX: Writing–Review & Editing. JC: Writing–Review & Editing. CS: Writing–Review & Editing ZZ: Writing–Review & Editing. YZ: Writing–Review & Editing. YX: Methodology, Validation, Writing–Review & Editing, Resources, Supervision, Project administration, Funding acquisition. HL: Resources, Project administration, Funding acquisition. JP: Project administration, Funding acquisition. ND: Supervision, Writing–Review & Editing. JL: Conceptualization, Validation, Supervision, Project administration, Funding acquisition.

Funding

National Natural Science Foundation of China under Grant No. 61905080.

Conflict of interest

The authors declare that the research was conducted in the absence of any commercial or financial relationships that could be construed as a potential conflict of interest.

Publisher's note

All claims expressed in this article are solely those of the authors and do not necessarily represent those of their affiliated organizations, or those of the publisher, the editors and the reviewers. Any product that may be evaluated in this article, or claim that may be made by its manufacturer, is not guaranteed or endorsed by the publisher.

References

1. Jiang M, Ma P, Huang L, Xu J, Zhou P, Gu X. KW-level, narrow-linewidth linearly polarized fiber laser with excellent beam quality through compact one-stage amplification scheme. *High Power Laser Sci Eng* (2017) 5:e30. doi:10.1017/hpl.2017.31

2. Wang Y, Feng Y, Feng Y, Wang X, Wang X-J, Yan H, et al. 6.5 GHz linearly polarized kilowatt fiber amplifier based on active polarization control. *Appl Opt* (2017) 56:2760. doi:10.1364/ao.56.002760

3. Deschamps T, Ollier N, Vezin H, Gonnet C. Clusters dissolution of Yb3+ in codoped SiO2-Al2O3-P2O5 glass fiber and its relevance to photodarkening. *J Chem Phys* (2012) 136:014503. doi:10.1063/1.3673792

4. Ma P, Xiao H, Liu W, Zhang H, Wang X, Leng J, et al. All-fiberized and narrow-linewidth 5 kW power-level fiber amplifier based on a bidirectional pumping configuration. *High Power Laser Sci Eng* (2021) 9:e45–7. doi:10.1017/hpl.2021.32

5. Liao S, Luo T, Xiao R, Chu Y, Li H, Xing Y, et al. Spectral broadening suppressed by a gain-enhanced fiber in polarization maintaining high-power systems. *IEEE Photon J* (2022) 14:1–6. doi:10.1109/JPHOT.2022.3221834

6. Russell PSJ, Culverhouse D, Farahi F. Theory of forward stimulated Brillouin scattering in dual-mode single-core fibers. *IEEE J Quan Electron* (1991) 27:836–42. doi:10.1109/3.81397

7. Liu X, Yao X, Cui Y. Real-time observation of the buildup of soliton molecules. *Phys Rev Lett* (2018) 121:023905. doi:10.1103/PhysRevLett.121.023905

8. Zhang Z, Zhang J, Chen Y, Xia T, Wang L, Han B, et al. Bessel terahertz pulses from superluminal laser plasma filaments. *Ultrafast Sci* (2022) 2022:20221–6. doi:10.34133/2022/9870325

9. Liu X, Pang M. Revealing the buildup dynamics of harmonic mode-locking states in ultrafast lasers. *Laser Photon Rev* (2019) 13:1800333–9. doi:10.1002/lpor.201800333

10. Li X, Feng J, Mao† W, Yin F, Jiang J. Emerging uniform Cu2O nanocubes for 251st harmonic ultrashort pulse generation. *J Mater Chem C* (2020) 8:14386–92. doi:10.1039/d0tc03622f

11. Zhang C, Li X, Chen E, Liu H, Shum PP, han CX. Hydrazone organics with third-order nonlinear optical effect for femtosecond pulse generation and control in the L-band. *Opt Laser Technol* (2022) 151:108016. doi:10.1016/j.optlastec.2022.108016

12. Zhang C, Liu J, Gao Y, Li X, Lu H, Wang Y, et al. Porous nickel oxide micron polyhedral particles for high-performance ultrafast photonics. *Opt Laser Technol* (2022) 146:107546. doi:10.1016/j.optlastec.2021.107546

13. Wang Y, Ke W, Peng W, Chang Z, Feng3 YW, Sun Y, et al. 3 kW, 0.2 nm narrow linewidth linearly polarized all-fiber laser based on a compact MOPA structure. *Laser Phys Lett* (2020) 17:075101. doi:10.1088/1612-202X/ab8e42

14. Ren S, Ma P, Li W, Wang G, Chen Y, Song J, et al. 3.96 kW all-fiberized linearly polarized and narrow linewidth fiber laser with near-diffraction-limited beam quality. *Nanomaterials* (2022) 12:2541. doi:10.3390/nano12152541

15. Wang Y., Sun Y., Peng W., Feng Y., Wang J., Ma Y., et al. 3.25 kW all-fiberized and polarization-maintained Yb-doped amplifier with a 20 GHz linewidth and near-diffraction-limited beam quality. *Aplied Opt* (2021) 60:6331–6. doi:10.1364/ao.431081

16. Chu Q, Shu Q, Chen Z, Li F, Yan D, Guo C, et al. Experimental study of mode distortion induced by stimulated Raman scattering in high-power fiber amplifiers. *Photon Res* (2020) 8:595. doi:10.1364/prj.383551

17. Li W, Ma P, Chen Y, Song J, Lai W, Liu W, et al. 694 W sub-GHz polarization-maintained tapered fiber amplifier based on spectral and pump wavelength optimization. *Opt Express* (2022) 30:26875. doi:10.1364/oe.463082

18. Hejaz K, Shayganmanesh M, Rezaei-Nasirabad R, Roohforouz A, Azizi S, Abedinajafi A, et al. Modal instability induced by stimulated Raman scattering in high-power Yb-doped fiber amplifiers. *Opt Lett* (2017) 42:5274. doi:10.1364/ol.42.005274

19. Zhou P, Ma P, Liu W, Xiao H, Ren S, Song J, et al. High power, narrow linewidth all-fiber amplifiers. *PROCEEDINGS SPIE* (2022) 37. doi:10.1117/12.2614414

20. Beier F, Hupel C, Nold J, Kuhn S, Hein S, Ihring J, et al. Narrow linewidth, single mode 3 kW average power from a directly diode pumped ytterbium-doped low NA fiber amplifier. *Opt Express* (2016) 24:6011. doi:10.1364/oe.24.006011

21. Tao R, Ma P, Wang X, Zhou P, Liu Z. Theoretical study of pump power distribution on modal instabilities in high power fiber amplifiers. *Laser Phys Lett* (2017) 14:025002. doi:10.1088/1612-202X/aa4f8e

22. Yang B, Wang P, Zhang H, Xi X, Shi C, Wang X, et al. 6 kW single mode monolithic fiber laser enabled by effective mitigation of the transverse mode instability. *Opt Express* (2021) 29:26366. doi:10.1364/oe.433630

23. Su R, Tao R, Wang X, Zhang H, Ma P, Zhou P, et al. 2.43 kW narrow linewidth linearly polarized all-fiber amplifier based on mode instability suppression. *Laser Phys Lett* (2017) 14:085102–19. doi:10.1088/1612-202X/aa760b

24. Wang Y, Wang Y, Wang Y, Feng Y, Feng Y, Ma Y, et al. 2.5 kW narrow linewidth linearly polarized all-fiber MOPA with cascaded phase-modulation to suppress SBS induced self-pulsing. *IEEE Photon J* (2020) 12:1–15. doi:10.1109/JPHOT.2020.2997935

25. Zhang Z, Lin X, Zhang X, Luo Y, Liao S, Wang X, et al. Low-numerical aperture confined-doped long-tapered Yb-doped silica fiber for a single-mode high-power fiber amplifier. *Opt Express* (2022) 30:32333. doi:10.1364/oe.466111

26. Gong M, Yuan Y, Li C, Yan P, Zhang H, Liao S. Numerical modeling of transverse mode competition in strongly pumped multimode fiber lasers and amplifiers. *Opt Express* (2007) 15:3236. doi:10.1364/oe.15.003236

27. Liao L, Zhang F, He X, Chen Y, Wang Y, Li H, et al. Confined-doped fiber for effective mode control fabricated by MCVD process. *Appl Opt* (2018) 57:3244. doi:10.1364/ao.57.003244

28. Yang B, Zhang H, Shi C, Wang X, Pan Z, Wang Z, et al. High power monolithic tapered ytterbium-doped fiber laser oscillator. *Opt Express* (2019) 27:7585. doi:10.1364/oe.27.007585

29. Ye Y, Xi X, Shi C, Yang B, Wang X, Zhang H, et al. Comparative study on transverse mode instability of fiber amplifiers based on long tapered fiber and conventional uniform fiber. *Laser Phys Lett* (2019) 16:085109. doi:10.1088/1612-202X/ab2acf

30. Khitrov V, Minelly JD, Tumminelli R, Petit V, Pooler ES. 3kW single-mode direct diode-pumped fiber laser. *Fiber Lasers XI: Technol Syst Appl* (2014) 896189610V. doi:10.1117/12.2037453

31. Enbin W, Ang M, Eng S, Hang L, Hou Q, Hen D, et al. 50 μm core diameter Yb3+/Al3+/F– codoped silica fiber with M^2<1.1 beam quality. *Opt Lett* (2016) 41:504–7. doi:10.1364/OL.41.000504

32. Liao S, Xiao R, Luo T, Zhang X, Xing Y, Chu Y, et al. kW-level, narrow-linewidth linearly polarized all-fiber amplifier based on homemade Yb-doped aluminosilicate polarization-maintaining fiber. *Opt Fiber Technol* (2023) 75:103163. doi:10.1016/j.yofte.2022.103163

33. Xu J, Ye J, Xiao H, Leng J, Liu W, Zhou P. In-band pumping avenue based high power superfluorescent fiber source with record power and near-diffraction-limited beam quality. *High Power Laser Sci Eng* (2018) 6:e46–6. doi:10.1017/hpl.2018.43

34. Ma P, Tao R, Wang X, Zhou P, Liu Z *High-Power Narrow-Band and Polarization-*, 27 (2015). p. 879–82.

35. Iangming JXU, Uang LONGH, Iang MANJ, Un JYE, Engfei PMA, Eng JIL, et al. Near-diffraction-limited linearly polarized narrow-linewidth random fiber laser with record kilowatt output. *Photon Res* (2017) 5:350–4. doi:10.1364/prj.5.000350

36. Du S, Qi T, Li D, Yan P, Gong M, Xiao Q. 10 kW fiber amplifier seeded by random fiber laser with suppression of spectral broadening and SRS. *IEEE Photon Technol Lett* (2022) 34:721–4. doi:10.1109/LPT.2022.3183025

37. Aoki Y, Tajima K, Murata S *s*, 6 (1987).Input power limits of optical fibers due to stimulated Brillouin scattering in fsk coherent optical transmission system

38. Zhang S, Zhang W, Jiang M, Liu W, Ma P, Li C, et al. Suppressing stimulated Raman scattering by adopting a composite cavity in a narrow linewidth fiber oscillator. *Appl Opt* (2021) 60:5984. doi:10.1364/ao.430054

39. Li T, Ke W, Ma Y, Sun Y, Gao Q. Suppression of stimulated Raman scattering in a high-power fiber amplifier by inserting long transmission fibers in a seed laser. *J Opt Soc America B* (2019) 36:1457. doi:10.1364/josab.36.001457

40. Tao R, Ma P, Wang X, Zhou P, Liu Z. Study of dopant concentrations on thermally induced mode instability in high-power fiber amplifiers. *Laser Phys* (2016) 26:065103. doi:10.1088/1054-660X/26/6/065103

41. Zhang F, Wang Y, Lin X, Cheng Y, Zhang Z, Liu Y, et al. Gain-tailored Yb/Ce codoped aluminosilicate fiber for laser stability improvement at high output power. *Opt Express* (2019) 27:20824. doi:10.1364/oe.27.020824

42. Tao R, Ma P, Wang X, Zhou P, Liu Z. Influence of core NA on thermal-induced mode instabilities in high power fiber amplifiers. *Laser Phys Lett* (2015) 12:085101. doi:10.1088/1612-2011/12/8/085101

43. Liu C-H, Galvanauskas A, Khitrov V, Samson B, Manyam U, Tankala K, et al. High-power single-polarization and single-transverse-mode fiber laser with an all-fiber cavity and fiber-grating stabilized spectrum. *Opt Lett* (2006) 31:17. doi:10.1364/ol.31.000017

44. Platonov N, Yagodkin R, De La Cruz J, Yusim A, Gapontsev V. 1.5kW linear polarized on PM fiber and 2kW on non-PM fiber narrow linewidth CW diffraction-limited fiber amplifier. *Components Packaging Laser Syst* (2017) III:10085100850M. doi:10.1117/12.2263926

45. Brar K, Savage-Leuchs M, Henrie J, Courtney S, Dilley C, Afzal R, et al. Threshold power and fiber degradation induced modal instabilities in high-power fiber amplifiers based on large mode area fibers. *Fiber Lasers XI: Technol Syst Appl* (2014) 896189611R. doi:10.1117/12.2042261

46. Yin L, Han Z, Shen H, Zhu R. Suppression of inter-modal four-wave mixing in high-power fiber lasers. *Opt Express* (2018) 26:15804. doi:10.1364/oe.26.015804

frontiers | Frontiers in Physics

TYPE Brief Research Report
PUBLISHED 23 February 2023
DOI 10.3389/fphy.2023.1155266

OPEN ACCESS

EDITED BY
Bofeng Zhu,
Nanyang Technological University,
Singapore

REVIEWED BY
Cheng Li,
Intel, United States
Suchun Feng,
Beijing Jiaotong University, China

*CORRESPONDENCE
Liwen Sheng,
shengliwen2008@163.com
Lin Huang,
huanglin@ceyear.com

SPECIALTY SECTION
This article was submitted to Optics and Photonics, a section of the journal Frontiers in Physics

RECEIVED 31 January 2023
ACCEPTED 14 February 2023
PUBLISHED 23 February 2023

CITATION
Qiao S, Sheng L, Huang L, Zhang A, Wei Y, Liu Z, Ju J, Zhang Z, Yin B, Li P, Han J, Zhang Y and Qu T (2023), High-SMSR wavelength-swept laser with a CL-band mode-hopping free tuning range. *Front. Phys.* 11:1155266. doi: 10.3389/fphy.2023.1155266

High-SMSR wavelength-swept laser with a CL-band mode-hopping free tuning range

Shan Qiao[1], Liwen Sheng[1,2,3]*, Lin Huang[1,2,4]*, Aiguo Zhang[1], Yu Wei[1], Zhiming Liu[1], Junwei Ju[1], Zhihui Zhang[1], Bingqi Yin[1], Peng Li[1], Jilei Han[1], Yiqi Zhang[1] and Tianyang Qu[1]

[1]Ceyear Technologies Co., Ltd., Qingdao, China, [2]Science and Technology on Electronic Test & Measurement Laboratory, Qingdao, China, [3]School of Electronic Engineering, Xidian University, Xi'an, China, [4]School of Information Science and Engineering, Shandong University, Qingdao, China

A high side-mode suppression ratio external-cavity wavelength-swept laser system with a wide mode-hopping free tuning range is developed. The proposed wavelength-swept laser is based on a single-angled facet gain chip in a classical Littman-Metcalf external-cavity configuration using a blazed diffraction grating as the feedback element. The output power, side-mode suppression ratio, and tunable range of the external-cavity wavelength-swept laser system are experimentally measured. Wide mode-hopping-free continuous wavelength tuning range about 100 nm in CL-band with a side-mode suppression ratio of more than 65.64 dB are realized. An output optical power of more than 14.12 dBm over the entire tunable region can also be achieved. The proposed external-cavity wavelength-swept laser system allows simultaneously high side-mode suppression ratio and no mode-hopping tunable radiation, thus opening a door for practical applications such as optical modulation schemes.

KEYWORDS

side-mode suppression ratio, mode-hopping free, wavelength-swept laser, Littman-Metcalf, narrow linewidth

1 Introduction

The highly controllable emission properties of wavelength-swept lasing sources are prior selected semiconductor lasers for a vast array of applications in fields including high-resolution spectroscopy [1,2], laser cooling [3], coherent optical orthogonal frequency division multiplexing (CO-OFDM) modulation schemes [4], space strontium optical clock [5–7], and optical frequency-domain reflectometry (OFDR) and so on [8–12]. Across these fields, the wavelength-swept lasing sources with higher side-mode suppression ratios (SMSRs) and increased mode-hopping free (MHF) tuning ranges continue to enable new applications. Therefore, it is critical to building a continuous wavelength-swept laser system with high SMSR.

Several types of wavelength-swept lasers, such as external-cavity semiconductor lasers (ECSLs), dye lasers, distributed Bragg reflector lasers, tunable solid-state lasers, vertical-cavity surface-emitting lasers, distributed feedback lasers, and optical non-linear frequency conversion-based lasers have been developed in the last 50 years [13–21]. Compared to other types of wavelength-swept laser, ECSL has the prestigious characteristics of a large tuning range, high signal-to-source spontaneous emission ratio, narrow linewidth, and low cost, which is one of the most versatile measuring tools [22–24]. An external-cavity diode laser

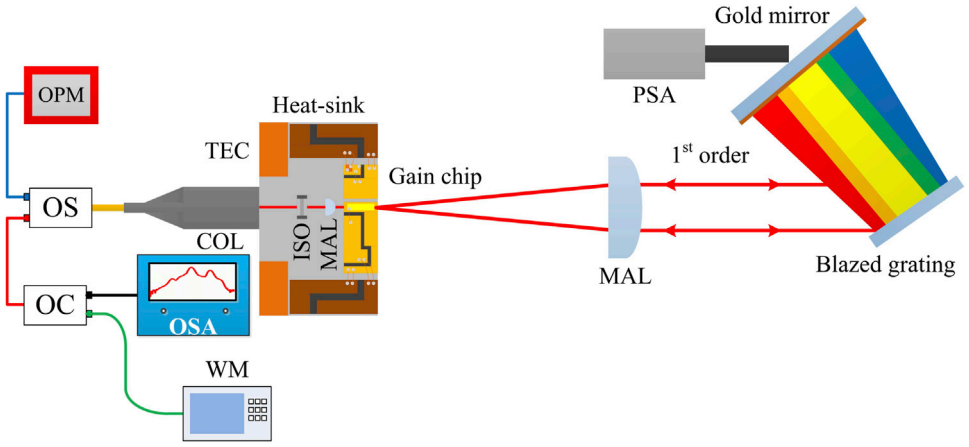

FIGURE 1
Schematic drawing of the proposed wavelength-swept laser setup built in the Littman-Metcalf configuration. OPM, optical power meter; OS, optical switch; TEC, thermoelectric cooler; MAL, molded aspherical lens; PSA, piezoelectric stack actuator; OC, optical coupler; OSA, optical spectrum analyzer; WM: wavelength meter; COL, collimator; ISO, isolator.

system with a maximum SMSR up to 50 dB at 1550 nm has been demonstrated by K. Fedorova et al., with a 173 nm tunable range of the proposed wavelength-swept laser system [25]. Using an InGaAsP/InP multiple quantum well (MQW) gain chip, an external-cavity diode laser configuration with a spectral range of 1320–1562 nm was achieved, where the SMSR covers the 17 dB–42 dB range [26]. Yuan et al. showed an extended-cavity InAs/InP quantum-dot (QD) laser operating at pulsed injection current with a maximum SMSR of around 20 dB, where the reported wavelength-swept laser system had a tuning range of 190 nm [27]. A high SMSR external-cavity laser scheme based on traditional Littman design was demonstrated by Gong *et al.*, with a maximum MHF range of 78 GHz [28]. A narrow linewidth external-cavity laser scheme was exhibited operating in C-band (1528.77–1568.36 nm in vacuum) by Zhang *et al.*, with an output power of around 13 dBm and with a SMSR around 55 dB [29]. Another C/L-band wavelength-tunable external cavity laser was demonstrated by K. Kasai *et al.*, with a spectral range of 1530–1570 nm or 1570–1610 nm without mode hopping and with a SMSR around 46 dB or 49 dB [30]. Recently, Wang *et al.* fabricated an ultra-high SMSR ECSL with a wide tunable range around 1550 nm, where a maximum wavelength tuning range of 209.9 nm was obtained, and the SMSR reached 65 dB [31]. Although many attempts focused on the widely tunable external-cavity laser configuration, this may not be the critical issue in many practical applications (typically in telecommunications) where the higher SMSR and the continuous tuning characteristics with MHF need to be paid more attention to.

In this work, based on an antireflection-coated single-angled facet gain chip in a Littman-Metcalf external cavity, a high-SMSR wavelength-swept laser with a CL-band (1520–1620 nm) MHF tuning range is experimentally demonstrated. By adjusting the length of the external cavity applied to the proposed configuration, a single mode tuning range of 100 nm without mode-hopping is obtained. The output power of the wavelength-swept laser is around 15.84 dBm with an injected current of 410 mA at the emitting wavelength of 1550 nm, and output power of more than 14.12 dBm over the entire tuning range is achieved. Meanwhile, the SMSR is more than 65.64 dB through the tuning range. The advantage of this proposed external-cavity wavelength-swept laser is that the lasing wavelength can be tuned finely in a range of C-band and L-band without mode-hoping, thus opening a door for practical application such as coherent optical modulation schemes.

2 Configuration of the wavelength-swept laser

A schematic drawing of the proposed wavelength-swept laser setup is shown in Figure 1. The customized single-angled facet gain chip is housed in a heat-sink with Peltier elements (or called thermoelectric cooler) attached to it is coated with an anti-reflection (0.005%) film on its angled facet and a reflectivity (10%) film on its normal facet. The temperature and the injection current of the single-angled facet gain chip are controlled with a homemade laser diode driver. The running temperature of the gain chip is typically stabilized at 25.0°C. The cavity length of the gain chip is 900 μm. A molded aspherical lens (NA = 0.55) with a focal length of 4.51 mm (Edmund, 87155) is applied to collimate the output continuous wave (CW) light from the gain chip. A gold-coated 900 grooves/mm blazed diffraction grating (Newport Richardson, 33025FL01-155R), with an average diffraction efficiency of 75%, is attached to the tilting face of the homemade mount. The collimated output beam is incident on the surface of the blazed diffraction grating. Depending on the incident angle of the light coming from the gain chip, a particular wavelength will be retroreflected from the gold-coated cavity mirror back into the gain chip to form the resonator. Tuning of the resonating wavelength is realized by rotating the gold-coated cavity mirror driven by a piezoelectric stack actuator with respect to the incident beam. The output of the lasing wavelength from the gain chip to the fiber is collected using a molded aspherical lens, an isolator and a

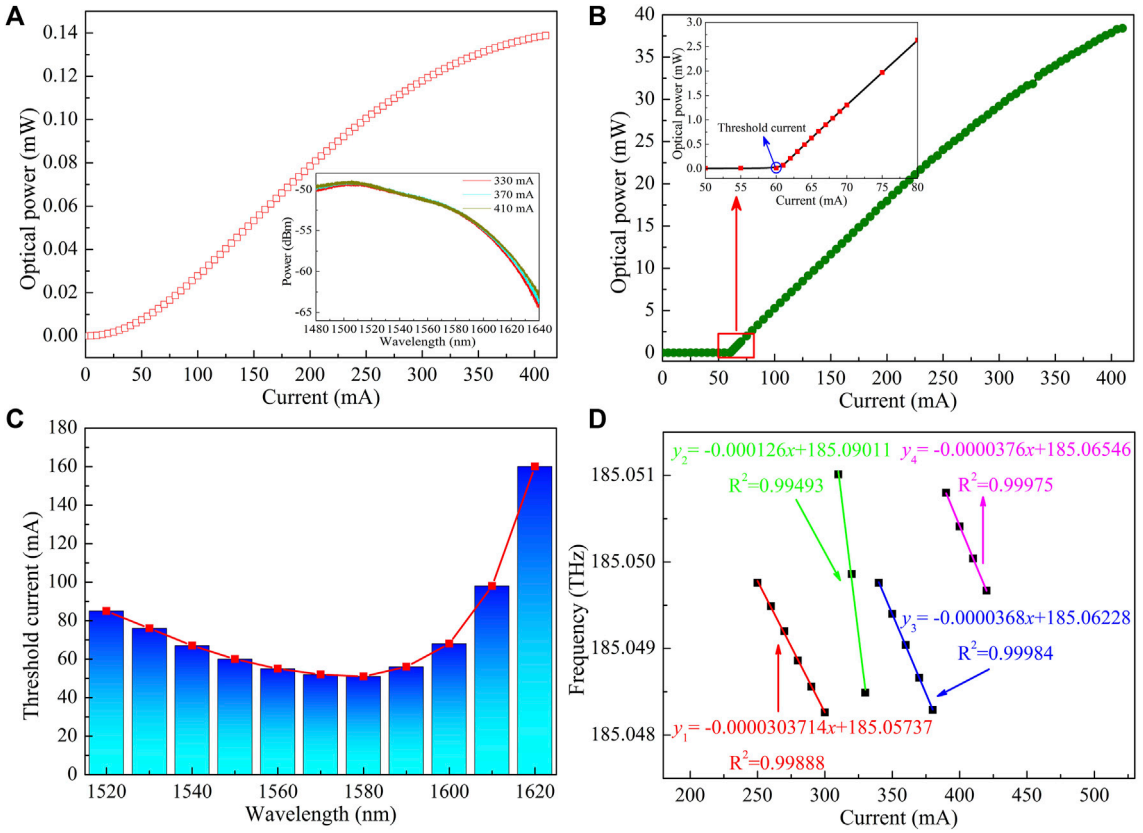

FIGURE 2
(A) Optical output power versus the injection current for the free-running single angled facet gain chip. Inset: gain spectra of the gain chip at different injection currents. **(B)** Measurement of the output power characteristics of the external-cavity wavelength-swept laser as a function of the injection current operating 1550 nm at a fixed temperature of 25.0°C. **(C)** Threshold current of the proposed external-cavity wavelength-swept laser at different lasing wavelength. **(D)** Measurement lasing frequency shift as a function of the injection current in the proposed external-cavity configuration.

single mode fiber pigtailed collimator, the coupling efficiency is higher than 50%. To measure the output lasing parameters, the output is picked out by an optical switch (OS) with low insertion loss. One channel of the OS is directed to the 3-dB optical coupler (OC), one port of the OC is directed into an optical spectrum analyzer (Yokogawa, AQ6370D) with a resolution of 0.02 nm for measuring the spectral changes, the other port is monitored by a wavelength meter (Yokogawa, AQ6151B), which is adapted to record the MHF traces over the entire tuning range. The other channel of the OS is connected to the calibrated optical power meter (Thorlabs, PM100D) to measure the output power of the lasing wavelength. It is worth noting that the overall external-cavity length from the gain chip output facet to the tuning mirror front facet is around 50 mm. The corresponding longitude mode space of the proposed wavelength-swept laser is equal to 23.1 pm (3 GHz) operating at 1520 nm, which will decide the maximum MHF tuning range theoretically.

3 Characterization and discussion

First, the typical P-I curves of the single-angled facet gain chip with and without an external cavity (namely, free-running) are measured and highlighted in Figures 2A, B, respectively. As can be seen in Figure 2A, since the single-angled facet gain chip is coated with the anti-reflection film, the maximum output power is around 0.14 mW at an injection current of 410 mA. The inset shown in Figure 2A show the gain spectra of the free-running single angled facet gain chip measured using the OSA with resolution of 0.02 nm. The results show the central wavelength is around 1510 nm. When the injection current is increased, the central wavelength slightly decreases along with an obvious increase in the spectra power at two edges of the gain spectra. In fact, by increasing the injection current, the output power at the edges of the full tuning range (1520 nm–1620 nm) of the external-cavity wavelength-swept laser can also be obviously increased.

After introducing optical feedback to the gain chip, as shown in Figure 2B, the threshold current of the proposed external-cavity wavelength-swept laser is around 60 mA, and the slope efficiency is about 0.11 mW/mA. Meanwhile, an output power of 15.84 dBm is achieved with an injection current of around 410 mA which is currently limited by the homemade laser diode driver. The output power of the gain chip based external cavity laser is 274.3 times as large as the output power of the freely running gain chip. The corresponding experimental result indicates that the external-cavity wavelength-swept laser of the presented

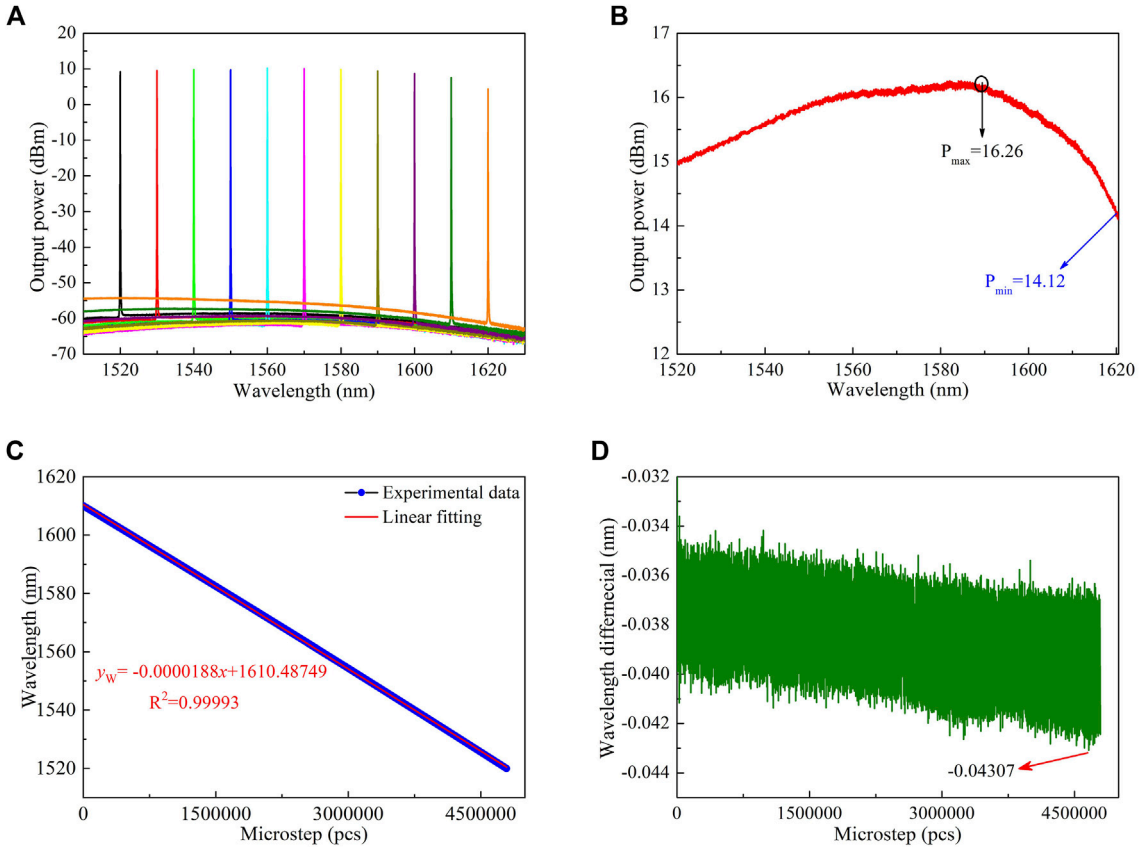

FIGURE 3
(A) The superimposed optical spectra at different lasing wavelengths. **(B)** Output power of the proposed external-cavity wavelength-swept laser. **(C)** The relationship between the lasing wavelength and the physical length of the wavelength-swept laser cavity. **(D)** The mode-hopping free performance of the proposed external-cavity wavelength-swept laser.

configuration runs in a strong optical feedback condition and completes optimum alignment.

The threshold current performance of the presented external-cavity wavelength-swept laser system is characterized by measuring the output optical power at different lasing wavelengths with the same calibrated optical power meter. The results for the threshold current as a function of lasing wavelength are plotted in Figure 2C, demonstrating a maximum threshold current of 160 mA. It can be seen that the threshold current of the proposed wavelength-swept laser system decreases at an intermediate tuning range (1560–1580 nm) and increases significantly when the lasing wavelength is changed toward the short wavelength (1520 nm) or long wavelength (1610 nm). Practically, except for the wavelength-dependent loss (i.e., the diffraction efficiency of the grating) of the cavity, this threshold current performance mainly comes from the spectral gain properties of the single-angled facet gain chip. To achieve a large range of wavelength tunable output, the working current therefore should be set above the maximum threshold current displayed in Figure 2C. Then, the effect of injection current (more than the maximum threshold current) on the tuning characteristics of the presented laser configuration output frequency (wavelength) is investigated. The injection current is increased from 250 mA to 420 mA with 10 mA/step. It can be observed in Figure 2D that, as mentioned in other ECTLs [5,32,33], the proposed external-cavity wavelength-swept laser also has a mode-hopping free current interval. The lasing frequency as a function of the injection current at a controlled laser temperature of 25.0°C is shown in Figure 2D, where linear regression is conducted to achieve the frequency tuning rate of the injection current, respectively, the mode-hopping is observed at an injection current of 300 mA–310, 330–340, and 390–400 mA. From this, the frequency tuning rate of the injection current can be determined to be approximately 0.0304 GHz/mA, 0.126 GHz/mA, 0.0368 GHz/mA and 0.0376 GHz/mA, respectively. Therefore, it is critical to choose a perfect working point to avoid this mode-hopping interval when the external-cavity wavelength-swept laser is working.

Subsequently, the basic tunability of the proposed external-cavity wavelength-swept laser system is characterized by an injection current of 410 mA. Figure 3A shows the measured spectra of the wavelength-swept laser. The resonance wavelength is increased from 1519.98 nm to 1619.98 nm with about 10 nm/step. It can be seen in Figure 3A that the tunable range is 100 nm. Meanwhile, as shown in Figure 3A, it is also easy to find that the wavelength-swept laser operates in a single-mode running state, and the SMSR is no less than 65.64 dB. The output power of the proposed external-cavity laser configuration at different resonance wavelengths is measured and the experimental results are

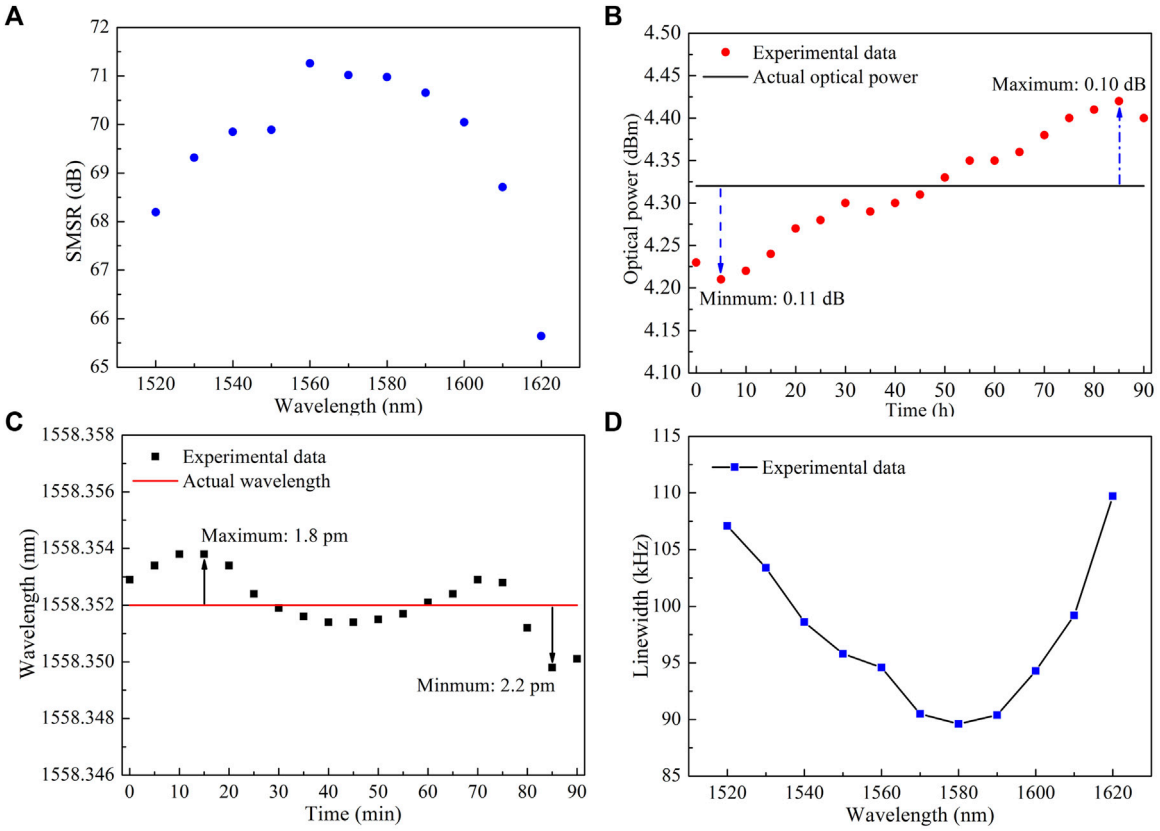

FIGURE 4
(A) Plot of the side-mode suppression ratio (SMSR) shown as the blue circles as a function of the lasing wavelength. **(B)** and **(C)** Output power and wavelength stability at wavelength 1558.352 nm with injection current of 410 mA, respectively. A variable optical attenuator is used to avoid the optical damage of the optical wavelength meter and the power meter. **(D)** Linewidth performance of the proposed system measured using the traditional DSH method with a total length of 24.5 km single-mode fiber and an 80 MHz fiber-coupled AOM. The injection current is 410 mA.

depicted in Figure 3B. The output power of the external-cavity laser configuration changes as the wavelength-swept laser is tuned. The maximum output power is 16.26 dBm operating at 1582.07 nm, and the minimum output power is 14.12 dBm operating at 1620.35 nm. Obviously, the proposed external-cavity wavelength-swept laser system exhibits an output power of more than 14.12 dBm over the entire tunable range when the injected current is 410 mA. A plot of the lasing wavelength as a function of the micro-step applied to the physical length of the external cavity is shown in Figure 3C, where linear regression is performed to obtain the MHF performance of the external-cavity wavelength-swept laser. The physical length of the external cavity is increased from 46.89 mm to 50 mm with 2048 micro-step (1.328 μm)/step. In fact, when the wavelength is tuned, the external-cavity wavelength-swept laser will experience a mode-hopping if the change of resonating wavelength decided by the change of the physical length of the external cavity mismatch with the change of wavelength decided by the first-order reflections from the blazed diffraction grating. As shown in Figure 3C, it is believed that the change in the physical length of the external cavity does match the changing wavelength fed back into the single-angled facet gain chip, the mode-hopping is suppressed as the external-cavity wavelength-swept laser is continuously tuned over 100 nm. Similar experimental results are obtained and highlighted in Figure 3D. The maximum change of the adjacent wavelength subtracts (43.07 pm) is no more than two mode spacing, which indicates an MHF tunable output is able to be achieved [32].

The SMSR of the proposed external-cavity wavelength-swept laser system at different lasing wavelengths is investigated and the corresponding results are shown in Figure 4A. With the blazed diffraction grating, the maximum output SMSR is around 71.26 dB operating at 1560 nm. Based on the classical grating equation, a large incident angle (80°) is beneficial to improve the blazed diffraction grating resolution. And the spontaneous emission noise can be suppressed with a large incident angle. Therefore, a higher SMSR can be obtained in the proposed external-cavity wavelength-swept laser configuration. Furthermore, a better SMSR is obtained at an intermediate tuning range, which is results from the match between the external-cavity lasing mode and the wavelength fed back to the internal chip as the first-order reflections from the blazed diffraction grating is rotated. However, in the longer lasing region, the edge of the material gain will occur, which will cause the growth in the spontaneous emission noise, meaning that the SMSR will decrease. Note that the mode-hopping-free tuning range is 1.69 times as large as the results in Ref. 33, while the SMSR in the full tuning range stay at a high level.

After warmup of 30 min, we monitored the stability of the wavelength and output power as shown Figures 4B, C, respectively, the duration is 90 min with 5 min step. As shown in the figure, the power deviation from the setting output power is less than ±0.11 dB and the wavelength deviation from the setting wavelength is less than 2.2 pm. The results show a good stability of the proposed external-cavity wavelength-swept laser system.

The laser linewidth performance is shown in Figure 4D, which is measured using the traditional delayed self-heterodyne (DSH) arrangement with a total length of 24.5 km single-mode fiber (Corning, SMF28e) and an 80 MHz fiber coupled acousto optic modulator (AOM). The linewidth of the laser output is less than 110 kHz within the full tuning range, the minimum linewidth is 90 kHz at the wavelength of 1580 nm. The linewidth at the central part of the full tuning range is narrower than the results in the two edges, which is most likely due to larger diffraction angles induced extra wavelength-dependent coupling loss at the edge of the full tuning range. The linewidth performance is similar to the results reported in Ref. [32].

4 Summary

In summary, a wide mode-hopping free external-cavity wavelength-swept laser with a high side-mode suppression ratio is designed, which is based on a traditional Littman-Metcalf configuration. Meanwhile, the tuning characteristics and side-mode suppression ratio of the proposed external-cavity diode laser are investigated experimentally. The external-cavity wavelength-swept laser can be continuously tuned over a range of 100 nm in the CL-band, with a maximum side-mode suppression ratio of 71.26 dB and an output optical power of more than 14.12 dBm. With the help of this designed external-cavity wavelength-swept laser, it has the potential applications for higher rate (e.g., 1 Tbit/s) coherent optical orthogonal frequency division multiplexing schemes. Future work shall focus on the optimization of the blazed grating diffraction efficiency to further suppress the spontaneous emission noise.

Data availability statement

The raw data supporting the conclusion of this article will be made available by the authors, without undue reservation.

Author contributions

Conceptualization, LS, SQ, and LH; methodology, LS, LH, AZ, and SQ; software, PL, JJ, TQ, and ZZ; validation, YZ, ZL, and BY; formal analysis, SQ and JH; investigation, YW and LS; resources, LH, ZL, AZ, and LS; data curation, SQ; writing—original draft preparation, LS and SQ; writing—review and editing, LH and LS; visualization, LS; supervision, LH; project administration, LS and LH; funding acquisition, LS, SQ, and LH. All authors have read and agreed to the published version of the manuscript.

Funding

This research was funded in part by National Key Research and Development Plan (2022YFF0705900); In part by National Natural Science Foundation of China (61605034); In part by Qingdao Postdoctoral Applied Research Project (20266153, 21290111); In part by Special Support for Postdoctoral Creative Funding in Shandong Province (202103076); And in part by Science and Technology on Electronic Test and Measurement Laboratory Foundation (ZF332).

Acknowledgments

Thanks to Hui Jin and Qiang Han for their support during the experiments.

Conflict of interest

Authors SQ, LS, LH, AZ, YW, ZL, JJ, ZZ, BY, PL, JH, YZ, and TQ were employed by Ceyear Technologies Co., Ltd.

Publisher's note

References

1. Robins N, Lance A, Close J, Sheng L, Liu J, Zhou S, et al. Piezo-locking a diode laser with saturated absorption spectroscopy. *Appl Opt* (2008) 47(28):5163–6. doi:10.1364/AO.47.005163

2. Doringsho K, Ernsting I, Rinkle R, Schiller S, Wicht A. Low-noise, tunable diode laser for ultra-high-resolution spectroscopy. *Opt Lett* (2007) 32(413):2876–8. doi:10.1364/OL.32.002876

3. Chi M, Jensen O, Petersen P. Tuning range and output power optimization of an external-cavity GaN diode laser at 455 nm. *Appl Opt* (2016) 55(9):2263–9. doi:10.1364/AO.55.002263

4. Ma Y, Yang Q, Tang Y, Chen S, Shieh W. 1-Tb/s single-channel coherent optical OFDM transmission over 600-km SSMF fiber with subwavelength bandwidth access. *Opt Express* (2009) 17(28):9421–7. doi:10.1364/OE.17.009421

5. Zhang L, Liu T, Chen L, Xu G, Jiang C, Liu J, et al. Development of an interference filter-stabilized external-cavity diode laser for space applications. *Photonics* (2020) 7(12):7010012. doi:10.3390/photonics7010012

6. Schioppo M, Brown R, McGrew W, Hinkley N, Fasano R, Beloy K, et al. Ultrastable optical clock with two cold-atom ensembles. *Nat Photon* (2017) 11(48):48–52. doi:10.1038/NPHOTON.2016.231

7. Yang X, Yin Y, Li X, Sheng L, Liu J, Zhou S, et al. External cavity diode laser as a stable-frequency light source for application in laser cooling of molecules. *Chin Opt Lett* (2016) 14(7):071403. doi:10.3788/COL201614.071403

8. Xu P, Yu X, Chen Z, Sheng L, Liu J, Zhou S, et al. Distributed refractive index sensing based on bending-induced multimodal interference and Rayleigh backscattering spectrum. *Opt Express* (2021) 29(14):21530–8. doi:10.1364/OE.430637

9. Zhao Z, Bai Z, Jin D, Qi Y, Ding J, Yan B, et al. Narrow laser-linewidth measurement using short delay self-heterodyne interferometry. *Opt Express* (2022) 30(17):30600–10. doi:10.1364/OE.455028

10. Sheng L, Huang L, Yan J, Qiao S, Zhang A, Jin H, et al. Distributed multi-parameter sensing based on the Brillouin scattering effect in orbital angular momentum guiding fiber. *Opt Continuum* (2022) 1(1):133–42. doi:10.1364/OPTCON.446952

11. Zhao Z, Bai Z, Jin D, Chen X, Qi Y, Ding J, et al. The influence of noise floor on the measurement of laser linewidth using short-delay-length self-heterodyne/homodyne techniques. *Micromachines* (2022) 13(8):1311. doi:10.3390/mi13081311

12. Qiao S, Sheng L, Song P, Zhang A, Guo H, Li P, et al. Measurement of distributed refractive index through Rayleigh backscattering spectra detection using a U-bent common fiber. In: Proc. SPIE 11907 Sixteenth National Conference on Laser Technology and Optoelectronics, 11907 (2021). p. 1190704. doi:10.1117/12.2600768

13. Mroziewicz B. External cavity wavelength tunable semiconductor lasers-a review. *Opto-Electronics Rev* (2008) 16:347–66. doi:10.2478/s11772-008-0045-9

14. Shank C, Bjorkholm J, Kogelnik H. Tunable distributed-feedback dye laser. *Appl Phys Lett* (1971) 18(9):395–6. doi:10.1063/1.1653714

15. Cai Y, Gao F, Chen H, Yang X, Bai Z, Qi Y, et al. Continuous-wave diamond laser with a tunable wavelength in orange–red wavelength band. *Opt Commun* (2023) 528: 128985. doi:10.1016/j.optcom.2022.128985

16. Bai Z, Zhao Z, Tian M, Jin D, Pang Y, Li S, et al. A comprehensive review on the development and applications of narrow-linewidth lasers. *Microwave Opt Tech Lett* (2022) 64(12):2244–55. doi:10.1002/mop.33046

17. Iga K. Forty years of vertical-cavity surface-emitting laser: Invention and innovation. *Jpn J Appl Phys* (2018) 57(8S2):08PA01. doi:10.7567/JJAP.57.08PA01

18. Gmachl C, Straub A, Colombelli R, Capasso F, Sivco DL, Sergent A, et al. Single-mode, tunable distributed-feedback and multiple-wavelength quantum cascade lasers. *IEEE J Quan Elect* (2002) 38(6):569–81. doi:10.1109/JQE.2002.1005407

19. Niu Y, Yan X, Chen J, Ma Y, Zhou Y, Chen H, et al. Research progress on periodically poled lithium niobate for nonlinear frequency conversion. *Infrared Phys Tech* (2022) 125:104243. doi:10.1016/j.infrared.2022.104243

20. Jin D, Bai Z, Lu Z, Fan R, Zhao Z, Yang X, et al. 22.5-W narrow-linewidth diamond Brillouin laser at 1064 nm. *Opt Lett* (2022) 47(20):5360–3. doi:10.1364/OL.471447

21. Bai Z, Zhao C, Gao J, Chen Y, Li S, Li Y, et al. Optical parametric oscillator with adjustable pulse width based on $KTiOAsO_4$. *Opt Mater* (2023) 136:113506. doi:10.1016/j.optmat.2023.113506

22. Komljenovic T, Srinivasan S, Norberg E, Davenport M, Fish G, Bowers J. Widely tunable narrow-linewidth monolithically integrated external-cavity semiconductor lasers. *IEEE J Selected Top Quan Elect* (2015) 21(6):214–22. doi:10.1109/JSTQE.2015.2422752

23. Li X, Shi J, Wei L, Ding K, Ma Y, Sun K, et al. Research progress of wide tunable Bragg grating external cavity semiconductor lasers. *Materials* (2022) 15(22):8256. doi:10.3390/ma15228256

24. Cui Q, Lei Y, Chen Y, Qiu C, Wang Y, Zhang D, et al. Advances in wide-tuning and narrow-linewidth external-cavity diode lasers. *Sci China Inf Sci* (2022) 65(8): 181401. doi:10.1007/s11432-021-3454-7

25. Fedorova K, Cataluna M, Kudryashov I, Khalfin V, Rafailov E. Broadly tunable InGaAsP-InP strained multi-quantum-well external cavity diode laser. *IEEE Photon Technol Lett* (2010) 22(413):1205–7. doi:10.1109/LPT.2010.2051661

26. Bagley M, Wyatt R, Elton D, Wicks H, Spurdens P, Seltzer C, et al. 242 nm continuous tuning from a GRIN-SC-MQW-BH InGaAsP laser in an extended cavity. *Electron Lett* (1990) 26(4):267–9. doi:10.1049/el:19900178

27. Yuan H, Gao F, Yang T. Ultra-broadband tunable single- and double-mode InAs/InP quantum dot external-cavity laser emitting around 1.65μm. *Opt Lett* (2018) 43(413): 3025–8. doi:10.1364/OL.43.003025

28. Gong H, Liu Z, Zhou Y, Zhang W. Extending the mode-hop-free tuning range of an external-cavity diode laser by synchronous tuning with mode matching. *Appl Opt* (2014) 53(33):7878–84. doi:10.1364/AO.53.007878

29. Zhang D, Zhao J, Yang Q, Liu W, Fu Y, Li C, et al. Compact MEMS external cavity tunable laser with ultra-narrow linewidth for coherent detection. *Opt Express* (2012) 20(18):19670–82. doi:10.1364/OE.20.019670

30. Kasai K, Nakazawa M, Tomomatsu Y, Endo T. 1.5 μm, mode-hop-free full C-band wavelength tunable laser diode with a linewidth of 8 kHz and a RIN of -130 dB/Hz and its extension to the L-band. *Opt Express* (2017) 25(18):22113–24. doi:10.1364/OE.25.022113

31. Wang Y, Wu H, Chen C, Zhou Y, Wang Y, Liang L, et al. An ultra-high-SMSR external-cavity diode laser with a wide tunable range around 1550 nm. *Appl Sci* (2019) 9: 4390. doi:10.3390/app9204390

32. Zhang A, Qiao S, Sheng L, Huang L, Liu Z, Ju J, et al. Study on external cavity diode laser with a wide mode-hopping free tuning range. *Front Phys* (2022) 10:1093179. doi:10.3389/fphy.2022.1093179

33. Repasky K, Nehrir A, Hawthorne J, Switzer G, Carlsten J. Extending the continuous tuning range of an external-cavity diode laser. *Appl Opt* (2006) 45(35): 9013–20. doi:10.1364/ao.45.009013

frontiers | Frontiers in Physics

TYPE Original Research
PUBLISHED 02 March 2023
DOI 10.3389/fphy.2023.1160287

OPEN ACCESS

EDITED BY
Shuo Liu,
Hebei University of Technology, China

REVIEWED BY
Hailiang Chen,
Yanshan University, China
Wei Liu,
Zhejiang Agriculture and Forestry University, China
Chen Shi,
National University of Defense Technology, China

*CORRESPONDENCE
Yingbin Xing,
jsxyb1232008@126.com

SPECIALTY SECTION
This article was submitted to Optics and Photonics, a section of the journal Frontiers in Physics

RECEIVED 07 February 2023
ACCEPTED 20 February 2023
PUBLISHED 02 March 2023

CITATION
Cai Y, Mai Y, Xiang S, Shi J, Zhu Q, Li R, Li J, Li C, Yan D and Xing Y (2023), Flexible beam delivery of ultrafast laser through vacuum-pumped anti-resonant hollow-core fiber.
Front. Phys. 11:1160287.
doi: 10.3389/fphy.2023.1160287

Flexible beam delivery of ultrafast laser through vacuum-pumped anti-resonant hollow-core fiber

Yiming Cai[1], Yifan Mai[2], Shen Xiang[1], Jianhong Shi[1], Qixin Zhu[1], Rong Li[2], Jinyan Li[1], Cheng Li[1], Dapeng Yan[1] and Yingbin Xing[1]*

[1]Huazhong University of Science and Technology, Wuhan, China, [2]Wuhan Raycus Fiber Laser Technologies Co., Ltd., Wuhan, China

We demonstrate the transmission of a 100 MW-peak-power ultrafast laser through a 5-m anti-resonant hollow-core fiber (AR-HCF) with a pumpable armored tube for air exhaust. The AR-HCF consists of a 45-μm-hollow-core and seven untouched capillaries with an attenuation of 0.11 dB/m measured at a wavelength of 1030 nm. We investigate the effect of air-filling and vacuum pumping on transmission efficiency and pulse distortion. The comparison reveals the importance of controlling air concentration in hollow-core fibers (HCFs) for achieving high transmission efficiency and pulse quality. With the suppression of air concentration, the transmission efficiency increases from 61% to 72%, and pulse distortion is effectively controlled. The results demonstrate the potential of AR-HCFs for high-power ultrafast laser delivery systems for various applications. The pumpable armored tube design provides a simple and effective solution to suppress self-phase modulation (SPM) and enable flexible beam delivery.

KEYWORDS

anti-resonant fiber, AR-HCF, flexible beam delivery, vacuum-pumped HCF, ultrafast laser delivery

1 Introduction

Ultra-fast laser sources with picosecond or femtosecond laser pulses have shown a wide range of application in micro-and nanofabrication [1–4]. The peak power intensity of ultrafast lasers determines the characteristics of their free-space transport structure, which to some extent increases the possible instability of the laser over a long period of time [5]. In contrast to fiber-delivered nanosecond or continuous lasers, ultrafast lasers are difficult to propagate in traditional silica fibers because the non-linear effects during fiber delivery and the pulse peak fluence induced self-focusing might exceed the damage threshold of those fibers [6]. Since 1999, researchers have examined the viability of employing a HCF to transmit laser beams in an effort to address the issue of flexible delivery of short-pulse laser beams [7]. Compared to the photonic-bandgap hollow-core fibers (PB-HCFs) [8], the AR-HCFs feature a comparatively simple micro-structured cladding [9] and a broad transmission bandwidth [10], which makes them suited for wide-spectrum, high peak power beam transmission. It has been reported that the visible spectral range lasers, which are generated by the use of second-harmonic generation (SHG) and third-harmonic generation (THG) of fiber or Nd: YAG ultrafast laser sources, have shown the achievement in beam flexible transmission of green [11] and ultraviolet [12, 13] lasers. The AR-HCF with cladding-tubes-touched structure has been utilized to transmit lasers with

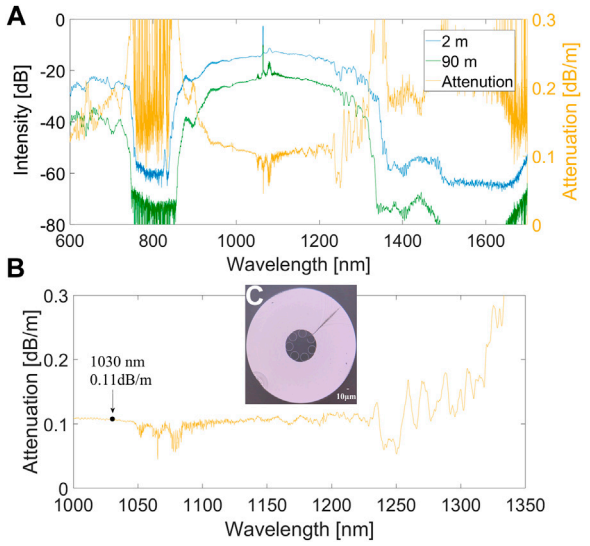

FIGURE 1
(A) Measured transmission spectra of the 2 m (solid blue curve) and the 90 m (solid green curve) AR-HCF and attenuation spectrum (solid yellow curve) in the range of 600 nm–1700 nm. **(B)** Detailed attenuation spectrum measured in the near-infrared range of 1,000 nm–1,350 nm (solid yellow curve). **(C)** Cross setion of seven capillaries AR-HCF with 45-μm-core diameter.

transmission bands ranging from 1 μm to 4 μm [14–16]. The 0.11 dB/m transmission losses of an ice-cream-structure AR-HCF have enabled the demonstration of a laser with a 63.1% coupling efficiency at 1,064 nm [17]. Theoretical advancements have indicated that AR-HCF fibers without nodes are being studied to reduce transmission loss [18, 19]. Recent studies have demonstrated a node-less AR-HCF for a 300 W laser guidance at 1,080 nm with a 0.05 dB/m attenuation [20]. Studies have shown a much higher transmission power of 1.167 kW with a high efficiency of 87.5% at the adjacent wavelength of 1,070 nm, by using an ice-cream structure AR-HCF [21]. Although HCFs have lower non-linear effects [22] and higher power damage thresholds [23] compared to conventional silica solid fibers, the effect of non-linearity could not be ignored for the laser transmission process of ultrafast lasers with high peak power over 30 MW [24]. Ultra-fast laser pulses transmitted along the HCFs have enough energy to interact with the air or gas in the hollow core to introduce the pulse chirp and thus broadening the pulse duration [25–27]. Factors found to be influencing power transmission limitations have been explored in several studies that show non-linear effects such as Raman scatting and SPM have played a critical role in ultra-fast laser delivering efficiency [28, 29]. Filling inert gas or vacuum states has been demonstrated and mentioned in research analyses as an effective method to modulate the non-linear effects in the beam transmission process [29–31]. Published studies have used gas-filled HCFs for spectral broadening and chirped mirror systems to compensate for dispersion and to compress for a shorter pulse duration [32–34]. However, the pulse recompression process lets the flexible beam delivery transfer to spatial transmission. Although there are proposed theoretical models showing that light transmission in the photonic crystal fibers of a negative refractive index metamaterial could compensate for dispersion [35]; however, this has not been achieved in practice. Our objective is to accomplish ultrafast laser transmission while keeping the light source's original properties. In this research, a vacuum chamber is concerned with preventing gas interactions and decreasing non-linear effects. The flexible beam delivery utilizes a 5-m AR-HCF with an attenuation of 0.11 dB/m at 1,030 nm. Laser transmission in air-filled and vacuum-pumped fiber is discussed separately. The pulsed laser is transmitted through an air-filled HCF, and the SPM interferes with the dispersion balance of the ultra-fast laser system, with a pulse spread of 16.5 ps. With the suppression of air concentration, the power transmission efficiency improves from 61% to 72% and the pulse duration is observed with slightly broadening from 500 fs to 670 fs.

2 Fiber structure and experimental setup

2.1 Fiber characteristic

The cross section of the fabricated AR-HCF fiber is shown in Figure 1C, which consists of seven untouched capillaries with an inscribed core diameter of 45 μm and a mode field diameter of 35 μm, the outer diameter of the capillaries of 22.6 μm and the jacked diameter of 314 μm. For multi-capillary anti-resonant fibers, the suppression of higher order modes (HOMs) is achieved with the increasing number of cladding holes, which is confirmed in Refs. [19, 36]. Moreover, bending loss of the AR-HCF could be suppressed by designing a smaller-core size [37]. The wall thickness of the capillaries and the gap distance between the capillaries also affect the transmission loss [19]. However, the increasing number of cladding capillaries and small core size are accompanied by a reduction in the fundamental mode field area, necessitating careful laser coupling to the AR-HCF [38]. The fundamental mode loss, bending loss and coupling efficiency are comprehensively considered for the future application, and the AR-HCF with mentioned parameters are designed and fabricated. The theoretical fundamental mode attenuation is calculated to be 0.89 dB/km at 1,030 nm by the expression discussed in Ref. [39].

The transmission spectra of the AR-HCF is measured by using a broadband light source (NKT Photonics) and a YOKOGAWA spectrometer, as shown in Figure 1A. The attenuation curve of wavelength from 600 nm to 1700 nm, as measured by the cut-back method (cut the 90 m fiber to 2 m). Figure 1B depicts the detailed decay curves covering the laser range from 1,000 nm to 1,350 nm. The positioning and deformation of the capillaries during fiber drawing, as well as the beam quality of the laser source, might result in variations between the theoretical and measured values. The calculated mode loss of LP01, LP11, and LP21 are 0.89 dB/km, 3.17 dB/km and 1.24 dB/km, respectively.

The low transmission loss is the combined result of the control of capillary and inter-capillary spacing consistency during the fiber drawing process as shown in Figure 1C. Measured transmit loss is 0.11 dB/m at 1,030 nm, which is much higher than the theoretical value, despite this, it shows an improvement comparison with a similar-structure seven capillaries AR- HCF in the most recent published article [40]. It is worth mentioning that the measured

TABLE 1 Performance comparison of recently reported attenuation of seven capillaries AR- HCFs.

Core diameter (μm)	Capillary thickness (μm)	Capillary diameter (μm)	Measured min. loss (dB/m at nm)	Time
28	0.78	18	0.11–1.2 at1,065	2022 [40]
35	0.355	17	0.05 at1,080	2021 [20]
31	0.78	23.6	0.07 at1,064	2021 [41]
28.3	0.43	10.6	0.7 at1,100	2021 [42]
17	0.132	7.3	0.26 at355	2018 [12]
35.8	0.775	7.67	0.028 at1,030	2018 [29]
30	0.83	17	0.03 at1,090	2016 [36]

The bold values are the core diameter of the AR-HCF.

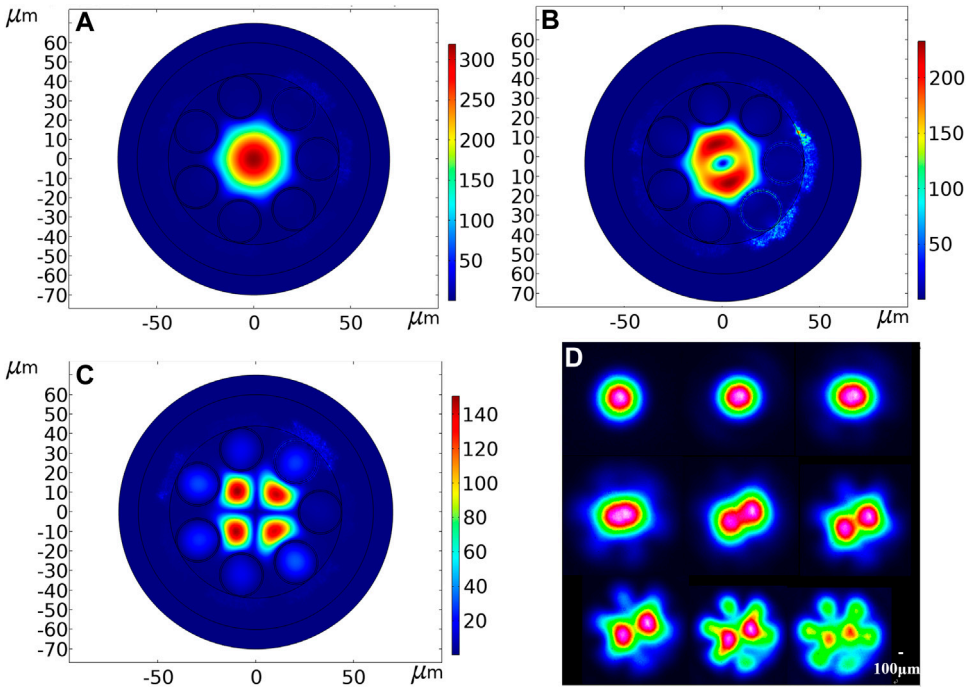

FIGURE 2
(A–C). Simulated mode field distribution of LP01, LP11 and LP31, respectively. **(D)** Measured mode profiles by the misalignment of the incident beam.

transmission loss of HCFs is related to fiber parameters such as core size, capillary diameter, and wall thickness; fiber drawing quality such as roughness; attenuation measurement methods such as fiber length, light source quality, etc. Table 1 summarizes the relevant parameters of seven capillaries AR- HCF published in recent years and their measured attenuation at certain wavelengths for reference.

2.2 Simulated and measured beam profiles

The finite element software COMSOL is used for simulating mode profiles AR-HCF as shown in Figures 2A–C. In the experiment, the focus lens is relocated away from the input side of the AR-HCF to misalign the focus point and stimulate HOMs. Figure 2D depicts the variation of the diameter mode field distribution of LP01 to LP11 obtained by adjusting the focusing mirror shown in Figure 3 to eccentricate the spot, with a fiber coiling diameter of 45 cm. It could be observed from the figure that no HOMs, such as LP21 and LP31, were observed after propagating 5 m. The reason is that the manufactured AR-HCF structure is not homogeneous, resulting in actual attenuation values for HOMs that are greater than their theoretical values. Moreover, the incident beam profile approaches the fundamental mode (M^2 = 1.167), and the contrast of the excited higher-order modes is rather low, so that only the LP01 and LP11 modes with reduced transmit loss could be examined. This result preliminarily shows that transmission in the AR-HCF has the effect of optimizing the beam quality.

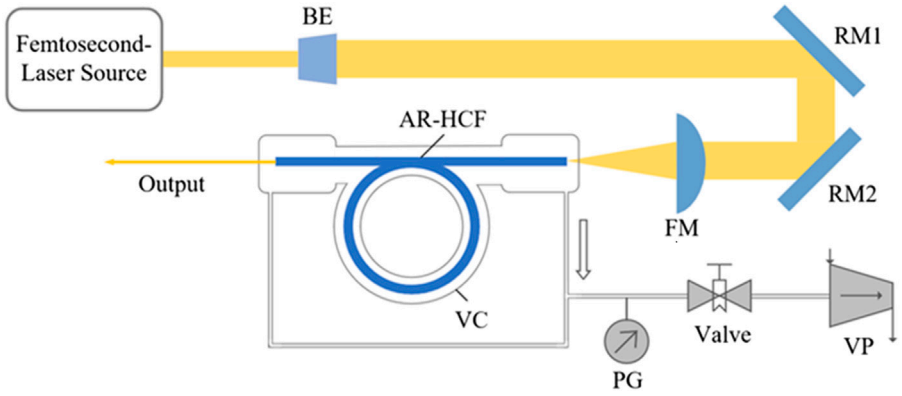

FIGURE 3
Experiment setup of the laser beam transmission system. BE: Beam expander; RM: Reflect mirror; FM: Focus mirror; VC: Vacuum chamber; PG: Pressure gauge; VP: Vacuum pump.

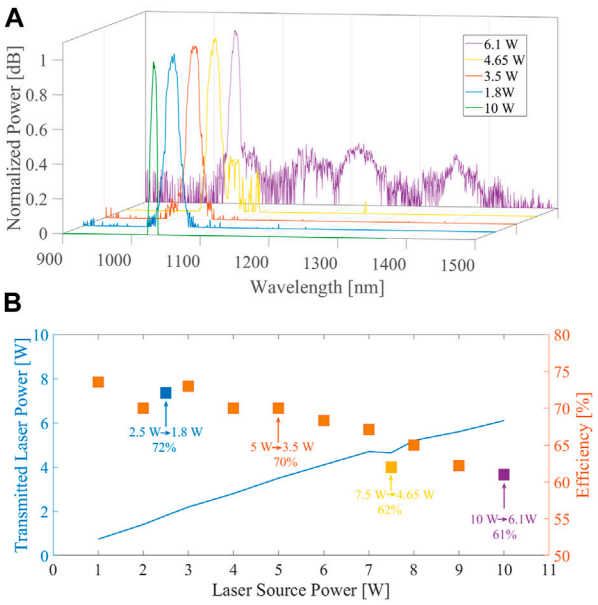

FIGURE 4
(A) Spectrum of the ultra-fast laser source (LS, green curve); Laser transmitted spectra measured after the air-filled AR-HCF: After transmissions, the input laser power drops from 2.5 W to 1.8 W (blue curve), 5 W–3.5 W (orange curve), 7.5 W–4.65 W (yellow curve) and 10 W–6.1 W (purple curve), respectively. **(B)** Transmitted laser power and transmission efficiency versus ultra-fast laser source power.

2.3 Experimental setup

The experimental setup is shown as Figure 3. A self-built 1,030 nm ultra-fast laser source with an average power of 10 W, a pulse duration of 500 fs, and a maximum single pulse energy of 50 μJ is used as the seed laser. The beam quality $M^2 = 1.167$, which is measured by a camera-based beam propagation analyzer (BeamSquared XC130). The output beam diameter is expanded from 1 mm to 2 mm by a beam expander. The two reflectors, RM1 and RM2, are crucial in adjusting the parallelism and perpendicularity of the laser beam. The RM1 and RM2 mirrors have a low group delay dispersion (GDD<30 fs^2) and a coating that ensures reflectance greater than 99.5% from 970 nm to 1,150 nm. The divergence angle of the AR-HCF is 0.035 mrad and the aspherical lens with a collimation distance of 30 mm focuses the beam into the AR-HCF with a focused spot diameter of 23.6 μm. An industrial high-precision optical fiber cleaver (Fujikura CT104 +) is used to cleave AR-HCF, and the cutting angle of the fiber is less than 0.5°. The length of 5 m of AR-HCF is placed inside an evacuable vacuum chamber to reduce gas interactions and minimize non-linear effects. The vacuum chamber is designed as an armored tube that could be coiled with a diameter ranging from 25 cm to 45 cm for flexible beam transmission. The air pressure is regulated by regulating the air flow through the valves, and the barometer is utilized to read the actual air pressure. A spectrum analyzer (YOKOGAWA AQ6370D) is used to record the laser's output spectrum, and an autocorrelator (APE Pulsecheck) is used to measure the pulse duration.

3 Results and discussion

Figure 4A shows the comparison between the measured spectrum of the ultra-fast laser source and the transmitted laser spectra at different laser powers. The spectral range of the femtosecond laser source is over 1,025 nm–1,040 nm, and after propagating through the AR-HCF, the spectral spread covers the range from 1,000 nm to 1,350 nm due to the non-linear effects. The spreading of the laser spectra in AR-HCF and the generation of deformation phenomena of the pulses is a complex non-linear process. Numerous theoretical and practical investigations on the transmission characteristics of ultrafast pulses in AR-HCF have been conducted [29, 30, 39, 43]. However, the mechanism behind their generation is still not fully comprehended. Many non-linear processes, including SPM, stimulated Raman scattering (SRS), four wave mixing, and higher-order soliton splitting, could be

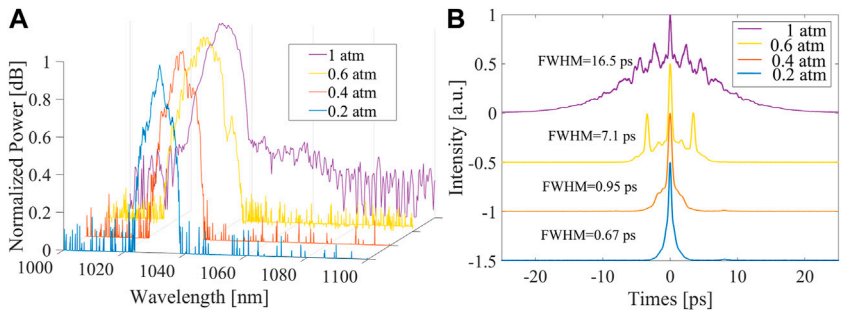

FIGURE 5
(A) Measured 6.1 W-output laser (input laser 10 W) transmission spectra after the vacuum-pumped AR-HCF. The curves from bottom to top show the spectral profiles that obtained under chamber pressure from p = 0.2 atm (blue curve), 0.4 atm (orange curve), 0.6 atm (yellow curve), and 1 atm (purple curve), respectively. **(B)** Autocorrelation curves under different pressures.

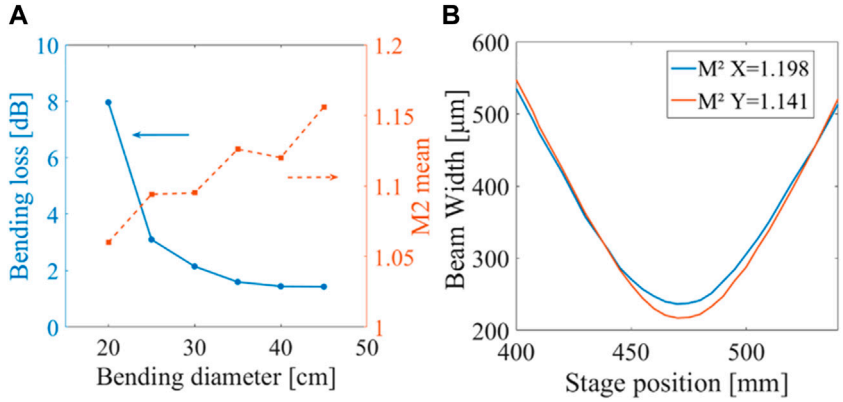

FIGURE 6
(A) Bending loss and M^2 versus bending diameter in the vacuum-pumped AR-HCF. **(B)** Measured laser source beam quality as a function of coiling diameter at 45 cm.

involved in optical pulse transmission [44]. As demonstrated in Figure 4A, the spectrum broadening is mostly caused by the SPM and SRS after laser beam propagation down the air-filled AR-HCF. The SPM phenomena may be detected more clearly if the associated laser power was increased. Since the femtosecond laser source is a broadband source with a measured spectral width of 9.56 nm at full width half maximum, it is going to be difficult to distinguish between the spectral frequency oscillation caused by the SPM and the Raman scattering peaks in the spectral range of 1,020 nm–1,040 nm; nonetheless, the Raman scattering peaks that could be observed in the range of 1,100 nm–1,450 nm at an incident optical power of 10 W. The Raman frequency shift around 1,140 nm, 1,220 nm and 1,350 nm is in agreement with the simulation results in Ref. [29]. The transmitted laser power, and transmission efficiency calculated by the ratio of input power/output power, versus laser source power are shown in Figure 4B. When the peak power of the light source exceeds 50 MW, a significant decrease drops to around 61% in transmission efficiency could be observed. The spectral range of the femtosecond laser source is over 1,025 nm–1,040 nm, and after propagating through the AR-HCF, the spectral spread covers the range from 1,000 nm to 1,350 nm. As the laser power increases, the non-linear effects that cause the spectrum to broaden intensify. This causes laser energy to be shifted to frequencies with higher losses, which leads to a decrease in transmission efficiency.

To reduce the Kerr effect of laser propagation in AR-HCF, we pumped out the air and measure the laser spectra at various air pressures, as shown in Figure 5A. Notably, at a pressure of 0.2 atm, the transmitted laser power increases from 6.1 W to 7.2 W when the input laser power is 10 W. The SPM is alleviated as the air concentration in the chamber decreases. As seen from the autocorrelation results in Figure 5B, the 500-fs laser pulse broadens to 16.5 ps (FWHM, Gaussian fit) after propagating through the 5-m length, air-filled fiber, which indicates that the pulse experiences a large non-linear phase shift in the fiber, enhanced by the SPM, and in agreement with the effect of SPM on pulses discussed in Ref [34]. This indicates that as the air is filled, the pulse waveform is broadened symmetrically, and oscillatory structures appear on both wings of the pulse. This demonstrates that the SPM effect is at work, and that the dispersion-induced non-linear effects are weaker. This is demonstrated by the later analysis:

when the pulse is transmitted in the fiber, both GVD and SPM cause the pulse to produce a frequency chirp, and while the pulse chirp introduced by GVD is linear, the pulse chirp introduced by SPM is far from linear within the whole pulse. Various portions of the pulse transmit at different speeds due to the non-linear character of the post-composite chirp. Especially in the situation of normal dispersion, the redshifted light near the leading edge of the pulse transmits faster than the non-redshifted light at the trailing end of the pulse's front; the opposite is true for the blue shifted light near the following edge. In both instances, the area of the front and rear edges of the pulse contains two different frequencies of light that interfere with one another, and the oscillations around the edge of the pulse are the result of this interference. As the air concentration decreases, the symmetrical oscillation structure of the pulse gradually weakens, which also indicates a gradual decrease of the phenomenon of SPM. The anti-resonant seven-core-touchless capillary hollow fiber is less sensitive to bending loss relative to other mechanisms that have been compared [29].

In our experiment, we investigate the laser propagation bending loss versus fiber coil diameters from 20 cm to 45 cm in the vacuum pumped AR-HCF, as shown in Figure 6A. In this configuration, the coiling diameter is greater than 35 cm, the bending loss is less than 1.5 dB, and the critical coiling value of the fiber is reached when the bending diameter is less than 30 cm. At this point, the fiber bending causes the fiber base mode to higher order mode transition, which causes most of the light to leak from the core, resulting in an increase in power loss. We also determined the relationship between beam quality and bending diameter. Figure 6B shows the measured transmitted laser source beam quality of M^2X = 1.198, M^2Y = 1.141 at the bending diameter of 45 cm. Although the beam quality factors vary only by 0.122 (1.182–1.06) when the fiber coiling diameter is varied in the range of 25 cm–45 cm, the dashed orange curve shows the decrease in the coiling diameter of the fiber is accompanied by a decreasing trend in M^2. The results indicate that the optimal coiling of the AR-HCF fibers could optimize transmission mode distribution.

4 Conclusion

In summary, we have achieved the conversion of space-transmitted ultrafast lasers into optical fiber transmission by focusing the laser into a core of AR-HCF. This provides the potential for subsequent application simplicity in industrial settings. We compared the ultrafast laser transmission between air-filled and vacuum-pumped seven-capillary AR-HCF. The transmit efficiency and the pulse shape that are affected by the SPM were discussed, and the method of extracting air could provide a simple solution. Results showed an improvement in laser transmission efficiency in vacuum-pumped fiber, and the efficiency improved from 61% to 72% with the suppression of air concentration, and the pulse distortion phenomenon could also be suppressed. The pulse broadening from 500 fs to 670 fs was recorded and might be improved in the future by using a more powerful pump at a lower atmospheric pressure. In addition, by modifying the fiber's structure so that it could support SHG or THG lasers, the experimental results could serve as a guide for other flexible beam transmission projects.

Data availability statement

The raw data supporting the conclusions of this article will be made available by the authors, without undue reservation.

Author contributions

YC: Conceptualization, Methodology, Data Curation, Writing—Original Draft. YM: Visualization, Software, Formal analysis. SX: Data curation. JS: Investigation QZ: Investigation. RL: Resources. JL: Supervision, Project administration. CL: Supervision. DY: Supervision. YX: Supervision, Funding Acquisition, Resources, Supervision, Writing—Review and Editing.

Funding

This work was supported by National Natural Science Foundation of China (Nos. 61975061 and 61735007).

Conflict of interest

YM and RL were empolyed by Wuhan Raycus Fiber Laser Technologies Co., Ltd.

The remaining authors declare that the research was conducted in the absence of any commercial or financial relationships that could be construed as a potential conflict of interest.

Publisher's note

References

1. Phillips KC, Gandhi HH, Mazur E, Sundaram SK. Ultrafast laser processing of materials: A Review. *Adv Opt Photon* (2015) 7(4):684. doi:10.1364/aop.7.000684

2. Malinauskas M, Žukauskas A, Hasegawa S, Hayasaki Y, Mizeikis V, Buividas R, et al. Ultrafast laser processing of materials: From science to industry. *Light: Sci Appl* (2016) 5(8):e16133–e.

3. Sakakura M, Lei Y, Wang L, Yu Y-H, Kazansky PGJLS. Applications. Ultralow-loss geometric phase and polarization shaping by ultrafast laser writing in silica glass. *Light: Sci Appl* (2020) 9(1):1–10.

4. Han H, Wang R, Cao H, Wen X, Dai C, Liu W, et al. Coded information storage pulsed laser based on vector period-doubled pulsating solitons. *Opt Laser Tech* (2023) 158:108894. doi:10.1016/j.optlastec.2022.108894

5. Yu L, Wang B, Han H, Dai C, Liu W, Wang Y. Passively Q-switched operation based on Sb2se3 and self-power near infrared photodetector. *J Lumin* (2022) 244: 118704. doi:10.1016/j.jlumin.2021.118704

6. Smith AV, Do BT, Hadley GR, Farrow RL. Optical damage limits to pulse energy from fibers. *IEEE J Sel Top Quan Electron* (2009) 15(1):153–8. doi:10.1109/jstqe.2008.2010331

7. Cregan RF, Mangan BJ, Knight JC, Birks TA, Russell PSJ, Roberts PJ, et al. Single-mode photonic band gap guidance of light in air. *Science* (1999) 285(5433):1537–9. doi:10.1126/science.285.5433.1537

8. Ishaaya AA, Hensley CJ, Shim B, Schrauth S, Koch KW, Gaeta AL. Highly-efficient coupling of linearly- and radially-polarized femtosecond pulses in hollow-core photonic band-gap fibers. *Opt express* (2009) 17(21):18630–7. doi:10.1364/OE.17.018630

9. Knight JC. Photonic crystal fibres. *Nature* (2003) 424(6950):847–51. doi:10.1038/nature01940

10. Poletti F, Petrovich MN, Richardson DJ. Hollow-core photonic bandgap fibers: Technology and applications. *Nanophotonics* (2013) 2(5-6):315–40. doi:10.1515/nanoph-2013-0042

11. Gao SF, Wang YY, Liu XL, Hong C, Gu S, Wang P. Nodeless hollow-core fiber for the visible spectral range. *Opt Lett* (2017) 42(1):61–4. Epub 2017/01/07. doi:10.1364/OL.42.000061

12. Yu F, Cann M, Brunton A, Wadsworth W, Knight J. Single-mode solarization-free hollow-core fiber for ultraviolet pulse delivery. *Opt express* (2018) 26(8):10879–87. Epub 2018/05/03. doi:10.1364/OE.26.010879

13. Gao SF, Wang YY, Ding W, Wang P. Hollow-core negative-curvature fiber for uv guidance. *Opt Lett* (2018) 43(6):1347–50. Epub 2018/03/16. doi:10.1364/OL.43.001347

14. Pryamikov AD, Biriukov AS, Kosolapov AF, Plotnichenko VG, Semjonov SL, Dianov EM. Demonstration of a waveguide regime for a silica hollow - core microstructured optical fiber with a negative curvature of the core boundary in the spectral region > 3.5 μm. *Opt express* (2011) 19(2):1441–8. doi:10.1364/OE.19.001441

15. Yu F, Wadsworth WJ, Knight JC. Low loss silica hollow core fibers for 3–4 Mm spectral region. *Opt express* (2012) 20(10):11153–8. doi:10.1364/OE.20.011153

16. Yu F, Knight JC. Spectral attenuation limits of silica hollow core negative curvature fiber. *Opt express* (2013) 21(18):21466–71. Epub 2013/10/10. doi:10.1364/OE.21.021466

17. Chen Y, Wang Z, Gu B, Yu F, Lu Q. Achieving a 15 μm fiber gas Raman laser source with about 400 kW of peak power and a 63 GHz linewidth. *Opt Lett* (2016) 41(21):5118–21. Epub 2016/11/03. doi:10.1364/OL.41.005118

18. Kolyadin AN, Kosolapov AF, Pryamikov AD, Biriukov AS, Plotnichenko VG, Dianov EM. Light transmission in negative curvature hollow core fiber in extremely high material loss region. *Opt express* (2013) 21(8):9514–9. Epub 2013/04/24. doi:10.1364/OE.21.009514

19. Belardi W, Knight JC. Hollow antiresonant fibers with low bending loss. *Opt express* (2014) 22(8):10091–6. Epub 2014/05/03. doi:10.1364/OE.22.010091

20. Zhu X, Wu D, Wang Y, Yu F, Li Q, Qi Y, et al. Delivery of cw laser power up to 300 watts at 1080 Nm by an uncooled low-loss anti-resonant hollow-core fiber. *Opt express* (2021) 29(2):1492–501. Epub 2021/03/18. doi:10.1364/OE.415494

21. Cui Y, Huang W, Zhou Z, Li H, Wang M, Chen Z, et al. Highly efficient and stable coupling of kilowatt-level continuous wave laser into hollow-core fibers. *Chin Opt Lett* (2022) 20(4):040602. doi:10.3788/col202220.040602

22. Ouzounov DG, Ahmad FR, Müller D, Venkataraman N, Gallagher MT, Thomas MG, et al. Generation of megawatt optical solitons in hollow-core photonic band-gap fibers. *Science* (2003) 301(5640):1702–4. doi:10.1126/science.1088387

23. de Matos CJS, Taylor JR, Hansen TP, Hansen KP, Broeng J. All-fiber chirped pulse amplification using highly-dispersive air-core photonic bandgap fiber. *Opt express* (2003) 11(22):2832–7. doi:10.1364/OE.11.002832

24. Wu S, Siwicki B, Carter RM, Biancalana F, Shephard JD, Hand DP. Impact of nonlinear effects on transmission losses of hollow-core antiresonant negative curvature optical fiber. *Appl Opt* (2020) 59(16):4988–96. Epub 2020/06/17. doi:10.1364/AO.382350

25. Emaury, F, Saraceno, CJ, Dutin, CF, Wang, YY, Schriber, C, Gerome, F, et al. *Efficient femtosecond operation of a kagome-type hc-pcf fiber at 75 W average power. CLEO: Science and innovations*. San Jose, CA: Optica Publishing Group (2013).

26. Li F, Yang Z, Lv Z, Wang Y, Li Q, Wei Y, et al. High energy femtosecond laser micromachining with hollow core photonic crystal fiber delivery. *Optik* (2019) 194: 163093. doi:10.1016/j.ijleo.2019.163093

27. Machinet, G, Debort, B, Kling, R, Lopez, J, Gerome, F, Benabid, F, et al. *High average power and high energy transport of ultrashort pulses with a low loss kagome hollow-core photonic crystal fiber for micromachining. The European Conference on Lasers and electro-optics*. Munich, Germany: Optica Publishing Group (2013).

28. Kolyadin AN, Alagashev GK, Pryamikov AD, Mouradian L, Zeytunyan A, Toneyan H, et al. Negative curvature hollow-core fibers: Dispersion properties and femtosecond pulse delivery. *Phys Proced* (2015) 73:59–66. doi:10.1016/j.phpro.2015.09.122

29. Mousavi SA, Mulvad HCH, Wheeler NV, Horak P, Hayes J, Chen Y, et al. Nonlinear dynamic of picosecond pulse propagation in atmospheric air-filled hollow core fibers. *Opt express* (2018) 26(7):8866–82. Epub 2018/05/03. doi:10.1364/OE.26.008866

30. Debord B, Alharbi M, Vincetti L, Husakou A, Fourcade-Dutin C, Hoenninger C, et al. Multi-meter fiber-delivery and pulse self-compression of milli-joule femtosecond laser and fiber-aided laser-micromachining. *Opt express* (2014) 22(9):10735–46. Epub 2014/06/13. doi:10.1364/OE.22.010735

31. Gladyshev AV, Yatsenko YP, Kosolapov AF, Myasnikov DV, Bufetov IA. Propagation of megawatt subpicosecond light pulses with the minimum possible shape and spectrum distortion in an air- or argon-filled hollow-core revolver fibre. *Quan Elect* (2019) 49(12):1100–7. doi:10.1070/qel17156

32. Sung JH, Park JY, Imran T, Lee YS, Nam CH. Generation of 0.2-tw 5.5-fs optical pulses at 1 khz using a differentially pumped hollow-fiber chirped-mirror compressor. *Appl Phys B* (2005) 82(1):5–8. doi:10.1007/s00340-005-2005-0

33. Suda A, Hatayama M, Nagasaka K, Midorikawa K. Generation of sub-10-fs, 5-mj-optical pulses using a hollow fiber with a pressure gradient. *Appl Phys Lett* (2005) 86(11):111116. doi:10.1063/1.1883706

34. Sartania Zc S, Lenzner M, Tempea G, Spielmann C, Krausz F. Generation of 0.1-tw 5-fs optical pulses at a 1-khz repetition rate. *Opt Lett* (1997) 22:1562. doi:10.1364/ol.22.001562

35. Chakrabarti K, Mostufa S, Paul AK. Design and analysis of a position chirped metamaterial photonic crystal array for confinement of light pulses. *J Opt* (2021) 23(11): 115201. doi:10.1088/2040-8986/ac2164

36. Michieletto M, Lyngso JK, Jakobsen C, Laegsgaard J, Bang O, Alkeskjold TT. Hollow-core fibers for high power pulse delivery. *Opt express* (2016) 24(7):7103–19. Epub 2016/05/04. doi:10.1364/OE.24.007103

37. Marcatili EAJ, Schmeltzer RA. Hollow metallic and dielectric waveguides for long distance optical transmission and lasers. *Bell Syst Tech J* (1964) 43(4):1783–809. doi:10.1002/j.1538-7305.1964.tb04108.x

38. Winzer PJ, Leeb WR. Fiber coupling efficiency for random light and its applications to lidar. *Opt Lett* (1998) 23(13):986–8. doi:10.1364/OL.23.000986

39. Wei D, Ying-Ying W, Shou-Fei G, Yi-Feng H, Pu W. Theoretical and experimental investigation of light guidance in hollow-core anti-resonant fiber. *Acta Physica Sinica* (2018) 67(12):124201. doi:10.7498/aps.67.20180724

40. Li H, Goel C, Zang J, Raghuraman S, Chen S, Abu Hassan MR, et al. Integration of an anti-resonant hollow-core fiber with a multimode Yb-doped fiber for high power near-diffraction-limited laser operation. *Opt express* (2022) 30(5):7928. doi:10.1364/oe.451033

41. Goel C, Li H, Abu Hassan MR, Chang W, Yoo S. Anti-resonant hollow-core fiber fusion spliced to laser gain fiber for high-power beam delivery. *Opt Lett* (2021) 46(17): 4374–7. Epub 2021/09/02. doi:10.1364/OL.436054

42. Xiong D, Wu X, Abu Hassan MR, Gavara T, Chang W. In-line hollow-core fiber-optic bandpass filter. *Opt Lett* (2021) 46(23):5918–21. Epub 2021/12/02. doi:10.1364/OL.447108

43. Fibich G, Gaeta AL. Critical power for self-focusing in bulk media and in hollow waveguides. *Opt Lett* (2000) 25(5):335–7. doi:10.1364/OL.25.000335

44. Chraplyvy AR. Limitations on lightwave communications imposed by optical-fiber nonlinearities. *J Lightwave Tech* (1990) 8(10):1548–57. doi:10.1109/50.59195

frontiers | Frontiers in Physics

TYPE Brief Research Report
PUBLISHED 08 March 2023
DOI 10.3389/fphy.2023.1159266

OPEN ACCESS

EDITED BY
Zhenxu Bai,
Hebei University of Technology, China

REVIEWED BY
Liguo Wang,
Dalian Nationalities University, China
Xiaobin Hong,
South China Normal University, China

*CORRESPONDENCE
Haibin Wu,
woo@hrbust.edu.cn

SPECIALTY SECTION
This article was submitted to Optics and Photonics, a section of the journal Frontiers in Physics

RECEIVED 05 February 2023
ACCEPTED 16 February 2023
PUBLISHED 08 March 2023

CITATION
Wang A, Song Y, Wu H, Liu C and Iwahori Y (2023), A hybrid neural architecture search for hyperspectral image classification.
Front. Phys. 11:1159266.
doi: 10.3389/fphy.2023.1159266

A hybrid neural architecture search for hyperspectral image classification

Aili Wang[1], Yingluo Song[1], Haibin Wu[1]*, Chengyang Liu[1] and Yuji Iwahori[2]

[1]Heilongjiang Province Key Laboratory of Laser Spectroscopy Technology and Application, Harbin University of Science and Technology, Harbin, China, [2]Department of Computer Science, Chubu University, Kasugai, Aichi, Japan

Convolution neural network (CNN)is widely used in hyperspectral image (HSI) classification. However, the network architecture of CNNs is usually designed manually, which requires careful fine-tuning. Recently, many technologies for neural architecture search (NAS) have been proposed to automatically design networks, further improving the accuracy of HSI classification to a new level. This paper proposes a circular kernel convolution-β-decay regulation NAS-confident learning rate (CK-βNAS-CLR) framework to automatically design the neural network structure for HSI classification. First, this paper constructs a hybrid search space with 12 kinds of operation, which considers the difference between enhanced circular kernel convolution and square kernel convolution in feature acquisition, so as to improve the sensitivity of the network to hyperspectral information features. Then, the β-decay regulation scheme is introduced to enhance the robustness of differential architecture search (DARTS) and reduce the discretization differences in architecture search. Finally, we combined the confidence learning rate strategy to alleviate the problem of performance collapse. The experimental results on public HSI datasets (Indian Pines, Pavia University) show that the proposed NAS method achieves impressive classification performance and effectively improves classification accuracy.

KEYWORDS

hyperspectral image classification, neural architecture search, differentiable architecture search (DARTS), circular kernel convolution, convolution neural network

1 Introduction

Hyperspectral sensing images (HSIs) collect rich spatial–spectral information in hundreds of spectral bands, which can be used to effectively distinguish ground cover. HSI classification is based on pixel level, and many traditional methods based on machine learning have been used, such as the K-nearest neighbor (KNN) [1] and support vector machine (SVM) [2]. The HSI classification method based on deep learning can effectively extract the robust features to obtain better classification performance [3–5].

Limited by the cost of computing resources and the workload of parameter adjustment, it is inevitable to promote the development of automatic design efficient neural network technology [6]. The goal of NAS (neural architecture search)is to select and combine different neural operations from predefined search spaces and to automate the construction of high-performance neural network structures. Traditional NAS work uses the

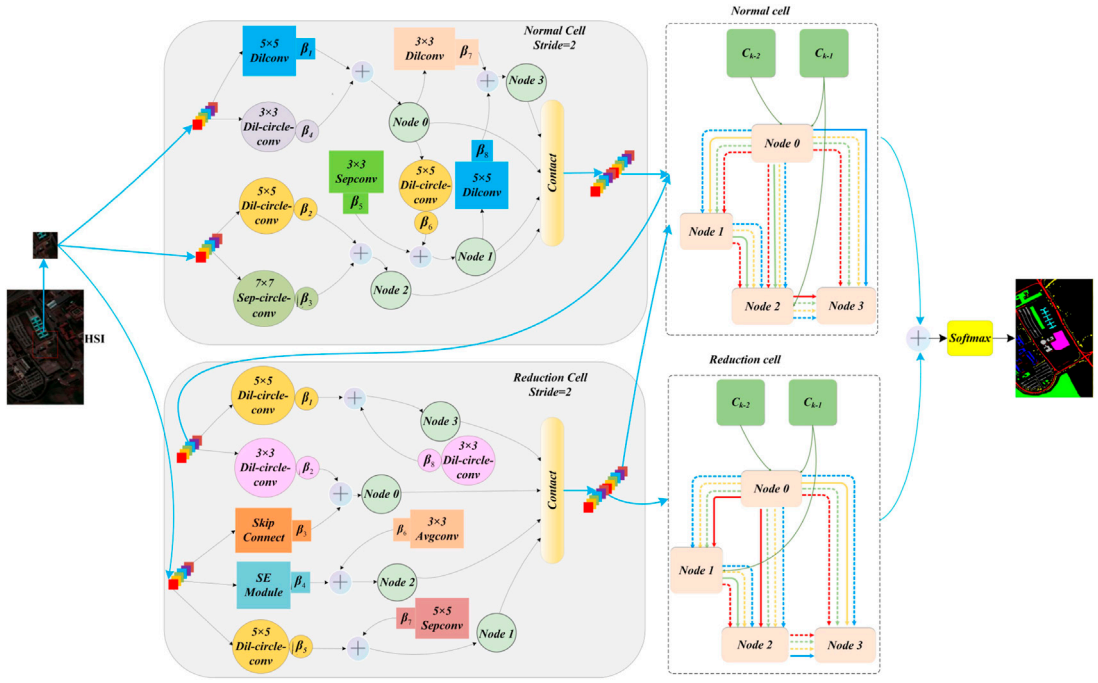

FIGURE 1
Overall framework of the proposed CK-βNAS-CLR model.

reinforcement learning algorithm (RL) [7], evolutionary algorithm (EA) [8], and the gradient-based method to conduct architecture search.

In order to reduce resource consumption, one-shot NAS methods based on supernet are developed [9]. DARTS is a one-shot NAS method with a distinguishable search strategy [10]. By introducing Softmax function, it expands the discrete space into a continuous search optimization process. Specifically, it can reduce the workload of network architecture design and reduce the process of a large number of verification experiments [9].

The method based on the automatic design of convolutional neural network for hyperspectral image classification (CNAS) introduces DARTS into the HSI classification task for the first time. The method uses point-by-point convolution to compress the spectral dimensions of HSI into dozens of dimensions and then uses DARTS to search for neural network architecture suitable for the HSI dataset [11]. Subsequently, based on the method of 3D asymmetric neural architecture search (3D-ANAS), a classification framework from pixel to pixel was designed, and the redundant operation problem was solved by using the 3D asymmetric CNN, which significantly improved the calculation speed of the model [12].

Traditional CNN design uses square kernel to extract image features, which brings significant challenges to the computing system because the number of arithmetic operations increases exponentially with the increase of network size. The features acquired by the square kernel are usually unevenly distributed [13] because the weights at the central intersection are usually large. Inspired by circular kernel (CK) convolution, this paper studies a new NAS paradigm to classify HSI data by automatically designing hybrid search space. The main contributions of this paper are as follows:

1) An effective framework is proposed to design the NAS, called CK-βNAS-CLR, which is composed of a hybrid search space of 12 operations of circular convolution with different convolution methods, different scales, and attention mechanism to effectively improve the feature acquisition ability.
2) β-decay regularization is introduced effectively to stabilize the search process and make the searched network architecture transferable among multiple HSI datasets.
3) We introduced the confident learning rate strategy to focus on the confidence level when updating the structure weight gradient and to prevent over-parameterization.

2 Materials and methods

As shown in Figure 1, the NAS framework for HSI proposed is described, called as CK-βNAS-CLR. Compared with other HSI classification methods, this method aims to alleviate the shortcomings of traditional microNAS methods from three aspects of search space, search strategy, and architecture resource optimization and effectively improve the classification accuracy.

DARTS is a basic framework which adopts weight sharing and combines hypernetwork training with the search of the best candidate architecture to effectively reduce the waste of computing resources. First, the hyperspectral image is clipped into patch by sliding window as input. Then, the hybrid search space of CK convolution and attention mechanism is constructed,

and the operation search between nodes is carried out in the hybrid search space to effectively improve the feature acquisition ability of the receptive field. At the same time, the architecture parameter set β, which represents the importance of the operator, is attenuated and regularized, effectively strengthening the robustness of DARTS and reducing the discretization differences in the architecture search process. After the search is completed, the algorithm stacks multiple normal cells and reduction cells to form the optimal neural structure, and then the classification results are obtained through Softmax operation. In addition, CLR is proposed to stack decay regularization to alleviate the performance crash of DARTS, improve memory efficiency, and reduce architecture search time.

2.1 The proposed NAS framework for HSI classification

2.1.1 Integrating circular kernel to convolution

The circular kernel is isotropic and can be realized from all directions. In addition, symmetric circular nuclei can ensure rotation invariance, which uses bilinear interpolation to approximate the traditional square convolution kernel to a circular convolution kernel, and uses matrix transformation to reparametrize the weight matrix, replacing the original matrix with the changed matrix to realize the offset of receptive field reception. Without considering the loss, the expression of receptive field H of standard 3 × 3 square convolution kernel with a dilation of 1 is written as follows:

$$H = \{(-1,1),(0,1),(1,1),(-1,0),(0,0),(1,0),(-1,-1),(0,-1),(1,-1)\}, \tag{1}$$

where H represents the offset set of the neighborhood convolved on the center pixel. By convolution, the feature map is $R \in H^{S\times S}$ and kernel is $J \in H^{M\times N}$. The output feature map $U \in H^{M\times N}$ can be obtained, and the coordinates of each position are shown in formula (2).

$$U_l \in \sum_{k\in H} R_k J_{l+k}. \tag{2}$$

So, we get $U = R \otimes J$, where $\otimes$ represents the classical convolution operation used by the CNN. Therefore, the change of receptive field of nucleus circularis 3 × 3 is shown in formula(3).

$$B = \left\{\left(-\frac{\sqrt{2}}{2},\frac{\sqrt{2}}{2}\right),(0,1),\left(\frac{\sqrt{2}}{2},\frac{\sqrt{2}}{2}\right),(-1,0),(0,0),(1,0),\left(-\frac{\sqrt{2}}{2},-\frac{\sqrt{2}}{2}\right),(0,-1),\left(\frac{\sqrt{2}}{2},-\frac{\sqrt{2}}{2}\right)\right\}. \tag{3}$$

For the sampling problem of circular convolution kernels, we selected the offset ($\{\Delta b\}$) of k for different discrete kernel positions and resampled the offset to input J to obtain circular receptive fields. Because the sampling receptive field of circular nucleus has a fraction, we use bilinear interpolation to approximate the sampling value of the receptive field.

$$U_l \in \sum_{k\in H} R_k J_{l+k+\Delta b}, \tag{4}$$

$$J_b = \sum_{k\in H} \mathcal{V}(k,b) J_k, \tag{5}$$

where b represents the grid position in the circular receptive field and k represents all grid positions in the square receptive field, which is the kernel of two-dimensional bilinear interpolation. According to the bilinear interpolation, $\mathcal{V}$ can be divided into two one-dimensional cores.

$$\mathcal{V}(k,b) = g(k_x,b_x)\cdot g\left(k_y,b_y\right), \tag{6}$$

$$g(q,e) = max\left(0,1-\left|q-e\right|\right). \tag{7}$$

Therefore, $\mathcal{V}(k,b) \neq 0$ and $\mathcal{V}(k,b) = 1$ only correspond to the corresponding grid k of receptive field B with grid location b. Then, we let $\hat{J}_{RF(l)} \in B^{S^2\times 1}$ and $\hat{R} \in B^{S^2\times 1}$ represent the adjusted receptive field centered on position i and nucleus, respectively. Generally, the standard convolution can be defined as shown in formula (8), so after replacing the circular convolution kernel, the circular convolution can be located as shown in formula (9).

$$U_l \in \hat{R}^T \hat{J}_{RF(l),} \tag{8}$$

$$U_l \in \hat{R}^T\left(C\hat{J}_{RF(l)}\right) = \left(\hat{R}^T C\right)\hat{J}_{RF(l),} \tag{9}$$

where $C \in B^{S^2\times S^2}$ is a fixed sparse coefficient matrix, so let $J \in B^{S^2\times S^2}$, $U \in B^{S^2\times S^2}$, and $R \in B^{S^2\times S^2}$ be the input feature map, output feature map, and kernel, respectively, so the corresponding definition of formula (9) can be written as formula (10).

$$U_l \in R \otimes (C^*J) = (R^*C) \otimes J, \tag{10}$$

where C^*J is the convolution process of changing the square receptive field into a circular receptive field. Thus, we can calculate the core weight to achieve operation C^*J. This calculation method can effectively avoid calculating the offset of multiple convolutions and reduce the cost of core operation. Next, we summarize the analysis of the actual effect of the transformation matrix. We let $\Delta R = R^{a+1} - R^a$, and the value of a change on the output is shown in formula (11). The squared value of a change on the output is shown in formula (12).

$$\Delta U = U^{a+1} - U^a, \tag{11}$$

$$\begin{aligned}\|\Delta U\|^2 &= (C^*J)^T \otimes \Delta R^T \Delta R \otimes (C^*J).\\ &= J^T \otimes \left(C^T{}^*\Delta R^T \Delta R^*C\right) \otimes J\end{aligned} \tag{12}$$

In contrast, ΔU of the traditional convolution layer is defined by $\Delta R^T \Delta R$. Therefore, it can be concluded that the transformation matrix C caused by the circular core can provide a better choice for the gradient descent path of DARTS.

2.1.2 β-decay regularization scheme

In order to alleviate unfair competition in DARTS, we introduced the β-decay regulation scheme [14] so as to improve its robustness and generalization ability and effectively reduce the search memory and the search cost to find the best architecture as shown in Figure 2.

$\alpha_o^{(m,n)}$ converts the discretization operation of the optional operation set $\mathcal{O}$ in the search space into an operable continuous set. After implementing Softmax operation, the architecture parameter set $\beta_l^{(m,n)}$ is obtained, which is attenuated and regularized.

$$\beta_l^{(m,n)} = \sum_{o\in\mathcal{O}} \frac{exp\left(\alpha_o^{(m,n)}\right)}{\sum_{l'=1} exp\left(\alpha_{o'}^{(m,n)}\right)}, \tag{13}$$

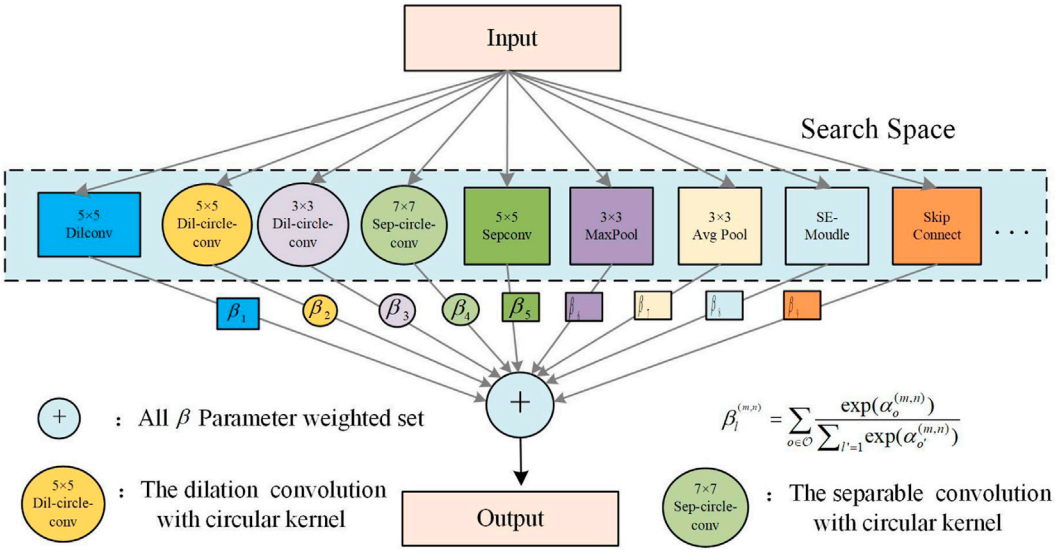

FIGURE 2
β-decay regularization scheme.

where $\beta_l^{(m,n)}$ is the combination of architecture parameters between node m and node n and l is the number of optional operations. Each cell can have up to N nodes, and $\alpha_o^{(m,n)}$ represents the architecture parameters. A special coefficient for each candidate operation $\beta_o^{(m,n)}$ is defined.

$$\beta_o^{(m,n)} = \frac{exp\left(\alpha_o^{(m,n)}\right)}{\sum_{o' \epsilon \mathcal{O}} \exp\left(\alpha_{o'}^{(m,n)}\right)}. \tag{14}$$

Starting from the default setting of regularization, consider the one-step update of architecture parameter α, where ς_α represents the learning rate a of architecture parameters.

$$\alpha_l^{t+1} \leftarrow \alpha_l^t - \eta_\alpha . \nabla_\alpha \mathcal{L}_{valid}. \tag{15}$$

For the special gradient descent algorithm of DARTS, these regularized gradients need to be normalized ($\mathcal{NL}$) through the sum size and to realize the average distribution of the total gradient without normalization.

$$\alpha_l^{t+1} \leftarrow \alpha_l^t - \eta_\alpha . \nabla_\alpha \mathcal{L}_{valid} - \varsigma_\alpha \delta \mathcal{NL}\left(\alpha_l^t\right), \tag{16}$$

$$\alpha_l^{t+1} \leftarrow \alpha_l^t - \eta_\alpha . \nabla_\alpha \mathcal{L}_{valid} - \varsigma_\alpha \delta \left(\alpha_k^y\right). \tag{17}$$

In the DARTS search process, the architecture parameter set, β, is used to express the importance of all operators. The research on explicit regularization of β can more clearly standardize the optimization of architecture parameters so as to improve the robustness and architecture universality of DARTS. We use the χ function with α as the independent variable to express the total impact of attenuation regularization.

$$\bar{\beta}_l^{t+1} = \chi_l^{t+1}\left(\alpha_l^t\right)\beta_l^{t+1}, \tag{18}$$

$$\alpha_l^{t+1} \leftarrow \alpha_l^t - \eta_\alpha . \nabla_\alpha \mathcal{L}_{valid} - \varsigma_\alpha \delta R\left(\alpha_k^t\right), \tag{19}$$

where the χ function (R is the independent variable) represents the overall influence of β attenuation regularization and R is the mapping function. We can iterate for dividing the single-step update parameter value β_l^{t+1} and parameter value weighted sum $\bar{\beta}_l^{t+1}$ of β.

$$\frac{\bar{\beta}_l^{t+1}}{\beta_l^{t+1}} = \frac{\sum_{l'=1}^{|\mathcal{O}|} exp\left(\alpha_{l'}^{t+1}\right)}{\sum_{l'=1}^{|\mathcal{O}|}\left[exp\left(R\left(\alpha_l^t\right) - R\left(\alpha_{l'}^t\right)\right)\right]^{\delta\varsigma_\alpha} exp\left(\alpha_{l'}^{t+1}\right)}. \tag{20}$$

It can be found that mapping function R determines the impact of α on β. To avoid excessive regularization and optimization difficulties, Softmax is used to normalize α.

$$R\left(\alpha_l\right) = \frac{exp\left(\alpha_l\right)}{\sum_{l'=1}^{|\mathcal{O}|} exp\left(\alpha_l'\right).} \tag{21}$$

We can obtain the impact and effect of our method.

$$\chi_l^{t+1}\left(\alpha_l^t\right) = \frac{\sum_{l'=1}^{|\mathcal{O}|} exp\left(\alpha_{l'}^{t+1}\right)}{\sum_{l'=1}^{|\mathcal{O}|}\left[exp\left(\frac{exp\left(\alpha_l^t\right) - exp\left(\alpha_{l'}^t\right)}{\sum_{l''=1}^{|\mathcal{O}|} exp\left(\alpha_{l''}^t\right)}\right)\right]^{\delta\varsigma_\alpha} exp\left(\alpha_{l'}^{t+1}\right)} \chi_l^{t+1}\left(\alpha_l^t\right). \tag{22}$$

2.1.3 Confident learning rate strategy

When the NAS method is used to classify hyperspectral datasets, a large number of parameters will be generated. When the training samples are limited, the performance of the network may be reduced due to the over-fitting phenomenon, which will lead to low memory utilization during the training process. CLR is used to alleviate these two problems [15].

After applying the Softmax operation, the structure is relaxed. The gradient descent algorithm is used to optimize the $\alpha = \{\alpha^{(m,n)}\}$ matrix, and the original weight of the network is called w. Then, the cross-entropy formula is used to calculate the loss value in the training stage and the parameters $\mathcal{L}_{train}$ and $\mathcal{L}_{valid}$ are updated.

In order to enable both to achieve the optimization strategy at the same time, it is necessary to fix the value of $\alpha = \{\alpha^{(m,n)}\}$ matrix on the training set, update w using the gradient descent algorithm,

TABLE 1 Performance comparison of different methods of the Indian Pines dataset.

Method	EMP-SVM	SSRN	ResNet	PyResNet	CNAS	MLP-Mixer	ANAS-CPA-LS	CK-βNAS-CLR
Alfalfa	51.16 ± 17.51	100 ± 0.00	95.36 ± 0.28	97.43 ± 0.36	95.14 ± 4.27	100 ± 0.00	99.39 ± 0.32	100.0 ± 0.75
Corn-no till	66.26 ± 3.37	88.95 ± 1.19	93.36 ± 3.76	98.87 ± 1.04	96.19 ± 1.21	96.56 ± 0.09	96.43 ± 0.79	96.93 ± 0.31
Corn-min till	70.40 ± 3.74	92.87 ± 0.54	95.64 ± 0.37	89.44 ± 0.34	92.86 ± 2.64	92.10 ± 0.03	94.25 ± 0.97	96.10 ± 0.34
Corn	56.63 ± 6.68	96.56 ± 0.91	94.99 ± 4.32	97.47 ± 0.57	96.56 ± 3.94	98.15 ± 0.68	99.07 ± 0.74	99.95 ± 0.00
Grass-pasture	87.04 ± 3.52	90.52 ± 7.56	97.69 ± 2.30	97.38 ± 0.95	97.13 ± 0.27	97.87 ± 1.16	99.56 ± 0.55	94.59 ± 1.16
Grass-trees	87.30 ± 1.82	96.91 ± 1.16	97.27 ± 1.80	98.40 ± 0.12	94.02 ± 0.22	96.98 ± 0.86	96.44 ± 0.97	98.39 ± 0.79
Grass-pasture-mowed	82.78 ± 8.11	86.60 ± 0.89	99.01 ± 0.00	100 ± 0.00	92.31 ± 0.88	100 ± 0.00	90.68 ± 2.66	95.21 ± 0.05
Hay-windrowed	89.45 ± 1.75	96.28 ± 3.71	93.64 ± 1.17	95.81 ± 1.68	99.44 ± 4.66	95.80 ± 0.60	97.91 ± 0.67	95.73 ± 1.95
Oats	64.83 ± 16.3	84.37 ± 0.06	96.66 ± 1.66	94.67 ± 1.11	98.96 ± 0.56	100 ± 0.00	99.51 ± 2.02	93.15 ± 2.87
Soybean-not till	71.90 ± 2.12	92.46 ± 0.07	92.88 ± 1.90	88.20 ± 7.13	92.00 ± 0.56	93.38 ± 0.34	95.02 ± 0.43	98.69 ± 1.04
Soybean-mint till	73.01 ± 1.62	95.33 ± 0.06	94.27 ± 0.11	95.26 ± 1.87	93.90 ± 0.92	95.34 ± 0.37	98.36 ± 0.65	99.04 ± 0.79
Soybean -clean	66.49 ± 4.56	94.69 ± 2.77	96.13 ± 1.43	95.42 ± 1.79	94.88 ± 0.19	94.34 ± 1.32	99.07 ± 0.83	98.38 ± 3.19
Wheat	88.62 ± 4.35	97.84 ± 1.14	99.02 ± 0.01	99.55 ± 0.62	94.65 ± 0.45	100 ± 0.00	95.28 ± 0.57	99.41 ± 0.12
Woods	90.44 ± 1.19	94.82 ± 2.31	93.97 ± 1.67	96.84 ± 1.14	98.33 ± 0.29	95.64 ± 0.06	95.57 ± 0.99	98.77 ± 0.62
Buildings-grass-trees-drivers	71.35 ± 7.39	91.29 ± 2.52	93.66 ± 0.11	93.56 ± 3.90	94.99 ± 0.45	95.55 ± 0.15	95.14 ± 1.66	98.65 ± 1.24
Stone-steel-towers	98.10 ± 1.82	86.70 ± 1.22	94.47 ± 1.43	96.34 ± 1.72	89.57 ± 2.66	88.12 ± 2.12	88.28 ± 0.96	85.30 ± 0.85
OA/%	81.64 ± 0.02	93.58 ± 1.12	94.53 ± 0.59	94.95 ± 1.07	95.00 ± 0.56	95.95 ± 0.17	96.57 ± 0.56	97.90 ± 0.31
AA/%	75.98 ± 5.36	92.88 ± 1.64	95.50 ± 1.39	95.91 ± 1.52	95.05 ± 1.51	96.23 ± 0.48	96.24 ± 0.98	96.76 ± 1.00
100 K	71.92 ± 2.82	92.67 ± 1.29	93.74 ± 0.67	94.31 ± 0.19	94.88 ± 0.87	95.38 ± 0.20	95.69 ± 0.39	96.97 ± 0.90

fix the w value on the verification set, update the $\alpha = \{\alpha^{(m,n)}\}$ value using the gradient descent algorithm, and obtain the best parameter value repeatedly. Stop the optimization after finding the best architecture neural architecture α_o^* and minimize the verification loss $\mathcal{L}_{valid}(w^*, \alpha^*)$.

$$\min_{\alpha} \mathcal{L}_{valid}(w^*(\alpha), \alpha), \tag{23}$$

$$\text{s.t. } w^*(\alpha) = arg\min_{w} \mathcal{L}_{train}(w, \alpha). \tag{24}$$

NAS architecture parameters will be over-parameterized with the increase of training time. Therefore, the gradient confidence obtained from the parameterized DARTS should increase with the training time of the architecture weight update.

$$LR_{Confident}(a) = \left(\frac{a}{A}\right)^{\tau} \times LR_{\alpha}, \tag{25}$$

where α represents the number of epochs currently trained, A represents the preset total epochs, and τ is the confidence factor of CLR. Through the update of the confidence learning rate, the network obtains $\mathcal{L}_{valid}$ and uses it for gradient update.

$$grad_{\alpha} = \nabla_{\alpha}\mathcal{L}_{valid}(w - \xi\nabla_{w}\mathcal{L}_{train}(\omega, \alpha), \alpha). \tag{26}$$

The confidence learning rate is established in the process of architecture gradient update.

$$grad_{\alpha} = LR_{confident} * \nabla_{\alpha}\mathcal{L}_{valid}(w - \xi\nabla_{w}\mathcal{L}_{train}(w, \alpha), \alpha). \tag{27}$$

3 Results

Our experiments are conducted using Intel (R) Xeon (R) 4208 CPU@2.10GHz Processor and Nvidia GeForce RTX 2080Ti graphics card. We selected the average of 10 experiments to compute the overall accuracy (OA), average accuracy (AA), and Kappa coefficient (K).

3.1 Comparison with state-of-the-art methods

In this section, we select some advanced methods to make comparison so as to evaluate the classification performance, which include extended morphological profile combined with support vector machine (EMP-SVM) [16], spectral spatial residual network (SSRN) [17], residual network (ResNet) [18], pyramid residual network (PyResNet) [19], multi-layer perceptron mixer (MLP Mixer) [20], CNAS [11], and efficient convolutional neural architecture search (ANAS-CPA-LS) [21]. All experimental results are shown in Tables 1, 2. The sample is clipped by using the sliding window strategy size of 32 × 32, and the overlap rate is set to 50%. We randomly selected 30 samples as the training dataset and 20 samples as the validation dataset. The training time is set to 200, and the learning rate of the three data sets is set to 0.001.

TABLE 2 Performance comparison of different methods of the Pavia University dataset.

Method	EMP-SVM	SSRN	ResNet	PyResNet	CNAS	MLP-Mixer	ANAS-CPA-LS	CK-βNAS-CLR
Asphalt	89.06 ± 1.33	90.59 ± 0.62	95.59 ± 3.43	94.01 ± 0.54	95.55 ± 0.25	95.56 ± 1.26	97.56 ± 1.34	98.75 ± 0.69
Meadows	88.12 ± 0.23	89.26 ± 1.05	97.10 ± 2.06	99.40 ± 0.70	98.91 ± 0.71	99.45 ± 0.15	100 ± 0.00	100 ± 0.00
Gravel	78.65 ± 3.05	78.89 ± 2.65	87.53 ± 5.27	98.26 ± 1.69	93.81 ± 4.60	93.83 ± 1.03	99.78 ± 0.03	98.73 ± 0.28
Trees	88.95 ± 0.53	89.05 ± 1.45	99.03 ± 0.33	98.73 ± 0.61	99.35 ± 0.28	98.78 ± 0.45	93.73 ± 1.64	97.12 ± 0.02
Metal	93.23 ± 1.29	94.55 ± 0.67	98.56 ± 1.36	99.64 ± 0.27	99.67 ± 0.17	99.81 ± 0.81	99.24 ± 0.01	98.93 ± 0.36
Bare soil	90.13 ± 0.54	90.23 ± 1.23	98.35 ± 1.06	99.28 ± 0.04	98.39 ± 0.18	98.97 ± 0.97	100 ± 0.00	100 ± 0.00
Bitumen	81.66 ± 3.31	83.69 ± 2.82	99.29 ± 0.51	96.35 ± 0.19	92.31 ± 0.88	99.22 ± 0.19	94.63 ± 0.24	97.61 ± 0.48
Bricks	83.05 ± 1.61	83.57 ± 2.91	94.61 ± 0.50	84.58 ± 1.34	89.44 ± 4.66	88.88 ± 1.92	92.89 ± 0.42	98.23 ± 0.69
Shadows	95.26 ± 0.56	94.68 ± 0.46	99.39 ± 0.58	99.74 ± 0.05	98.96 ± 0.56	98.92 ± 1.46	96.33 ± 0.32	97.16 ± 0.91
OA/%	91.07 ± 0.85	91.32 ± 1.22	96.49 ± 1.78	96.97 ± 1.32	97.05 ± 0.45	97.55 ± 0.13	97.61 ± 0.87	98.46 ± 0.57
AA/%	87.57 ± 1.38	88.28 ± 1.54	96.61 ± 1.68	96.67 ± 0.13	96.27 ± 1.36	97.05 ± 0.91	97.12 ± 0.44	98.50 ± 0.34
100 K	88.72 ± 1.44	89.43 ± 1.09	95.31 ± 2.41	96.07 ± 0.41	96.22 ± 0.11	96.76 ± 0.18	96.86 ± 0.74	98.06 ± 0.67

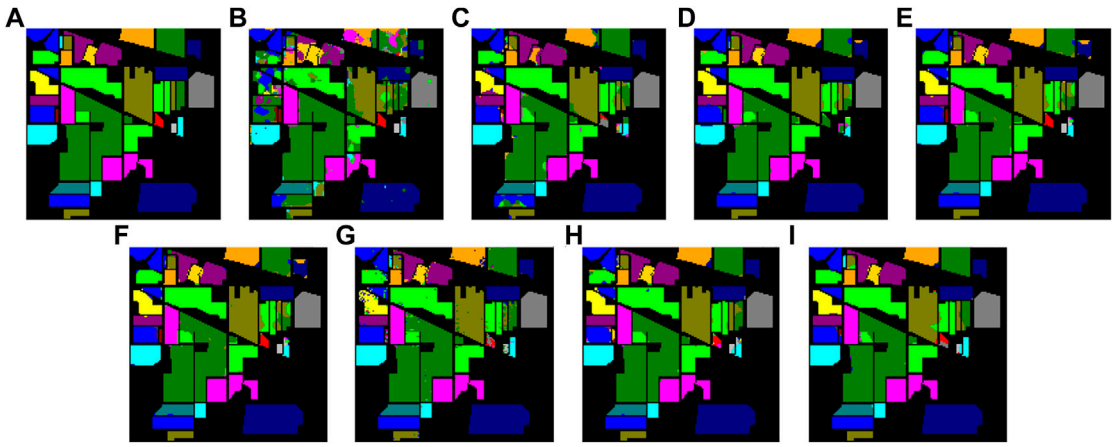

FIGURE 3
Classification results of the Indian pines dataset. **(A)** Ground-truth map, **(B)** EMP-SVM, **(C)** SSRN, **(D)**ResNet, **(E)** PyResNet, **(F)** CNAS, **(G)** MLP-Mixer, **(H)** ANAS-CPA-LS, and **(I) (I)** CK-*β*NAS-CLR.

In Table 1, compared with EMP-SVM, SSRN, ResNet, PyResNet, CNAS, MLP Mixer, and ANAS-CPA-LS, OA obtained by our proposed method is increased by 16.26%, 4.32%, 3.37%, 2.95%, 2.9%, 1.95%, and 1.33%, respectively, on the Indian Pines dataset. Figures 3, 4 shows the classification diagram obtained from a visual perspective. By comparing the classification diagrams obtained, we can draw a conclusion that our algorithm achieves better performance. Compared with CNAS, our method uses a hybrid search space, which can effectively expand the receptive field acquired by pixels, improve the flexibility of different convolution kernel operations to process spectrum and space, and achieve higher classification accuracy.

4 Discussion

The ablation study results are provided in Table 3. When CNAS is combined with hybrid search space, OA increases by 0.70%, 0.35%, and 0.54%, which proves that the hybrid search space can improve the sensitivity of the network to hyperspectral information features and slightly improve the classification performance of the model. Compared with CNAS, CK-NAS has no time change in the search time on the three datasets but has achieved better classification accuracy. CK-βNAS-CLR search gets better results with fewer parameters and involves less computational complexity.

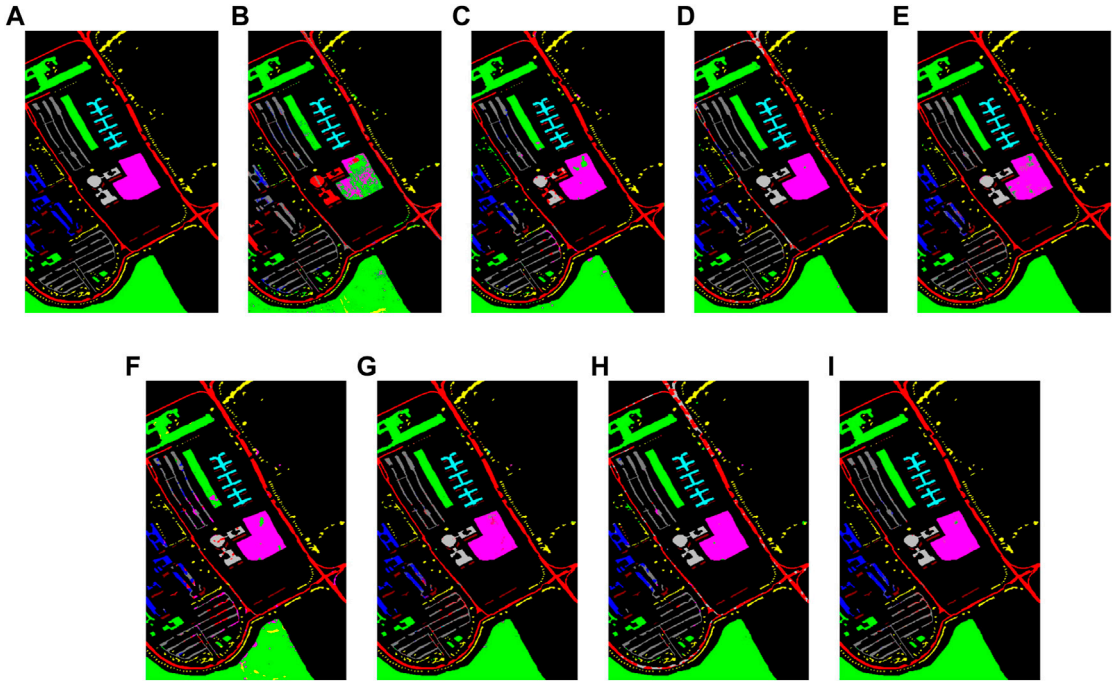

FIGURE 4
Classification results of the Pavia University dataset. **(A)** Ground-truth map, **(B)** EMP-SVM, **(C)** SSRN, **(D)**ResNet, **(E)** PyResNet, **(F)** CNAS, **(G)** MLP-Mixer, **(H)** ANAS-CPA-LS, and **(I)** CK-βNAS-CLR.

TABLE 3 Ablation results on the two datasets.

Dataset	Index	CNAS	CK + NAS	CK+β+NAS	CK+β+NAS + CLR
Indian Pines	OA (%)	95.00 ± 0.56	95.70 ± 0.87	96.80 ± 0.31	97.82 ± 0.31
	AA (%)	95.05 ± 1.51	93.12 ± 0.42	94.60 ± 0.42	96.76 ± 1.00
	100 K	94.88 ± 0.87	95.11 ± 0.17	96.95 ± 0.17	96.87 ± 0.90
	Search cost (h)	2.702	2.687	2.562	2.473
	Params (M)	0.082	0.075	0.075	0.070
Pavia University	OA (%)	97.05 ± 0.45	97.40 ± 0.29	97.82 ± 0.20	98.46 ± 0.57
	AA (%)	96.27 ± 1.36	97.14 ± 1.36	97.51 ± 1.83	98.50 ± 0.86
	100 K	96.22 ± 0.11	96.65 ± 0.79	97.25 ± 2.51	98.06 ± 0.67
	Search cost (h)	3.054	3.013	2.867	2.733
	Params (M)	0.176	0.172	0.172	0.168

5 Conclusion

In this paper, the neural network structure CK-βNAS-CLR is proposed. First of all, we introduce a hybrid search space with circular kernel convolution, which can not only enhance the robustness of the model and the ability of receptive field acquisition but also achieve a better role in optimizing the path. Second, we quoted the β-decay regulation scheme, which reduced the discretization difference and the search time. Finally, the confidence learning rate strategy is introduced to improve the accuracy of model classification and reduce computational complexity. The experiment was conducted on two HSI datasets, and CK-βNAS-CLR is compared with seven methods, and the experimental results show that our method achieves the most advanced performance while using less computing resources. In future, we will use an adaptive subset of the data even when training the final architecture, which may lead to faster runtime and lower regularization term.

Data availability statement

Publicly available datasets were analyzed in this study. These data can be found here: https://www.ehu.eus/ccwintco/index.php?%20title=Hyperspectral-Remote-Sensing-Scenes.

Author contributions

All authors listed have made a substantial, direct, and intellectual contribution to the work and approved it for publication.

Funding

This work was funded by the Reserved Leaders of Heilongjiang Provincial Leading Talent Echelon of 2021, high and foreign expert's introduction program (G2022012010L), and the Key Research and Development Program Guidance Project (GZ20220123).

Conflict of interest

The authors declare that the research was conducted in the absence of any commercial or financial relationships that could be construed as a potential conflict of interest.

Publisher's note

All claims expressed in this article are solely those of the authors and do not necessarily represent those of their affiliated organizations, or those of the publisher, the editors, and the reviewers. Any product that may be evaluated in this article, or claim that may be made by its manufacturer, is not guaranteed or endorsed by the publisher.

References

1. Chandra B, Sharma RK. On improving recurrent neural network for image classification. In: Proceeding of the International Joint Conference on Neural Networks. Alaska, USA: IJCNN (2017). p. 1904–7. doi:10.1109/IJCNN.2017.7966083

2. Samadzadegan F, Hasani H, Schenk T. Simultaneous feature selection and SVM parameter determination in classification of hyperspectral imagery using Ant Colony Optimization. *Remote Sens* (2012) 38:139–56. doi:10.5589/m12-022

3. Hu W, Huang Y, Wei L, Zhang F, Li H. Deep convolutional neural networks for hyperspectral image classification. *J Sensors* (2015) 2015:1–12. doi:10.1155/2015/258619

4. Makantasis K, Karantzalos K, Doulamis A, Doulamis N. Deep supervised learning for hyperspectral data classification through convolutional neural networks. In: 2015 IEEE International Geoscience and Remote Sensing Symposium (IGARSS). Milan, Italy: IGARSS (2015). p. 4959–62.

5. Li W, Wu G, Zhang F, Du Q. Hyperspectral image classification using deep pixel-pair features. *IEEE Trans Geosci Remote Sensing* (2017) 55(2):844–53. doi:10.1109/tgrs.2016.2616355

6. Kaifeng B, Lingxi X, Chen X, Longhui W, Tian Q. *GOLD-NAS: Gradual,one-level, differentiable* (2020). p. 03331. arXiv:2007.

7. Real E, Aggarwal A, Huang Y, Le QV, "Regularized evolution for image classifier architecture search," in Proc. AAAI Conf. Artif. Intell (2019) 33, 4780–9. doi:10.1609/aaai.v33i01.33014780

8. Tan M, Chen B, Pang R, V asudevan V, Sandler M, Howard A, et al. *MnasNet: Platform-aware neural architecture search for mobile*. Long Beach, CA, USA: CVPR (2019). 2820–8.

9. Liang H. *DARTS+: Improved differentiable architecture search with early stopping* (2020). arXiv:1909.06035. [Online]. Available: https://arxiv.org/abs/1909.06035 (Accessed October 20, 2020).

10. Guo Z, "Single path one-shot neural architecture search with uniform sampling," in Proc. IEEE Eur. Conf. Comput. Vis (2020), 544–60.

11. Chen Y, Zhu K, Zhu L, He X, Ghamisi P, Benediktsson JA. Automatic design of convolutional neural network for hyperspectral image classification. *IEEE Trans Geosci Remote Sensing* (2019) 57(9):7048–66. doi:10.1109/tgrs.2019.2910603

12. Zhang H, Gong C, Bai Y, Bai Z, Li Y. *3d-anas: 3d asymmetric neural architecture search for fast hyperspectral image classification* (2021). arXiv preprint arXiv: 2101.04287, 2021.[Online]. Available: https://arxiv.org/abs/2101.04287 (Accessed Janunary 12, 2021).

13. Li G, Qian G, Delgadillo IC, Muller M, Thabet A, Ghanem B. Sgas: Sequential greedy architecture search. In: Proc. IEEE Conf. Comput. Vis. Pattern Recognit (2020). p. 1620–30.

14. Ye P, Li B, Li Y, Chen T, Fan J, Ouyang W, et al. beta$-DARTS: Beta-Decay regularization for differentiable architecture search, in Proceeding of the 2022 IEEE/CVF Conference on Computer Vision and Pattern Recognition (CVPR), New Orleans, LA, USA (2022), 10864–73.

15. Ding Z, Chen Y, Li N, Zhao D. BNAS-v2: Memory-Efficient and performance-collapse-prevented broad neural architecture search. *IEEE Trans Syst Man, Cybernetics: Syst* (2022) 52(10):6259–72. doi:10.1109/TSMC.2022.3143201

16. Melgani F, Bruzzone L. Classification of hyperspectral remote sensing images with support vector machines. *IEEE Trans Geosci Remote Sensing* (2004) 42(8):1778–90. doi:10.1109/tgrs.2004.831865

17. Zhong Z, Li J, Luo Z, Chapman M. Spectral–spatial residual network for hyperspectral image classification: A 3-D deep learning framework. *IEEE Trans Geosci Remote Sensing* (2018) 56(2):847–58. doi:10.1109/tgrs.2017.2755542

18. Liu X, Meng Y, Fu M, "Classification research based on residual network for hyperspectral image,"In, Proceeding of the 2019 IEEE 4th International Conference on Signal and Image Processing (IC) (2019). 911–5.

19. Paoletti ME, Haut JM, Fernandez-Beltran R, Plaza J, Plaza AJ, Pla F. Deep pyramidal residual networks for spectral–spatial hyperspectral image classification. *IEEE Trans Geosci Remote Sensing* (2019) 57(2):740–54. doi:10.1109/TGRS.2018.2860125

20. He X, Chen Y. Modifications of the multi-layer Perceptron for hyperspectral image classification. *Remote Sensing* (2021) 13(17):3547. doi:10.3390/rs13173547

21. Wang A, Xue D, Wu H, Gu Y. Efficient convolutional neural architecture search for LiDAR DSM classification. *IEEE Trans Geosci Remote Sensing* (2022) 60:1–17. Art no. 5703317. doi:10.1109/TGRS.2022.3171520

frontiers | Frontiers in Physics

TYPE Brief Research Report
PUBLISHED 08 March 2023
DOI 10.3389/fphy.2022.1115557

OPEN ACCESS

EDITED BY
Shuo Liu,
Hebei University of Technology, China

REVIEWED BY
Liwen Sheng,
Ceyear Technologies Co., Ltd, China
Hui Yang,
Southwest Jiaotong University, China

*CORRESPONDENCE
Hongli Wang,
wanghl@nuc.edu.cn

SPECIALTY SECTION
This article was submitted to Optics and Photonics, a section of the journal Frontiers in Physics

RECEIVED 04 December 2022
ACCEPTED 20 December 2022
PUBLISHED 08 March 2023

CITATION
Wang H, Shan S and Wang G (2023), Experimental optimization of compact double-cell stimulated Brillouin scattering pulse compressor.
Front. Phys. 10:1115557.
doi: 10.3389/fphy.2022.1115557

Experimental optimization of compact double-cell stimulated Brillouin scattering pulse compressor

Hongli Wang[1,2]*, Shimin Shan[3] and Gao Wang[1]

[1]School of Information and Communication Engineering, North University of China, Taiyuan, China, [2]Department of Physics, Korea Advanced Institute of Science and Technology, Daejeon, South Korea, [3]School of Semiconductors and Physics, North University of China, Taiyuan, China

To optimize the output of SBS sub-nanosecond pulse compression, two kinds of compact double-cell structures are carried out and compared experimentally. The beam parameters of the compact double-cell structure are calculated theoretically, which provides the selection guidance of structural parameters such as lens focal length and SBS cell size. The dependence of lens parameters and medium parameters on SBS output parameters are experimentally studied. Results show that SBS pulse compression enters the saturation region at a low injection energy with a long focal length lens or a large gain coefficient medium. For compact double-cell setup with one lens, it is easy to obtain narrow pulses for the medium FC40 with a short phonon lifetime. While in setup with two lenses, it is easy to obtain SBS output with a high energy efficiency and narrow pulse width for HT110 medium with a large gain coefficient. The pulse width compression ratio is up to 16 times after optimization. These experimental results can provide references for the experimental design of SBS pulse compression.

KEYWORDS

high-energy laser, stimulated Brillouin scattering, pulse compression, sub-nanosecond pulse, beam parameter

1 Introduction

A single-longitudinal mode sub-nanosecond pulse laser with good beam quality has important applications in the fields of fast ignition lasing radiation [1], space debris detection [2, 3], medical laser cosmetology [4], Doppler wind radar [5], and high spatial resolution in LIDAR Thomson scattering diagnostics [6], *etc.* Stimulated Brillouin scattering (SBS) has proved to be an effective technical means to compress long nanosecond pulses to sub-nanosecond pulses and improve the beam quality of the laser system [7–9]. The compact double-cell structure based on liquid media, with the advantages of a high pulse compression ratio, no high pressure, a small absorption coefficient, and a high laser damage threshold compared with gas and solid media, are commonly and widely used in high-energy sub-nanosecond pulse laser systems [10–14]. SBS pulse compressors with a compact double-cell structure have received considerable attention by employing the medium of perfluorocarbon-compounds (PFCs) liquids and perfluoropolyether (PFPE) liquids.

Many previous theoretical and experimental studies have been conducted to obtain a high-reflected energy efficiency and narrow-pulse width beam laser by optimizing the structure parameters and medium parameters. Feng et al. stated that the interaction length between the Stokes and pump pulses is the key parameter in achieving sub-phonon lifetime pulse compression and experiment was conducted by employing an energy-scalable generator-

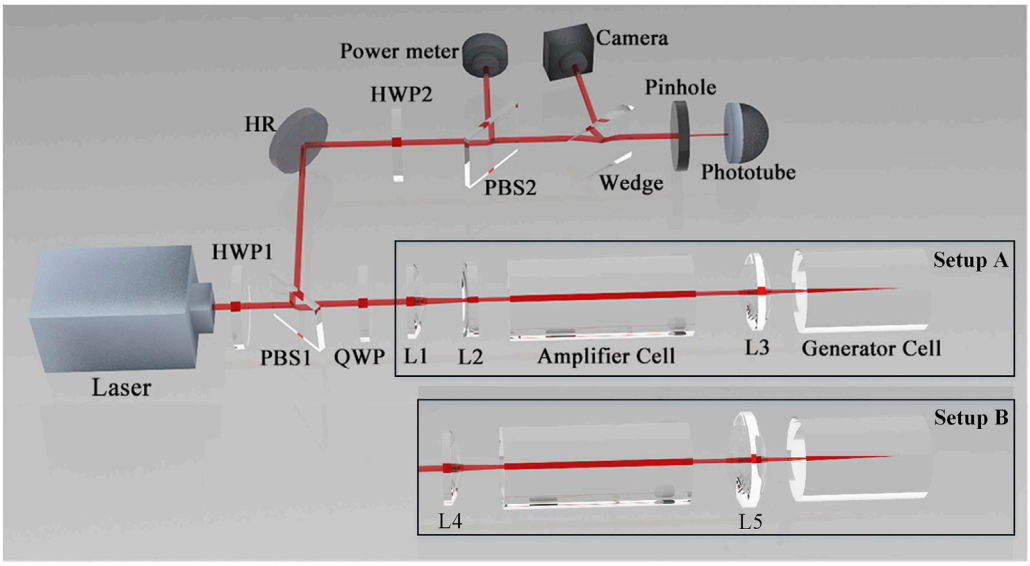

FIGURE 1
Schematic of experimental setups for compact double-cell SBS compressor. QWP, quarter wave plate; HWP1~2, half wave plate; L1~5, lens. In setup A, the input beam is introduced into the SBS amplifier cell through a QWP and a pair of lenses L1 and L2 and focused into the generator cell through a lens L3. In setup B, the input beam is introduced into the SBS amplifier cell through a QWP and a lens L4 and focused into the generator cell through a focusing lens L5.

amplifier setup [12]. Xu et al. used a combination of theoretical modeling and experiments to identify and optimize all critical parameters, including optical configuration, interaction length, intensity matching, choice of gain medium and thermal stability in an energy-scalable generator-amplifier setup [15]. Yoshida et al. achieved a high compression ratio by SBS consisting of two long cells [11]. Guo et al. designed a single-cell experiment to study the energy reflectivity property for the SBS medium of PFCs and PFPE in high peak power laser [16], and Park et al. also measured the SBS characteristics in several liquids [17]. Hasi et al. stated the characteristics of four PFCs media for two-stage SBS pulse compression structure [18]. Therefore, the optimization of the structure parameters and medium parameters for compact double-cell structures is required to study systematically to obtain good SBS compression with a high energy reflectivity.

In this study, to obtain sub-nanosecond pulses with a high reflected energy efficiency, the SBS pulse compression for two types of compact double-cell structure setups are experimentally studied and compared. The focal depth and focal spot size in the compact double-cell structure are calculated, which provides theoretical guidance for structural design such as lens focal length and medium cell size. The experimental setup is described in Section 2. In Section 3, calculation of beam parameters in compact double-cell structure is presented. In Section 4, the experimental results and discussion are presented, and Section 5 concludes the paper. This work has important reference value for the design of SBS experimental structure in high-energy laser systems.

2 Experimental setup

The experimental setup employed in this research is shown in Figure 1. The pumping source is p-polarized light originating from an injection seeded single-longitudinal-mode laser at a fundamental wavelength of 1,064 nm. The pump beam has a pulse width of 10 ns operating at a repetition rate of 10 Hz. The laser propagates from left to right. A half-wave plate (HWP1) and a polarization beam splitter (PBS1) were used to control the input beam energy. Two setups are employed in this research. The input beam is introduced into the SBS amplifier cell through a quarter-wave plate (QWP) and a pair of lenses L1 and L2 with focal lengths of 30 cm and −20 cm, respectively in setup A. The pump beam size is reduced from 8 mm to 5.2 mm using a beam reducer. The laser is focused into the generator cell through a focusing lens L3 with focal lengths of 20 cm or 50 cm, respectively. In setup B, the input beam is introduced into the SBS amplifier cell through a QWP and a lens L4 with focal length of 200 cm and focused into the generator cell through a focusing lens L5 with focal length of 50 cm or 75 cm, respectively.

In the process of SBS pulse compression, the phonon lifetime and the gain coefficient are two significant parameters affecting the compressed pulse width. The influence weight between the two parameters, the phonon lifetime and the gain coefficient, is necessary to obtain a good SBS compression [7]. Based on this, we choose two commonly used media of perfluoropolyether liquid HT110 and heavy fluorocarbon liquid FC40 as the objectives due to the large difference between their phonon lifetimes and gain coefficients, which are made by Solvay Company and 3M Company, respectively. Phonon lifetimes of the medium of HT110 and FC40 are .6 ns and .2 ns, respectively. SBS gain coefficients of the medium of HT110 and FC40 are 4.7 cm/GW and 1.8 cm/GW, respectively [7].

3 Calculation of beam parameters in compact double-cell structure

To avoid damaging the lens and window mirror of SBS cell in the design of compact double-cell structure, it is necessary to select the

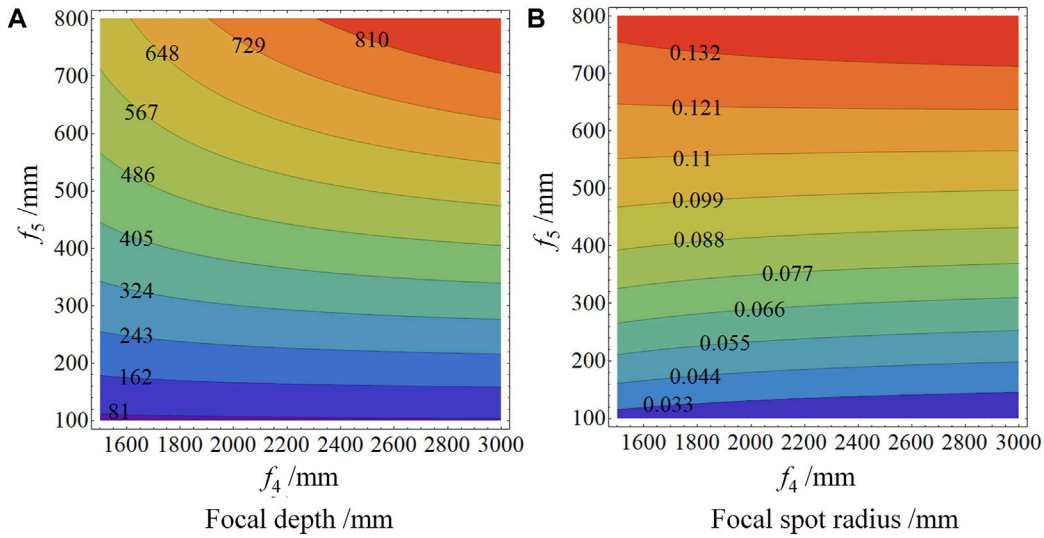

FIGURE 2
Contour map of beam parameters with respect to focal lengths of lens in setup B.

lens and SBS cell with appropriate parameters. Taking setup B as an example, the focal depths and focal spot sizes within the generator cell are theoretically calculated. It is generally believed that the generation position of the Stokes beam is at the focal point within the generator cell. The focal depth indicates the interaction length between the pump beam and the Stokes beam, which affects the compressed pulse width of SBS. It is easy to cause optical breakdown and permanent damage to the optical window mirror of SBS cell if the beam size of the focus spot in the generator cell is too small. Therefore, it is important to select the generator cell with the appropriate physical length.

In the compact double-cell structure, the contour maps of the focal depth and focal spot radius in the generator cell are shown in Figure 2. Physical parameters used for the simulation are as follows. The pump beam quality of M^2 is 2. The radius of the pump beam spot is 4 mm, and the distance from the waist position of the pump beam to the lens of L4 is 50 cm. The physical length of the amplifier cell is 100 cm, and the distance between the lens L5 and the window mirror of generator cell is 5 cm. The refractive index of SBS liquid medium is 1.28. The optical wavelength is 1,064 nm.

According to ABCD matrix theory, the variations of focal depth and focal spot radius with the focal lengths of lens L4 and L5 can be calculated as shown in Figure 2 f_4 and f_5 represent the focal lengths of lens L4 and L5, respectively. It can be seen from Figure 2A that, within the range of focal length f_4 of lens L4 less than 200 cm, the focal depth within the generator cell is jointly affected by the focal lengths of lens L4 and L5. When focal length of lens L4 is greater than 200 cm, the focal depth of the generator cell is more sensitive to the focal length of lens L5. In Figure 2B, the focal spot size varies greatly with the focal length of lens L5, and it is not sensitive to the focal length of lens L4. When the focal length of lens L5 is fixed, the focal depth and the focal spot size gradually become stable with the increase of the focal length of lens L4. According to the theoretical calculation, a generator cell with a physical length of 80 cm is required when the focal length f_5 of the lens L5 is 50 cm, and a generator cell with a physical length of 20 cm is required when the focal length f_5 of lens L5 is 15/20 cm.

4 Experimental results and discussion

To optimize the output parameters of SBS pulse compression and obtain the optimization rules, the experiments for setup A and setup B are respectively studied. A comparison of the output parameters under different focal lengths of lens L3 and SBS media is shown in Figure 3 using setup A. The experimental results show that the energy extraction efficiency improves and the compressed pulse width becomes narrow with an increase of the input energy. In this experiment, the focal length of lens L3 is 20 cm or 50 cm, respectively. Figure 3A shows the reflected energy efficiency under different focal lengths of lens L3 and media. The average energy efficiencies are 74.8%, 68.5%, and 77.1% for the cases of L3 lens of 50 cm with FC40 medium, 50 cm with HT110, and 20 cm with HT110, respectively, at the pump energy of 70 mJ. Comparing the cases of lens L3 with focal lengths of 20 cm and 50 cm in HT110 medium, the reflected energy efficiency of the shorter focusing lens of 20 cm is obviously greater than that of the focusing lens of 50 cm. This is because as the focal length of lens L3 increases, the focal spot size in the generator cell also increases, which causes the decrease of the pump power density at the generation position of the Stokes seed beam under the same pumping conditions, thus leading to the reduction of the energy reflectivity. For the setup A with a focal length of 50 cm and HT110 medium, the reflected energy efficiency enters the saturation region when the injected energy is 30 mJ, which is not conducive to further improvement of the reflected energy. The corresponding compressed pulse width using HT110 is shown in Figure 3B, with the increase of injected energy, the SBS compressed pulse width gradually narrows and finally enters the saturation region. The minimum pulse widths are 649 ps ± 14 ps at the pump energy of 50 mJ and 654 ps ± 9 ps at 70 mJ for the lens focal lengths of 50 cm and 20 cm, respectively. With the focal length of L3 lens increasing, the compressed pulse width becomes narrower as the injection energy and enters the saturation region at the lower pump energy. The longer focal length of the focusing lens, the lager the focal depth within the generator cell, which indicates that the longer interaction length

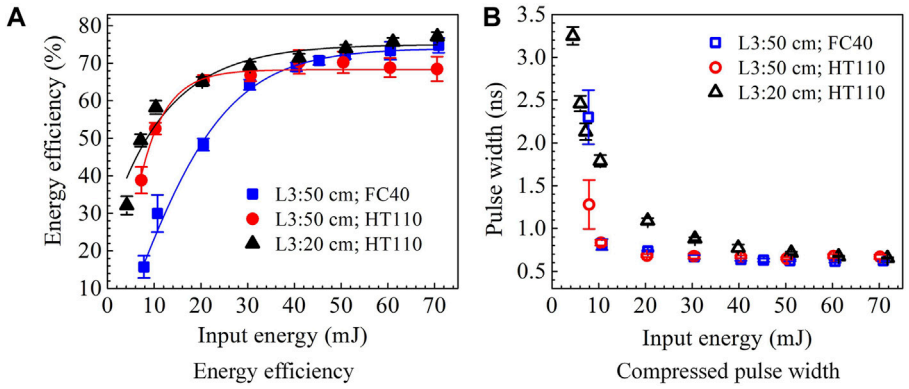

FIGURE 3
Output parameters with different focal lengths of lens L3 and media for setup A.

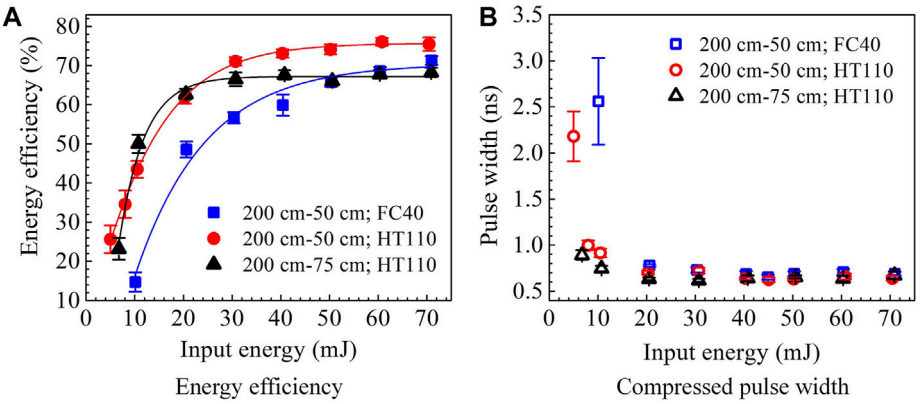

FIGURE 4
Output parameters with different focal lengths of lens and media for setup B.

between the pump beam and Stokes beam is easier to obtain the narrow compressed pulse width. According to the experimental results, the pump power density and interaction length both affect the energy efficiency and compressed pulse width. Setup A with short focusing lenses is easy to obtain a high reflection energy, while with long focusing lenses is easy to obtain narrow compressed pulse width.

With the focusing lens L3 of 50 cm, compared with the medium of FC40 and HT110 in Figure 3A, the energy efficiency obtained by the two media is the same at the pump energy of 40 mJ. When the injected energy is less than 40 mJ, the reflected energy efficiency with HT110 is higher than that of FC40 medium. When the injected energy is greater than 40 mJ, the reflected energy used FC40 medium is greater than that of HT110. The experimental results show that it is easy to obtain a high energy efficiency in the case of a medium with a high gain coefficient. So the energy efficiency with HT110 medium is higher than that of FC40 at a low injection pump power. With the increase of injection pump power, the energy efficiency for HT110 with a high gain coefficient enters the gain saturation region earlier than the case for FC40 with a low gain coefficient, then the energy efficiency of FC40 is higher than that of the medium HT110. The relationship between the compressed pulse width and the injected energy for different media is shown in Figure 3B. At low injection energy, the compressed pulse width using HT110 medium is slightly narrower than that of FC40, this is because the medium with a high gain coefficient can effectively amplify the front part of the Stokes pulse. With the increase of injection energy, the compressed pulse width using FC40 medium is narrower than that of HT110, which is because during the amplification process of the Stokes pulse, the front part and back part are both amplified resulting in the broadening of the compresses pulse. Under the injection energy of 70 mJ, the average pulse widths measured in FC40 and HT110 media are 620 ps ± 12 ps and 660 ps ± 26 ps, respectively. For compact double-cell setup A, it is easy to obtain narrow pulses for the medium FC40 with a short phonon lifetime.

In setup B, the focal length of lens L4 is 200 cm, and it is 50 cm or 75 cm for the lens L5, respectively. The SBS output parameters under different lenses and media employing setup B are shown in Figure 4. Figure 4A illustrates the reflected energy efficiency under different lens focal lengths and media. The average energy efficiencies are 71.3%, 75.5%, and 68.3% for the cases of lens group of 200–50 cm with FC40 medium, 200–50 cm with HT110, and 200–75 cm with HT110, respectively, at the pump energy of 70 mJ. Comparing the cases of lens

L5 with focal lengths of 50 cm and 75 cm in HT110 medium, the reflected energy efficiency with a short focusing lens of 50 cm is larger than that of the focusing lens of 75 cm. For the case with lens focal length of 75 cm, the reflected energy efficiency enters the saturation region when the injected energy is 30 mJ, which is not conducive to further improvement of the reflected energy. The corresponding compressed pulse widths are shown in Figure 4B. The minimum pulse widths are 626 ps ± 27 ps ns at the pump energy of 45 mJ and 619 ps ± 16 ps at 60 mJ for the lens focal lengths of 50 cm and 75 cm, respectively, and the pulse width compression ratio is up to 16 times. With the increase of injected energy, the SBS compressed pulse width gradually narrows and finally enters the gain saturation region. In the case of 75 cm, the pulse width become widening when the injected energy exceeds 30 mJ.

With the focusing lens L5 of 50 cm, compared with the medium of FC40 and HT110 in Figure 4A, the reflected energy used HT110 medium is much higher than that of FC40 medium at the same pump energy. The relationship between the compressed pulse width and the injected energy under different media is shown in Figure 4B. Under the injection energy of 45 mJ, the average pulse widths measured in FC40 and HT110 media are 653 ps ± 25 ps and 626 ps ± 27 ps, respectively. The compressed pulse width of HT110 medium is slightly narrower than that of FC40. This is because the medium with a high gain coefficient can effectively amplify the front part of Stokes pulse. Therefore, in compact double-cell setup B, it is easy to obtain a high energy efficiency and narrow pulse width for the medium HT110 with a large gain coefficient.

5 Conclusion

In this study, experiments in the compact double-cell structure are conducted to optimize the output parameters of SBS pulse compression. Firstly, the focal depth and focal spot size in the compact double-cell structure are calculated, which provides theoretical guidance for the structural parameter design such as lens focal length and SBS cell size. Then, the influence of the lens and medium parameters on output parameters of SBS pulse compression is experimentally studied for setup A and setup B, respectively. For setup A, it is easy to obtain a high reflection energy efficiency with a short focal length lens, while easy to obtain a narrow compressed pulse width with a long focal length lens. As the focal length of focusing lens increases, the injection energy at which the compressed pulse width enters the saturation region becomes small, and the compressed pulse width is narrower. The experimental results show that it is easy to obtain a high energy efficiency in the case of a medium with a large gain coefficient. With the increase of injection pump power, the energy efficiency for HT110 with a high gain coefficient enters the gain saturation region earlier than the case for FC40 with a low gain coefficient. For compact double-cell setup A, it is easy to obtain narrow pulses for the medium FC40 with a short phonon lifetime. However, in compact double-cell setup B, it is easy to obtain a high energy efficiency and narrow pulse width for the medium HT110 with a large gain coefficient. The pulse width compression ratio is up to 16 times after optimization. These experimental results can provide output optimization guidance for the experimental design of SBS pulse compression in high-energy laser systems.

Data availability statement

The original contributions presented in the study are included in the article/supplementary material, further inquiries can be directed to the corresponding author.

Author contributions

HW conducted the experiment and wrote the manuscript, SS did the simulation, and GW checked the writing.

Funding

National Natural Science Foundation of China (62105303); Fundamental Research program of Shanxi Province (20210302124026); Shanxi Scholarship Council of China (2020-102); Scientific and Technological Innovation Programs in Shanxi (2020L0265); 2021 China-Korea Young Scientist Exchange Program.

Conflict of interest

The authors declare that the research was conducted in the absence of any commercial or financial relationships that could be construed as a potential conflict of interest.

Publisher's note

All claims expressed in this article are solely those of the authors and do not necessarily represent those of their affiliated organizations, or those of the publisher, the editors and the reviewers. Any product that may be evaluated in this article, or claim that may be made by its manufacturer, is not guaranteed or endorsed by the publisher.

References

1. Zhang F, Cai HB, Zhou WM, Dai ZS, Shan LQ, Xu H, et al. Enhanced energy coupling for indirect-drive fast-ignition fusion targets. *Nat Phys* (2020) 16(7):810–4. doi:10.1038/s41567-020-0878-9

2. Quinn MN, Jukna V, Ebisuzaki T, Dicaire I, Soulard R, Summerer L, et al. Space-based application of the CAN laser to LIDAR and orbital debris remediation. *Eur Phys Journal-Special Top* (2015) 224(13):2645–55. doi:10.1140/epjst/e2015-02577-5

3. Li HW, Zhao B, Jin LW, Wang DM, Gao W. Flat gain over arbitrary orbital angular momentum modes in Brillouin amplification. *Photon Res* (2019) 7(7):748–53. doi:10.1364/Prj.7.000748

4. Baumler W, Weiss KT. Laser assisted tattoo removal - state of the art and new developments. *Photochem Photobiol Sci* (2019) 18(2):349–58. doi:10.1039/c8pp00416a

5. Zhang X, Dai J, He T, Zhao C, Huang J, Li X, et al. Overview of the Chinese lidar satellite development. In: *LIDAR imaging detection and target recognition 2017*. Washington, United States: International Society for Optics and Photonics (2017). doi:10.1117/12.2296275

6. Gowers CW, Brown BW, Fajemirokun H, Nielsen P, Nizienko Y, Schunke B. Recent developments in LIDAR Thomson scattering measurements on JET (invited). *Rev Scientific Instr* (1995) 66(1):471–5. doi:10.1063/1.1146321

7. Wang H, Cha S, Kong HJ, Wang Y, Lu Z. Minimizing cross sectional pulse width difference between central and edge parts of SBS compressed beam. *Opt Express* (2019) 27(2):1646–59. doi:10.1364/OE.27.001646

8. Cao C, Wang Y, Bai Z, Li Y, Yu Y, Lu Z. Developments of picosecond lasers based on stimulated Brillouin scattering pulse compression. *Front Phys* (2021) 9:524. doi:10.3389/fphy.2021.747272

9. Kang Z, Fan Z, Huang Y, Zhang H, Ge W, Li M, et al. High-repetition-rate, high-pulse-energy, and high-beam-quality laser system using an ultraclean closed-type SBS-PCM. *Opt Express* (2018) 26(6):6560–71. doi:10.1364/OE.26.006560

10. Bai ZX, Yuan H, Liu ZH, Xu PB, Gao QL, Williams RJ, et al. Stimulated Brillouin scattering materials, experimental design and applications: A review. *Opt Mater* (2018) 75:626–45. doi:10.1016/j.optmat.2017.10.035

11. Yoshida H, Hatae T, Fujita H, Nakatsuka M, Kitamura S. A high-energy 160-ps pulse generation by stimulated Brillouin scattering from heavy fluorocarbon liquid at 1064 nm wavelength. *Opt Express* (2009) 17(16):13654–62. doi:10.1364/oe.17.013654

12. Feng C, Xu X, Diels JC. High-energy sub-phonon lifetime pulse compression by stimulated Brillouin scattering in liquids. *Opt Express* (2017) 25(11):12421–34. doi:10.1364/OE.25.012421

13. Shin JS, Kong HJ. Phase fluctuation of self-phase-controlled stimulated Brillouin scattering waves via K8 glass. *Opt Commun* (2012) 285(13-14):2977–9. doi:10.1016/j.optcom.2012.02.055

14. Zhang A, Qiao S, Sheng L, Huang L, Liu Z, Ju J, et al. Study on external cavity diode laser with a wide mode-hopping free tuning range. *Front Phys* (2022) 10:1093179. doi:10.3389/fphy.2022.1093179

15. Xu X, Feng C, Diels JC. Optimizing sub-ns pulse compression for high energy application. *Opt Express* (2014) 22(11):13904–15. doi:10.1364/OE.22.013904

16. Guo X, Hasi W, Zhong Z, Jin C, Lin D, He W, et al. Research on the SBS mediums used in high peak power laser system and their selection principle. *Laser Part Beams* (2012) 30(4):525–30. doi:10.1017/S0263034612000390

17. Park H, Lim C, Yoshida H, Nakatsuka M. Measurement of stimulated Brillouin scattering characteristics in heavy fluorocarbon liquids and perfluoropolyether liquids. *Jpn J Appl Phys Part 1-Regular Pap Brief Commun Rev Pap* (2006) 45(6A):5073–5. doi:10.1143/Jjap.45.5073

18. Hasi W, Zhao H, Lin DY, He WM, Lu ZW. Characteristics of perfluorinated amine media for stimulated Brillouin scattering in hundreds of picoseconds pulse compression at 532 nm. *Chin Opt Lett* (2015) 13(6):061901–5. doi:10.3788/col201513.061901

frontiers | Frontiers in Physics

TYPE Brief Research Report
PUBLISHED 22 March 2023
DOI 10.3389/fphy.2023.1163555

OPEN ACCESS

EDITED BY
Zhenxu Bai,
Hebei University of Technology, China

REVIEWED BY
Yonghong Wang,
Hefei University of Technology, China
Lei Wang,
Harbin Institute of Technology, China

*CORRESPONDENCE
Aili Wang,
ailli925@hrbust.edu.cn

SPECIALTY SECTION
This article was submitted to Optics and Photonics,
a section of the journal
Frontiers in Physics

RECEIVED 10 February 2023
ACCEPTED 03 March 2023
PUBLISHED 22 March 2023

CITATION
Wu H, Li M and Wang A (2023), A novel meta-learning-based hyperspectral image classification algorithm.
Front. Phys. 11:1163555.
doi: 10.3389/fphy.2023.1163555

A novel meta-learning-based hyperspectral image classification algorithm

Haibin Wu, Meixin Li and Aili Wang*

Heilongjiang Province Key Laboratory of Laser Spectroscopy Technology and Application, Harbin University of Science and Technology, Harbin, China

Aimed at the hyperspectral image (HSI) classification under the condition of limited samples, this paper designs a joint spectral–spatial classification network based on metric meta-learning. First, in order to fully extract HSI fine features, the squeeze and excitation (SE) attention mechanism is introduced into the spectrum dimensional channel to selectively extract useful HSI features to improve the sensitivity of the network to information features. Second, in the part of spatial feature extraction, the VGG16 model parameters trained in advance on the HSRS-SC dataset are used to realize the transfer and learning of spatial feature knowledge, and then, the higher-level abstract features are extracted to mine the intrinsic attributes of ground objects. Finally, the gated feature fusion strategy is introduced to connect the extracted spectral and spatial feature information on HSI for mining more abundant feature information. In this paper, a large number of experiments are carried out on the public hyperspectral dataset, including Pavia University and Salinas. The results show that the meta-learning method can achieve fast learning of new categories with only a small number of labeled samples and has good generalization ability for different HSI datasets.

KEYWORDS

hyperspectral image, meta-learning, limited samples, transfer learning, attention mechanism

1 Introduction

Hyperspectral image (HSI) refers to a spectral image with a spectral resolution in the range of nanometers, and its rich spectral information can be obtained while obtaining spatial information on ground objects [1]. The unique advantage of hyperspectral imagery is that it can not only obtain multi-channel spectral information on ground objects but also complex spatial information on different types of ground objects, and its spatial spectrum fusion features can effectively distinguish ground objects [2].

HSI classification methods based on deep learning can automatically extract spectral features, spatial features, or spectral–spatial features. Chen et al. [3] proposed a stacked autoencoder (SAE) to extract joint spectral–spatial features for HSI classification. Li et al. [4] utilized deep belief networks (DBNs) to extract spectral–spatial features and achieved better classification performance than SVM-based methods. Makantasis et al. [5] introduced 2D-CNN to HSI classification and obtained satisfactory performance by using CNN to encode spectral–spatial information and using multi-layer perceptron. Chen et al. [6] used 3-D CNN to simultaneously extract spectral–spatial features of HSI and achieved better classification results. Nevertheless, training very deep CNNs is still somewhat difficult due to the information loss produced by the vanishing gradient problem. To solve this problem, Wang et al. [7] introduced ResNet into HSI

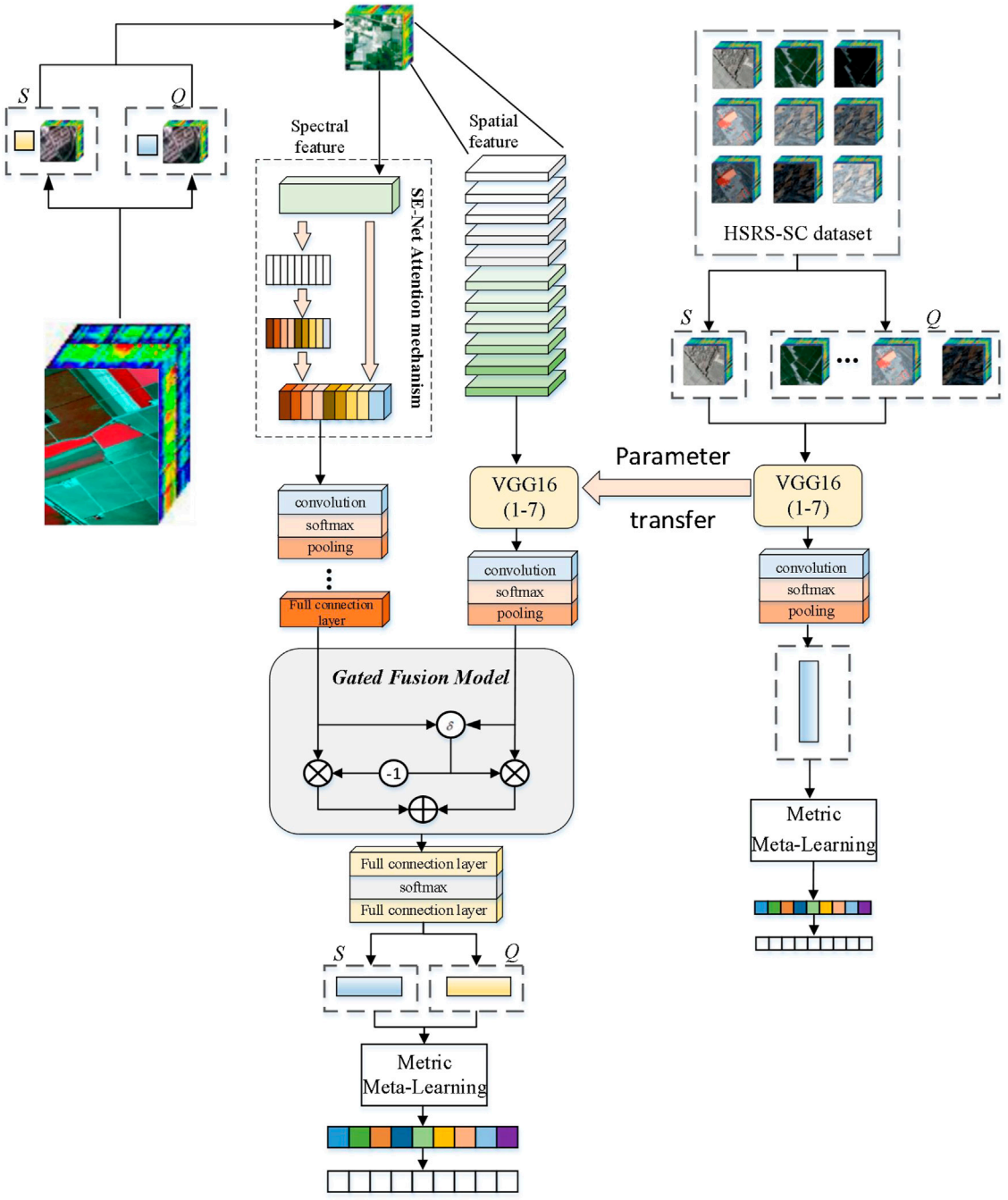

FIGURE 1
Joint spectral–spatial classification network based on the metric meta-learning model.

classification. Zhong et al. [8] designed a spectral–spatial residual network (SSRN) to identify HSI spectral properties and spatial context using spectral and spatial residual blocks and achieved state-of-the-art HSI classification accuracy. Furthermore, Paoletti proposed deep pyramidal residual networks (PyResNet) [9] to learn more robust spectral–spatial representations from HSI cubes and provide competitive advantages over state-of-the-art HSI classification methods in both classification accuracy and computation time aspect.

Hyperspectral image classification based on deep learning has achieved great success, but deep learning methods require a large number of labeled training samples, and the acquisition of labeled samples is very difficult, requiring great manpower, material, and financial resources. In practical classification applications, new scene images often have very few labeled samples, but other scene images often have enough labeled samples. Meta-learning is an effective method to achieve few-sample classifications. The learned meta-knowledge can help predict the target domain data and solve the

problem of hyperspectral image classification when there are only a few labeled samples for each class. Meta-learning is proposed to solve the problem of the insufficient generalization performance of traditional neural network models and the adaptability of new types of tasks. As early as the beginning of the 21st century, Hochreiter et al. verified that neural networks with memory modules could be used to deal with the proposition of meta-learning problems [10]. Such networks cache information efficiently and accurately through learning and then input it into the memory module to complete the conversion of the output. Subsequently, Munkhdalai et al. proposed a meta-network that applied the idea of meta-learning to the memory network to solve the problem of small-sample learning [11]. This network extracts task-independent meta-level knowledge to achieve rapid parameterization of common tasks. The matching network model proposed by O. Vinyals et al. [12] is the earliest method of combining metric learning with meta-learning. Subsequently, Snell et al. proposed prototypical networks by further improving and optimizing the matching network [13]. The prototype network uses simple ideas to effectively reduce the number of parameters, simplify the training process, and achieve good classification results. C. Finn et al. proposed a model-independent meta-learning algorithm named model-agnostic meta-learning (MAML) [14], which can be seen as a meta-learning tool for training basic meta-learners. Andrei A. Rusu et al. [15] proposed a meta-learning idea by optimizing hidden layer embedding on the basis of MAML, constructing a hidden space in which the parameters can complete its inner loop update, which effectively adapts the behavior of the model.

The contributions of the proposed method are as follows:

1. According to the few training samples and scarce labeled samples of HSI, this paper proposes a joint transfer classification framework based on the metric meta-learning method.
2. In order to mine the spatial–spectral features of HSI, this paper proposes a novel spatial–spectral feature extraction module. Moreover, the squeeze and excitation (SE) attention mechanism is introduced into the spectral dimension channel in the spatial–spectral feature migration network module to capture global information, selectively extract useful HSI features, reduce the influence of useless information, and increase the attention of important features.
3. The gated feature fusion strategy is introduced, the feature information on spectral–spatial HSI is utilized, and the method of recursive merging is adopted to gradually fuse the images, thereby enhancing the ability of the network to adapt to the characteristics of HSI. Through gated fusion, the network can select a reasonable combination scheme for each pixel, enhance the appropriate features and suppress the inappropriate features, and extract more abundant HSI feature information.

2 Materials and methods

Figure 1 shows the overall block diagram of the spectral–spatial joint transfer classification network based on the metric meta-learning of HSI.

First, the hyperspectral dataset is divided into many different metatasks. Each task contains a small number of labeled samples (the support set) and unlabeled samples (the query set). Then, the support set and query set samples are simultaneously sent to the spectral–spatial joint transfer network module constructed to extract the spatial and spectral embedded features. The parameters in the spatial features are initialized by the network parameters trained on the HSRS-SC dataset to realize the transfer learning of spatial feature knowledge, which provides a new idea for hyperspectral image classification when training samples are insufficient. Then, the extracted spatial and spectral features are fused to gain more knowledge about general HSI features. Finally, the fused spectral–spatial features are sent into the metric meta-learning classification module and feature information is mapped into an embedding space by making full use of the metric space in the prior knowledge so that the model can achieve the effect of quickly and efficiently classifying the image categories.

2.1 Spatial–spectral feature extraction module combined with transfer learning

This section starts from the perspective of joint spatial–spectral features and aims at optimizing feature extraction and proposes a spatial–spectral joint transfer network. For HSI classification, spectral feature extraction exclusively leads to difficult interpretation of high-level semantic information on features of HSI scenes. It is shown that modeling through the synergy of spatial and spectral information can combine the spectral and spatial advantages of images to better reveal the proprieties of HSI. The two branches of the network extract spatial features and spectral features of HSI, respectively, and a channel attention mechanism is applied after extracting spectral features. This mechanism can strengthen the extracted features and make them more discriminative, thus improving the classification effect of HSI. After the spatial features and spectral features are extracted, the two features are combined by the gated fusion method. The gated fusion method can selectively fuse the spatial–spectral features for the classification of different positions, according to the feature appearance of the input image.

2.1.1 Spectral feature extraction combined with SE attention mechanisms

For the spectral feature extraction model, the network is configured with one 1-D convolutional layer, one spectral residual block, one 1-D convolutional layer, and one FC layer. SE-Net adds attention mechanisms to channels, including two key operations: squeeze and incentive. It can be observed that the module obtains the best weight value through autonomous learning, which is generally implemented by the neural network. A feature recalibration mechanism based on the network model is proposed, which enables the model to find some small amount of information that needs to be focused on in a large amount of data, thus avoiding a waste of computing power on unimportant information.

The input X of any size is first given, then the input is mapped by F_{tr}, resulting in its special transformation into a feature map U ($U \in \mathrm{R}^{H\times W\times C}$). The convolutional neural network is then used to construct a corresponding SE block, which is used to re-calibrate the features. The calibration step is to generate an embedded global

TABLE 1 Classification results of different methods on the Pavia University dataset.

Class	EMP-SVM	DCNN	ResNet	RLNet	DCFSL	HFSL	Ours
Asphalt	80.24 ± 2.45	79.38 ± 3.08	76.59 ± 0.58	84.03 ± 1.89	85.25 ± 2.55	86.47 ± 0.83	87.06 ± 3.47
Meadows	79.25 ± 0.76	83.42 ± 1.47	82.98 ± 1.49	76.96 ± 3.55	90.64 ± 0.84	89.33 ± 0.56	90.90 ± 0.85
Gravel	63.59 ± 2.07	72.18 ± 0.86	75.36 ± 3.67	80.13 ± 2.76	82.09 ± 1.62	84.81 ± 1.94	87.58 ± 1.06
Trees	78.67 ± 1.89	80.03 ± 2.43	85.52 ± 0.44	87.34 ± 0.81	88.84 ± 3.91	89.45 ± 2.85	90.70 ± 2.19
Metal sheets	76.41 ± 0.95	77.26 ± 4.16	82.71 ± 0.83	85.03 ± 1.43	91.70 ± 4.27	93.93 ± 3.06	93.57 ± 3.54
Bare soil	72.72 ± 2.44	87.84 ± 3.81	89.92 ± 4.75	91.06 ± 0.72	88.28 ± 1.66	89.49 ± 2.07	91.36 ± 4.82
Bitumen	76.06 ± 0.58	78.61 ± 0.84	75.34 ± 1.40	78.68 ± 3.53	87.12 ± 3.82	90.41 ± 3.82	92.71 ± 1.53
Bricks	78.52 ± 3.06	74.86 ± 2.59	73.57 ± 3.61	74.65 ± 2.86	83.51 ± 2.77	86.24 ± 0.91	87.03 ± 2.06
Shadows	86.43 ± 1.54	87.66 ± 1.06	88.67 ± 2.84	90.64 ± 4.39	92.79 ± 0.93	94.81 ± 1.64	96.54 ± 0.31
OA/%	77.89 ± 0.75	79.84 ± 2.14	80.85 ± 3.72	82.97 ± 1.68	85.02 ± 2.51	86.15 ± 3.19	89.26 ± 1.95
AA/%	75.76 ± 1.63	80.32 ± 1.86	81.49 ± 1.95	83.41 ± 2.11	84.47 ± 0.83	85.88 ± 2.83	88.75 ± 3.08
100 K	70.09 ± 3.71	72.56 ± 0.92	73.24 ± 0.86	75.91 ± 3.54	79.04 ± 1.69	80.73 ± 1.52	82.51 ± 0.76

TABLE 2 Classification results of different methods on the Salinas dataset.

Class	EMP-SVM	DCNN	ResNet	RLNet	DCFSL	HFSL	Ours
Bg_weeds_1	77.57 ± 1.56	85.29 ± 0.16	86.85 ± 0.05	87.63 ± 0.22	89.47 ± 3.25	91.40 ± 2.12	92.49 ± 0.09
Bg_weeds_2	82.43 ± 0.85	88.20 ± 2.03	89.97 ± 2.20	91.09 ± 1.14	92.47 ± 0.85	93.76 ± 3.14	95.41 ± 2.54
Fallow	86.95 ± 2.12	89.45 ± 2.28	88.47 ± 3.48	89.01 ± 2.21	91.05 ± 1.94	92.86 ± 0.82	94.94 ± 0.51
Fr_plow	82.11 ± 0.22	84.31 ± 3.05	86.52 ± 1.80	88.54 ± 2.05	93.75 ± 2.29	94.55 ± 0.08	95.97 ± 1.15
Fallow_smooth	80.29 ± 0.23	82.24 ± 2.19	84.20 ± 0.43	85.98 ± 0.55	86.45 ± 0.61	88.70 ± 0.74	89.85 ± 3.24
Stubble	85.36 ± 0.45	88.85 ± 1.06	87.28 ± 2.22	89.47 ± 2.29	91.73 ± 2.74	92.52 ± 0.25	94.62 ± 1.07
Celery	84.39 ± 0.13	86.69 ± 2.01	88.98 ± 3.01	90.81 ± 3.64	92.61 ± 1.45	93.88 ± 1.59	94.31 ± 0.46
Grapes_untrained	74.99 ± 0.05	76.40 ± 1.28	78.90 ± 3.74	80.74 ± 0.76	81.11 ± 3.23	82.57 ± 2.49	85.84 ± 0.51
Sv_develop	86.09 ± 1.87	89.25 ± 3.16	90.64 ± 0.05	91.13 ± 3.09	92.35 ± 0.25	93.59 ± 0.41	94.94 ± 3.08
Cs_green_weeds	85.45 ± 0.37	88.72 ± 0.29	89.01 ± 1.64	90.98 ± 1.85	91.53 ± 0.19	92.42 ± 1.54	94.51 ± 2.94
Lr_4wk	81.25 ± 0.29	84.15 ± 1.57	86.86 ± 0.47	85.99 ± 0.19	87.03 ± 3.09	88.61 ± 3.61	89.63 ± 1.46
Lr_5wk	77.22 ± 0.07	79.65 ± 0.32	80.67 ± 1.23	81.13 ± 0.43	83.15 ± 2.54	85.93 ± 0.37	86.27 ± 2.13
Lr_6wk	77.30 ± 1.08	83.63 ± 0.66	84.04 ± 3.67	86.34 ± 0.51	88.54 ± 0.52	89.30 ± 0.69	89.71 ± 0.88
Lr_7wk	81.84 ± 0.15	84.56 ± 2.09	85.61 ± 0.82	84.06 ± 0.02	86.43 ± 0.68	88.85 ± 0.43	90.29 ± 2.69
Vinyard_untrained	69.52 ± 1.23	71.02 ± 3.01	73.97 ± 3.54	74.54 ± 1.67	75.18 ± 0.28	77.38 ± 1.88	80.53 ± 0.43
Vv_trellis	81.45 ± 0.19	86.41 ± 0.46	89.91 ± 1.28	92.65 ± 2.98	94.39 ± 1.73	95.22 ± 3.66	96.61 ± 0.79
OA (%)	79.85 ± 1.38	84.20 ± 0.38	86.39 ± 2.28	88.67 ± 0.76	90.65 ± 2.38	91.43 ± 0.57	93.96 ± 1.58
AA (%)	85.24 ± 0.42	87.56 ± 1.29	89.01 ± 0.46	90.90 ± 0.60	91.42 ± 0.84	92.59 ± 1.26	94.39 ± 0.76
100 K	78.68 ± 2.54	82.46 ± 0.24	84.95 ± 3.13	85.52 ± 0.93	87.32 ± 3.13	88.84 ± 2.04	89.08 ± 2.93

distribution channel feature response and aggregate the features with a dimension size of $C \times H \times W$ to obtain a feature size of $C \times 1 \times 1$ so that the layer closest to the input layer can obtain the global receptive field. After the squeeze operation, an excitation operation is performed, which is to re-input the new feature and aggregate a new weight generated by each channel, which will be mapped to U again to obtain the final output $\tilde{X}$ combined with the weight.

2.1.2 Spatial feature extraction network combined with transfer learning

As shown in Figure 1, the three parts of spectral feature extraction, spatial feature extraction, and spectral–spatial feature extraction constitute the joint spatial–spectral feature extraction network. However, a meta-learning training strategy is used to learn the embedding feature space suitable for the HSRS-SC dataset. The pre-trained VGGNet's first seven-layer structure and parameters are used to train the data on the target domain, and the parameters are transferred to the feature extraction model of the HSRS-SC dataset. Then, a CNN with 2D convolution, 2D max-pooling, and FC layers is designed to extract spatial features. The 2D convolution layer is followed by the BN layer, ReLU activation function, and maximum pooling. A batch normalization (BN) layer is added after the 2D convolutional layer to solve gradient disappearance and improve the generalization ability of the model. The activation function is added after the normalization layer. Finally, an FC layer is added to generate spatial feature vectors.

After the spatial features and spectral features are extracted, the two features are combined by the gated fusion method, which can selectively fuse the spectral–spatial features for the classification of different positions according to the feature appearance of the input image. Through gated fusion, the network can select a reasonable combination scheme for each pixel, enhance suitable features and suppress inappropriate features, and extract richer HSI feature information.

2.2 Metric meta-learning classification module

As shown in Figure 1, the obtained spectral–spatial feature vector used to be classified by comparing the distance of labeled samples and unlabeled samples based on metric element learning. The method in this paper is an improvement on the classic algorithm of metric-based meta-learning. The estimated metric function minimizes the difference between similar tasks, which maximizes the distance between dissimilar tasks and improves the efficiency of task processing. The known support samples x_j and query samples x_i generate the eigenvector sums of two sets of $E_\varphi(x_i)$ and $E_\varphi(x_j)$ through the spectral–spatial transfer network module, and then generate eigenvectors through splicing operation $C(*,*)$. The distance between samples can be used to obtain sample attributes Con_i^j without using all the features of samples, which can make more effective use of HSI features and reduce the model's dependence on training samples.

$$\mathrm{Con}_i^j = C\left(E_\varphi(x_i), E_\varphi\left(x_j\right)\right). \tag{1}$$

M_ϕ is a neural network consisting of three regular convolutional layers. The first two convolution layers, with the size of $1 \times 1 \times 64$, are followed by the Leaky-ReLU activation function for non-linear mapping. The sigmoid activation function is then used to output the similarity between samples, then the output feature vector is mapped to M_ϕ and convolved by a convolutional layer. By analyzing the similarity between samples to obtain class x_j, feature vectors and relationship scores $m_{i,j}$ are generated xj.

In order to determine the label of the query sample, the feature mapping of each combination is input into M_ϕ to generate a similarity, which is defined to indicate the similarity between any two embedded samples. The value of the output $m_{i,j}$ is a range of $[0,1]$, in which the samples with high similarity scores are considered to be more similar.

$$m_{i,j} = M_\phi\left(C\left(E_\varphi(x_i), E_\varphi\left(x_j\right)\right)\right). \tag{2}$$

The comparison measurement model uses the mean squared error (MSE) loss function to calculate the relationship score and conduct training. When the training samples belong to the same category, the loss value is 1; otherwise, it is 0. The loss function is shown as follows: $(m_{i,j} - 1(y_i == y_j))^2$

$$\phi, \varphi \leftarrow \arg\min_{\phi,\varphi} \sum_{x_i}. \tag{3}$$

3 Results

In order to prove the effectiveness of this method, classification experiments are carried out on public datasets, namely, Pavia University and Salinas datasets, and the transfer learning dataset selects the HSRS-SC dataset. All experiments were conducted using the Intel (R) Xeon (R) 4208 CPU @ 2.10 GHz processor and Nvidia GeForce RTX 2080Ti graphics card. The number of training iterations is set to 1,000. For each training iteration, K is set to 1 and N is set to 19, which is the number of categories in the HSI dataset; that is, 1 labeled sample and 19 unlabeled samples were selected randomly to form a training set for model training. In addition, the model in this paper is optimized using Adam, and the learning rate is set to 0.001.

3.1 Comparison with state-of-the-art methods

In order to evaluate the effectiveness of the meta-learning method, this paper compares the meta-learning method with deep learning and few-shot supervised learning methods including extended morphological profile support vector machine (EMP-SVM) [16], deep convolutional neural network (DCNN) [17], residual network (ResNet) [18], and current few-shot learning methods including relation network (RLNet) [19], deep cross-domain few-shot learning (DCFSL) [20], and heterogeneous few-shot learning (HFSL) [21]. In order to ensure the fairness of the experiment, this paper randomly selects five labeled samples in each type of HSI dataset as the supervised samples. All experiments were performed 10 times to remove the effect of random sampling. Tables 1, 2 show the accuracy values of OA, AA, and kappa of Pavia University and Salinas datasets.

From Tables 1, 2, it can be seen that the proposed method in this paper achieves almost the highest classification accuracy in each class. In particular, it improves the classification accuracy more for classes with lower heights, such as the asphalt road class and the grass class in the Pavia University dataset. As shown in Table 1, the OA value of the Pavia University dataset is as high as 82.96%, and compared with EMP-SVM, DCNN, ResNet, RLNet, DCFSL, and HFSL, it has increased by 11.37%, 9.42%, 8.41%, 6.29%, 4.24%, and 3.11%, respectively. These results demonstrate the superiority of meta-learning methods in HSI

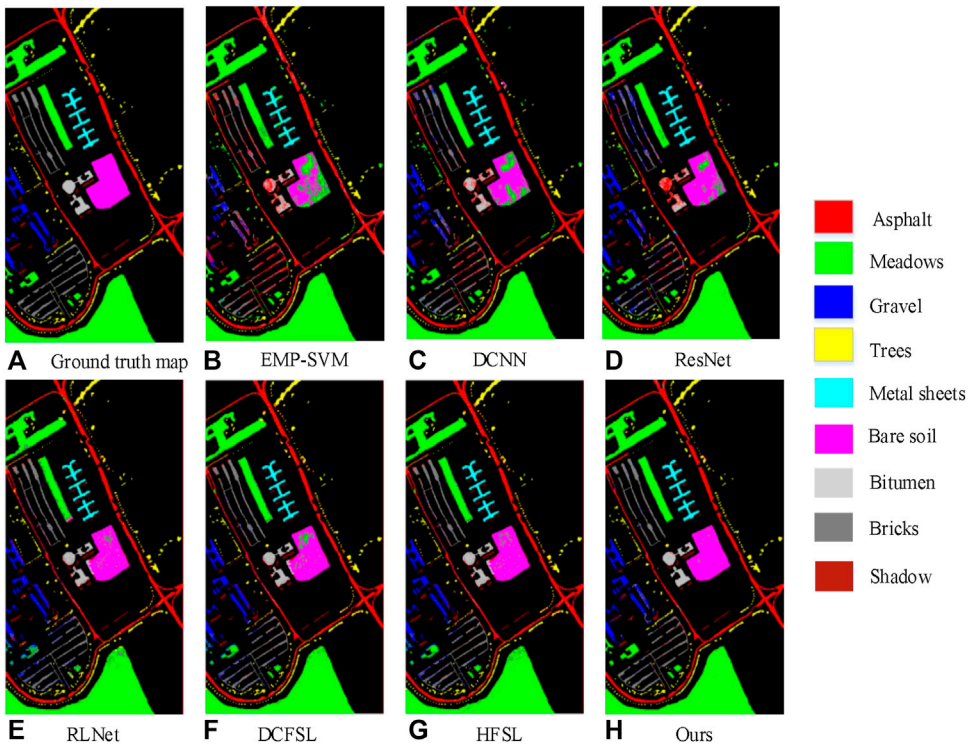

FIGURE 2
Classification maps of the Pavia University dataset. **(A)** ground truth; **(B)** EMP-SVM; **(C)** DCNN; **(D)** ResNet; **(E)** RLNet; **(F)** DCFSL; **(G)** HFSL; **(H)** Ours.

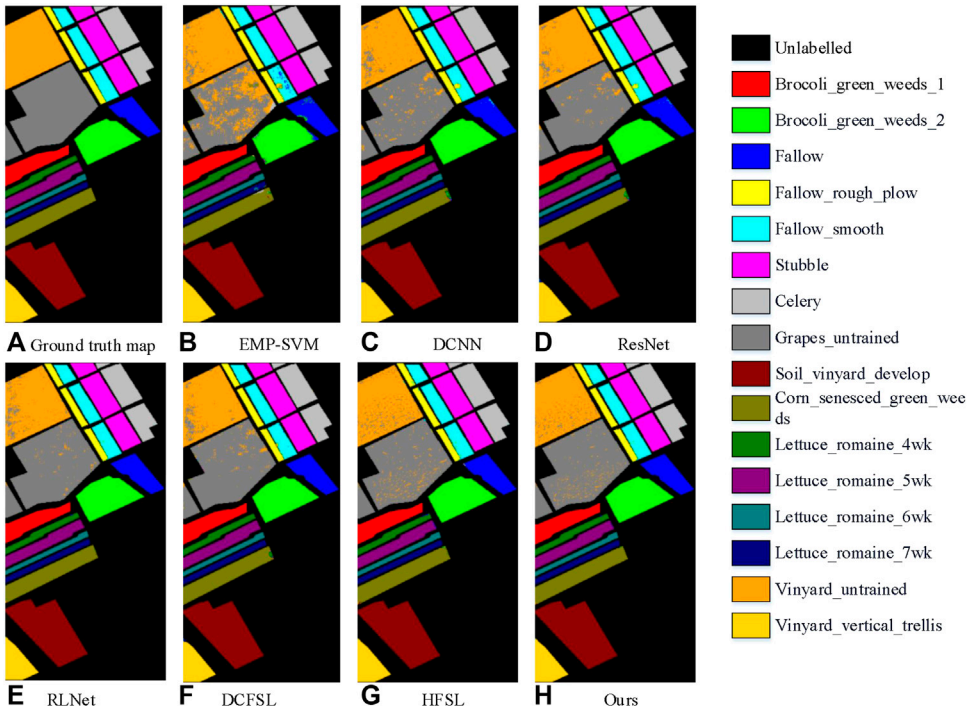

FIGURE 3
Classification maps of the Salinas dataset. **(A)** ground truth; **(B)** EMP-SVM; **(C)** DCNN; **(D)** ResNet; **(E)** RLNet; **(F)** DCFSL; **(G)** HFSL; **(H)** Ours.

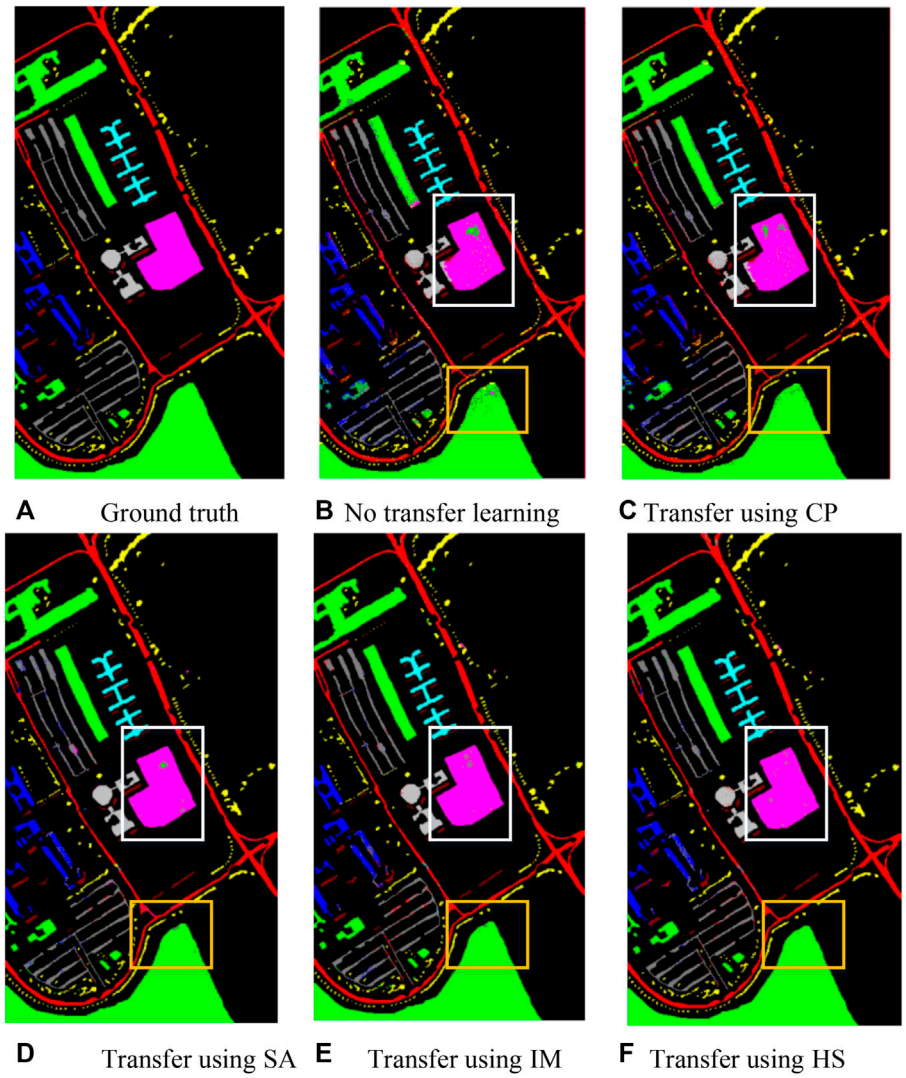

FIGURE 4
Classification visualization result diagram using different transfer datasets. **(A)** Ground truth; **(B)** No transfer learning; **(C)** Transfer using CP; **(D)** Transfer using SA; **(E)** Transfer using IM; **(F)** Transfer using HS.

classification. For categories that other methods cannot accurately classify, such as gravel, bare soil, asphalt, and bricks, the meta-learning method can obtain more accurate classification results, further demonstrating its effectiveness.

Figures 2, 3, respectively, show the HSI ground truth maps and the false color image maps of the classification results. In the small-sample ground objects, the error features such as gravel and bricks have been significantly improved, and it can correct various types of ground objects with a small number of training samples.

In Figure 3, the SVM algorithm only considers the spectral feature, and the misclassification rate for Vinyard_untrained and Grapes_untrained is higher. DCNN and other deep learning algorithms are better than SVM in the classification of Vinyard_untrained and Grapes_untrained, which shows that it has good feature extraction ability in large-scale landforms. On this dataset, the meta-learning algorithm has greatly improved compared with other algorithms, and the classification effect is the best.

4 Discussion

In order to verify the HSI classification framework based on model transfer, the influence of different datasets on the classification results in transfer learning was studied to construct the optimal classification framework. Figure 4 shows the results of classification using different datasets for transfer learning, where CP means the center of Pavia dataset, SA means the Salinas dataset, HS means the HSRS-SC dataset, and IM means the natural image dataset ImageNet. Through the visualization of experimental data, it can be found that the model-based transfer learning method is effective. As shown in Figure 4F, the classification result obtained by using the HSRS-SC as the source dataset is better than the other three types and is closer to the ground truth map in terms of spatial correlation and completeness, especially the soil class. Rich information on source domain data facilitates the learning of pre-trained models. By using the HSRS-SC

dataset to train the model, the obtained model has a stronger feature extraction ability and is able to learn more general features rather than features limited to a specific dataset so that the migration of the pre-trained model to the target domain can better adapt to the new learning task well.

5 Conclusion

In order to improve the classification accuracy of hyperspectral images, this paper designs a spatial–spectral joint transfer classification network based on metric meta-learning. Furthermore, to combine the spectral and spatial superiority of HSI, a joint spatial–spectral transfer learning network module is proposed in this paper, which can extract finer HSI features and capture cross-dimensional and spatial interaction information. The experimental results on two publicly available HSI datasets show that the meta-learning method proposed in this paper is more competitive and outperforms other classical methods and existing few-shot learning methods. In the future, we will study model compression and pruning to reduce the complexity of the proposed model and improve real-time performance without affecting the classification ability.

Data availability statement

The original contributions presented in the study are included in the article/Supplementary Material; further inquiries can be directed to the corresponding author.

Author contributions

All authors listed have made a substantial, direct, and intellectual contribution to the work and approved it for publication.

Funding

This work was funded by the Reserved Leaders of Heilongjiang Provincial Leading Talent Echelon of 2021, the High-end Foreign Expert's Introduction Program (G2022012010L), and the Key Research and Development Program Guidance Project (GZ20220123).

Conflict of interest

The authors declare that the research was conducted in the absence of any commercial or financial relationships that could be construed as a potential conflict of interest.

Publisher's note

References

1. Tong QX, Zhang B, Zhang LF. Current progress of hyperspectral remote sensing in China. *J Remote Sensing* (2016) 20(5):689–707. doi:10.11834/jrs.20166264

2. Julie T, Raphael DA, Alexandre M, Defourny P. Survey of hyperspectral earth observation applications from space in the sentinel-2 context. *Remote Sensing* (2018) 10(3):157. doi:10.3390/rs10020157

3. Chen Y, Lin Z, Zhao X, Wang G, Gu Y. Deep learning-based classification of hyperspectral data. *IEEE J.-STARS* (2014) 7:2094–107. doi:10.1109/jstars.2014.2329330

4. Li T, Zhang J, Zhang Y. Classification of hyperspectral image based on deep belief networks. In: 2014 IEEE International Conference on Image Processing (ICIP); 27-30 October 2014; Paris, France (2014). p. 5132–6. doi:10.1109/ICIP.2014.7026039

5. Makantasis K, Karantzalos K, Doulamis A, Doulamis N. Deep supervised learning for hyperspectral data classification through convolutional neural networks. In: 2015 IEEE International Geoscience and Remote Sensing Symposium (IGARSS); 26-31 July 2015; Milan, Italy (2015). p. 4959–62. doi:10.1109/IGARSS.2015.7326945

6. Chen Y, Jiang H, Li C, Jia X, Ghamisi P. Deep feature extraction and classification of hyperspectral images based on convolutional neural networks. *IEEE Trans. Geosci. Remo. Sen.* (2016) 54:6232–51. doi:10.1109/tgrs.2016.2584107

7. Wang L, Peng J, Sun W. Spatial-spectral squeeze-and-excitation residual network for hyperspectral image classification. *Remote Sens* (2019) 11:884–90. doi:10.3390/rs11070884

8. Zhong Z, Li J, Luo Z, Chapman M. Spectral-spatial residual network for hyperspectral image classification: A 3-d deep learning framework. *IEEE T Geosci Remote* (2017) 56:847–58. doi:10.1109/tgrs.2017.2755542

9. Paoletti ME, Haut JM, Ez-Beltran R, Plaza J, Plaza AJ, Pla F. Deep pyramidal residual networks for spectral-spatial hyperspectral image classification. *IEEE T Geosci Remote* (2018) 57:740–54. doi:10.1109/tgrs.2018.2860125

10. Santoro A, Bartunov S, Botvinick M, Wierstra D, Lillicrap T. One-shot learning with memory-augmented neural networks. In: International Conference on Machine Learning; 19, May 2016; Sydney, Australia (2016).

11. Munkhdalai T, Yu H. Meta networks. In: International Conference on Machine Learning; Sydney, Australia (2017). p. 2554–63.

12. Vinyals O, Blundell C, Lillicrap T, Kavukcuoglu K, Wierstra D, et al. Matching networks for one shot learning. *Adv Neural Inf Process Syst* (2016) 29:3630–8. doi:10.48550/arXiv.1606.04080

13. Snell J, Swersky K, Zemel RS. Prototypical networks for few-shot learning. *Neural Inf Process Syst* (2017) 1703:05175. doi:10.48550/arXiv.1703.05175

14. Finn C, Abbeel P, Levine S. Model-agnostic meta-learning for fast adapt ation of deep networks. In: International Conference on Machine Learning; Sydney, Australia (2017). p. 1126–35.

15. Rusu AA, Rao D, Sygnowski J, Vinyals O, Pascanu R, Osindero S Meta-learning with latent embedding optimization. In: 7th International Conference on Learning Representations; New Orleans, LA, USA (2018). p. 671–83.

16. Gu YF, Liu TZ, Jia XP, Benediktsson JA, Chanussot J. Nonlinear multiple kernel learning with multiple-structure-element extended morphological profiles for hyperspectral image classification. *IEEE Trans Geosci Remote Sensing* (2016) 54(6): 3235–47. doi:10.1109/tgrs.2015.2514161

17. Song W, Li S, Fang L, Lu T Hyperspectral image classification with deep feature fusion network[J]. *IEEE Trans Geosci Remote Sensing* (2018) 56(6):1–12. doi:10.1109/TGRS.2018.2794326

18. Paoletti ME, Haut JM, Plaza J, Plaza A A new deep convolutional neural network for fast hyperspectral image classification[J]. *Isprs J Photogrammetry Remote Sensing* (2017) 145PA(NOV):120–47. doi:10.1016/j.isprsjprs.2017.11.021

19. Deng B, Shi D. Relation network for hyperspectral image classification. In: 2019 IEEE International Conference on Multimedia and Expo Workshops (ICMEW); 08-12 July 2019; Shanghai, China. IEEE (2019).

20. Li Z, Liu M, Chen Y, Xu Y, Li W, Du Q. Deep cross-domain few-shot learning for hyperspectral image classification. *IEEE Trans Geosci Remote Sensing* (2021) 60(99): 1–18. doi:10.1109/tgrs.2021.3057066

21. Wang Y, Liu M, Yang Y, Li Z, Du Q, Chen Y, et al. Heterogeneous few-shot learning for hyperspectral image classification. *IEEE Geosci Remote Sens Lett* (2022) 19: 1–5. doi:10.1109/lgrs.2021.3117577

frontiers | Frontiers in Physics

TYPE Original Research
PUBLISHED 06 April 2023
DOI 10.3389/fphy.2023.1181692

OPEN ACCESS

EDITED BY
Zhenxu Bai,
Hebei University of Technology, China

REVIEWED BY
Andrey Pryamikov,
Prokhorov General Physics Institute (RAS), Russia
Xiaohui Li,
Shaanxi Normal University, China

*CORRESPONDENCE
Wenguang Liu,
lwg.kevin@163.com
Xiaolin Wang,
chinaphotonics@163.com
Jiangbin Zhang,
zhangjiangbin@nudt.edu.cn

SPECIALTY SECTION
This article was submitted to Optics and Photonics, a section of the journal Frontiers in Physics

RECEIVED 07 March 2023
ACCEPTED 28 March 2023
PUBLISHED 06 April 2023

CITATION
Chai J, Liu W, Wen Y, Wang X, Xie K, Zhou Q, Zhang H, Zhang J, Liu P, Zhang D, Lu Y, Jiang Z and Zhao G (2023), Dynamic modal characteristics of transverse mode instabilities in ytterbium-doped fiber laser oscillator. *Front. Phys.* 11:1181692. doi: 10.3389/fphy.2023.1181692

Dynamic modal characteristics of transverse mode instabilities in ytterbium-doped fiber laser oscillator

Junyu Chai[1,2,3], Wenguang Liu[1,2,3]*, Yujun Wen[1,2,3], Xiaolin Wang[1,2,3]*, Kun Xie[4], Qiong Zhou[1,2,3], Hanwei Zhang[1,2,3], Jiangbin Zhang[1,2,3]*, Pengfei Liu[1,2,3], Dan Zhang[1,2,3], Yao Lu[1,2,3], Zongfu Jiang[1,2,3] and Guomin Zhao[1,2,3]

[1]College of Advanced Interdisciplinary Studies, National University of Defense Technology, Changsha, China, [2]Nanhu Laser Laboratory, National University of Defense Technology, Changsha, China, [3]Hunan Provincial Key Laboratory of High Energy Laser Technology, National University of Defense Technology, Changsha, China, [4]Xi'an Satellite Control Center, Xi'an, China

In recent years, transverse mode instability (TMI) has been widely observed in fiber laser amplifier systems. The transverse mode instability phenomenon in fiber laser oscillators is less studied. Here, we focus on the dynamical output properties, i.e., its temporal signal and modal characteristics in a 30-μm-core-diameter ytterbium (Yb)-doped fiber laser oscillator. The TMI occurs at a pumping power around 310 W. Different from amplifiers, the basic oscillation frequency is quite low, at around 100 Hz, changing with time and pump power. When the fiber laser oscillator operates beyond TMI threshold at 357 W or 377 W for a while, the temporal fluctuation slowly disappears together with a decreased oscillation frequency, and appears again later. Based on the mode decomposition technique, we find that during the period of fluctuation disappearance at 357 W, the power output stays low and the output beam is still a mixture of fundamental mode and higher-order modes. The fundamental mode content is calculated to be averagely higher when temporal fluctuation disappears, increasing from ~57% to ~63%. Our results indicate complex interaction between the fiber laser oscillation and the TMI effect, and calls for more attention into understanding TMI in fiber laser oscillators.

KEYWORDS

transverse mode instability, fiber laser oscillator, modal coupling, refractive index gratings, modal interference pattern

1 Introduction

High power fiber lasers (HPFLs) have attracted much attention in scientific research and industrial field due to their high conversion efficiency, excellent beam quality and convenient heat management [1–3]. There are currently three operations of fiber lasers, including pulse wave, quasi continuous wave (QCW), and continuous wave (CW). The progress of ultra-fast optics and ultra-intense laser technology has promoted the development of pulsed wave fiber laser [4–8]. They provide the advantages of high repetition rate and high peak power, which can be widely used in laser cutting. QCW fiber laser refers to a pulsed laser of ms magnitude with a duty cycle of 10%, which can be

applied in drilling [9–11]. By contrast, CW fiber laser can continuously output light with stable power and play an important role in welding [12–14].

The rapid progress of high-brightness laser diodes (LDs) and large-mode-area (LMA) fiber fabrication technology quickly pushed the CW fiber laser power to exceed 20 kW in a multimode fiber [15–20]. However, such trend was prohibited by a thermo-optical effect called transverse mode instability (TMI). In this effect, the heat generated from the amplification affects the refractive index of the fiber, inducing dynamical energy transfer between the fundamental mode and higher-order modes. This coupling typically results in unstable output beam profile, which exhibits temporal fluctuations up to a few kHz. Therefore, the beam quality and laser output performance degrade. As mentioned in the field of ultrafast photonics, pulsed optical fiber laser is generated from complex interactions among photons, electrons, and phonons under laser excitation conditions [21–23]. TMI process in CW fiber laser is also related to the dynamics of complex non-linear systems [24]. In order to mitigate TMI effect, researchers use several methods, such as imposing external bend loss of HOMs for mode selection [25–27], optimizing the fiber parameters [28–30], changing the fiber laser architecture as well as changing pumping schemes [31–33]. These mitigation strategies using passive optical devices are promising, but are only applicable in specific operation regimes [34]. Considering the physical origin of TMI (dynamic in nature) and taking the idea from adaptive optics, active mode control in a closed-loop system may provide a universal way to stabilize the beam beyond TMI threshold [35]. In principle, active mode control aims to control the direction of mode coupling, allowing energy transfer to flow between fundamental mode and higher-order modes.

In order to accurately measure the direction of energy, different methods have been developed to detect the TMI effect, such as utilizing photodiode (PD) [30] and high-speed camera (HSC) [36–38]. The PD is widely used to detect power fluctuation. The HSC method, in combination with modal analysis algorithm can measure the beam fluctuation spatially and temporally, but is not cheap. The fluctuation of power and modal analysis can provide the detailed information about dynamic mode coupling, showing the dynamic energy transfer between two or more modes. Such information is prior to perform proper mode control.

What's more, there are usually two configurations for CW fiber lasers, including master oscillator power amplifier (MOPA) and fiber laser oscillator. Currently, the MOPA architecture is more studied due to its high-power output [39–41]. In comparison with MOPA, the monolithic fiber laser oscillators exhibit the advantages of simpler structure, easier manipulation, and less sensitivity against backward coupled light. The output power level from the fiber oscillators has reached over 8 kW [42]. Therefore, more attention should be paid on investigating and suppressing TMI effect in fiber laser oscillators.

In this paper, we characterize TMI in a co-pumping fiber laser oscillator by measuring its temporal variation and performing modal analysis. We first describe the adopted all-fiber laser oscillator configuration and methods to characterize TMI properties. Then, we measure the laser output performance and observe transverse mode coupling. Furthermore, proper physical explanations are provided according to the experimental phenomenon.

2 Experimental setup

We build a co-pumping all-fiber laser oscillator with a low TMI threshold. The advantage of researching such laser is that the TMI process can be carefully observed at a low output power. Thus, the laser system is safe to operate around and beyond TMI threshold for a long time. The fiber laser oscillator setup is shown in Figure 1. We use fiber-coupled LDs with a stabilized emission wavelength of 976 nm as optical pump sources. A forward (6 + 1)×1 pump-signal combiner (PSC) enables a number of pump LDs to inject into the laser oscillation cavity. Six pump ports of the PSC are used, while the unoccupied central pump port of the PSC is angle cleaved to avoid facet reflection. The co-pumping light is launched into the laser oscillation cavity *via* the high-reflection fiber Bragg grating (HR-FBG). A length of ~20 m Ytterbium (Yb)-doped fiber (YDF) with 30/400 μm core/cladding diameters (NA_{core} = 0.064) is applied as gain fiber. The HR-FBG is inscribed on the end of YDF, and it provides a reflectivity of ~99.9% with a 3 dB bandwidth of ~4 nm at the central wavelength of ~1,080 nm. An output coupler fiber Bragg grating (OC-FBG) provides a reflectivity of ~10% with a 3 dB bandwidth of ~1.7 nm at the central wavelength of ~1,080 nm. After the OC-FBG, a length of 3 m 30/400 μm delivery fiber is spliced and a quartz endcap is used to output the signal laser without facet reflection. A cladding light stripper (CLS) is realized by removing the polymer cladding of delivery fiber and coating the inner cladding with high refractive index ointment. Thus, the CLS ensures the cladding light to leak into the air and only the amplified signal light reaches the fiber output. To avoid the heat accumulation, the whole all-fiber laser oscillator is attached on a water-cooled plate, and the gain fiber is coiled in a figure-8 shape with a minimum bend diameter of 85 mm.

As depicted in Figure 1, we employ several methods to characterize TMI. In the experiment, the output beam is collimated by a lens, and then a high reflection (HR) mirror reflects ~99.99% of the laser into the power meter (PM). A photodiode (PD) receives the scattered lights to monitor the temporal traces of output power *via* the oscilloscope. Part of the light is coupled into multimode fiber and transmitted to an optical spectrum analyzer (OSA) for recording spectral information. A mode decomposition system is applied to analyze the real-time modal variation of the co-pumping optical fiber oscillator. A spatial light modulator (SLM) and a HSC are the main components of the mode decomposition device with optical correlation filter (OCF) method [43]. To match the polarization requirement of the SLM, the incident light passes through a polarized beam splitter (PBS). A computer-generated-hologram containing the first six linearly polarized (LP) modes (LP_{01}, LP_{11e}, LP_{11o}, LP_{21e}, LP_{21o} and LP_{02}) related transmission functions is loaded on the SLM. The first order of the diffracted light is captured *via* a HSC. The neutral density filters (NDF) and optical bandpass filters are applied to adjust the incident power level onto the HSC and remove any residual pump light. A low-speed camera (LSC), which assists in judging the accuracy of the placement position and tilt angle of optical components, is used

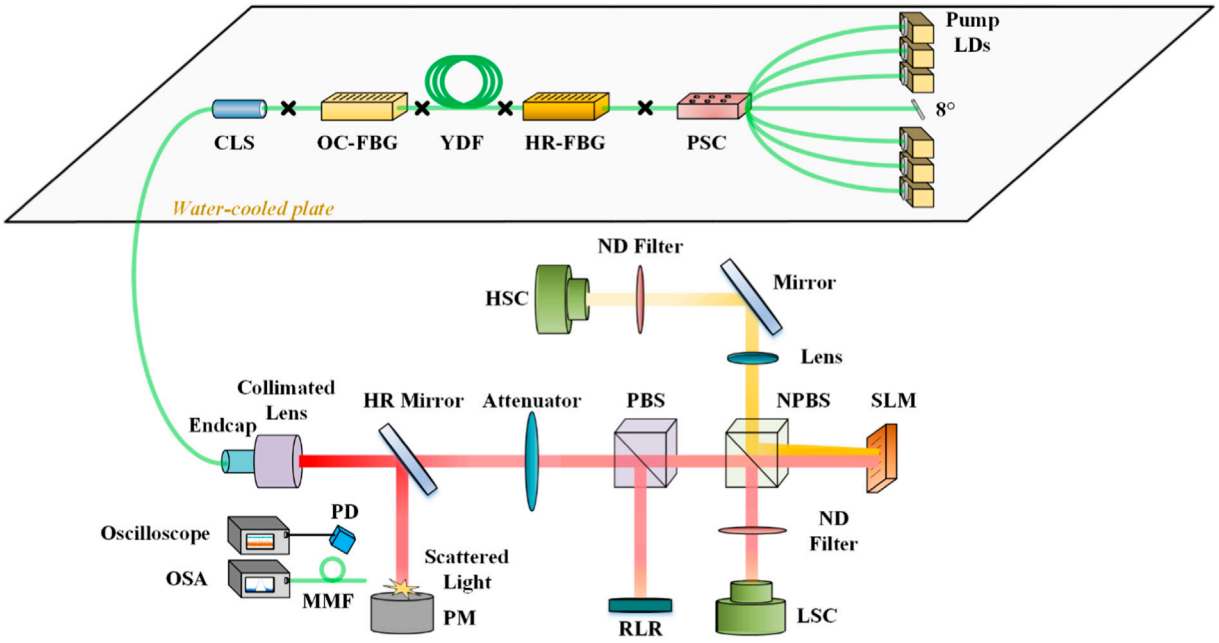

FIGURE 1
A schematic diagram of all-fiber laser oscillator and measurement system. (LDs, Laser diodes; PSC, Pump-signal combiner; HR, High reflection; FBG, Fiber Bragg grating; OC, Output coupler; YDF, Ytterbium-doped fiber; CLS, Cladding light stripper; PD, Photo-diode; OSA, Optical spectrum analyzer; MMF, Multi-mode fiber; PM, Power meter; PBS, Polarizing beam splitter; NPBS, Non-Polarizing beam splitter; SLM, Spatial light modulator; ND, Neutral density; RLR, Residual light receiver; LSC, Low-speed camera; HSC, High-speed camera).

to calibrate the measurement system. A residual light receiver (RLR) is applied to receive the unused polarized light during the entire measurement.

3 Results and discussion

3.1 Laser output characteristic

In the experiment, we first measure the spectrum and output power of the fiber laser oscillator. As depicted in Figure 2A, the central wavelength is around 1,080 nm at 155 W, and there are no pump light or ASE in the spectrum. Figure 2B depicts the output power dependence on the pump power and the standard deviations (STD) of the temporal signals at different power levels. The fiber laser oscillator shows a rollover output power of 180 W at the co-pumping power of 318 W, along with a rising instability, quantified by the STD of the temporal signal. We set the fiber laser oscillator to operate at three pumping powers (318, 357, and 377 W) over TMI threshold for 60 s, and recorded their temporal fluctuations using a PD per 10 s, as shown in Figure 2C. When the pumping power is 318 W, the time domain STD suddenly increases after 10 s, marking the appearance of TMI, and the intensity of STD fluctuates with time. When the pumping power reaches 357 and 377 W, we observe there is no fluctuation for the temporal signal at 40 and 50 s, respectively. Each stable period lasts for more than 10 s, and then the fluctuation re-appears again with the varied intensity over times.

In order to watch the time variation at the pumping power beyond TMI, we take the 357 W power input, and plot six normalized temporal intensities in a short period of 50 ms (The data is recorded every 10 s), as shown in Figure 2D. The signal shows periodic change, except at 40 s when the signal becomes quite stable. To better visualize the related frequency information, we perform Fourier transformation in Figure 2E. The fundamental frequency is initially 100 Hz, which decreases to around 75 Hz at 20 s, and returns to 100 Hz at 30 s. There is no obvious peak signal around 100 Hz at 40 s, but reappears at 150 Hz afterwards. We see that the signal variation frequency changes with time. Interestingly, there is a period which lasts around 10 s, when the time variation disappears. This indicates that TMI may be suppressed at power beyond the threshold.

3.2 Transverse modal properties

To research the transverse mode coupling process when TMI occurs, the temporal variation of the laser output profile is recorded. The far-field spot for mixed modes and the +1st diffraction pattern from mode decomposition is simultaneously captured *via* a HSC at 2,000 fps. A hole with a diameter of 4.5 μm is chosen at the centroid of the far-field spot, and the power change in this circle is monitored. When the pumping power is 357 W, we record the quasi-periodic fluctuation of power in the far-field bucket at selected time slices, as shown in Figures 3A–F. The waveform presents a superposition of two sine waves with a certain phase

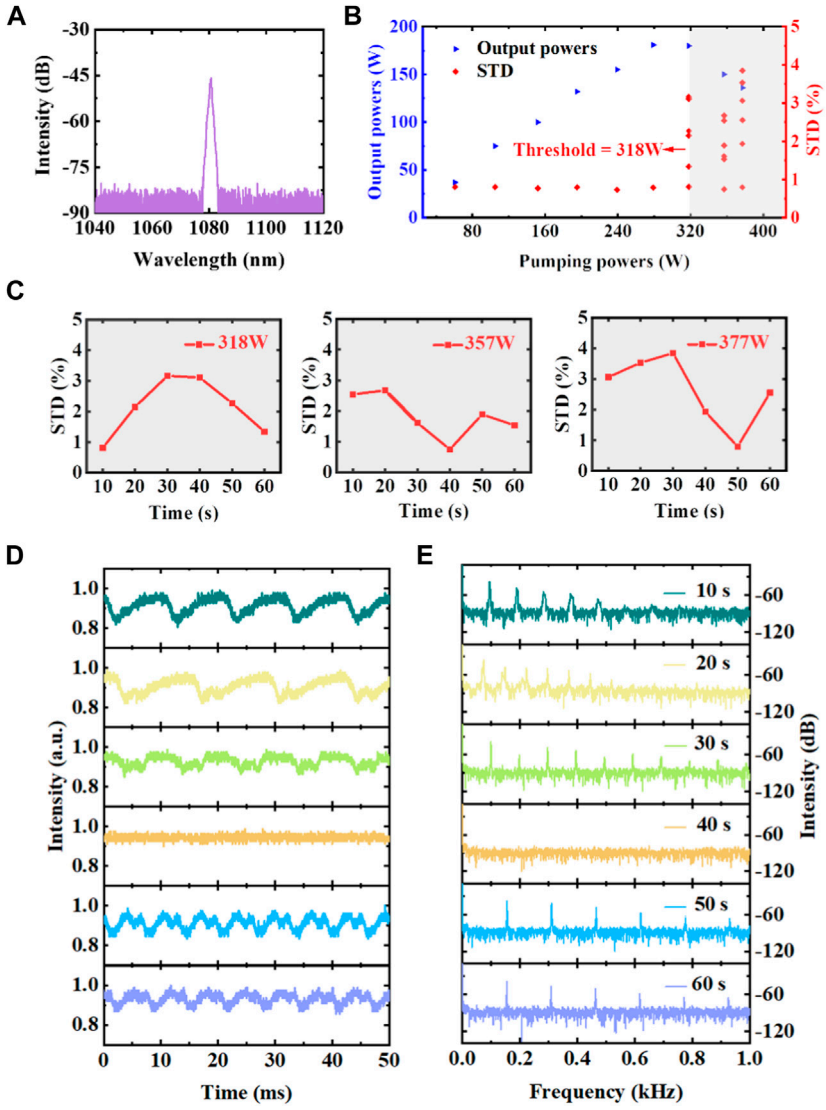

FIGURE 2
The spectrum and evolution of the output power and stability of the beam emitted by the co-pumping fiber laser oscillator: **(A)** The output spectrum at the output power of 155 W. **(B)** The output power and STD of the temporal signal at distinct pumping power. **(C)** Six recordings within 60 s of the time domain STDs at three pumping powers of 318, 357, and 377 W (The data is collected every 10 s). **(D)** Six temporal traces with first 50 ms in every 10 s in sequence at the pumping power of 357 W. **(E)** Fourier spectra of intensity variations.

difference. When there are no distinct temporal fluctuations (Figure 3D), the normalized intensity is relatively stable but at a low level around 0.6. Although the temporal fluctuation disappears, the TMI still occurs due to the reduced output power. This low output power is assumed a dynamic multimode coupling of some frequency combinations or a static energy transfer (mode coupling).

We then perform mode decomposition and the corresponding modal content is shown in Figures 4A–F. The accuracy of mode decomposition can be up to 98% in our experiment. When the modal coupling occurs at adjacent modes, these two modes are recognized as a coupling pair. According to the variation of modal contents, the modal coupling presents a reverse periodic change among one coupling pair. When one mode intensity decreases, the other mode in the coupling pair will increase in a similar trend. It can be clearly seen that there is a strong coupling between LP_{01} and LP_{11e} mode in the state of TMI. The degenerate modes (LP_{11e} and LP_{11o}, LP_{21e} and LP_{21o}) have mutual energy exchange. Besides, the results of the modal analysis demonstrate that the periodic modal coupling changes with time. In Figure 4D, when the laser output is relatively stable which lasts for about 18 s, the mode content of the fundamental mode stays around 65%, increasing from 58% in the unstable case. This result demonstrates a static mode coupling in the time range of 18 s. And then the output power oscillates again, accompanied by dynamic mode coupling.

To figure out the properties of the modal coupling frequencies, we compute Fourier spectrum of the individual mode content in 30 s. We compare it with the frequency of the

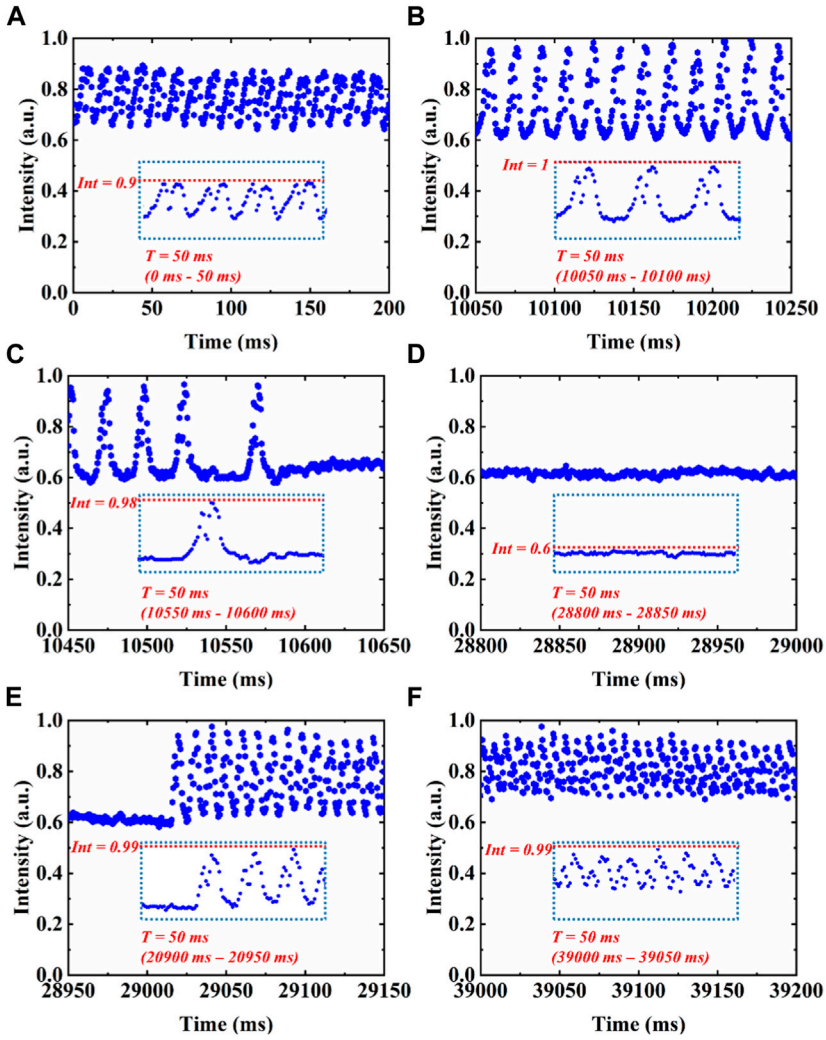

FIGURE 3
Variation of power in the far-field bucket within multiple 200 ms at the pumping power of 357 W. Inset: selected 50 ms time window, where Int denotes the maximum intensity.

power in the far-field bucket. The power fluctuation of the far-field bucket in 50 ms is shown in Figure 5A. The intensity has a periodic quasi-triangle waveform in this time window. The characteristic peaks of the Fourier spectrum are independent below 1 kHz. As depicted in Figure 5B, the characteristic frequencies of the individual modes are similar as that of the power change of the far-field mixed modes. The basic frequencies are all around 150 Hz. Thus, we consider 1.5 kHz may be an essential frequency for controlling mode coupling for this fiber laser oscillator in an active control system.

3.3 Physical explanations and analysis

The above experimental results show that the frequencies of the temporal fluctuation are several times lower than the dynamic TMI in fiber amplifiers, which are mostly in kHz level. This phenomenon is consistent with that of Ref. [44] that the characteristic frequency of a fiber laser oscillator is lower than that of a fiber laser amplifier.

In recent years, it is generally agreed that TMI is induced by the refractive index gratings (RIG) [11]. But there are still two different theories explaining the physical origin of TMI. One of the theories is based on non-adiabatic waveguide changes which are thermally induced [39]. The other theory relies on modal interference pattern (MIP) between fundamental mode and higher-order modes with slightly different frequencies [45].

The energy transfer between the transverse modes for the dynamic TMI is related to the non-adiabatic longitudinal change of the transverse refractive index distribution along the fiber. From the Ref. [39] and the results of our experiments, the energy exchange is a ripple-shape in one cycle. This ripple-shape will change slightly over time compared with the previous ones. That is to say, the energy oscillation can remain unchanged within a certain time range, but it will suddenly vary to a new state, and then keep this state for a moment. What's more, the net energy

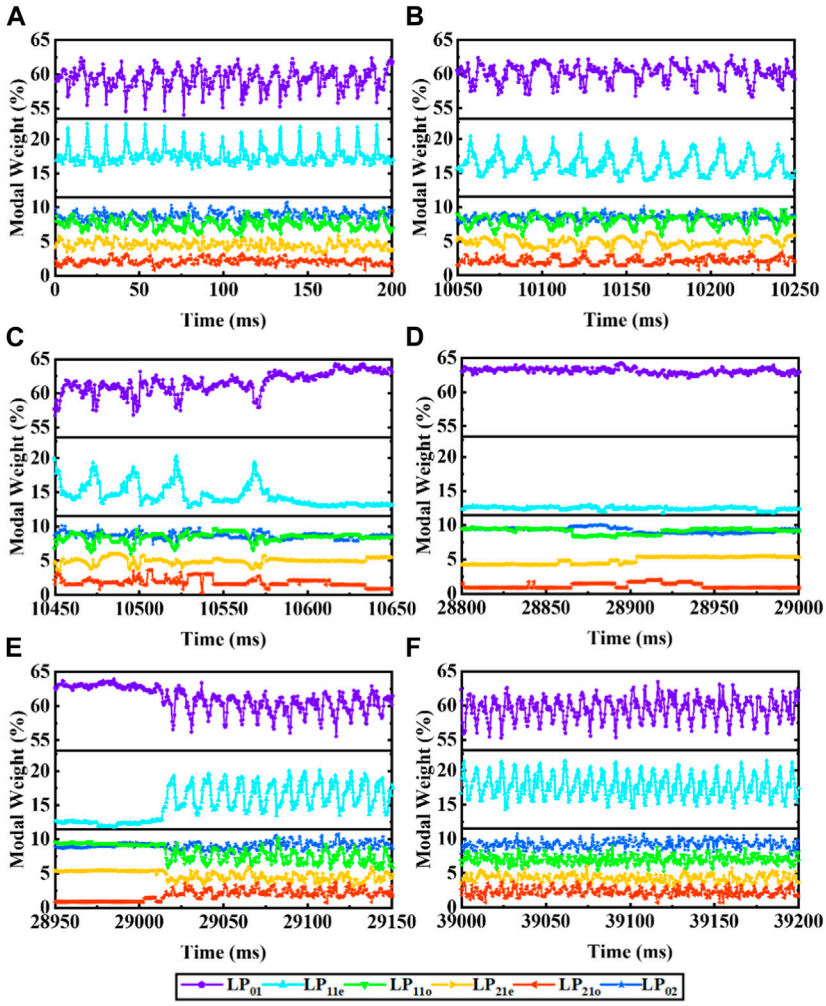

FIGURE 4
The variation of transverse mode coupling at the pumping power of 357 W.

transfer after each period will be equal to zero, since the energy transfer in the first half cycle will be completely reversed in the second half cycle.

We observe that the TMI effect switches from an unstable temporal state to a stable temporal state. Even though, this phenomenon is demonstrated as a static mode coupling in the selected time window at 357 W (Figure 4D). When the system operates for a period at the pumping power point above TMI threshold, it is also recorded that the system switches back and forth between the stable and the unstable state (at 357 and 377 W). This may be still a dynamic energy transfer with a certain set of the coupling frequencies, which can induce a plausible balanced state. Otherwise, the temporal stability may be occurred when the dynamic energy transfer relaxes to a stable state of the system over time. A weak external perturbation, such as air turbulence/convection, mechanical vibration, or the thermally-induced change, is enough to trigger the modal interference conditions and induce the unstable evolution of the system again. Besides, the RIG at the fiber end amplifies the impact of these perturbations. The TMI will occur when this amplification factor is higher than the damping of perturbation. This also requires in-depth researches to explore the physical origin of this relaxation.

In additon, according to Ref. [46], Hui Cao from Yale University calculated that multiple mode excitation can reduce the thermo-optical non-linearity and instability compared to two mode excitation. As there are at least 6 supported modes in 30 μm Yb-doped fiber, multiple mode excitation is highly likely to exist and may change over time. When the mode coupling results in more mode distribution, the TMI threshold increases so that TMI

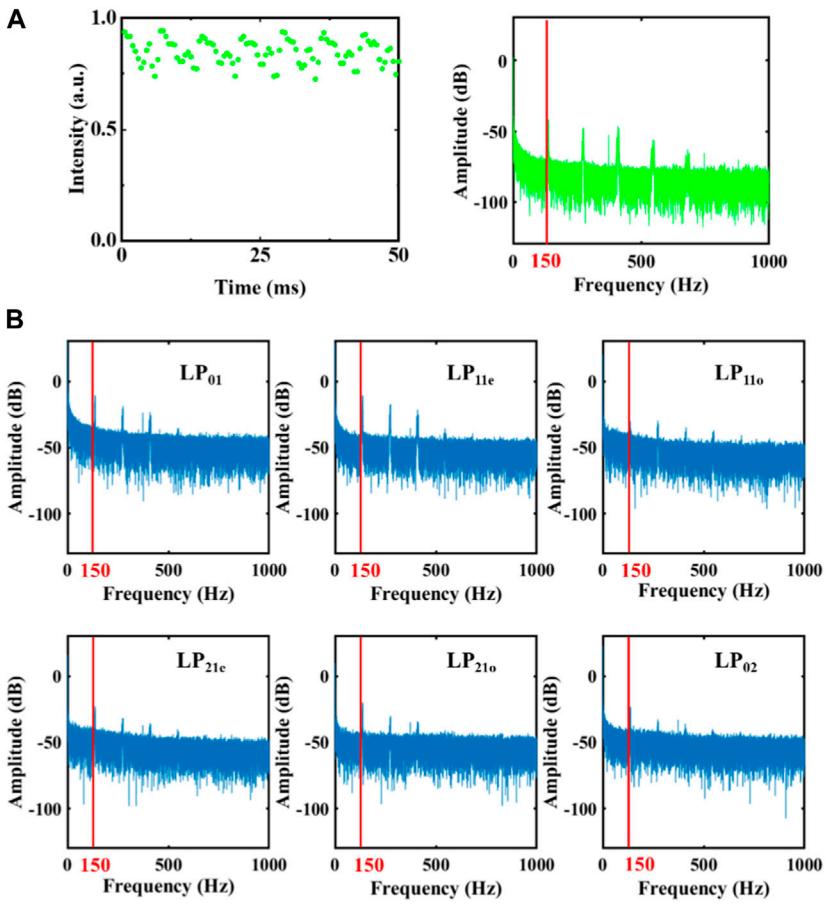

FIGURE 5
The variation of the power fluctuation in the bucket of far-field spot and modal coupling frequencies. **(A)** The power fluctuation of the far-field bucket in 50 ms and the related Fourier spectrum; **(B)** The characteristic frequencies of the individual modes (LP_{01}, LP_{11e}, LP_{11o}, LP_{21e}, LP_{21o}, LP_{02}) in 30 s.

phenomenon may not occur. On the other hand, when the mode coupling reduces the number of modes, the TMI may jump in again due to the reduced threshold.

4 Conclusion

In summary, we have experimentally studied the TMI phenomenon in a 30 μm Yb-doped fiber laser oscillator in detail and validate the modal energy transfer during TMI using temporal analysis and mode decomposition. The TMI threshold is measured at a pumping power around 310 W. The basic characteristic frequency is quite low, around 100 Hz, changing with time and pump power. When the fiber laser oscillator operates above TMI threshold at 357 W or 377 W, to our surprise, the temporal fluctuation slowly disappears with a reduced frequency, and re-appears after more than 10 s. During the period of fluctuation disappearance at 357 W, the mode content of fundamental mode increases from 57% to 63%, while the output power stays low. This demonstrates a static mode coupling in the selected time window. We provide proper physical explanations and analysis for several complex nonlinear dynamics of TMI, which could be helpful for the recognition and suppression of TMI in the fiber laser oscillator.

Data availability statement

The original contributions presented in the study are included in the article/supplementary material, further inquiries can be directed to the corresponding authors.

Author contributions

Investigation, JC, WL, and XW; resources, YW, KX, QZ, PL, HZ, DZ, YL, and ZJ; writing—original draft preparation, JC; writing—review and editing, JC, JZ, and XW; supervision, WL, XW, and GZ. All authors have read and agreed to the submitted version of the manuscript.

Funding

The authors appreciate the financial support from the National Natural Science Foundation of China (NSFC) under Grant Nos. 12074432 and 12204540; Science and Technology Innovation Program of Hunan Province under Grant No. 2021RC3038.

Acknowledgments

The authors would like to thank Lingfa Zeng, Penglin Zhong, and Xiaoyong Xu for their assistance in the whole experiment.

Conflict of interest

The authors declare that the research was conducted in the absence of any commercial or financial relationships that could be construed as a potential conflict of interest.

Publisher's note

All claims expressed in this article are solely those of the authors and do not necessarily represent those of their affiliated organizations, or those of the publisher, the editors and the reviewers. Any product that may be evaluated in this article, or claim that may be made by its manufacturer, is not guaranteed or endorsed by the publisher.

References

1. Jauregui C, Limpert J, Tünnermann A. High-power fibre lasers. *Nat Photon* (2013) 7(11):861–7. doi:10.1038/nphoton.2013.273

2. Nilsson J, Payne D. High-power fiber lasers. *Science* (2011) 332(6032):921–2. doi:10.1126/science.1194863

3. Zervas M, Codemard C. High power fiber lasers: A review. *IEEE J Sel Top Quan Electron.* (2014) 20(5):219–41. doi:10.1109/jstqe.2014.2321279

4. Zhang C, Liu J, Gao Y, Li X, Lu H, Wang Y, et al. Porous nickel oxide micron polyhedral particles for high-performance ultrafast photonics. *Opt Laser Technol* (2022) 146:P107546. doi:10.1016/j.optlastec.2021.107546

5. Li X, Feng J, Mao W, Yin F, Jiang J. Emerging uniform Cu2O nanocubes for 251st harmonic ultrashort pulse generation. *J Mater Chem C* (2022) 8(41):14386–92. doi:10.1039/d0tc03622f

6. Li X, Xu W, Wang Y, Zhang X, Hui Z, Zhang H, et al. Optical-intensity modulators with PbTe thermoelectric nanopowders for ultrafast photonics. *Appl Mater Today* (2022) 28:101546. doi:10.1016/j.apmt.2022.101546

7. Zhao Y, Wang W, Li X, Lu H, Shi Z, Wang Y, et al. Functional porous MOF-Derived CuO octahedra for harmonic soliton molecule pulses generation. *ACS Photon* (2022) 7(9):2440–7. doi:10.1021/acsphotonics.0c00520

8. Zhang C, Li X, Chen E, Liu H, Shum P, Chen X. Hydrazone organics with third-order nonlinear optical effect for femtosecond pulse generation and control in the L-band. *Opt Laser Technol* (2022) 151:108016. doi:10.1016/j.optlastec.2022.108016

9. Wang L, Zhang H, Wang P, Yang B, Wang X, Ning Y, et al. A 6.4-kw peak power near-single-mode quasi-continuous wave fiber laser oscillator employing spindle-shaped ytterbium-doped fiber. *Opt Laser Technol* (2022) 154.

10. Hong Z, Wan Y, Xi X, Zhang H, Wang X, Xu X. High-peak-power pump-modulated quasi-CW fiber laser. *Appl Opt* (2022) 61(7):1826–33. doi:10.1364/ao.452604

11. Leone C, Mingione E, Genna S. Laser cutting of CFRP by quasi-continuous wave (QCW) fibre laser: Effect of process parameters and analysis of the HAZ index. *Compos B-eng* (2021) 0224:109146. doi:10.1016/j.compositesb.2021.109146

12. Limpert J, Liem A, Zellmer H, Tünnermann A. 500 W continuous-wave fibre laser with excellent beam quality. *Electron Lett* (2003) 39:645–7. doi:10.1049/el:20030447

13. Jeong Y, Sahu J, Payne D, Nilsson J. Ytterbium-doped large-core fiber laser with 1.36 kW continuous-wave output power. *Opt Express* (2004) 12:6088–92. doi:10.1364/opex.12.006088

14. Pakniat M, Ghaini F, Torkamany M. Hot cracking in laser welding of Hastelloy X with pulsed Nd:YAG and continuous wave fiber lasers. *Mater Des.* (2016) 16:177–83. doi:10.1016/j.matdes.2016.05.124

15. Richardson D, Nilsson J, Clarkson W. High power fiber lasers: Current status and future perspectives [invited]. *J Opt Soc Am B* (2010) 27(11):B63. B63–B92. doi:10.1364/josab.27.000b63

16. Fang Q, Shi W, Qin Y, Meng X, Zhang Q. 2.5 kw monolithic continuous wave (cw) near diffraction-limited fiber laser at 1080 nm. *Laser Phys Lett* (2014) 11(10):105102. doi:10.1088/1612-2011/11/10/105102

17. Yu H, Zhang H, Lv H, Wang X, Leng J, Xiao H, et al. 315 kW direct diode-pumped near diffraction-limited all-fiber-integrated fiber laser. *Appl Opt* (2015) 54(14):4556–60. doi:10.1364/ao.54.004556

18. Shi C, Su R, Zhang H, Yang B, Wang X, Zhou P, et al. Experimental study of output characteristics of bi-directional pumping high power fiber amplifier in different pumping schemes. *IEEE Photon J* (2017) 9(3):1–10. doi:10.1109/jphot.2017.2679753

19. Beier F, Hupel C, Kuhn S, Hein S, Nold J, Proske F, et al. Single mode 4.3 kw output power from a diode-pumped yb-doped fiber amplifier. *Opt Express* (2017) 25(13):14892. doi:10.1364/oe.25.014892

20. Beier F, Hupel C, Nold J, Kuhn S, Hein S, Ihring J, et al. Narrow linewidth, single mode 3 kw average power from a directly diode pumped ytterbium-doped low na fiber amplifier. *Opt Express* (2016) 24(6):6011. doi:10.1364/oe.24.006011

21. Guan M, Chen D, Hu S, Zhao H, You P, Meng S. Theoretical insights into ultrafast dynamics in quantum materials. *Ultrafast Sci* (2022) 16:9767251. doi:10.34133/2022/9767251

22. Liu X, Yao X, Cui Y. Real-time observation of the buildup of soliton molecules. *Phys Rev Lett* (2018) 121(2):023905. doi:10.1103/physrevlett.121.023905

23. Liu X, Popa D, Akhmediev N. Revealing the transition dynamics from Q switching to mode locking in a soliton laser. *Phys Rev Lett* (2019) 123(9):093901. doi:10.1103/physrevlett.123.093901

24. Hansen K, Alkeskjold T, Broeng J, Lægsgaard J. Theoretical analysis of mode instability in high-power fiber amplifiers. *Opt Express* (2013) 21:1944–71. doi:10.1364/oe.21.001944

25. Hejaz K, Norouzey A, Poozesh R, Heidariazar A, Roohforouz A, Nasirabad R, et al. Controlling mode instability in a 500 W ytterbium-doped fiber laser. *Laser Phys* (2014) 24(2):025102. doi:10.1088/1054-660x/24/2/025102

26. Smith A, Smith J. Mode instability in high power fiber amplifiers. *Opt Express* (2011) 19(11):10180–92. doi:10.1364/oe.19.010180

27. Ward B, Robin C, Dajani I. Origin of thermal modal instabilities in large mode area fiber amplifiers. *Opt Express* (2012) 20(10):11407–22. doi:10.1364/oe.20.011407

28. Haarlammert N, Sattler B, Liam A, Strecker M, Nold J, Schreiber T, et al. Optimizing mode instability in low NA fibers by passive strategies. *Opt Lett* (2015) 40(10):2317–20. doi:10.1364/ol.40.002317

29. Brar K, Savage-Leuchs M, Henrie J, Courtney S, Dilley C, Afzal R, et al. "Threshold power and fiber degradation induced modal instabilities in high-power fiber amplifiers based on large mode area fibers," In Proc. SPIE (2014) San Francisco, California, USA. 8961.

30. Otto H, Stutzki F, Jansen F, Eidam T, Jauregui C, Limpert J, et al. Temporal dynamics of mode instabilities in high-power fiber lasers and amplifiers. *Opt Express* (2012) 20(14):15710–22. doi:10.1364/oe.20.015710

31. Tao R, Wang X, Zhou P. Comprehensive theoretical study of mode instability in high-power fiber lasers by employing a universal model and its implications. *IEEE J Sel Top Quan Electron.* (2018) 24(3):1–19. doi:10.1109/jstqe.2018.2811909

32. Smith A, Smith J. Increasing mode instability thresholds of fiber amplifiers by gain saturation. *Opt Express* (2013) 21(13):15168–82. doi:10.1364/oe.21.015168

33. Jauregui C, Otto H, Stutzki F, Jansen F, Limpert J, Tünnermann A. Passive mitigation strategies for mode instabilities in high-power fiber laser systems. *Opt Express* (2013) 21(16):19375–86. doi:10.1364/oe.21.019375

34. Jauregui C, Stihler C, Limpert J. Transverse mode instability. *Adv Opt Photon* (2020) 12(2):429–84. doi:10.1364/aop.385184

35. Chai J, Liu W, Zhang J, Xie K, Lu Y, Li C, et al. Influence of aberrations on modal decomposition for LMA fiber laser systems. *Front Phys* (2022) 9:9. doi:10.3389/fphy.2021.796666

36. Eidam T, Wirth C, Jauregui C, Stutzki F, Jansen F, Otto H, et al. Experimental observations of the threshold-like onset of mode instabilities in high power fiber amplifiers. *Opt Express* (2011) 19(14):13218–24. doi:10.1364/oe.19.013218

37. Christensen S, Johansen M, Michieletto M, Triches M, Maack M, Lægsgaard J. Experimental investigations of seeding mechanisms of TMI in rod fiber amplifier using spatially and temporally resolved imaging. *Opt Express* (2020) 28(18):26690–705. doi:10.1364/oe.400520

38. Stutzki F, Otto H, Jansen F, Gaida C, Jauregui C, Limpert J, et al. High-speed modal decomposition of mode instabilities in high-power fiber lasers. *Opt Lett* (2011) 36(23):4572–4. doi:10.1364/ol.36.004572

39. Jauregui C, Eidam T, Otto H, Stutzki F, Jansen F, Limpert J, et al. Physical origin of mode instabilities in high-power fiber laser systems. *Opt Express* (2012) 20(12): 12912–25. doi:10.1364/oe.20.012912

40. Karow M, Tünnermann H, Neumann J, Kracht D, Wessels P. Beam quality degradation of a singlefrequency Yb-doped photonic crystal fiber amplifier with low mode instability threshold power. *Opt Lett* (2012) 37(20):4242–4. doi:10.1364/ol.37.004242

41. Naderi S, Dajani I, Madden T, Robin C. Investigations of modal instabilities in fiber amplifiers through detailed numerical simulations. *Opt Express* (2013) 21(13): 16111–29. doi:10.1364/oe.21.016111

42. Wang Y, Kitahara R, Kiyoyama W, Shirakura Y, Kurihara T, Nakanishi Y, et al. "8-kW single-stage all-fiber Yb-doped fiber laser with a BPP of 0.50 mm-mrad." In Proc. SPIE (2020) San Francisco, California, USA, 1126022.

43. Xie K, Liu W, Zhou Q, Huang L, Jiang Z, Xi F, et al. Adaptive phase correction of dynamic multimode beam based on modal decomposition. *Opt Express* (2019) 27(10): 13793–802. doi:10.1364/oe.27.013793

44. Yang B, Zhang H, Shi C, Wang X, Zhou P, Xu X, et al. Mitigating transverse mode instability in all-fiber laser oscillator and scaling power up to 2.5 kW employing bidirectional-pump scheme. *Opt Express* (2016) 24(24):27828–35. doi:10.1364/oe.24.027828

45. Smith A, Smith J. Spontaneous Rayleigh seed for stimulated Rayleigh scattering in high power fiber amplifiers. *IEEE Photon J* (2013) 5(5):7100807. doi:10.1109/jphot.2013.2280526

46. Chen C, Wisal K, Eliezer Y, Stone A, Cao H, "Suppressing transverse mode instability through multimode excitation in a fiber amplifier." in Proceeding of the Cleo: Science and innovations 2022 (2022) San Jose, California, USA, 15438.

frontiers | Frontiers in Physics

TYPE Brief Research Report
PUBLISHED 12 April 2023
DOI 10.3389/fphy.2023.1185068

OPEN ACCESS

EDITED BY
Shuo Liu,
Hebei University of Technology, China

REVIEWED BY
Zhichao Liu,
Changchun University of Science and Technology, China
Wang Gao,
North University of China, China

*CORRESPONDENCE
Meixuan Li,
limx@jlenu.edu.cn

RECEIVED 13 March 2023
ACCEPTED 03 April 2023
PUBLISHED 12 April 2023

CITATION
Ding W, Li M, Liang F, Gao Y, Qin W and Zhang H (2023), Research on on-line assembly and calibration system based on laser scanning and optical fiber sensor. *Front. Phys.* 11:1185068.
doi: 10.3389/fphy.2023.1185068

Research on on-line assembly and calibration system based on laser scanning and optical fiber sensor

Weijie Ding[1], Meixuan Li[2]*, Fang Liang[3], Yan Gao[1], Wei Qin[1] and Hong Zhang[1]

[1]Department of Physics, Xinzhou Normal University, Xinzhou, Shanxi, China, [2]Institute for Interdisciplinary Quantum Information Technology, Jilin Engineering Normal University, Changchun, China, [3]Department of Electronics, Xinzhou Normal University, Xinzhou, Shanxi, China

In order to improve the degree of assembly automation, an online assembly calibration system is designed based on laser scanning and optical fiber sensors. The optical fiber sensing module is used to obtain the stress field information, and the laser scanning module is used to obtain the point cloud information of the assembly structure. The position offset caused by the stress field can be compensated to the 3D point cloud for improving the target reconstruction accuracy. It consists of laser scanning module, optical fiber sensor module, demodulator, data analysis module, *etc.* Analyzing the structural characteristics of the module, the stress field distribution of the module structure is obtained through simulation analysis, and an appropriate optical fiber sensor network layout is constructed. When the force is applied in different directions, the stress field distribution of the assembly structure is simulated and analyzed. The results show that the magnitude and direction of the residual stress have an impact on the distribution of the stress field. At the same time, the stress field diffusion degree had been also analyzed in different strength conditions. In the calibration test of FBG sensor, the functional relationship between wavelength variation and stress is about 0.0011 nm/N. In the assembly test, the stress test trends of different FBGs were obtained, and the relative error was concentrated between 4.0% and 9.0%, which had good stability. After correcting the position of the point cloud for optical fiber sensing data, the position deviation between the test point and the digital analog has been significantly reduced, with the average value decreasing from 2.953. to 0.095 mm. It has good applicability in factories with large interference of working environment, and can improve the application field of intelligent assembly.

KEYWORDS

optical fiber network, laser scanning, assembly calibration, automation, stress field analysis

1 Introductions

Intelligent assembly technology is the development direction of the future manufacturing industry, and it is the closed-loop control of online real-time monitoring and feedback as demonstrated [1]. The existing online adjustment methods of intelligent assembly mainly include laser scanning method and image matching method [2]. The image matching method mostly uses a trinocular measuring instrument. Boeing adopts intelligent assembly technology, and large parts were realized by iGPS and AGV. It greatly reduces time for assembly time [3–5]. A high-precision online correction module was provided by the

modular positioning technology, which can use laser positioning to obtain real-time assembly information Arnaldo G [6]. Had a very high level of intelligence as demonstrated.

Lidar technology [7–11] has the advantages of high precision and good repeatability in intelligent assembly, and the image matching method has the advantages of strong applicability and good stability. Both of them use the method of collecting light waves at the target position to obtain the assembly state. In the existing intelligent assembly system, it can often only be applied to large components with a simple structure or an assembly process with a single process, and at the same time, it is necessary to ensure the low noise of the assembly environment. It also limits the application of the two technologies in the more general assembly process, so these two technologies are currently mainly used in the aviation field. Multi-sensor measurement methods have low dependence on working conditions, good real-time performance and strong adaptability. Mulle et al. [12] completed the measurement of mechanical structures under moving conditions through FBG strain measurement and vibration demodulation. Stress fluctuation range test; Anany [13] used multi-core fiber to achieve the acquisition of three-dimensional strain field distribution, so as to invert the structural shape change; Arnaldo [14] detected the bending shape and solved the problem of the installation process of the aircraft boom. The force condition assists the assembly. Qu Daoming et al. [6] used optical fiber sensing technology to complete the flexible skin detection, and provided experimental reference data for the automatic adjustment of variable wings. Jiang Xintong et al. [15] obtained the pre-assembled stress model through the optical fiber network to improve the assembly accuracy. In order to directly obtain the assembly state information during the assembly process for realizing online correction, it can achieve the purpose of being suitable for various assembly fields.

An intelligent assembly trajectory correction system was designed by optical fiber sensing. The tool distributed sensor network was used to solve the problem of visual blind spots, and the differential correction was used to solve the problem of environmental interference.

2 Principle of the system

During the assembly process, the assembly tool needs to move the workpiece to a suitable position. During the process, it is often affected by the error between the preset trajectory and the actual assembly trajectory. Translation error, pose error, *etc.*, will cause improper assembly, interference assembly or assembly interference, *etc.* In order to realize the self-adaptive correction in the assembly process of large-scale structural workpieces, it is necessary to obtain the real-time assembly status information. Obtaining the stress field distribution through optical fiber sensing technology can complete the real-time correction of assembly trajectory, the echo offset of any FBG can be expressed as.

$$\frac{\Delta\lambda_B}{\lambda_B} = (1 - P_\varepsilon) \cdot \varepsilon + \left(\alpha_f + \xi\right)\Delta T \tag{1}$$

Among them, λ_B is the initial value of the center wavelength of the FBG, α is the thermal expansion coefficient, ξ is the thermo-optic coefficient, ΔT is the temperature change, ε is the strain, and P_ε is the elastic-optic coefficient. Since the influence of temperature on FBG can be realized by performing temperature compensation in the same working environment, the temperature term in the above formula can be replaced by a constant coefficient.

Let the feature point set on the tape-mounted product be A (x, y, z), and the actual point set be A' (x, y, z). The reason for the deviation is the deformation caused by stress, then the point set change ΔA (x, y, z) can be expressed as

$$\Delta A(x, y, z) = \left|A(x, y, z) - A'(x, y, z)\right| \tag{2}$$

The strain position function $f(\varepsilon)$ can be expressed as

$$f(\varepsilon) = \Delta A(x, y, z)/A(x, y, z) \tag{3}$$

The test group data can be obtained through the experiment to complete the fitting of the $f(\varepsilon)$ function, and then use this function to compensate for the unknown position offset.

A sufficient number of FBG sensors are pasted on the entire tool according to the sensitive locations that may change significantly. The stress field distribution of the entire tool can be obtained at one time. Then, through the difference of stress field distribution, the analysis of the assembly deviation was completed, and the assembly trajectory was corrected according to the difference. According to Hooke's law, the stress value at any position on the workpiece has

$$F = \frac{2xEI}{l - x}(\Delta\lambda_B - \lambda_C)[\lambda_B \cdot (1 - P_\varepsilon)]^{-1} \tag{4}$$

Among them, x is the corresponding position, l is the size of the building element, I is the moment of inertia, E is the elastic modulus, ε is the strain value, and λ_C is the wavelength offset compensation coefficient obtained by temperature calibration. Since l、 E and I are all constants, and x is the position corresponding to the test, it can be used as an input. The wavelength change of all FBGs corresponding to the x position becomes the only variable for the calculation of the stress value, that is, the stress field distribution matrix can be obtained through the wavelength matrix. Since the theoretical trajectory position can be obtained by multiplying the matrix of the test position P by the trajectory compensation matrix, the trajectory compensation matrix C_{xy} affected by the stress field can be expressed as the test position matrix P and the wavelength offset is all the test values and the wavelength offset $\Delta\lambda_B$, there is

$$C_{xy} = P_{xy} \cdot \Delta\lambda_B\big|_{xy} \tag{5}$$

Among them, z is a constant; x and y respectively represent the two-dimensional coordinates of the workpiece marking point. By calculating the parameters of the trajectory compensation matrix corresponding to the two-dimensional coordinates at any time, it can complete the real-time correction of the assembly.

3 Assembling the calibration system

The traditional multi-sensor measurement method requires multiple types of sensors to monitor the stress of the product installation location, vibration parameter measurement, temperature compensation test and so on. There are many factors that need to be considered to complete the layout of various sensors and the placement of processing circuits on the

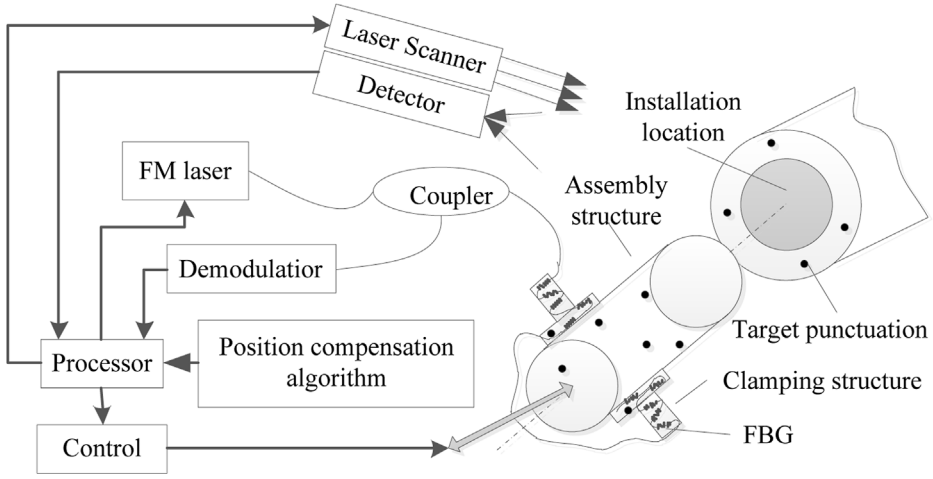

FIGURE 1
Based on laser scanning and optical fiber detection and correction system.

entire robotic arm. Otherwise, interference problems, electronic interference problems, and signal crosstalk problems during the movement process may be affected. Test results and lead to feedback errors affecting the installation effect. The system consists of a frequency-modulated laser, a coupler, a demodulation module, a fiber grating (FBG, Fiber Bragg Grating) and a laser scanning module. The overall structure is shown in Figure 1. The optical fiber sensor network itself is a passive sensor and is not affected by electromagnetic radiation; the front section has only optical fiber, the processing module can be completely separated from the sensing part, and the optical fiber sensing part is small in size, and can simultaneously obtain the stress through combined measurement. The laser scanning module can obtain three-dimensional point cloud data of the assembly structure. After converting the geometric deformation relationships sensed by optical fibers into offset parameters, the 3D point cloud of the assembly structure is imported to achieve correction of the assembly trajectory.

4 Simulation analysis

In the intelligent detection and correction system, the transmission of the test physical quantity is from stress to wavelength change value, wavelength change value to position offset, and position offset to detection correction value. Among them, the wavelength change value to the position offset is realized by fitting the experimental data. The position offset to the detection correction value is realized by the control structure, and the stress to the wavelength change is obtained through the test data. It can affect the original data directly and the calibration accuracy, so the simulation analysis of its parameters is very necessary. The FBG distribution position and FBG axial direction are guided by the simulation results, which provide theoretical support for accurately obtaining stress distribution data. Taking the common jack-type installation structure in Figure 1 as an example, the simulation analysis is carried out for the two main error forms of position deviation and angle deviation, and the results are shown in Figure 2.

Two different abnormal position states common in the product installation process are simulated and analyzed. It shows the stress distribution caused by the deviation of the installation position in Figure 2A. The assembly depth is too large, so that there is a stress effect of extrusion between the insertion end and the installation hole, the stress field distribution is shown in Figure 2A, and its stress is mainly concentrated on the insertion end. When the residual stress is 10N, the maximum position offset is about 2.6 μm. It shows the stress distribution caused by the deviation of the installation angle in Figure 2B. There is an angular deviation between the axis of the insert and the axis of the installation hole during assembly. The stress field distribution is shown in Figure 2B, and the stress is mainly concentrated at the end of the installation hole. When the residual stress is 30N, the maximum position offset is about 1.82 μm. The size of the components and the force applied by the assembly robot are corresponding to the weight of the workpiece and the clamping requirements, so the stress range changes greatly.

5 Experiments

5.1 Calibration test

The stress test of the FBG array was calibrated before completing the stress acquisition at the assembly location. The test mainly completes the test of the temperature compensation data and the test of the variation law of stress and wavelength. The stress test adopts the classic cantilever beam structure. The effective distance is 5.0 cm. The FBG length is 2.5 mm. The material is steel. The elastic modulus is 6.54×10^{10} Pa, and the expansion coefficient is 21.6 μm/mk. The external force value was increased from 0 to 400 N, and the test data was recorded every 100 N. The functions of wavelength with respect to stress are

$$\lambda = 0.00043F + 1550.32 \quad (6)$$

The target location uses a stress sensitive FBG, and the stress test results are shown in Figure 3. At the same time, temperature FBG is used to compensate for the temperature drift of the stress FBG. The

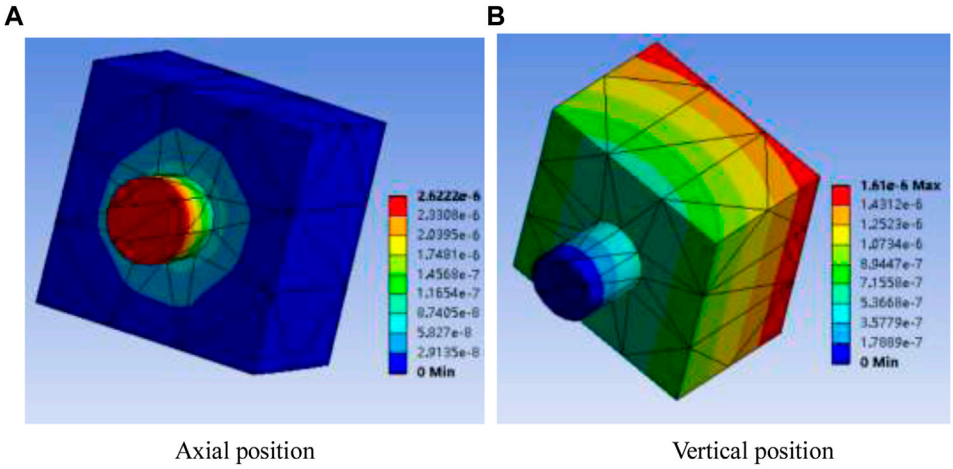

FIGURE 2
Simulation of stress under different states.

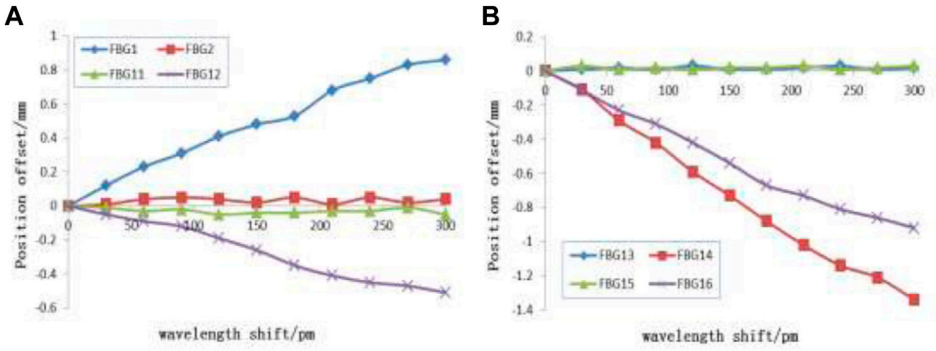

FIGURE 3
Wavelength offset values at different positions.

relationship between stress and wavelength shift is linear. The average slope is 0.43 p.m./N. In order to improve the test range of the system application, the strain value of the test point can be calibrated by calibrating the database, so that it is suitable for a larger stress response range that conforms to elastic deformation.

5.2 Assembly structure test experiment

The stress distribution position has the regularity of gradient diffusion. The structure distribution design of the FBG in the insert and the mounting hole is completed, and the FBG is numbered.

In the insert clamping structure, comparing the test results of No. 1 to 12 FBGs, it can be seen that the relationship between the axial position and the direction of stress is very important. The effect of FBG's response effect is very obvious. According to the positive and negative values of the test, it can also be concluded that when the stress distribution position is in the compression transition state, its value is negative, and when it is in the tensile state, its value is positive. By comparing No. 1, 5, 9 and No. 4, 8, and 12 FBGs, it can be seen that the stress distribution of the insert is affected by the depth of the insertion position. The more inward the stress value is, the greater the position deviation is. It can be seen from FBG No. 14, 16, 18, and 20 that there is an obvious stress gradient in the area of the mounting hole, which is basically consistent with the simulation results. It can be seen from the test results that the system has an obvious response law to the position deviation caused by the stress change, and the inversion accuracy is also compared with the visual inspection system. The relative error is concentrated between 4.0% and 9.0%, which has good stability. The experiment is expressed by the comparison relationship between stress and wavelength offset value and position offset value in the range of 0–400 N. Four groups of FBGs were selected for the comparison detection position, and there were No. 1 and No. 2, No. 11 and No. 12, No. 13 and No. 15, No. 14 and No. 16. The test changes are shown in Figure 3.

The corresponding relationship between the wavelength offset and the position offset is shown in Figure 3A. The two groups of orthogonally distributed FBGs are No. 1 and No. 2, No. 11 and No. 12, respectively. The distribution of stress on the insert had obvious directionality, and the sensitive direction of

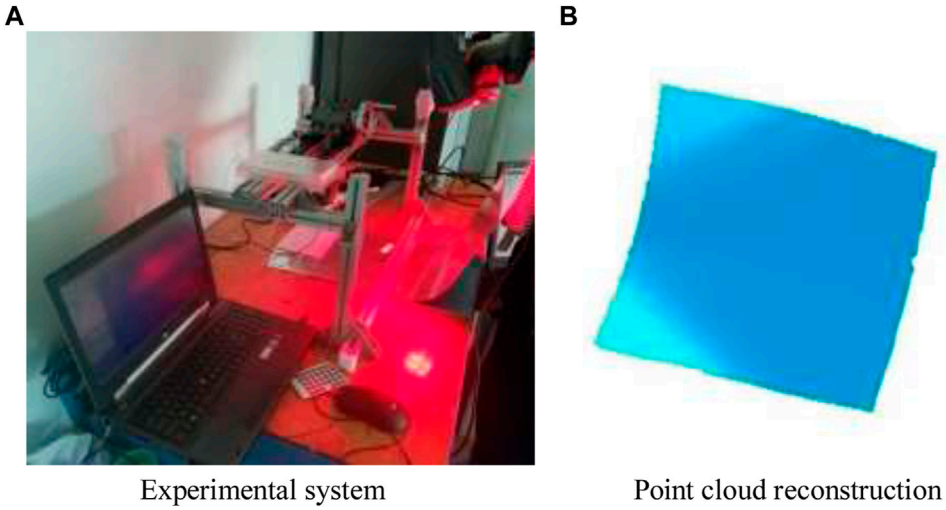

FIGURE 4
Comparative experimental system.

TABLE 1 Position test data.

Force/N	Deformation degree by FBG/mm	Position deviation/mm		Force/N	Deformation degree by FBG/mm	Position deviation/mm	
		Before correction	After correction			Before correction	After correction
0	0	0.024	0.025	160	2.154	3.658	0.096
20	0.851	0.198	0.029	180	2.684	4.035	0.115
40	1.254	0.266	0.035	200	3.148	4.426	0.129
60	1.634	0.651	0.042	220	3.587	4.869	0.135
80	2.012	0.955	0.049	240	4.068	5.261	0.139
100	2.451	1.369	0.057	260	4.517	5.635	0.152
120	2.866	1.533	0.069	280	4.928	6.025	0.168
140	3.171	1.952	0.081	300	5.248	6.415	0.197

FBG No. 1 and No. 12 is consistent with the axial direction of FBG, so they had a good response. No. 2 and No. 11 were basically unchanged. It can be seen that when the force is applied perpendicular to the current force direction, the test result is just the opposite. For the mounting holes, the corresponding relationship between the wavelength offset and the position offset is shown in Figure 3B. The two groups of orthogonally distributed FBGs were No. 13 and No. 15, No. 14, and No. 16 respectively, the distribution of stress on the mounting hole also had obvious directionality, FBGs No. 14 and No. 16 are sensitive test points, and FBG No. 13 and No. 15 were insensitive points. For FBGs No. 1, No. 12, No. 14, No. 16, the fitting curve was basically close to linear, so the wavelength offset and position offset of the system in this stress test interval are linear functions. The center wavelength of the wave can effectively compensate the deviation of the assembly position, which verifies the feasibility of the system.

5.3 Comparative experiment analysis

In order to verify that the optical fiber sensing system can provide trajectory correction data for the assembly control module, the test data of R1X 3D laser scanner is used as the standard test data, with a sight distance of 50.0 cm and an accuracy of 120 μm, which can accurately reflect the assembly the position trajectory of the structure. The comparison experiment is shown in Figure 4.

A three-dimensional strain field monitoring system based on FBG sensors is established, and the physical diagram of the experimental device is shown in Figure 4. The type of FBG strain sensor used in the experiment; the bandwidth of the six sensors is 0.213 nm; the edge-to-mode rejection ratio is 16.21 dB; the length of the grid region is 20mm; , 1,536.124, 1,540.347, 1,542.428, 1,546.758, and 1,549.224 nm. The target points for comparing the position information are pasted on the assembly

structure, so as to analyze the position trajectory test accuracy of the method. The thickness of the structural parts used in the test is 20.0 mm, and the diameter of the axle is 40.0 mm, which is smaller than the simulation body. Therefore, considering its structural bearing capacity and avoiding plastic deformation, the force strength used in the test is from 10 to 200 N, and the test results are deviated. The degree is shown in Table 1.

In Table 1, when the external force gradually increases, the maximum position offset of the test position also increases, which can be known by linear fitting. It can be seen that in the range of 0–300.0 N, the relationship between the deformation offset and the applied force satisfies the change relationship of 0.0214 mm/N. The mean absolute value of the test error using this system is 0.124 mm, the maximum relative error is 1.92%, and the mean value is −0.96%. And from the distribution of test data, it can be seen that with the increase of the force, the test error decreases significantly. The analysis believes that this is because the increase of the test stress increases the signal energy. Compared with the basic white noise, the overall signal-to-noise ratio is improved. The average relative error is about −0.96%, and it meets the design requirements. Before and after correction, the distance deviation between the assembly position and the digital analog position has been significantly improved. With the increase of external stress, the effect of correction becomes more and more obvious. When the stress is 300 N, the average position deviation before correction is 6.415 mm, while after correction, it is only 0.197. The position deviation between the test point and the digital analog has been reduced from 2.953 to 0.095 mm. Correction can significantly suppress positional deviation over the entire stress application range.

5 Conclusion

The optical fiber sensor network is applied in the field of trajectory correction of assembly by taking advantage of the characteristics of small size, high sensitivity and anti-electromagnetic interference. The sensor array corresponding to the assembly structure is designed, and the stress distribution under different assembly abnormal conditions is simulated and analyzed. The experiment applies optical fiber sensing data to three-dimensional point cloud reconstruction from laser scanning, and obtains a target surface reconstruction model with higher positional accuracy. The experimental results show that the position deviation accuracy of the system is close to the average relative error of standard test data, which meets the design requirements. The system has certain application prospects in the trajectory correction of assembly.

Data availability statement

The original contributions presented in the study are included in the article/Supplementary Material, further inquiries can be directed to the corresponding author.

Author contributions

WD proposes the idea of combining optical fiber and laser scanning; ML deduced and calculated the mathematical models of two kinds of data fusion, and FL simulated and analyzed the design; YG and WQ completed the test of optical fiber sensing; HZ completed the laser scanning test. All authors contributed to the article and approved the submitted version.

Funding

This work was supported in part by Teacher Education Fund of Xinzhou Teachers University (JZ201701).

Conflict of interest

The authors declare that the research was conducted in the absence of any commercial or financial relationships that could be construed as a potential conflict of interest.

Publisher's note

All claims expressed in this article are solely those of the authors and do not necessarily represent those of their affiliated organizations, or those of the publisher, the editors and the reviewers. Any product that may be evaluated in this article, or claim that may be made by its manufacturer, is not guaranteed or endorsed by the publisher.

References

1. Mesquita E, Pereira L-I, Theodosiou A, Alberto N, Melo J, Marques C, et al. Optical sensors for bond-slip characterization and monitoring of RC structures. *Sensors Actuators A: Phys* (2018) 280(1):332–9. doi:10.1016/j.sna.2018.07.042

2. Zhi-chao L, Jin-hua Y, Zhang L, et al. Granary temperature measurement network based on chirped FBG. *Spectrosc Spectral Anal* (2016) 36(10):3377–80.

3. Sun B, Li J, Zhang W. Fiber Bragg grating sensor. *Opt Fiber Sensing Struct Health Monit Technol* (2019) 26(4):77–148.

4. Sun L, Hao H, Zhang BB, Ren B, Li J. Strain transfer analysis of embedded fiber Bragg grating strain sensor. *J Test Eval* (2016) 44(6):20140388–2320. doi:10.1520/jte20140388

5. Wang J, Liu Z, Lin X, et al. Fiber Bragg grating strain detection system for digital calibration. *Laser Technol* (2020) 44(5):570–4.

6. Qu D, Sun G, Hong L, et al. Optical fiber sensing and reconstruction method for deformable wing flexible skin shape. *J Instrument Instrument* (2018) 39(2):460–40.

7. Zhi-chao L, Zhang L-J, Jin-hua Y, et al. Research on Bragg spectral distribution based on refractive index modulation matrix. *Spectrosc Spectral Anal* (2018) 32(12): 3718–23.

8. Zhao Z, Bai Z, Jin D, Qi Y, Ding J, Yan B, et al. Narrow laser-linewidth measurement using short delay self-heterodyne interferometry. *Opt Express* (2022) 30(17):30600–10. doi:10.1364/OE.455028

9. Zhao Z, Bai Z, Jin D, Chen X, Qi Y, Ding J, et al. The influence of noise floor on the measurement of laser linewidth using short-delay-length self-heterodyne/homodyne techniques, *Micromachines* (2022) 13(8): 1311. doi:10.3390/mi13081311

10. Chen H, Bai Z, Cai Y, Yang X, Ding J, Qi Y, et al. Order controllable enhanced stimulated Brillouin scattering utilizing cascaded diamond Raman conversion. *Appl Phys Lett* (2023) 122(9):092202. doi:10.1063/5.0137542

11. Jin D, Bai Z, Li M, Yang X, Wang Y, Mildren RP, et al. Modeling and characterization of high-power single frequency free-space Brillouin lasers. *Opt Express* (2023) 31(2):2942–55. doi:10.1364/oe.476759

12. Mulle M, Yudhanto A, Lubineau G, Yaldiz R, Schijve W, Verghese N. Internal strain assessment using FBGs in a thermoplastic composite subjected to quasi-static indentation and low-velocity impact. *Compos Structures* (2019) 215(32):305–16. doi:10.1016/j.compstruct.2019.02.085

13. Al A, Yasser M, Tait MJ. Fiber-reinforced elastomeric isolators for the seismic isolation of bridges. *Compos Structures* (2016) 160(7):300–11.

14. Leal-Junior AG, Díaz CAR, Anselmo F, Marques C, Ribeiro MR, Pontes MJ. Simultaneous measurement of pressure and temperature with a single FBG embedded in a polymer diaphragm. *Opt Laser Technol* (2019) 112(93):77–84. doi:10.1016/j.optlastec.2018.11.013

15. Guo YX, Li X, Kong JY, Zhang Zan-yun 张, Qin Li 秦丽. Sliding type fiber Bragg grating displacement sensor. *Opt Precision Eng* (2017) 25(1):50–8. doi:10.3788/ope.20172501.0050

frontiers | Frontiers in Physics

TYPE Original Research
PUBLISHED 03 May 2023
DOI 10.3389/fphy.2023.1146208

OPEN ACCESS

EDITED BY
Bofeng Zhu,
Nanyang Technological University, Singapore

REVIEWED BY
Lei Gao,
Chongqing University, China
Zhenxu Bai,
Hebei University of Technology, China

*CORRESPONDENCE
Wenguang Liu,
lwg.kevin@163.com
Xiaolin Wang,
chinaphotonics@163.com

RECEIVED 17 January 2023
ACCEPTED 20 April 2023
PUBLISHED 03 May 2023

CITATION
Chai J, Liu W, Wang X, Zhou Q, Xie K, Wen Y, Zhang J, Liu P, Zhang H, Zhang D, Jiang Z and Zhao G (2023), High-speed modal analysis of dynamic modal coupling in fiber laser oscillator. *Front. Phys.* 11:1146208. doi: 10.3389/fphy.2023.1146208

High-speed modal analysis of dynamic modal coupling in fiber laser oscillator

Junyu Chai[1,2,3], Wenguang Liu[1,2,3]*, Xiaolin Wang[1,2,3]*, Qiong Zhou[1,2,3], Kun Xie[4], Yujun Wen[1,2,3], Jiangbin Zhang[1,2,3], Pengfei Liu[1,2,3], Hanwei Zhang[1,2,3], Dan Zhang[1,2,3], Zongfu Jiang[1,2,3] and Guomin Zhao[1,2,3]

[1]College of Advanced Interdisciplinary Studies, National University of Defense Technology, Changsha, China, [2]Nanhu Laser Laboratory, National University of Defense Technology, Changsha, China, [3]Hunan Provincial Key Laboratory of High Energy Laser Technology, Changsha, China, [4]Xi'an Satellite Control Center, Xi'an, China

Up till now, the spatial and temporal dynamics of transverse mode instability (TMI) in fiber laser oscillator have increasingly attracted a worldwide attention. Here, we develop a high-speed modal decomposition (MD) system to analyze the modal coupling for fiber laser oscillator above the TMI threshold. A set of angular-multiplexing transmission functions (TFs) are designed for simultaneous MD and monitoring the far-field beam profile. The TMI threshold of the deployed fiber laser oscillator is 181 W at a co-pumping power (CPP) of 279 W. As the CPP increases from 318 W to 397 W, the power fluctuations of the output laser become more drastic. The changes of the far-field beam profile and the centroid of far-field spot (COFFS) indicate an increased velocity of energy transfer between modes. The high-speed MD verifies above process and analyzes the modal components, indicating that the single cycle of modal coupling decreases from 11 ms to 4 ms. Otherwise, the strong mode coupling occurs between modes with relatively large weights. The high-speed MD provides a powerful tool to research the TMI effect.

KEYWORDS

transverse mode instability, mode decomposition, modal coupling, fiber laser, optical correlation filter

1 Introduction

With the remarkable progress of high-power fiber laser (HPFL) in recent years [1, 2], the demands of large-mode-area (LMA) fibers have been increasing. The LMA fibers are commonly referred to as few mode fibers. The V-number of this fiber is normally greater than the cut-off value for single-mode operation (i.e., V = 2.405), since it has a larger core diameter than the single mode fiber (i.e., 8 μm–10 μm) [3]. This leads to an increase weight in the higher-order mode (HOM). Although the HOMs can be reduced by the bending and coiling of optical fiber, the existence of HOMs will cause transverse mode instability (TMI) [4]. When the power reaches a certain threshold, the beam quality degrades [5].

The conventional beam diagnostic methods mainly include the records of spectrum, power and beam quality. However, mode coupling in fiber laser after the occurrence of TMI has not been fully researched. Modal decomposition (MD) is used to analyze transverse

mode components in LMA fibers. In recent years, a variety of MD methods have been proposed, involving the spatially and spectrally resolved imaging (S^2) [6, 7], low-coherence interferometry [8, 9], numerical analysis [10], wavefront analysis [11], and ring-resonators [12, 13]. The method of S^2 and low-coherence interferometry are realized by measuring the interference between different transverse modes according to their different group velocities in the fiber. They are completed by spatial scanning or wavelength scanning, thus consuming several minutes [14]. For numerical analysis, it is mainly based on the iterative optimization algorithm [15]. It takes over hundreds of steps and several minutes due to the large number of optimization parameters. Even though there are several reports based on S^2 and numerical analysis with a high-speed, they need off-line data processing [16]. The wavefront analysis relies on the use of wavefront sensors [17]. The method of ring-resonators involves a piezo translator (PZT) [13]. However, the error of these two methods exceeds 10% since the measurement accuracy of HOMs cannot be guaranteed. Compared with other techniques, optical correlation filter (OCF) is suitable for high-speed MD because it only requires straightforward algebraic calculation to obtain the modal weights with a high accuracy above 95% [18]. The implementation of high-speed cameras and high-performance processors using OCF can help to achieve a fast MD.

In this paper, we propose a method of high-speed modal analysis based on OCF, which is beneficial to analyze modal coupling when the TMI occurs. A set of transmission functions (TF)s for the measurement of modal weight and monitoring far-field beam profile are designed and encoded into one computer-generated hologram (CGH). In addition to the use of conventional beam diagnostic methods, the change of modal weight with the increase of pumping power after the occurrence of TMI is monitored.

2 Theory

2.1 The modes of weakly guiding fibers

The weakly guided fibers commonly used in HPFL systems are step-index fibers (SIFs) with a small refractive index difference between the core and the cladding. In the weakly guiding approximation, the electromagnetic fields can be recognized as linearly polarized (LP) modes system [19]. The optical field of each polarization component can be expressed by using the orthogonal basis functions:

$$U(r) = \sum_{k=1}^{K} c_k \psi_k(r) \tag{1}$$

where k is the total number of modes supported by the fiber, $\psi_k(r)$ representing the set of LP eigenmodes, and the k_{th} modal coefficient c_k is shown below

$$c_k = \rho_k e^{j\varphi_k} = \iint_{R^2} d^2 r \psi_k^*(r) U(r) = \langle \psi_k, U \rangle \tag{2}$$

with ρ_k denoting the k_{th} modal amplitude, φ_k representing the k_{th} intermodal phase difference (the phase difference between the HOM and the fundamental mode). d is a sign for differentiation in the formula of integral. The modal coefficients fulfill the relation $\sum_{k=1}^{K} |c_k|^2 = \sum_{k=1}^{K} |\rho_k|^2 = 1$. Hence, the modal weight can be acquired *via* the measurement of amplitude based on modal analysis.

2.2 The MD based on OCF

The OCF is a powerful technique for modal analysis [20–22]. The core of OCF is TFs by design, which play key roles as matched filters. The TF is composed of amplitude and conjugate phase information related to eigenmode of LMA fiber laser $T_k(r) = \psi_k^*(r)$. A set of TFs can be superimposed at certain spatial frequencies for simultaneous measurement for multimode. The total TFs are expressed as follows

$$T_{total}(r) = \sum_{k=1}^{K} T_k(r) \cdot e^{iFreq_k(r)} \tag{3}$$

where, $Freq_k(r)$ denoting a certain spatial carrier frequency, which is induced to realize a spatial separation of each diffraction pattern in the Fourier plane. The total TFs are then converted into a phase-only CGH *via* certain coding process. This CGH is loaded on a spatial light modulator (SLM). When the laser beam illuminates the SLM, the beam is diffracted according to the CGH. Then, we realize the modulation of laser beam under TFs. Only the light containing the same modes as the designed filters can be diffracted and converge at the specified positions (sub-optical axes $r = 0$) in the far-field plane. e.g., when LP_{11o} mode passes its filter, LP_{11o} mode will be superposed with the filter containing its conjugate phase. Then, there is a certain intensity on the sub-optical axis of the +first order diffracted light. However, other transverse modes cannot go through LP_{11o} mode filter, and no relevant intensity can be detected at the same position. The ratios of the intensities at sub-optical axes represent the modal coefficients $I \infty |c_n|^2$. Thus, the modal weight can be directly accessible *via* a simple intensity measurement to investigate the modal coupling [23].

Since the Ytterbium (Yb)-doped fiber (YDF) of the fiber laser oscillator to be test has a core diameter of 30 μm (NA = 0.064), the supported eigenmodes at an operating wavelength λ of 1,080 nm are LP_{01}, LP_{11e}, LP_{11o}, LP_{21e}, LP_{21o}, LP_{02}, LP_{31e}, LP_{31o}, LP_{12e}, and LP_{12o}. The mode filtering can be realized *via* certain bending and coiling of fiber [24–26]. After repeated experiments, we find ten eigenmodes can be limited to six by coiling the YDF in a ∞ shape with a minimum bend diameter of 85 mm. The other four higher HOMs of LP_{31e}, LP_{31o}, LP_{12e} and LP_{12o} sustain complete transmission loss. Thus, we design a total TF which can measure the contents of six modes simultaneously. Removing the TFs of non-transmission modes can help to shrink the range of interest (ROI) of far-field camera to increase the computational efficiency. Besides, a mirror-like TF with a tilting phase is added to monitor the far-field beam profile.

$$T_{far-field}(r) = e^{iFreq_{far-field}(r)} \tag{4}$$

The final TF in our experiments can be expressed as

$$\begin{aligned} T_{final}(r) &= T_{total}(r) + T_{far-field}(r) \\ &= \sum_{k=1}^{6} T_k(r) \cdot e^{iFreq_k(r)} + e^{iFreq_{far-field}(r)} \end{aligned} \tag{5}$$

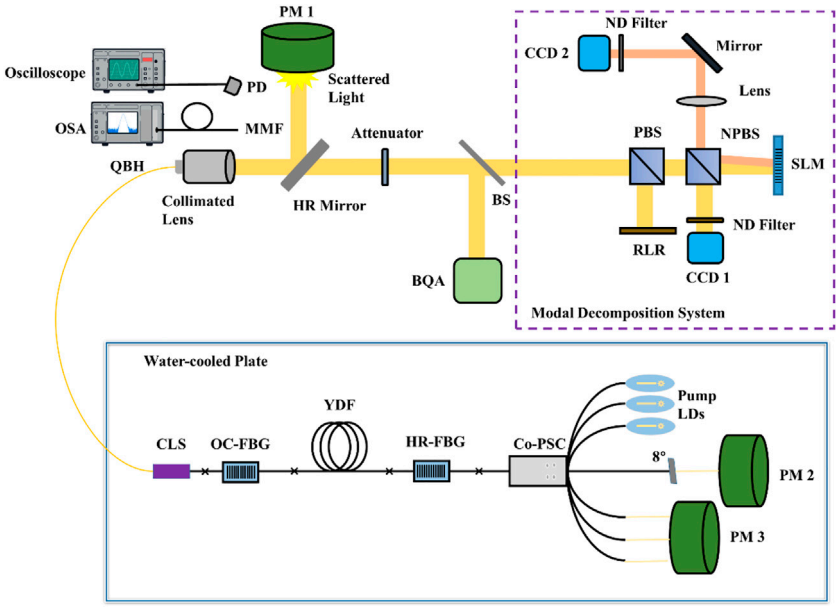

FIGURE 1
A setup of all-fiber laser oscillator and beam diagnostic system.

Then, the final TF is encoded into a phase-only CGH *via* a coding technique introduced by Arrizón et al. [27].

3 Experimental setup

The experimental system mainly involves an all-fiber laser oscillator and beam diagnostic equipment, as shown in Figure 1. The all-fiber laser oscillator is co-pumped via fiber-coupled laser diodes (LDs) with a stabilized emission wavelength of 976 nm. A number of pump LDs are grouped by a co-sided (6 + 1) × 1 pump-signal combiner (Co-PSC) and inject into the laser oscillation cavity. Three pump ports of the Co-PSC are applied, and the central pump port of the Co-PSC is angle cleaved to prevent facet reflection. The remaining three ports are not used in this experiment. The co-pumping light enters the laser cavity through a high reflection fiber Bragg grating (HR-FBG). The gain fiber is a length of ~20 m YDF with 30/400 μm core/cladding diameters (NA_{core} = 0.064), which is coiled in a ∞ shape with a minimum bend diameter of about 85 mm. The length, bend diameter and shape of YDF mainly affect TMI threshold and the number of transmission modes in the fiber. The HR-FBG is inscribed on the end of YDF, which provides a reflectivity of ~99.9% with a 3 dB bandwidth of ~4 nm around a central wavelength of ~1,080 nm. The transmitted light goes through an output coupler fiber Bragg (OC-FBG) with a reflectivity of ~10% and a 3 dB bandwidth of ~1.7 nm at a central wavelength of ~1,080 nm. Then, it is received by a length of 3 m delivery fiber (30/400 μm) and the laser beam output *via* a quartz block head (QBH). A part of the polymer cladding of delivery fiber is stripped and the inner cladding is coated with high refractive index ointment. The entire all-fiber laser oscillator is water-cooled to avoid thermal damage.

(OSA: Optical spectrum analyzer; PD: Photodiode; MMF: Multimode fiber; QBH: Quartz block head; PM: Power meter; HR: High reflection; BS: Beam splitter; BQA: Beam quality analyzer; PBS: Polarizing beam splitter; RLR: Residual light receiver; NPBS: Non-Polarizing beam splitter; ND: Neutral density; CCD1: Near-field camera; SLM: Spatial light modulator; CCD2: Far-field camera; CLS: Cladding light stripper; OC: Output coupler; FBG: Fiber Bragg grating; YDF: Ytterbium-doped fiber; Co-PSC: Co-sided pump-signal combiner; LD: Laser diode).

In the experiment, the spectrum, temporal trace, beam quality, and modal content are monitored simultaneously as shown in Figure 1. The collimated beam first passes through a high reflection (HR) mirror. The 99.99% of the light is reflected into the power meter 1 (PM1), and the remaining 0.01% of the light is weaken by the attenuator and then split into two beams via a beam splitter (BS). A beam of light directs to the beam quality analyzer (BQA) to obtain the data of M^2, and the second beam of light enters the MD system. The near-field beam profile is monitored by charge-coupled device 1 (CCD1, pixel size: 10 μm, 62.23 fps) for the calibration of the entire optical path before the experiment and the investigation of the beam at a fixed time under test. The specially designed CGH is loaded on the SLM (resolution: 1920 × 1,152, pixel size: 9.2 μm). The beam illuminates the CGH, and then the reflected light is Fourier transformed by a lens. The +first order diffracted light in the far-field plane is recorded *via* a CCD2 (pixel size: 4.5 μm, 2000 fps) for modal analysis. Besides, the scattered light from the photosensitive surface of PM1 is received by optical spectrum analyzer (OSA), photodetector (PD) and oscilloscope to record the data of spectrum and temporal trace. PM2 and PM3 are applied to monitor the power vibrations of the end-face reflected light and the residual pump light.

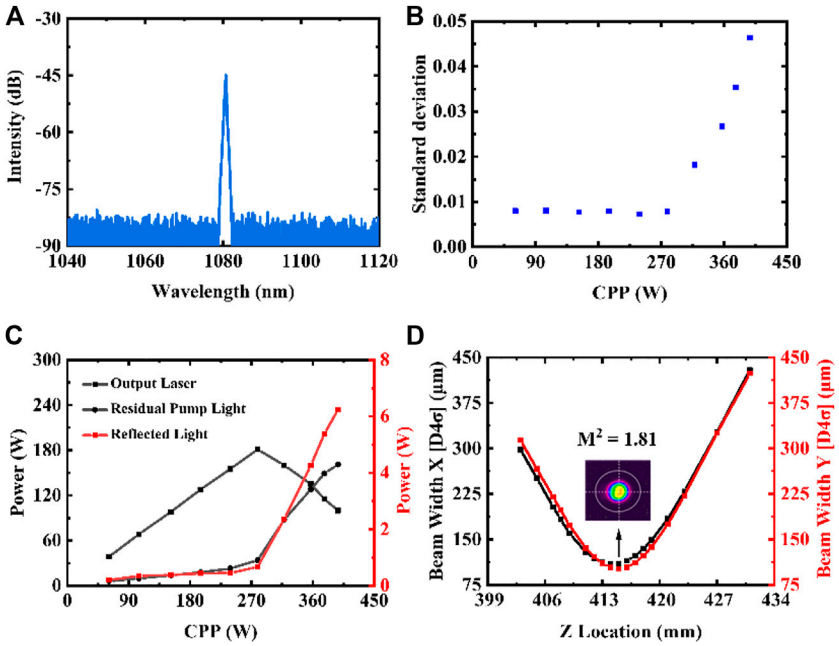

FIGURE 2
Laser output characteristics. **(A)** The spectrum at 100 W. **(B)** The STD variation of the temporal trace with the increase of CPP. **(C)** The power changes of output laser, residual pump light and end-face reflected light with the increase of CPP. **(D)** The beam quality at 181 W.

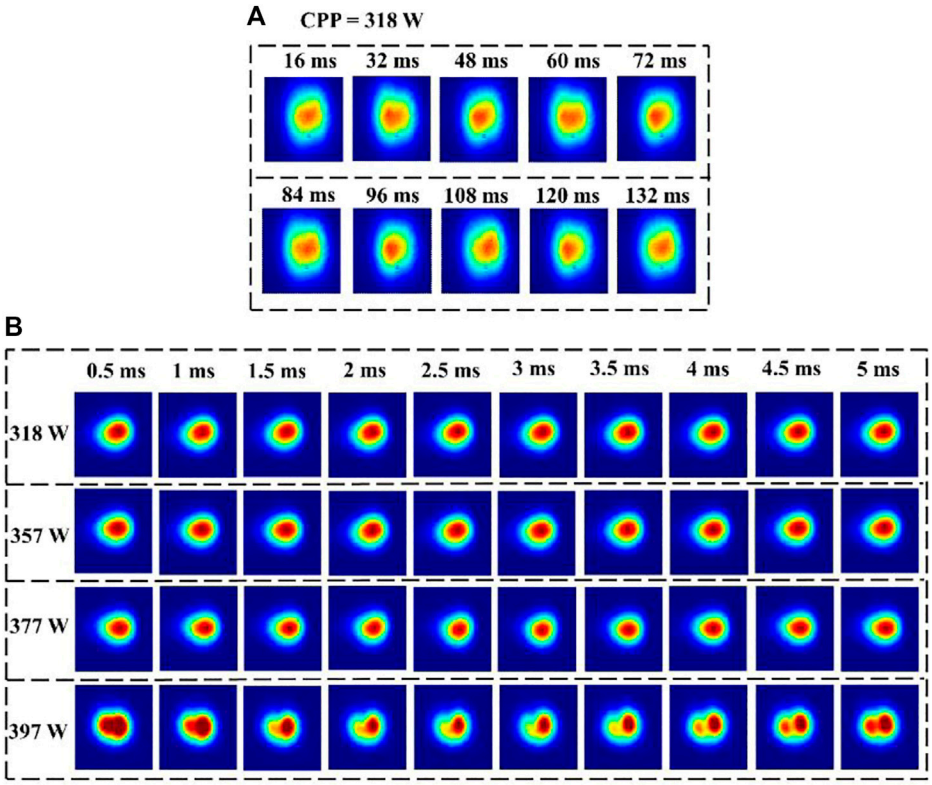

FIGURE 3
The beam profiles of near-field **(A)** and far-field **(B)** captured from CCD1 and CCD2.

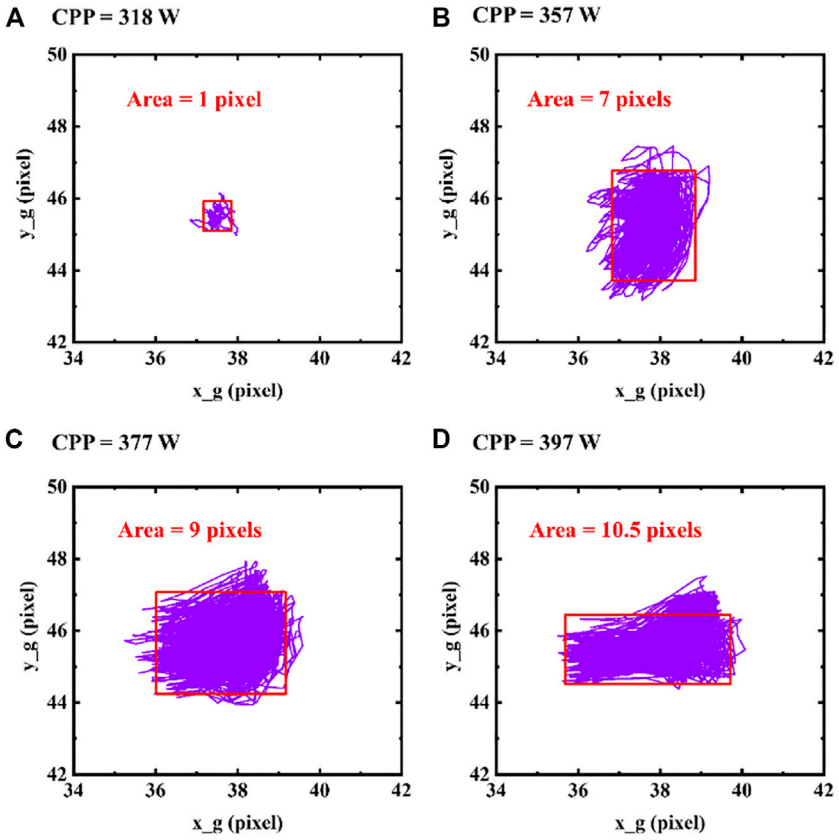

FIGURE 4
The fluctuation of the COFFS at the CPP of **(A)** 318 W, **(B)** 357 W, **(C)** 377 W, and **(D)** 397 W.

4 Results and discussion

The spectrum, output power and beam quality are measured in the experiment. Figure 2A depicts that the central wavelength of the output laser at 100 W is around 1,080 nm, and the full width at half maxima (FWHM) is ~2 nm. Figure 2B shows the change of standard deviation (STD) of the temporal trace with the increase of co-pumping power (CPP). This fiber laser oscillator has a TMI threshold of 181 W under a CPP of 279 W. The power changes of output laser, residual pump light and end-face reflected light with the increase of CPP are depicted in Figure 2C. After the occurrence of TMI, the output power continues to decrease from 181 W to 100 W with the increase of CPP from 318 W to 397 W. The decrease of the output laser results in the increase of residual pump light and end-face reflected light. Compared with drastic vibrations of the output laser and the residual pump light, the change of the end-face reflected light is relatively weak, i.e., only from 0.7 W to 6.2 W. The is because that the central pump port of Co-PSC is cleaved with an angle of 8, which weakens the return light. When there is no TMI, the beam quality remains at 1.55. Figure 2D shows that the beam quality is about 1.81 at the TMI threshold of 181 W.

When TMI occurs, the near-field beam profile is captured *via* CCD1. Figure 3A extracts ten frames of the pictures during 132 m at 318 W. Even the low-speed of 63.2 fps can catch the beam fluctuation. The far-field beam profile is recorded *via* CCD2 with a speed of 2000 fps. Figure 3B depicts the variation in the first 5 ms at multiple CPPs (318 W, 357 W, 377 W, and 397 W). It can be clearly seen that the velocity of energy transfer is accelerated with the increase of CPP. Especially when the CPP is 397W, the far-field beam profile is obviously split from one lobe to two lobes. This implies intense modal couplings between fundamental mode and higher-order modes.

To clearly investigate beam fluctuation above the TMI threshold, we compute the centroid of the far-field spot (COFFS) at each CPP, as shown in Figure 4. At the beginning of TMI, the area of COFFS is only within one pixel (Figure 4A). Then, it is mainly distributed within seven pixels (Figure 4B) and nine pixels (Figure 4C) at the CPP of 357 W and 377 W. As the CPP reaches 397 W, it is further broadened to ten point five pixels (Figure 4D). This gradual expansion implies an intensified strength of the multimode coupling.

To analyze the change of modal component, we carry out a high-speed MD with a rate of 2 kHz.The MD results are shown in Figure 5, and the accuracies are about 98%. The modal coupling reflects the energy transfer between multimode and it clearly shows periodic change within the selected 50 ms window at multiple CPPs. At the onset of TMI, modal coupling is mainly among LP_{01}, LP_{11e}, LP_{11o}, and LP_{02}, while LP_{21e} and LP_{21o} are relatively stable (Figure 5A). As the CPP increases from 318 W to 397W, the single coupling cycle shortens from 11 ms to 4 ms, indicating an increased velocity of energy transfer

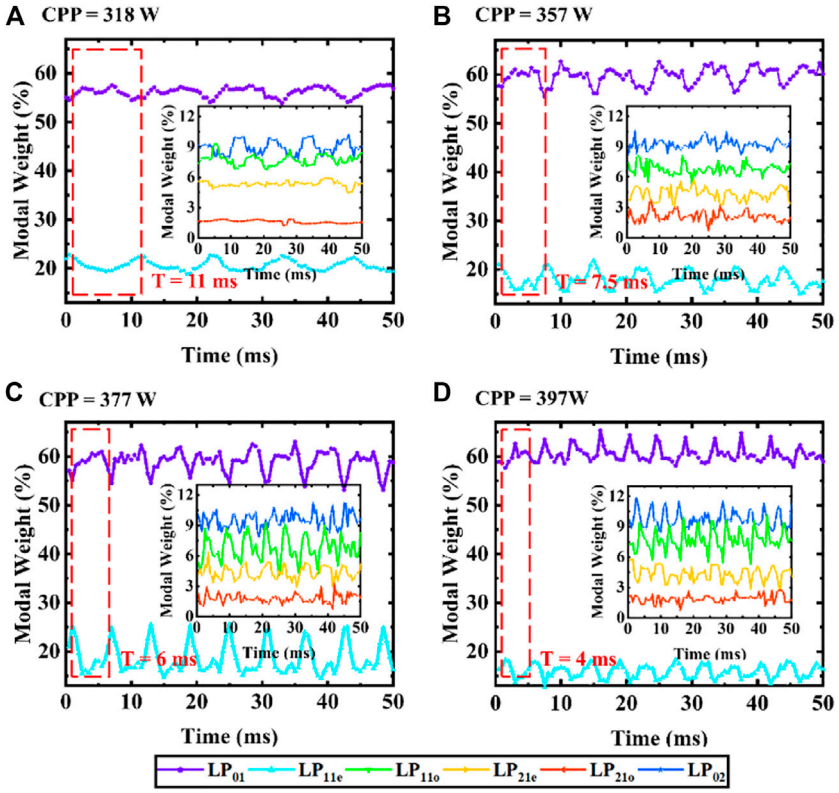

FIGURE 5
MD results in 50 ms windows at the CPP of **(A)** 318 W, **(B)** 357 W, **(C)** 377 W, and **(D)** 397 W.

(Figure 5A–D). More modes (LP_{21e} and LP_{21o}) are involved in the coupling process from 357 W. The MD results demonstrate the modal coupling becomes complex with the increase of CPP. Otherwise, there is a drastic modal coupling between modes with large modal weights (LP_{01}, LP_{11e}, LP_{11o}, and LP_{02}), while those with less modal weight (LP_{21e} and LP_{21o}) have relatively weak coupling. Thus, it is inferred that TMI can be suppressed by mainly breaking the coupling between modes with large modal weight.

Furthermore, the rate of MD depends on the performance of far-field camera and processors. The high-performance processors in current system are based on FPGA with a bandwidth of 100 kHz. To realize a faster MD for investigating TMI with even faster coupling speed, multi-element PD with pin-holes can be used to replace the far-field camera. Each beam of + first diffracted light with modal information illuminates on a photosensitive surface. Then, the intensities on the sub-optical axes are collected by the multi-element PD with pin holes, and they are transmitted to the FPGA for the calculation of modal weights. Then, the performance of this MD system can be improved to~100 kHz with current processors. However, it is complicated to calibrate the optical path and locate the modal detection point, since the beam profile cannot be viewed *via* the multi-element PD. Besides, the power of diffracted light behind the hole is weak to a few nanowatts and hard to be detected, thus an extra system for weak opto-electrical signal processing is needed.

5 Conclusion

In summary, we present a high-speed MD to characteristic modal coupling properties above the TMI threshold. A set of angular-multiplexing TFs is designed for simultaneous MD and monitoring the far-field beam profile. The TMI threshold of the deployed fiber laser oscillator is 181 W at a CPP of 279 W. We find the velocity of energy transfer accelerates with the increase of CPP from 318 W to 397 W. The high-speed MD demonstrates this and analyzes the change of modal components. The MD results show the single cycle of modal coupling decreases from 11 ms to 4 ms. The strong modal coupling occurs mainly between modes with relatively large weight. The characteristic of modal coupling obtained from high-speed MD is conducive to evaluate the effect of TMI mitigation in fiber lasers.

Data availability statement

The original contributions presented in the study are included in the article/supplementary material, further inquiries can be directed to the corresponding author.

Author contributions

Investigation, JC, WL, and XW; resources, QZ, PL, HZ, DZ, ZJ, KX, and YW; writing—original draft preparation, JC; writing—review and

editing, JC, JZ, and XW; supervision, WL and GZ. All authors have read and agreed to the published version of the manuscript.

Funding

This work was supported by National Natural Science Foundation of China (12074432, 12204540); Science and Technology Innovation Program of Hunan Province (2021RC3038).

Acknowledgments

The authors would like to thank Lingfa Zeng, Penglin Zhong, and Xiaoyong Xu for their assistance in the whole experiment.

Conflict of interest

The authors declare that the research was conducted in the absence of any commercial or financial relationships that could be construed as a potential conflict of interest.

Publisher's note

All claims expressed in this article are solely those of the authors and do not necessarily represent those of their affiliated organizations, or those of the publisher, the editors and the reviewers. Any product that may be evaluated in this article, or claim that may be made by its manufacturer, is not guaranteed or endorsed by the publisher.

References

1. Nilsson J, Payne DN. High-power fiber lasers. *Science* (2011) 332:921–2. doi:10.1126/science.1194863

2. Zervas MN, Codemard CA. High power fiber lasers: A review. *IEEE J Sel Top Quan Electron.* (2014) 20:219–41. doi:10.1109/jstqe.2014.2321279

3. Richardson DJ, Fini JM, Nelson LE. Space-division multiplexing in optical fibres. *Nat Photon* (2013) 7(5):354–62. doi:10.1038/nphoton.2013.94

4. Jauregui C, Limpert J, Tünnermann A. High-power fibre lasers. *Nat Photon* (2013) 7(11):861–7. doi:10.1038/nphoton.2013.273

5. Jauregui C, Stihler C, Limpert J. Transverse mode instability. *Adv Opt Photon* (2020) 12:429–84. doi:10.1364/aop.385184

6. Nicholson JW, Yablon AD, Ghalmi S. Spatially and spectrally resolved imaging of modal content in large-mode-area fibers. *Opt Express* (2008) 16:7233–43. doi:10.1364/oe.16.007233

7. Nicholson JW, Yablon AD, Fini JM, Mermelstein MD. Measuring the modal content of large-mode-area fibers. *IEEE J Sel Top Quan Electron.* (2009) 15:61–70. doi:10.1109/jstqe.2008.2010239

8. Ma YZ, Sych Y, Onishchukov G, Ramachandran S, Peschel U, Schmauss B, et al. Fiber-modes and fiber-anisotropy characterization using low-coherence interferometry. *Appl Phys B* (2009) 96:345–53. doi:10.1007/s00340-009-3517-9

9. Demas J, Ramachandran S. Sub-second mode measurement of fibers using C2 imaging. *Opt Express* (2014) 22:23043–56. doi:10.1364/oe.22.023043

10. Brüning R, Gelszinnis P, Schulzes C, Flamm D, Duparré M. Comparative analysis of numerical methods for the mode analysis of laser beams. *Appl Opt* (2013) 52:7769–77. doi:10.1364/ao.52.007769

11. Paurisse M, Lévèque L, Hanna M, Druon F, Georges P. Complete measurement of fiber modal content by wavefront analysis. *Opt Express* (2012) 20:4074–84. doi:10.1364/oe.20.004074

12. Andermahr N, Theeg T, Fallnich C. Novel approach for polarization-sensitive measurements of transverse modes in few-mode optical fibers. *Appl Phys B* (2008) 91:353–7. doi:10.1007/s00340-008-3011-9

13. Andermahr N, Fallnich C. Interaction of transverse modes in a single-frequency few-mode fiber amplifier caused by local gain saturation. *Opt Express* (2008) 16:8678–84. doi:10.1364/oe.16.008678

14. Gray DR, Sandoghchi SR, Wheeler NV, Jasion GT, Wooler JP, Petrovich MN, et al. Towards real-time mode content characterization of multimode fibers. In: 2014 The European Conference on Optical Communication (ECOC); 21-25 September, 2014; Cannes, France (2014). p. 1–3.

15. Shapira O, Abouraddy AF, Joannopoulos JD, Fink Y. Complete modal decomposition for optical waveguides. *Phys Rev Lett* (2005) 94:143902. doi:10.1103/physrevlett.94.143902

16. Stutzki F, Otto H-J, Jansen F, Gaida C, Jauregui C, Limpert J, et al. High-speed modal decomposition of mode instabilities in high-power fiber lasers. *Opt Lett* (2011) 36:4572–4. doi:10.1364/ol.36.004572

17. Lizhi D, Wenjin L, Ping Y, Hu Y, Xiang L, Shuai W, et al. Transformations of high-order mode Hermite–Gaussian beams using a deformable mirror. *Laser Phys* (2013) 23:035004. doi:10.1088/1054-660x/23/3/035004

18. Xie K, Liu W, Zhou Q, Huang L, Jiang Z, Xi F, et al. Adaptive phase correction of dynamic multimode beam based on modal decomposition. *Opt Express* (2019) 27:13793–802. doi:10.1364/oe.27.013793

19. Flamm D, Schulze C, Naidoo D, Schroter S, Forbes A, Duparre M. All-digital holographic tool for mode excitation and analysis in optical fibers. *J Lightwave Technol* (2013) 31(7):1023–32. doi:10.1109/jlt.2013.2240258

20. Kaiser T, Flamm D, Schröter S, Duparré M. Complete modal decomposition for optical fibers using CGH-based correlation filters. *Opt Express* (2009) 17:9347–56. doi:10.1364/oe.17.009347

21. Flamm D, Schmidt OA, Schulze C, Borchardt J, Kaiser T, Schröter S, et al. Measuring the spatial polarization distribution of multimode beams emerging from passive step-index large-mode-area fibers. *Opt Lett* (2010) 35:3429–31. doi:10.1364/ol.35.003429

22. Schulze C, Naidoo D, Flamm D, Schmidt OA, Forbes A, Duparré M. Wavefront reconstruction by modal decomposition. *Opt Express* (2012) 20:19714–25. doi:10.1364/oe.20.019714

23. Chai J, Liu W, Zhang J, Xie K, Lu Y, Li C, et al. Influence of aberrations on modal decomposition for LMA fiber laser systems. *Front Phys* (2022) 9. doi:10.3389/fphy.2021.796666

24. Hansen K, Alkeskjold T, Broeng J, Lægsgaard J. Theoretical analysis of mode instability in high-power fiber amplifiers. *Opt Express* (2013) 21(2):1944–71. doi:10.1364/oe.21.001944

25. Tao R, Wang X, Xiao H, Zhou P, Liu Z. Theoretical study of the threshold power of mode instability in high-power fiber amplifiers. *Acta Opt Sin* (2014) 34(1):0114002. doi:10.3788/aos201434.0114002

26. Tao R, Su R, Ma P, Wang X, Xiao H, Zhou P. Suppressing mode instabilities by optimizing the fiber coiling methods. *Laser Phys Lett* (2017) 14(2):025101. doi:10.1088/1612-202x/aa4fbf

27. Arrizón V, Ruiz U, Carrada R, González LA. Pixelated phase computer holograms for the accurate encoding of scalar complex fields. *J Opt Soc Am A* (2007) 24:3500–7. doi:10.1364/josaa.24.003500

frontiers | Frontiers in Physics

TYPE Brief Research Report
PUBLISHED 05 May 2023
DOI 10.3389/fphy.2023.1195052

OPEN ACCESS

EDITED BY
Bofeng Zhu,
Nanyang Technological University,
Singapore

REVIEWED BY
Xiao Han,
Harbin Engineering University, China
Huiying Zhang,
Jilin Institute of Chemical Technology,
China

*CORRESPONDENCE
Shoufeng Tong,
tsf1998@sina.com
Peng Zhang,
zp@cust.edu.cn

RECEIVED 28 March 2023
ACCEPTED 19 April 2023
PUBLISHED 05 May 2023

CITATION
Dong B, Tong S, Zhang P and Wang J (2023), Research on underwater wireless dynamic optical communication system based on PPM modulation.
Front. Phys. 11:1195052.
doi: 10.3389/fphy.2023.1195052

Research on underwater wireless dynamic optical communication system based on PPM modulation

Bing Dong[1], Shoufeng Tong[1]*, Peng Zhang[1]* and Jiaxing Wang[2]

[1]National and Local Joint Engineering Research Center of Space Optoelectronics Technology, Changchun University of Science and Technology, Changchun, China, [2]College of Optoelectronic Engineering, Changchun University of Science and Technology, Changchun, China

In order to achieve underwater wireless dynamic optical communication, a laser communication system is proposed based on Pulse Position Modulation (PPM). In order to achieve underwater laser communication accurately, the mathematical model of underwater laser communication was constructed with small angle analysis. The pulse position modulation demodulation algorithm is designed, and the workflow of modulation and demodulation is given in the transmit module and the receive module. In the experiment, Lumileds-470 nm light source was selected for data communication for testing at a communication rate of 15 Mbp/s. In the servo control process, the square wave signal used for stepping motor drive had a stable amplitude output and a stable time width. It can well simulate the testing process of underwater dynamic scanning. In the experiment, laser light spots were obtained under different attenuation states, and the characteristics of the light spot distribution were analyzed. The numerical reconstruction of the light spot energy was completed in MATLAB. Three types of light attenuators, 1.0%, 0.1%, and 0.01%, were used to simulate different light attenuations underwater. The test results show that the system error rate is better than 10^{-6} when attenuation chip is 1.0%. When attenuation chip is 0.1%, the error rate of the system is reduced to 10^{-4}. When attenuation chip is 0.01%, a valid signal cannot be obtained by the system. The feasibility of the system is verified.

KEYWORDS

laser communication, underwater communication, servo control, dynamic testing, PPM

1 Introduction

Underwater wireless communication technology is widely used in resource exploration [1], abnormal sea state monitoring [2], sensor monitoring [3], underwater imaging [4], underwater robots [5], and airspace integration [6]. It is important advantages for blue or green laser, such as good penetration ability, strong anti-interference, large communication depth, and high transmission rate in seawater. It has become a research hotspot.

The characteristics of underwater laser communication include: a) high transmission rate. Due to the use of high-frequency information transmission, the transmission rate can reach Mbit/s, far due to traditional acoustic equipment. b) Large information capacity. The blue light of laser communication is about 620 THz, which can support the construction of large capacity link systems. It has the underwater transmission requirements of image signals and multi-channel video signals, and its high bit rate is generally around the GHz level. c) Strong anti-interference. The laser transmission process is not affected by electromagnetic interference. It is not significantly affected by seawater temperature, concentration, etc. d) High safety and density. Light wave has strong directionality and small beam divergence

angle. If the communication signal is truncated, the receiving end will lose the signal, which is easy to be detected in a timely manner, so its security and confidentiality are very good. e) The system structure is compact. Underwater laser communication systems have a compact structure and low power, making them more concealable.

Duntley [7] found that lasers with a wavelength range of 470–525 nm can effectively reduce the light wave absorption of seawater. Shimura S [8] had experimentally verified that the visible light band has a low loss window, and its propagation loss was only 1% of that of other light waves. This discovery will have greatly advanced for the underwater laser communication research. Tivey et al. [9] developed an underwater wireless communication system. It still had the ability to transmit data underwater. The system achieves effective communication of signals within a range of 5 m. Huang A P et al. [10] designed an optical communication system with acoustic systems. This system used low-power receivers and it could achieve underwater data transmission of 10–20 Mbit/s within 100 m. Campagnaro F et al. [11] used a 405 nm wavelength laser to conduct communication tests in 4.8 m long clear water, when the communication rate is 1.45 Gbit/s, the bit error rate is only 9.1×10^{-4}. Fu et al. [12] studied the impact of communication aperture on the bit error rate of underwater wireless optical communication systems under medium intensity turbulence. Han et al. [13] used electro-optical crystal modulation to generate communication signals, and completed the extinction characteristics of underwater communication systems on modulated signals by Monte Carlo method. Based on the analysis of transmission link span and laser divergence angle, Vali et al. [14] analyzed and discussed the effects of system aperture and field of view on underwater communication under turbulent conditions.

In summary, this paper studies an underwater laser communication system based on PPM (Pulse Position Modulation [15]) modulation. The system uses a servo mechanism to align the optical path at both ends of the laser communication, then uses PPM modulation technology to complete data communication, and simulates underwater communication by using an attenuator.

2 Underwater laser communication system design

In this paper, a blue laser communication experimental system based on PPM modulation and demodulation is constructed. The overall structure of the system is shown in Figure 1.

The entire laser communication system consists of a transmitter and a receiver. The transmitter is mainly composed of a data transmission module, a PPM modulator, and a laser. The data transmission module is used to input the data to be transmitted and transmit it to the PPM modulator through USB interface. The PPM modulator converts the modulated data into an output signal and drives the laser to emit light through the laser interface. A laser beam emits a signal in the form of a carrier wave. The laser adopts a tunable semiconductor blue laser with a central wavelength of 470 nm and a maximum communication rate of 15 Mbps. In the experiment, in order to simulate the optical attenuation effect from 10 to 20 m underwater, variable optical attenuators were added to the communication path, achieving 30%, 50%, and 80% optical attenuation, respectively. In actual experiments, the distance between the two laser communication modules after using the attenuator will be set to be 2–4 m.

The receiving module is mainly composed of a receiving optical path, a PPM demodulator, and a data receiving terminal. After the certain attenuation, the laser pulse containing modulation information is transmitted to the receiving optical path. After photoelectric conversion is completed by the APD (Avalanche Photodetector [16]) detector, it is sent to the PPM demodulation module. The demodulated data can be displayed on the LCD panel of the PPM demodulator. Data can also be transferred to a computer through a USB port to complete operations such as storing and recording.

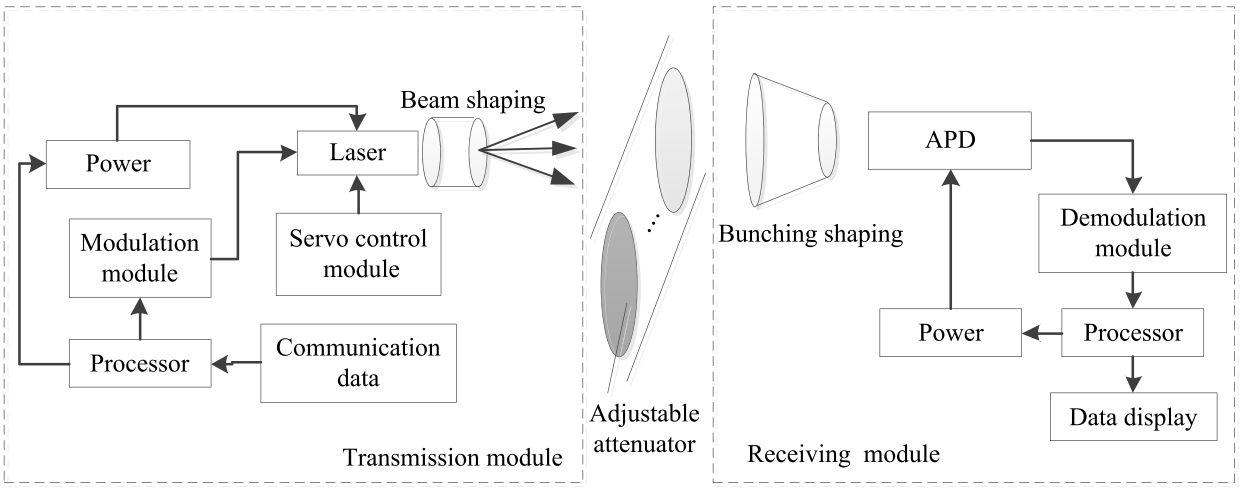

FIGURE 1
Receiving and transmitting module of underwater laser communication system.

3 Small angle analysis mathematical model

Small angle analysis is a typical method for studying underwater laser propagation [17]. During communication, the laser transmitter and receiver can achieve good position alignment through a servo mechanism, so their transmission divergence angle is small. The mathematical model is constructed from the particle nature of light, and the scattering process between photons and suspended particles is described using a small angle approximation method, which is more consistent with the actual test situation.

The laser beam is transmitted in water along the z-axis, and the light source coordinates are set to the origin (0, 0, 0). During transmission, seawater molecules and impurity molecules can cause laser light to scatter, assuming this scattering angle is θ_i.

The movement displacement L per unit time is

$$\frac{dL}{dt} = \left[\left(\frac{dx}{dt}\right)^2 + \left(\frac{dy}{dt}\right)^2 + \left(\frac{dz}{dt}\right)^2\right]^{\frac{1}{2}} \tag{1}$$

x, y, z represents the numerical value on the corresponding coordinate axis, and t represents time. According to the scattering theory, assume that the single scattering rate is w, the unilateral scattering angle is θ, and the optical thickness is τ. There are

$$\frac{dL}{dz} = \left[1 + \left|\frac{d(r)}{dz}\right|^2\right]^{\frac{1}{2}}, r = \sqrt{w\tau\theta^2} \tag{2}$$

Then r is the photon scattering projection angle.

Due to the small value of r, the above formula can be simplified and approximated as follows:

$$L = \frac{8z}{27w\tau\theta^2}\left[\left(1 + \frac{9}{4}w\tau\theta^2\right)^{\frac{3}{2}} - 1\right] \tag{3}$$

According to the principle of optical communication [18], it is possible to calculate the time delay of the small angle analysis method as follows:

$$t_m = \frac{zn}{c}\left\{\frac{3}{10w\tau\theta^2}\left[\left(1 + \frac{9}{4}w\tau\theta^2\right)^{\frac{3}{2}} - 1\right] - 1\right\} \tag{4}$$

Where c is the speed of light and n is the refractive index of the water transmitting medium [19]. Therefore, the optical power at the receiving end of the system can be expressed as

$$P_s(t) = E_L\frac{t}{t_m^2}\exp\left(-\frac{t}{t_m}\right) \tag{5}$$

Then E_L is the energy value of the received light. In communication systems, the width of laser pulses affects time domain broadening. After the laser pulse passes through the water, since only the pulse broadening is considered, the shock response of the initial time domain waveform p (t) can be assumed to be P_c (t). After the transmission distance z of the initial pulse p (t), the broadened waveform can be expressed as

$$I(t) = p(t) \otimes P_c(t) \tag{6}$$

I(t) represents the energy value that varies with time t. From this energy value, the energy distribution of the communication laser spot at the receiving end can be calculated, thereby completing the inversion of communication efficiency.

4 PPM demodulation algorithm

The PPM communication pulse sequence is composed of several frames, each frame being divided into protection segments and information segments. When a pulse is included in the K time slots of the communication period, the pulse width is set to ΔT. One frame period is equivalent to one optical pulse period, which is also the repetition frequency of the laser.

The protection segment is related to the characteristics of the laser and is the minimum time interval for the laser to reach the threshold condition again. Use J light pulse lengths JΔT represents. K determines the number of bits k of modulated information, which can be expressed as:

$$k = \log_2 K \tag{7}$$

In PPM modulation, the transmitted information corresponds to the position of the laser pulse one by one. The analysis of the pulse position can calculate the transmitted data value, which belongs to a phase modulation.

PPM modulation transmits information using a laser pulse from K time slots in the information segment. In a system, a frame period is the period of a light pulse, i.e., (K + J)ΔT. When the energy of a single laser pulse is high, the average power over the entire cycle is very small, reducing the need for average power in signal transmission. In terms of transmission rate, PPM modulation achieves log2M bit data transmission, and its speed can be expressed as

$$V_b = \log_2\frac{K}{(K+J)\Delta T} \tag{8}$$

To further improve speed, you can increase the information time slot or reduce the protection time slot. However, this increase and decrease is not arbitrary, and is limited by the characteristics of the laser.

4.1 Transmission module

The laser emission module with a microprocessor as its core achieves timing output through a high-speed timer. Controllable output at a certain port is achieved by controlling the timer amount. Specific process: First, the timer operates in a high-speed timing state, and counts with the minimum resolution time slot. Then, when the algorithm controls the time corresponding to the modulated information data, a pulse is generated, and the rising edge of the pulse is its modulation information. Next, a similar rising edge is generated through the PPM conversion module to control this narrow pulse and complete the PPM modulation output. Finally, the output signal can be connected to the modulation interface of the laser to control the laser to emit a modulated optical pulse sequence.

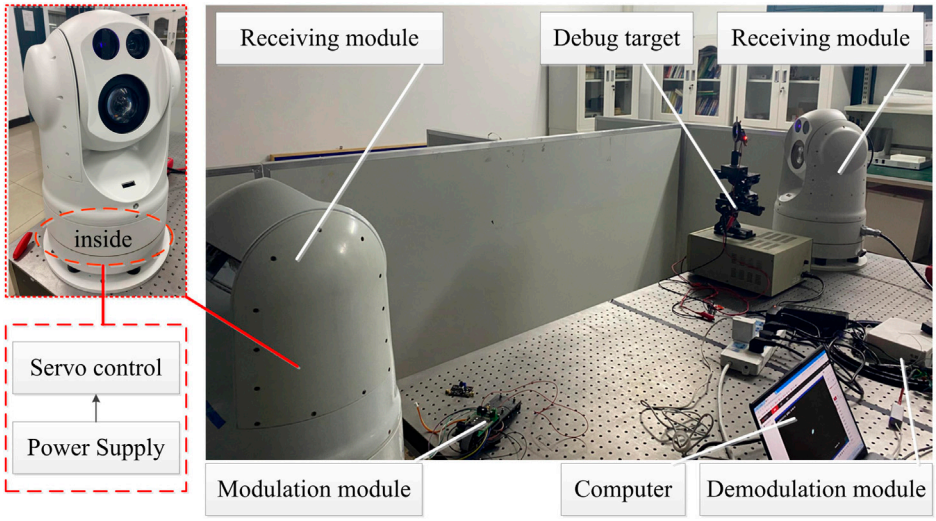

FIGURE 2
Laser communication experimental system.

4.2 Receiving module

The PPM demodulator, as the core device of the reception section, converts the received pulses containing modulation information into slot positions and demodulates the information. Firstly, it is implemented using the comparison and capture module of high-speed timers. As long as the received signal meets the trigger conditions after processing, it can accurately capture the pulse jump edge and achieve accurate timing. Secondly, a high-speed clock is used for timing decisions, and the positions of each pulse are recorded in the form of time counts. Finally, the modulation information is obtained through the corresponding demodulation algorithm.

5 Experiments

5.1 Experimental system

The main structure of the system includes a transmitting light module and a receiving light module. In the receiving module, the computer controls the modulation module to complete the uploading and modulation of data. In the receiving module, the computer controls the demodulation module to complete data download and demodulation. Lumileds-470 nm type light source is selected as the emission laser. At a communication rate of 15 Mbps, a single LED has a luminous power of about 200 mW and a divergence angle of 120°. The output power of the entire LED array is above 1 W, which can meet the system requirements. In the receiving module, the APD detector selected by Hamamatsu Company is C12702-12. The processing part uses ALINX's AN108 A/D module and FPGA development board to work together. The system is shown in Figure 2.

Before the experimental test, first use a test target to calibrate the position of the receiving module and the transmitting module, and then add attenuation pads to the communication link to complete the simulation of underwater communication attenuation. The emitting laser spot is collected by the receiving end after passing through the medium. The original spot signal is restored through demodulation processing. Processing system is used to calculate the energy loss of the light spot, thereby analyzing the communication efficiency of the system.

5.2 Servo control

Servo control modules are installed in the transmitting and receiving parts respectively, which are used to adjust the laser and detector by step scanning, thereby achieving effective alignment of communication angles. The servo control module is shown in Figure 3A, and its control response signal is shown in Figure 3B.

The system drives the stepper motor through a servo control module to achieve adjustable control of the position and angle of the optical module, achieving alignment of the irradiation position and posture during communication. By Figure 3B, the maximum signal value is 0.75 V, and the minimum signal value is 0.14 V in Ch1 channel. This is a control command issued by the control module that completes stepping control through a square wave level signal. After adjustment by the servo module, the corresponding command signal is displayed on the Ch2 channel. The maximum value of the signal in Ch2 channel is 2.41 V, and the minimum value is 1.23 V. After amplifying the step signal, the amplitude has significantly increased, and the time interval has not changed. This control module can effectively control the scanning system through a stepper motor. In the servo system, a stepper motor is used to complete the scanning of the communication module, simulating the characteristics of underwater dynamic communication.

5.3 Receiving spot energy test

In underwater laser communication, the spot energy of the communication laser is an important indicator to judge the

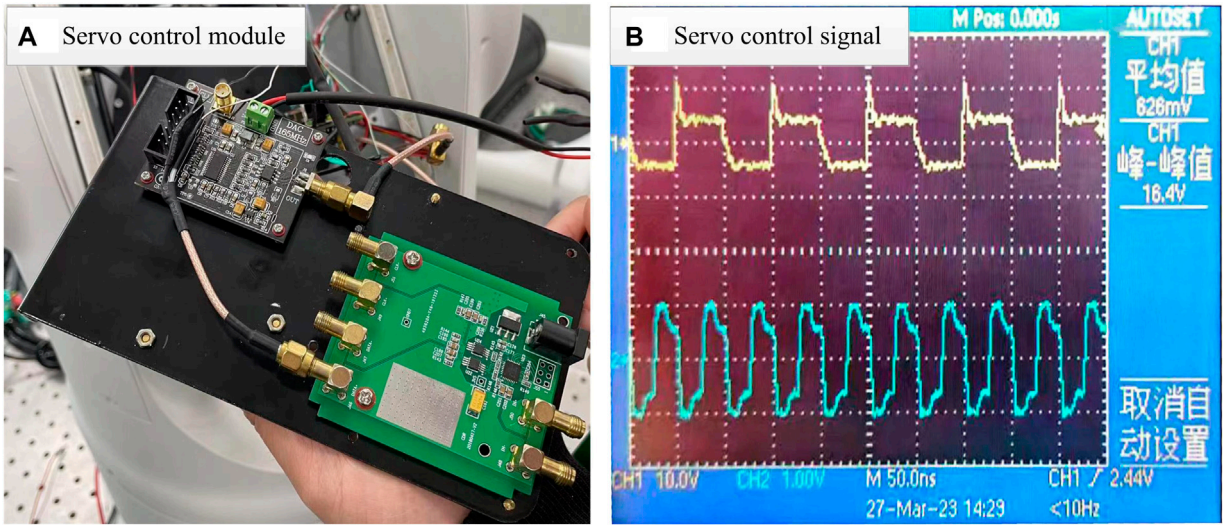

FIGURE 3
Wavelength offset values at different positions. **(A)** Servo control module. **(B)** Servo control signal

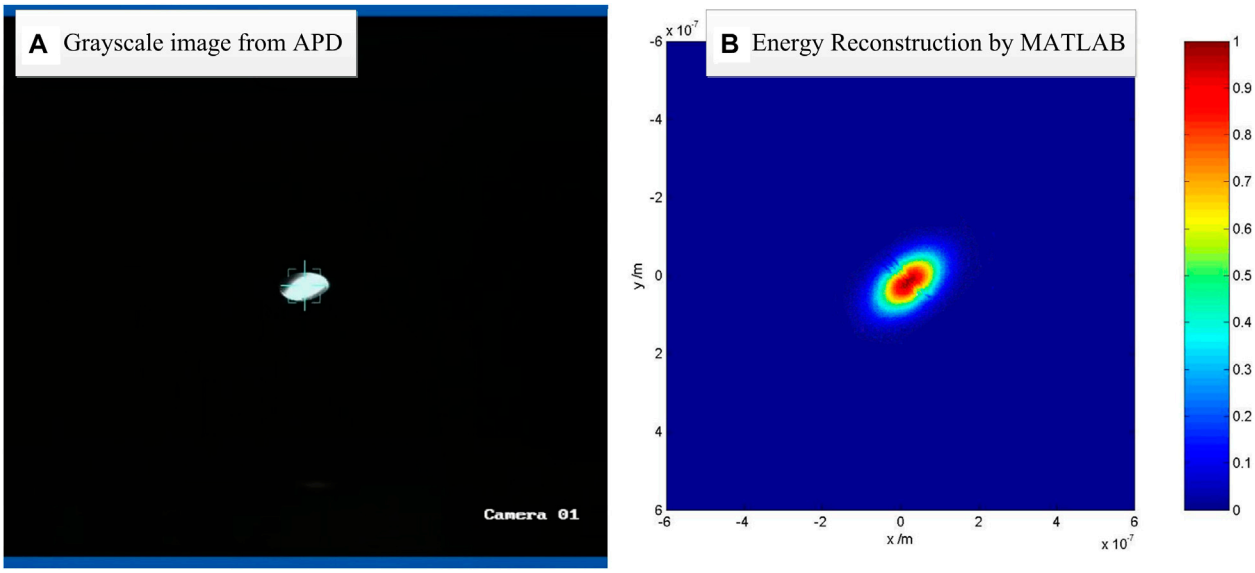

FIGURE 4
Laser spot acquisition and energy distribution reconstruction. **(A)** Grayscale image from APD. **(B)** Energy Reconstruction by MATLAB

communication quality. The attenuation and turbulent disturbance of water on the laser spot can significantly affect the energy distribution characteristics of the laser spot. Therefore, it is necessary to measure the energy of laser spots with energy attenuation and turbulence disturbances. In the experiment, 50% attenuation plates were used to simulate the attenuation effect of seawater medium on laser light. The energy of the actual test laser spot obtained by the APD detector is shown in Figure 4A. The energy distribution is reconstructed using MATLAB software, as shown in Figure 4B.

As shown in Figure 4A, over a communication distance of 10 m, when 1.0% attenuation chip was used, the laser spot still undergoes significant deformation. When 0.1% attenuation chip was used, the energy peak decreases significantly and the signal-to-noise ratio decreases. When 0.01% attenuation chip was used, the laser communication receiver cannot obtain a valid signal. The deformation of the laser spot tends to be elliptical, and the analysis shows that its deviation angle is caused by alignment deviation between the receiving module and the transmitting module. This situation will exist in actual laser communication. On this basis, the energy distribution of the light spot is simulated and reconstructed, and the reconstruction results are shown in Figure 4B. The energy map shows that the energy distribution of the light spot is elliptical, consistent with the actual test results. The intensity of energy meets the energy requirements of laser communication, which can achieve effective information transmission.

As the pass rate of the attenuator decreases, the input power decreases. The laser spot energy becomes weaker, and the packet loss of communication data gradually increases. Under the condition of using 1.0% attenuator, the test results show that the error rate of the system is better than 10^{-6}. Under the condition of using 0.1% attenuator, the test results show that the error rate of the system is better than 10^{-4}. It can be seen that when the energy attenuation exceeds an order of magnitude, the bit error rate significantly increases. With a 0.01% attenuator, the effective signal is submerged in noise.

6 Conclusion

An underwater laser communication system was proposed based on PPM modulation. The system is mainly composed of a transmitting module and a receiving module. The system applies PPM modulation and demodulation technology to the transmitting module and the receiving module. The control of step scanning in the servo module was tested and analyzed in the experiment, for verifying the stability of clock matching. In the spot energy analysis test, the laser spot intensity at different attenuation states was obtained. The system communication error rate under different laser spot energy intensities was tested and studied. The feasibility of this system has been verified, and it has certain application prospects in the field of underwater laser communication.

Data availability statement

The original contributions presented in the study are included in the article/supplementary material, further inquiries can be directed to the corresponding authors.

Author contributions

BD completed the paper. ST completed the system theoretical analysis. PZ completed the simulation calculation. JW completed the experimental test.

Funding

This work was supported in part by Natural Science Foundation of Jilin Province (YDZJ202301ZYTS394); Science and Technology Research Project of Jilin Provincial Department of Education (JJKH20230814KJ).

Conflict of interest

The authors declare that the research was conducted in the absence of any commercial or financial relationships that could be construed as a potential conflict of interest.

Publisher's note

All claims expressed in this article are solely those of the authors and do not necessarily represent those of their affiliated organizations, or those of the publisher, the editors and the reviewers. Any product that may be evaluated in this article, or claim that may be made by its manufacturer, is not guaranteed or endorsed by the publisher.

References

1. Zhao Z, Bai Z, Jin D, Qi Y, Ding J, Yan B, et al. Narrow laser-linewidth measurement using short delay self-heterodyne interferometry. *Opt Express* (2022) 30(17):30600–10. doi:10.1364/OE.455028

2. Zhao Z, Bai Z, Jin D, Chen X, Qi Y, Ding J, et al. The influence of noise floor on the measurement of laser linewidth using short-delay-length self-heterodyne/homodyne techniques. *Micromachines* (2022) 13(8):1311. doi:10.3390/mi13081311

3. Xiang WD, Yang P, Wang S, Xu B, Liu H. Underwater image enhancement based on red channel weighted compensation and gamma correction model. *Opto-Electronic Adv* (2018) 1(10):18002401–9. doi:10.29026/oea.2018.180024

4. Sui MH. *The key technology research on underwater wireless optical communication systems*. Qingdao: Ocean University of China (2009).

5. Kim J, Joe H, Yu SC, Lee JS, Kim M. Time-delay controller design for position control of autonomous underwater vehicle under disturbances. *IEEE Trans Ind Electro* (2016) 63(2):1052–61. doi:10.1109/tie.2015.2477270

6. Zhang Y, Li X, Lv W, Chen J, Zheng M, Xu J, et al. Link structure of underwater wireless optical communication and progress on performance optimization. *Opto-Electronic Eng* (2020) 47(9):190734.

7. Duntley SQ. Light in the sea. *J Opt Soc America* (1963) 53(2):214–536. doi:10.1364/josa.53.000214

8. Shimura S, Ichimura SE. Selective transmission of light in the ocean waters and its relation to phytoplankton photosynthesis. *J Oceanography* (1973) 29(6):257–66. doi:10.1007/bf02108845

9. Tivey M, Fucile P, Sichel E. A low power, low cost, underwater optical communication system. *Ridge* (2000) 2(1):1–32.

10. Huang AP, Tao LW. Monte Carlo based channel characteristics for underwater optical wireless communications. *Ieice Trans Commun* (2017) 100(4):612–8. doi:10.1587/transcom.2016ebp3266

11. Gampagnaro F, Favaro F, Guerra F, Sanjuan V, Casari P Simulation of multimodal optical and acoustic communications in underwater networks. In: OCEANS 2015; May 18-21, 2015; Genoa, Italy. New York. IEEE (2015). p. 15473725.

12. Fu YQ, Huang CT, Du YZ. Effect of aperture averaging on mean bit error rate for UWOC system over moderate to strong oceanic turbulence. *Opt Commun* (2019) 451:6–12. doi:10.1016/j.optcom.2019.06.030

13. Han B, Wang W, Zheng Y, Shi K, Zhao W Influence of electro-optical crystal flatness on indirect modulation signal for underwater blue-green laser communication. *Proc SPIE* (2019) 11068:1106823.

14. Vali Z, Gholami A, Ghassemlooy Z, Michelson DG. System parameters effect on the turbulent underwater optical wireless communications link. *Optik* (2019) 198:163153. doi:10.1016/j.ijleo.2019.163153

15. Shen P, Yang L, Chen YS. Characteristics and development status of underwater laser communication technology. *China Plant Eng* (2018)(4) 214–5.

16. Wu T-C, Chi Y-C, Wang HY, Tsai CT, Lin GR. Blue laser diode enables underwater communication at 12.4 Gbps. *Nature* (2017) 25(13):40480–14765. doi:10.1038/srep40480

17. ValiGholami ZASGHAR, Ghassemlooy Z, Michelson DG, Omoomi M, Noori H. Modeling turbulence in underwater wireless optical communications based on Monte Carlo simulation. *J Opt Soc America, A. Opt image Sci Vis* (2021) 34(8):1187. doi:10.1364/josaa.34.001187

18. Chen H, Bai Z, Cai Y, Yang X, Ding J, Qi Y, et al. Order controllable enhanced stimulated Brillouin scattering utilizing cascaded diamond Raman conversion. *Appl Phys Lett* (2023) 122(9):092202. doi:10.1063/5.0137542

19. Jin D, Bai Z, Li M, Yang X, Wang Y, Mildren RP, et al. Modeling and characterization of high-power single frequency free-space Brillouin lasers. *Opt Express* (2023) 31(2):2942–55. doi:10.1364/oe.476759

frontiers | Frontiers in Physics

TYPE Original Research
PUBLISHED 09 May 2023
DOI 10.3389/fphy.2023.1192965

OPEN ACCESS

EDITED BY
Zhenxu Bai,
Hebei University of Technology, China

REVIEWED BY
Jian Li,
Taiyuan University of Technology, China
Xu Wu,
Shenzhen Technology University, China

*CORRESPONDENCE
Guochen Wang,
wanggc@hit.edu.cn

RECEIVED 24 March 2023
ACCEPTED 20 April 2023
PUBLISHED 09 May 2023

CITATION
Gao H, Wang G, Gao W, Zhao B, Zhang R, Zhang B and Yang F (2023), An impact-insensitive fiber optic current transformer based on polarization maintaining photonic crystal fiber delay coil. *Front. Phys.* 11:1192965. doi: 10.3389/fphy.2023.1192965

An impact-insensitive fiber optic current transformer based on polarization maintaining photonic crystal fiber delay coil

Hongze Gao[1], Guochen Wang[1]*, Wei Gao[1], Bo Zhao[1,2], Runfeng Zhang[2], Boya Zhang[3] and Fan Yang[4]

[1]School of Instrumentation Science and Engineering, Harbin Institute of Technology, Harbin, China, [2]HIT (An Shan) Institute of Industrial Technology, Anshan, China, [3]Military Office of Rocket Armaments Department in Harbin District, Harbin, China, [4]Shaanxi Dongfang Aviation Instrument Co., Ltd., Hanzhong, China

When the polarization-maintaining fiber (PMF) delay coil of a fiber optic current transformer (FOCT) is impacted, external forces on the optical fibers and change of their birefringence may lead to extra phase errors during the propagation of optical signals in the fibers. These errors increase the error in current measurement. In the paper, the environmental impact mechanisms influencing the PMF delay coil of FOCT were investigated with a mathematical error model. The method of replacing PMF with a polarization-maintaining photonic crystal fiber (PCF) as the delay coil was proposed. Also, the relationship between structural parameters of air holes and linear birefringence of the polarization maintaining PCF subjected to stress was investigated. The structural parameters of optical fibers were also optimized subsequently. Simulated impact experiments of FOCT with polarization-maintaining PCF and PMF as the delay coil, respectively, demonstrated the effective impact resistance of FOCT with polarization-maintaining PCF delay coil after the optimization of its structural parameters. The current measurement errors of the FOCTs with polarization maintaining PCF delay coil reduced by approximately 35% with respect to the FOCT with PMF delay coil.

KEYWORDS

polarization maintaining fiber delay coil, fiber optic current transformer, polarization maintaining photonic crystal fiber, environmental impact, current measurement error

1 Introduction

As a kind of current transformer based on the Faraday effect, the fiber optic current transformer (FOCT) can be used as one of the key test instruments for the ship's integrated power system due to its good insulation and high reliability or later [1–6]. Due to the high-energy weapons (electromagnetic guns, laser systems, *etc.*) and detection systems equipped in modern ships, the impact and large ambient temperature fluctuations resulting from the impulse load greatly increase the current measurement error of FOCT. This error increase causes the protection circuit on the ship to trigger incorrectly [7–9]. Consequently, the FOCT loses its original monitoring and control function of the integrated power system of the ship. Therefore, the integrated power system of the ship puts forward higher requirements on the environmental adaptability of the FOCT.

As one of the important applications of FOCT, the integrated power system of a ship has been proposing the requirements of high environmental adaptability to FOCT, which mainly involves adaptability to temperature and impact. Reference [10] proposed the appropriate delay length of a $\lambda/4$ wave plate to compensate for the change in the Verdet constant of a fiber sensing coil, which could compensate for the influence of temperature on current measurement error well. So we need to focus on the effect of environmental impact on the FOCT and compensate for the current measurement error.

The effect of external impacts on FOCT is mainly through a polarization-maintaining fiber (PMF) delay coil [11], but the winding method of the PMF delay coil has not been taken into consideration so far in the research. In fact, different layers of a fiber coil have different forces. Reference [12] analyzed the forces of a PMF delay coil under an impact environment and established a resulting phase error model. However, the model is not applicable to FOCT, and the error model needs to be rebuilt to analyze the relationship between environmental impact and current measurement error quantitatively. In addition, there have been no studies to provide a suitable solution for the current measurement error of FOCT caused by an impact. Taking practical application into account, the requirements for FOCT to be lightweight and of small size are proposed, so adding an impact-proof shell to FOCT cannot satisfy our requirements. Therefore, we believe that it is of great significance to establish the error model of impacts on a fiber delay coil and to explore appropriate solutions.

In the article, we first analyzed the force of the PMF delay coil in in-line Sagnac FOCT under an impact condition. We subsequently established the phase error model of the fiber delay coil and revealed the essential relationship between linear birefringence, phase error, and current measurement error. Based on this error model, a polarization-maintaining photonic crystal fiber (PCF) was proposed to replace PMF as the delay coil. Then, the change of linear birefringence under forces of polarization maintaining PCFs with different sectional structural parameters was analyzed. Based on the analysis, the structural parameters of the polarization maintaining PCF were optimized. The study proved that the linear birefringence fluctuation of the PCF with the optimized structural parameters is smaller compared to that of the PMF under the impact environment in theory. Finally, this study verified the accuracy and rationality of the model and confirmed the effectiveness of the proposed solution using the two types of optical fibers. The optical fibers were used for the test of the current measurement error of the FOCT fiber delay coil under the normal and the impact environments, respectively. It is proved that the proposed solution can improve the current measurement stability of the FOCT under impact by using the optimized design of the polarization-maintaining PCF delay coil.

2 The establishment of the error model of FOCT

2.1 Optical circuit and force analysis of FOCT

Figure 1 shows the optical circuit structure of FOCT as the mainstream scheme [4]. The natural light from a super-luminescent diode (SLD), which has a center wavelength of 1,310 nm, is converted into a linearly polarized light along the x-axis (slow axis) of the panda PMF after passing through a fiber coupler and a polarizer. The linearly polarized light is split into two orthogonal linearly polarized lights after entering the next PMF through the 45° fusion point one. The two orthogonal linearly polarized beams are changed into left-handed and right-handed fundamental mode lights after passing through the 45° fusion point two and $\lambda/4$ wave plate. The lights enter a fiber sensing coil and are reflected back to the $\lambda/4$ wave plate by the reflector at the end of

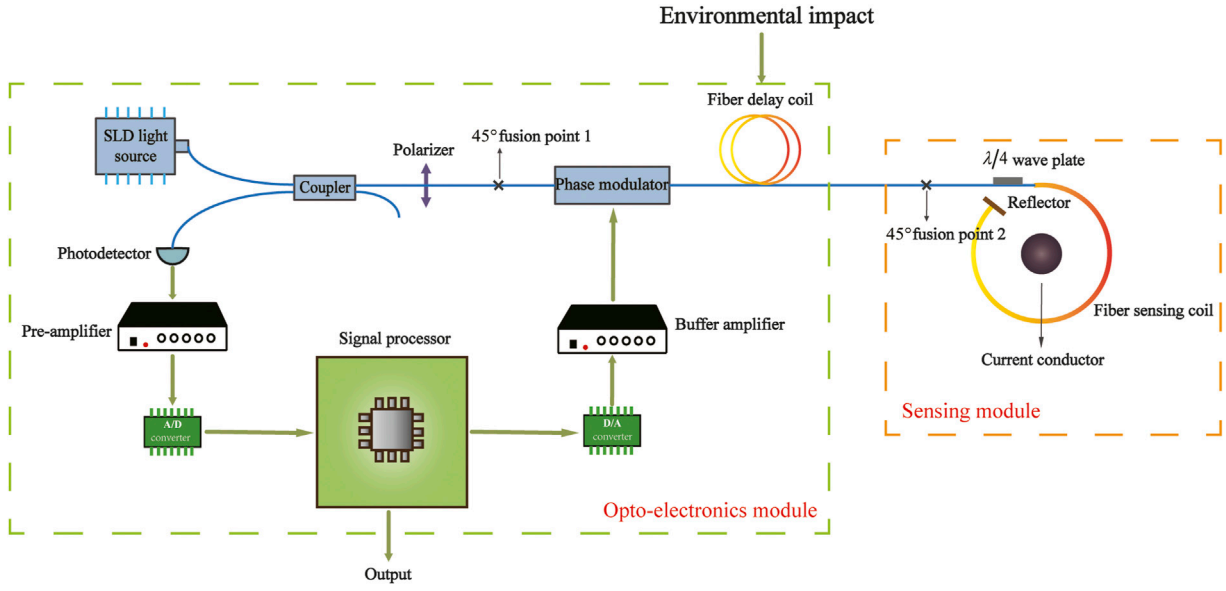

FIGURE 1
The schematic diagram of the in-line Sagnac FOCT structure.

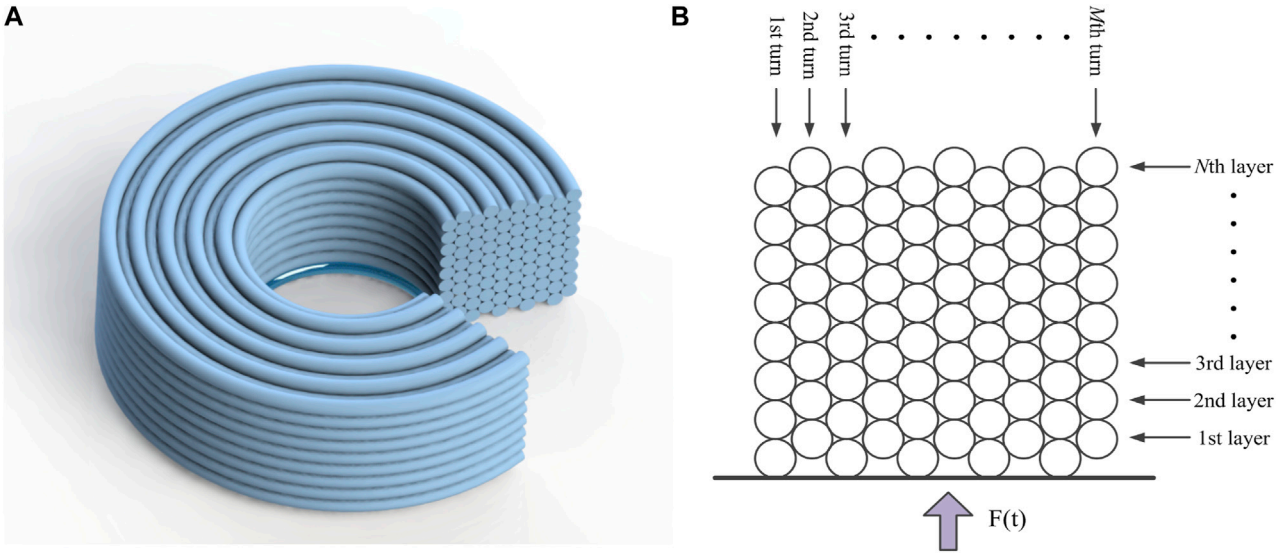

FIGURE 2
The structural diagram of PMF delay coil. **(A)** The three-dimensional structure of the PMF delay coil. **(B)** The side view structural diagram of the PMF delay coil.

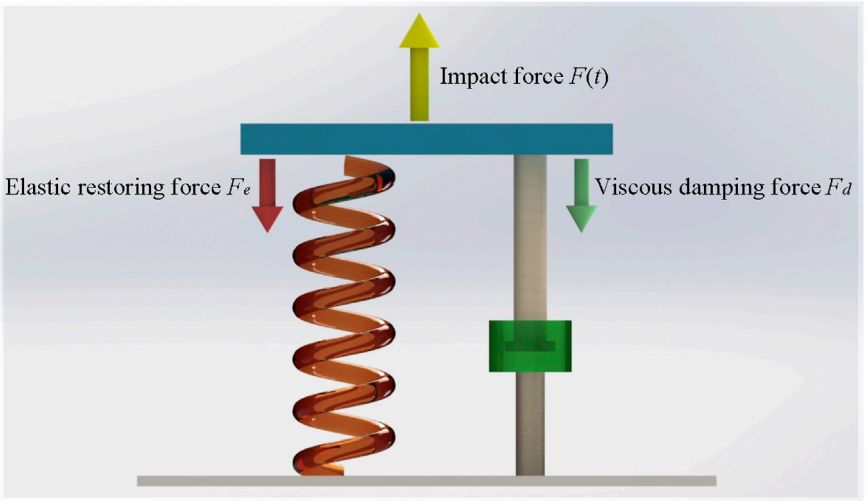

FIGURE 3
The equivalent model of the PMF delay coil system.

the optical fiber to change back to the linearly polarized light at the same time. The information of the measured current carried in the optical signal is finally interfered with by two linearly polarized light beams at the polarization, and the optical signal is converted into an electrical signal by a photoreceptor. Finally, the information of the measured current is outputted as a digital signal by a signal processing system.

When a FOCT is affected by external impacts, only the photoelectric devices related to optical fiber are influenced. Since the lengths of the fiber coupler, phase modulator, and $\lambda/4$ wave plate are very short compared to the length of the PMF delay coil and fiber sensing coil, the effect of impacts on these devices can be ignored. With respect to the fiber sensing coil, based on the analysis of the above system, the relative magnitude that the impacts brought to the left-handed and right-handed fundamental mode light and their respective polarization directions are small and can also be ignored. Therefore, the PMF delay coil is affected mostly by the impacts in FOCT. The above theoretical analysis has also been verified by the experimental results of Ref. [11]. Therefore, only specific force analysis will be conducted on the PMF delay coil.

When a ship is sailing in the sea, the impact on the ship's integrated power system generally comes from sudden changes in

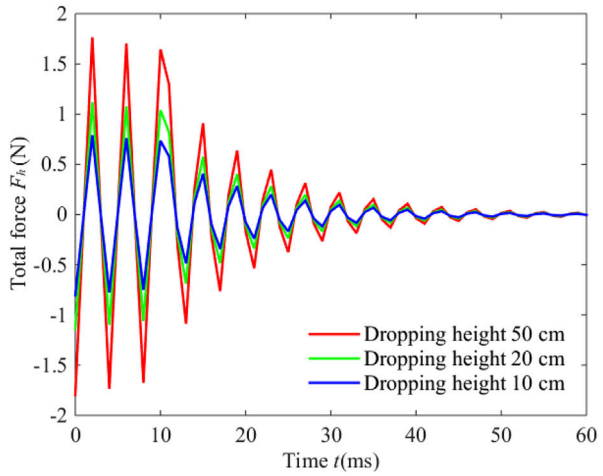

FIGURE 4
The curves of the variation of total force F_h with the time increase.

TABLE 1 Simulation parameters.

Parameters	Value
Impact time τ	10 m
Turns M	8
Layers N	10
The mass of PMF delay coil m_{coil}	7×10^{-11} kg (for 200 m length of the fiber)
Viscosity coefficient γ	0.2
Center optical wavelength of light source λ	1,310 nm
Original beat length of PMF L_{B0}	5.43 mm
Light speed c	3×10^8 m/s
Average refractive index n_0	1.45
Longitudinal elastic optical coefficient B_1	6.9×10^{-13} m^2/N
Transverse elastic optical coefficient B_2	41.9×10^{-13} m^2/N
Diameter of fiber D	250 μm
Turns of fiber sensing coil N_{sc}	10
Verdet constant of the fiber V	1.1×10^{-6} rad/A
Measured current I	640 A
Gravitational acceleration g	10 m/s^2
Damping coefficient η	0.01
Elasticity modulus of the fiber E	7×10^{10} Pa

the underwater environment, such as an explosion. Impact experiments usually use waveforms such as rectangular, semi-sinusoidal, and back-peak serrated to simulate different impacts. According to Refs. [12,13], the impulse signal can be equivalent to an ideal semi-sinusoidal pulse, and the change of its force over time can be expressed as

$$F_0(t) = \begin{cases} F_0 \sin\left(\frac{\pi}{\tau} t\right), & 0 \le t \le \tau \\ 0, & t > \tau \end{cases} \tag{1}$$

where τ represents the duration of impact received by the fiber delay coil of the polarization-maintaining fiber, and F_0 represents the amplitude of the function $F_0(t)$. t represents the time. The winding structure diagram of the PMF delay coil is shown in Figure 2.

Figure 2A shows the three-dimensional structure of the PMF delay coil [14]. Figure 2B shows the side structure of the delay coil. All fibers are closely connected using an ultraviolet-curing adhesive. It is defined that each horizontal line represents a layer wound of the optical fiber, and each vertical line represents a turning wound of the optical fiber. Assuming that the total number of the turning wound is M, and the number of layers is N, an optical fiber at any position is defined to be in the nth (n = 1, 2. . . .N) layer and mth (m = 1, 2. . . , M) turning. As can be seen from Figure 2B, there are dense arrangements between any two optical fibers. Considering that the actual conditions can only be suitable for simulated impulse experiments, the impact force applied on the PMF delay coils is in the vertical direction, and it is considered that the force between each turning wind of the fiber in the same layer is uniform. Under the above premise, we simplify the fixed model and consider that a small damped oscillation system is formed between each layer of fiber when the whole PMF delay coil is impacted. Subsequently, we establish the corresponding under-damping oscillation model with a single degree of freedom. To analyze the specific motion and force of the PMF delay coil, we need to carry out a two-step analysis. First, we need to consider the PMF delay coil as a whole system and analyze its motion and force. Then, based on the above conditions, we separately analyze the motion and force of each layer of the PMF delay coil. The motion and force of the whole PMF delay coil system are shown in Figure 3.

Here, the blue part represents the PMF delay coil whole system. The movement of the whole system can be considered equivalent to a simple harmonic vibration of a spring with gradual attenuation amplitude in the vertical direction, and the corresponding equation of motion is

$$m_{coil}\frac{d^2x}{dt^2} = F_0(t) - F_e - F_d \tag{2}$$

where m_{coil} represents PMF delay coil mass, $F_0(t)$ represents the external impact force, and F_e represents the elastic restoring force, which is equal to kx. k and x represent the stiffness coefficient and displacement in the vertical direction of the equivalent spring, respectively. F_d represents the viscous damping force, which is equal to $\gamma dx/dt$. γ and dx/dt represent the viscosity coefficient and velocity of spring, respectively. According to Eq. 2, the displacement of the spring x_1 during the process of impact ($t < \tau$) can be expressed as

$$\begin{aligned} x_1 &= be^{-\delta t}\sin\left(\sqrt{\omega_0^2 - \delta^2}\cdot t + \varepsilon\right) + b\sin(\omega t - \varepsilon) \\ b &= a_0 \Big/ \sqrt{\left(\omega_0^2 - \omega^2\right)^2 + 4\delta^2\omega^2} \\ \varepsilon &= \arctan\left[2\delta\omega/\left(\omega_0^2 - \omega^2\right)\right] \\ a_0 &= F_0/m_{coil} = 2\sqrt{2gh_d}/\tau \end{aligned} \tag{3}$$

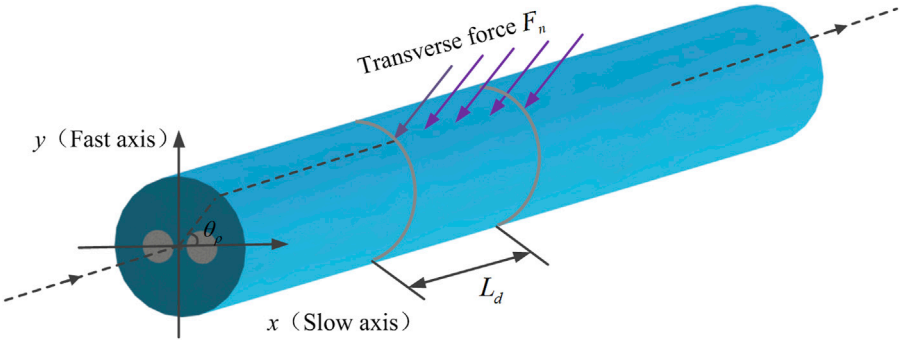

FIGURE 5
The diagram for the force analysis of PMF delay coil.

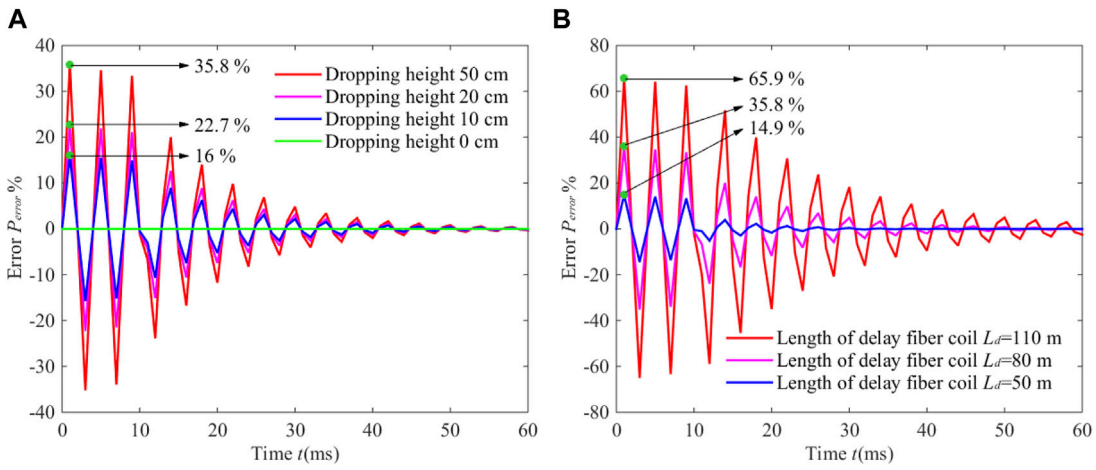

FIGURE 6
FOCT current measurement error caused by impacts under a PMF delay coil. **(A)** The variation of FOCT current measurement error with different free-fall heights when the length of the fiber delay coil is 80 m. **(B)** The variation of FOCT current measurement error with different lengths of fiber delay coil when the free-fall height is 50 cm.

where ω_0 represents the natural angular frequency of the whole system with the value of $\sqrt{k/m_{coil}}$, δ represents the damping coefficient of the whole system with the value of $\gamma/2m_{coil}$, ω represents the impact frequency with the value of π/τ, g represents gravitational acceleration, and h_d represents the falling height. When the impact is over ($t > \tau$), the displacement of spring x_2 can be calculated as

$$\begin{aligned} x_2 &= Ae^{-\delta t}\sin\left(\sqrt{\omega_0^2-\delta^2}\cdot t+\theta\right)\\ A &= \sqrt{x_0^2+(v_0+\delta x_0)^2/(\omega_0^2-\delta^2)}\\ \theta &= \arctan\left[\left(x_0\sqrt{\omega_0^2-\delta^2}\right)/(v_0+\delta x_0)\right] \end{aligned} \tag{4}$$

where x_0 and v_0 represent the displacement and velocity, respectively, of the equivalent spring when $t = \tau$. For each layer of the PMF delay coil, the whole motion is the same as the process described in Figure 3. According to Ref. [12], for the nth line fiber, the stiffness coefficient of the equivalent spring can be calculated as $k = E\Delta S/L$, and the damping coefficient of the fiber is η. E represents the elasticity modulus of the fiber. L represents the distance between the bottom of the fiber coil and each layer of the fiber with the value of $(2n\text{-}1)D/2$. ΔS represents the basal area of the fiber coil with the value of $(\sqrt{3}(M\text{-}1)L_dD)/(2NM)$. L_d represents the length of the PMF delay coil, and D represents the diameter of the fiber. Therefore, the stiffness coefficient k can be calculated as

$$k = \frac{\frac{\sqrt{3}}{2}(M-1)\frac{EL_dD}{N\times M}}{\frac{2n-1}{2}D} \tag{5}$$

In the actual process, when the whole system vibrates due to force, each line of the fiber and its coil bottom move simultaneously, and the corresponding dynamic equation of each line of fiber can be expressed as

10.3389/fphy.2023.1192965

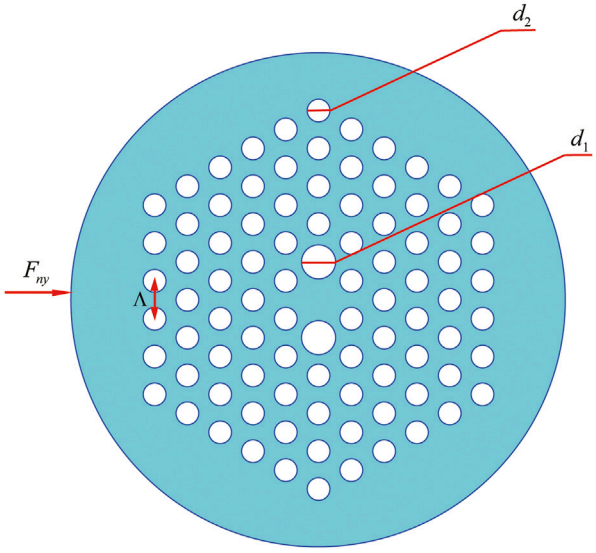

FIGURE 7
The cross-sectional structure diagram of the polarization maintaining PCF.

$$\begin{cases} \frac{m_{coil}}{N}\frac{d^2x}{dt^2} + \eta\left(\frac{dx}{dt} + \frac{dx_1}{dt}\right) + k(x + x_1) = 0, & 0 < t \le \tau \\ \frac{m_{coil}}{N}\frac{d^2x}{dt^2} + \eta\left(\frac{dx}{dt} + \frac{dx_2}{dt}\right) + k(x + x_2) = 0, & t > \tau \end{cases} \tag{6}$$

Here, the first differential equation of motion corresponds to the stage of continuous impact ($t < \tau$), and the second differential equation of motion corresponds to the stage of no impact ($t < \tau$). Finally, the solutions of Eq. 6 are

$$\begin{cases} x = e^{-\alpha_0 t}[C_1\cos(\beta t) - C_2\sin(\beta t)] - e^{-\alpha_0 t}\cos(\beta t)H + e^{-\alpha_0 t}\sin(\beta t)I, 0 < t \le \tau \\ x = e^{-\alpha_0 t}[C_3\cos(\beta t) - C_4\sin(\beta t)] - e^{-\alpha_0 t}\cos(\beta t)HH + e^{-\alpha_0 t}\sin(\beta t)II, t > \tau \end{cases} \tag{7}$$

According to Eq. 7, we can solve the impact force F_n of the nth layer PMF delay coil at two stages of $0 < t \le \tau$ (F_{1n}) and $t > \tau$ (F_{2n}). The total impact force F_h can be written as

$$F_h = \begin{cases} \sum_{i=1}^{n} F_{1n}, & 0 \le t \le \tau \\ \sum_{i=1}^{n} F_{2n}, & t > \tau \end{cases} \tag{8}$$

The specific values and names of all the symbols in Eqs 7, 8 are shown in the Supplementary Material S1. The relationship between F_h and t is shown in Figure 4. The simulation parameters can be found in Table 1 [13].

As shown in Figure 4, the change curve of force with time shows a sinusoidal trend of decay. During the first stage of $t \le 10$ ms, the external impact force plays a leading role, causing a small degree of attenuation of the total impact force. During the second stage of $t >$ 10 ms, there is no external impact force acting on the fiber delay coil. The damping of the ultraviolet curing adhesive plays a leading role, causing a gradual decrease in the amplitude of the total force. The higher the dropping height is, the smaller the total force will be. The results in Figure 4 prove that the total force variation trend over time is consistent with the motion process analyzed above.

2.2 Phase delay error of FOCT caused by impact

To simplify the force analysis mechanism and process of the optical fiber, the force analysis of the nth layer of the PMF delay coil is carried out in this study, and the force analysis diagram of the layer is shown in Figure 5 [15].

Figure 5 represents the diagram for the force analysis of the PMF delay coil. There is a transverse force F_n in the fiber; from the direction of the force, the x-axis is deviated by an angle θ_ρ. n_x and n_y are the refractive indices of the x and y-axes of the PMF delay coil, respectively. Δn is the linear birefringence of the PMF delay coil with a value of n_x-n_y. Considering the external force of the PMF delay coil, the refractive index of the axis of the PMF delay coil can be calculated according to Eq. 4 in Ref. [16].

$$\begin{cases} n_x = n_{x0} + B_1\sigma_x + B_2\sigma_y \\ n_y = n_{y0} + B_1\sigma_y + B_2\sigma_x \end{cases} \tag{9}$$

where n_{x0} and n_{y0} represent the original refractive index without the external force of the x and y-axes, respectively. σ_x and σ_y represent the transverse stress along the x and y-axes, respectively. B_1 and B_2 represent the longitudinal and transverse elastic optical coefficients, respectively. The specific equations for stress are

$$\begin{cases} \sigma_x = \frac{2F_{ny}}{\pi L_d D} \\ \sigma_y = -\frac{6F_{ny}}{\pi L_d D} \end{cases} \tag{10}$$

where F_{ny} denotes the component of the external force F_n along the y-axis with a value of $F_n\sin\theta_\rho$. According to Eqs 9, 10, the relationship between Δn and F_n is

$$\Delta n = \left(n_{x0} - n_{y0}\right) + \frac{4F_n\sin\theta_\rho}{\pi L_d D}(B_1 - B_2) \tag{11}$$

In practice, the angle between the direction of the external force and that of the x-axis is a residual value. Hence, we need to consider the greatest effect of the impact on the fiber. So, we consider a maximum value of 90° for the residual value. The above analysis focused on the change of the birefringence of any layer of the fiber under impact, and the extra phase error is marked as $\Delta\phi_{sn}$ and obtained by summing up the phase error of each layer. According to Eq. 4 in Ref. [10], the specific equation for the extra phase error is

$$\Delta\phi_s = \sum_{n=1}^{n}\Delta\phi_{sn} = \sum_{n=1}^{n}\frac{2\pi L_d}{L_B^2}\frac{\partial L_B}{\partial F_n}\frac{\partial F_n}{\partial t}\tau_{sn} \tag{12}$$

where L_B represents the beat length of the PMF delay coil and is equal to $\lambda/\Delta n$. λ denotes the center optical wavelength of the light source, and τ_{sn} represents the light transmission time of a single-layer PMF delay coil and is equal to $n_0 L_d/c$. c and n_0 represent the light speed and average refractive index of fiber, respectively. According to Eqs 8, 11, 12, the final current measurement error can be simplified as

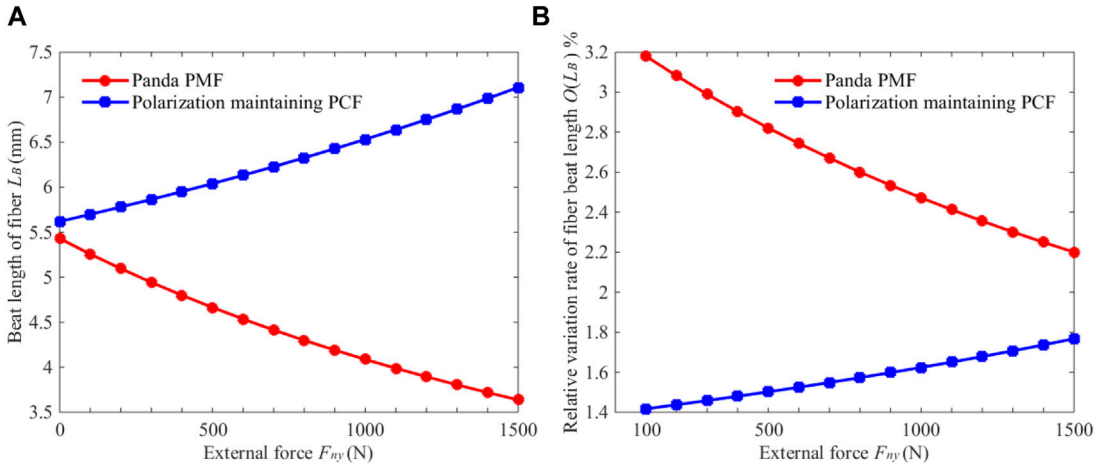

FIGURE 8
(A) The beat length variation with the change of force of the two kinds of fiber. **(B)** The beat length relative variation rate with the change of force of two kinds of fiber.

$$P_{error} = \frac{\Delta\phi_s}{4N_{sc}VI} = \frac{2\lambda n_0 L_d (B_1 - B_2)\sin\theta_\rho}{cDL_{B0}^2 \Delta n^2 N_{sc} VI} \cdot \sum_{n=1}^{n} \frac{\partial F_n}{\partial t} \quad (13)$$

where N_{sc} represents the number of turns of the fiber sensing coil, V represents the Verdet constant of the fiber sensing coil, and I denotes the measured current. From Eq. 13, the simulation results of the current measurement error of FOCT caused by impacts are shown in Figure 6. The simulation parameters can be found in Table 1.

As can be seen from Figure 6, the error of the fiber delay coil reaches the maximum value when the time duration of impacts is less than 10 ms, and the error at each peak value almost does not attenuate and is close to the maximum error value. When the time duration lasts for more than 10 ms, the error decreases over time and becomes even smaller when the time duration reaches 60 m. As can be seen from Figure 6A, the peak error decreases with the decrease in the free-fall height of the FOCT. The peak errors of the FOCT in free falling at 50, 20, and 10 cm are 35.8, 22.7, and 16%, respectively. As can be seen from Figure 6B, with the shortening of the length of the fiber delay coil, the peak error also decreases gradually. The peak errors corresponding to the lengths of 110, 80, and 50 m are 65.9, 35.8% and 14.9%, respectively. The above results proved that the phase error of the FOCT will be affected by different impact forces or changes in the fiber length of the fiber delay coil during the impacts.

3 Theoretical analysis of the polarization maintaining PCF

It can be seen from Eq. 13 that the phase error of the FOCT induced by impacts is mainly affected by its length, the beat length of the PMF delay coil, the beat length variation rate with the force, and the force variation rate with time. The change of force with time is determined by the external environment. In a panda PMF, the beat length is generally fixed. The length of optical fiber is mainly affected by the modulation speed of the FOCT circuit, so the choice of length reduction for phase error minimization is limited. Therefore, to greatly reduce the phase error, the way of reducing the sensitivity to forces of the beat length should be followed. The beat length of the fiber is related to the linear birefringence, and the linear birefringence of the fiber can be considered as the linear birefringence of the fiber core. The fundamental reason why the linear birefringence of the fiber changes with the force is the elastic effect. Therefore, from the perspective of weakening the elastic effect of the fiber core, polarization maintaining PCF can fundamentally solve the problem of the high sensitivity of linear birefringence of the fiber to force [17]. Reference [18] also pointed out that the air hole covering of the PCF can effectively reduce the influence of the elastic optical effect of the fiber core.

3.1 Force analysis of polarization maintaining PCF under impacts

The structure of the polarization maintaining the PCF of this research is shown in Figure 7. The cross-sectional structure of the polarization-maintaining PCF shown in Figure 7 contains five layers, and the air holes in each layer are arranged in a hexagonal pattern. Among the six air holes in the innermost layer, the diameters d_1 of two holes are larger than the diameters d_2 of the other air holes, and the distance between every two adjacent holes is Λ (lattice constant). Although the polarization maintaining PCF is not only limited to this structure, the panda PMF is adopted in the fiber tails of all the optical devices in the FOCT system. Therefore, the optical fiber with the structure shown in Figure 7 as the fiber delay coil of FOCT can make the mode fields between fibers more similar, allowing easier axis fusion and ensuring relatively small fusion loss. As for the force of the fiber, although the direction of force cannot be determined, it can be clearly seen from Eq. 11 that when the force direction of the fiber coincides with the y-axis (fast axis) of the fiber, the linear birefringence caused by elastic optical effect changes the most. Meanwhile, the polarization maintaining PCF of this structure is similar to the ordinary panda PMF structure. Although Eq. 11 cannot be completely used for quantitative analysis, its properties are similar to those of the panda PMF, so the

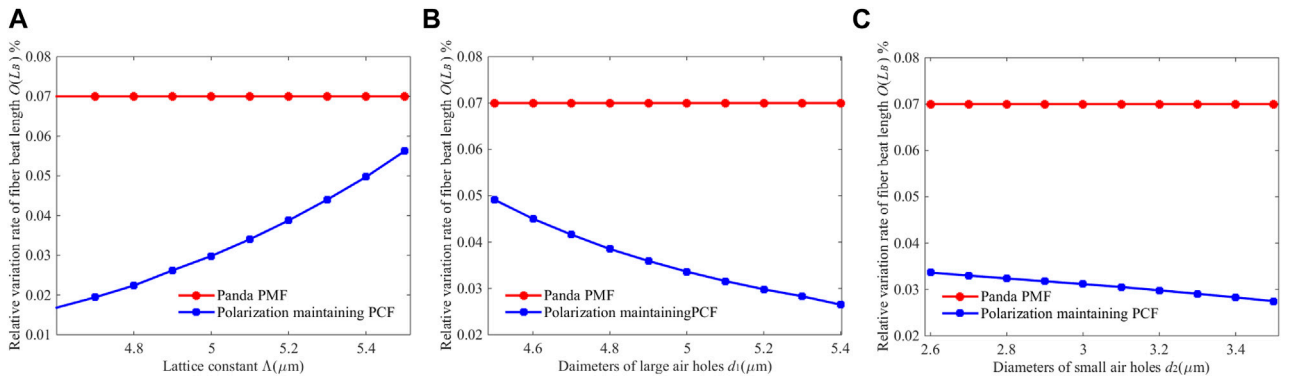

FIGURE 9
(A) The variation of relative change rate O (L_B) of beat length of fiber with the change of lattice constant Λ, d_1 = 5.2 μm and d_2 = 3.2 μm. **(B)** The variation of relative change rate O (L_B) of beat length of fiber with the change of large air holes d_1, Λ = 5 μm, and d_2 = 3.2 μm. **(C)** The variation of relative change rate O (L_B) of beat length of fiber with the change of small air holes d_2, d_1 = 5.2 μm and Λ = 5 μm.

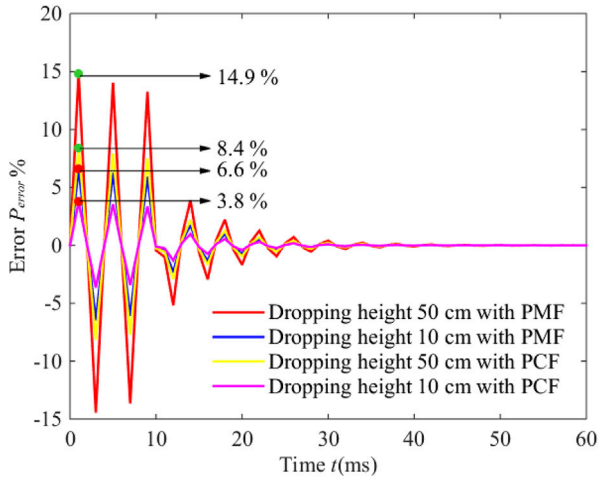

FIGURE 10
The current measurement error caused by FOCT after using polarization maintaining PCF with optimized parameters as the fiber delay coil.

same qualitative analysis method as the one in the case of the panda PMF can be used. In addition, since we believe that the optical fiber receives a uniform force in the vertical direction and the changes in the length and refractive index of the optical fiber in the vertical direction can be ignored, the force of the optical fiber can be simplified as two-dimensional. The force direction of the polarization maintaining PCF is marked in Figure 7.

Combined with a finite element method according to Eq. 11, we gradually increase the stress of the two kinds of optical fibers, and the relationship between the change of fiber beat length and the change of force can be obtained, respectively, as shown in Figure 8A. The red solid line represents the panda PMF, while the blue full line represents the polarization maintaining PCF. The parameters corresponding to the two kinds of optical fiber in the simulated experiment can be found in Table 1.

Although it can be seen from Figure 8A that the beat length of the two kinds of optical fibers changes with the increase of the force, it cannot be intuitively seen which optical fiber beat length is less sensitive to the external force. Therefore, we defined the relative change rate O (L_B) of an optical fiber (when the beat length changes with the force of the optical fiber) as

$$O(L_B) = \left| \frac{L_B(F_{ny2}) - L_B(F_{ny1})}{L_B(F_{ny1})} \right| \times 100\% \quad (14)$$

In Eq. 14, L_B (F_{ny1}) and L_B (F_{ny2}) represent the beat lengths of the optical fibers corresponding to the initial and changed force condition, respectively. According to the original data of the beat lengths of the optical fiber corresponding to the force conditions in Figure 8A, the calculation and processing are performed according to Eq. 14. It can be concluded that the relative change rates of beat lengths of the two kinds of PMFs vary with their forces, as shown in Figure 8B. It can also be clearly seen from Figure 8B that during the process of the force increasing from 0 to 1,500 N, the relative change rate of beat length of panda PMF is always greater than 2.2%, while that of the polarization maintaining PCF is always less than 1.8%. Therefore, it can be proved from the results of the simulated experiment that, under appropriate structural parameters, the polarization-maintaining PCF has less sensitivity compared to the panda PMF to the beat length force, and the results are also consistent with those of Ref. [17]. Therefore, according to Eqs 12, 14, under the same force, compared with the panda PMF, the polarization-maintaining PCF has lower beat length change rates. As the fiber delay coil of FOCT, the polarization-maintaining PCF can reduce the current measurement error caused by impacts.

3.2 Optimization of structural parameters of a polarization maintaining PCF

To increase the impact resistance ability of the polarization maintaining PCF as a delay coil of FOCT, we need to analyze and

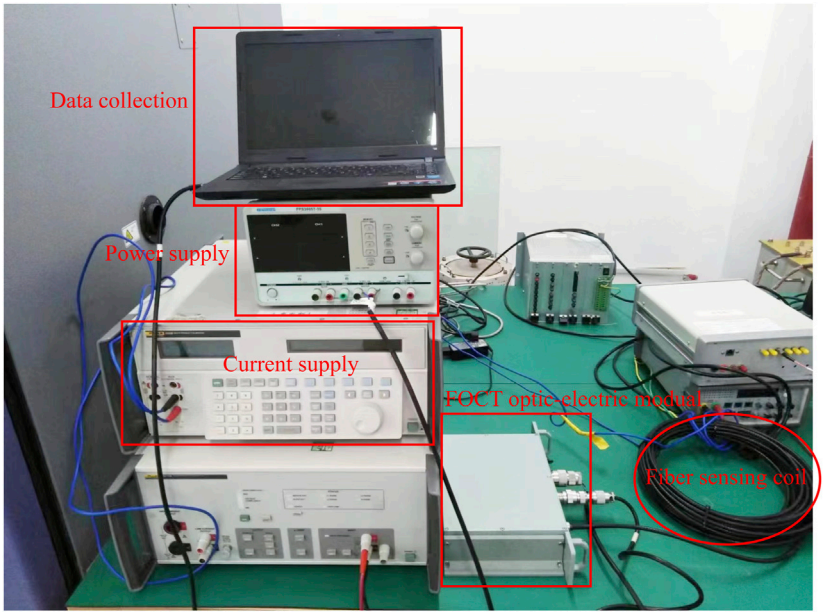

FIGURE 11
The process of the simulated impact experiment.

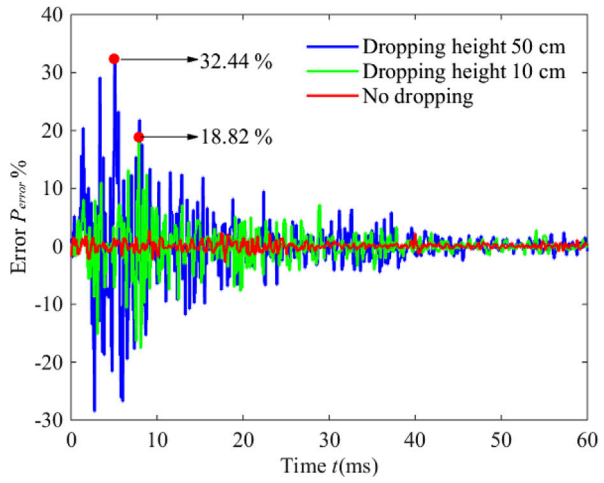

FIGURE 12
The actual current measurement error of the FOCT under different free-fall heights.

optimize the structural parameters of the air holes of the optical fiber. In the polarization maintaining PCF, the main structural parameters are the diameters of the two larger air holes (d_1), the diameters of smaller outer air holes (d_2), and the lattice constant (Λ) of the optical fiber. The influence of the changes of each of these three parameters on the relative change rate of the beat length is studied under the same force with the other two parameters fixed. The simulated results are shown in Figure 9, where the red solid line represents the panda PMF, and the blue solid line represents the polarization maintaining PCF.

It can be clearly seen from Figure 9A that for polarization maintaining PCFs, the relative change rate of the corresponding fiber beat length increases from 0.02% to 0.06% with the increase of lattice constant. As can be observed from Figures 9B, C, the increase of diameters d_1 and d_2, respectively, decreases the relative change rate of the optical fiber beat length. In particular, the change of diameters of the larger air holes has a greater impact on the relative change rate of optical fiber beat length compared to the change of diameter of the smaller air holes. Notably, the relative change rate of optical fiber beat length decreases from 0.05% to 0.027% and from 0.034% to 0.028% for the change of the larger and smaller holes' diameters, respectively. The reason for the above results is that the decrease of lattice constant or the increase of the diameters of the air holes increases the filling ratio of air in the fiber. In fact, the function of air holes can be equal to that of the protective layer of the optical fiber core, which can reduce the interference of external force when the light is transmitted in the fiber core. The increase of the air-filling ratio further reduces such interference, weakens the change of refractive index caused by the elastic optical effect, and reduces the force sensitivity of the optical fiber beat length. If the changes in the diameters of the air holes remain the same, compared with the smaller air holes, the increase in the diameter of larger air holes can significantly reduce the relative change rate of the optical fiber beat length. The reason for this significant reduction is that the increase in the diameter of the larger air holes can significantly change the optical fiber beat length. So, in conclusion, the range of the relative change rate of the optical fiber beat length of large air holes is more obvious.

To further reduce the influence that impacts bring to the beat length of the polarizing maintaining PCF delay coil and taking the

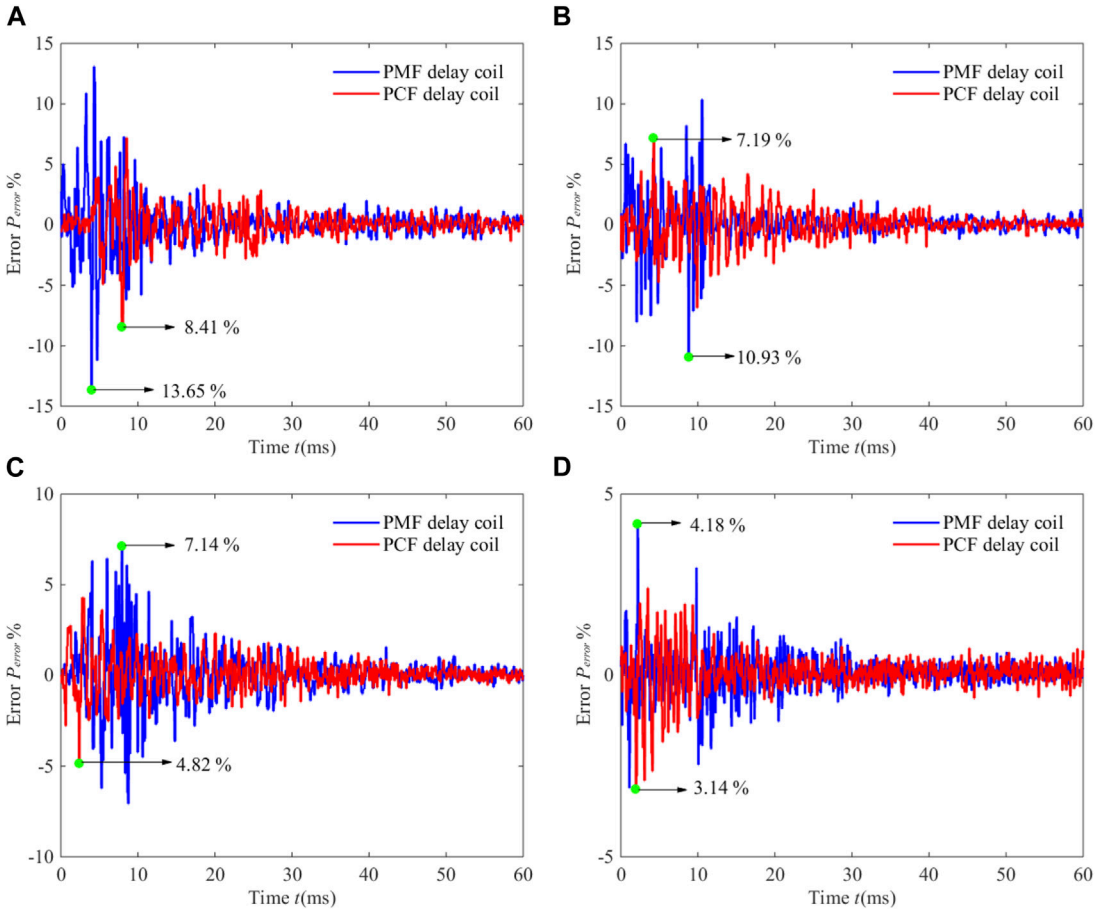

FIGURE 13
The comparison of current measurement errors of two kinds of fiber delay coils with different free-fall heights. **(A)** 50 cm free falling height. **(B)** 20 cm free falling height. **(C)** 10 cm free falling height. **(D)** 5 cm free falling height.

TABLE 2 The comparison of current measurement errors with two kinds of FOCT fiber delay coils.

Free falling height	Current measurement error with PMF the delay coil (%)	Current measurement error with the polarization maintaining PCF the delay coil (%)
50 cm (63 g)	13.65	8.14
20 cm (40 g)	10.93	7.19
10 cm (28 g)	7.14	4.82
5 cm (20 g)	4.18	3.14

mathematical rationality of the actual size of the optical fiber and the possibility of production into account, the structural parameters of the optical fiber are designed accordingly. The final values are lattice constant $\Lambda = 4.8$ μm, $d_1 = 5$ μm, and $d_2 = 3$ μm. According to Eq. 13, the decrease in the length of the fiber delay coil can also reduce the aftermath brought by impacts. However, considering the limitation brought by the modulation period of the FOCT signal processing unit, the length of the fiber delay coil is reduced to 50 m here. After the polarization maintaining PCF corresponding to the above structural parameters serves as the fiber delay coil of the FOCT, the additional phase delay error curve diagram can be obtained during impacts according to Eq. 13. The diagram is shown in Figure 10.

As can be seen in Figure 10, for a 50 m-long fiber delay coil, when the free falli height of the FOCT is 50 cm, the current measurement error of FOCT with the polarization maintaining PCF delay coil is reduced to 8.4%, compared to the 14.9% with the PMF delay coil. When the free fall height of the FOCT is 10 cm, the current measurement error of the FOCT with the PCF delay coil is reduced to 3.8% compared with the 6.6% error of FOCT with the PMF delay coil. The above results proved that the FOCT with the polarization maintaining PCF delay coil can reduce

the influence of extra phase error caused by impacts better in theory.

4 Comparison and analysis of experiment results

4.1 The verification of the current measurement error model

To verify the reasonableness of the impact-induced FOCT current measurement error model, PMF was adopted as the optical fiber delay coil of the FOCT, the length of which was set at 80 m. Other relevant parameters were consistent with the parameters in Table 1. The specific experimental process is shown in Figure 11.

In the experiment, we simulate the effect of free fall impact on the whole FOCT from free-fall under different heights of the photoelectric module of the FOCT. First, the height of the free-fall is measured to the left side of the FOCT photoelectric module and marked. Then, the FOCT photoelectric module is lifted to the height of the marked position. Finally, the FOCT photoelectric module is allowed to free fall and the impact is captured by the data acquisition software.

The free-fall height of the FOCT photoelectric module is set to 50 and 10 cm, respectively, and the actual current measurement error of the FOCT can be obtained, as shown in Figure 12.

As can be seen from Figure 12, when the height of the FOCT in free falling is 50 and 10 cm, the corresponding peak current measurement errors are 32.44% and 18.82%, and both errors reach the peak within 10 ms. After 10 ms, the errors corresponding to the two free-fall heights tend to decrease gradually, and the errors can be reduced to the range of noise current at about 60 ms. The results are roughly the same as those shown in Figure 6A in terms of trend and peak current errors, which can prove the rationality and accuracy of the impact-induced error model in this paper.

4.2 Comparison of current measurement errors of two kinds of optical fibers as the fiber delay coils results

To verify the error suppression effect under the impact of the polarization maintaining PCF as the FOCT fiber delay coil, we conducted a comparative experiment of polarization maintaining PCF and PMF as the FOCT fiber delay coils, respectively. The lengths of the two optical fiber delay coils are 50 m, and the free-fall heights of the FOCT photoelectric module are 50, 20, 10, and 5 cm, respectively. The corresponding current measurement errors are shown in Figure 13, and the specific values are shown in Table 2.

For the convenience of comparison, the current measurement error values marked in Figure 13 are all absolute values. As can be seen from Figure 13 and Table 2, compared with the FOCT corresponding to the PMF delay coil, the peak current measurement error in the FOCT using the polarization maintaining PCF delay coil reduced by about 35%, which proved that the method of using polarization maintaining PCF as the FOCT delay coil can reduce the current measurement error caused by impacts more effectively.

5 Conclusion

In this article, the forces on the polarization-maintaining fiber (PMF) delay coil of a fiber optic current transformer (FOCT) under environmental impact were investigated, and a current measurement error model based on the delay coil winding method was established. Also, the essential correlation of linear birefringence with phase error and current measurement error was derived. According to the proposed model, both the magnitude and force sensitivity of the beat length of fibers contribute to current measurement errors induced when FOCT is impacted. Apart from reasonably reducing the delay coil length, a polarization-maintaining photonic crystal fiber (PCF) is proposed as the delay coil of FOCT to reduce its phase error under impact conditions. Changes in linear birefringence of fibers under stress were also analyzed based on the structural parameters of different cross-sections of polarization maintaining PCF to optimize its structural parameters. This analysis thereby demonstrated by numerical simulation that the fluctuation of the linear birefringence of the polarization maintaining PCF under environmental impact is reduced by optimizing the structural parameters. In addition, the current measurement errors of FOCT with the two delay coils under environmental impact were investigated. The current measurement errors of FOCT based on the PMF delay coil in cases of different free fall heights obtained by measurements were compared with corresponding simulation results. The proposed current measurement error model is accurate for the FOCT under environmental impact. The current measurement results of FOCT with PMF and polarization maintaining PCF as the delay coil, respectively, in cases of different free-fall heights were compared. The comparison demonstrated that the FOCT with optimized polarization maintaining PCF as the fiber delay coil shows less current measurement error than the FOCT with PMF as the fiber delay coil. Specifically, the peak error of the current measurement of FOCT with the polarization maintaining PCF as the fiber delay coil was 35% less than that with the PMF as the fiber delay coil when the delay coil has a length of 50 m. Hence, the polarization maintaining PCF as the delay coil in FOCT provides an effective measure for the improvement of the environmental impact adaptability of the FOCT.

Data availability statement

The raw data supporting the conclusion of this article will be made available by the authors, without undue reservation.

Author contributions

All authors listed have made a substantial, direct, and intellectual contribution to the work and approved it for publication.

Funding

This work was supported by the National Natural Science Foundation of China (52271315, 51909048), the China Postdoctoral Science Foundation (2019T120260), the Heilongjiang Postdoctoral Science Foundation (LBH-TZ1015), and the Fundamental Research Funds for the Central Universities.

Conflict of interest

FY was employed by Shaanxi Dongfang Aviation Instrument Co., Ltd.

The remaining authors declare that the research was conducted in the absence of any commercial or financial relationships that could be construed as a potential conflict of interest.

Publisher's note

Supplementary material

The Supplementary Material for this article can be found online at: https://www.frontiersin.org/articles/10.3389/fphy.2023.1192965/full#supplementary-material

References

1. Chung Y, Liu WX, Schoder K, Cartes DA Integration of a bi-directional DC–DC converter model into a real-time system simulation of a shipboard medium voltage DC system. *Electr Power Syst Res* (2011) 81:1051–9. doi:10.1016/j.epsr.2010.12.010

2. Bohnert K, Gabus P, Nehring J, Brandle H Temperature and vibration insensitive fiber-optic current sensor. *J Lightwave Technol* (2002) 20(2):267–76. doi:10.1109/50.983241

3. Zhang F, Lit JWY Temperature and strain sensitivity measurements of high-birefringent polarization-maintaining fibers. *Appl Opt* (1993) 32(13):2213–8. doi:10.1364/ao.32.002213

4. Short SX, de Arruda JU, Tselikov AA, Blake JN Elimination of birefringence induced scale factor errors in the in-line Sagnac interferometer current sensor. *J Lightwave Technol* (1998) 16(10):1844–50. doi:10.1109/50.721071

5. Li YS, Zhang WW, Liu XY, Liu J Characteristic analysis and experiment of adaptive fiber optic current sensor technology. *Appl Sci* (2019) 9:333. doi:10.3390/app9020333

6. Qi YF, Wang MJ, Zhang FX, Zhang X, Cong BT, Liu YY Novel fiber optic current transformer with new phase modulation method. *Photonic Sensors* (2020) 10(3):275–82. doi:10.1007/s13320-020-0581-6

7. Roger AF, Moghaddam AA, Diaz ER, Vasquez JC, Guerrero JM J. Uceda. Dynamic assessment of COTS converters-based DC integrated power systems in electric ships. *IEEE Trans Ind Inform* (2018) 14(2):5518–29. doi:10.1109/TII.2018.2810323

8. Menis R, da Rin A, Vicenzutti A, Sulligoi G Dependable design of all electric ships integrated power system: Guidelines for system decomposition and analysis. In: IEEE conference: Electrical Systems for Aircraft, Railway and Ship Propulsion; 2-4 Nov 2016 (2012). p. 13193142.

9. Shen QY, Ramachandran B, Srivastava SK, Andrus M, Cartes DA Power and energy management in integrated power system. In: IEEE Electric Ship Technologies Symposium; 10-13 April 2011 (2011). p. 12008016.

10. Short SX, Tselikov AA, de Arruda JU, Blake JN Imperfect quarter-waveplate compensation in Sagnac interferometer-type current sensors. *J Lightwave Technol* (1998) 16(7):1212–9. doi:10.1109/50.701399

11. Short SX, Tantaswadi P, de Carvalho RT, Russell BD, Blake J An experimental study of acoustic vibration effects in optical fiber current sensors. *IEEE Trans Power Deliv* (1996) 11(4):44–5. doi:10.1109/mper.1996.4311007

12. Gao ZX, Zhang YG, Zhang Y Modeling for IFOG vibration error based on the strain distribution of quadrupolar fiber coil. *Sensors* (2016) 16:1131. doi:10.3390/s16071131

13. He XM, Wang GC, Gao W, Wang YG, Gao HZ The effect analysis of impact on a fiber optic current sensor. *Optik* (2021) 238:166724. doi:10.1016/j.ijleo.2021.166724

14. Wang ZC, Wang GC, Wang YY, Wang Z, Gao W Research on the birefringence distribution of the fiber coil with quadrupole symmetrical winding method. *IEEE Sensors J* (2022) 22(4):3219–27. doi:10.1109/JSEN.2021.3139626

15. Tsubokawa M, Higashi T, Negishi Y Mode couplings due to external forces distributed along a polarization-maintaining fiber: An evaluation. *Appl Opt* (1988) 27(1):166–73. doi:10.1364/ao.27.000166

16. Szpulak M, Martynkien T, Urbanczyk W Effects of hydrostatic pressure on phase and group modal birefringence in microstructured holey fibers. *Appl Opt* (2004) 43(24):4739–42. doi:10.1364/ao.43.004739

17. Li S, Li YB, Lv HW, Ji CT, Gao HZ, Sun Q Chiral dual-core photonic crystal fiber for an efficient circular polarization beam splitter. *Photonics* (2023) 10:45. doi:10.3390/photonics10010045

18. Zhu ZM, Brown TG Stress-induced birefringence in microstructured optical fibers. *Opt Lett* (2003) 28(23):2306–9. doi:10.1364/ol.28.002306

frontiers | Frontiers in Physics

TYPE Brief Research Report
PUBLISHED 15 May 2023
DOI 10.3389/fphy.2023.1208411

OPEN ACCESS

EDITED BY
Zhenxu Bai,
Hebei University of Technology, China

REVIEWED BY
Zhichao Liu,
Changchun University of Science and Technology, China
Mingming Luo,
Hebei University of Technology, China

*CORRESPONDENCE
Dajun Chang,
changdajun@mails.cust.edu.cn

RECEIVED 19 April 2023
ACCEPTED 05 May 2023
PUBLISHED 15 May 2023

CITATION
Chang Y, Chang D and Su L (2023), Based on adaptive modulation laser communication multi-microgrids scheduling system.
Front. Phys. 11:1208411.
doi: 10.3389/fphy.2023.1208411

Based on adaptive modulation laser communication multi-microgrids scheduling system

Ying Chang[1], Dajun Chang[2]* and Li Su[3]

[1]School of Computer Engineering and Artificial Intelligence, Jilin University of Architecture and Technology, Changchun, Jilin, China, [2]School of Electrical Information, Changchun University of Architecture and Civil Engineering, Changchun, Jilin, China, [3]Jilin Academy of Chinese Medicine Sciences, Changchun, Jilin, China

In order to improve the data sharing and comprehensive information processing capabilities between multi-microgrids in the power system, the multi-microgrids scheduling system based on laser communication has been proposed. In order to reduce the error rate of laser communication and reduce the impact of atmospheric turbulence on signal acquisition, an adaptive modulation algorithm has been designed. A mathematical model for laser communication modulation and demodulation based on adaptive modulation algorithm has been constructed. In simulation analysis, the target signal was extracted from the original signal superimposed with atmospheric turbulence noise through filtering and demodulation. The energy fluctuation of the extracted signal decreased from 47.3 to 5 mV. The energy attenuation trend of communication lasers within the range of 0–6 km was experimentally tested. Within 2.0 km, the energy demodulation results of both algorithms are similar, both below 10%. After exceeding 2.0 km, the calculation error of the adaptive modulation algorithm remains basically unchanged, while the error of traditional algorithms increases by about twice. For the APD response value, the adaptive modulation algorithm demodulation has a higher response range concentration ratio and the higher envelope recognition. Under different nominal atmospheric turbulence values, the maximum error rates of the adaptive modulation algorithm are 5.8×10^{-8}, 8.9×10^{-8}, and 1.2×10^{-7}, respectively, while the maximum error rates of the amplitude coherent algorithm are 2.9×10^{-5}, 6.3×10^{-5}, and 1.05×10^{-4}, respectively. It can effectively suppress the impact of atmospheric turbulence on the error rate of laser communication by adaptive modulation algorithm.

KEYWORDS

laser communication, multi-microgrids scheduling, adaptive modulation, error rate, demodulation analysis

1 Introduction

With the development of the Internet and microgrids technology, a single microgrid is no longer able to meet existing energy needs. In order to improve the reliability of large-scale power supply, sub-microgrids are constructed into interconnected and interconnected multi-microgrids systems [1]. “Internet plus + multi micro network” can realize the intelligence of energy, and realize the comprehensive management of energy storage, energy transmission and energy use through big data, cloud computing and other technologies [2]. A multi-microgrids

system can achieve reliable power supply for multiple loads, and by combining micro sources, multiple sources can complement each other and improve energy utilization efficiency. The coordinated control technology of Internet plus multi-microgrids connection is one of the important research directions [3]. In order to achieve efficient communication of multi-microgrids data, laser communication technology is used to construct high-speed data communication transmission channels in the multi-microgrids system.

With the continuous maturity of equipment such as lasers, detectors, and optical amplifiers, laser communication technology has also made significant progress in the civilian field. In 2017, Ratnam V [4] completed laser communication experiments between airships using an FSOC optical transceiver. Its communication distance exceeds 100 km and communication rate is 130Mbps. In 2018, Horwath [5] used airborne terminals MLT-70 and GS-200 ground stations to achieve communication, with a communication rate of up to 10Gbps and a communication distance of 10 km. In 2018, Hu H [6] completed laser communication between vehicles using a 15ZFF optical transceiver, with a central wavelength of 1550 nm. At a distance of 0.5km, the communication rate is 2.5Gbps. At a distance of 10km, the communication rate is 155Mbps. In 2019, Li L [7] completed laser communication experiments between buildings using an Artolink optical transceiver. In the experiment, a 1550 nm laser was used, with a system link distance of 4.4 km and a communication rate of 1.25Gbps. In 2019, Sayan O F [8] completed laser communication between aircraft using the MLT-30 optical transceiver, with a communication link of up to 40 km and a communication rate of 10Gbps. In 2019, Von Rhein J [9] used a 15YDF optical transceiver for malicious communication between two buildings, with a communication distance of 500 m and a communication speed of 10Gbps. In 2020, Yu X [10] used a full cycle laser terminal for real-time communication of 12.7 km dynamic targets, and the system adopted a full cycle dynamic servo mechanism, with a communication rate of up to 2.5Gbps. In 2021, Quintana C [11] conducted laser communication between ground and unmanned aerial vehicles, constructing a data link through the combination of modulators and reflectors. The system has achieved an effective aperture of 11mm, with a communication rate of up to 500Mbps and an error rate of 7.6E-4 over a testing distance of 560 m. In 2023, Chen Hui [12] completed the measurement of Brillouin scattering in laser communication. In 2023, Jin D [13] achieved precise control of modulation frequency by using a narrow linewidth laser modulation. In 2023, Bai Z [14] achieved laser amplitude modulation using a tunable pulse width oscillator, improving the stability of laser communication.

In summary, laser communication has the advantages of large communication capacity and no electromagnetic interference in laser signals. It is very suitable for massive data calculation and communication between multiple microgrids. Therefore, this article proposes a multi micro network networking system based on laser communication.

2 Multi-microgrids scheduling system with laser communication

The multi-microgrids scheduling system based on laser communication is shown in Figure 1. The electrical energy of the main power grid is transmitted to various electricity consuming units through Power transmission lines. The power generation department also transmits electrical energy to the Energy storage system through the main power grid. The load end includes industrial power units, urban power units, etc. All modules use Transformers to complete current matching and circuit breakers to complete circuit protection before being connected to the main power grid. The main information such as power consumption of each output and input unit will be transmitted to the LCU (Laser communication unit) through Data communication. Lidar sends data information from the power microgrids to another. After summarizing all electrical energy transmission information, it is transmitted by the microgrids management system to the Power Grid dispatch center, ultimately completing control of power network distribution, grid connection, etc. In the system, LiDAR can not only achieve data interaction between sub units and the main control unit, but also complete data communication between sub units. Each laser communication unit can be a power data communication terminal in an industrial factory area or a power data communication terminal in an urban area.

The Laser communication unit mainly includes atmospheric channels, lasers, detectors, optical antennas, terminal equipment, power supplies, etc. The information is controlled by the processing system and modulated onto the optical carrier generated by the laser using a modulator. Then transmit it to the receiving end through an optical transmitting antenna. The optical signal reaches the receiving end through an atmospheric channel. The optical receiving antenna focuses the laser signal, which is then converted into an electrical signal by the detector. After amplification and filtering, it enters the processing system of the receiving end.

3 Adaptive laser modulation model

Due to the fact that there is more than one communication location in the power network, the entire system is a laser communication network. For networks, the order of communication between laser communication modules, channel occupancy ratio, and communication time allocation can have an impact on communication efficiency. So in the process of laser communication, it is necessary to adaptively modify the modulation degree and demodulation method under different distances and atmospheric turbulence interference conditions. The adaptive algorithm proposed in this article is to improve the efficiency of laser communication by introducing adaptive parameters during the modulation process.

3.1 Signal expression

In order to achieve higher communication efficiency [15] and reduce the error rate of laser communication, a mathematical model based on adaptive laser modulation was constructed. The signal sequence can be represented by the state values of 1 and 0, that is, 1 and 0 in the carrier amplitude. Firstly, set the main data parameters in the system.

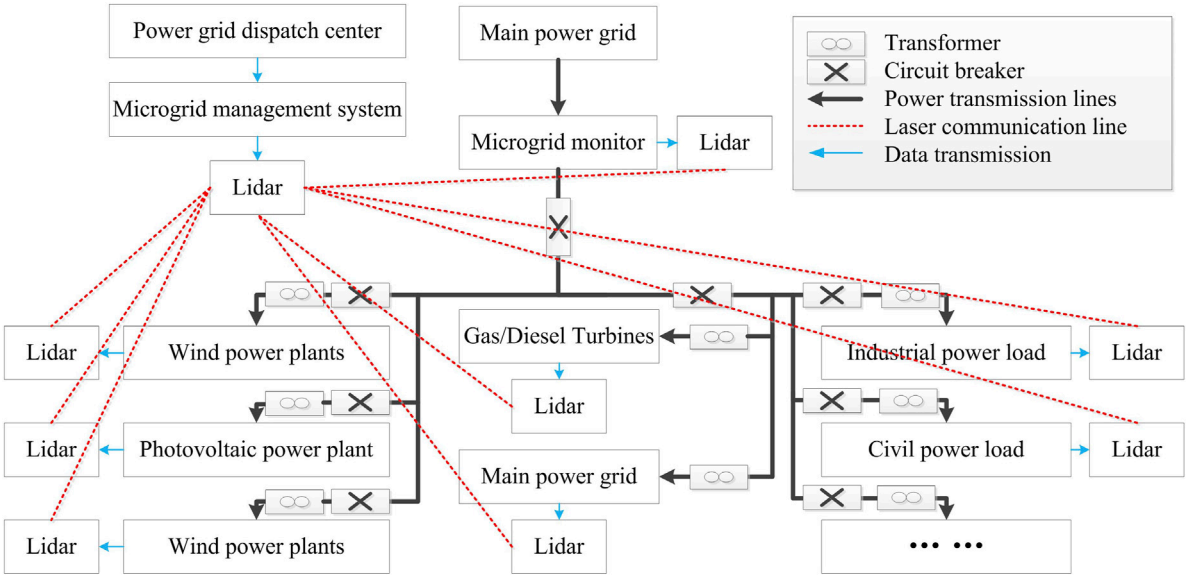

FIGURE 1
Power microgrids monitoring system by laser communication.

a) Signal amplitude. The data amplitude modulation in laser communication is achieved by modulating the basic signal [16], and its formula is as follows

$$V(x) = \sum_i x_i h(x - kX_i) \tag{1}$$

Among them, x_i is the amplitude of ith signal. X_i is the period. $h(x)$ is the pulse waveform. k is the compensation coefficient within the cycle.

b) Frequency shift signal and phase shift signal. Frequency shift signal is the carrier wave of information achieved by the system by overlaying signals of different frequencies [17]. A phase shift signal is the phase shift of a signal. Let the two communication states be 0 and 1, where 0 represents the basic carrier frequency f_1 and 1 represents the carrier frequency f_2. The frequency shift signal and phase shift signal have

$$\begin{cases} Q_f(x) = G\sum_i (x - kX_i)^{\phi_i} \\ Q_p(x) = G\sum_i (x - kX_i)^{\phi - \phi_i} \end{cases} \tag{2}$$

Among them, G is the amplitude. φ is the initial phase. φ_i is the phase of ith test position.

3.2 Modulation model design

Set the power data in the power communication process as the modulation signal $f(x)$, and the carrier signal as $e(x) = \cos\alpha_0 x$, where α_0 is the carrier frequency [18]. The output signal $y(x)$ of the system can be expressed as

$$y(x) = f(x)\cos\alpha_0 x \tag{3}$$

According to Eq. 1, there is a proportional relationship between y x) and f x), which is the amplitude modulation of the laser signal [16]. According to the frequency domain convolution calculation, its spectral expression is

$$Y(i\alpha) = \frac{1}{2\pi} F(i\alpha)^* E(i\alpha) \tag{4}$$

$F(i\alpha)$ and $E(i\alpha)$ can be modulated to achieve signal loading and parsing. The spectrum $Y(i\alpha)$ of y(x) will generate a controllable frequency shift during modulation, which can be automatically aligned during laser communication through adaptive algorithms. The sideband signal in the system can be represented as

$$c(x) = kf(x)\cos\alpha_i x \tag{5}$$

Among them, k represents the processing coefficient. The above formula can suppress noise entering the communication system and achieve real-time adjustment of the system sideband signal amplitude [19]. In order to enable the communication system to automatically switch communication targets in different subunits, an adaptive function is set to classify communication data. The setting parameters for classification are achieved by adding a high pass filtering module, and modifying the filter to perform secondary processing on the updated signal. Set the noise phase shift of the signal in the subunit as an independent state parameter, which has a uniformly distributed feature in the signal interval. Then, calculate the phase offset of different units through processing functions, and obtain the phase setting value for the optimal overall communication. In sub unit communication, initialize the setting data of the processing function. Then, the preset modulation parameters are substituted into the system to complete the adaptive iterative calculation. Finally, the parameter settings that match the overall communication optimal solution will be combined as the updated control parameters.

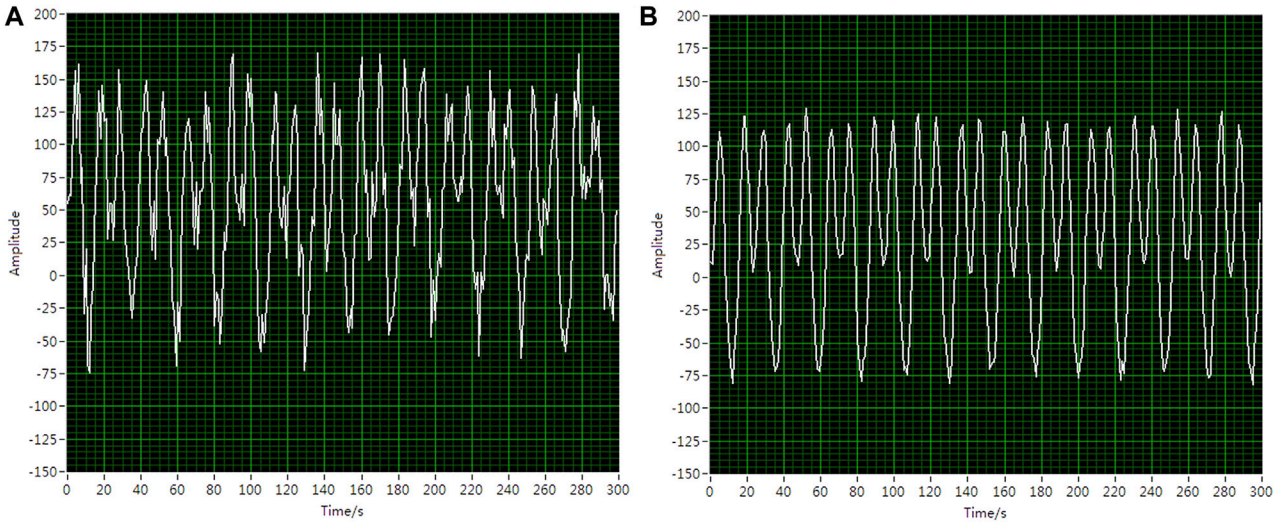

FIGURE 2
Signal curve before and after filtering.

4 Filter simulation analysis

When laser communication is completed between mult-microgrids, communication data will be attenuated in the atmospheric transmission channel, and stray light will interfere with the reception of laser signals. However, due to the significant difference in frequency between other interference signals such as stray light and the modulation signal of the system, the adaptive laser modulation algorithm proposed in this article can be used for filtering. Filter and process the loaded noise signal through Labview. The root mean square value of the noise is 200.0 mV, and the root mean square value of the signal source is 250.0 mV. The noise reduction filtering in this article adopts the built-in filtering program in Labview software, namely, the Cutoff function. Select its bandpass function and set the frequency to 10–100 Hz. Analyze two sets of superimposed signals and extract modulated signals from the mixed signals. The mixed signal and the signal is shown in Figure 2.

As shown in Figure 2A, the laser modulation signal emitted by the laser communication system is affected by atmospheric attenuation and atmospheric turbulence when passing through the atmospheric channel, and the signal will mix with noise, mainly Gaussian white noise. During the simulation, the root mean square value of the noise was set to 200.0 mV, indicating that the modulation waveform experienced peak to peak bifurcation and signal mean shift. The average value of the entire test curve was 58.5 mV, with fluctuations of approximately 47.3 mV. If this signal is directly used for demodulation, it will result in a significant increase in the error rate of the communication system. Therefore, the original signal needs to be filtered first, and the modulated waveform after processing is shown in Figure 2B. The laser modulation signal becomes smooth, and there is no longer a bifurcation phenomenon at each peak position, presenting a single main peak waveform. The average of the entire test curve is 52.3 mV, with fluctuations of less than 5.0 mV, which is about an order of magnitude lower than before optimization. The overall mean shift is very small, and the signal output is stable. Throughout the entire communication process, the error changes of all sampling point test data are basically consistent with it.

5 Experiments

The experimental system includes a laser, a modulation and transmission module, and a reception and demodulation module. The laser adopts Lumileds' c-band infrared laser, with a luminous power superior to 300 mW and a divergence angle of 100 at a communication rate of 10.0Mbps. The collimator adopts the RC08FC collimation system from THORLABS company, with a transmission power of −3.38dBm. The adaptive modulation galvanometer adopts OIM103 electromagnetic galvanometer, with a control voltage of 0- ± 10 V and a maximum rotation amplitude of 25.3 mrad. The APD detector uses the S8664 photoelectric sensor from Hamamatsu Company, with a detection bandwidth of 20Mbps. The AD7605 AD chip is selected in the signal acquisition module to complete rapid data processing.

5.1 Communication laser energy testing

In the process of laser communication, the communication distance has the most significant impact on the communication effect. On the one hand, as the communication distance increases, the degree of spot divergence increases, resulting in a decrease in received laser energy and a decrease in signal-to-noise ratio. On the other hand, the longer the distance through the atmospheric channel, the more obvious the effect of atmospheric disturbances and turbulence. In order to verify the better communication capability of the laser communication system based on adaptive modulation, the same system hardware is used to receive the same

TABLE 1 Laser energy test data under different communication distances.

Test distance (*km*)	TH-M900HDJG (*mA*)	Adaptive modulation algorithm (*mA*)	Error (%)	Amplitude coherence algorithm (*mA*)	Eror (%)
0.5	43.55	41.36	5.03	40.36	7.32
1.0	35.61	33.58	5.70	32.58	8.32
1.5	28.89	27.69	4.15	25.89	9.46
2.0	20.36	18.95	6.93	18.25	9.84
2.5	16.57	16.85	1.69	14.15	14.60
3.0	12.35	11.48	7.04	10.48	15.14
3.5	9.48	8.81	7.07	7.81	17.62
4.0	6.35	5.79	8.82	5.19	18.27
4.5	3.64	3.31	9.07	2.91	20.05
5.0	0.52	0.47	6.77	0.41	21.15
5.5	0.26	0.24	8.69	0.21	23.56
6.0	0.11	0.09	9.25	0.07	24.35

set of laser test signals, and the adaptive modulation algorithm and amplitude coherence algorithm are respectively used for analysis. The test results are shown in Table 1.

The test results show that the received optical power conforms to the logarithmic normal distribution within 2.0 km. Its energy is mainly distributed in the range of 20–40 mA, with a variance of approximately 0.0825. After adopting adaptive modulation, the optical power tends to stabilize, with its energy mainly distributed in the range of 20–25 mA, and the variance reduced to 0.0064. Experiments have shown that adaptive modulation can effectively suppress signal power fluctuations caused by turbulence. Within the range of 2.0–6.5 km, the output optical power of APD exhibits a negative exponential distribution. Its energy is mainly distributed in the range of 0.5–20.0 mA, with a variance of approximately 0.9258. Compared to the test results below 2.0 km, it can be seen that there is energy attenuation and the fluctuation has increased by nearly an order of magnitude. As the communication distance increases, the energy of the communication laser weakens and the variance fluctuation significantly increases. The signal energy calculation results of the two algorithms are similar within 3.0 km. After exceeding 3.0 km, the solution performance of the adaptive modulation algorithm gradually outperforms that of the amplitude coherence algorithm. The testing of laser energy is to analyze the signal amplitude during laser communication, as it is proportional to the laser energy.

5.2 Signal demodulation analysis

In order to verify the good demodulation performance of the adaptive modulation algorithm signal, demodulation analysis was conducted on the laser signal at the receiving end. The signal was obtained using the receiving module in the laser communication system, and 600s of test data were intercepted, as shown in Figure 3.

As shown in Figure 3, the original signal (blue curve in the figure) contains a large amount of noise after passing through the atmospheric channel. The response current fluctuation range on the APD detector is 5–70 mA, with an average of about 38.5 mA and a large variance. After filtering, the filtered signal can be obtained through the demodulation calculation of the adaptive modulation algorithm (red curve in the figure). After filtering and demodulation calculation, the response current fluctuation range on the APD detector is reduced to 22.0–53.0 mA, with an average of about 39.3 mA and a significant reduction in variance. The APD response current demodulated using an adaptive modulation algorithm has good output characteristics. The curve can roughly see the signal envelope in the range of about 100 s, and after data processing, the modulated data can be well recognized. By performing Fourier transform on filtered signals, their frequency domain information can be obtained, and their Frequency shift signal and Phase shift signal can be solved. By comparing with the original modulated signal of the laser communication signal, the frequency shift signal and phase shift signal of the received signal relative to the original signal can be calculated.

5.3 Error rate comparison test

From the received light intensity and the response current of the APD detector, it can be seen that the signal-to-noise ratio has been improved after adopting adaptive modulation. In order to further validate the advantages of this design in laser communication, the error rate of the adaptive modulation algorithm and the amplitude coherence algorithm under different atmospheric turbulence nominal values were compared. The nominal values of atmospheric turbulence are taken as $C_1 = 10^{-15}$, $C_2 = 10^{-16}$ and $C_3 = 10^{-17}$, respectively, and the test results are shown in Figure 4. C_1, C_2 and C_3 are the error rate of a laser communication system, calculated by subtracting the total amount of communication data

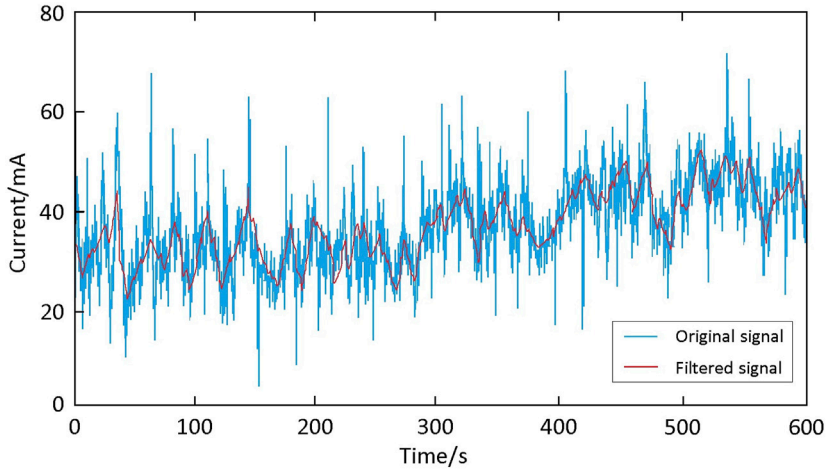

FIGURE 3
APD response current value before and after filtering.

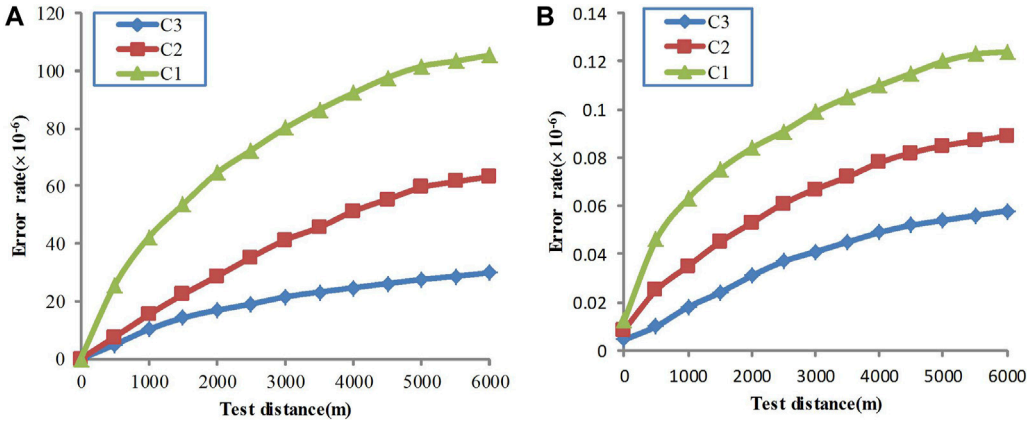

FIGURE 4
Bit error rates before and after adaptive modulation optimization.

from the amount of error data during the communication process and dividing it by the total amount of communication. It is often used to analyze the transmission accuracy of communication systems.

As shown in Figure 4A, as the communication distance increases, the error rate also increases. The testing distance has increased from 0 to 6 km. When $C_1 = 10^{-15}$, the error rate increases from 4.5×10^{-9} to 2.9×10^{-5}; When $C_2 = 10^{-16}$, the bit error rate increases from 8.5×10^{-9} to 6.3×10^{-5}. When $C_3 = 10^{-17}$, the error rate increases from 1.3×10^{-8} to 1.05×10^{-4}. As the nominal value of atmospheric turbulence decreases, the error rate of laser communication systems is also gradually decreasing. In contrast, when $C_1 = 10^{-15}$, the bit error rate using adaptive modulation algorithms increases from 4.3×10^{-9} to 5.8×10^{-8}; When $C_2 = 10^{-16}$, the bit error rate increases from 8.2×10^{-9} to 8.9×10^{-8}. When $C_3 = 10^{-17}$, the error rate increases from 1.2×10^{-8} to 1.2×10^{-7}. The error rate variation amplitude of the adaptive modulation algorithm is much smaller than the calculation result of the amplitude coherence algorithm. The error rate of the adaptive modulation algorithm is also less disturbed by the nominal value of atmospheric turbulence than that of the amplitude coherence algorithm. The superiority of this algorithm has been verified.

6 Conclusion

This article focuses on the problem of requiring a large amount of data transmission in the multi-microgrids scheduling process of power systems, and designs a multi-microgrids scheduling system based on laser communication. Apply adaptive modulation algorithms in laser communication systems to modulate and demodulate communication signals. The impact of atmospheric

turbulence on communication laser energy, APD response value, and laser communication error rate was analyzed through simulation and experimental testing. We compared the testing results of adaptive modulation algorithm and amplitude coherence algorithm, analyzed the error rate of laser communication in different states, and verified the feasibility of the system and the superiority of the algorithm.

Data availability statement

The original contributions presented in the study are included in the article/supplementary material, further inquiries can be directed to the corresponding author.

Author contributions

YC proposed the design concept of the paper and wrote it. DC completed the simulation analysis. LS participated in the experimental testing. All authors contribute to the paper. All authors listed have made a substantial, direct, and intellectual contribution to the work and approved it for publication.

Funding

This work was supported in part by Key R&D of Jilin Provincial Department of Science and Technology, project name: "Research on Key Technologies for Multi-microgrids Connection and Coordinated Control" (20230203050SF).

Conflict of interest

The authors declare that the research was conducted in the absence of any commercial or financial relationships that could be construed as a potential conflict of interest.

Publisher's note

All claims expressed in this article are solely those of the authors and do not necessarily represent those of their affiliated organizations, or those of the publisher, the editors and the reviewers. Any product that may be evaluated in this article, or claim that may be made by its manufacturer, is not guaranteed or endorsed by the publisher.

References

1. Vali Z, Gholami A, Ghassemlooy Z, Michelson DG System parameters effect on the turbulent underwater optical wireless communications link. *Optik* (2019) 198:163153. doi:10.1016/j.ijleo.2019.163153

2. Akyildiz IF, Pompili D, Melodia T. Challenges for efficient communication in underwater acoustic sensor networks. *ACM SIGBED Rev* (2004) 1(2):3–8. doi:10.1145/1121776.1121779

3. Kim J, Joe H, Yu SC, Lee JS, Kim M. Time-delay controller design for position control of autonomous underwater vehicle under disturbances. *IEEE Trans Ind Electron* (2016) 63(2):1052–61. doi:10.1109/tie.2015.2477270

4. Ratnam V, Krishnan P. Bit error rate analysis of ground-to-high altitude platform free-space optical communications using coded polarization shift keying in various weather conditions[J]. *Opt Quan Electron* (2022) 54(1):1–18. doi:10.1007/s11082-021-03398-6

5. Horwath J, Diaz Gonzalez D, Martin Navajas L, Souto AL, Haque F, Grier A, et al. Test results of error-free bidirectional 10 Gbps link for air-to-ground optical communications. In: Free-Space Laser Communication and Atmospheric Propagation XXX; 29-30 January 2018; San Francisco, California, USA. San Jose, California, USA: SPIE (2018).

6. Hu H, Oxenlowe LK, Morioka T, Yankov MP, Da Ros F, Amma Y, et al. Ultrahigh-spectral-efficiency WDM/SDM transmission using PDM-1024-QAM probabilistic shaping with adaptive rate. *J lightwave Technol* (2018) 36(6):1304–8. doi:10.1109/jlt.2017.2787340

7. Li L, Zhang R, Liao P, Cao Y, Song H, Zhao Y, et al. Mitigation for turbulence effects in a 40-Gbit/s orbital-angular-momentum-multiplexed free-space optical link between a ground station and a retro-reflecting UAV using MIMO equalization. *Opt Lett* (2019) 44(21):5181–4. doi:10.1364/ol.44.005181

8. Sayan OF, Gercekcioglu H, Baykal Y. Hermite Gaussian beam scintillations in weak atmospheric turbulence for aerial vehicle laser communications. *Opt Commun* (2020) 458:124735. doi:10.1016/j.optcom.2019.124735

9. Von Rhein J, Henze GP, Long N, Fu Y. Development of a topology analysis tool for fifth-generation district heating and cooling networks. *Energ Convers Manage* (2019) 196(9):705–16. doi:10.1016/j.enconman.2019.05.066

10. Yu X, Zhang L, Zhang Y, Song Y, Tian M, Wang T, et al. 2.5Gbps free-space optical transmission between two 5G airship floating base stations at a distance of 12km. *Opt Lett* (2021) 46(9):2156–2159. doi:10.1364/ol.419690

11. Quintana C, Wang Q, Jakonis D, Oberg O, Erry G, Platt D, et al. A high speed retro-reflective free space Optics links with UAV. *J Lightwave Technol* (2021) 39(18):5699–705. doi:10.1109/jlt.2021.3091991

12. Hui C, Bai Z, Cai Y, Yang X, Ding J, Qi Y, et al. Order controllable enhanced stimulated Brillouin scattering utilizing cascaded diamond Raman conversion. *Appl Phys Lett* (2023) 122(9):092202. doi:10.1063/5.0137542

13. Jin D, Bai Z, Lu Z, Fan R, Zhao Z, Yang X, et al. 22.5-W narrow-linewidth diamond Brillouin laser at 1064 nm. *Opt Lett* (2022) 47(20):5360–5363. doi:10.1364/ol.471447

14. Bai Z, Zhao C, Gao J, Chen Y, Li S, Li Y, et al. Optical parametric oscillator with adjustable pulse width based on KTiOAsO4. *Opt Mater* (2023) 136:113506. doi:10.1016/j.optmat.2023.113506

15. Jin D, Bai Z, Li M, Yang X, Wang Y, Mildren RP, et al. Modeling and characterization of high-power single frequency free-space Brillouin lasers. *Opt Express* (2023) 31(2):2942–2955. doi:10.1364/oe.476759

16. Chen B, Bai Z, Hun X, Wang J, Cui C, Qi Y, et al. Gain characteristics of stimulated Brillouin scattering in fused silica. *Opt Express* (2023) 31(4):5699–5707. doi:10.1364/oe.480391

17. Lin Y Application of neural network-based nonlinear intelligent control in electro-optical tracking systems. *Opt Precision Eng* (2018) 26(12):2949–55. doi:10.3788/ope.20182612.2949

18. Talmora G, Harding JH, Chen CC. Two –axis gimbal for air-to-air and air-to-ground laser communications. *Proc 2016 SPIE* (2016) 9739:1–8. Baltimore. SPIE. doi:10.1117/12.2218097

19. Yang JS. Design and implementation of large scale internet of things laser communication system. *Laser J* (2019) 40(4):92–96.

frontiers | Frontiers in Physics

TYPE Brief Research Report
PUBLISHED 01 June 2023
DOI 10.3389/fphy.2023.1190569

OPEN ACCESS

EDITED BY
Shuo Liu,
Hebei University of Technology, China

REVIEWED BY
She Shengfei,
Chinese Academy of Sciences (CAS), China
Quan Sheng,
Tianjin University, China
Wang Pengyuan,
Chinese Academy of Sciences (CAS), China

*CORRESPONDENCE
Yu Shen,
shenyu@mail.ipc.ac.cn
Qin-Jun Peng,
pengqinjun@mail.ipc.ac.cn

RECEIVED 21 March 2023
ACCEPTED 09 May 2023
PUBLISHED 01 June 2023

CITATION
Chang J-Q, Bian Q, Bo Y, Shen Y and Peng Q-J (2023), 2.85-kW cryogenic Nd:YAG slab laser operating at 946 nm. *Front. Phys.* 11:1190569. doi: 10.3389/fphy.2023.1190569

2.85-kW cryogenic Nd:YAG slab laser operating at 946 nm

Jin-Quan Chang[1,2,3], Qi Bian[1,2], Yong Bo[1,2], Yu Shen[1,2]* and Qin-Jun Peng[1,2]*

[1]Key Lab of Solid State Laser, Technical Institute of Physics and Chemistry, Chinese Academy of Sciences, Beijing, China, [2]Key Lab of Function Crystal and Laser Technology, Technical Institute of Physics and Chemistry, Chinese Academy of Sciences, Beijing, China, [3]University of Chinese Academy of Sciences, Beijing, China

A several-kilowatt level laser at 946 nm is demonstrated in a cryogenically cooled diode-pumped Nd:YAG slab system. The oscillator realizes the record of the output power of 2.85 kW in a compact cavity with the homemade cryogenically cooled Nd:YAG crystal slab. The pulse repetition rate and pulse width of the laser are 400 Hz and 200 μs, respectively, and the center wavelength under full power is 946.2 nm with a bandwidth of about 0.5 nm. The absorption linewidth at 808 nm is a little narrowed and blue shifts at the cryogenic temperature, while the cooling temperature decreases from 300 to 77 K. The measured thermal conductivity increases from 10 to 70 W/m·K, and the thermal expansion coefficient decreases from $7.5*10^{-6}$ to $1.5*10^{-6}$/K. These results could guide us in simulating the temperature gradient and thermal-induced stress distributions in the crystal slab.

KEYWORDS

high power, cryogenically cooled, diode-pumped, Nd:YAG, slab laser, 946 nm

1 Introduction

High-power lasers with special wavelengths offer a wide range of applications in the fields of medical aesthetics, laser processing, and nonlinear optics [1–5]. As the most widely used solid-state gain medium, neodymium-doped yttrium aluminum garnet (Nd:YAG) crystals with different shapes have received widespread attention in the fields of high-power laser oscillators and short-pulse laser amplifiers [6–8]. The common radiation wavelengths of Nd:YAG include 946 nm, 1064 nm, and 1319 nm [9, 10]. The $^4F_{3/2}\rightarrow{}^4I_{9/2}$ transition of Nd:YAG is attractive for achieving a high-power radiant source with a wavelength of 946 nm. Such laser sources are suitable for differential absorption LiDAR systems or for generating into the blue at 473 nm radiation for various applications, such as medical imaging, data storage, manufacturing and processing, and remote sensing [11–14]. However, the 946-nm laser radiation from Nd:YAG with the quasi-three-level transition suffers from some limitations, including significant reabsorption losses, a small stimulated emission cross section compared to the 1064-nm transition, and an intense thermal loading of the gain medium [15]. However, the laser performance could be enhanced for the quasi-three-level 946-nm Nd:YAG laser by cryogenic cooling, which breaks the physical limitation of thermodynamics at room temperature and is inspired from the demonstration of cryogenic Yb:YAG lasers [16–18]. In recent years, extensive research has since been performed toward power scaling of 946-nm Nd:YAG lasers. For example, a 3.8-W continuous wave 946-nm Nd:YAG laser was demonstrated under cryogenic cooling with the temperature range of 90 K–290 K [19]. A 30.2-W 946-nm laser was obtained by using an 8-mm Nd:YAG crystal at 130 K [20]. A 60-W cryogenically cooled Nd:YAG laser at 946 nm

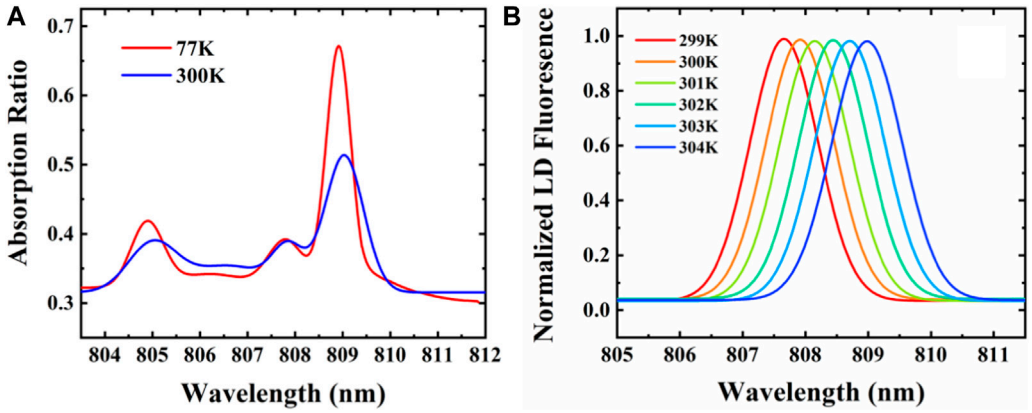

FIGURE 1
(A) Absorption spectrum of Nd:YAG at 77 K and 300 K and **(B)** output spectrums of the diode laser array at the coolant temperatures of 299 K, 300 K, 301 K, 302 K, 303 K, and 304 K.

was reported with a high-brightness pumping diode laser array of 869 nm [21]. In addition, G Shayeganrad broke through the 100-W level Nd:YAG laser at 946 nm with a closed-cycle cryogenically cooled laser [22]. In our previous reports, a 1.06-kW quasi-continuous wave surface-pumped cryogenically cooled 946-nm Nd:YAG slab laser was developed [23]. These demonstrations suggest that cryogenic cooling is an excellent solution for achieving high-power 946-nm laser radiation.

In this paper, a cryogenically cooled Nd:YAG crystal slab laser with quasi-continuous wave operation having an output power of 2.85 kW at 946 nm is demonstrated. We first thoroughly measure the absorption spectra of the 0.6-at.% Nd:YAG crystal at the temperatures of 300 K and 77 K. Then, the temperature-dependent thermal expansion coefficient and thermal conductivity of the 0.6-at.% Nd:YAG crystal were studied simultaneously. The results indicate that the peak of absorption is shift to 808.9 nm when the sample is cooled to 77 K and the bandwidth of the absorption spectrum is narrowed. The conversion efficiency can be improved according to the optimization of the wavelength of the pumped diode laser. To date, this is the highest power laser at 946 nm, acquired in a single Nd:YAG slab, to the best of our knowledge. These results can be used in simulating the temperature gradient and thermal-induced stress distributions in the crystal slab, which guides in optimizing the cooling system of the module.

2 Experimental setup

The key for the performance enhancement of Nd:YAG slab lasers is to increase the overlap region of the Nd:YAG absorption spectrum and the pump laser emission spectrum. The stimulated absorption spectra of the Nd:YAG crystal are measured at the temperatures of 77 K and 300 K. Figure 1A gives the absorption spectra of 0.6 at % Nd:YAG samples from $^4F_{3/2}$ to $^4I_{9/2}$ transition, which is carried out using a fluorescence spectrometer (Edinburgh FLSP980) with a 0.02-nm resolution. It can be observed that the absorption intensity around 809 nm is increased as the temperature

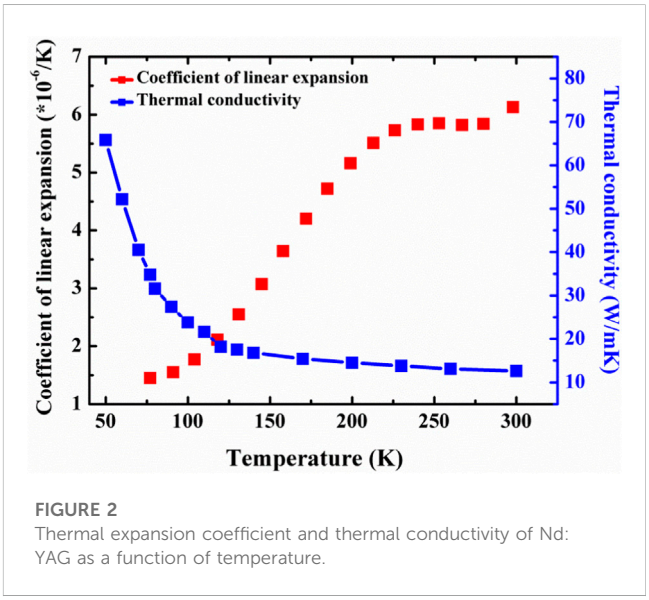

FIGURE 2
Thermal expansion coefficient and thermal conductivity of Nd:YAG as a function of temperature.

decreases, where the bandwidth of the absorption spectrum is narrowed from ~1 nm to 0.6 nm, with the temperature decreasing from 300 K to 77 K. Meanwhile, the peak wavelength was decreased by 0.1 nm over this range. Traditionally, diode lasers are used as pump sources for high-power solid-state lasers due to their merits, including a high conversion efficiency, wavelength tunability, and compactness. Taking the measured absorption spectrum of Nd:YAG in a cryogenic environment, we optimized the pump absorption efficiency at different coolant temperatures of diode laser arrays. As shown in Figure 1B, the emission spectra of the pump sources were measured using an Aurora 4000 spectrum analyzer. The wavelength of a laser diode array (LDA) was temperature-tuned to reach the maximum absorption when it passes through the slab that is cryogenically cooled. This can be realized when the coolant temperature is 303.5 K and the corresponding center wavelength is 809.0 nm with a bandwidth of 1.3 nm.

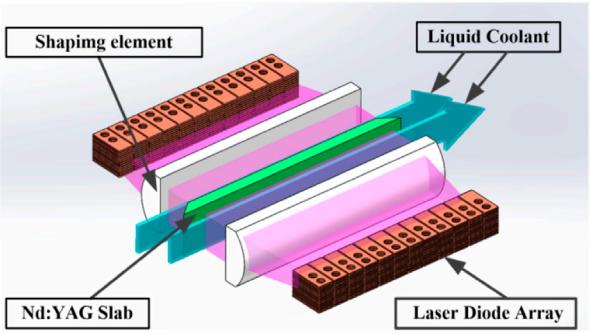

FIGURE 3
Schematic diagram of the experimental setup of the Nd:YAG slab laser.

In order to enhance the output performance of the 946-nm laser, the cryogenic temperature for the cooling slab needs to be reduced to below 140 K to practically eliminate the reabsorption loss [24]. Moreover, we need to minimize the temperature excursion and thermal stress across the slab to ensure the reliability of the laser operation due to the large size of the slab. Therefore, the temperature-dependent thermal expansion coefficient and thermal conductivity of the gain medium should be studied.

It was demonstrated that the cooling of the gain medium to cryogenic temperatures resulted in a significant increase in thermal and mechanical properties compared to that at the room temperature [25, 26]. The measurements presented in this paper were carried out with the φ3 × 9-mm Nd:YAG sample. Thermal conductivity was measured using PPMS-9 by the steady-state longitudinal heat-flow method, and thermal expansion was measured in the temperature range of 77–300 K using a Linseis L75 thermal dilatometer whose accuracy deviation is estimated to be within 1%. The measured thermal conductivity and thermal expansion of Nd:YAG versus the temperature is shown in Figure 2. It can be seen that the thermal expansion coefficient tends to get substantially lower when the cryogenic temperature decreases below 300 K, and the thermal conductivity increases up to almost an order of magnitude as the temperature decreases to 77 K.

The heat transfer coefficient could be affected by the physical characteristics of the gain medium, geometry of the slab, and parameters of the coolant. Slab lasers are well-suited for high-efficiency cooling systems, thus exhibiting favorable results, further realizing the high output power with a high beam quality [27], compared to rod active media. Considering the growth size of the crystals and the absorption efficiency for a pumping laser, the 0.6 at.% doping concentration of the Nd:YAG slab is cut into 173.6 mm × 66 mm × 10 mm. The two end faces of the crystal slab with the angle of 40° are polished and anti-reflection-coated at 1061 nm and 946 nm to reduce the surface reflection. To suppress the parasitic oscillation, we adopt the non-parallel structure with small angle deviations between the two opposite side faces along the length of the slab. At the same time, the two large side faces need to be rough in order to suppress effectively the ASE along the width direction of the slab [28].

Figure 3 shows the experimental setup of the LDA-pumped double face-cooled Nd:YAG slab laser. It is quite important for obtaining a good performance of the slab laser by controlling the intensity distribution and irradiation size of the pump beam [29]. Here, the spot of the LDA-adopted micro-lens array and cylindrical lens is shaped into a well for the overlapping and uniformity pumping intensity. The cooling liquid flows along the two large side faces, entraining the heat when the 946-nm beam passes through the slab in a zigzag path. For improving the cooling efficiency, liquid nitrogen usually flows in a turbulent manner along the large side faces of the slab within the 1.2-mm gap between the shaping element and the slab. A large flow rate is beneficial for improving the heat transfer coefficient; however, a large flow rate also can break down the sealing structure. In addition, a strong turbulent flow may generate vortices that will affect the pump laser transmission, suggesting that the heat transfer coefficient

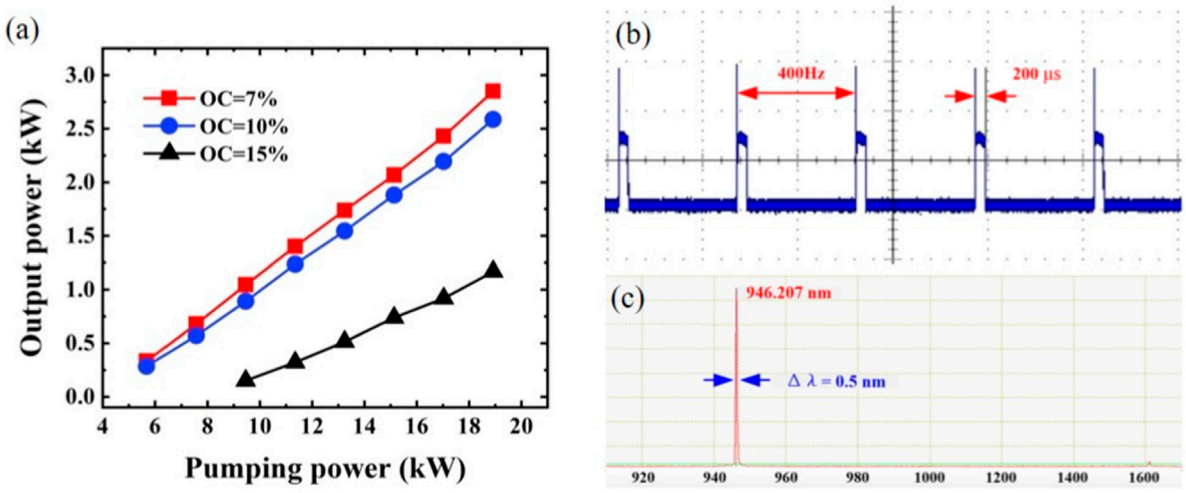

FIGURE 4
(A) Output power of the 946-nm Nd:YAG cryogenic slab laser as a function of diode pump power with 7%, 10%, and 15% optical couplers. **(B)** Oscillator trace of output pulses. **(C)** Emission spectrum for Nd:YAG under full power.

is about 15 kW/K-m^2 between the crystal and the liquid nitrogen coolant at a flow rate of 60 kg/min.

According to the measured result of the absorption spectrum ($\alpha = 0.9\ cm^{-1}$), with a low doping concentration, the absorption ratio for the pumping laser is around 60%. In the simulation, we adopt the curves of thermal conductivity and thermal expansion of the Nd:YAG crystal versus temperature. When the pumping power reaches up to 20 kW, the simulated temperature gradient in the slab is about 39 K and the highest value of thermal stress is about 45 MPa, which is quite smaller than the limit of the fracture [30]. The simulated results indicate that the cooling structure we designed can effectively remove the extra heat in the slab under the high power pumped. Thus, the meticulous design of thermal management for the gain medium can play a role in developing the high-power quasi-three-level lasers.

3 Experimental results

In order to evaluate the laser performance of the cryogenic Nd:YAG slab module operating at 946 nm, we adopted the short cavity structure. A plano-concave mirror with a radius of 750 mm was chosen for its high reflectivity at 946 nm and high transmission at 1061 nm to suppress parasitic lasing. Moreover, we use different plane–plane output coupler transmissions of Toc = 7%, 10%, and 15% to examine the laser performance, considering it as the low-stimulated emission cross section.

The output power of the Nd:YAG slab laser at 946 nm is measured using the Ophir Nova II power meter. Figure 4A shows the results of output power by comparing it with three OCs as a function of the pump power. The maximum optical efficiency was obtained with the output coupling of 7%. We can see that the average output power at 946 nm approximately increases linearly in accordance with the incident pump power. At the pumping power of 18.9 kW, the maximum output power is 2.85 kW, with a corresponding optical-to-optical efficiency of 15.1%. In order to achieve high output power, the profile of the laser beam is in multiple transverse modes, owing to the short cavity setup [31]. The pulse profile of 946-nm laser is measured using a Thorlabs DET200 photodetector whose increase in time is less than 25 ns. The oscillator trace of laser pulses is shown in Figure 4B. The output-pulse temporal characteristics of the 946-nm laser are measured under the maximum output power, and it indicated that the pulse repetition rate of the laser is 400 Hz; the pulse width is about 200 μs. Emission wavelengths of the Nd:YAG slab laser are measured using an Ocean Optics NIRQuest256-2.5 optical spectrum analyzer, as shown in Figure 4C. It can be seen that the center peak of the laser spectrum is 946.2 nm with a bandwidth of 0.5 nm under the full output laser and no evident peak at 1 μm.

4 Discussion and conclusion

We have undertaken a thorough examination of the variations of adsorption, thermal expansion coefficients, and thermal conductivity of the Nd:YAG crystal with temperature. Employing this measured data source, a model temperature gradient and thermal stress distribution in laser slabs can be simulated and calculated to optimize the cooling system design during the development of a high-power laser module. Based on the design parameters, such as the characteristics of the coolant flow, wavelength of the pumping laser, and gain medium geometry, the cryogenic cooling of the multi-kilowatt QCW double face-pumped 946-nm Nd:YAG slab is realized. The laser oscillator delivers a record high average power of 2.85 kW at 946.2 nm, with the conversion efficiency of 15%. The oscillator operates at a repetition frequency of 400 Hz with a pulse width of 200 μs.

Data availability statement

The raw data supporting the conclusion of this article will be made available by the authors, without undue reservation.

Author contributions

Conceptualization, Q-JP and YB; methodology, Q-JP; software, J-QC; validation, J-QC; writing—original draft preparation, J-QC; writing—review and editing, QB and YS; project administration and funding acquisition, Q-JP and YS. All authors contributed to the article and approved the submitted version.

Funding

This research was funded by the National Key Research and Development Program of China (Key Special Projects, Young Scientist, No. 2022YFB3607900); the Key Laboratory Foundation of the Chinese Academy of Sciences, Key Lab of Solid-State Laser (No. CXJJ-22S020); and the National Special Support Program for High-Level Talents in Science and Technology (Innovation Leading Talent Program of the Defense Technology Innovation Foundation, no. SQ2022RA24910010).

Acknowledgments

The authors acknowledge some crystal support from Chengdu Dien Photoelectric Technology Co., Ltd. (DIEN TECH).

Conflict of interest

The authors declare that the research was conducted in the absence of any commercial or financial relationships that could be construed as a potential conflict of interest.

Publisher's note

References

1. Liang L, Yuan J, Lin G Effect of the scanning speed on the microgroove formation regime in nanosecond-pulsed laser scanning ablation of cermet. *Int J Adv Manufacturing Technol* (2020) 107:97–107. doi:10.1007/s00170-020-05017-2

2. Kerse C, Kalaycıoğlu H, Elahi P, Çetin B, Kesim DK, Akçaalan Ö, et al. Ablation-cooled material removal with ultrafast bursts of pulses. *Nature* (2016) 537:84–8. doi:10.1038/nature18619

3. Jin D, Bai Z, Lu Z, Fan R, Zhao Z, Yang X, et al. 22.5-W narrow-linewidth diamond Brillouin laser at 1064 nm. *Opt Lett* (2022) 47:5360–3. doi:10.1364/ol.471447

4. Jin D, Bai Z, Li M, Yang X, Wang Y, Mildren RP, et al. Modeling and characterization of high-power single frequency free-space Brillouin lasers. *Opt Express* (2023) 31:2942–55. doi:10.1364/oe.476759

5. Chen H, Bai Z, Cai Y, Yang X, Ding J, Qi Y, et al. Order controllable enhanced stimulated Brillouin scattering utilizing cascaded diamond Raman conversion. *Appl Phys Lett* (2023) 122:092202. doi:10.1063/5.0137542

6. Zhou B, Kane TJ, Dixon GJ, Byer RL. Efficient, frequency-stable laser-diode-pumped Nd: YAG laser. *Opt Lett* (1985) 10(2):62–4. doi:10.1364/ol.10.000062

7. Bai Z, Zhao C, Gao J, Chen Y, Li S, Li Y, et al. Optical parametric oscillator with adjustable pulse width based on $KTiOAsO_4$. *Opt Mater*, 2023 136, 113506 doi:10.1016/j.optmat.2023.113506

8. Li K, Wang Y, Yu Y, Yue J, Song C, Cao C, et al. Amplification of high repetition-rate, picosecond laser pulses using a zig-zag slab configuration. *Opt Laser Technol* (2023) 157:108717. doi:10.1016/j.optlastec.2022.108717

9. Lü Y, Zhao L, Zhai P, Xia J, Fu X, Li S. Simultaneous three-wavelength continuous wave laser at 946 nm, 1319 nm and 1064 nm in Nd: Yag. *Opt Commun* (2013) 286:257–60. doi:10.1016/j.optcom.2012.08.073

10. Li X, Javed F, Zhang H, Liu X, Chen T, Yang S, et al. High power diode end-pumped 1.3 μm Nd: YAG InnoSlab laser. *Results Phys* (2022) 37:105468. doi:10.1016/j.rinp.2022.105468

11. Mackenzie JI. An efficient high-power 946 nm Nd:YAG planar waveguide laser. *Appl Phys B* (2009) 97(2):297–306. doi:10.1007/s00340-009-3693-7

12. Fan TY, Bye RL. Continuous-wave operation of a room-temperature, diode-laser-pumped, 946-nm Nd:YAG laser. *Opt Lett* (1987) 12(10):809–11. doi:10.1364/ol.12.000809

13. Zhou R, Li E, Li H, Wang P, Yao J. Continuous-wave, 15.2 W diode-end-pumped Nd:YAG laser operating at 946 nm. *Opt Lett* (2006) 31(12):1869–71. doi:10.1364/ol.31.001869

14. Freitag I, Henking R, Tünnermann A, Welling H. Quasi-three-level room-temperature Nd: YAG ring laser with high single-frequency output power at 946 nm. *Opt Lett* (1995) 20(24):2499–501. doi:10.1364/ol.20.002499

15. Bjurshagen S, Koch R. Modeling of energy-transfer upconversion and thermal effects in end-pumped quasi-three-level lasers. *Appl Opt* (2004) 43(24):4753–67. doi:10.1364/ao.43.004753

16. AggarwalRipinOchoa RLDJJR, Fan TY. Measurement of thermo-optic properties of Y3Al5O12, Lu3Al5O12, YAIO3, LiYF4, LiLuF4, BaY2F8, KGd(WO4)2, and KY(WO4)2 laser crystals in the 80–300K temperature range. *J Appl Phys* (2005) 98(10):103514. doi:10.1063/1.2128696

17. Yasuhara R, Furuse H, Iwamoto A, Kawanaka J, Yanagitani T. Evaluation of thermo-optic characteristics of cryogenically cooled Yb:YAG ceramics. *Opt Express* (2012) 20(28):29531–9. doi:10.1364/oe.20.029531

18. Zhou R, Zhang T, Li E, Ding X, Cai Z, Zhang B, et al. 8.3 W diode-end-pumped continuous-wave Nd: YAG laser operating at 946-nm. *Opt express* (2005) 13(25):10115–9. doi:10.1364/opex.13.010115

19. Cho CY, Lee CY, Chang CC, Tuan PH, Huang KF, Chen YF. 24-W cryogenically cooled Nd:YAG monolithic 946-nm laser with a slope efficiency >70%. *Opt Express* (2015) 23(8):10126–31. doi:10.1364/oe.23.010126

20. Cho CY, Huang TL, Cheng HP, Huang KF, Chen YF. Exploring the power scaling of the cryogenic 946 nm monolithic laser. *Laser Phys Lett* (2018) 15(8):085801. doi:10.1088/1612-202x/aac357

21. Cante S, Valle S, Yoon SJ, Mackenzie JI. 60-W 946-nm cryogenically-cooled Nd:YAG laser. *Appl Phys B* (2019) 125(7):135–6. doi:10.1007/s00340-019-7244-6

22. Shayeganrad G, Cante S, Mosquera JP, Bailey WOS, Mackenzie JI. Highly efficient 110-W closed-cycle cryogenically cooled Nd: YAG laser operating at 946 nm. *Opt Lett* (2020) 45(19):5368–71. doi:10.1364/ol.401011

23. Song ZX, Wang BS, Shen Y, Bo Y, Chang JQ, Chen ZZ, et al. QCW surface-pumped cryogenically cooled single-slab laser with 1 kW level at 946 nm. *Appl Opt* (2022) 61(10):2898–902. doi:10.1364/ao.451288

24. Yoon SJ, Mackenzie JI. Cryogenically cooled 946 nm Nd:YAG laser. *Opt Express* (2014) 22(7):8069–75. doi:10.1364/oe.22.008069

25. Schulz PA, Henion Scott R. Liquid-nitrogen-cooled Ti:Al/sub 2/O/sub 3/laser. *IEEE J Quan Electron* (1991) 27(4):1039–47. doi:10.1109/3.83339

26. Brown DC. Ultrahigh-average-power diode-pumped Nd:YAG and Yb:YAG lasers. *IEEE J Quan Electron* (1997) 33(5):861–73. doi:10.1109/3.572162

27. Xie W, Tam SC, Yang H, Gu J, Zhao G, Lam YL, et al. Heat transfer for diode side-pumped YAG slabs. *Opt Laser Technol* (1999) 31(7):521–8. doi:10.1016/s0030-3992(99)00111-5

28. Hackel LA, Soules TF, Fochs SN, Rotter MD. Letts S A, U.S. *patent* 7, 496B2 (2011).

29. Meng S, Chen ZZ, Bo Y, Yuan L, Li Y, Guo YD, et al. 6.2 kW quasi-continuous-wave diode-pumped Yb:YAG ceramic slab laser. *Laser Phys* (2020) 30(1):015802. doi:10.1088/1555-6611/ab570c

30. Koechner W. *Solid-state laser engineering*. 6th ed. Springer (2006). Chap. 2.

31. Furuse H, Kawanaka J, Takeshita K, Miyanaga N, Saiki T, Imasaki K, et al. Total-reflection active-mirror laser with cryogenic Yb:YAG ceramics. *Opt Lett* (2009) 34(21):3439–41. doi:10.1364/ol.34.003439

frontiers | Frontiers in Physics

TYPE Original Research
PUBLISHED 06 July 2023
DOI 10.3389/fphy.2023.1207182

OPEN ACCESS

EDITED BY
Tonglei Cheng,
Northeastern University, China

REVIEWED BY
Yulai She,
Guilin University of Electronic Technology, China
Huaiqing Liu,
West Anhui University, China
Bin Yin,
Ocean University of China, China
Haisu Li,
Beijing Jiaotong University, China

*CORRESPONDENCE
Yudong Lian,
ydlian@hebut.edu.cn

RECEIVED 17 April 2023
ACCEPTED 28 June 2023
PUBLISHED 06 July 2023

CITATION
Qi X and Lian Y (2023), Photonic crystal fiber with double-layer rings for the transmission of orbital angular momentum.
Front. Phys. 11:1207182.
doi: 10.3389/fphy.2023.1207182

Photonic crystal fiber with double-layer rings for the transmission of orbital angular momentum

Xingyu Qi[1,2] and Yudong Lian[1,2]*

[1]Center for Advanced Laser Technology, Hebei University of Technology, Tianjin, China, [2]Hebei Key Laboratory of Advanced Laser Technology and Equiment, Hebei University of Technology, Tianjin, China

In this paper, we propose a novel photonic crystal fiber (PCF) with double-layer rings for transmitting orbital angular momentum (OAM). The substrate of PCF is a pure silicon base. The inner circle is doped with Fluoride to reduce the refractive index (RI), and the transmission domain is doped with Germanium dioxide to increase the RI. On the outer side of the transmission ring, air holes are regularly arranged to restrict the beam transmission within the transmission layer. After calculation, the proposed OAM fiber can effectively support 118 OAM modes in the range of 1.3–1.75 μm with excellent characteristics. In addition, we also found that proposed fiber has "bandgap-like" mode field characteristics.

KEYWORDS

orbital angular momentum, photonic crystal fiber, doped fiber, double layer rings, bandgap-like

1 Introduction

Optical communication is one of the important communication methods, and is highly favored with its high capacity and high speed. In recent years, conventional optical communication technology is getting closer to Shannon's limit. Therefore, wavelength division multiplexing (WDM) [1], mode division multiplexing (MDM) [2] and other multiplexing technologies have become the primary directions of optical communication. Among them, orbital angular momentum (OAM) beam is an excellent carrier beam [3–5]. OAM was proposed by Allen [6] in 1992 and has made a big splash in the field of optical communication. The vortex beam has the phase factor of $e^{il\varphi}$ and the phase distribution is vortex-shaped. Most importantly, OAM theoretically has infinite orthogonal modes in Hilbert space, which provides a very ideal transmission channel for optical communication.

In recent years, the research of OAM transmission fibers has focused on ring core fibers (RCFs) and photonic crystal fibers (PCFs).OAM-RCFs include step index RCF [7], graded index RCF [8], refractive index modulated (RI- modulated) RCF [9], etc. OAM-RCFs improve the characteristics by making corresponding changes of transmission layer rings to make them more compatible with OAM transmission. The design principle of OAM-PCF is that the periodic arrangement of air holes restricts the beam propagating in the fiber core. By adjusting the number [10], arrangement [11], shape [12] of air holes, the supported OAM number by the fiber is greatly increased. There are also some studies on setting transmission rings in PCF, which are RI-modulated. The transmission layer works with the air holes to confine the beam. The fiber combining RCF and PCF has good characteristics for

transmitting OAM. In addition, some special rotating fibers [13] also have unique advantages in transmitting OAM.

In this paper, we propose a PCF containing a double layer of rings. The inner ring is doped with Fluoride to reduce the RI, and the transmission layer is doped with Germanium dioxide to increase the RI. Air holes are regularly arranged on the outside of the transmission layer to restrict the beam within the transmission layer. After calculation, our proposed fiber can support 118 OAM modes in the range of 1.3 μm–1.75 μm and has excellent features such as large mode field and flat dispersion. In addition, proposed fiber also shows characteristics of "bandgap-like PCF".

2 Structure of the designed PCF with double-layer rings

The schematic diagram of our proposed OAM fiber with double layer rings is shown in Figure 1. We dope two layers of rings in the silicon-based PCF. The inner ring is fluoride doped to reduce the RI, and the outer ring is germaniμm dioxide doped to improve the RI. The double-layer circular structure fiber effectively improves the RI difference between the transmission layer and the substrate. The radius of the fiber cladding *r1* is 62.5 μm *r2* is 32 μm, and the thickness of the fluoride doped layer is *d1* = 1 μm with a RI of 1.43. The thickness of the high refractive index layer (HRIL) of the germanium dioxide doped layer is *d2* = 2 μm with a RI of 1.48.

Outside the HRIL we set the air holes arranged periodically. *r3* is 37 μm, and the diameter of the air holes *d* is 6 μm. The air hole spacing Λ is 2 μm. The number of air holes from the inner layer to the outer layer is 30, 36, and 40. In the outermost layer, we set the perfect match layer (PML) with a thickness of 7.5 μm. PML acts as a near-ideal absorber or radiator domain. Therefore, PML reduces the influence of beam reflection and improves the calculation accuracy.

3 Characteristics of PCF with double-layer rings

3.1 Number of OAM modes

According to the fiber coupling mode theory, OAM can be formed by coupling the even and the odd mode of the same vector mode in the fiber [14]:

$$\begin{cases} \sigma^{\pm} OAM_{\pm l} = HE^{even}_{l+1,1} \pm jHE^{odd}_{l+1,1} \\ \sigma^{\mp} OAM_{\pm l} = EH^{even}_{l-1,1} \pm jEH^{odd}_{l-1,1} \end{cases} \tag{1}$$

where l represents the order of the OAM and vector modes. The positive and negative of σ represents the spin direction. *even* and *odd* denote the even and odd modes of the vector modes, respectively. The imaginary number j represents the phase difference of $\pi/2$.

In the field of optical communication, increasing the communication capacity is very important. And using OAM as a transmission carrier, the number of modes determines the communication capacity. For OAM transmission fibers, increasing the RI of the transmission layer will increase the OAM numbers. But this results in higher losses. For example, Sulfur-based doping is chosen as the HRIL. Although this increases the number of supported OAM modes, it raises the confinement loss (CL), which is not conducive to the long-distance transmission of the beam.

The purpose of our design is to reduce the RI difference between the transmission layer and the substrate as much as possible if the loss caused by the doped HRIL is acceptable. This will result in a significant improvement in the number of transmission modes. The outer ring is doped with Germanium dioxide and HRILis doped with Fluoride. On the outside of the HRIL, air holes are periodically arranged, which can reduce the RI of the substrate. Figure 2 shows the mode field distribution of higher order modes. After calculation,

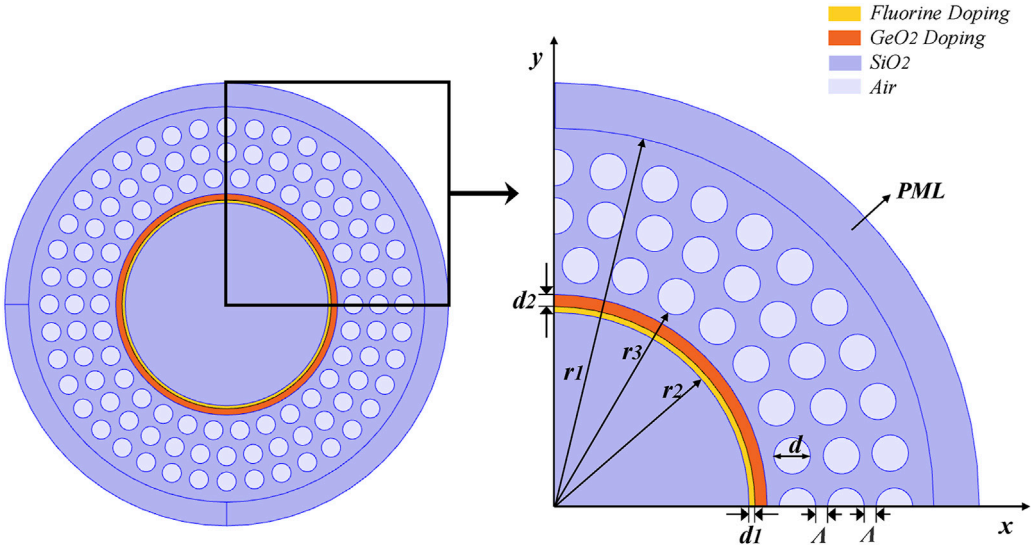

FIGURE 1
The schematic diagram of proposed OAM fiber with double-layer rings.

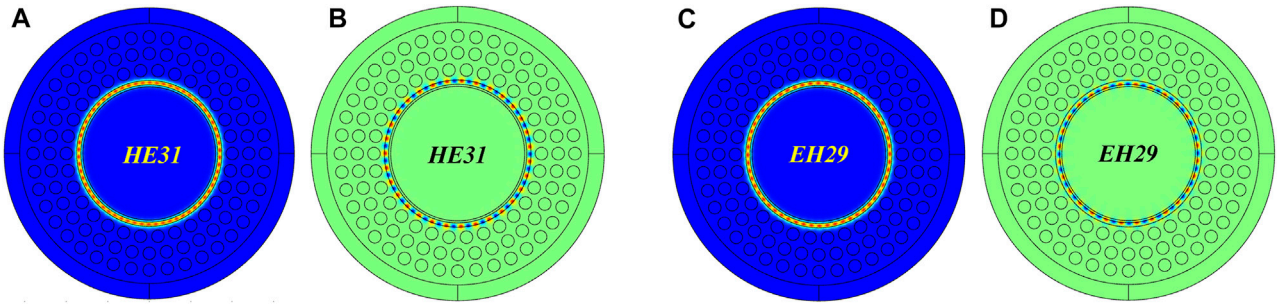

FIGURE 2
(A) Mode field distribution of $HE_{31,1}$. **(B)** Z-direction electric field of $HE_{31,1}$. **(C)** Mode field distribution of $EH_{29,1}$. **(D)** Z-direction electric field of $EH_{29,1}$.

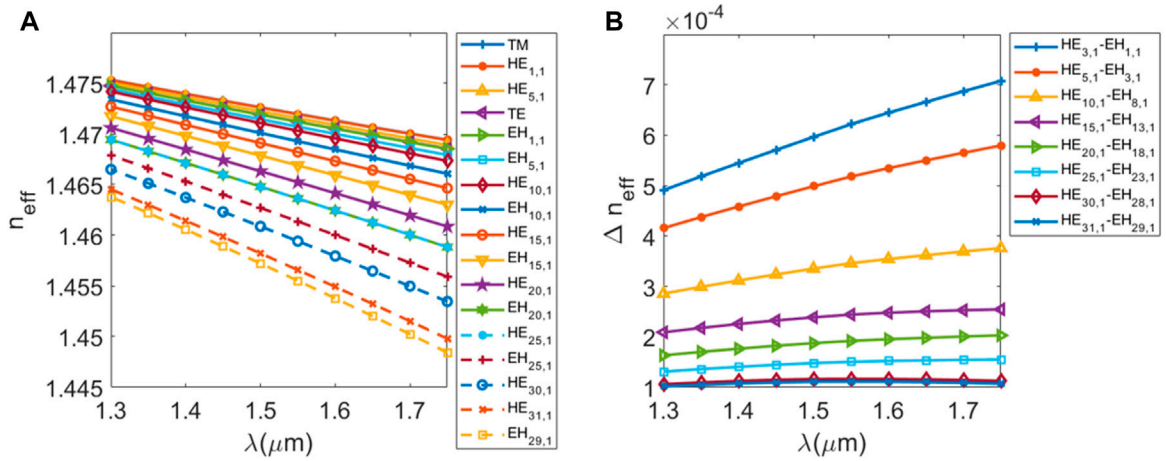

FIGURE 3
(A) n_{eff} of the some vector modes. **(B)** Δn_{eff} of some vector modes.

the OAM fiber can effectively support 118 modes in range of 1.3 μm–1.75 μm.

3.2 Effective refractive index and its differences

We analyzed the supported modes from 1,300 nm to 1750 nm. The effective refractive index (ERI) is defined as:

$$n_{eff} = \frac{\beta}{k_0} \tag{2}$$

where β is the propagation constant, k_0 is the wave number in a vacuum. Figure 3A shows the variation of the ERI with wavelength for some vector modes. As the wavelength increases, the ERI of the vector modes all decrease. Among them, the ERI of the higher-order mode $EH_{29,1}$ is the lowest, and the ERI is 1.44832 at 1.75 μm. In addition, the ERI's variation between different wavelengths of the same mode increases gradually as the mode order rises.

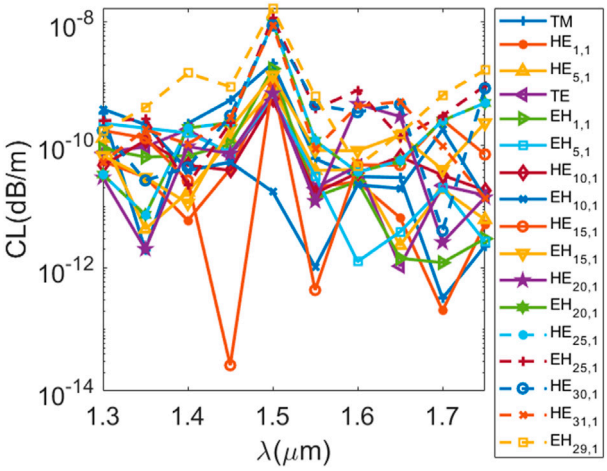

FIGURE 4
CL of some vector modes.

TABLE 1 The number of OAM modes and CL of the recently proposed OAM fiber.

References	CL	OAM number	Year
[12]	10^{-8}~10^{-6} dB/m	42	2020
[24]	10^{-8} dB/m	56	2020
[25]	10^{-10}–10^{-8} dB/m	30	2020
[26]	10^{-8} dB/m	80	2020
[27]	10^{-9} dB/m	76	2018
This Paper	10^{-11}–10^{-9} dB/m	118	2023

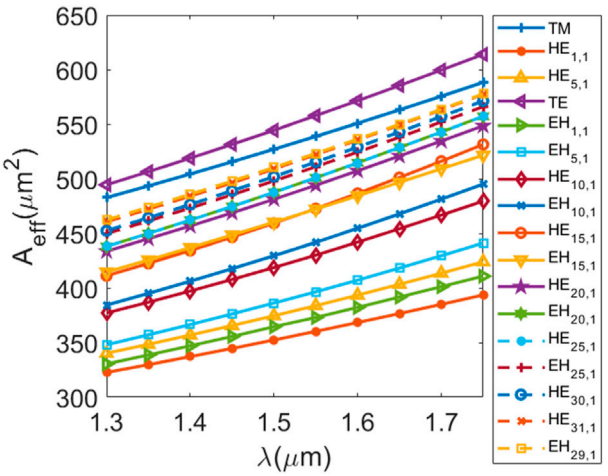

FIGURE 5
EMA of some vector modes.

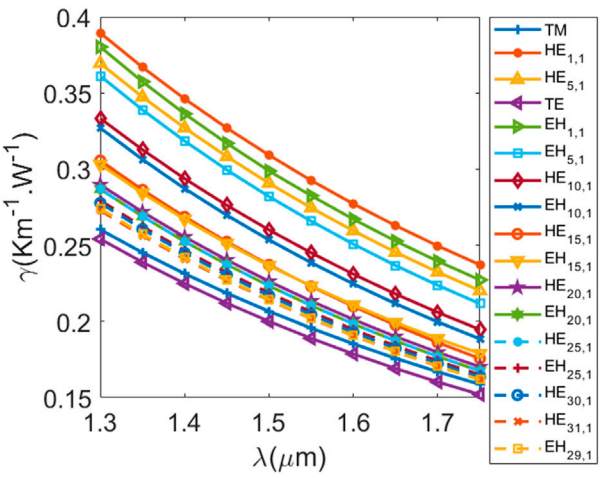

FIGURE 6
Nonlinear coefficient of some vector modes.

ERID reflects the quality of the OAM formed by vector mode coupling. According to the fiber degeneracy mode theory, $HE_{l+1,1}$ and $EH_{l-1,1}$ will degenerate when the ERI is close to forming the LP mode.

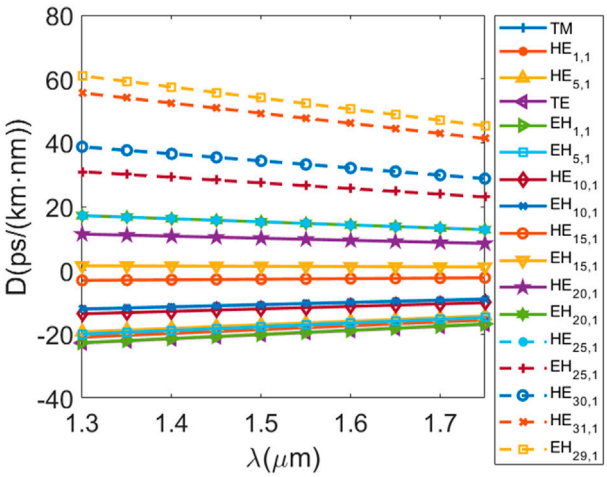

FIGURE 7
Dispersion of some vector modes.

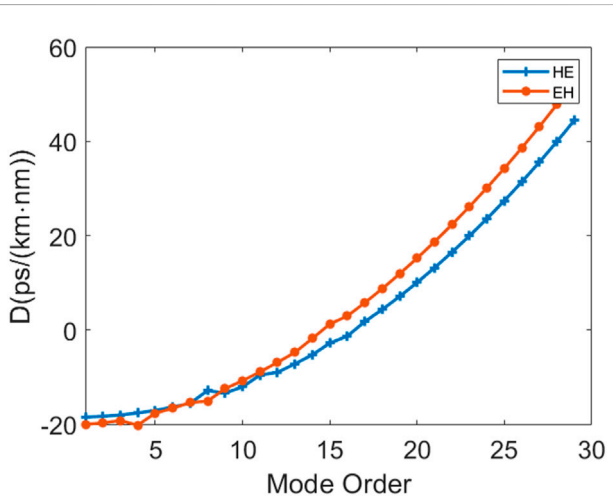

FIGURE 8
Dispersion values for all vector modes at 1550 nm.

This is unfavorable for the formation of OAM because we prefer the coupling of odd and even modes of the same vector mode. It is generally believed that when the ERID of $HE_{l+1,1}$ and $EH_{l-1,1}$ is above 10^{-4}, the formation of LP mode will be avoided. Figure 3B shows the variation of ERID with wavelength. The ERID decreases as the mode order increases. Among them, the ERID between $HE_{31,1}$ and $EH_{29,1}$ is the lowest to 0.000102. Although the model we designed can also support higher-order vector modes, we discarded them because they do not satisfy the ERID condition for forming OAM.

3.2.1 Confinement loss

The CL reflects the loss of the light propagating through the fiber. The CL is defined as [15, 16]:

$$CL = -\frac{2\pi}{\lambda}\frac{20}{\ln(10)}10^6 Im\left(n_{eff}\right)(dB/m) \quad (3)$$

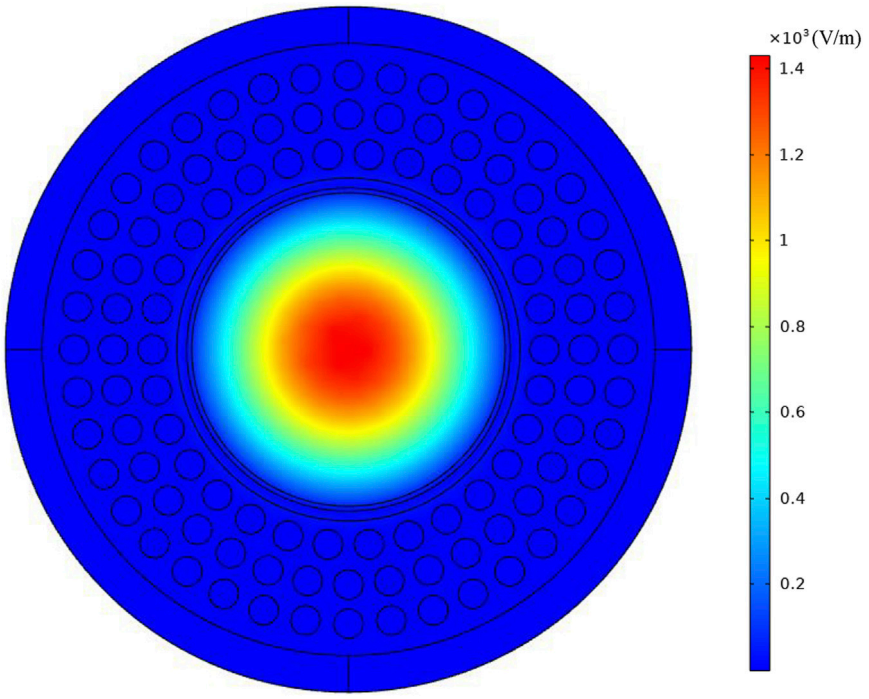

FIGURE 9
Base-mode of bandgap-like fiber.

TABLE 2 The EMA and ERI of some of the bandgap-like modes.

Mode	EMA(μm²)	n_{eff}
TE	2,247.9	1.443720765
$HE_{2,1}^{even}$	2,248.6	1.443720919
$HE_{2,1}^{odd}$	2,248.9	1.44372092
TM	2,249.8	1.443721093
$HE_{1,1}^{even}$	1,660.5	1.443890031
$HE_{1,1}^{odd}$	1,660.5	1.443890032

where λ is wavelength, and $Im(n_{eff})$ is the imaginary part of the n_{eff}. Figure 4 shows the CL's variation of some vector modes over wavelength. For wavelength from 1.3 μm to 1.75 μm, the CL of most vector modes oscillates in the range of 10^{-11}–10^{-9} dB/m. The lower transmission loss can ensure more effective transmission of information. Table 1 shows the number of OAM modes and CL of other OAM fibers. It indicates that the number of OAM modes supported by designed OAM fiber is higher, and the CL is smaller.

Theoretically, light is confined inside transmission layer owe to the HRIL [17, 18], but it will also be leaked out inevitably because the outer layer of the HRIL is a silicon-based substrate with higher RI than the inner low refractive index layer (LRIL), and the leakage from the outer layer will be more serious. Air holes outside the HRIL can effectively prevent the leakage of light waves and thus reduce CL.

3.3 Effective mode area and nonlinear coefficient

The effective mode area (EMA) and nonlinear coefficient are important parameters to evaluate the beam propagation quality [19]. The EMA represents the energy concentration, and the nonlinear coefficient is used to characterize the nonlinear effect of the fiber [20]. Since the effective mode field area is inversely proportional to the nonlinear coefficient, we need to increase the effective mode field area in optical communication. The higher effective mode field area and the lower nonlinear coefficient improve the optical signal-to-noise ratio. The EMA is given by [21, 22]:

$$A_{eff} = \frac{\left(\iint |E(x,y)|^2 dxdy\right)^2}{\iint |E(x,y)|^4 dxdy} \tag{4}$$

where $E(x, y)$ is the field distribution of the transverse electric field. The nonlinear coefficient is defined as [21]:

$$\gamma = \frac{2\pi n_2}{\lambda A_{eff}} \tag{5}$$

where n_2 is the nonlinear index for fused silica, and $n_2 = 2.6 \times 10^{-20} m^2 W^{-1}$. Figure 5 shows the variation of the EMA with wavelength for some modes. The EMA becomes larger with the increase of mode order. The EMA of all vector modes is above 320 μm², and the EMA of $HE_{31,1}$ reaches 577.763 μm² at 1.75 μm. The greater EMA reflects the higher energy concentration and smaller nonlinear coefficient.

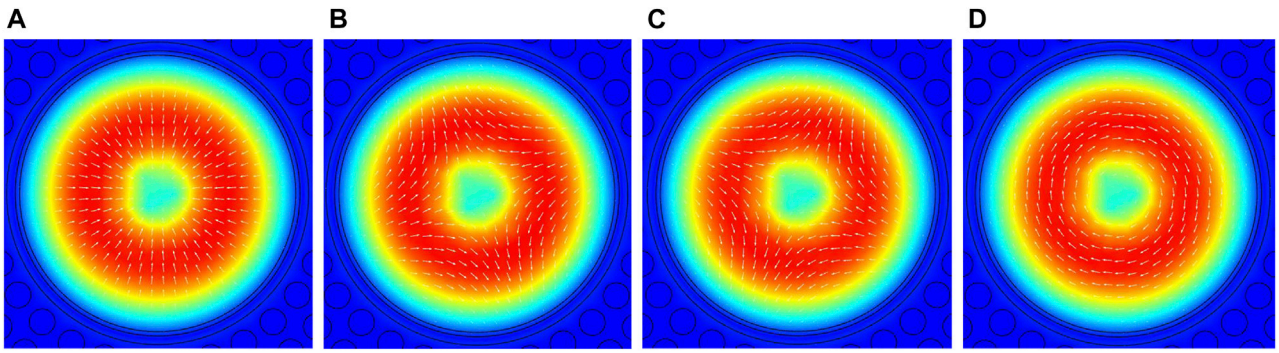

FIGURE 10
Mode field distribution of the bandgap-like vector mode and its polarization direction. **(A)** TM **(B)** $HE_{2,1}^{odd}$ **(C)** $HE_{2,1}^{even}$ **(D)** TE.

Figure 6 shows the nonlinear coefficient variation of some modes over wavelength. As the wavelength increases, the nonlinear coefficient decreases. In addition, the nonlinear coefficient decreases with the mode order, which indicates that the nonlinear effect of the higher-order mode is weaker and more conducive to transmission. The nonlinear coefficients are all below 0.4 km^{-1} W^{-1}, which indicates the OAM mode supported by proposed fiber has good transmission characteristics.

3.3.1 Dispersion

In optical communications, dispersion has a significant effect on the efficiency of information transmission. A large dispersion causes a high delay. The definition of dispersion is [23]:

$$D = -\frac{\lambda}{c}\frac{\partial^2 n_{eff}}{\partial \lambda^2} \tag{6}$$

Where λ is the wavelength, and c is the speed of light in a vacuum. Figure 7 shows the variation of partial vector mode dispersion with wavelength. When the mode's order is below $HE_{16,1}$ and $EH_{14,1}$, the dispersion is negative. When the order is higher than these two modes, the dispersion value is positive. And the absolute value of dispersion increases with the wavelength. The positive and negative distribution of dispersion is beneficial to the dispersion compensation of optical communication network and can improve the accuracy of information transmission.

In addition, the vector mode has a smaller dispersion and a flat variation. In the calculated band, the $HE_{31,1}$ mode has the highest absolute dispersion value of 60.962 ps/(km·nm) at 1.75 μm and a flat dispersion curve slope of 0.00348 ps/(km·nm^2). Figure 8 shows the variation of dispersion value with mode order for all vector modes at 1.55 μm. The dispersion values show a monotonic increase with the increase of mode order.

4 "Bandgap-like" properties of OAM fiber

Due to the LRIL in proposed fiber, the fiber exhibits the characteristics of a bandgap-PCF. We call this property "bandgap-like". Figure 9 shows the fundamental mode of the bandgap-like mode field. The main feature is that the beam propagates on a pure silicon-based substrate with a LRIL doped with fluoride in its outer layer. Intuitively, the beam appears to be confined by the LRIL, like light propagating through air in a bandgap PCF. The ERI of the bandgap-like mode is lower than the normal vector mode. The fundamental mode of the bandgap-like mode starts to appear at 1,550 nm when the ERI is 1.44389.

These bandgap-like modes propagate at the central base with a large EMA. Table 2 shows the EMA and ERI of some bandgap-like modes. Furthermore, these modes are highly degenerate. According to fiber mode theory, the ERI of vector modes that degenerate to form the same LP mode are very close. Figure 10 shows the mode field distribution of the "bandgap-like" vector modes and their polarization direction. The white arrow shows the polarization direction of the electric field. Combined with the optical fiber mode theory, we can analyze the beam mode by the polarization of the electric field. The bandgap-like mode $HE_{2,1}^{odd}$, $HE_{2,1}^{even}$, TM and TE have a very low difference in ERI, which is consistent with this feature. Although this "bandgap-like" mode cannot be used to form OAM mode, its large EMA and highly degenerate properties make it unique. "Bandgap-like" mode of proposed fiber can be used for optical communication because of its large field area.

5 Conclusion

In this paper, we propose a PCF fiber with double-layer rings for transmitting OAM. The RI is modulated by different doping of the rings. This increases the RI difference between the transmission layer and the substrate, increasing the supported OAM numbers. The regular arrangement of air holes also restricts the light beam. After calculation, the fiber can support 118 OAM modes in the range of 1.3–1.75 μm. The CL of most vector modes oscillates in the range of 10^{-11}–10^{-9} dB/m. The EMA of all vector modes is above 320μm^2, and the nonlinear coefficients of all modes are below 0.4 km^{-1} W^{-1}. The dispersion value is small and changes gently. In addition, the "bandgap-like"

mode field appears in the optical fiber, which is characterized by large EMA and high degeneracy.

Data availability statement

The original contributions presented in the study are included in the article/Supplementary Material, further inquiries can be directed to the corresponding author.

Author contributions

XQ proposed the idea and wrote this manuscript, YL revised the manuscript. All authors contributed to the article and approved the submitted version.

Acknowledgments

We are grateful to the people in the laboratory who have helped us. The authors gratefully acknowledge financial support from the National Natural Science Foundation of China (61905062).

Conflict of interest

The authors declare that the research was conducted in the absence of any commercial or financial relationships that could be construed as a potential conflict of interest.

Publisher's note

Supplementary material

The Supplementary Material for this article can be found online at: https://www.frontiersin.org/articles/10.3389/fphy.2023.1207182/full#supplementary-material

References

1. Zhu L, Zhu G, Wang A, Wang L, Ai J, Chen S. 18 km low-crosstalk OAM + WDM transmission with 224 individual channels enabled by a ring-core fiber with large high-order mode group separation. *Opt Lett* (2018) 43(8):1890–3. doi:10.1364/OL.43.001890

2. Zhu J, Zuo M, Yang Y, Ge D, Shen L, Chen Z, et al. Multiple-ring-core FM-EDF for weakly-coupled MDM amplification with low differential modal gain. *IEEE Photon J* (2021) 13(1):7100511. doi:10.1109/JPHOT.2021.3051455

3. Lian Y, Qi X, Wang Y, Bai Z, Wang Y, Lu Z. OAM beam generation in space and its application. *Opt Lasers Eng* (2022) 151:106923. doi:10.1016/j.optlaseng.2021.106923

4. Ma M, Lian Y, Wang Y, Lu Z. Generation, transmission and application of orbital angular momentum in optical fiber: A review. *Front Phys* (2021) 9:773505. doi:10.3389/fphy.2021.773505

5. Lian Y, Yu Y, Han S, Luan N, Wang Y, Lu Z. *IEEE Sensors J* (2022) 22(5):3828–43. doi:10.1109/JSEN.2022.3145833

6. Allen L, Beijersbergen MW, Spreeuw RJ, Woerdman JP. Orbital angular momentum of light and the transformation of Laguerre-Gaussian laser modes. *Phys Rev A* (1992) 45(11):8185–9. doi:10.1103/physreva.45.8185

7. Wang H, Liang Y, Zhang X, Chen S, Shen L, Zhang L. Low-loss orbital angular momentum ring-core fiber: Design, fabrication and characterization. *J Lightwave Technol* (2020) 38(22):6327–33. doi:10.1109/jlt.2020.3012285

8. Zhu G, Hu Z, Wu X, Du C, Luo W, Chen Y. Scalable mode division multiplexed transmission over a 10-km ring-core fiber using high-order orbital angular momentum modes. *Opt Express* (2018) 26(2):594–604. doi:10.1364/OE.26.000594

9. Zhang J, Liu J, Shen L, Zhang L, Luo J, Liu J. Mode-division multiplexed transmission of wavelength-division multiplexing signals over a 100-km single-span orbital angular momentum fiber. *Photon Res* (2020) 8(7):1236–42. doi:10.1364/prj.394864

10. Jia C, Jia H, Wang N, Chai J, Xu X, Lei Y. Theoretical analysis of a 750-nm bandwidth hollow-core ring photonic crystal fiber with a graded structure for transporting 38 orbital angular momentum modes. *IEEE Access* (2018) 6:20291–7. doi:10.1109/access.2018.2817577

11. Nandam A, Shin W. Spiral photonic crystal fiber structure for supporting orbital angular momentum modes. *Optik* (2018) 169:361–7. doi:10.1016/j.ijleo.2018.05.055

12. Kabir MA, Hassan MM, Hossain MN, Paul BK, Ahmed K. Design and performance evaluation of photonic crystal fibers of supporting orbital angular momentum states in optical transmission. *Opt Commun* (2020) 467:125731. doi:10.1016/j.optcom.2020.125731

13. Zhang Z, Liu X, Wei W, Ding L, Tang L, Li Y. The simulation of vortex modes in twisted few-mode fiber with inverse-parabolic index profile. *IEEE Photon J* (2020) 12(3):1–8. doi:10.1109/jphot.2020.2994819

14. Kuiri B, Dutta B, Sarkar N, Santra S, Mandal P, Mallick K, et al. Design and optimization of photonic crystal fiber with low confinement loss guiding 98 OAM modes in THz band. *Opt Fiber Technol* (2022) 68:102752. doi:10.1016/j.yofte.2021.102752

15. Kuiri B, Dutta B, Sarkar N, Santra S, Atta R, Patra AS. Development of photonic crystal fiber supporting 124 OAM modes with flat dispersion and low confinement loss. *Opt Quan Electron* (2022) 54:527. doi:10.1007/s11082-022-03942-y

16. She Y, Zhou D, Chen X, Ni J. Bend-resistant low bending loss and large mode area single-mode fiber with low NA. *Opt Fiber Technol* (2019) 51:101–6. doi:10.1016/j.yofte.2019.05.006

17. Wang W, Wang N, Li K, Geng Z, Jia H. A novel dual guided modes regions photonic crystal fiber with low crosstalk supporting 56 OAM modes and 4 LP modes. *Opt Fiber Technol* (2020) 57:102213. doi:10.1016/j.yofte.2020.102213

18. Zhang L, Meng Y. Design and analysis of a photonic crystal fiber supporting stable transmission of 30 OAM modes. *Opt Fiber Technol* (2021) 61:102423. doi:10.1016/j.yofte.2020.102423

19. Wang W, Sun C, Wang N, Jia H. A design of nested photonic crystal fiber with low nonlinear and flat dispersion supporting 30+50 OAM modes. *Opt Commun* (2020) 471:125823. doi:10.1016/j.optcom.2020.125823

20. Lei Y, Xu X, Wang N, Jia H. Numerical analysis of a photonic crystal fiber for supporting 76 orbital angular momentum modes. *J Opt* (2018) 20(10):105701. doi:10.1088/2040-8986/aaddb8

21. Zhang L, Zhang K, Peng J, Deng J, Yang Y, Ma J. Circular photonic crystal fiber supporting 110 OAM modes. *Opt Commun* (2018) 429:189–93. doi:10.1016/j.optcom.2018.07.014

22. She Y, Zhang W, Tu S, Liang G. Large mode area single mode photonic crystal fiber with ultra-low bending loss. *Optik* (2021) 229:165556. doi:10.1016/j.ijleo.2020.165556

23. Hassan MM, Kabir MA, Hossain MN, Nguyen TK, Paul BK, Ahmed K. Numerical analysis of circular core shaped photonic crystal fiber for orbital angular momentum with efficient transmission. *Appl Phys B* (2020) 126(9):145. doi:10.1007/s00340-020-07497-2

frontiers | Frontiers in Physics

TYPE Brief Research Report
PUBLISHED 14 July 2023
DOI 10.3389/fphy.2023.1225869

OPEN ACCESS

EDITED BY
Zhenxu Bai,
Hebei University of Technology, China

REVIEWED BY
Zhenzhen Song,
Nanjing University of Information Science and Technology, China
Xiangqian Quan,
Chinese Academy of Sciences (CAS), China

*CORRESPONDENCE
Shoufeng Tong,
tsf1998@sina.com
Peng Zhang,
zp@cust.edu.cn

RECEIVED 20 May 2023
ACCEPTED 03 July 2023
PUBLISHED 14 July 2023

CITATION
Dong B, Tong S, Zhang P and Du Y (2023), Research on duplex underwater wireless laser communication system.
Front. Phys. 11:1225869.
doi: 10.3389/fphy.2023.1225869

Research on duplex underwater wireless laser communication system

Bing Dong[1], Shoufeng Tong[1]*, Peng Zhang[1]* and Yangfan Du[2]

[1]National and Local Joint Engineering Research Center of Space Optoelectronics Technology, Changchun University of Science and Technology, Changchun, China, [2]College of Optoelectronic Engineering, Changchun University of Science and Technology, Changchun, China

To improve the bit error rate (BER) of underwater wireless laser communication and increase communication speed, a duplex underwater wireless laser communication system is designed. The system uses both blue and green lasers to transmit signals simultaneously, and adopts an improved modulation and demodulation algorithm to achieve separate modulation of the two sets of signals. A duplex underwater wireless laser communication system builds based on 440 and 550 nm lasers. On the basis of analyzing the absorption and scattering characteristics of seawater in laser communication, the influence of turbulence on communication efficiency is discussed. Improved the traditional duplex modulation algorithm and conducted communication testing at a depth of 2.0 m underwater. The experimental results show that when the communication distance increases from 5 to 50 m, the BER of the unoptimized duplex mode increases from 2.34×10^{-7} to 3.5×10^{-5}. After adopting the optimization algorithm, the BER increases from 2.81×10^{-7} to 1.18×10^{-6}, and the signal attenuation has been significantly suppressed. The duplex communication structure and algorithm can effectively reduce the impact of communication distance on bit BER.

KEYWORDS

underwater wireless laser communication, duplex mode communication, modulation algorithm, bit error rate, optimization model

1 Introduction

The ocean contains abundant biological and mineral resources, and about 70% of the Earth's surface is covered by the ocean. The development and utilization of marine resources is a trend. The application of information and communication technology to ocean development and utilization is inevitable. Studying underwater communication for the ocean is one of the important directions for future development. Underwater wireless laser communication technology is a communication technology with important application value. Underwater wireless optical communication (UWOC) is an emerging communication technology [1]. It usually uses the blue green light band (450–570 nm) as an information carrier to achieve information transmission underwater [2]. Due to the characteristics of large bandwidth, high speed, and high security, UWOC has become a substitute communication technology for traditional underwater acoustic communication [3].

In 1960, Gilbert et al. [4] experimentally tested the low attenuation of blue-green light in water. In 1963, Duntley [5] tested the attenuation characteristics of light in various water bodies, verifying that the 450–550 nm blue-green band was a weak attenuation band in seawater, providing important design ideas for UWOC. In 1976, Karp et al. [6] used lasers to achieve bidirectional communication between satellites and underwater submarines, and designed

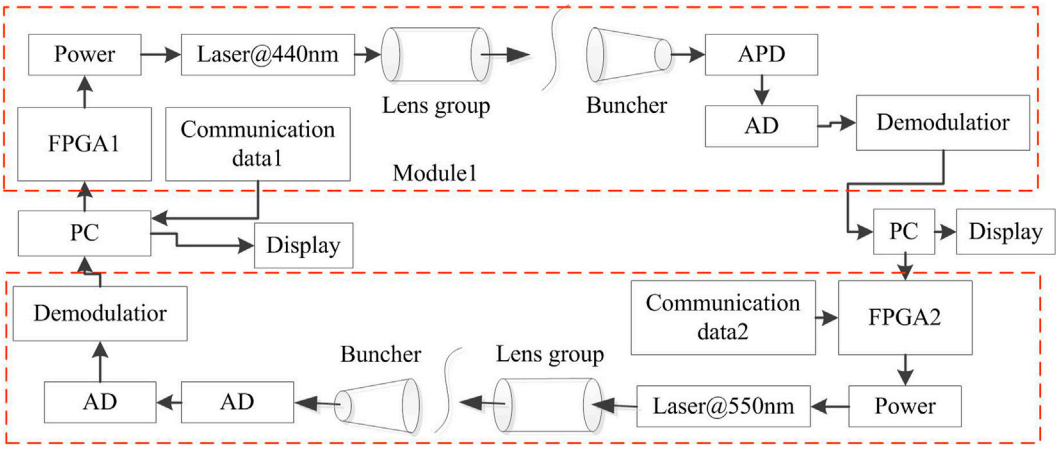

FIGURE 1
Duplex underwater wireless laser communication system.

corresponding communication models [7]. In 1991, Puschell J. J. [8] used duplex communication between aircraft and underwater submarines, and the laser used in the experiment was a blue green laser. In 1992, Snow et al. [9] completed underwater wireless laser communication of 5 m at a communication rate of 50 Mbps. In 2008, Hanson et al. [10] used the Monte Carlo method to analyze the optical communication characteristics of different water bodies. It achieves 1 Gbps/m underwater communication, and its 532 nm laser operates in an externally modulated mode. In 2012, John F. Muth et al. [11] designed an underwater wireless laser communication system with dual end transceiver. In 2017, Ho C. M. [12] achieved 10 Gbps transmission rate over a length of 10 m using a 405 nm blue laser and a 16 Quadrature-Amplitude-Modulation Orthogonal-Frequency-Division- Multiplexing modulation module. In 2019, Hong et al. [13] implemented 18.09 Gbps/m underwater optical communications using Discrete Multi Tone (DMT) modulation and shaping algorithms. In 2019, Wang J. [17] achieved indoor underwater optical communication of 100 m/500 Mbps with a transmission power of only 7.25 mW. Chi Nan et al. [14] utilized hardware equalization to achieve underwater transmission at a rate of 3.075 Gbps. Zhou Y [15] achieved 15.7 Gbps underwater visible light communication using GaN based LEDs and 64 Quadrature Amplitude Modulation technology. In 2019, Wang et al. [16] achieved underwater optical communication of 100 m/500 Mbps using a 520 nm laser and Non-Return-Zero On-Off-Keyed modulation in tap water.

In summary, underwater communication systems are developing towards multi wavelength, long-distance, and high-speed directions. In order to further improve the efficiency and stability of underwater wireless laser communication systems, we design a duplex laser communication system. By placing narrowband filters in front of the receiving window at different wavelengths, the signal-to-noise ratio of the sensing module is improved, thereby suppressing mutual interference.

2 System design

The Duplex underwater wireless laser communication system is shown in Figure 1. The system includes two parts: reception and transmission. The Transmission module includes Personal Computer (PC), modulation system, communication data database, modulation power supply, blue laser (at 440 nm), green laser (at 550 nm), and lens group. The Receiving module includes buncher, Administrative Distance (AD), Avalanche Photo Diode (APD), demodulator, PC, and display unit. The system modulates communication signals on both green and blue lasers simultaneously, and the receiving end obtains a duplex communication signal.

Multiple forms of encoding and modulation can be performed on the original source electrical signals. The system performs pre equalization processing on underwater fading channels. It drives the light source to emit a modulation signal. The photodetector in the receiving end receives the corresponding optical signal. After signal amplification, filtering, and other processing, the system can complete the collection and analysis of dual wavelength signals. Due to the fact that in real underwater application scenarios, the receiving and transmitting ends may be dynamic and cannot always maintain a good optimal state, which seriously affects the communication performance of the system. Therefore, the receiving end can design acquisition, pointing, and tracking modules, namely, APT modules, with the aim of maintaining the optical link alignment between the receiving and transmitting ends as much as possible. Corresponding optical components such as lenses and filters, it can be configured at both ends of the light source and detector to further optimize and improve the transmission performance of the beam.

3 Seawater characteristics analysis

3.1 Absorption and scattering

The underwater communication environment is complex, but it can be mainly divided into two categories: dissolved organic matter and suspended particles. The optical properties of these components are mainly manifested as absorption and scattering properties, corresponding to absorption coefficient and scattering coefficient. Therefore, attention coefficient can be expressed as:

$$c(\lambda) = \alpha(\lambda) + \beta(\lambda) \tag{1}$$

Among them, $\alpha(\lambda)$ represents the absorption coefficient, and $\beta(\lambda)$ represents the scattering coefficient, both in units of m^{-1}. The two parameters exhibit different absorption and scattering effects on different water bodies. When light waves propagate in water, absorption refers to the conversion of photon energy into thermal or biological energy of substances in the water and their disappearance. Scattering refers to the phenomenon where photons interact with substances in seawater, causing the direction of photon transmission to randomly change without loss of energy. Therefore, scattering changes the energy distribution of the light field.

Seawater refers to water without any impurities, mainly composed of a mixture of dissolved salt and pure water. Therefore, the absorption effect mainly comes from water molecules and dissolved salts, including $NaCl$, $MgCl_2$, $CaCl_2$, etc. The absorption characteristics of pure seawater and pure water are very similar, with the lowest coefficient of absorption approximately in the 400–500 nm wavelength range, namely, the blue-green light band, while the absorption coefficients of other wavelengths are relatively high. This characteristic basically determines that blue-green light is the main wavelength band for underwater wireless optical communication.

Assuming the length of water passing through is l, the incident light power is P_i, the absorbed light power is P_α, and the scattering angle θ corresponds to the scattered light power P_θ. The absorption coefficient and scattering coefficient are:

$$\alpha(\lambda) = \lim_{l\to 0} \frac{P_\alpha(\lambda)}{P_i(\lambda)l}, \beta(\lambda) = \lim_{l\to 0} \frac{P_s(\lambda)}{P_i(\lambda)l} \tag{2}$$

When the water environment for communication is known, the testing of absorption coefficient and scattering coefficient can be completed through calibration methods.

The scattering phenomenon is the result of the water molecules combined action and suspended particles in seawater on light, and is also related to factors such as temperature, pressure, and salinity. To the complex size and distribution of different particles, it is difficult to find a unified scattering model. If the scattering effect generated by particle size is analyzed, it can be divided into Rayleigh scattering and Mie scattering. Rayleigh scattering is a common scattering phenomenon, and it refers to the scattering of incident light by particles with a diameter much smaller than the wavelength of light (less than one tenth of the wavelength), and the intensity of the scattered light is inversely proportional to the fourth power of the wavelength of light, that is, the shorter the wavelength, the stronger the scattering effect. The scattering of seawater mainly comes from Mie-Scattering, and it refers to the scattering phenomenon that occurs when the diameter of particles is equivalent to the radiation wavelength. The scattering intensity of Mie scattering is proportional to the square of frequency, and Forward scatter is stronger than backward scattering, with obvious directionality, while Rayleigh scattering is almost symmetrically distributed. Mie-Scattering can be simply understood as a random collision between photons and suspended particles that change the direction of transmission, and typically involves multiple collisions.

3.2 Turbulent interference

There are similarities between water and the atmospheric environment. Ocean turbulence in water is the chaotic movement of water. Turbulence refers to the flow where the velocity and direction of motion at any point in a water body change in an disordered manner, and there is a strong mixing phenomenon between different layers of fluid. The random changes in parameters such as temperature, salinity, and pressure of water result in significant fluctuations in the refractive index of the water body. The phase and intensity of underwater transmitted optical signals will fluctuate randomly and cause beam wanders, resulting in scintillation at the receiving end. Its phenomenon will reduce the transmission performance of laser communication systems. The turbulence intensity can be expressed as

$$\mathrm{Re} = Lv/k \tag{3}$$

Among them, L represents the characteristic length of water flow, v represents the velocity of water flow, and k represents the kinematic/eddy viscosity coefficient of water flow, expressed in m^2/s. When $Re > 2700$, the water exhibits a significant turbulence phenomenon. The fading intensity caused by turbulence can be expressed as the scintillation index, with

$$\sigma_I^2(l, L, \lambda) = \frac{E\left[I^2(l, L, \lambda)\right] - E^2\left[I^2(l, L, \lambda)\right]}{E^2\left[I^2(l, L, \lambda)\right]} \tag{4}$$

Among them, I (l, L, λ) is the instantaneous intensity at the position vector (l, L), l is the previous position coordinate (x, y), L is the link distance, and E (I) represents the expected value.

In fluid mechanics, a dimensionless parameter characterizing the relative importance of momentum exchange and heat exchange in fluid flow. It indicates the relationship between the temperature boundary layer and the flow boundary layer, reflecting the influence of fluid physical properties on the convective heat transfer process, which can be defined as:

$$P_l = \frac{k}{\chi} \tag{5}$$

Among them, k represents the kinematic viscosity and χ represents the diffusion rate, expressed in m^2s^{-1}. The range of Prandtl numbers depends on the possibility of turbulence in the given medium. Each wavenumber can appear within the inertial or viscous range of its energy spectrum, or within the convective or diffusive range of its scalar spectrum.

The underwater environment also varies with changes in vertical depth, resulting in changes in optical properties. When the final system is applied to communication in seawater, the top layer is called the Euphoto zone, which is about 200 m deep in ocean water and can generate a large amount of solar radiation, such as phytoplankton. Therefore, the absorption coefficient of light in this area is relatively high. The middle layer is called the weak light zone, where there is insufficient sunlight, resulting in fewer algae and plants. The bottom layer is called the opaque zone, where sunlight is extremely scarce. The salinity, temperature, and other parameters of each layer vary, changes in the refractive index of the medium. Therefore, separate link modeling is required. This layering is meaningful for the weight matching of absorption and scattering parameters in the modeling process of underwater wireless laser communication.

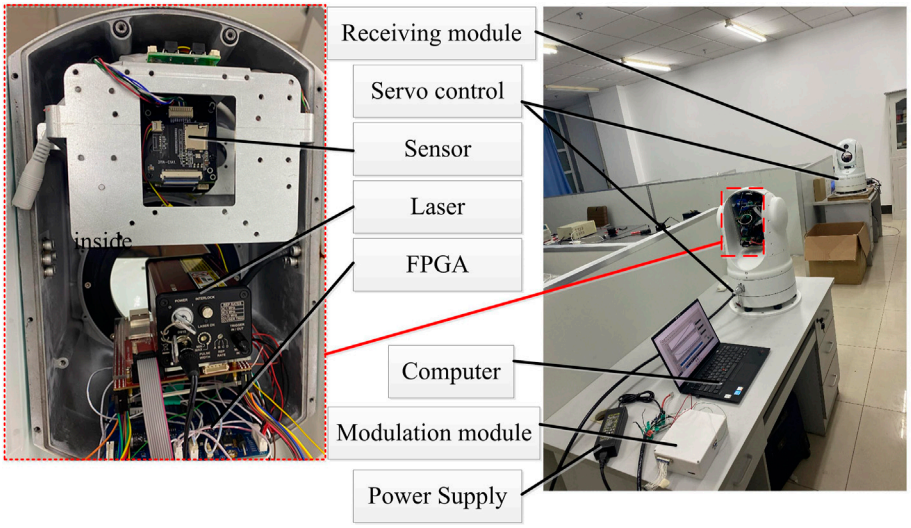

FIGURE 2
Duplex laser communication system.

3.3 Improved duplex modulation algorithm

Based on the impact of underwater environment on laser communication, the traditional laser modulation function is optimized and improved. In single wavelength laser communication, the echo waveform can be represented as

$$I(t) = p(t) \otimes P_c(t) \tag{6}$$

Among them, p(t) is the initial time-domain waveform, and P_c(t) is the impact response.

When using duplex communication, the hardware part uses bandpass filters to filter the corresponding wavelengths. At the same time, the processing algorithm performs differential calculations on the two sets of echo data. When the time difference between the emission laser of two wavelengths is Δ T, the phase difference is ΔÅ. During duplex modulation, the correction parameters are

$$c = \frac{I_1(t)}{I_2(t + \Delta\varphi)} \tag{7}$$

By calculating the correction parameters, the amplitude ratio of two echo intensities can be solved. Meanwhile, the time difference between the two times is determined by the pre-set phase difference. This can achieve feedback control of the modulation state and suppress mutual crosstalk by correcting parameters.

4 Experiments

4.1 Experimental system

The system consists of a transmitter and a receiver. The emitting laser adopts dual lasers with center wavelengths of 440 and 550 nm, respectively. Each laser has a luminous power of approximately 200 mW. The detector adopts the APD detector of S8664-1010. Choose FPGA as the data acquisition module to achieve high-speed data acquisition. The modulator is used to modulate the signal of a duplex laser. The system is shown in Figure 2.

During laser communication, servo control used to achieve alignment between two modules. Due to the use of duplex communication, it is necessary to first determine which laser to communicate with during the alignment process, and then complete the alignment of laser communication. The reception process adopts time-sharing communication. There is a filter in front of the corresponding receiving window that is used to suppress other stray light.

4.2 Duplex signal sampling

Blue laser and green laser are used to emit laser signals respectively, and then APD is used to obtain the two optical signals. To distinguish the response results of laser signals, single laser pulses of 1 and 3 μs were used, respectively. The test results are shown in Figure 3.

The amplitude of the signal after filtering and amplification is about 400 mV, and the operating frequency is 25 MHz. When using duplex communication, it is first necessary to filter and denoise the two laser signals. The original signal contains a lot of noise, and using bandpass filtering can filter out high-frequency noise and low-frequency noise separately. The laser signals of green and blue light can be modulated using different pulse periods and phases, which facilitates data separation during later processing. As shown in Figure 3A, the input signal pulse width of the blue light signal source is 1 us, and the signal pulse width of the receiving end is 3.3 μs When modulating the amplitude strength of the input signal, the carrier signal is used to generate the envelope of communication data. It can be seen that the ripple noise of the blue response curve has been significantly filtered out. The square wave shape is obvious and can well reflect the peak and phase relationship of the input signal. As shown in Figure 3B, the input signal pulse width of the

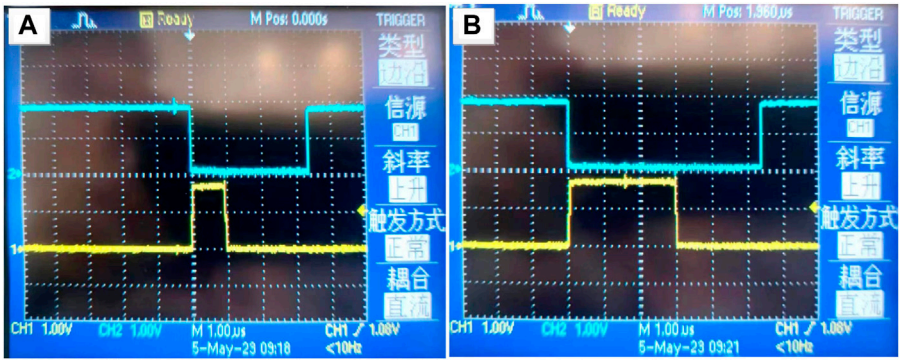

FIGURE 3
Response waveform of duplex signal **(A)** blue laser response **(B)** green laser response.

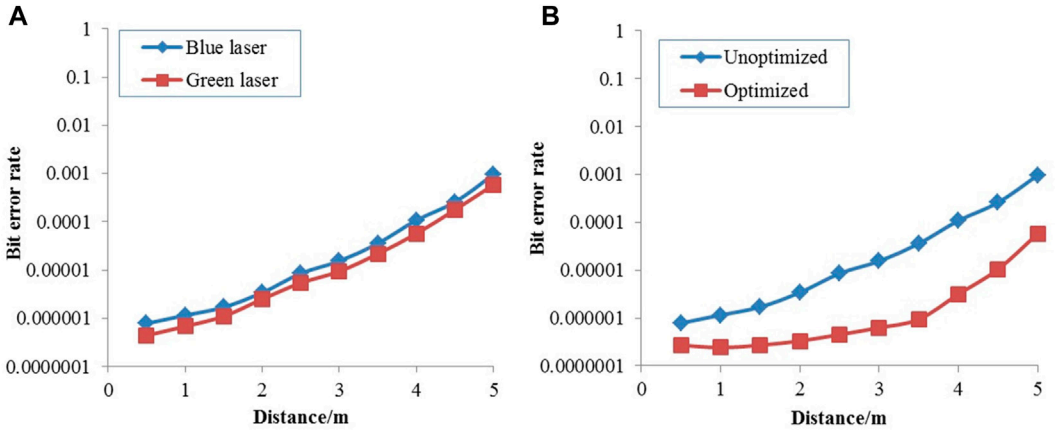

FIGURE 4
Response waveform of duplex signal. **(A)** Bit error rate of single laser **(B)** before and after optimization of dual laser.

green light signal source is 3.0 μs, and the signal pulse width of the receiving end is 5.4 μs. When modulating the amplitude strength of the input signal, the carrier signal is used to generate the envelope of communication data. The energy analysis of signals can calculate the degree of energy drift during the modulation process. Comparing the two sets of test signals, it can be seen that using the filtering processing of this system can obtain better data waveform curves.

4.3 BER analysis of duplex communication

At a depth of 2.0 m, a duplex laser communication system was tested using single pass and dual pass tests, respectively. Direct communication and signal modulation communication methods were used during dual pass operation. The test results of BER with different communication distances are shown in Figure 4.

As shown in Figure 4A, blue laser and green laser completed a 2.0 m deep underwater wireless laser communication test separately. When the communication distance increases from 5 to 50 m, the BER of blue laser increases from 1.54×10^{-7} to 9.57×10^{-4}, and the BER of green laser increases from 1.03×10^{-7} to 5.88×10^{-5}. The communication efficiency of the two monochromatic lasers is similar, and when the communication distance is the same, the BER does not differ significantly. As shown in Figure 4B, using duplex mode, compare whether to choose the optimization algorithm in this article. When the communication distance increases from 5 to 50 m, the bit error rate of the unoptimized duplex mode increases from 1.63×10^{-7} to 9.24×10^{-5}, which is basically similar to the communication BER of monochromatic laser. After using the algorithm optimization in this article, the bit error rate increased from 2.81×10^{-7} to 1.18×10^{-6}. In contrast, after optimization, the growth rate of the system's bit error rate significantly decreases, and the trend of bit error rate variation with respect to distance weakens. It can be seen that using the duplex modulation optimization design in this article has good results.

5 Conclusion

A duplex underwater wireless laser communication system is proposed. The system uses a 440 nm green laser and a 550 nm blue laser to communicate together. On the basis of analyzing the characteristics of seawater, a modulation and demodulation algorithm for suppressing seawater interference is proposed. The experiments were conducted on monochromatic laser communication and duplex communication, respectively. After optimization, the growth rate of the system's bit error rate significantly decreases, and the trend of bit error rate variation with respect to distance weakens. It can be seen that using the duplex modulation optimization design in this article has good results. This design can slow down the increase in bit error rate and has better application prospects in the field of underwater wireless laser communication.

Data availability statement

The original contributions presented in the study are included in the article/Supplementary Material, further inquiries can be directed to the corresponding authors.

Author contributions

BD proposed this idea and wrote this paper. ST provided theoretical guidance and analysis. PZ completed the experiment. YD participated in experimental data analysis and paper revision. All authors contributed to the article and approved the submitted version.

Funding

This work was supported in part by Natural Science Foundation of Jilin Province (YDZJ202301ZYTS394) and Science and Technology Research Project of Jilin Provincial Department of Education (JJKH20230814KJ).

Conflict of interest

The authors declare that the research was conducted in the absence of any commercial or financial relationships that could be construed as a potential conflict of interest.

Publisher's note

References

1. Zhou H, Zhang M, Wang X, Ren X. Design and implementation of more than 50m real-time underwater wireless optical communication system. *J Lightwave Tech* (2022) 40(12):3654–68. doi:10.1109/jlt.2022.3153177

2. Al-Zhrani S, Bedaiwi NM, El-Ramli IF, Barasheed AZ, Abduldaiem A, Al-Hadeethi Y, et al. Underwater optical communications: A brief overview and recent developments. *Engineered Sci* (2021) 16:146–86. doi:10.30919/es8d574

3. Khan IU, Iqbal B, Songzou L. Full-duplex underwater optical communication systems: A review//2021 international bhurban conference on applied Sciences and technologies (ibcast). *IEEE* (2021) 886–93.

4. Gilbert A, Stoner TR, Jernigan JL. Underwater experiments on the polarization, coherence, and scattering properties of a pulsed blue-green laser. *Proc Underwater Photo Opt* (1966) I.

5. Duntley SQ. Light in the sea. *J Opt Soc America* (1963) 53(2):214–33. doi:10.1364/josa.53.000214

6. Karp S. Optical communications between underwater and above surface (satellite) terminals. *IEEE Trans Commun* (2003) 24(1):66–81. doi:10.1109/tcom.1976.1093200

7. Khalil RA, Babar MI, Saeed N, Jan T, Cho HS. Effect of link misalignment in the optical-internet of underwater things. *Electronics-Switz* (2020) 9(4):646. doi:10.3390/electronics9040646

8. Puschell JJ, Giannaris RJ, Stotts L. The autonomous data optical relay experiment: First two way laser communication between an aircraft and submarine. In: proceedings of the Telesystems Conference; 19-20 May 1992; Washington (1992).

9. Snow JB, Flatley JP, Freeman DE, Landry MA, Lindstrom CE, Longacre JR, et al. Underwater propagation of high-data-rate laser communications pulses. In: Proceedings of SPIE - The International Society for Optical Engineering; 31 December 1992; San Diego, CA (1992). p. 1750.

10. Hanson F, Radic S. High bandwidth underwater optical communication. *Appl Opt* (2008) 47(2):277. doi:10.1364/ao.47.000277

11. Simpson JA, Hughes BL, Muth JF. Smart transmitters and receivers for underwater free-space optical communication. *IEEE J Selected Areas Commun* (2012) 30(5):964–74. doi:10.1109/jsac.2012.120611

12. Ho CM, Lu CK, Lu HH, Huang S, Cheng M, Yang Z, et al. A 10m/10Gbps underwater wireless laser transmission system; 19-23 March 2017; Los Angeles (2017). *proceedings Opt Fiber Commun Conf Exhibition*

13. Hong X, Fei C, Zhang G, Du J, He S. Discrete multitone transmission for underwater optical wireless communication system using probabilistic constellation shaping to approach channel capacity limit. *Opt Lett* (2019) 44(3):558–61. doi:10.1364/ol.44.000558

14. Nan C, Yuanyuan W, Yiguang W, Xingxing H, Xiaoyuan L. Ultra-high-speed single red–green–blue light-emitting diode-based visible light communication system utilizing advanced modulation formats. *Chin Opt Lett* (2014) 12(001):22–5. doi:10.3788/COL201412.010605

15. Zhou Y, Zhu X, Hu F, Shi J, Wang F, Zou P, et al. Common-anode LED on a Si substrate for beyond 15 Gbit/s underwater visible light communication. *Photon Res* (2019) 7(9):1019. doi:10.1364/prj.7.001019

16. Wang J, Lu C, Li S, Xu Z. 100 m/500 Mbps underwater optical wireless communication using an NRZ-OOK modulated 520 nm laser diode. *Opt Express* (2019) 27(9):12171–81. doi:10.1364/oe.27.012171

frontiers | Frontiers in Physics

TYPE Original Research
PUBLISHED 24 July 2023
DOI 10.3389/fphy.2023.1230203

OPEN ACCESS

EDITED BY
Bofeng Zhu,
Nanyang Technological University,
Singapore

REVIEWED BY
Dongdong Pang,
Beijing Institute of Technology, China
Liu Yuan,
Nanjing University of Science and Technology, China

*CORRESPONDENCE
Xiaohong Mi,
hongxiaomi@163.com
JinYu Han,
407262854@qq.com

RECEIVED 28 May 2023
ACCEPTED 07 July 2023
PUBLISHED 24 July 2023

CITATION
Mi X, Sun H, Liu Z and Han J (2023), Research on far-field spot search and centre location algorithms.
Front. Phys. 11:1230203.
doi: 10.3389/fphy.2023.1230203

Research on far-field spot search and centre location algorithms

Xiaohong Mi[1]*, Haodong Sun[2], Zhaoyu Liu[2] and JinYu Han[3]*

[1]Business School, Henan University of Science and Technology, Luoyang, China, [2]College of Intelligent Engineering, Zhengzhou University of Aeronautics, Zhengzhou, China, [3]Basic Experiment and Training Center, Tianjin Sino-German University of Applied Technology, Tianjin, China

The energy distribution of the far-field spot is uneven, and the background is complex. Therefore, the identification of far-field points and the positioning of the centre are difficult. This article proposes an algorithm for multi-scale Gaussian cyclic convolution for locating the centre of far-field spots. First, wavelet denoising is performed on the image of multiple far-field spots, and the images of adjacent frames are subtracted. Then, the absolute values of the differences are added. Due to the large size of the far-field spot, the Gaussian distribution of the laser energy is not obvious. Therefore, a multi-scale Gaussian convolution kernel is used to perform circular convolution on these images. To preserve low-scale Gaussian features, features are spliced between two convolutions. In this article, we also design multi-angle combination filters to filter the enhanced Gaussian distribution features. Finally, curved polynomials are fitted to the reconstructed Gaussian energy distribution to obtain the maximum value; at this point, the position where the maximum value lies is the centre of the far-field spot. The experiments showed that this method has better robustness.

KEYWORDS

wavelet denoising, multi-scale, circular convolution, combination filters, far-field spot

1 Introduction

The classic laser spot centre positioning methods include the Hough transform method [1], the circular fitting method [2], and the grey-scale centroid [3]. The aforementioned methods have some shortcomings in terms of positioning accuracy, computational complexity, and robustness. The Hough transform method requires a large amount of computation. The circular fitting method requires high integrity of far-field spots. The grey-scale centroid method is susceptible to the uniformity of the digital number (DN) value. Therefore, there is a need to devise more advanced algorithms for laser spot centre localisation.

To be specific, Zhou et al. used iterative thresholding for coarse localisation, followed by interpolation, to achieve the positioning of sub-pixels in the centre of the spot [4]. Liu et al. proposed a curve-fitting algorithm that was introduced to improve the positioning accuracy of the laser spot centre based on the centroid method, but the algorithm is only suitable for images that conform to the Gaussian distribution. Liu, Z. R., et al. proposed laser spot centre localisation accuracy, but the algorithm is only suitable for the case where the grey scale of the spot image conforms to a Gaussian distribution [5]. Zhang et al. proposed an algorithm for laser spot localisation based on a weighted interpolation algorithm; the principle is to use weighted processing for spot positioning, which not only improves the accuracy and stability of the positioning but also provides accurate positioning to the edge of the spot. However, the algorithm is computationally complex and susceptible to saturated image elements within the speckle [6]. Thomas et al. propose a simple approach for the estimation of the circular arc

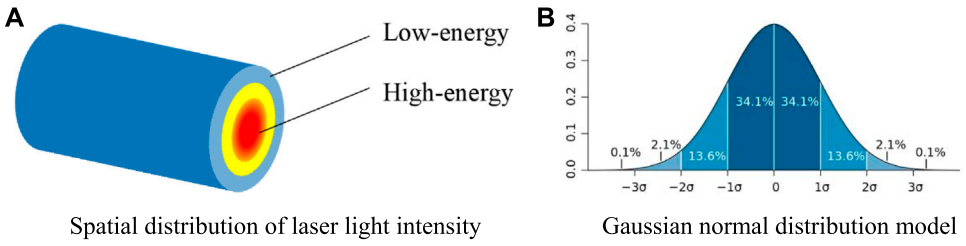

FIGURE 1
Light intensity distribution of an ideal Gaussian beam. **(A)** Spatial distribution of laser light intensity. **(B)** Gaussian normal distribution model.

centre and its radius [7], which can be used for laser spot centring. The aforementioned algorithm relies on the image of the ideal spots.

In our study, we found that the far-field spot has a weak Gaussian distribution at multiple scales but not at other locations in the image [8]. To enhance this feature, a multi-scale convolution kernel is used to perform cyclic convolution on the image. Then, features are spliced between two convolutions. The presence of low-scale Gaussian features results in the high-scale convolutions. Finally, the binomials of the results are fitted to the Gaussian distribution; at this point, the position where the global maximum value lies is the coordinate of the centre point.

2 Theoretical analysis

2.1 Model for the energy distribution of laser beams

The energy distribution of laser beams has multiple stable modes, including fundamental and higher-order modes. The fundamental mode is the ideal Gaussian beam, which is usually represented as a plane wave, denoted by I_0. As shown in Figure 1A, red indicates the distribution points with high intensity, and blue indicates the spatial distribution of weak intensity; most of the energy is concentrated near the propagation axis to form an Airy spot [9]. The Gaussian beam is represented as the plane wave when z is equal to a constant. As shown in Figure 1B, the amplitude of the light field decreases gradually from the propagation axis to the edge as a Gaussian function $\exp(-r2/r20)$. When the amplitude is reduced to a central value of $1/e$, r is defined as the radius of the spot. Therefore, the amplitude of the optical field A of a Gaussian beam at a certain cross section is expressed as follows:

$$A(\mathrm{r}) = A_0 \exp\left(-\frac{r^2}{{r_0}^2}\right). \quad (1)$$

In the formula, r_0 is the distance from the centre of the spot. The energy of the laser, I, is expressed as

$$I(\mathrm{r}) = I_0 \exp\left(-\frac{2r^2}{{r_0}^2}\right). \quad (2)$$

Due to the long distance of the far-field spot, the following effects can occur.

FIGURE 2
Effect of the unprocessed far-field spot image.

2.1.1 Light spot drift

Due to the long distance of the far-field spot, there is an effect on the beam propagation, resulting in a certain change in the direction of propagation and a consequent change in the position of the spot. The effect on the beam is manifested in several ways, and the spot drift effect refers to the change in the spatial position of the spot. Furthermore, with time, the spot drift exhibits a certain superposition effect, which is the beam expansion. The effects of this phenomenon must be taken into account in applications such as optical tracking systems and targeted designs should be created.

2.1.2 Beam extension

Based on the previous analysis, it is clear that the superposition effect of spot drift over time creates a beam expansion. This results in a beam drift phenomenon, which means that the beam after passing through the medium has changed, resulting in an increase in the spot size trend. When beam expansion occurs, the spot size increases and the light intensity at the centre is reduced [10].

2.1.3 Intensity fluctuations of the laser

The transmission of the laser light over long distances is subjected to laser undulation, which is the random undulation of

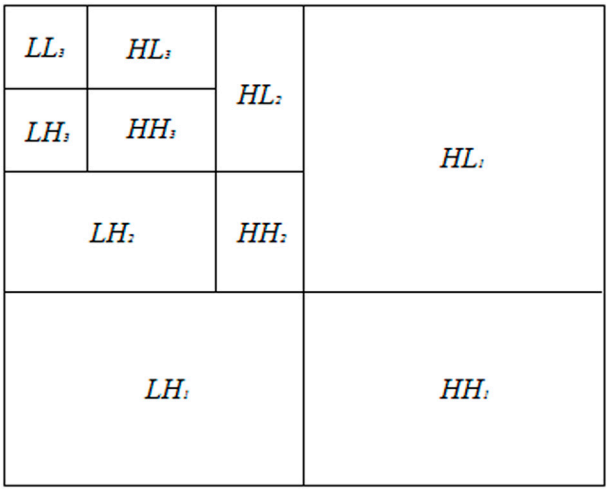

FIGURE 3
Diagrams of the orthogonal wavelet transform.

the laser. Affected by the light beam, scattering and other phenomena occur in the medium, resulting in continuous changes in the intensity of the receiving surface. This is known as the intensity fluctuations of the laser [11].

The aforementioned effects weaken the Gaussian characteristics of the laser spot, as shown in Figure 2.

2.2 Image pre-processing

2.2.1 Wavelet denoising

In this article, wavelet denoising is used to denoise the captured images to eliminate the effect of noise on positioning accuracy [12]. We believe that suppressing the high-frequency noise of the speckle helps resolve the inhomogeneity of the far-field spot and improve the accuracy of speckle image segmentation [13, 14]. The process can be expressed as shown in Figure 3. After image wavelet decomposition, the image noise is reflected in the high-frequency components, and the absolute value of the wavelet coefficient is small; however, the part with uniform laser energy is reflected in the high-frequency component, and the wavelet coefficient is large [15]. According to the idea of wavelet threshold denoising proposed by Johnstone, when the wavelet coefficient is less than a certain threshold, it is considered to be mainly noise components, and the part larger than the threshold is retained.

2.2.2 Background removal

Background removal is required for far-field spot images after wavelet denoising. Figure 4 represents the background removal process. Two adjacent frame images are subtracted, and the absolute value is calculated. Due to the frequency of the laser, there are four cases of adjacent frames: no laser spot in both frames; a laser spot in both preceding and following frames; a laser spot in the preceding frame and no laser spot in the following frame; and no laser spot in the preceding frame and a laser spot in the following frame. In the first and second cases, image

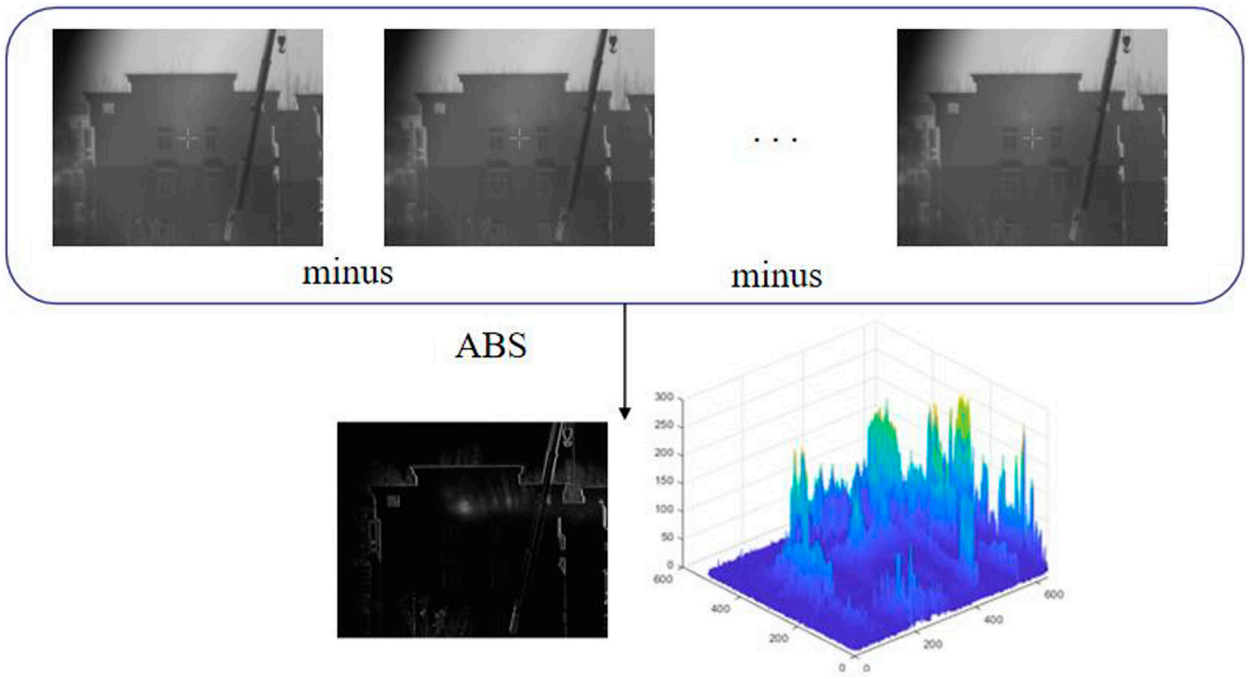

FIGURE 4
Background removal results.

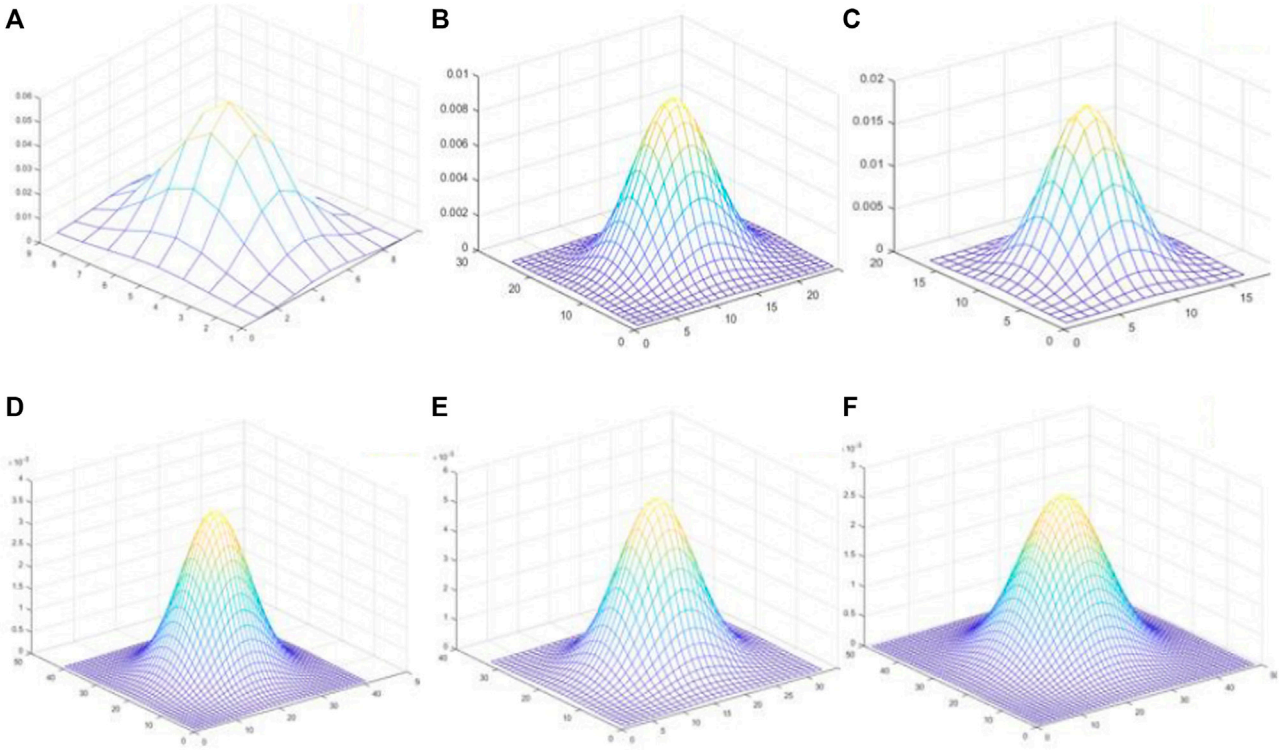

FIGURE 5
Gaussian kernels of different sizes. **(A)** shows the Gaussian kernel generated by ksize/2, **(B)** shows the Gaussian kernel generated by ksize/4, **(C)** shows the Gaussian kernel generated by ksize/6, **(D)** shows the Gaussian kernel generated by ksize/8, **(E)** shows the Gaussian kernel generated by ksize/10, and **(F)** shows the Gaussian kernel generated by the function, which is the Gaussian kernel that best meets the algorithm's needs.

subtraction results in zero, while in the third and fourth cases, image subtraction of the laser spot energy can be retained; however, the former has positive laser spot pixels and the latter has negative laser spot pixels. Finally, the spot pixels are unified to obtain a positive value by calculating the absolute value.

2.3 Gaussian kernel

Due to the Gaussian nature of the laser, a two-dimensional Gaussian kernel needs to be selected to convolve the image. A one-dimensional Gaussian kernel can be obtained by solving the following equation.

The one-dimensional Gaussian kernel function is defined by

$$f(x) = \frac{1}{\sigma\sqrt{2\pi}} e^{-(x-\mu)^2/2\sigma^2}, \tag{3}$$

where μ is the mean of x and σ is the variance of x. Because when calculating the average, the centre point is the origin and μ is equal to 0 by default, which then provides the following equation:

$$f(x) = \frac{1}{\sigma\sqrt{2\pi}} e^{-x^2/2\sigma^2}. \tag{4}$$

A two-dimensional Gaussian can then be derived as follows:

$$G(x, y) = \frac{1}{2\pi\sigma^2} e^{-(x^2+y^2)/2\sigma^2}. \tag{5}$$

The value of σ in the formula determines the width of the resulting Gaussian convolution kernel. The larger the value of σ, the wider the graph, the smaller the spikes, and the flatter the graph; the smaller the value of σ, the narrower and more concentrated the graph, the larger the spikes, and the more dramatic the graph changes. To ensure consistency in the transformation of images at different sizes in the Gaussian kernel, the value of σ can be calculated using the following formula:

$$\sigma = 0.3 \times ((ksize - 1) \times 0.5 - 1) + 0.8. \tag{6}$$

Figure 5 shows images of Gaussian kernels of different sizes according to the function.

2.4 Multi-scale Gaussian cyclic convolution

Deeper features in images rely heavily on convolution for extraction [16, 17]. The laser spot features in the pre-processed image are submerged in the background, which are still not extracted and localised, so a multi-scale Gaussian convolution is designed to suppress the background features and highlight the laser spot features. The structure diagram is as follows:

In this article, the Gaussian characteristics of the laser are combined with the choice of using multiple Gaussian

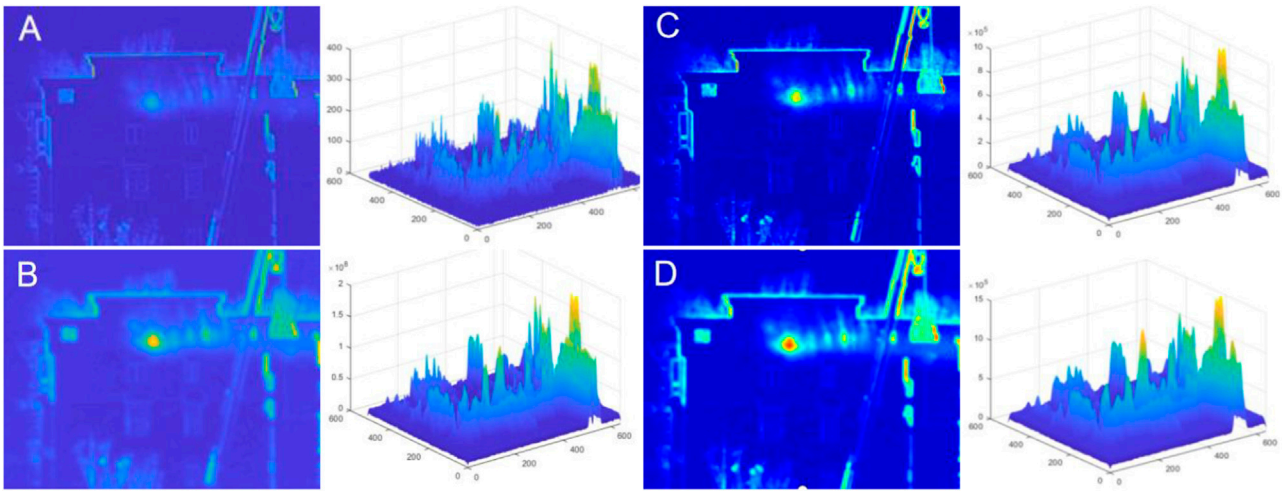

FIGURE 6
Multi-scale Gaussian convolution before and after comparison and its histogram. Plot **(A)** represents the result of looping the convolution 1 time, plot **(B)** represents the result of looping 3 times, plot **(C)** represents the result of looping 5 times 5 times, and plot **(D)** represents the result of looping 7 times.

convolution kernels of different sizes, i.e., weight matrices, to obtain the convolution feature results at different scales, and then all the feature results are normalised to finally extract the Gaussian features of the light spot image.

Figure 6 shows the effect of the image after multi-scale circular convolution. From the figure, it can be seen that the original image has no obvious spot features; the spot features are enhanced by 3 times of circular convolution, but the difference in the surrounding background is small; the Gaussian features in the spot area are more obvious by 6 times of circular convolution; and the difference between the Gaussian features of the spot and the surrounding Gaussian distribution can be clearly observed by 8 times of circular convolution and above. More detail of the source image is retained in the high-frequency features [18]. The multi-scale cyclic convolution method can effectively enhance the Gaussian characteristics of the spot and improve its distinctness.

Gaussian features in the spot region are significantly improved after multi-scale cyclic convolution, and the background detail information in the darker regions of the spot image is improved, but the search for locating the centre of the spot requires the removal of information such as background detail that interferes with the experimental results. To solve this problem, a multi-angle-based combination filter is proposed to extract contour information and that information is subtracted from each iteration of the cycle. The rotation matrix γ_i is used to construct the kernel function for the ith angle. Let θ_i be the rotation angle of the kernel function; then, the rotation matrix A for the i th angle is as follows:

$$\gamma_i = \begin{bmatrix} \cos\theta_i & -\sin\theta_i \\ \sin\theta_i & \cos\theta_i \end{bmatrix}. \tag{7}$$

If $P(x, y)$ is a point on the kernel function under the coordinate system, the point $\breve{P}$ at the ith angle $U - V$ coordinate after the rotation process is as follows:

$$\breve{P}(u, v) = P\gamma_i = \begin{bmatrix} x & y \end{bmatrix} \begin{bmatrix} \cos\theta_i & -\sin\theta_i \\ \sin\theta_i & \cos\theta_i \end{bmatrix}. \tag{8}$$

In order to uniformly filter the spot background while extracting contour and detail information from the image, i.e., if the response of the background region (i.e., non-contour and detail information) after stencil filtering is zero, the filter kernel function $\breve{G}(x, y)$ for the ith angle is defined as follows:

$$\breve{G}(x, y) = \left[\lambda \cdot \exp\left(-\frac{x^2 + y^2}{\sigma^2}\right) - \sum_{\breve{P}\epsilon\mathbb{Q}} K/N\right] + \gamma_i Lap \cdot (x, y), \tag{9}$$

where a is the weight and b belongs to the neighbourhood. $\mathbb{Q} = \{|u| \le 3\varepsilon, |v| \le L/2\}$; K is the number of grey values in the neighbourhood $\mathbb{Q}$ at the ith angle; $\lceil\ \rceil$ is rounded; Lap is the $Laplace$ operator, which is used to extract the background detail information of each angle of the image [19].

Figure 7 shows the images and feature histograms before and after the multi-angle-based filter combined with multi-scale circular convolution processing. The comparison shows that the spot features are more pronounced after processing than before processing.

The contrast of the laser spot image is significantly improved by comparison with the multi-angle-based combination filter. The background of the image is filtered out, while the Gaussian characteristics of the laser spot are enhanced.

3 Verification of the accuracy of the central positioning algorithm

3.1 Selection of evaluation indicators

Commonly evaluated metrics for laser spot-centring algorithms are repeatability verification and accuracy verification. Repeatability means that the spot is photographed and measured several times in the same position with a stable far-field spot, and the individual measurements are analysed in comparison with the maximum

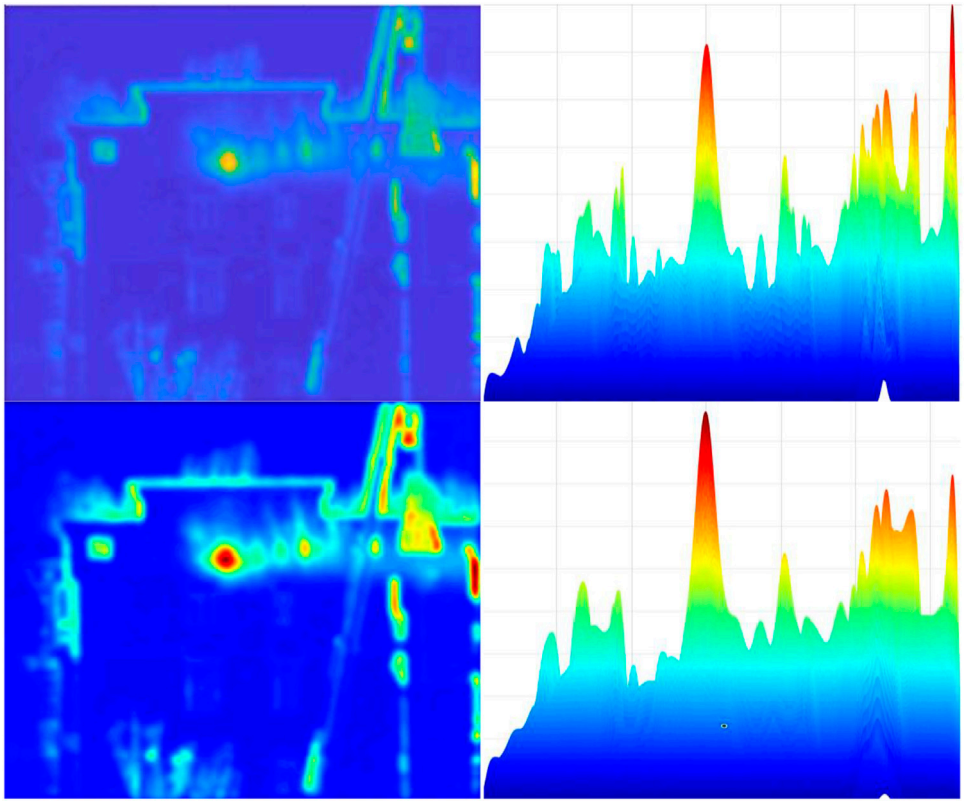

FIGURE 7
Image histograms and features before and after multi-angle combination filter processing.

TABLE 1 Coordinates of spot centres calculated by several positioning algorithms.

Algorithm	Group A		Group B		Group C		Group D		Group E		Group F		Standard deviation	
	x	y	X	y	x	y	x	y	X	y	x	y	σ x	σ y
Current study	301.21	202.14	302.94	203.88	303.46	203.94	304.21	202.61	299.46	204.14	300.92	205.13	1.6398	0.9940
Hough transform	301.83	204.07	299.44	202.66	297.31	202.90	304.67	209.38	302.39	204.84	301.01	204.25	2.3118	2.2331
Circular fitting	300.90	202.34	299.44	202.64	297.12	201.35	311.64	202.94	302.08	206.33	300.51	204.26	4.5956	1.6016
Grey-scale centroid	300.90	202.34	299.56	200.25	297.31	202.89	304.67	209.38	302.40	204.85	301.01	204.25	2.2776	2.8219

difference between the average values of the measurements. Accuracy is the difference between the measured value of the laser position coordinates and the true value [20]. In practice, however, it is not possible to know the definitive true value of the laser position coordinates, so straightness is used to evaluate the accuracy of the positioning algorithm. When the laser beam moves along a certain straight line, the movement of the spot centre coordinates must be a straight line, and the straightness of the fitted line is chosen as the evaluation index. The smaller the straightness, the better the accuracy of the positioning algorithm.

3.2 Repetitive experimental results

Eight randomly selected far-field spot images with different noises added were taken at the same location, and the spot centre should remain the same. The effect of the spot after the algorithm is shown in Figure 8.

The coordinates of the spot centres calculated by several positioning algorithms are shown in Table 1.

The comparison results show that the standard deviation of the algorithm proposed in this paper is smaller, and its stability and accuracy are higher than those of other classical algorithms.

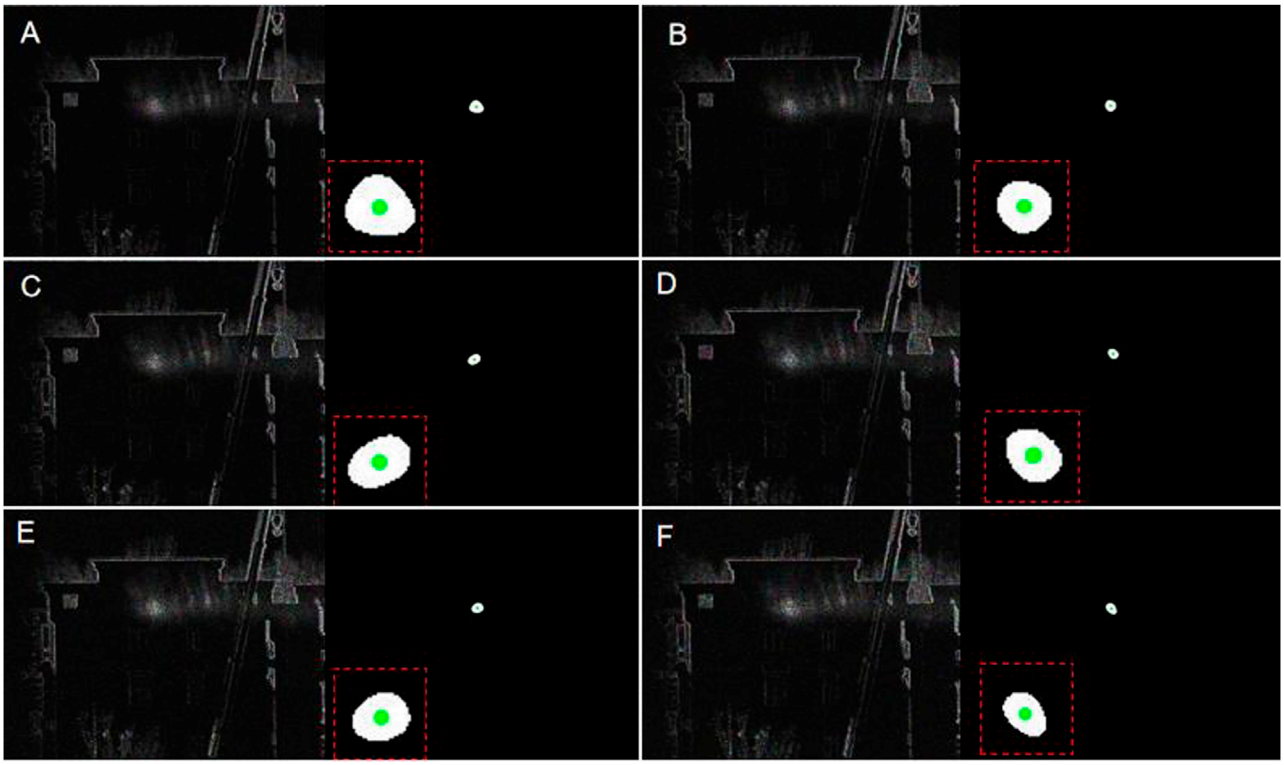

FIGURE 8
Corresponding light spot effect after adding different noise images and algorithm processing, **(A–F)** images with speckle noise added for (0.02, 0.04, 0.06, 0.08, 0.1, 0.12 noise parameters, respectively).

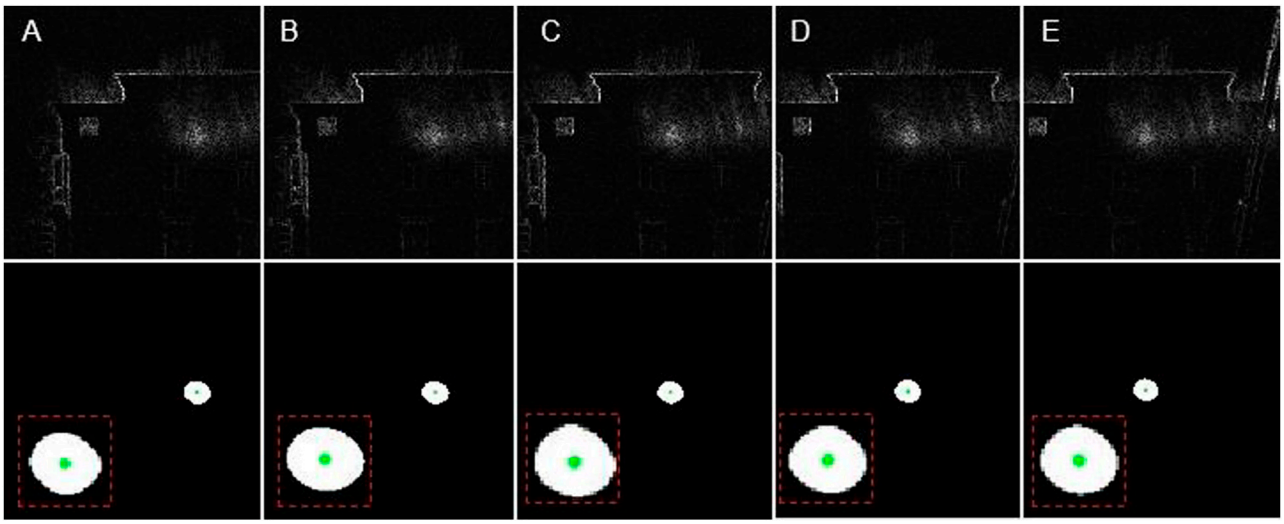

FIGURE 9
Far-field spot translation and positioning results. The **(A–E)** image represents the image after moving 20, 40, 60, 80, 100 units to the X-axis respectively.

3.3 Accuracy experiment results

The far-field spot image is panned to obtain five frames, and the same level of noise is added. As only horizontal panning is performed, the spot centre coordinates should only change on the y-axis. The results of the far-field spot panning and positioning are shown in Figure 9.

When moving in the horizontal direction, the centre of the extracted spot must also be a straight line in the vertical

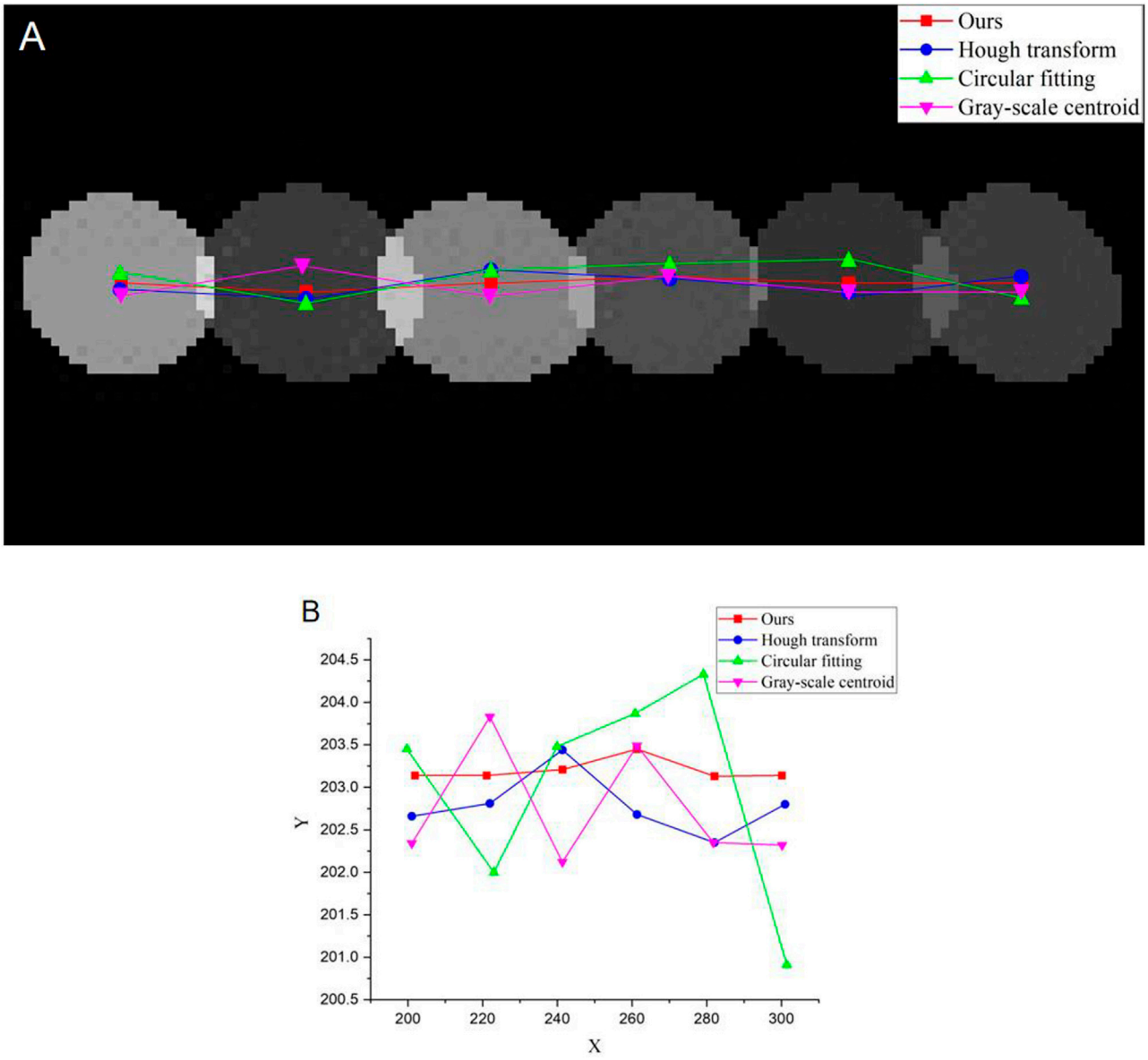

FIGURE 10
Centre coordinate connections calculated by several algorithms. **(A)** represents a graph of the effect of several light-point localisation algorithms after panning the image, **(B)** represents a line graph of the variation of several light-point localisation algorithms on the Y-axis after panning the image.

direction, and the straightness of this line is used as a criterion to evaluate the accuracy of the localisation algorithm. Figure 9 shows the straightness results for several localisation algorithms at different step sizes.

The results of each algorithm were linearly fitted, and the results of the fit are shown in Figure 10A. The three coloured lines in the figure indicate the fitting results for several algorithms in the horizontal direction. Figure 10B shows the fit results for several algorithms in the horizontal direction.

From the aforementioned data, it is intuitively clear that our method is the best fit, meaning that each coordinate is very close to the trajectory of the motion, which matches the trajectory of the laser. The Hough transform method is the second most effective method, with coordinates that are essentially identical to the trajectory of the motion, and the residual sum of squares in the circular fitting method transformation is the largest.

4 Conclusion

The main research in this paper is an algorithm based on multi-scale Gaussian convolution for locating the centre of the far-field spot. To improve the accuracy of the segmentation, several methods are proposed in this paper. First, wavelet denoising is performed on images of multiple far-field spots,

and the images of adjacent frames are subtracted. Second, due to the large size of the far-field spots, the Gaussian distribution of the laser energy is not obvious, so a multi-scale Gaussian convolution kernel is used to perform circular convolution on the denoised images. We also designed a multi-angle-based combination filter to filter the enhanced Gaussian distribution features. Finally, a bending polynomial is fitted to the reconstructed Gaussian energy distribution to obtain the maximum value; i.e., the location where the maximum value lies is the centre of the far-field point. In this article, three classical algorithms are chosen for comparison, and the proposed algorithm is more stable and accurate than the other three classical algorithms. Thus, the algorithm in this paper demonstrates that a laser point centre localisation algorithm based on multi-scale Gaussian convolution can be applied to the detection of far-field spot centres.

Data availability statement

The raw data supporting the conclusion of this article will be made available by the authors, without undue reservation.

Author contributions

XM proposed the idea and wrote the original manuscript. XM and HS performed the simulation work. HS helped collect the data. ZL helped in revising the original manuscript. JH and ZL supervised the research work and helped complete the experiment. All authors contributed to the article and approved the submitted version.

Conflict of interest

The authors declare that the research was conducted in the absence of any commercial or financial relationships that could be construed as a potential conflict of interest.

Publisher's note

All claims expressed in this article are solely those of the authors and do not necessarily represent those of their affiliated organizations, or those of the publisher, the editors, and the reviewers. Any product that may be evaluated in this article, or claim that may be made by its manufacturer, is not guaranteed or endorsed by the publisher.

References

1. Yang YQ, Shi R. An algorithm to improve the accuracy of laser spot centre positioning by Hough transform[J]. *J Opt* (1999) 19(12): 6. doi:10.3321/j.issn:0253-2239.1999.12.013

2. Wu ZK, Li GQ, Wang WT, Ma C. Laser spot center detection based on improved circle fitting algorithm. *Laser & Infrared* (2016) 46(3):346–50. doi:10.3969/j.issn.1001-5078.2016.03.021

3. Xi JH, Bao H. Laser stripe center extraction algorithm based on improved centroid method. *Fire Control & Command Control* (2019) 44(5):149–53. doi:10.3969/j.issn.1002-0640.2019.05.032

4. Zhou HF, Ailing G. Research on sub-pixel localization of CCD spot centres in images. *Metrology Tech* (2007) (11) 21–3. doi:10.3969/j.issn.1000-0771.2007.11.007

5. Liu ZR, Wang ZQ, Liu SJ, Shen CW. Research on algorithm for accurate positioning of laser spot centre[J]. *Comput Simul* (2011) 28(5): 399–401. doi:10.3969/j.issn.1006-9348.2011.05.097

6. Zhang J. Research on the measurement accuracy of different laser spot center location. In: Proceedings Volume 11052, Third International Conference on Photonics and Optical Engineering; 110520K; 2019 Jan 24 (2019). doi:10.1117/12.2521709

7. Thomassamuel M, Chany T. A simple approach for the estimation of circular arc center and its radius. *Comp Vis Graphics Image Process* (1989) 45:362–70. doi:10.1016/0734-189x(89)90088-1

8. Liu K, Zhiping J, Fang H. Laser spot effective area detection technology[J]. *Comput Modernization* (2011) 8(10):70–3. doi:10.3969/j.issn.1006-2475.2011.10.020

9. Bai Z, Zhao Z, Tian M, Jin D, Pang Y, Li S, et al. A comprehensive review on the development and applications of narrow-linewidth lasers. *Microwave Opt Tech Lett* (2022) 64(12):2244–55. doi:10.1002/mop.33046

10. Andrews LC, Al-Habash MA, Hopen CY, Phillips RL. Theory of optical scintillation: Gaussian-Beam wave model. *Waves Random Media* (2001) 11:271–91. doi:10.1080/13616670109409785

11. Yang C, Goguen J. The Mars exploration rovers descent image motion estimation system. *IEEE Intell Syst* (2004) 3(19):13–21. doi:10.1109/MIS.2004.18

12. Tosellia I, Andrews LC, Phillips RL, Ferrero L. Angle of arrival fluctuations for free space laser beam propagation through non Kolmogorov turbulence. *SPIE* (2007) 6551: 65510E-1–65510E-12. doi:10.1117/12.719033

13. Chen H, Bai Z, Yang X, Ding J, Qi Y, Yan B, et al. Enhanced stimulated Brillouin scattering utilizing Raman conversion in diamond. *Appl Phys Lett* (2022) 120(18): 181103. doi:10.1063/5.0087092

14. Bai Z, Williams RJ, Kitzler O, Sarang S, Spence DJ, Wang Y, et al. Diamond Brillouin laser in the visible. *APL Photon* (2020) 5(3):031301. doi:10.1063/1.5134907

15. Guo XC, Ma PG, Pang DD, Sun J, Jin Q, Wei H. Research on laser center positioning under CV model segmentation[J]. *Front Phys* (2022): 104–5. doi:10.3389/fphy.2022.1021950

16. Luo W, Xue Q, Zhang Y, Shen J, Cao X. Enhancing sketch-based image retrieval by CNN semantic Re-ranking. *IEEE Trans Cybernetics* (2019) 50(7):3330–42. doi:10.1109/TCYB.2019.2894498

17. Tu Z, Xie W, Dauwels J. Semantic cues enhanced multi-modality multi-stream CNN for action recognition[J]. *IEEE Trans Circuits Syst Video Tech* (2018) 29(99): 1423–37. doi:10.1109/TCSVT.2018.2830102

18. Zhang ZH, Wu X, Xu T. Combining multi-scale decomposition and octave convolution for infrared and visible image fusion[J]. *Chin J Image Graphics* (2023) 28(1):181. doi:10.11834/jig.220517

19. Lu HX, Liu ZB, Zhang J. Infrared image enhancement combining multiscale circular convolution and multiclustering space[J]. *J Elect* (2022)(2) 419. doi:10.12263/DZXB.2021017

20. Jiang JW, Kang JH, Wu B. Research on high-precision positioning compensation algorithm for laser spot centre[J]. *Adv Laser Optoelectronics* (2021) 58(14):141202–5.

frontiers | Frontiers in Physics

TYPE Brief Research Report
PUBLISHED 04 August 2023
DOI 10.3389/fphy.2023.1223755

OPEN ACCESS

EDITED BY
Shuo Liu,
Hebei University of Technology, China

REVIEWED BY
Zhaohong Liu,
Hebei University of Technology, China
Ying He,
Harbin Institute of Technology, China

*CORRESPONDENCE
Fang Liang,
liangfang423@163.com

RECEIVED 16 May 2023
ACCEPTED 10 July 2023
PUBLISHED 04 August 2023

CITATION
Liang F, Xun Y, Wu W and Fu J (2023), Based on laser energy absorption ratio differential algorithm methane concentration detection system. *Front. Phys.* 11:1223755. doi: 10.3389/fphy.2023.1223755

Based on laser energy absorption ratio differential algorithm methane concentration detection system

Fang Liang*, Yanqin Xun, Wenyi Wu and Jianmei Fu

Department of Electronics, Xinzhou Normal University, Xinzhou, Shanxi, China

To reduce the interference of other gases and improve the detection accuracy in CH_4 concentration detection, a CH_4 concentration detection system is proposed, and a ratio differential algorithm is designed. The difference value of the absorbed light intensity between chamber 1 and chamber 2 used to suppress the calculation of CH_4 concentration by other component gases. The high concentration of CH_4 gas in chamber 3 used to obtain the accurate position of the characteristic absorption peak, and it is applied as a boundary condition for data extraction in chamber 1. Two sets of gases chamber differential calculations were used, one set was used to calculate the differential value of laser energy at the characteristic position of CH_4 absorption, and the other set was used to calculate the differential value of laser energy for the other gases. Then, calculate the proportion coefficients of the two sets of difference values to obtain the CH_4 concentration inversion function using this structure. The interfering gases include C_2H_6, SO_2 and CO_2. A total of 1,000 sets for sample data were collected for the mixed gas, with 400 sets as the sample data and the rest as the test samples. The results show that the accuracy of CH_4 concentration inversion by this algorithm is about 3 times that of traditional algorithm. The algorithm modeling time is approximately 1/4 of that of traditional methods. It has certain advantages in detecting CH_4 concentration in environments with interfering gases.

KEYWORDS

CH_4, ratio differential algorithm, infrared laser, characteristic absorption peak, interfering gas

1 Introduction

Methane (CH_4) [1–3] gas is a common combustible gas in underground coal mining. Real time monitoring of gas concentration is crucial. The research can quickly identify methane gas in a mixture of gases, which is of great significance to ensure the life safety of underground personnel and the development of coal industry. Methane is often mixed with other gases, which can affect the detection accuracy of methane gas concentration. Therefore, the design and improvement of methane gas concentration detection systems are of great significance.

In 1985, K. Chan [4] used InGaAs material LEDs as light sources to align the absorption peak of methane gas at 1665.4 nm. It was also combined with narrowband interference filters, which doubled the sensitivity of the system. In 1992, H. Tai [5] reported on the use of two DFB lasers with central wavelengths of 1.66 and 1.53 μm to form a composite light

source, and used harmonic detection technology to achieve simultaneous detection of methane and acetylene concentrations. V. Weldon [6] reported in 1993 an experimental study on the simultaneous measurement of methane and carbon dioxide with a tunable DFB laser with a wavelength of 1.64 μm. In 1998, B. Culshaw [7] from Strathclyde University in the UK reported on a multipoint fiber optic gas sensing network operating by space division multiplexing. In 2000, Miha Zavrsnik [8] reported on a series fiber gas sensing network based on coherent multiplexing. In 2003, G. Stewart [9] reported on a gas concentration detection system for landfills, and used the fiber optic sensing network with 45 sensors and a coverage area of 5 square kilometers. In 2004, the Institute of Physics of the Russian Academy of Sciences reported an experiment with a single frequency laser to measure the absorption of methane gas at 1,654 nm. In 2006, Crawford Massie [10] reported on a portable gas optical sensor with an absorption wavelength of 1660 nm. In 2018, Zang Yipeng, et al. [11] designed CH_4 detection system by the 1,850 nm laser, and its accuracy is 1.14 ppm. In 2021, Chen Wenwen, et al. [12] had an accuracy of 1.0 ppm for detecting CH_4 concentration, and its accuracy is 0.13 ppm. In 2022, Dong Mao [13] achieved modulation of the laser using birefringence managed normal dissection fiber laser, resulting in a significant increase in phase matching during the birefringence process and a modulation energy enhancement of about 10 times. It can achieve a stronger signal-to-noise ratio when selecting methane characteristic wavelengths. In 2023, Yanjun Chen [14] used a high-power diode laser to detect trace methane gas concentration. The center wavelength of the light source was 1650.96 nm, with an optical power of up to 38 mW. The sensor was implemented by 3D printing, with a minimum detection limit of 14.93 ppm. In 2023, Kazuki Hashimoto [15] used a combination of broadband mid infrared spectroscopy and ultrafast Fourier transform to obtain high-resolution broadband TSIR. Its maximum wavenumber resolution is 0.017 cm^{-1}. In 2023, Yufei Ma [16] completed ammonia concentration detection by thermoelastic spectroscopy technology, and its minimum detection accuracy is 80 ppm. In 2023, Chu Zhang [17] used photoacoustic technology to detect the concentration of acetylene gas, and improved the signal-to-noise ratio through time accumulation detection. It increased the detection accuracy by 1.65 times compared to traditional methods.

In summary, most researchers use more advanced hardware devices or optimized data processing algorithms to improve the detection accuracy of methane gas concentration [18]. The article mainly focuses on proposing a novel detection method that improves detection accuracy and stability. It proposes a method of first differentiating laser energy, and calculates the ratio to calculate the proportional coefficient. Based on the analysis of characteristic absorption spectra of CH_4, a ratio differential algorithm by adaptive SVM (Support Vector Machine [19]) is designed. It provides a new approach for methane gas concentration detection, and this method can coexist with traditional optimization methods.

2 System design

In Figure 1 chamber 1 and chamber 2 are filled with tested gas, and it can be discharged through the "Output" channel; Chamber 3 is filled methane with a concentration of 80%. In order to obtain more accurate information on the special absorption band, methane with a concentration of 80% used in addition to methane. Gas entering two chambers requires a filter. In the filter, it is filled with molecular sieves. It can adsorb water vapor, dust, coal dust, etc., thereby reducing the impact of other pollutants in the test gas on the calculation of CH_4 concentration. Chamber 3 is filled with high concentration of CH_4, and it used to over-absorb the characteristic absorption of CH_4.

The signal modulation module is controlled to output modulation waves by CPU. The modulated signal controls the driver to emit laser signals from the infrared laser. According to the basic principle of characteristic spectral absorption, the absorption energy of CH_4 molecule is just equal to the photon of the difference between the energies of two energy levels. The other gases in the well absorb photons of different frequencies due to different atomic structures and chemical bond, so different characteristic absorption peaks inhibit the impact of other gases concentration. The main characteristic wavelength of CH_4 is 1650.8 nm, Analyzing the spectral distribution can determine the concentration of CH_4 gas.

3 Design of adaptive SVM algorithm

3.1 SVM algorithm

There are many methods for processing spectral data, such as least squares, artificial neural networks, etc. The core idea of the SVM algorithm is to map data into a high-dimensional space, making it easier for data to be separated in that space. In the spectral calculation process, due to the large amount of spectral data and high dimensionality, this algorithm is more suitable. Meanwhile, the SVM algorithm has strong generalization ability, making it more applicable when the type and concentration of mixed gases are unknown. After comprehensive comparison, it is believed that the SVM algorithm is the most suitable method in this system.

SVM is often applied to solve classification and regression problems, and it is suitable for the separation of multi-component gas. It has high applicability and robustness, and is suitable for multi-component separation situations. Assuming the training data (xi, yi), i = 1, 2, 3, . . ., n (n represents the number of samples), x_i and y_i belong to R, x_i is the sample input, y_i is the expected output, and its fitting function is

$$f(x) = \omega \cdot x + b \tag{1}$$

Among them, ω is the space hyperplane, and b offset.

According to the minimum structural risk criterion [20], it can be optimized as

$$V = \min \frac{1}{2}\|\omega\|^2 + C\sum_{i=1}^{l}\left(\xi_i + \xi_i^*\right) \tag{2}$$

And its parameters comply with:

$$s.t. = \begin{cases} \left(y_i - \omega x_i - b \le \varepsilon + \xi_i, -y_i + \omega x_i + b \le \varepsilon + \xi_i^*\right) \\ \xi_i + \xi_i^* \ge 0 \, (i = 1, 2, ..., l) \end{cases} \tag{3}$$

Among them, C represents the penalty factor, which is used to adjust the degree of punishment for sample error exceeding the

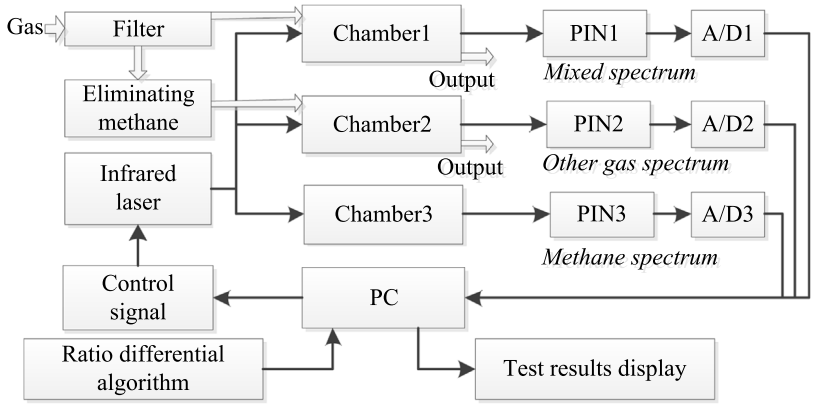

FIGURE 1
Improved laser modulated methane concentration detection system.

limit; ξ represents the relaxation factor; Å represents an insensitive parameter used to reflect the system's tolerance for errors.

$$\max\left[-\frac{1}{2}\sum_{i,j=1}^{l}(\alpha_i-\alpha_i^*)(\alpha_j-\alpha_j^*)(x_i\cdot x_j)-\sum_{i=1}^{l}\alpha_i(\varepsilon+y_i)\right]$$
$$s.t.\begin{cases}\sum(\alpha_i-\alpha_i^*)=0\\ 0\le\alpha_i,\alpha_i^*\le C(i=1,2,...,l)\end{cases} \tag{4}$$

According to the test condition, the output can be calculated as follows:

$$f(x)=\sum_{i=1}^{l}(\alpha_i-\alpha_i^*)(x_i\cdot x)+\frac{1}{N_s}\sum_{S}\left[t_s-\varepsilon-\sum_{m\in S}^{l}(\alpha_m-\alpha_m^*)(x_m\cdot x_S)\right] \tag{5}$$

3.2 Adaptive SVM

The formula for finding the optimal solution through information exchange between sample individuals is

$$\begin{cases}X_{ij}^{k+1}=X_{ij}^{k}+V_{ij}^{k+1}\\ V_{ij}^{k+1}=c_1r_1\left(P_{ij}^{k}-X_{ij}^{k}\right)+c_2r_2\left(P_{gj}^{k}-X_{ij}^{k}\right)+\sigma V_{ij}^{k}\end{cases} \tag{6}$$

Among them, $i\in N$ (N represents the total number of particles), j represents the dimension, and σ represents the inertia weight; D represents the dimension; k. $k+1$ represents the current and next iteration algebra, respectively; V_{ij} represents particle velocity; X_{ij} represents the particle position; P_{ij} and P_{gj} represent the extreme values of individuals and groups, respectively, while c_1 and c_2 represent the acceleration factor.

By setting constraints on the spectral characteristics of measured gas, the corresponding particles are mutated, thereby guiding the population to achieve the optimal convergence effect; The second is to improve SVM by setting a dynamic change insensitive region $\varepsilon(y_i)$ in support vector regression calculation, which is to replace $\varepsilon(y_i)$ in the original algorithm. On the basis of this improvement idea, Eq. 4 is replaced and simplified to obtain

$$f(x)=\sum_{i=1}^{l}(\alpha_i-\alpha_i^*)(x_i\cdot x)+\frac{1}{N_s}\sum_{S}\left[t_s-\varepsilon(y_i)-\sum_{m\in S}^{l}(\alpha_m-\alpha_m^*)(x_m\cdot x_S)\right] \tag{7}$$

The introduction of $\varepsilon(y_i)$ can suppress the effect of over-learning model.The specific process for completing the optimization is shown in Figure 2.

3.3 CH_4 concentration

When the incident light intensity I_0 (λ) and transmitted light intensity I_t (λ), as well as the absorption coefficient and effective length L of the gas chamber, are known or can be calculated [21], the concentration of the measured gas c_{CH4} can be expressed as

$$c_{CH4}=\left|\frac{\ln(I_t(\nu)-I_0(\nu))}{\alpha(\nu)L}\right| \tag{8}$$

In the formula, ν represents the wavenumber, and it is the reciprocal of the wavelength. α (ν) represents the absorption coefficient of light intensity. The light intensity between chamber 1 and 2 is I_{12}. The light intensity between chamber 2 and 3 is I_{23}. The light intensity between chamber 1 and 3 is I_{13}.

With T_{13}, Eq. 8 is substituted into:

$$c_{CH4}=\left|\frac{\ln I_{12}(\lambda)}{\alpha(\nu)L}\right| T_{13}\ge T_0 \tag{9}$$

When $T_{13} > T_0$, it indicates that the absorption intensity of methane gas at this wavelength is positively correlated with methane concentration, and it is considered as a characteristic absorption wavelength with high contribution rate. When $T_{13} < T_0$, it indicates that the absorption capacity of methane gas at this wavelength is relatively weak. There is the characteristic absorption, and it is susceptible to interference from other

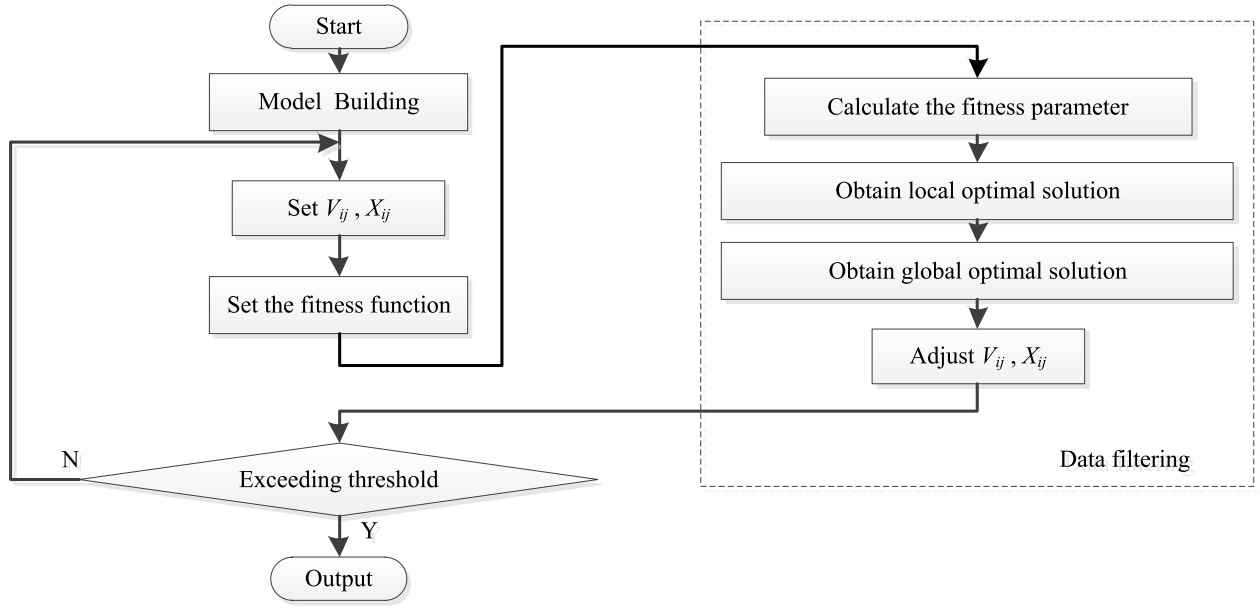

FIGURE 2
The chart of algorithm flow.

gases. Therefore, this wavelength is not selected during the testing and calculation processing, and zero value will be set for its concentration. The difference in light intensity within this range is calculated, and it can significantly suppress the interference of stray signals on the system.

3 Algorithm design

The improved Adaptive SVM algorithm completes classification calculations after setting mutation particles and dynamic insensitivity regions. Take one-third of the total spectral test data as training samples, and the rest as test samples; Initialize C and ξ to construct an SVM model; Set the particle swarm dimension to 2, select 20 particles for each dimension, set the iteration number to 200 generations, optimize V_{ij} and X_{ij} according to the set range, and calculate the mean square error of the fitness function; Set the direction of convergence for mutation particle constraints and improve learning efficiency by setting ε (y_i); Compare the fitness of each particle, and calculate the local and global optimal values of each particle; Adjust V_{ij} X_{ij} based on the first two steps; If the ending conditions are not met, re learn until the requirements are met.

To improve the sensitivity of system and achieve narrowband filtering effect, a high concentration CH_4 gas filtering window was designed. T_0 is determined by the calibration method. Firstly, match the standard concentration of methane gas, and find the position of the methane characteristic absorption peaks. Then, iteratively select different bands for methane concentration inversion, and sort the positions of the bands that affect methane concentration inversion; Take the position of the band with a contribution rate exceeding 80% and set the corresponding T value of this band position to T_0.

The process shows in Figure 2.

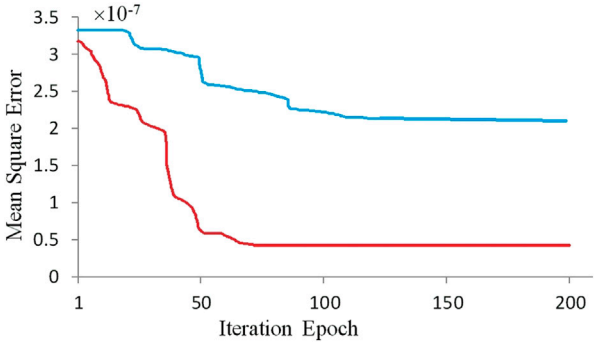

FIGURE 3
Mean square error with the number of iteration epoch.

4 Experiments

The source is 1,650 nm infrared laser, and its half width is 10 nm. The length of chamber is 40.0 cm. The test gas is simultaneously input into chamber 1 and chamber 2. A gas analyzer was used, and the detection accuracy of methane concentration is ±1 ppm. During the testing process, two methods are used: individual gas testing and mixed gas testing. For mixed gases, the basis for selecting mixed gases is from the perspective of practical applications. In coal mining environments, methane gas is often mixed with C_2H_6, SO_2, and CO_2, so the above three gases are used as interference gases. The specific mixing ratio is completed in the form of multiple proportion combination experiments, with a focus on discussing situations similar to coal mine gas mixtures.

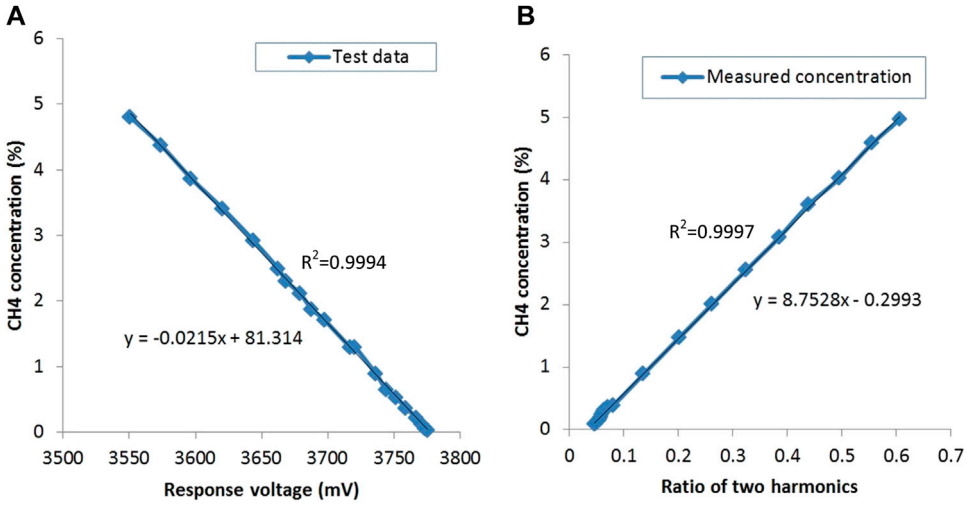

FIGURE 4
CH_4 concentration calculation based on harmonic ratio. **(A)** Response voltage by two harmonics and **(B)** CH_4 concentration by harmonic ratio.

4.1 Errors comparison

The underground gas contains a large amount of coal dust, dust, and water vapor. So the measured gases are introduced into a filter for dust and moisture removal treatment, and they introduce into the gas chamber for detection. The testing mainly focuses on CH_4 (0%–10%), C_2H_6 (0%–1%), SO_2 (0%–1%), and CO_2 (0%–1%). A total of 800 sets of sample data were collected for the mixed gas, with 400 sets as the sample data and the rest as the test samples. Perform baseline correction, noise reduction, and normalization on the samples to complete the preprocessing of spectral data. It shows in Figure 3.

In Figure 3, the blue curve represents the relationship between the average relative error and the iteration number when traditional algorithms calculate methane concentration. The red curve represents the relationship between the average relative error and the iteration number when calculating methane concentration using this algorithm. In the first 20 iterations, the error of this algorithm decreased from 3.2×10^{-7} to 2.4×10^{-7}, while the traditional algorithm remained almost unchanged during this stage. When the number of iterations exceeds 50, the error of this algorithm almost reaches a stationary state, with a value of 4.6×10^{-8}. However, traditional algorithms achieve a stationary state through 100 iterations, with a value of 2.1×10^{-7}. Thus, this algorithm has advantages in Rate of convergence and error.

In order to provide the model with fast and efficient prediction capabilities, independent modeling was conducted for different gas components. For the main detection gas CH_4, the particle swarm dimension was set to 2, with 20 particles per dimension. The optimization iteration was 200 generations, with an inertia weight of 0.9 and a termination value of 0.4, completing the generation by generation calculation. The particle swarm optimization error curve is obtained after optimization according to the above model. As shown in Figure 3, the improved particle swarm optimization algorithm only needs 43 steps to reach the global optimal solution, which has high convergence. The optimization time of the 200 generation is about 4,012 *s*, $c = 58.46$, $\sigma = 4.67$. By incorporating the optimization results into SVM, the predicted mean square error of the test sample is 4.8×10^{-8}. At the same time, the same set of spectral data was separated and the concentrations of each component were inverted using a back propagation network (due to space limitations, only three typical values within the testing range were selected).

4.2 Detection results analysis

In experiments, the response voltage is tested with CH_4 concentration, and the test curve is shown in Figure 4A. The algorithm is used for proportional calculation, and the function curve between proportional value and CH_4 concentration is shown in Figure 4B.

In Figure 4A, when the response voltage increases, the concentration of CH_4 increases, too. There is a linear relationship between them. Its slope value is −0.0215, with good linearity. The sensor response and concentration change trend are consistent with the analysis results, and the curve is linear. Throughout the entire testing process, the maximum response voltage was 3775.217 mV and the minimum was 3551.060 mV. The fitted linearity is 0.9994, with relative errors less than 5.0%. It can be seen that the system linearity meets the design requirements.

In Figure 4B, it can be seen that the CH_4 concentration is linear with respect to the ratio of first harmonic to second harmonic, and the slope of the fitted polynomial is 8.752, with a linearity of 0.997. The linearity is relatively in the 0%–10.0% range, and it meets requirements. The maximum response voltage in the first harmonic is 4938.25 mV, and the minimum value is 4442.89 mV; The maximum response voltage in the second harmonic is 2694.24 mV, and the minimum value is 226.58 mV. It can be seen that there is a significant difference in the voltage ratio between the first and second harmonics, resulting in a significant improvement in their signal-to-noise ratio. Their relative errors are all less than 1.0%, and the testing stability has been improved.

When there is no methane gas, the second harmonic is not zero, which is caused by factors such as circuit and optical path noise, as well as nonlinearity of wavelength modulation. When calculating the ratio of second harmonic to first harmonic, the second harmonic amplitude value at each non-zero concentration should be subtracted from the second harmonic amplitude value in the absence of methane, and then divided by the first harmonic amplitude at that concentration to obtain a result that is closer to the actual concentration value. From the table, it can be seen that when the concentration of methane gas is 1%, the measurement error is the largest.

5 Conclusion

A spectral data processing algorithm for quantitative analysis of multi-component games has proposed. Prediction accuracy Improved and the convergence period decreased with mutation particle constraint method. Compared with traditional SVM algorithm, the absorption ratio differential algorithm has faster optimization time, higher model prediction accuracy, and significantly improved modeling efficiency. The model verified to meet practical testing requirements and has certain practical application value in improving the accuracy of methane concentration detection.

Data availability statement

The original contributions presented in the study are included in the article/Supplementary Material, further inquiries can be directed to the corresponding author.

Author contributions

FL proposed the design and wrote this article. YX completed the theoretical analysis of the paper. WW completed the experimental testing. JF completed the test data. All authors contributed to the article and approved the submitted version.

Funding

This work was supported in part by the Shanxi Teaching Reform Research Project “Research on the Construction of practical Teaching System of Applied Electronic Information Specialty under the background of new engineering” (No. J2021572).

Conflict of interest

The authors declare that the research was conducted in the absence of any commercial or financial relationships that could be construed as a potential conflict of interest.

Publisher’s note

All claims expressed in this article are solely those of the authors and do not necessarily represent those of their affiliated organizations, or those of the publisher, the editors and the reviewers. Any product that may be evaluated in this article, or claim that may be made by its manufacturer, is not guaranteed or endorsed by the publisher.

References

1. Bai Z, Zhao C, Gao J, Chen Y, Li S, Li Y, et al. Optical parametric oscillator with adjustable pulse width based on KTiOAsO4. *Opt Mater* (2023) 136(1):113506. doi:10.1016/j.optmat.2023.113506

2. Farooq A, Alquaity ABS, Raza M, Nasir EF, Yao S, Ren W. Laser sensors for energy systems and process industries: Perspectives and directions. *Prog Energ Combustion Sci* (2022) 91(1):100997. doi:10.1016/j.pecs.2022.100997

3. Liu C, Xu L. Laser absorption spectroscopy for combustion diagnosis in reactive flows: A review. *Appl Spectrosc Rev* (2019) 54(1):1–44. doi:10.1080/05704928.2018.1448854

4. Chan K, Inaba H, Ito H, Furuya T. 10 km-long fibre-optic remote sensing of CH_4 gas by near infrared absorption. *Appl Phys B* (1985) 38(1):11–5. doi:10.1007/bf00691764

5. Tai H, Yamamoto K, Uchida M, Osawa S, Uehara K. Long distance simultaneous detection of methane and acetylene by using diode lasers coupled with optical fibers. *IEEE Photon Technol* (1992) 4(7):804–7. doi:10.1109/68.145278

6. Weldon V, Phelan P, Hegarty J. Methane and carbon dioxide sensing using a DFB laser diode operating at 1.64 μm. *Electron Lett* (1993) 29(6):560–1. doi:10.1049/el:19930374

7. Culshaw B, Stewart G, Dong F, Tandy C, Moodie D. Fibre optic techniques for remote spectroscopic methane detection—From concept to system realisation. *Sensors and Actuators B* (1998) 51(1):25–37. doi:10.1016/s0925-4005(98)00184-1

8. Zavrsnik M, Stewart G. Coherence addressing of quasi-distributed absorption sensors by the FMCW method. *J Light-wave Technol* (2000) 18(1):57–65. doi:10.1109/50.818907

9. Stewart G, Culshaw B, Johnstone W, Whitenett G, Atherton K, McLean A. Optical fibre sensors and networks for environmental monitoring. *Manage Environ Qual* (2003) 14(2):181–90. doi:10.1108/14777830310470413

10. Crawford M, Stewart G. Design of a portable optical sensor for methane gas detection. *Sensors and Actuators B* (2006) 113(1):830–6. doi:10.1016/j.snb.2005.03.105

11. Zang Y, Nie W, Xu Z, et al. Measurement of trace water vapor based on tunable diode laser absorption spectroscopy. *Acta Optica Sinica* (2018) 38(11):393–8. doi:10.3788/AOS201838.1130004

12. Chen W, Zheng K, Cao Y, et al. Sensing system of dissolved methane in water based on cavity-enhanced laser spectroscopy. *Acta Photonica Sinica* (2021) 50(9):168–76. doi:10.3788/gzxb20215009.0930002

13. Dong M, He Z, Gao Q, et al. Birefringence-managed normal-dispersion fiber laser delivering energy-tunable chirp-free solitons. *Ultrafast Sci* (2022) 9760631(1):1–12. doi:10.34133/2022/9760631

14. Chen Y, Liang T, Qiao S, Ma Y. A miniaturized 3D-printed quartz-enhanced photoacoustic spectroscopy sensor for methane detection with a high-power diode laser. *Sensors* (2023) 23(1):4034–41. doi:10.3390/s23084034

15. Hashimoto K, Nakamura T, Kageyama T, Badarla VR, Shimada H, Horisaki R, et al. Upconversion time-stretch infrared spectroscopy. *Light: Sci Appl* (2023) 12(48):48–10. doi:10.1038/s41377-023-01096-4

16. Ma Y, Liang T, Qiao S, Liu X, Lang Z. Highly sensitive and fast hydrogen detection based on light-induced thermoelastic spectroscopy. *Ultrafast Sci* (2023) 3(1):0024. doi:10.34133/ultrafastscience.0024

17. Zhang C, Qiao S, He Y, Zhou S, Qi L, Ma Y. Differential quartz-enhanced photoacoustic spectroscopy. *Appl Phys Lett* (2023) 122(1):241103. doi:10.1063/5.0157161

18. Lu W, Zhu X, Li Y, Yao Shunchun 姚, Lu Zhimin 卢, Qu Yi 曲艺, et al. Comparison of direct absorption and wavelength modulation methods for online measurement of CO2 by TDLAS. *Infrared Laser Eng* (2018) 47(7):0717002. doi:10.3788/irla201847.0717002

19. Jin D, Bai Z, Li M, Yang X, Wang Y, Mildren RP, et al. Modeling and characterization of high-power single frequency free-space Brillouin lasers. *Opt Express* (2023) 31(2):2942–55. doi:10.1364/oe.476759

20. Chen B, Bai Z, Hun X, Wang J, Cui C, Qi Y, et al. Gain characteristics of stimulated Brillouin scattering in fused silica. *Opt Express* (2023) 31(4):5699–707. doi:10.1364/oe.480391

21. Jin D, Bai Z, Lu Z, Fan R, Zhao Z, Yang X, et al. 22.5-W narrow-linewidth diamond Brillouin laser at 1064 nm. *Opt Lett* (2022) 47(20):5360–3. doi:10.1364/ol.471447

Frontiers in Physics

Investigates complex questions in physics to understand the nature of the physical world

Addresses the biggest questions in physics, from macro to micro, and from theoretical to experimental and applied physics.

Discover the latest Research Topics

See more →

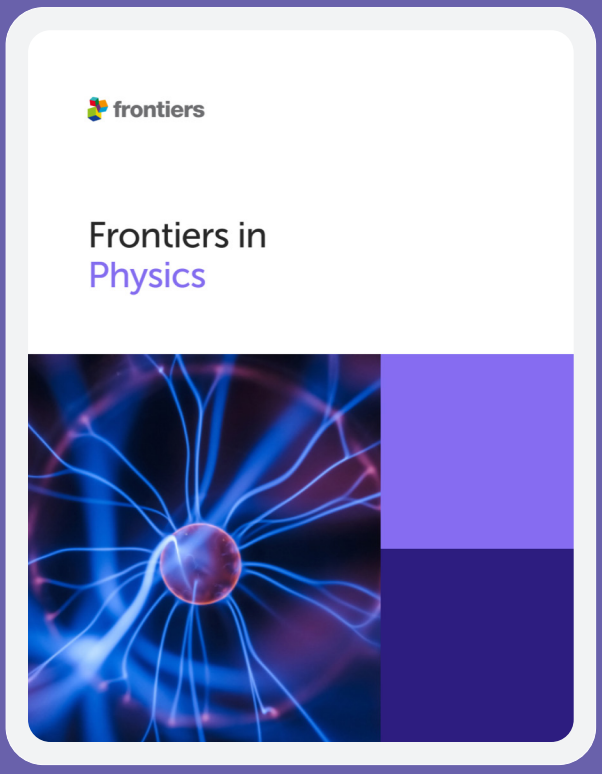

Frontiers

Avenue du Tribunal-Fédéral 34
1005 Lausanne, Switzerland
frontiersin.org

Contact us

+41 (0)21 510 17 00
frontiersin.org/about/contact